

---

**Characterization and establishment of advanced  
intestinal cell culture models and the evaluation of  
potential new biomarkers for the prediction of drug-  
induced intestinal toxicity**



**Genehmigte Dissertation**

zur Erlangung des akademischen Grades eines

**Doctor rerum naturalium (Dr. rer. nat.)**

von

**Stefanie Hoffmann**

Erstgutachter: Prof. Dr. Bodo Laube

Zweitgutachterin: Prof. Dr. Beatrix Süß

Darmstadt 2023

Fachbereich Biologie

der Technischen Universität Darmstadt

---

Hoffmann, Stefanie: Characterization and establishment of advanced intestinal cell culture models and the evaluation of potential new biomarkers for the prediction of drug-induced intestinal toxicity

Darmstadt, Technische Universität Darmstadt

Jahr der Veröffentlichung: 2023

Tag der mündlichen Prüfung: 19. Januar 2023

Veröffentlicht unter CC BY-SA 4.0 International

<https://creativecommons.org/licenses/>

---

„In der Wissenschaft gleichen wir alle nur den Kindern, die am Rande des Wissens hier und da einen Kiesel aufheben, während sich der weite Ozean des Unbekannten vor unseren Augen erstreckt.“

Isaac Newton

---

---

## Declaration of originality

---

Ich erkläre hiermit, dass ich die vorliegende Arbeit entsprechend den Regeln guter wissenschaftlicher Praxis selbstständig und ohne unzulässige Hilfe Dritter angefertigt habe.

Sämtliche aus fremden Quellen direkt oder indirekt übernommenen Gedanken sowie sämtliche von Anderen direkt oder indirekt übernommenen Daten, Techniken und Materialien sind als solche kenntlich gemacht.

Die Arbeit wurde bisher bei keiner anderen Hochschule zu Prüfungszwecken eingereicht. Die eingereichte elektronische Version stimmt mit der schriftlichen Version überein

---

Datum,

---

Stefanie Hoffmann

I herewith formally declare that I, Stefanie Hoffmann, have prepared the present work independently and without the undue help of third parties in accordance with the rules of good scientific practice.

All thoughts taken directly or indirectly from external sources as well as all data, techniques and materials taken over directly or indirectly from others are identified as such. The thesis has not yet been submitted to any other university for examination purposes.

I am aware, that in case of an attempt at deception based on plagiarism (§38 Abs. 2 APB), the thesis would be graded with 5,0 and counted as one failed examination attempt. The thesis may only be repeated once.

---

Date,

---

Stefanie Hoffmann



---

---

## Acknowledgement

---

First, I would like to thank all colleagues, friends, and relatives who supported me during the years of my thesis. Many thanks go to Dr. Paul Germann, Dr. Brigitte Simon-Hettich and Dr. Philip Hewitt for giving me the opportunity to work on this doctoral thesis on this interesting project in the early clinical safety department at Merck Healthcare KGaA, Darmstadt.

My special thanks to Dr. Philip Hewitt for supporting my work and the continuous useful support, suggestions and help whenever I needed it during the whole time of this project. Your vast knowledge and constant ability to link with more scientists has given me many opportunities for new perspectives.

Many thanks as well to Prof. Dr. Bodo Laube and Prof. Dr. Beatrix Süß who supported this thesis. Your useful suggestions always helped me to think outside the box and inspired me with new possibilities during our meetings.

For the great support in the lab, I would like to thank many great colleagues in the toxicology department. Special thanks to Isabel Koscielski, Bettina von Eiff and Claudia Klement for all the continuous support in lab. Many thanks as well to Jessica Dieckhoff for the great discussions about our PhD projects and doing the DGPT courses together. Last but not least, special thanks to Janike Sensbach who was always open for wonderful discussions of my results and the permanent motivation. I would also like to thank Julian Kreis for performing the statistical analysis of the gene expression data and Thomas Wild for the analysis of the protein samples. Special thanks go to Angelika Schäfer-Schwebel for the great support and advice in the immunohistology practice and Anja Knippel for the great support on the evaluation of the microdissections. Many thanks go as well to all other eNCS colleagues. Thank you for making me feel comfortable, making me smile and smiling back. You all have contributed to the fact that I have felt very well during the whole time.

However, the biggest thanks go to my mother and father, Petra and Willi and my sister Jennifer. Without you I probably would have given up at some points and doubted myself. Your constant moral support and faith in me has brought me to this point. Very special thanks as well to my life partner, Jan. Your continuous support, understanding and patience made me to the person I am today. You always encouraging me to overcome all challenges for meanwhile 16 years. You have always supported me in all my decisions without scrutinize them and have backed me up and kept my back free in every situation. Thanks so much!

---

## Abstract

---

Drug discovery and development is a very time consuming and expensive process which requires a high number of *in vitro* and *in vivo* experiments (Guengerich, 2006; Paul *et al.*, 2010; DiMasi, Grabowski and Hansen, 2016). Especially *in vivo* experiments are very complex and often under ethical discussion. Beside this many drug candidates fail during the development. One of the main reasons why a drug development gets stopped or the drug gets withdrawn from the market is due to enormous side effects, specifically in the GI tract.

The aim of this thesis was to establish advanced intestinal cell culture models (Caco-2 2D, Caco-2 in the OrganoPlate® and colon organoids as a 3D model) and evaluate novel biomarkers, which can predict more reliable and sensitive drug-induced gastrointestinal injury. The characterization of the 3D colon organoid model showed high similarity of the human intestine in structure and function. This could be shown e.g. by polarized, connected intestinal epithelial cells in 3D structure or by immunofluorescence staining of intestine specific proteins (E-cadherin,  $\alpha$ -tubulin, Zonula occludens-1 (ZO-1), Ezrin, CYP2C9 or Claudin7). The metabolic activity in the three cell culture models could be shown by measuring intestine specific genes (Phase I, II and III enzymes).

The best predictivity of toxic effects of drugs could be observed in the 3D organoid model which recapitulate high similarity to the human colon. After 24h of treatment the colon organoids showed the strongest response to toxic compounds. This could be shown with lower IC<sub>50</sub> values compared to the two other models with Caco-2 cells.

For the prediction of toxic effects, the use of biomarkers is a reliable tool. But so far in pre-clinical studies a lack of predictive and reliable biomarkers is existing (John-Baptiste *et al.*, 2012; Carr *et al.*, 2017). Specifically, the 3D organoid model used in this thesis showed the possible application as tool for the study of potential biomarkers to predict drug-induced gastrointestinal injury events. After the treatment of these models with compounds which are known for the damage in the GI tract, the secreted and expressed markers were examined. This study demonstrated the suitability of some proteins and genes as potential biomarkers. In the 3D colon organoid model Lipocalin-2 (*LCN-2*), C-reactive protein (*CRP*) and Histidine decarboxylase (*HDC*) were higher expressed in the treated samples compared to the control, but no significant differences could be calculated here. In comparison, the Caco-2 2D and Organ-on-a-chip (OoC) model showed better application in the use of biomarkers for early detection of drug-induced damage in the intestine. The genes *LCN-2* and Myosin light chain kinase (*MLCK*) were significantly higher expressed in treated samples compared to the control sample. Also measurable was a damage and thus decrease in enterocytes using the biomarker citrulline, so far only used *in vivo*. This biomarker

---

was measured in significantly lower amounts in the treated samples of the Caco-2 models (2D and OoC) compared to the control samples.

In conclusion, advanced intestinal cell culture models are a promising tool to recapitulate the human intestine and helps to evaluate the potential effects of drugs. These models can be used to study intestinal biology, metabolic and toxicologic profiles and to evaluate potential biomarkers for the prediction of drug-induced gastrointestinal injury in a more physiological environment. The models can for example be integrated into the drug development process as early screening tool and help to identify toxic side effects of drugs. The main benefit of these models is that these models can help to translate *in vitro* results to the human and can thereby bridge the gap between simple 2D and complex *in vivo* models.

Overall, it could be said that not one specific model is suitable for all tested assays. Each model has his advantages and can be used for different questions.

---

## Zusammenfassung

---

Die Entwicklung eines neuen Medikaments ist ein sehr zeitaufwändiger und teurer Prozess, der eine große Anzahl von *in vitro* und *in vivo* Experimenten erfordert (Guengerich, 2006; Paul *et al.*, 2010; DiMasi, Grabowski and Hansen, 2016). Vor allem die Tierversuche sind oft sehr komplex und ethisch umstritten. Außerdem scheitern viele Arzneimittelkandidaten während der Entwicklung. Einer der Hauptgründe, warum die Entwicklung eines Medikaments gestoppt oder das Medikament vom Markt genommen wird, sind die enormen Nebenwirkungen, insbesondere im Magen-Darm-Trakt.

Ziel dieser Arbeit war es, fortschrittliche Darmzellkulturmodelle (Caco-2 2D, Caco-2 in der OrganoPlate® und Dickdarmorganoide als 3D-Modell) zu etablieren und neu Biomarker zu evaluieren, die eine zuverlässigere und empfindlichere Vorhersage von arzneimittelinduzierten gastrointestinalen Schäden ermöglichen. Die Charakterisierung des 3D Dickdarmorganoid Modells zeigte eine Ähnlichkeit des menschlichen Darms in Struktur und Funktion. Dies konnte z.B. durch polarisierte, verbundene Darmepithelzellen in 3D-Struktur gezeigt werden oder durch Immunfluoreszenzfärbungen von darmspezifischen Proteinen (E-cadherin,  $\alpha$ -Tubulin, ZO-1, Ezrin, CYP2C9 oder Claudin7). Die Stoffwechselaktivität in den drei Zellkulturmodellen konnte gezeigt werden durch die Messung von darmspezifischen Genen (Phase I, II und III Enzyme).

Die beste Vorhersagbarkeit toxischer Wirkungen von Arzneimitteln konnte ebenso im 3D-Organoidmodell nachgewiesen werden. Nach 24h Behandlung zeigten die Dickdarmorganoide die stärkste Reaktion auf toxische Substanzen. Dies konnte mit niedrigeren  $IC_{50}$  Werten, im Vergleich zu den beiden Modellen mit Caco-2 Zellen, gezeigt werden.

Für die Vorhersage toxischer Wirkungen ist die Verwendung von Biomarkern eine zuverlässige Methode. In präklinischen Studien fehlt es jedoch bisher an prädiktiven und zuverlässigen Biomarkern (John-Baptiste *et al.*, 2012; Carr *et al.*, 2017). Nach der Behandlung der verwendeten Zellkulturmodelle mit Substanzen, die für die Schädigung des Magen-Darm-Trakts bekannt sind, wurden die sezernierten und exprimierten Marker untersucht. Diese Studie zeigte die Eignung einiger Proteinprodukte als potenzielle Biomarker. Im 3D Dickdarmorganoid Model waren *LCN-2*, *CRP* und *HDC* in den behandelten Proben stärker exprimiert im Vergleich zur Kontrolle, jedoch konnten hier keine signifikanten Unterschiede berechnet werden. Im Vergleich hierzu zeigte das Caco-2 2D und OoC Model bessere Anwendungsmöglichkeiten bei der Nutzung von Biomarkern zur frühen Erkennung von medikamenteninduzierten Schäden im Darm. Die Gene *LCN-2* und *MLCK* waren signifikant höher exprimiert in behandelten Proben im Vergleich zur Kontrollprobe. Ebenso messbar war eine Schädigung und somit Abnahme der Enterozyten mithilfe des Biomarkers Citrullin, welcher bisher nur Anwendung in Patienten findet. Dieser konnte in

---

signifikant niedrigeren Mengen in den behandelten Proben der Caco-2 Modelle (2D und OoC) gemessen werden im Vergleich zu den Kontrollproben.

Zusammenfassend lässt sich sagen, dass fortgeschrittene Darmzellkulturmodelle ein vielversprechendes Modell sind, um den menschlichen Darm *in vitro* abzubilden und die potenziellen Auswirkungen von Arzneimitteln zu bewerten. Diese Modelle können zur Untersuchung der Darmbiologie, der metabolischen und toxikologischen Profile und zur Bewertung potenzieller Biomarker für die Vorhersage arzneimittelinduzierten gastrointestinalen Schäden in einer physiologischeren Umgebung verwendet werden. Sie können z.B. in den Prozess der Arzneimittelentwicklung als frühes Screening-Instrument integriert werden und helfen, toxische Nebenwirkungen von Arzneimitteln zu erkennen. Der Hauptvorteil dieser Modelle besteht darin, dass sie dazu beitragen können, Ergebnisse dieser *in vitro* Versuche zu nutzen für die präzisere Vorhersage von Nebenwirkungen im Menschen und somit auch die Lücke zwischen einfachen 2D- und komplexen Tier-Modellen zu schließen.

---

## Table of Contents

<b>Declaration of originality</b>	<b>V</b>
<b>Acknowledgement</b>	<b>VI</b>
<b>Abstract</b>	<b>VII</b>
<b>Zusammenfassung</b>	<b>IX</b>
<b>Table of figures</b>	<b>XV</b>
<b>List of tables</b>	<b>XX</b>
<b>List of abbreviations</b>	<b>XXVIII</b>
<b>1. .... Introduction</b>	<b>1</b>
1.1. Toxicology	1
1.2. Toxicology in drug development and discovery	2
1.2.1. Early safety assessment methods and models	3
1.2.2. The need for new cell culture models	9
1.3. Gastrointestinal Tract (GI)	12
1.3.1. Structure of the GI tract	12
1.3.2. Small intestine	14
Function of the small intestine	16
1.3.3. Large intestine	16
Function of the large intestine	17
1.3.4. Intestinal epithelium – Barrier shield against environment	18
1.3.5. Transporters and xenobiotic metabolism in the human intestine	23
1.4. Toxicology of the gastrointestinal tract	25
1.5. Compounds that affect the GI tract	26
1.5.1. Chemotherapeutics	26
5-Fluorouracil (5-FU)	26
Gefitinib (Gef)	27
Irinotecan hydrochloride (Irino)	28
Oxaliplatin hydrochloride (Oxali)	28
1.5.2. Nonsteroidal anti-inflammatory drugs (NSAIDs)	28
Diclofenac sodium (Diclo)	29
1.5.3. Anti-diarrheal drugs	30
Alosetron hydrochloride (Alo) - Lotronex	30
Loperamide hydrochloride (Lop)	30
1.5.4. Other compounds	31
Flavopiridol hydrochloride (Flavo)	31
Terfenadine (Terf)	31
1.6. Intestinal <i>in vitro</i> models	32
	XI

---

Caco-2 cell line	33
Organoids – <i>in vitro</i> mini tissues	35
Organs-on-a-chip – The new promising tool for drug discovery	36
1.7. The utility of biomarkers	38
1.8. Aim of the work	42
1.9. Personal contribution	43
<b>2.....Material and methods</b>	<b>44</b>
2.1. Materials	44
2.1.1.Cells	44
2.1.2.Compounds	44
2.1.3.Kits	45
2.1.4.Antibodies, conjugates, and dyes	45
2.1.5.Consumables	47
2.1.6.Reagents and chemicals	49
2.1.7.Instruments & Equipment	52
2.1.8.Software	54
2.2. Methods	55
2.2.1.Cell culture techniques	55
2.2.2.Caco-2	55
2.2.2.1. Used cell culture formats for cultivation of Caco-2 cells	55
2.2.2.2. Coating of 96-well plates, transwell inserts and OrganoPlate®	56
Determination of cell number and cell viability	56
2.2.2.3. Media formulations	57
2.2.2.4. Thawing, culturing, and passaging of Caco-2	57
2.2.2.5. Seeding of Caco-2 cells	58
2.2.3. iPSC derived colon organoids	59
2.2.3.1. Determination of cell number and cell viability	60
2.2.3.2. Media formulations	60
2.2.3.3. Thawing, culturing, and passaging of iPSC derived colon organoids	60
2.2.3.4. Culturing and passaging of iPSC derived colon organoids	60
2.2.3.5. Single cell passaging of organoids	61
2.2.3.6. Implementation of organoids into OrganoPlate®	62
2.2.4.Compound concentrations	63
2.2.5.Widefield microscope	64
2.2.6.Cell viability	64
2.2.6.1. CellTiter-Glo® assay	64
2.2.6.2. Resazurin assay	65

2.2.7. Cell layer integrity	66
2.2.7.1. Barrier Integrity (BI) Assay	66
2.2.7.2. Data analysis for the Barrier Integrity Assay	67
2.2.7.3. Measurement of the transepithelial electrical resistance	68
2.2.8. Immunofluorescent staining	71
2.2.8.1. Immunofluorescent staining in the 2D model	71
2.2.8.2. Immunofluorescent staining in 3D organoid model	72
2.2.8.3. Immunofluorescent staining in OoC model	72
2.2.9. Immunohistochemistry	74
2.2.9.1. Preparation of paraffin blocks and alcohol serial	74
2.2.9.2. H&E staining	75
2.2.9.3. Antibody staining of different cell types in organoids	76
2.2.9.4. Alcian blue staining	77
2.2.10. Transcriptomics (QuantiGene™ Plex Assay Kit)	78
2.2.10.1. Sample preparation	80
2.2.10.2. Target hybridization	81
2.2.10.3. Signal amplification	82
2.2.11. Proteomics	83
2.2.11.1. Cell culture	83
2.2.11.2. Sample preparation	84
2.2.11.1. Measurement of samples with Mass spectrometry	85
2.2.11.2. Data analysis	85
2.2.12. Measurement of microRNA 194 (QuantiGene™2.0 miRNA Assay)	86
2.2.12.1. Sample preparation and target hybridization (day 1)	86
2.2.12.2. Signal amplification and detection (day 2)	87
2.2.13. Citrulline measurement	88
2.2.14. Calprotectin measurement	89
<b>3. .... Results and discussion</b>	<b>91</b>
3.1. Morphology assessment of the cell culture models	91
3.1.1. Caco-2 2D	91
3.1.2. Caco-2 OoC	93
3.1.3. Colon organoids	95
3.2. Morphological characterization of organoids by using immunohistology stainings	98
3.3. Morphological characterization of all three cell culture models by using immunofluorescent (IF) stainings	103
3.4. Functional characterization of all three cell culture models by using immunofluorescent (IF) stainings	109



---

3.5.	Functional characterization of all three cell culture models: Gene expression	121
3.6.	Comparative study on the evaluation of cytotoxic effects of compounds	125
3.7.	Comparative study on the evaluation of barrier integrity effects of compounds	132
3.7.1.	Evaluation of the TEER after treatment with test compounds in 2D and OoC	132
3.7.2.	Evaluation of the BI assay after treatment with test compounds in the OrganoPlate®	137
3.8.	Evaluation of protein expression between the advanced cell culture models	139
3.8.1.	Global protein expression	141
3.8.2.	Expression profiles of proteins for tight and adherens junction	143
3.8.3.	Expression profiles of drug metabolizing enzymes	147
3.9.	Gene expression measurements for the detection of new biomarker for GI damage	155
3.9.1.	Statistical comparison of gene expression of drug induced GI toxicity compounds and the DMSO control	161
3.10.	Expression levels of mir194 for the evaluation of drug-induced toxicity	164
3.11.	Measurement of <i>in vivo</i> used biomarkers for the prediction of GI damage <i>in vitro</i>	165
3.11.1.	L-Citrulline	166
3.11.2.	Calprotectin	168
3.12.	Evaluation of human intestine specific pathways	171
3.12.1.	Impact of drugs targeting intestinal major pathways	177
3.13.	Assessment of iPSC derived colon organoids into the OrganoPlate®	177
<b>4.....</b>	<b>Conclusion</b>	<b>185</b>
<b>5.....</b>	<b>Further perspectives</b>	<b>192</b>
<b>6.....</b>	<b>References</b>	<b>194</b>
<b>7.....</b>	<b>Appendix</b>	<b>225</b>
	<b>Curriculum vitae</b>	<b>286</b>
	<b>Publications, posters, and awards</b>	<b>288</b>

---

---

## Table of figures

---

Figure 1: The drug development process.....	2
Figure 2: Purpose of animal use in 2019.....	6
Figure 3: Percent success and failure rate of new compounds entering the specific phases of development.....	7
Figure 4: Reason for failures of drug candidates.....	7
Figure 5: The 3R principles.....	8
Figure 6: Estimated number of cancer incidence proportions of both sexes and all ages worldwide in 2012 (total: 14090149 cases) .....	10
Figure 7: Occurrence of side effects based on the databank side effect resource (SIDER) 4.124. 11	11
Figure 8: Structure and anatomy of the gastrointestinal tract. ....	12
Figure 9: Main important cell types and the organization of the intestinal epithelium of the small intestine .....	13
Figure 10: Structural overview of the anatomy of the small intestine .....	15
Figure 11: Microscopic structure of the enlargement of the plicae circulares (mucosal folds of the small intestine) and the villus structures.....	15
Figure 12: Structure of the large intestine .....	17
Figure 13: Structure of intestinal enterocytes.....	18
Figure 14. Composition of the cell-cell connections of enterocytes .....	19
Figure 15: Overview of the intestinal epithelium of the small intestine with all included cell types. ....	20
Figure 16: Wnt signaling pathway.....	21
Figure 17: Simplified overview of the EGFR signaling pathway .....	22
Figure 18: Overview of the notch signaling pathway. ....	23
Figure 19: Important drug transporters expressed at the intestinal epithelium.....	24
Figure 20: Overview of the pathophysiological mechanism of gastrointestinal toxicity.....	25
Figure 21: Caco-2 cell culture in cell culture flasks. Bar =100µm .....	33
Figure 22: Overview of the GI tract, its cells, and the localization of intestinal cells in an organoid. ....	35
Figure 23: Compared complexity, relevance, controllability, and reproducibility of used in vitro and in vivo models.....	37
Figure 24: Possible benefits of biomarkers during drug discovery and development phases.....	38

Figure 25: Used cell culture formats for the cultivation of Caco-2 cells.....	55
Figure 26: a.) Overview of the 3lane OrganoPlate® in the 384-well format. ....	59
Figure 27: Cultivation format of colon organoids in Matrigel® hemispheres in 24-well plates..	61
Figure 28: Principle of CellTiter-Glo® (Promega, 2015) .....	65
Figure 29: Principle of Resazurin.....	65
Figure 30: Volume scheme for immunofluorescence staining in OrganoPlate®.....	67
Figure 31: Imaging and selection of areas for the barrier integrity assay .....	67
Figure 32: Experimental setup for TEER measurement in 2D.....	69
Figure 33:OrganoPlate® and OrganoTEER® instrument set up and measurement principle. ....	70
Figure 34: Plate position during incubation and wash steps for Immunofluorescent stainings of the OrganoPlate®.....	73
Figure 35: Overview of the used volumes for immunofluorescence stainings in the OrganoPlate®. .....	73
Figure 36: Example for a.) embedding molds and b.) plastic cassettes for the paraffin embedding of colon organoids.....	74
Figure 37: Principle for the QuantiGene™ Plex Assay.....	79
Figure 38: Assay workflow for the measurement of miRNA .....	86
Figure 39: Caco-2 cells growing in cell culture plates.....	92
Figure 40: a.) ATP content over time in the Caco-2 2D model. ....	93
Figure 41: Cultivation of Caco-2 cells in chips of the OrganoPlate from Mimetas.....	94
Figure 42.a.) ATP content over time in Caco-2 cells growing in the OrganoPlate®. ....	94
Figure 43: Increasing size and area of organoids during culture.....	96
Figure 44: a.) Organoid growth and shape formation during cultivation. ....	96
Figure 45: ATP content in colon organoids after several days in culture.....	97
Figure 46: a.) Overview of Ki67 staining of iPSC derived colon organoids microdissection.....	99
Figure 47: a.) Overview of H&E stained colon organoid microdissections showed different size and shape of organoids. ....	99
Figure 48: a.) & b.) H&E stained colon organoid microdissections showed specific intestine structures.....	100
Figure 49: a.) With Alcian blue stained colon organoid microdissections showed presence of goblet cells within the organoids.....	101

Figure 50: a.) With Lysozyme C stained colon organoid microdissections showed presence of Paneth cells within the organoids. ....	102
Figure 51: Staining of stem cells with the antibody LGR5 (green) within the organoids. Nuclei were counterstained with Hoechst (blue). 10x magnification, bar = 50 $\mu$ m. ....	103
Figure 52: Immunofluorescent stainings with the antibody $\alpha$ -tubulin to stain the structures of the cytoskeleton. ....	104
Figure 53: Immunofluorescent stainings with the antibody ZO-1 to stain specific proteins of the tight junctions. ....	105
Figure 54: Immunofluorescent stainings with the antibody claudin 7 to stain for a specific tight junction protein. ....	107
Figure 55: Immunofluorescent stainings with the antibody E-cadherin to stain for a specific protein of the adherens junctions. ....	108
Figure 56: Immunofluorescent stainings with the antibody CYP2C9 to stain for a specific phase I enzyme. ....	110
Figure 57: Immunofluorescent stainings with the antibody <i>CYP2D6</i> (green) to stain for a specific phase I enzyme of the intestine. ....	111
Figure 58: Immunofluorescent stainings with the antibody <i>NAT 1/2</i> (green) to stain for a specific phase II enzyme of the intestine. ....	113
Figure 59: Immunofluorescent stainings with the antibody <i>MRP2</i> (green) to stain for a specific drug transporter of the intestine. ....	115
Figure 60: Immunofluorescent stainings with the antibody Ezrin (green) to stain for a specific component of the microvilli of the intestine. ....	117
Figure 61: Immunofluorescent stainings with the antibody CDX2 (green) to stain for a specific intestinal transcription factor. ....	118
Figure 62: Immunofluorescent stainings with the antibody EpCAM (green) to stain for a specific intestinal molecule, responsible for maintenance of intestinal barrier and homeostasis. ...	119
Figure 63: Immunofluorescent stainings of Organoids 3D with the antibody Muc5B (green) to stain for goblet cells and their capability to secrete mucin. ....	120
Figure 64: Column plots of basal gene expression of phase I (a.) and II (b.) enzymes in the three cell culture models. ....	122
Figure 65: Column plots of basal gene expression of phase III efflux transporter (a.) and phase II uptake transporter (b.) enzymes in the three cell culture models. ....	123
Figure 66: Column plots of basal gene expression of a.) <i>Muc2</i> and <i>Muc5AC</i> . ....	124
Figure 67: a.) Scatterplot of $IC_{50}$ values derived from ATP content measurements after exposure to the nine different test compounds for 24h. ....	127

Figure 68:a.) Scatterplot of IC <sub>50</sub> values derived from Resazurin assay after exposure to the nine different test compounds for 24h.....	131
Figure 69: Measured TEER values after different time points in culture.....	133
Figure 70: Measured TEER values after different time points in culture.....	134
Figure 71: Measured TEER values after different time points in culture.....	135
Figure 72: Measured TEER values after different time points in culture.....	136
Figure 73: Comparison of the results of the BI and TEER assay.....	138
Figure 74: Number of all measured proteins in the different cell culture formats. The samples were analysed via LC-MS. N=1.....	139
Figure 75: Heatmap representation of the 4070 overlapping proteins identified in all cell models including hierarchical clustering.....	141
Figure 76: Principal component analysis (PCA) of all measured protein samples in the LC-MS.....	142
Figure 77: Heatmap representing the hierarchical clustering of the basal expression levels of tight junction formation involved proteins.....	144
Figure 78: Heatmap representing the hierarchical clustering of the basal expression levels of adherens junction involved proteins.....	145
Figure 79: Heatmap representing the hierarchical clustering the basal expression levels of different CYP450 enzymes.....	147
Figure 80: Heatmap representing the hierarchical clustering of the basal expression levels of different phase II enzymes.....	149
Figure 81: Major drug transporters proteins expressed in the intestinal epithelium (Estudante <i>et al.</i> , 2013).....	151
Figure 82: Heatmap representing the hierarchical clustering of the basal expression levels of different phase II enzymes.....	153
Figure 84: Fold change in gene expression of potential biomarkers <i>MLCK</i> and <i>CRP</i> .....	158
Figure 85: Fold change in gene expression of potential biomarkers <i>HDC</i> and <i>FABP-2</i> .....	159
Figure 86: Statistically significant differences between GI toxicity drugs and DMSO control in the Caco-2 2D model.....	161
Figure 87: Statistically significant differences between GI toxicity drugs and DMSO control in the Caco-2 OoC model.....	162
Figure 88: Statistically significant differences between GI toxicity drugs and DMSO control in the colon organoid 3D model.....	163
Figure 89: Fold change in mir194 expression.....	164

Figure 90: Boxplot chart of the L-citrulline concentrations in the cell culture systems.....	166
Figure 91: Bar graph of the L-citrulline concentration in the different models.....	167
Figure 92: Boxplot chart of the calprotectin concentrations in the cell culture systems.....	169
Figure 93: Bar graph of the calprotectin concentration in the different models.....	170
Figure 94: Immunofluorescent stainings with the antibody $\beta$ -catenin to stain a major component of the Wnt-signaling pathway.....	171
Figure 95: Immunofluorescent stainings with the antibody $\beta$ -catenin to stain a major component of the Wnt-signaling pathway.....	172
Figure 96: Immunofluorescent stainings with the antibody YAP to stain a major component of the Hippo-signaling pathway.....	173
Figure 97: Immunofluorescent stainings with the antibody YAP to stain a major component of the Hippo-signaling pathway.....	174
Figure 98: Immunofluorescent stainings with the antibody notch to stain a major component of the Notch-signaling pathway.....	175
Figure 99: Immunofluorescent stainings with the antibody notch to stain a major component of the Notch-signaling pathway.....	176
Figure 100: Overview of the implementation of organoids into the OoC system after coating the top channel with vitronectin.....	179
Figure 101: Overview of the implementation of organoids into the OoC system after coating the top channel with Laminin.....	180
Figure 102: Overview of the implementation of organoids into the OrganoPlate <sup>®</sup> after coating the top channel with Matrigel <sup>®</sup> .....	182
Figure 103: Overview of the implementation of organoids into the OrganoPlate <sup>®</sup> after coating the top channel with collagen.....	183
Figure 104: Overview of the implementation of organoids into the OrganoPlate <sup>®</sup> after coating the top channel with geltrex.....	183
Figure 105: Summary of the used cell culture models and their advantages and limitations.....	189
Figure 106: 3D models can bridge the gap between simple 2D models and animal experiments and can thereby help to support the 3R principle (Fitzgerald <i>et al.</i> , 2015).....	191
Figure 107: Immunofluorescent stainings with the antibody occludin to stain for a specific claudin family member to build tight junctions.....	226
Figure 108: Immunofluorescent stainings with the antibody occludin to stain for a specific claudin family member to build tight junctions.....	227
Figure 109: Immunofluorescent stainings with the antibody <i>GSTA1</i> to stain for a specific phase II enzyme.....	227

---

Figure 110: Immunofluorescent stainings with the the antibody <i>SULT1E1</i> to stain for a specific phase II enzyme. ....	228
Figure 111: Immunofluorescent stainings with the antibody <i>MDR1</i> to stain for a specific phase III enzyme.....	228
Figure 112: Immunofluorescent stainings with the antibody <i>BCRP</i> to stain for a specific phase III enzyme.....	229
Figure 113: Overview of differences in size, shape and structure of iPSC derived colon organoids. ....	229
Figure 114: Formula for the calculation of the Papp values. Values are calculated after treating the Caco-2 cells in the OrganoPlate® and performing the BI-assay.....	273
Figure 115: Pictures of the long-term cultivation of iPSC derived colon organoids. ....	284
Figure 116: Schematic overview of the hippo pathway in intestinal .....	285

---

## List of tables

---

Table 1: Safety guidelines and corresponding study types harmonized by the ICH.....	4
Table 2: <i>In vitro</i> assays used in the drug discovery and development phases used by companies.	5
Table 3: Overview of the most important physiologically parameters of gastrointestinal cell culture models (Costa and Ahluwalia, 2019 modified). ....	32
Table 4: List of existing in vivo biomarkers for human intestinal tissues and potential in vitro biomarkers.....	39
Table 5: Potentially novel biomarker for the prediction of drug-induced toxicity of the GI tract in <i>in vitro</i> models .....	40
Table 6: Overview of the used volumes of coating solution (50µg/ml collagen in 0.2% acetic acid) for the different cell culture formats.....	56
Table 7: Media compositions for the culture of Caco-2 cells.....	57
Table 8: Summary of the seeding densities and pre-cultivation times of caco-2 cells across all used cell culture models .....	58
Table 9: Seeding densities of single-cell organoids for the experiments in 96-well plates.....	62
Table 10: Overview of the tested seeding densities, coating solutions and attachment times for the implementation of organoids into the OrganoPlate® .....	63
Table 11: Overall compound concentrations that were used in this study. ....	64
Table 12: Cell culture model specific differences for viability measurements using CellTiter-Glo® .....	65
Table 13: Cell densities and pre-cultivation times of Caco-2 cells for the TEER measurement experiments .....	68

Table 14: Used compounds and concentrations for the treatment of cells and then the measurement of the TEER.....	70
Table 15: Buffer compositions for immunofluorescent staining of cells in different cultivation systems.....	71
Table 16: Staining procedure for H&E staining of paraffin sections of organoids .....	75
Table 17: Buffer for immunofluorescent stainings of organoids paraffin sections.....	76
Table 18: Antibody dilution for immunohistochemistry staining.....	76
Table 19: Staining procedure for the Alcian blue staining of paraffin sections of organoids .....	77
Table 20: Used compounds and concentrations for the gene expression experiment.....	79
Table 21: Volumes for the working lysis mixture for the QuantiGene™ Plex Assay .....	80
Table 22: Preparation of working bead mix for RNA samples and RNA control, each volume is calculated for one well .....	81
Table 23: Used dilutions of samples for different cell culture systems.....	81
Table 24: Pre-cultivation times and seeding densities for the proteomics experiment .....	83
Table 25: Volumes for the detachment of cells for the proteomics experiment .....	83
Table 26: Used parameters and their set up for the raw data analysis of the proteomics mass spectrometry data.....	85
Table 27: Preparation of working bead mix for the samples and standard serial, calculated volume is for one well of a 96-well plate.....	87
Table 28: Dilutions of samples for miRNA Assay .....	87
Table 29: Dilution series for citrulline standard.....	88
Table 30: Dilution series of calprotectin standard .....	89
Table 31: Characteristic parameters used for the evaluation of organoid health using H&E stained, paraffin embedded microdissections .....	98
Table 32: Selected representative primary antibodies against phase I, II and III for the assessment of metabolic capacity of the different cell culture systems.....	109
Table 33: Used targets for the analysis of gene expression in the used cell culture models.....	121
Table 34: Selected test compounds and final concentration ranges for the cytotoxicity comparison of the three cell culture models. ....	126
Table 35: List of investigated potential genetic biomarkers for drug-induced GI damage.....	155
Table 36: Tested coating solutions and concentrations for the assessment of seeding single cell .....	184
Table 37: Specifications of one chip of the Mimetas OrganoPlate®.....	225



Table 38: Luminescence signals of the ATP measurement for the morphological assessment of Caco-2 cells growing in the OrganoPlate® (OoC) .....	225
Table 39: Luminescence signals of the ATP measurement for the morphological assessment of iPSC derived colon organoids in 3D.....	225
Table 40: Luminescence signals of the ATP measurement for the morphological assessment of Caco-2 cells growing in 2D. ....	226
Table 41: Results from two replicates of the gene expression of phase I enzymes for the functional characterization of the three cell culture models. ....	230
Table 42: Results from two replicates of the gene expression phase II enzymes for the functional characterization of the three cell culture models. ....	230
Table 43: Results from two replicates of the gene expression of efflux transporter for the functional characterization of the three cell culture models. ....	230
Table 44: Results from two replicates of the gene expression of uptake transporter for the functional characterization of the three cell culture models. ....	231
Table 45: Results from two replicates of the gene expression of two mucins for the functional characterization of the three cell culture models. ....	231
Table 46: Luminescence signals of the ATP measurements after the treatment with Gefitinib for 24h in the Caco-2 2D model .....	232
Table 47: Luminescence signals of the ATP measurements after treatment with Alosetron for 24h in the Caco-2 2D model .....	232
Table 48: Luminescence signals of the ATP measurements after treatment with 5-FU for 24h in the Caco-2 2D model .....	233
Table 49: Luminescence signals of the ATP measurements after treatment with Diclofenac for 24h in the Caco-2 2D model .....	233
Table 50: Luminescence signals of the ATP measurements after treatment with Flavopiridol for 24h in the Caco-2 2D model .....	234
Table 51: Luminescence signals of the ATP measurements after treatment with Irinotecan for 24h in the Caco-2 2D model .....	234
Table 52: Luminescence signals of the ATP measurements after treatment with Loperamide for 24h in the Caco-2 2D model .....	235
Table 53: Luminescence signals of the ATP measurements after treatment with Oxaliplatin for 24h in the Caco-2 2D model .....	235
Table 54: Luminescence signals of the ATP measurements after treatment with Terfenadine for 24h in the Caco-2 2D model .....	236
Table 55: Luminescence signals of the ATP measurements after treatment with Staurosporine for 24h in the Caco-2 2D model .....	236

Table 56: Luminescence signals of the ATP measurements after treatment with Metformin 750µM (a) and 0.5% DMSO (b) for 24h in the Caco-2 2D model .....	237
Table 57: Luminescence signals of the ATP measurements after treatment with Gefitinib for 24h in the Caco-2 OoC model .....	237
Table 58: Luminescence signals of the ATP measurements after treatment with Alosetron for 24h in the Caco-2 OoC model .....	238
Table 59: Luminescence signals of the ATP measurements after treatment with 5-FU for 24h in the Caco-2 OoC model .....	238
Table 60: Luminescence signals of the ATP measurements after treatment with Diclofenac for 24h in the Caco-2 OoC model .....	239
Table 61: Luminescence signals of the ATP measurements after treatment with Flavopiridol for 24h in the Caco-2 OoC model .....	239
Table 62: Luminescence signals of the ATP measurements after treatment with Irinotecan for 24h in the Caco-2 OoC model .....	240
Table 63: Luminescence signals of the ATP measurements after treatment with Loperamide for 24h in the Caco-2 OoC model .....	240
Table 64: Luminescence signals of the ATP measurements after treatment with Oxaliplatin for 24h in the Caco-2 OoC model .....	241
Table 65: Luminescence signals of the ATP measurements after treatment with 0.5% DMSO (a) and Metformin 750µM (b) for 24h in the Caco-2 OoC model .....	241
Table 66: Luminescence signals of the ATP measurements after treatment with Staurosporine for 24h in the Caco-2 OoC model .....	242
Table 67: Luminescence signals of the ATP measurements after treatment with Gefitinib for 24h in the organoid 3D model .....	243
Table 68: Luminescence signals of the ATP measurements after treatment with Alosetron for 24h in the organoid 3D model .....	243
Table 69: Luminescence signals of the ATP measurements after treatment with 5-FU for 24h in the organoid 3D model .....	244
Table 70 Luminescence signals of the ATP measurements after treatment with Diclofenac for 24h in the organoid 3D model .....	244
Table 71 Luminescence signals of the ATP measurements after treatment with Flavopiridol for 24h in the organoid 3D model .....	245
Table 72: Luminescence signals of the ATP measurements after treatment with Irinotecan for 24h in the organoid 3D model .....	245
Table 73 Luminescence signals of the ATP measurements after treatment with Loperamide for 24h in the organoid 3D model .....	246

Table 74: Luminescence signals of the ATP measurements after treatment with Oxaliplatin for 24h in the organoid 3D model.....	246
Table 75: Luminescence signals of the ATP measurements after treatment with Terfenadine for 24h in the organoid 3D model.....	247
Table 76: Luminescence signals of the ATP measurements after treatment with 0.5% DMSO (a) and Metformin 750µM (b) for 24h in the organoid 3D model.....	247
Table 77: Luminescence signals of the ATP measurements after treatment with Staurosporine for 24h in the organoid 3D model .....	248
Table 78: TEER values of the Caco-2 2D model after the treatment on day 21 with the controls (DMSO, Metformin, Staurosporine) and 5-FU .....	249
Table 79: TEER values of the Caco-2 2D model after the treatment on day 21 with the controls (DMSO, Metformin, Staurosporine) and Alosetron .....	250
Table 80: TEER values of the Caco-2 2D model after the treatment on day 21 with the controls (DMSO, Metformin, Staurosporine) and Diclofenac.....	251
Table 81: TEER values of the Caco-2 2D model after the treatment on day 21 with the controls (DMSO, Metformin, Staurosporine) and Flavopiridol .....	252
Table 82: TEER values of the Caco-2 2D model after the treatment on day 21 with the controls (DMSO, Metformin, Staurosporine) and Gefitinib.....	253
Table 83: TEER values of the Caco-2 2D model after the treatment on day 21 with the controls (DMSO, Metformin, Staurosporine) and Loperamide .....	254
Table 84: TEER values of the Caco-2 2D model after the treatment on day 21 with the controls (DMSO, Metformin, Staurosporine) and Terfenadine .....	255
Table 85: TEER values of the Caco-2 OoC model. Shown are the TEER values of the experiment with Lop, Terf, Flav, Dic and Met. Platelayout (a.), TEER values before treatment on day 3 (b.), day 4 (c.) and day 5 (d.) .....	256
Table 86: TEER values of the Caco-2 OoC model. Shown are the TEER values of the experiment with Lop, Terf, Flav, Dic and Met. TEER values before treatment on day 6 (a.), on day 6 (1h after treatment) (b.), on day 6 (4h after treatment) (c.) and on day 7 (24h of treatment) (d.) .....	257
Table 87: TEER values of the Caco-2 OoC model after treatment with 5-FU, Med and Stau. Shown are the TEER values of the experiment with 5-FU, Med and Stau. Platelayout (a.), TEER values before treatment on day 3 (b.), day 4 (c.) and day 5 (d.) .....	258
Table 88: TEER values of the Caco-2 OoC model. Shown are the TEER values of the experiment with 5-FU, Med and Stau. TEER values before treatment on day 6 (a.), on day 6 (1h after treatment) (b.), on day 6 (4h after treatment) (c.) and on day 7 (24h of treatment) (d.)....	259
Table 89: TEER values of the Caco-2 OoC model. Shown are the TEER values of the experiment with 5-FU, Alo, Gef and DMSO. Platelayout (a.), TEER values before treatment on day 3 (b.), day 4 (c.) and day 5 (d.) .....	260

Table 90: TEER values of the Caco-2 OoC model. Shown are the TEER values of the experiment with 5-FU, Alo, Gef and DMSO. TEER values before treatment on day 6 (a.), on day 6 (1h after treatment) (b.), on day 6 (4h after treatment) (c.) and on day 7 (24h of treatment) (d.)	261
Table 91: TEER values of the Caco-2 OoC model. Shown are the TEER values of the experiment with Terf, Flav and DMSO. Platelayout (a.), TEER values before treatment on day 4 (b.), day 5 (c.) and day 5 (1h after treatment) (d.)	262
Table 92: TEER values of the Caco-2 OoC model. Shown are the TEER values of the experiment with Terf, Flav and DMSO. TEER values on day 5 (4h after treatment) (a.), on day 5 (6h after treatment) (b.) and on day 6 (24h after treatment) (c.)	263
Table 93: TEER values of the Caco-2 OoC model. Shown are the TEER values of the experiment with Gef, Alo, Met, Lop and Med. Platelayout (a.), TEER values before treatment on day 4 (b.), day 5 (c.) and day 5 (1h after treatment) (d.)	264
Table 94: TEER values of the Caco-2 OoC model. Shown are the TEER values of the experiment with Gef, Alo, Met, Lop and Med. TEER values on day 5 (4h after treatment) (a.), on day 5 (6h after treatment) (b.) and on day 6 (24h after treatment) (c.)	265
Table 95: TEER values of the Caco-2 OoC model. Shown are the TEER values of the experiment with Dic, Stau and Med. Platelayout (a.), TEER values before treatment on day 4 (b.), day 5 (c.) and day 5 (1h after treatment) (d.)	266
Table 96: TEER values of the Caco-2 OoC model. Shown are the TEER values of the experiment with Dic, Stau and Med. TEER values on day 5 (4h after treatment) (a.), on day 5 (6h after treatment) (b.) and on day 6 (24h after treatment) (c.)	267
Table 97: TEER values of the Caco-2 OoC model. Shown are the TEER values of the experiment with Flav, Gef, Terf, Lop, Dic and Med. Platelayout (a.), TEER values before treatment on day 3 (b.), day 4 (c.) and day 5 (d.)	268
Table 98: TEER values of the Caco-2 OoC model. Shown are the TEER values of the experiment with Flav, Gef, Terf, Lop, Dic and Med. TEER values on day 6 (a.), on day 6 (1h after treatment) (b.) and on day 6 (4h after treatment) (c.) and on day 7 (24h after treatment)	269
Table 99: TEER values of the Caco-2 OoC model. Shown are the TEER values of the experiment with Dic, Stau and DMSO. Platelayout (a.), TEER values before treatment on day 3 (b.), day 4 (c.) and day 5 (d.)	270
Table 100: TEER values of the Caco-2 OoC model. Shown are the TEER values of the experiment with Dic, Stau and DMSO. TEER values on day 6 (a.), on day 6 (1h after treatment) (b.) and on day 6 (4h after treatment) (c.) and on day 7 (24h after treatment)	271
Table 101: TEER values of the Caco-2 OoC model. Shown are the TEER values of the experiment with 5-FU, Alo, Flavo, Met and DMSO. Platelayout (a.), TEER values before treatment on day 3 (b.), day 4 (c.) and day 5 (d.)	272
Table 102: TEER values of the Caco-2 OoC model. Shown are the TEER values of the experiment with 5-FU, Alo, Flavo, Met and DMSO. TEER values on day 6 (a.), on day 6 (1h after	

treatment) (b.) and on day 6 (4h after treatment) (c.) and on day 7 (24h after treatment). .....	273
Table 103: Papp values of the BI assay after treatment with 5-FU (a), Alo (b) and Diclo (c) in the Caco-2 OoC model. ....	274
Table 104: Papp values of the BI assay after treatment with Flavo (a), Gef (b) and Terf (c) in the Caco-2 OoC model. ....	274
Table 105: Papp values of the BI assay after treatment with Lop in the Caco-2 OoC model.....	275
Table 106: Protein expression levels of tight junction proteins.....	275
Table 107: Protein expression levels of adherens junction proteins .....	275
Table 108: Protein expression levels of phase I enzymes.....	276
Table 109: Protein expression levels of phase II enzymes .....	276
Table 110: Protein expression levels of phase III enzymes (SLC transporter) .....	277
Table 111: Results from three replicates of the gene expression of potential novel tested biomarkers ( <i>LCN-2, FABP-1, GSTA1, MLCK, CRP, HDC, GAST</i> ) of the Caco-2 2D model. Values are normalized to the gene expression of the housekeepers <i>PPIA, PIB, HPRT1</i> and <i>LDHA</i> and given as fold changes towards the vehicle control. ....	279
Table 112: Results from three replicates of the gene expression of potential novel tested biomarkers ( <i>LCN-2, FABP-1, GSTA1, MLCK, CRP, HDC, GAST</i> ) of the Caco-2 OoC model. ....	279
Table 113: Results from three replicates of the gene expression of potential novel tested biomarkers ( <i>LCN-2, FABP-1, GSTA1, MLCK, CRP, HDC, GAST</i> ) of the organoid 3D model. ....	280
Table 114: Statistically significant differences in gene expression between the DMSO control and treated samples. ....	280
Table 115: Fold changes in mir194 expression after 7 days treatment in Caco-2 2D (a), caco-2 OoC (b) and organoid 3D (c). ....	281
Table 116: Statistically significant differences in mir194 expression between treated and non-treated samples. Normal distribution was pretested with a Shapiro-Wilk test.....	281
Table 117: Statistically significant differences in citrulline concentrations between the used cell culture models. Normal distribution was pretested with a Shapiro-Wilk test.....	281
Table 118: Measured absorbance and interpolated concentrations of L-citrulline in the used cell culture models after 7days treatment with GI toxic and non-toxic compounds.....	282
Table 119: Statistically significant differences in L-citrulline concentrations between treated and non-treated samples. Normal distribution was pretested with a Shapiro-Wilk test. ....	282
Table 120: Statistically significant differences in calprotectin concentrations between the used cell culture models. Normal distribution was pretested with a Shapiro-Wilk test.....	283

---

Table 121: Measured absorbance and interpolated concentrations of calprotectin in the used cell culture models after 7 days treatment with GI toxic and non-toxic compounds. .... 283

Table 122: Statistically significant differences in calprotectin concentrations between treated and non-treated samples. Normal distribution was pretested with a Shapiro-Wilk test. ... 284

---

## List of abbreviations

---

°	Degree
°C	Degree Celsius
%	Percent
≥	Greater-than or equal to
Xg	Relative centrifugal force
\$	Dollar
µg/ml	Microgramm per Milliliter
µl	Microliter
µM	Micro Mol
2D	Two-dimensional
3D	Three-dimensional
5-FU	5- Fluorouracil
3R	Replace, Reduce, Refine
AC	Altering current
ABC	ATP-binding cassette
<i>ABCB1</i>	ATP-binding cassette sub-family B member 1 (synonym <i>P-gp</i> / <i>MDR1</i> )
<i>ABCC2</i>	ATP-binding cassette sub-family C member 2 (synonym <i>MRP2</i> / <i>cMOAT</i> )
<i>ABCG2</i>	ATP-binding cassette sub family G member 2 (synonym <i>BCRP</i> )
CAN	Acetonitrile
ADME	Absorption, distribution, metabolism, excretion
ADMET	Absorption, distribution, metabolism, excretion, toxicity
AJ	Adherens junctions
Alo	Alosetron hydrochloride
AP	Alkaline phosphatase
ATP	Adenosintriphosphate
<i>BCRP</i>	Breast cancer resistance protein (synonym <i>ABCG2</i> )
bDNA	Branch DNA
Caco-2	Cancer coli 2 (cell line of human colorectal adenocarcinoma cells)
CATs	Cationic amino acid transporters
CA I	Carbonic anhydrase I

---

CDK	Cyclin-dependant kinase
<i>CDX2</i>	Caudal-type homeobox 2
CK20	Cytokeratin 20
cm <sup>2</sup>	Square centimeter
<i>cMOAT</i>	Canalicular multispecific organic anion transporter 1 (synonym <i>ABCC2</i> / <i>MRP2</i> )
CO <sub>2</sub>	Carbon dioxide
COX	Cyclooxygenases
<i>CRP</i>	C-reactive protein
CYP	Cytochrome P
Da	Dalton
DC	Direct current
DE	Definitive endoderm
DI-H <sub>2</sub> O	Deionized water
Dic	Diclofenac sodium
DMSO	Dimethyl sulfoxide
DNA	Desoxyribonucleic acid
DMEs	Drug metabolizing enzymes
DMETs	Drug metabolizing enzymes and transporters
DPBS -/-	Dulbecco's Phosphate buffered saline (calcium- and magnesium free)
DPBS +/-	Dulbecco's Phosphate buffered saline (with calcium and magnesium)
ECM	Extracellular matrix
EFPIA	European Federation of Pharmaceutical Industries and Associations
EGF	Epidermal growth factor
EGFR	Epidermal growth factor receptor
EMEM	Eagle's Minimum Essential Medium
EtOH	Ethanol
<i>FABP-1</i>	Fatty acid binding protein 1 (synonym <i>L-FABP</i> )
<i>FABP-2</i>	Fatty acid binding protein 2 (synonym <i>I-FABP</i> )
FBS	Fetal bovine serum
FITC	Fluorescein-5-isothiocyanat
Flav	Flavopiridol hydrochloride



---

g	Gram
g/L	Gram per liter
Gef	Gefitinib
GFR	Growth Factor reduced
GI	Gastrointestinal Tract
GLP <sup>^</sup>	Good Laboratory Practice
GO	Gene Ontology
<i>GSTA-1</i>	Glutathione-S-Transferase Alpha 1
h	Hours
HATs	Heteromeric amino acid transporter
H&E	Hematoxin and eosin
HBSS	Hanks Balanced Salt Solution
HCS	High Content Screening
<i>HDC</i>	Histidine decarboxylase
Hz	Hertz
IBS	Inflammatory bowel syndrome
IC <sub>20</sub>	Inhibitory concentration 20
IC <sub>50</sub>	Half maximal inhibitory concentration
ICH	International Conference on harmonisation
<i>I-FABP</i>	Intestine fatty acid binding protein
IL25	Interleukin 25
iPSC	Induced pluripotent stem cells
Irino	Irinotecan
ISX	Intestine-specific homeobox
JPMA	Japan Pharmaceutical Manufactureres Associations
kDa	Kilo Dalton
kPa	Kilopascal
Lats	L-type amino acid transporters
LC	Liquid chromatography
<i>LCN-2</i>	Lipocalin 2
<i>L-FABP</i>	Liver-type acid binding protein

---

Lop	Loperamide hydrochloride
M	Molar
mg/ml	Milligram per Milliliter
min	Minutes
ml	Milliliter
mm	Millimeter
mM	Millimolar
mm <sup>2</sup>	Square millimeter
mV	Milli Volt
<i>MCT</i>	Monocarboxylate transporter protein
<i>MDR1</i>	Multidrug resistance protein 1 (synonym P-gp / ABCB1)
MHLW	Japanese Ministry of Health, Labour and Welfare
miRNAs	Micro RNAs
<i>MLCK</i>	Myosin light chain kinase
<i>MRP1</i>	Multidrug resistance protein 1 (synonym <i>ABCC1</i> )
<i>MRP2</i>	Multidrug resistance protein 2 (synonym <i>cMOAT</i> / <i>ABCC2</i> )
<i>MRP3</i>	Multidrug resistance protein 3 (synonym <i>ABCC3</i> )
<i>MRP4</i>	Multidrug resistance protein 4 (synonym <i>ABCC4</i> )
<i>MRP5</i>	Multidrug resistance protein 5 (synonym <i>ABCC5</i> )
MS	Mass spectrometry
<i>Muc2</i>	Mucin 2
<i>Muc5Ac</i>	Mucin 5Ac
nm	Nanometer
nl/min	Nanoliter per minute
NaHCO <sub>3</sub>	Sodium bicarbonate
<i>NAT 1/2</i>	N-Acetyltransferase 1/2
NEAA	Non-essential amino acids
NICD	Notch intracellular domain
NSAIDs	Nonsteroidal anti-inflammatory drugs
NSCLC	Non-small-cell lung cancer
<i>OATP</i>	Organic anion transporting polypeptide

---

<i>OCT</i>	Organic cation transporter
<i>OCTN</i>	Carnitine/organic cation transporter
OoC	Organ on a chip; in this case OrganoPlate®
Oxali	Oxaliplatin
pg/ml	Picogram per milliliter
ppm	Parts per million
Pa	Pascal
Papp	Apparent permeability
PCA	Principal component analysis
<i>PEPT</i>	Peptide transporter protein
PhRMA	Pharmaceutical manufacturers' associations Pharmaceutical research and Manufacturers of America
<i>P-gp</i>	Multidrug efflux pump P-glycoprotein (synonym <i>MDR1</i> / <i>ABCB1</i> )
<i>PMAT</i>	Plasma membrane monoamine transporter
RNA	Ribonucleic acid
ROCKi	Rock inhibitor
Rpm	Rounds per minute
RT	Room temperature
SAPE	Streptavidin-conjugated R-Phycoerythrin
Sec	Seconds
SI	Sucrase-Isomaltase
SLC	Solute carrier transporter
Stau	Staurosporine
<i>SULT1E1</i>	Sulfotransferase 1E1
Terf	Terfenadine
TFA	Trifluoroacetic acid
TG	Technical guideline
TMT	Tandem mass tag
TRITC	Tetramethylrhodamine
TS	Thymidylate synthase
TJs	Tight junctions
<i>TJAP1</i>	Tight junction associated protein 1

---

TKIs	Tyrosine Kinase Inhibitors
WHO	World Health Organization
WT	Wild type
xMAP®	Multi-analyte proflin beads
ZO-1/-2/-3	Zonula occludens 1/2/3



---

## 1. Introduction

---

### 1.1. Toxicology

The study of adverse side effects of xenobiotics, chemical, physical, or biological agents is called toxicology. The interdisciplinary scientific field of toxicology provides the society information about how to protect the environment, animals and humans from toxicants and to speed up and better understand the development of new drug candidates for clinical use (Hodgson, 2004).

The knowledge and especially the intuition about poisons reaches back into the earliest times of human existence, when contact with animal and plant poisons was a matter of life and death. Very early the Greeks described drugs as "*pharmaka*" or "*pharmakon*" but without any classification relating to their potential. Later these terms received the meaning of poison (Hayes and Gilbert, 2009). In the 17<sup>th</sup> century the term toxicology, from Greek "*toxicon*" (poison) and "*logos*" (science) was introduced. Probably every toxicologist is familiar with the statement of Paracelsus (born Philippus Theophrastus Aureolus Bombastus von Hohenheim, 1493-1541):

*"Alle Dinge sind Gift, und nichts ist ohne Gift; allein die Dosis machts, daß ein Ding kein Gift sei."*

Which means "all things are poison, and nothing is without poison, only the dose permits something not to be poisonous". This statement today is still a fundamental concept in toxicology and is defined nowadays as a dose-response relationship. The field of toxicology has developed over many years (and after several important occurrences, for example the thalidomide scandal in the 60s (Vargesson, 2015) or the TeGenero incident in 2006, where all six human volunteers had multiorgan failure (Attarwala, 2010)), to a more descriptive discipline focusing more on the mechanisms of toxicity (Hodgson, 2004). Nowadays toxicology is an interdisciplinary field and can be found in a wide range of areas, e.g. forensic, environmental, occupational, food, pharmaceutical and clinical toxicology.

Toxicology is always focused on the adverse effect an agent may cause to animals, environment, or humans. A big focus here is in the area of drug development, where a safe dose of a new drug that is safe is determined. To reach this goal of dose finding, risk assessment studies and a battery of experiments, including expensive and time-consuming animal experiments, which are required by law in the pharmaceutical industry are performed.

## 1.2. Toxicology in drug development and discovery

The drug development process is a very time consuming and costly process in which a new drug is designed, developed, and finally approved for use in patients. The complete development process from pre-clinical to clinical studies up to marketing takes around 12-15 years and costs approx. \$1-2.6 billion. The costs depend on the type of the new drug, e.g. a new molecular entity (NME) or a new biological entity (NBE) (Guengerich, 2006; Paul *et al.*, 2010; DiMasi, Grabowski and Hansen, 2016; Mohs and Greig, 2017) and is shown in Figure 1. Before a new drug can be used for patients, it must go through various research phases to determine whether it is safe and effective, as well as its correct dosage/exposure.

The development of a new drug starts in the discovery phase with basic research and discovery of solid knowledge to understand the molecular mechanisms of the disease of interest. The biological target, usually a gene or protein, is identified and validated. The target must interact with and be affected by the potential drug candidate.

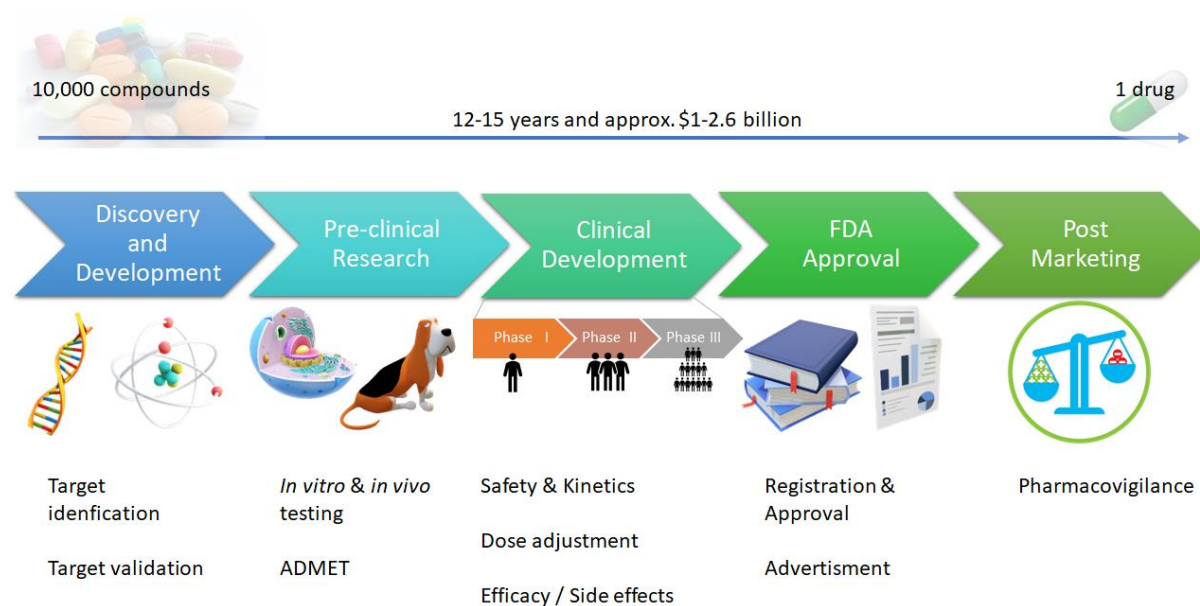


Figure 1: The drug development process. Consecutive phases from discovery and development to post-marketing. Number of tested compounds decreasing continuously.

The pre-clinical phase consists primarily of the *in silico*, *in vitro* and *in vivo* experiments. Within this phase a large number of compounds are screened to select and find the best candidates and to identify their ability to alter the target activity. The choice of compounds is determined by the results of the early tests on efficacy (*in vitro* and *in vivo*), absorption, distribution, metabolism, excretion, toxicity (ADMET; *in vitro* and *in vivo*). A major goal of the pre-clinical and clinical trials is to distinguish between positive therapeutic effects of pharmacological drugs and their

---

potentially adverse side effects. Liver, kidney, heart, skin and muscle are the most affected organs (Daly, 2013).

*In vitro* models are used to help identify such effects as early as possible. Preferably, these experiments should be performed on specific cells or tissues to best mimic the natural properties of human responses to drugs (Grabinger *et al.*, 2014). The pre-clinical phase serves to determine if the drug candidate is efficacious and safe enough to enter the clinical trial and testing in humans. The clinical phase is divided into phase I, II and III, usually a small group of healthy volunteers (with the exception of oncology studies) are treated to achieve information on the tolerability and pharmacokinetics. With this knowledge phase II follows in which a small group of patients (100-500) is involved. This stage serves as the proof of concept, in which the therapeutic efficacy is determined. Finally, in phase III a larger group of patients (1,000-5,000) is treated (depending on the indication), and the results of efficacy must be confirmed and compared to a placebo or reference drug. In addition, dose-response relationships and risk-benefit analyses are conducted. After all phases have been successfully completed, the registration and approval of the drug can be initiated. After the drug has been launched on the market, the final phase (post-marketing or pharmacovigilance) begins in which the safety, risks and benefits of the drug are monitored. In this phase its always possible to take action e.g. reducing the risks by changing the field of application or in extreme cases to withdraw the drug from the market.

### **1.2.1. Early safety assessment methods and models**

To assess the safety of a new drug, to understand the potential hazardous effect of chemicals or drugs and for predicting their effect on humans many experiments are performed during pre-clinical drug development. All experiments are performed under strict compliance with regulations and guidelines (both internal, national and international). Studies for more advanced molecules are conducted in accordance with the recommendations of regulatory authorities (e.g., European Medicines Agency (EMA) and U.S. Food and Drug Administration (FDA)). Both are responsible for approving the conduct of clinical trials and grant marketing authorization of new drugs. These later studies are also (mostly) performed under Good Laboratory Practice (GLP) or under company specific quality regulations.

The International Conference on Harmonisation of Technical Requirements for Registration of Pharmaceuticals for Human Use (ICH) has harmonized multiple scientific guidelines and includes safety ICH guidelines, which are listed in Table 1.



Table 1: Safety guidelines and corresponding study types harmonized by the ICH

ICH guideline	Study types
S1	Carcinogenicity studies
S2	Genotoxicity studies
S3	Toxicokinetic and pharmacokinetics studies
S4	Repeat-dose toxicity studies
S5	Reproductive toxicology studies
S6	Biotechnological products studies
S7	Safety pharmacology studies
S8	Immunotoxicology studies
S9	Therapeutic area-specific
S10	Photosafety evaluation studies
S11	Non-clinical safety in paediatric medicines studies

Already in the early drug discovery *in silico* models are used which enables the use of structure activity relationships and computer-based prediction models (Simon-Hettich, Rothfuss and Steger-Hartmann, 2006) to help to identify and prioritize drug candidates. Subsequently, among other tests, the cell-based (*in vitro* studies) experiments follow (Eisenbrand *et al.*, 2002). In the pre-clinical phase, the goal is to identify the efficacy, toxicity, the pharmacokinetic and the safety of a new drug candidate. This will be reached by a wide range of tests which are successfully integrated by pharmaceutical companies in their drug discovery and development process. Table 2 summarizes the already included studies to cover the corresponding endpoints to gain more knowledge on compound toxicity. But most of the pharmaceutical companies handle the type of assay and order differently. Several *in vitro* methods have passed regulatory scrutiny and are integrated in official ICH guidelines.

Table 2: *In vitro* assays used in the drug discovery and development phases used by companies. The underlined assays indicate those included in the technical guidelines (TGs) of the Organisation for Economic Co-operation and development (OECD). CYP (Cytochrome P).

<b>Endpoint</b>	<b>In vitro assay</b>	<b>OECD technical guidelines</b>
Cytotoxicity	ATP assay, MTT assay, LDH leakage	
CYP induction potential	mRNA induction, reporter gene assay	
Cellular and oxidative stress	GSH depletion, activation of Nrf2 antioxidant-response or heat shock response pathways, p53 activation	
Genotoxicity	<u>Ames test</u>	TG471
	<u>Chromosome aberration assay</u>	TG473, 475, 483
	<u>Micronucleus test</u>	TG487
	Mouse lymphoma assay, Comet assay	
Phototoxicity	<u>3T3 Neutral Red Uptake</u>	TG432
Eye irritation	<u>Bovine Cornea Opacity Test</u>	TG437
	<u>Isolated chicken eye</u>	TG438
Skin corrosion / irritation	Human skin models ( <u>EpiSkin™</u> , <u>EpiDerm™</u> )	TG431
		TG439

In a later stage additionally *in vivo* toxicity studies are conducted. These are more informative but also more expensive. Compared to *in vitro* models, animal models retain proper physiological conditions, are more complex and a change in the behavior after drug treatment can be observed as well. But all the positive sides cannot solve the main problem of species-specific differences by translating the results to humans. For example the expression, catalytic activities of drug metabolizing enzymes or the isoform composition that differ between them can be critical (Martignoni, Groothuis and de Kanter, 2006).

Animals are not only used in pharmaceutical research these models were as well use in other areas. Figure 2 shows that most animals are used in basic research which includes for example main research on the complexity of the immune or nerve system, which cannot be covered with simple *in vitro* models. Another application area of animals in the manufacturing or quality control of medical products (Radtke, 2022). This includes for example the testing of stents or cardiac valves.

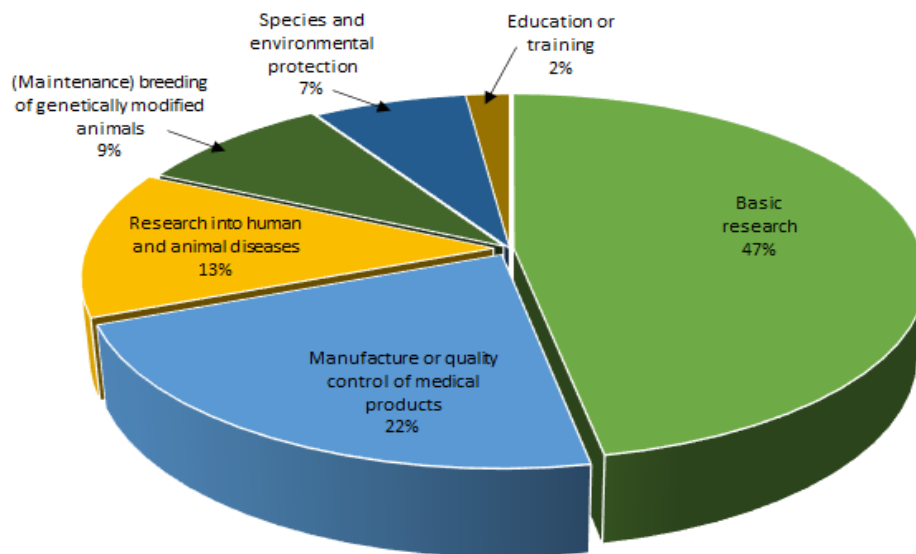


Figure 2: Purpose of animal use in 2019. The percentages are based on 2902348 animals used in 2019 in Germany (*Statistiken zu Tierversuchen, 2022*)

One major aim of the whole development process of new pharmaceuticals includes the characterization of a safety profile, the generation of a complete risk assessment of the drug and the compliance to regulatory requirements.

Despite all these experiments during the development of a drug, there are unfortunately (but rarely) drugs that have been approved but either cause side effects during use by the patient that severely restrict the quality of life or are so severe that they have to be withdrawn from the market.

In each phase of the drug development process failure rates occur. Between 2010 and 2013 the estimated attrition rates in the pre-clinical research was 89.5 %, in the clinical phases the success is a little bit higher. In Phase I 55.5 %, in phase II 80.4%, in phase III 68.8 % and in the registration phase 28.7 % of the drugs fail (Pammolli *et al.*, 2020). Figure 3 shows that the highest attrition rate is in clinical development (phase II and III), where the highest costs are also incurred. Even during the process of registration one of four drug candidates fail (approx. 23 %) (Kola and Landis, 2004).

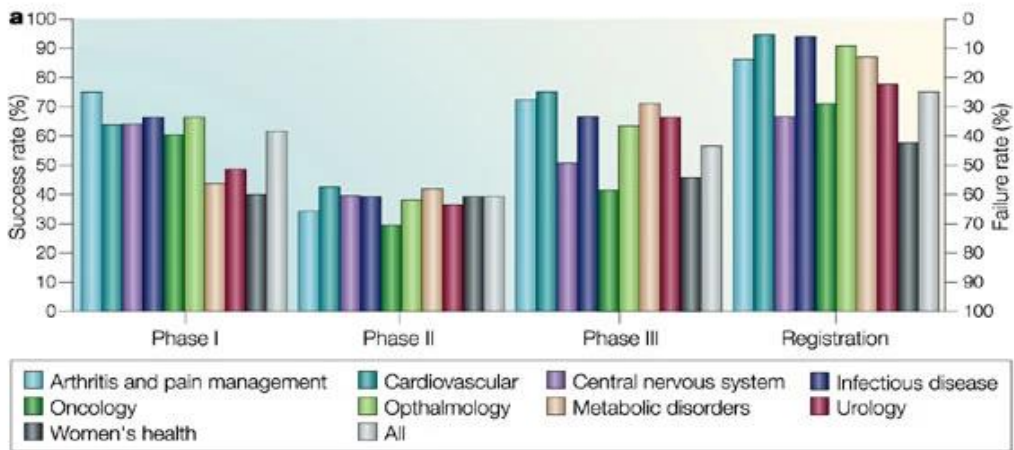


Figure 3: Percent success and failure rate of new compounds entering the specific phaseses of development. Divided after certain therapeutic areas (Kola and Landis, 2004).

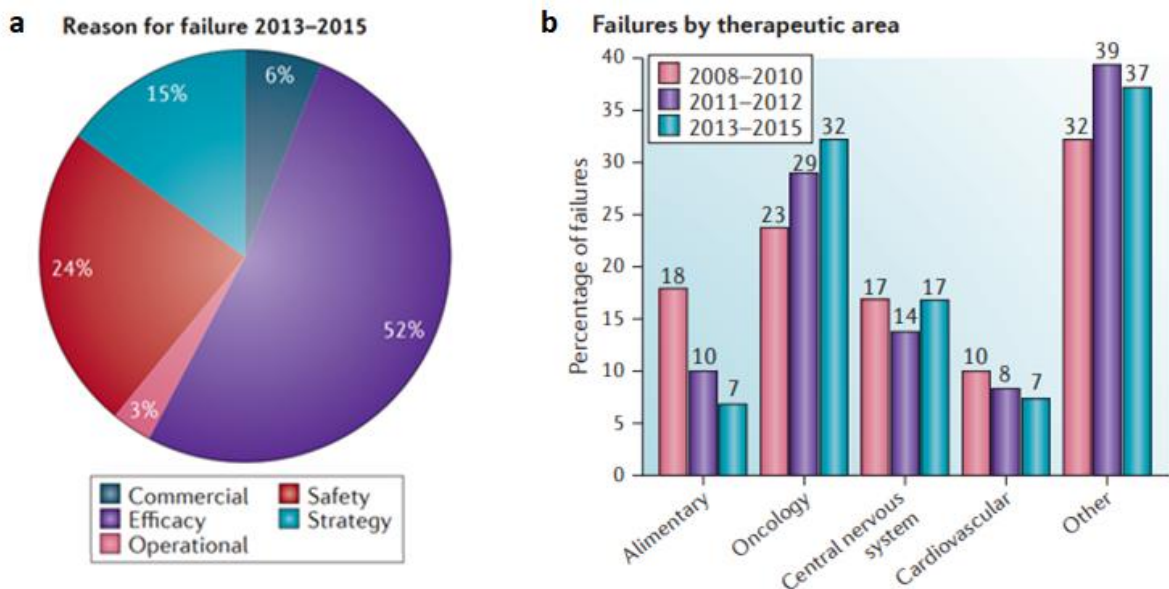


Figure 4: Reason for failures of drug candidates a.) Reasons for failures of drug candidates between 2013 and 2015. b.) Phase II and III clinical failures by therapeutic area (Harrison, 2016).

Figure 4a shows that the most problems which cause drug attritions during drug development are due to either poor pharmacokinetics/bioavailability/efficacy or safety (Harrison, 2016). In 2000 approximately 30 % of drug failures were due to safety issues (Kola and Landis, 2004). The most critical area is the therapeutic field of oncology and central nervous system (Figure 4b). The increasing trend of drugs with new, complex pharmaceutical mechanisms are one reason for the high rates of attritions (Harrison, 2016) - especially in the two indication areas. Although the number of drugs entering phase III is steadily increasing, the total number of drug candidates in the early stages of development has been decreasing in recent years (Derek Lowe, 2019).

---

The very high failure rate of compounds during phase III is often due to the poor predictability of toxic effects, which cannot be reproduced in cell culture models and the difficulty of translating experimental results from animal studies to humans.

To overcome these problems scientists are trying to develop new methods and new advanced cell culture models. Pharmaceutical companies which are under pressure, try to intensify their research and invest a lot of effort and money into scientific innovations. They have the goal to better predict and recapitulate the complex human body, to improve the current situation and to develop new screening strategies which improve the assessment of the toxicological profile of new drugs and better determine the efficacy and safety pharmacology.

Many of these improvements are in line with the 3R principle. The 3Rs stand for “replace, reduce, and refine” and refers to the conducting of experiments with animals (Figure 5). In 1959, the British scientists William Russel and Rex Burch published the principle of 3R’s as a tenet of experimental scientific work (Bundesinstitut für Risikobewertung, 2020). The main goal is to avoid or replace animal testing whenever possible not only because of ethical reasons, but also because of legal and economic reasons and as well by good scientific practice.

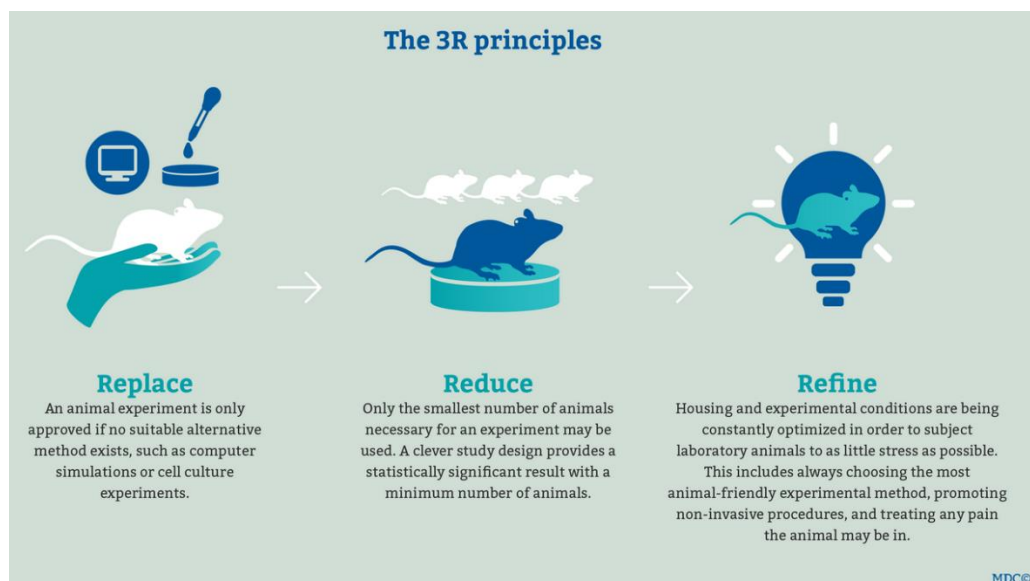


Figure 5: The 3R principles (MDC Berlin, 2020).

Already in the 1980s the European pharmaceutical industries founded the European federation of pharmaceutical industries and associations research and animal welfare working group (RAW). At the same time the first discussion took place regarding the EU-directive 86/609 on the protection of animal used for scientific purposes. Now the pharmaceutical industry not only complies with the provisions of this guideline, but also the companies support and foster higher

---

animal welfare standards and the 3R's. This explicitly shows the incorporation of 3R requirements of the EU-directive (directive 2010/63/EU) to protect more animals in scientific experiments (Fleetwood *et al.*, 2015; Vinken, 2020).

In order to be able to reproduce more the complex and dynamic structures of the human body and also to reduce, refine or replace animal experiments, scientists and pharmaceutical industries more and more invest in new *in vitro* cell culture models and research. Early screening models to better filter molecules with more toxic effects have been developed in recent years (Goh *et al.*, 2015). For example, co-culture models or 3D models could be developed.

### **1.2.2. The need for new cell culture models**

The field of intestinal *in vitro* models is a good alternative to animal models to investigate physiological and pathophysiological processes in the gastrointestinal (GI) system. Even if animal testing cannot be avoided completely to this day, there is at least the possibility of using a suitable cell culture model to reduce them to a minimum.

The development of clinically relevant *in vitro* models of the GI tract has received tremendous interest due to the global spread of intestinal disease (Hynds and Giangreco, 2013). Especially the cancer frequency has increased recently.

In 2012 the three most common types of cancer among the population are lung (13 %), breast (11.9 %) and colorectal cancer (9.7 %) (Stewart and Wild, 2016) (Figure 6). Besides the increase in colorectal cancer cases, another common problem is the use of chemotherapeutic drugs, which unfortunately often have severe side effects in the gastrointestinal tract. However, severe side effects do not only occur when taking chemotherapeutics, but also with a variety of other medicines.

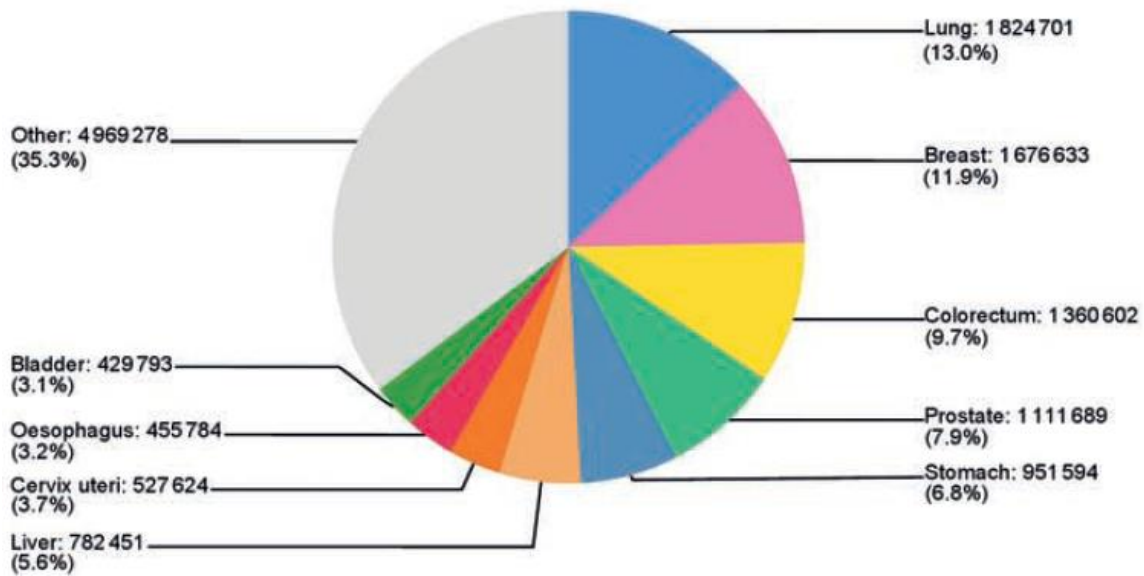


Figure 6: Estimated number of cancer incidence proportions of both sexes and all ages worldwide in 2012 (total: 14090149 cases) (Stewart and Wild, 2016).

Adverse drug effects can be divided into two types, pharmacological effects, which are dose-dependent and reversible (Pirmohamed *et al.*, 1998; Carr and Pirmohamed, 2018). They can be minimized by reducing the dose or gain full health by withdrawing the drug (Panarelli, 2014). And idiosyncratic effects which cannot be predicted and are very complicated and usually more harmful. Luckily around 80% of adverse effect are pharmacological side effects (Pirmohamed *et al.*, 1998). The five most common pharmacological side effects worldwide, based on the Databank side effect Resource (SIDER) 4.124, are headache, nausea, diarrhea, dizziness, and vomiting (Galeano *et al.*, 2020) (Figure 7).

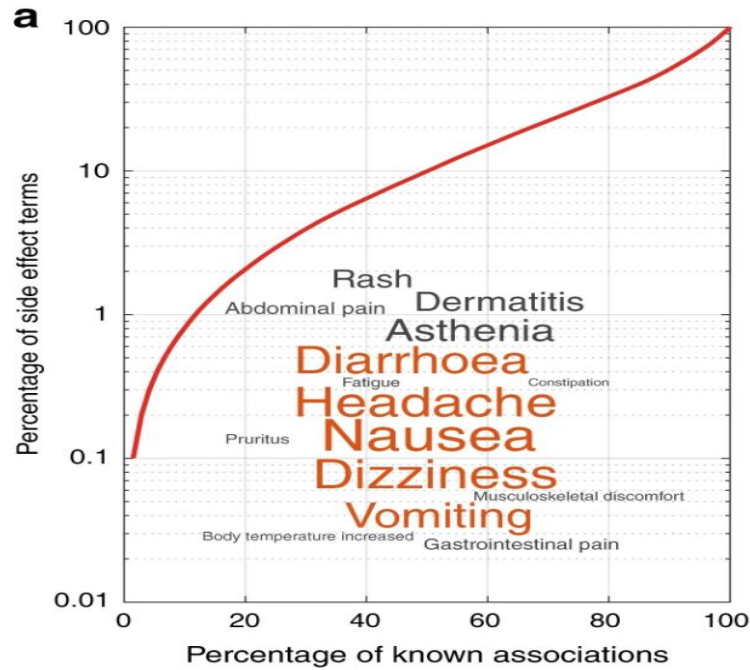


Figure 7: Occurrence of side effects based on the databank side effect resource (SIDER) 4.124. Shown are the 15 most frequent side effects. The size of the word is proportional to its popularity and the five most common adverse effects are coloured in orange. Side effects are ordered on the y-axis in decreasing order of popularity. (Galeano *et al.*, 2020).

The drugs which have specific side effects on the GI tract can affect any section of the intestine (Makins and Ballinger, 2003a). The small and large intestine are more often affected and approximately 20-40% of side effects occur in these parts of the intestine (Zeino, Sisson and Bjarnason, 2010).



---

### 1.3. Gastrointestinal Tract (GI)

#### 1.3.1. Structure of the GI tract

The GI tract is an open-ended and hollow-like tube and starts with the mouth and ends in the anus. Between mouth and anus, the esophagus, stomach, small and large intestine are located directly next to other organs like the liver and the pancreas. Each part of the GI tract has its own structural features and different accessory glands which support the digestion of food (Welcome, 2018).

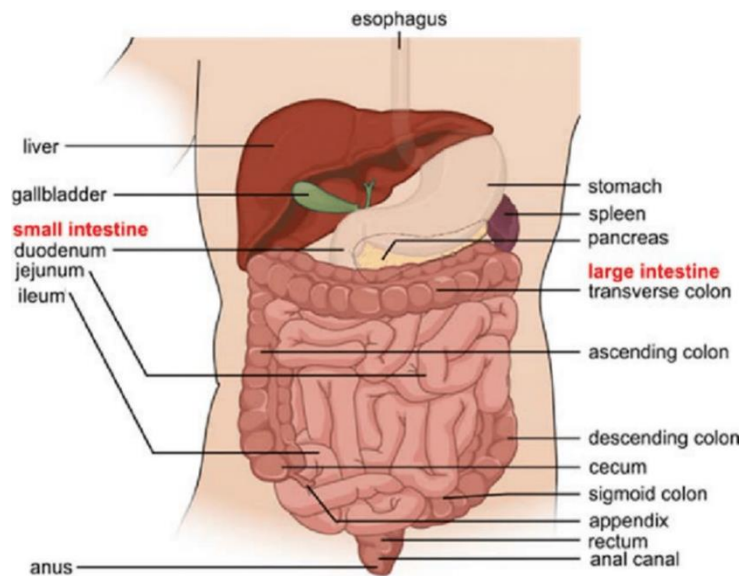


Figure 8: Structure and anatomy of the gastrointestinal tract. Overview of the structure of the GI tract of the human body (Mühlemann, 2018)

The intestine has various functions like food reception and storage, transport of food, digestion, absorption and protection against xenobiotics by building a barrier or by elimination (Nigam Y, Knight J, 2019).

The main functions of the GI tract are digestion, absorption, excretion, and protection. The intestine is not only the key organ for absorption and metabolism of nutrients, xenobiotics and drugs but also plays an important role in immune, neuromotor and endocrine system and is the main defense barrier (Rodrigues *et al.*, 2019).

The GI tract contains different cells from different tissues – cells of the nervous system, muscle cells, connective tissues cells and accessory cells from the gut.

In particular, the five main epithelial cells of the GI tract can be subdivided according to their function or morphology: enterocytes, goblet, enteroendocrine, paneth and stem cells (Figure 9). All these cells are formed from a single lineage, which is localized at the crypts. The cells in the intestinal epithelium are organized into crypts and villi structures. Enterocytes are the main cells in the villi parts of the intestinal epithelium. They include on the apical side closely packed microvilli which allows the absorption of nutrients. The tips of the enterocytes contain negatively charged, integral membrane mucin-like glycoproteins and these form a continuous, filamentous brush border. This layer forms a diffusion barrier against particles, bacteria and viruses (Snoeck, Goddeeris and Cox, 2005).

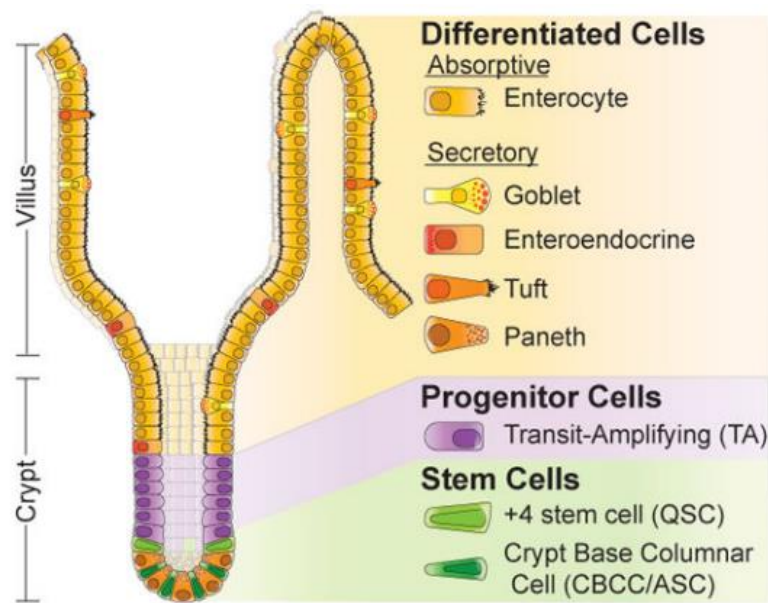


Figure 9: Main important cell types and the organization of the intestinal epithelium of the small intestine (Carulli, Samuelson and Schnell, 2014).

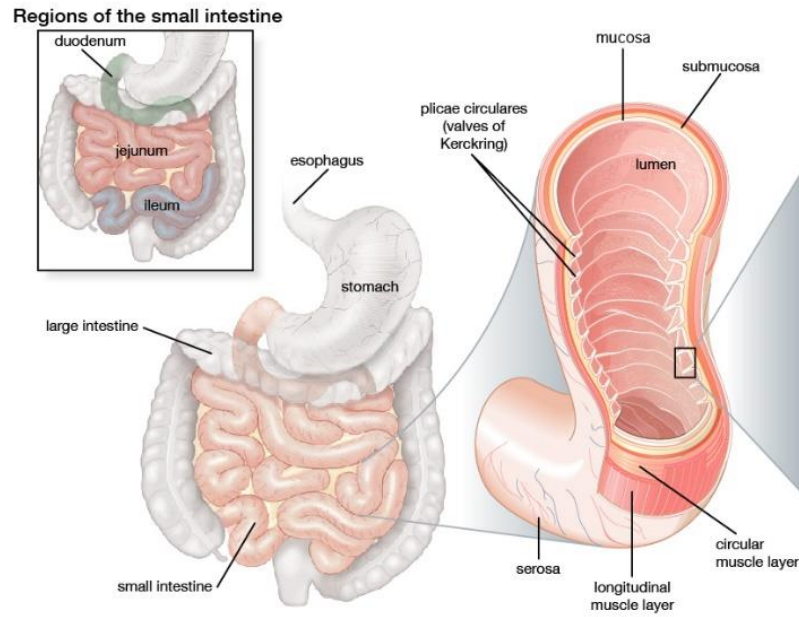
For the maintenance of the intestinal homeostasis the goblet cells play an important role. Goblet cells are columnar epithelial cells which are four times as high as wide and have microvilli at the apical end. Below the microvilli is the cytoplasm which contains large mucin granules necessary for mucin secretion (Guzman-Aranguez and Argüeso, 2010). Mucins bind water to build a gel-like structure and this helps to prevent against pathogenic microorganisms (Yang and Yu, 2021) and coat the inner layer (Collins, Nguyen and Badireddy, 2017; Welcome, 2018). The enteroendocrine cells are key regulators of food digestion and absorption, insulin secretion and appetite by producing and secreting important hormones (Gribble and Reimann, 2019). Enteroendocrine cells can be divided in open-type and closed-type cells based on the cytoarchitecture and location. Open-type cells have a bottle-neck shape and an apical end with microvilli which have direct contact to the intestinal lumen. Closed-type cells are based on the basal membrane, have no

---

microvilli, and have no contact to the lumen (Sundler *et al.*, 1989). Very rare are the tuft cells, which produce some effector molecules like IL-25 or the neurotransmitter acetylcholine. Tuft cells have a unique morphology with their dominant tuft of long and thick microvilli on the apical side of the cell (Sato, 2007). The tuft cells work as immune sentinels (Gerbe, Legraverend and Jay, 2012). Paneth cells, which are localized in the crypts and characterized by a huge endoplasmic reticulum and Golgi network which direct large dense core secretory granules to the apical membrane, are containing high amounts of antimicrobial peptides, like  $\alpha$ -defensin (Chelakkot, Ghim and Ryu, 2018), and immunomodulating proteins for the regulation of the intestinal flora (Bevins and Salzman, 2011; Lueschow and McElroy, 2020). The enterocytes are responsible for the uptake of ions, water, nutrients, vitamins and are involved in the epithelial barrier function and antigen uptake (Snoeck, Goddeeris and Cox, 2005). The other main cell types in the crypts are the stem cells which continuously self-renew and differentiate into the specialized cells named above (Barker, 2014). Further cells, the caveolated and motilin cells are less abundant (Welcome, 2018). Paneth cells, goblet cells and absorptive epithelial cells maintain the balance between gut microbiota and host immunity (Okumura and Takeda, 2017). Microfold cells or M cells are responsible for the immune sensing of bacteria and have at the apical surface short irregular microvilli and a poor brush border (Corr *et al.*, 2008).

### **1.3.2. Small intestine**

With approximately 6 m the small intestine is the longest part of the GI tract and is divided into duodenum, jejunum and ileum (Zorn and Wells, 2009; Vasković, 2021) (Figure 10). The duodenum is the shortest part and gets chyme from the stomach, pancreatic enzymes, and bile from the liver. In this part the food gets mixed and digested and the absorption starts (Collins, Nguyen and Badireddy, 2017). The second section, the jejunum measures around 2.5 m, it is responsible for absorption of digested products and contains muscular flaps (plicae circulares). The ileum is the last part and is approximately 3 m long and has the function to absorb specific vitamins, bile acids and any final nutrients (Collins, Nguyen and Badireddy, 2017).



© 2014 Encyclopædia Britannica, Inc.

Figure 10: Structural overview of the anatomy of the small intestine (The Editors of Encyclopaedia Britannica, 1998).

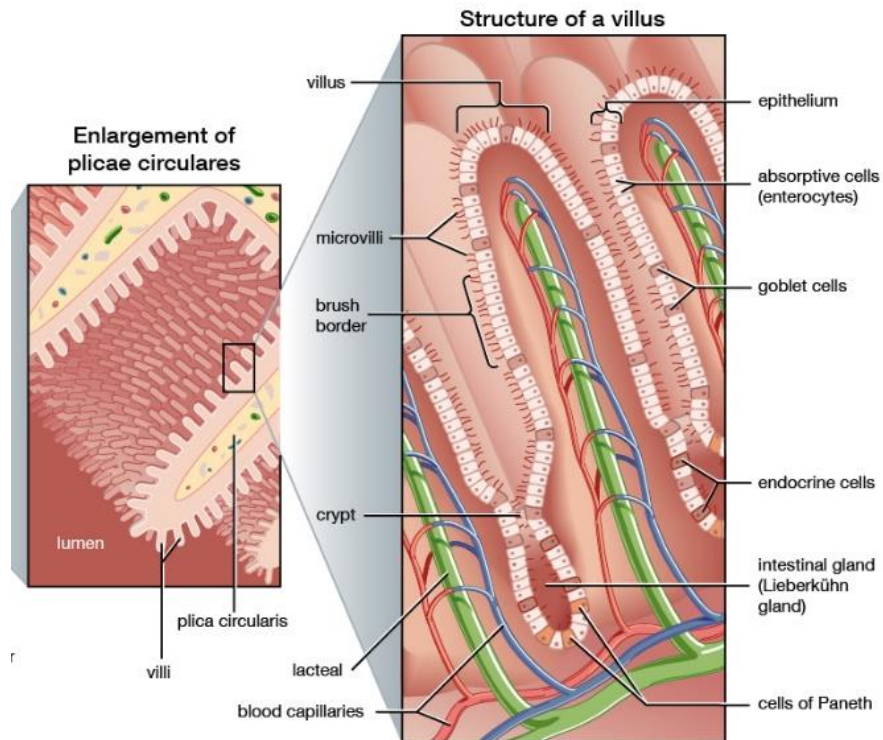


Figure 11: Microscopic structure of the enlargement of the plicae circulares (mucosal folds of the small intestine) and the villus structures (The Editors of Encyclopaedia Britannica, 1998)

The small intestine consists of 4 layers. The serosa is the outer layer and is formed by epithelium and mesothelium. It is responsible for keeping the GI tract in place. The next layer is called

---

muscularis. It is a four-part muscle layer which is responsible for lengthening, shortening the intestine and for contractions and peristaltic motion which are required for mechanical breaking down of the food. The third very thick and highly vascularized layer contains blood vessels, lymphatics and nerves and is called submucosa. The inner wall of the small intestine, the mucosa, has mucosal folds and is the place of absorption (Figure 10). The mucosa is covered with villi which include epithelial cells with microvilli, which maximize the surface area. The mucosal folds, also called plicae circulares, extend the surface area of the small intestine (Figure 11). A villus is about 1µm long and the main cells of it are absorptive enterocytes with microvilli (brush border), hormone-secreting enteroendocrine cells and goblet cells. In addition to these cells, paneth cells and stem cells are also found in the small intestine, which are mainly located in the Lieberkühn crypts (Figure 11) (Mühlemann, 2018).

### **Function of the small intestine**

The main functions of the small intestine are digestion and absorption. The chyme, the semi-fluid mass of half-digested food, is transported from the stomach to the duodenum and is mechanically mixed and crushed. The duodenum receives digesting enzymes from the liver and pancreas (bile acids and pancreatic juice) which help to digest the chyme. The pancreatic juice contains digestive enzymes like proteases, amylase and lipase and hormones like insulin, glucagon, somatostatin, and gastrin. These hormones help to regulate the body's metabolism (Henderson, no date). After food is digested, the nutrients (carbohydrates, fat, proteins, vitamins, and minerals), water and electrolytes are absorbed into the bloodstream. The produced mucus, from the goblet cells, helps to transport the chyme through the jejunum and ileum to the colon (Christiansen, 2020; Karunahatamoorthy, 2021).

### **1.3.3. Large intestine**

The human large intestine is divided into cecum, colon and rectum and is approximately 1.5 m long (Zorn and Wells, 2009). It has a very similar macroscopic structure compared to the small intestine but without any microvilli within the mucosa (Nigam Y, Knight J, 2019). The shortest part of the large intestine, the cecum is about 6 cm long. It ends with the appendix and towards the other end into the colon, which is divided into ascending, transverse, and descending colon (Figure 12).

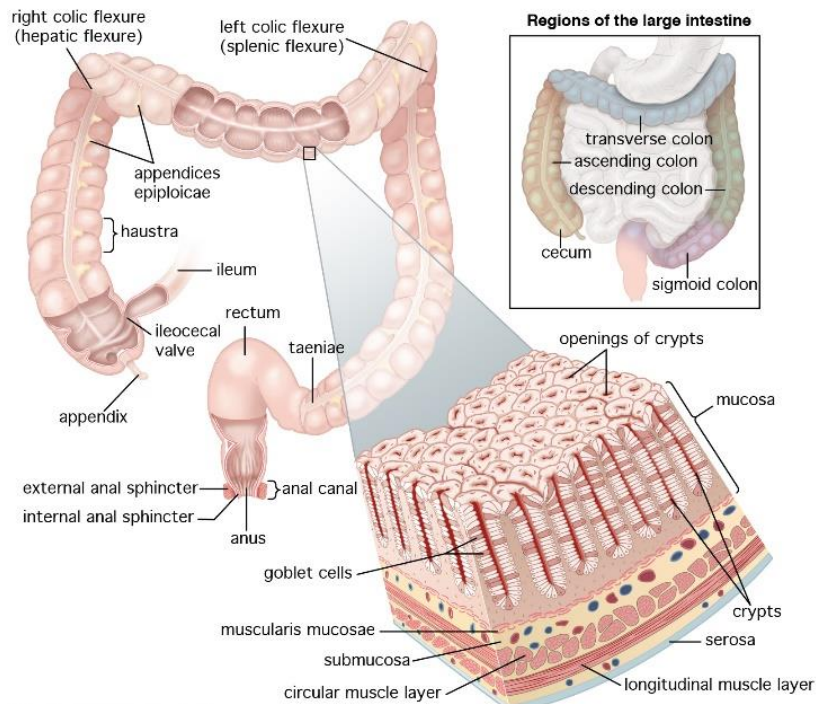


Figure 12: Structure of the large intestine (The Editors of Encyclopaedia Britannica, 2020).

Like the small intestine, the large intestine also consists of 4 layers, namely mucosa, submucosa, muscular layer, and serosa (Figure 12). The muscular layer consists of two layers, the inner (smooth muscle) and the outer (circular, longitudinal) layer, which are responsible for the motility function of the large intestine. Two different contraction types are active. On the one hand haustral (bulges in the colon wall that give the colon a segmented appearance) contraction gets activated by chyme and transport the chyme from haustra to haustra (sacculas in the colon) and on the other hand mass movement which transport the chyme very quickly in the direction of the rectum (Azzouz and Sharma, 2018). The number of goblet cells are much higher in the large intestine compared to the small intestine, which results in a very thick mucus layer (Okumura and Takeda, 2017) (Figure 12).

### Function of the large intestine

The large intestine has 3 main functions, absorbing water and electrolytes and producing vitamins, especially from the bacteria present (Azzouz and Sharma, 2018). After the chyme has remained in the small intestine for about 8-9 h and the digestion and absorption process have started and most nutrients are already absorbed, the chyme is transported further into the large intestine (Azzouz and Sharma, 2018; Nigam Y, Knight J, 2019). The large intestine completes the digestive process with the help of bacteria which produce vitamin K & B<sub>12</sub> and thiamin and riboflavin. Beside absorption of electrolytes and water (The Editors of Encyclopaedia Britannica,



---

2020), the large intestine also has the function of forming and transporting faeces toward the rectum for elimination (Nigam Y, Knight J, 2019).

The main differences between small and large intestine are that the colon contains no villi and has a flat surface epithelium.

### 1.3.4. Intestinal epithelium – Barrier shield against environment

Since the GI tract is the one of the first barrier that comes into contact with external contaminants, toxins, foreign substances or food, it has an important protective function. This can be divided into 4 functional barriers: immune barrier, biological barrier, chemical barrier and mechanical barrier, whereby the mechanical barrier has the most important function (Wu *et al.*, 2019).

The protective barrier of the GI tract is the intestinal epithelium which is a single-cell layer organized into crypts and villi. It works as a protective shield against toxins, bacteria, antigens and foreign substances (Jeon, 2013) and is the largest of the body's mucosal surfaces with approximately 400m<sup>2</sup> (Peterson and Artis, 2014). The functional barrier is characterized by an intestinal epithelium of polarized absorptive enterocytes connected via different junctional complexes. The connections and the produced mucus from the goblet cells are necessary for maintaining the physical defense. The connections are divided in tight junctions, adherens junctions, desmosomes, and gap junctions (Figure 13).

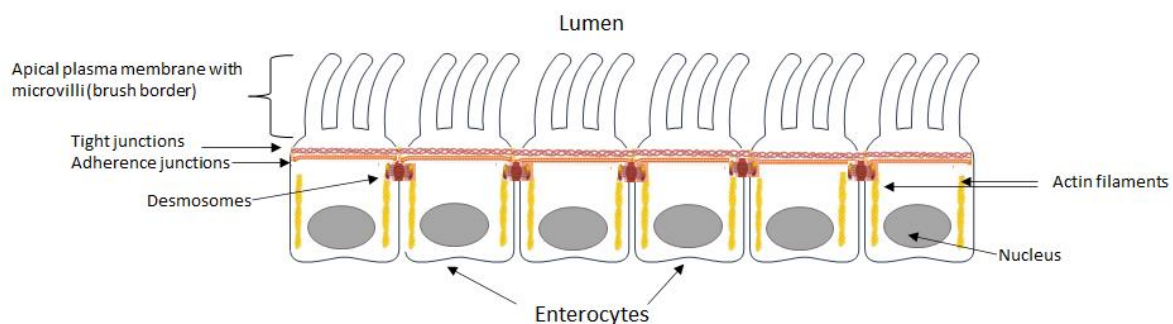


Figure 13: Structure of intestinal enterocytes. Structure and organization of the enterocytes-enterocytes formation.

The tight junctions (TJs) are structures which connect neighboring cells and control the permeability of compounds. TJs integrity is based on the interaction of integral transmembrane and peripheral membrane proteins with actin. The integral membrane proteins are composed of different proteins from occludin, claudin family members, cingulin, member of the Zonula occludens (ZO) family and junctional adhesion molecules (JAMs) 1-3 (Lee, Moon and Kim, 2018) (Figure 14). The main function of tight junctions is to maintain homeostasis through their ability

to act as a paracellular gate which discriminates the diffusion on size and charge of molecules (Zihni *et al.*, 2016). The disruption of the TJs homeostasis can be induced for example by proinflammatory cytokines, pathogenic bacteria, lipopolysaccharides (LPS), and pathological conditions and this can lead to serious diseases (Lee, Moon and Kim, 2018).

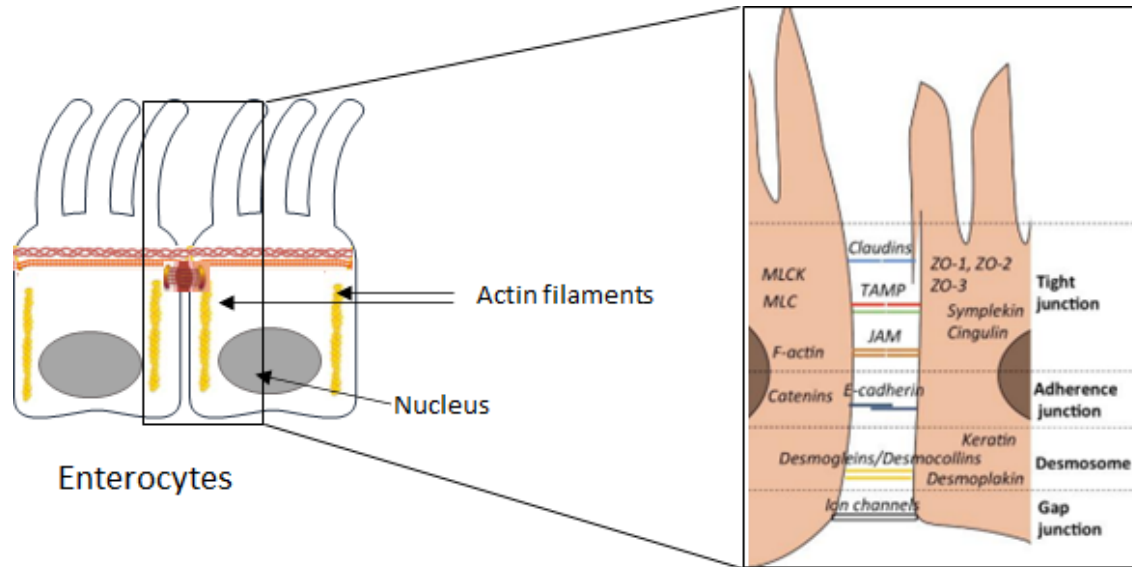


Figure 14. Composition of the cell-cell connections of enterocytes (Schoultz and Keita, 2020 modified)

The adherens junctions are connections between cells on the lateral membrane. They are mostly formed by catenin-cadherin interactions. The cadherins contain an intracellular C-terminus and an extracellular N-terminus. The N-domain is the part which connect to the cadherins of the neighbor cells which promotes the cell-cell adhesion (Groschwitz and Hogan, 2009) and in the GI tract the most abundant cadherin is the e-cadherin (Takeichi, 1990; Troxell *et al.*, 1999; Guo *et al.*, 2003; Schoultz and Keita, 2020) (Figure 14). These strong e-cadherin mediated cell-cell adhesions plays an important role in the maintenance of intestinal epithelial barrier function and is involved in the regulation of tight junctions through the transmitted signals through the adherens junctions (Takeichi, 1990; Man *et al.*, 2000; Angst, Marozzi and Magee, 2001).

The third part which contributes to the apical junctional complex in enterocytes are the desmosomes. The cell-cell adhesion of desmosomes is based on desmoglein and desmocollin (Figure 14), both are specific cadherin types (Harrison *et al.*, 2016; Gross *et al.*, 2018). They are localized on the lateral basal membrane side and play an important role in the barrier function and in the pathogenesis of inflammatory bowel disease (Ungewiß, 2019).

Gap junctions are plasma membrane ion channels between neighboring cells (Figure 14). They allow direct cytoplasmic exchange of ions and small molecule metabolites (Evans and Martin, 2002; Goodenough and Paul, 2009; Nielsen *et al.*, 2012). Gap junctions are formed by six



connexins, which build together a connexon. Gap junctions are responsible for the electrical communication and the transport of ions (Wong *et al.*, 2019).

One of the main characteristics beside absorption is the very fast, periodic cell renewal of the epithelial cells in the intestine (every 4-5 days in humans) and therefore it is the most vigorously self-renewing tissue of adult mammals (Van Der Flier and Clevers, 2009). The cells differentiate in the base of the crypts and then migrate upwards while maturing along the villi (Figure 15).

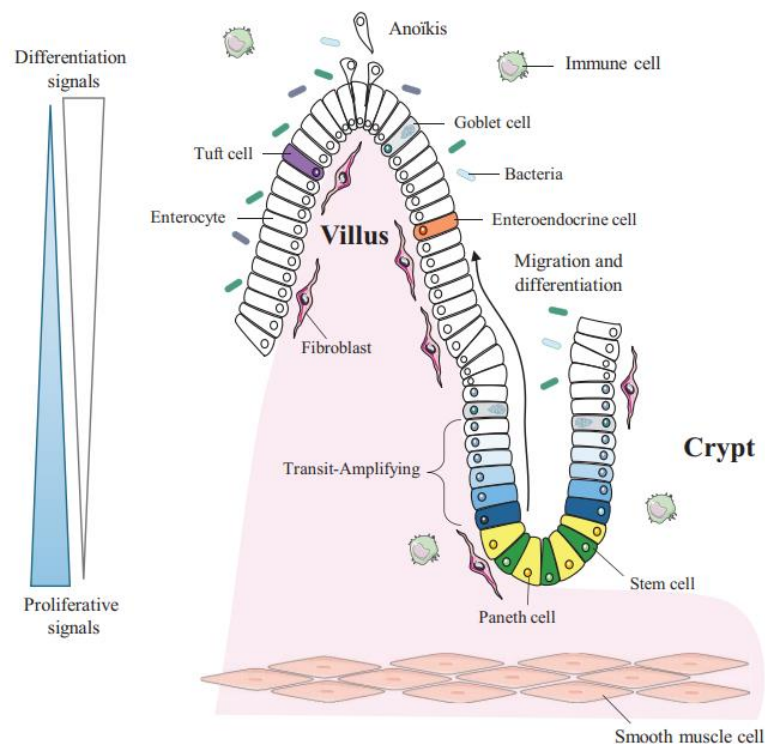


Figure 15: Overview of the intestinal epithelium of the small intestine with all included cell types. Renewal of the intestinal epithelium by LGR5<sup>+</sup> intestinal stem cells (ISC) in the crypt. The cells migrate upwards and maturing along the villi towards the lumen (Creff, Malaquin and Besson, 2021)

The differentiation needs specific signaling molecules, specifically Wnt, epidermal growth factor (EGF) and notch ligands which are provided in the small intestine by the paneth cells (Rees *et al.*, 2020). The Wnt signaling pathway is the key factor for the proliferation of intestinal epithelial cells (Van Der Flier and Clevers, 2009). The main molecule in the Wnt pathway is  $\beta$ -catenin, which is the key signal transducer in the cytoplasm for this pathway. If no Wnt signal is present, the proteasomal degradation of  $\beta$ -catenin begins and the transcription of Wnt target genes stops. On the other hand, Wnt signaling binds the Wnt ligand to Frizzled receptor which leads to activation of the protein disheveled protein which inhibits the degradation process.  $\beta$ -catenin can then enter the nucleus and induce the transcriptional regulation of Wnt target genes (Figure 16) (Fevr *et al.*

2007; Komiya and Habas, 2008; Van Der Flier and Clevers, 2009; Mah, Yan and Kuo, 2016), like cyclin D1 or MYC, which are important for cell proliferation (García-Gutiérrez, Delgado and León, 2019). Inhibition of Wnt pathway leads to a complete loss of crypt epithelial progenitor cells and also to no renewal and formation of cell types of the intestine (Gerbe *et al.*, 2011).

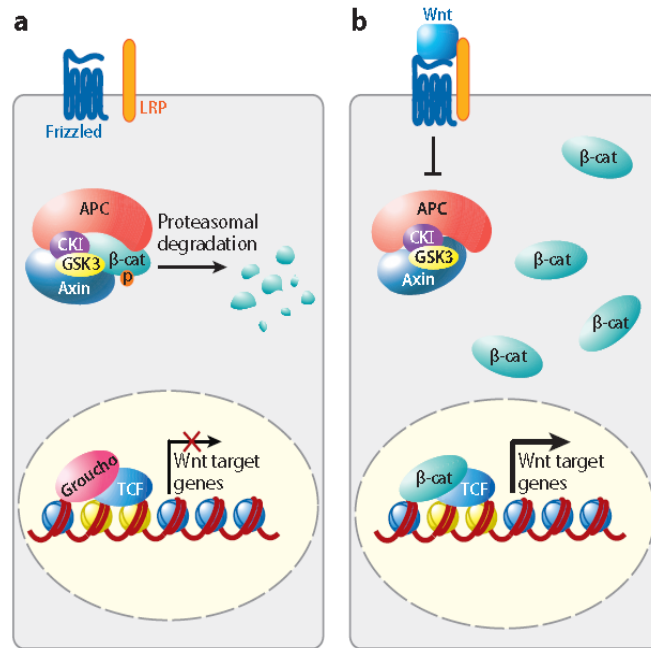


Figure 16: Wnt signaling pathway. a.) Deactivated Wnt pathway which leads to proteasomal degradation. b.) Activation of Wnt pathways by binding Wnt to frizzled receptor which leads to the entering of  $\beta$ -catenin into the nucleus (Van Der Flier and Clevers, 2009).

The resident stem cells are responsible for the fast cell renewal in the intestine and are located at the base of the crypts. Beside these cells, paneth cells, are localized between the stem cells, and play an important role by secreting signaling molecules like Wnt, EGF and notch ligands which are needed for the maturation and differentiation of stem cells to enterocytes, goblet cells, tuft cells and enteroendocrine cells (Rees *et al.*, 2020).

The epidermal growth factor receptor (EGFR) pathway (Figure 17) plays an important role in cell survival, proliferation, differentiation and growth (Oda *et al.*, 2005). EGF is an amino acid peptide which plays a main role in cell growth, survival, migration, apoptosis, proliferation and differentiation (Takahashi and Shiraishi, 2020). After binding of EGF to the EGFR this induces the receptor

tyrosine kinase autophosphorylation and thus leads to the subsequent activation of different signal transduction pathways like Ras/mitogen-activated protein kinases (Ras/MAPK), phosphatidylinositol 3-kinase /AKT (PI3K/AKT), phospholipase C- $\gamma$  /protein kinase C (PLC-/PKC) and STATs signal pathways (Tang *et al.*, 2016) (Figure 17). These signal pathways regulate tight junction protein expression (Basuroy *et al.*, 2006), reduce cell autophagy (Maynard *et al.*, 2010), regulate mucin secretion (Tang *et al.*, 2016) or promote intestinal development (Bedford *et al.*, 2015).

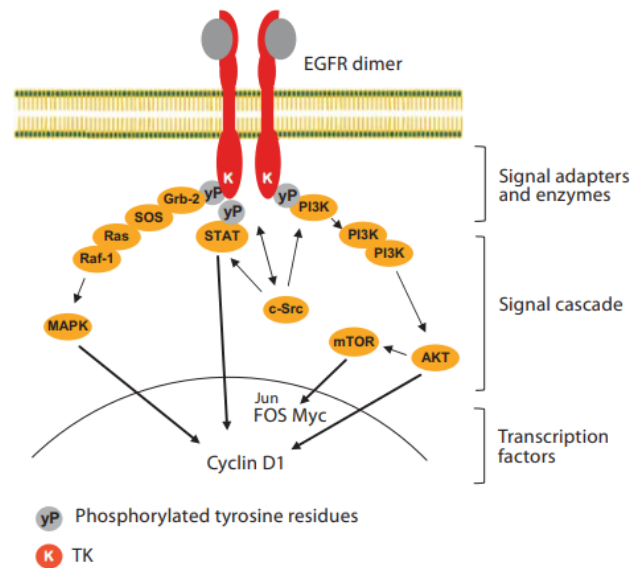


Figure 17: Simplified overview of the EGFR signaling pathway (Lurje and Lenz, 2010).

The notch signaling (Figure 18) is a further important pathway in the intestine. Notch receptors have five ligands, Delta-like1, -3, -4 and Jagged-1 and -2, which bind and activate the receptor. After activation two proteolytic cleavage follows. The first cleavage is catalyzed by metalloproteases, like ADAM10, and the second by  $\gamma$ -secretase. The second cleavage leads to a transport of the notch intracellular domain (NICD) into the nucleus. In the nucleus NICD binds to the protein RBP-J which activates transcription of genes (Bray, 2006; Borggreffe and Oswald, 2009; Takahashi and Shiraishi, 2020) which are involved in cell differentiation, proliferation and apoptosis in the intestine (Artavanis-Tsakonas, Rand and Lake, 1999; Penton, Leonard and Spinner, 2013).

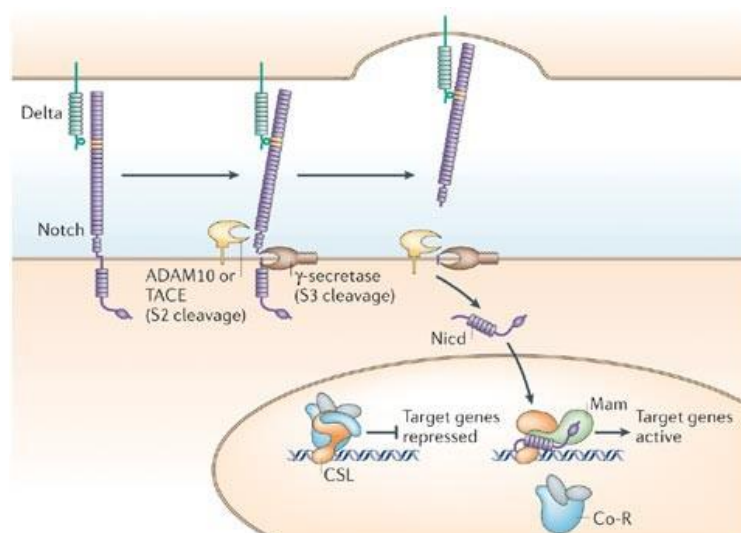


Figure 18: Overview of the notch signaling pathway. After ligand binding to notch leads this to cleavage and release of NICD into the nucleus. NICD binds to DNA binding protein which starts transcription (Bray, 2006).

### 1.3.5. Transporters and xenobiotic metabolism in the human intestine

The main route for drug treatment is oral administration, which is convenient for the patient as they can take the drug themselves and, compared to an intravenous injection, there is no risk of infection and no need to consult a doctor (Harwood *et al.*, 2007; Oostendorp *et al.*, 2010). The first route of exposure to a drug is through the mucosa of the gut wall (Estudante *et al.*, 2013). The bioavailability of orally taken drugs are dependent on their absorption via efflux or uptake transporters in the apical or basolateral membrane of enterocytes and the metabolic enzymes expressed in the cells (Terada and Hira, 2015). For drug transport two different mechanism exist, via passive diffusion or via transporter activity. The transporter related absorption can be divided in active and passive transport. Passive transport occurs by the passage of drugs/solutes via their electrochemical gradient and without energy consumption across the membrane. In comparison, active transport needs energy-coupling processes, which create ion or solute gradients across the membrane (Estudante *et al.*, 2013). Into date, more than 400 membrane transporters have been identified in humans, 49 ATP-binding cassette (ABC) and 395 solute carrier (SLC) transporters (Estudante *et al.*, 2013; Ölander *et al.*, 2016), but not all are involved in drug absorption and transport. The major transporters at the apical membrane of enterocytes are P-glycoprotein (P-gp or MDR1, also named as ABCB1), breast cancer resistance protein (BCRP, also named ABCG2) and multidrug resistance protein 2 (MRP2 or cMOAT, also named as ABCC2). Several transporters in the cell membrane help to absorb and distribute the drugs and determine the bioavailability of orally taken drugs (Yoshida, Maeda and Sugiyama, 2013).

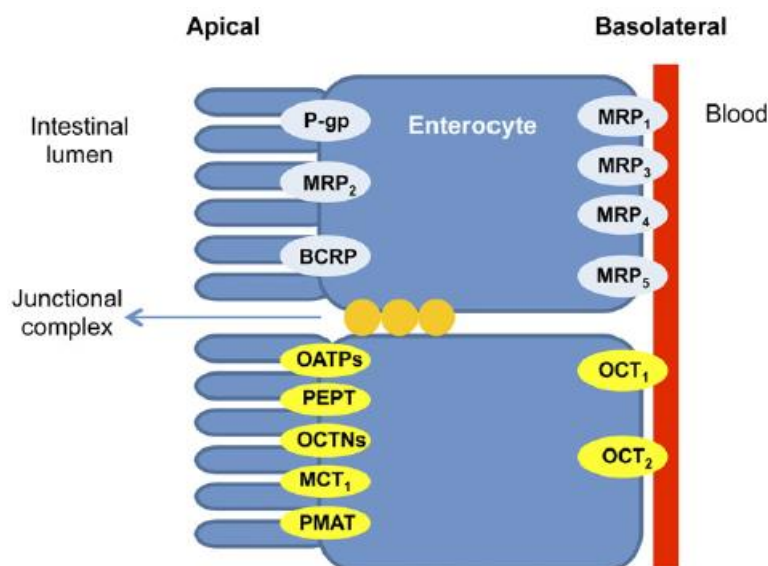


Figure 19: Important drug transporters expressed at the intestinal epithelium. Coloured in yellow are the uptake transporter and in light blue the efflux transporter. MDR1 (P-glycoprotein), MRP, BCRP, monocarboxylate transporter protein (MCT), peptide transporter protein (PEPT), organic anion transporting polypeptide (OATP), organic cation transporter (OCT), carnitine/organic cation transporter (OCTN), and plasma membrane monoamine transporter (PMAT) (Estudante *et al.*, 2013).

And major basolateral transporters are the multidrug resistance protein 1 (MRP1 or ABCC1), MRP3 (or ABCC3), MRP4 (or ABCC4), MRP5 (or ABCC5), OCT1 (also named SLC22A1) and OCT2 (or SLC22A2).

After drug uptake the drugs gets metabolized via several enzymes. The small intestine is the first site of drug metabolism of orally taken drugs. The main present CYPs in the human intestine are CYP3A4, 2C9, 2C19 (Obach *et al.*, 2001), 1A1, 1B1, 2D6, 2E1, 3A5 (Kaminsky and Zhang, 2003; Galetin and Houston, 2006) and 2J2 (Galetin and Houston, 2006). These CYPs can eliminate a large part of orally taken drugs before they reach the systemic circulation, which can have a high impact on their bioavailability.

#### 1.4. Toxicology of the gastrointestinal tract

Not only the development of intestinal toxicity but also the important role of the intestine and the impairment of health and well-being of the patients leads to the fact that the gastrointestinal tract is increasingly investigated during drug development (Rodrigues *et al.*, 2019). Since most drugs are taken orally and absorbed through the GI tract, most of them also cause moderate to severe side effects (Zentler-Munro and Northfield, 1979). Either one part or the entire GI tract can be affected by drug toxicity. Drug-induced toxicity can manifest itself in a variety of clinical symptoms. From the one hand the very harmless, but very common and benign drug-induced diarrhea to the other end to serious side effects such as fatal bleeding or perforation of the GI tract (Pusztaszeri, Genta and Cryer, 2007). Symptoms can vary from constipation due to anticholinergic medication to tissue toxicity and damages following NSAID treatment or changes in gut microbiota following antibiotic treatment with subsequent infection (Philpott *et al.*, 2014). In total 20-40% of all appearing drug side effects show up in the small and large intestine (Zeino, Sisson and Bjarnason, 2010). In 2006 the Medical Subject headings introduced the term “mucositis” as a keyword for intestinal damage by xenobiotics and therapeutics. The main problems arise from the destruction of the mucous membrane and the loss of mucosal integrity. Drug toxicity can emerge due to direct therapeutic action or related to direct mucosal destruction (Panarelli, 2014). But overall, GI toxicity manifests itself in several pathophysiological mechanisms (Figure 20). For example, it may affect enzyme release or activation, directly affect the cell membrane, affect mucosal proliferation or intracellular signal transduction and even many more (Gelberg, 2018).

<i>Mechanisms</i>	<i>Examples</i>
Direct effects on cell membrane	Plant lectins, alcohol, NSAIDs, bile acids, sodium chloride
Stimulation of mucosal proliferation	Dioxins, aromatic hydrocarbons, pancreatic enzyme preparations, alcohol
Inhibition of mucosal proliferation	Anticancer drugs
Nerve damage	Surfactants, capsaicin
Reduced blood flow	NSAIDs, alcohol
Activation of emetic pathways	Anticancer agents, 5-HT, dopamine
Disruption of intracellular signal transduction	Cholera toxin
Release of regulatory substances	Antigens, endotoxins, inflammation. NSAIDs
Generation of oxygen free radicals	NSAIDs, laxatives, lipid hydroperoxides, inflammatory responses
Chemotaxis and activation of granulocytes	Endotoxins, antigens
Release of enzymes	Endotoxins, antigens, cytokines
Activation of enzymes	Cholera toxin, nitric oxide
Inhibition of enzymes	NSAIDs, AChE pesticides
Increase susceptibility to H <sup>+</sup>	NSAIDs
Intracellular toxicity	Heavy metals

Figure 20: Overview of the pathophysiological mechanism of gastrointestinal toxicity (Gelberg, 2018)

---

## 1.5. Compounds that affect the GI tract

### 1.5.1. Chemotherapeutics

Unfortunately, when taking chemotherapeutic agents for the treatment of cancer, severe side effects often occur in the GI tract. Adverse effects during taking chemotherapeutics include alopecia, infertility, sterility, nausea, and vomiting (Amjad, Chidharla and Kasi, 2021). Beside these effects some others like diarrhea, pain, constipation, weight loss or infections can occur (Lee, Ryan and Doherty, 2014; McQuade *et al.*, 2016; Forsgård *et al.*, 2017). Constipation and diarrhea are often the reasons for reducing the treatment concentration of chemotherapeutic agents or even discontinuing the treatment. In recent years, chemotherapy has been greatly improved and the survival of patients with some cancer diagnoses has increased enormously. The goal of chemotherapy is to inhibit tumor growth and thereby the proliferation and multiplication of tumor cells. Chemotherapeutics interfere either with DNA and RNA or protein synthesis or affecting the function of the target molecules. All lead to cell death of the tumor cells due to the direct effect of the chemotherapeutic agent or the activation of apoptosis (Amjad, Chidharla and Kasi, 2021). However, the main problem with chemotherapy is the generally cytotoxic effect of the drugs (McQuade *et al.*, 2016). Chemotherapeutics cannot distinguish between healthy tissue and tumor tissue (Mitchell, 2006). In particular, the very rapid cell renewal of enterocytes and the high metabolic activity in the intestine make the GI tract very susceptible to drug-induced damage.

### 5-Fluorouracil (5-FU)

5-FU, a Fluoropyrimidine, was introduced to the market in 1962 by the pharmaceutical company Hoffmann-La Roche. It is an antimetabolic chemotherapeutic agent which is widely used in the treatment of cancers, including breast and colorectal cancers (Longley, Harkin and Johnston, 2003) later also for the treatment of neck or head cancer (Zhang *et al.*, 2008). Due to its heterocyclic aromatic organic structure 5-FU is very similar to the pyrimidine molecules of DNA and RNA. It is an analogue of uracil. That's why 5-FU interacts with nucleoside metabolism due to its structure and can be incorporated into DNA or RNA. 5-FU is converted to fluorodeoxyuridine monophosphate and then forms a stable complex with thymidylate synthase (TS). TS can then inhibit deoxythymidine monophosphate production which is essential for DNA replication and repair. This leads to cytotoxicity and cell death. A major part of 5-FU catabolism (> 80 %) is run by an enzyme called dihydropyrimidine dehydrogenase which is abundantly expressed in the liver. The remaining 20 % act through fluorouridine triphosphate and fluorodeoxyuridine monophosphate and induce the inhibition of DNA and RNA synthesis, which in turn is responsible for cell death (Song, Park and Sung, 2013).

---

Some cells have developed ways to overcome the effect of 5-FU. They developed a resistance against the drug e.g. due to the polymorphic TS gene promotor which means high TS expression leads to a poor response to 5-FU-based therapy (Longley, Harkin and Johnston, 2003). The hydrophilic drug 5-FU has a low oral and rectal absorption which can be improved by a prodrug (Buur *et al.*, 1996). If 5-FU is used in combination with irinotecan or oxaliplatin the response rates increases from around 10% to 60% (Noordhuis *et al.*, 2004; Zhang *et al.*, 2008).

But the use of 5-FU also shows often intestinal injury, such as epithelial ulceration in the mucosa (mucositis) which manifests mainly in pain and dyspeptic syndromes and inflammation due to cytokine participation (Soares *et al.*, 2013). As well as damage of intestinal barrier function, reduced enterocyte proliferation and crypt cell apoptosis is observed. After treatment with 5-FU, around 80% of patients have reported gastrointestinal mucositis (Song, Park and Sung, 2013). In pre-clinical experiments with colon and small intestinal organoids a high concentration (1000  $\mu$ M) of 5-FU leads to cell death, decreased organoid size, change in morphology and increased caspase 3/7 activity. Additionally cell cycle related genes are downregulated (Rodrigues *et al.*, 2021).

### **Gefitinib (Gef)**

Gefitinib, also known under the brand name Iressa (AstraZeneca), is used for the treatment of metastatic non-small-cell lung cancer (NSCLC). It was the first commercially available tyrosine kinase inhibitor of the epidermal growth factor receptor (EGFR) (Frampton *et al.*, 2004). EGFR is highly expressed in many human tumors, has an intracellular domain and an extracellular ligand-binding domain (Knight *et al.*, 2004). After ligand binding and receptor dimerization the tyrosine kinase gets activated which leads to a signal-transduction cascade which is involved in survival, apoptosis, invasion and metastasis, angiogenesis and cell proliferation (Muhsin, Graham and Kirkpatrick, 2003). Gefitinib is used as monotherapy after failure of chemo- and platinum-based therapies. Gefitinib has shown in *in vitro* tests a potential to inhibit the cardiac action potential repolarization process, but this could not be seen as causal association in clinical trials. GI related effects could not be seen in pre-clinical trials (Emc, 2021).



---

### **Irinotecan hydrochloride (Irino)**

Irinotecan hydrochloride is a semisynthetic derivative of camptothecin, an active agent from the plant *Camptotheca acuminata* (Alimonti *et al.*, 2004; Fujita *et al.*, 2015). In 1994 it was approved in Japan for the treatment of ovarian, cervical and lung cancer (Fujita *et al.*, 2015, 2016).

A major side effect of Irinotecan medication is diarrhea. Two types of diarrhea are common, early onset diarrhea which occurs within several hours during administration and late onset diarrhea which mainly resulted from direct toxicity (Lee, Ryan and Doherty, 2014). Further very common undesirable effects are vomiting, nausea, abdominal pain and constipation (Emc, 2018). The main gastrointestinal toxicity is due to the OATP1A2-mediated accumulation of the activated metabolite SN-38 in the enterocytes (Fujita *et al.*, 2016). SN-38 inhibits the DNA topoisomerase I by inducing irreversible DNA damage in tumor cells and accumulates in the intestinal mucosa (Lee, Ryan and Doherty, 2014). In pre-clinical experiments it could be shown that Irinotecan has mutagenic potential. Irinotecan showed in pre-clinical animal experiments with dogs delayed diarrhea which was associated with atrophy and focal necrosis of the intestinal mucosa (Emc, 2018).

### **Oxaliplatin hydrochloride (Oxali)**

The third-generation platinum derivative Oxaliplatin hydrochloride is nowadays a routine cancer therapy, especially for the treatment of advanced colorectal cancer. It is often used in combination with 5-FU (Cassidy and Misset, 2002). It is a modification of the well-known drug cisplatin, which has significant clinical toxicity (Graham, Muhsin and Kirkpatrick, 2004). During oxaliplatin therapy the most common adverse effects are gastrointestinal, hematologic and neurologic toxicity (Cassidy and Misset, 2002). Very common undesirable effects of the GI tract are nausea, diarrhea, vomiting, mucositis, abdominal pain, and constipation. In pre-clinical experiments with mice, rats, dogs and monkeys it could be shown that the bone marrow, the kidney, the testes, the nervous system, the heart and the GI tract showed organ toxicities (Emc, 2019).

### **1.5.2. Nonsteroidal anti-inflammatory drugs (NSAIDs)**

With around 30 million patients taking NSAIDs/day (Gunaydin and Bilge, 2018), they are among the most prescribed medicines in the world (Baigent *et al.*, 2013). Unfortunately, NSAIDs are among the drugs that most frequently correlate with drug-induced GI injury. Intestinal inflammation and increased intestinal permeability are the pathophysiologic components of NSAID enteropathy (Pusztaszeri, Genta and Cryer, 2007). If inflammatory bowel disease is already present and NSAIDs are taken, this often leads to a flare-up of this disease (Leong and Chan, 2006).

---

Known side effects by taking NSAIDs which can be seen frequently in clinical field are cramping, bloody diarrhea, upper abdominal discomfort, central lower abdominal pain, passage of mucus and focal right iliac fossa pain (Leong and Chan, 2006). Perforation, erosion, ulceration and obstruction of the lower GI tract are as well common side effects during taking NSAIDs (Lim and Yang, 2012; Tajima, 2013). The main effect of the NSAIDs occurs by interfering with the defensive properties of the mucosa. Thus, the mucosa is more susceptible to acid in the lumen which has two main complications. First is by increasing drug absorption and second by diffusing from the lumen into the mucosa and this can lead to necrosis or perforation or irritation of the barrier (Cohen, 1988; Ivey, 1988; Scarpignato, 1995). Another site of attack are the cyclooxygenases (COX), which produce prostaglandins that are partly responsible for maintaining barrier integrity. NSAIDs inhibits COX1 and this results in a cessation of prostaglandin synthesis (Owen, no date; Vane and Botting, 1998a, 1998b).

### **Diclofenac sodium (Diclo)**

The globally used active ingredient diclofenac is a nonsteroidal anti-inflammatory drug (NSAID). It is commercially available in various formulations as a gel, oral, intravenous, suppository or as a transdermal patch and nowadays available in approximately 120 countries. Since its introduction Diclofenac is one of the eight largest selling drugs in the world (Shobha Rani, Goundalkar and Prakasam, 1994). Diclofenac is used for the treatment of hyperthermia, chronic and acute inflammation, and pain (Todd and Sorkin, 1988).

Diclofenac is commonly used to treat a variety of acute and chronic pain, for example rheumatic or non-rheumatic conditions. It's mechanism of action is via anti-inflammatory, antipyretics, and analgesic processes (Gan, 2010). The anti-inflammatory effect and some other pharmacological effects are generally assumed to be related to the inhibition of prostaglandin synthesis via the inhibition of COX (Todd and Sorkin, 1988; Gan, 2010). After oral administration diclofenac is absorbed very quickly and efficiently.

A common major side effect of taking diclofenac is bleeding, inflammation and ulceration in the small intestine (Ramirez-alcantara, Loguidice and Boelsterli, 2021). Beside this nausea, vomiting, diarrhea, dyspepsia, abdominal pain are further common side effects. Rare or very rare hemorrhage, gastrointestinal ulcer, colitis, or constipation could be observed. Pre-clinical experiments showed that diclofenac leads to lesions and ulcers in the GI tract but only after high systemic levels after topical application of 1% diclofenac gel (Emc, 2020).

---

### 1.5.3. Anti-diarrheal drugs

Diarrhea can be a side effect of many drugs or several diseases and which is the leading cause of death in children under 5 (Gupta *et al.*, 2015). The pathophysiology of diarrhea manifests itself mainly in reduced absorption efficiency (Schiller, 2017). The typical symptoms of diarrhea are increased water content in the stool and loss of potassium and dehydration in the case of more severe illnesses. In very rare cases the illness can lead to a potentially deadly situation due to electrolyte loss and no nutrient uptake (Drancourt, 2017). The most anti-diarrhetic drugs work through a binding to the opioid receptors and then the release of acetylcholine and subsequently prostaglandins are inhibited which slows down the peristalsis and transit time of stool.

#### **Alosetron hydrochloride (Alo) - Lotronex**

Alosetron is a drug which is used for the treatment of severe diarrhea-predominant irritable bowel syndrome (IBS) which is a common disorder of the large intestine (Camilleri *et al.*, 1999). In 2000 Alosetron was the first drug approved for the treatment of IBS by the FDA (Friedel, Thomas and Fisher, 2001). It is a highly potent 5-HT<sub>3</sub> receptor antagonist and improves abdominal pain and can slow down colonic transit (Camilleri *et al.*, 1999 and Balfour, Goa and Perry, 2000). The 5-HT<sub>3</sub> receptors are localized on sensory neurons or enterochromaffin cells of the mucosa and are responsible for the mediation of motility, bowel function, secretion and perception of pain in the intestine (Camilleri *et al.*, 2001). Due to some reports of severe side effects the drug was voluntarily withdrawn from the market by GlaxoWellcome in the same year as it was approved. Side effects included severe constipation, ischaemic colitis and death (Hyman and Garvey, 2002). In *in vitro* experiments with mice no carcinogenic or genotoxic effect could be found and the fertility and reproductivity was not negatively influenced (Inc., 2008). In 2002 the FDA allowed the reintroduction of Alosetron to the market with more restricted medications (Lucak, 2010).

#### **Loperamide hydrochloride (Lop)**

The first loperamide formulation was first approved in 1976 (Vandenbossche *et al.*, 2010) for the treatment of acute and chronic diarrhea and is well absorbed from the GI-Tract. Loperamide is a nonprescription opioid which changes the transport of water and electrolytes in the intestine by stimulated absorption, and induces the antisecretory action mediated by calmodulin antagonism (Regnard *et al.*, 2011; Miller *et al.*, 2017) and the blocking of intestinal calcium channels (Wu and Juurlink, 2017). By binding to the opioid receptors the release of acetylcholine and prostaglandins are inhibited which slows down the peristalsis and transit time, whereby the antagonistic activity against calcium channels exacerbating this (Miller *et al.*, 2017). Loperamide has a very low bioavailability (0.3%) and that's why there is a very wide margin of safety. The main metabolism takes place by cytochrome P450 3A4 and CYP2C8 in the liver and the intestine. A key factor of the

---

pharmacokinetics of loperamide is the multidrug efflux pump P-glycoprotein (P-gp or MDR1). This active transporter is responsible for the absorption of loperamide and is among others located in the small intestinal epithelium (Wu and Juurlink, 2017). The P-gp/MDR1 pump is responsible for the active efflux of loperamide. When taking loperamide constipation, nausea, vomiting, dyspepsia and abdominal pain are potential known effects which can occur (Emc, 2022).

#### **1.5.4. Other compounds**

Some medications do not show direct GI toxicity but sometimes have mild to severe side effects in the GI tract, which can lead to a significant impact on quality of life.

##### **Flavopiridol hydrochloride (Flavo)**

Flavopiridol is a semisynthetic analog of a natural alkaloid isolated from the leaves and stems of the plants *Amoora rohituka* and *Dysoxylum binectariferum*. It is a potent inhibitor of a wide range cyclin-dependent kinases (CDK) and the first CDK inhibitor to enter clinical trials (Tomaszewski et al., 2002; Cimini et al., 2017). Flavopiridol causes cell cycle arrest and inhibits cyclin dependent kinase 2 (CDK2) and CDK1 (Tomaszewski *et al.*, 2002; Blagosklonny, 2004; Cimini *et al.*, 2017). This results in an cell cycle arrest in G2 to M and G1 to S phases (Ferry and Kerr, 2002). It also has anticancer effects due to the induction of apoptosis of cancer cells or the inhibition of angiogenesis (Cimini et al., 2017). The fact that flavopiridol also inhibits CDK9 and CDK7 explains its characteristic to inhibit transcription, because CDK9 is the transcriptional elongation factor P-TEFb which is essential for the control of RNA polymerase II elongation (Blagosklonny, 2004). In pre-clinical experiments it could be shown that the major toxicity when taking flavopiridol appears in the bone marrow and GI tract in rodents (Kelland, 2005). In clinical trails the dose-limiting toxicity is secretory diarrhea (Innocenti *et al.*, 2000).

##### **Terfenadine (Terf)**

$\alpha$ -(4-tert-butylphenyl)-4-( $\alpha$ -hydroxy- $\alpha$ -phenylbenzyl)-1-piperidine butanol, also known as Terfenadine (Kulshrestha *et al.*, 1978) was first approved in 1985 for the treatment of allergic reaction, especially to relieve symptoms of allergic rhinitis (World Health Organization, 1997). Terfenadine is a selective second-generation H<sub>1</sub>-histamine receptor antagonist. It works as a competitive inhibitor of histamine, which plays an important role in allergic responses (McTavish, Goa and Ferrill, 1990; Desager and Horsmans, 2012). Compared to other antihistamines it has no effect on the central nervous system (Kulshrestha *et al.*, 1978). An adverse side effect of terfenadine is the occurrence of prolongation of the QT interval and the development of torsades de pointes which often leads to fatal ventricular arrhythmia (DuBuske, 1999). Other side effects

are confusion, fatigue, dizziness, insomnia, headache, depression, drowsiness, muscle tremors and gastrointestinal problems (Nonnenmacher, 2021). Pre-clinical experiments showed that terfenadine is relative nontoxic for animals (Gibson, Huffmann and Newberne, 1982). But due to it's potential to prolongate the QT interval the WHO formulated an alert to non-use of terfenadine and suggested to withdraw this drug from the market and use an alternative since 1997. The FDA received reports of severe and fatal cardiac side effects at the time (World Health Organization, 1997).

### 1.6. Intestinal *in vitro* models

Due to rising average age and increased incidence of serious diseases and cancers, more and more medicines are needed which need to be developed (Zeino, Sisson and Bjarnason, 2010). In addition, more and more complex drugs are coming onto the market, which often lead to undesirable and unexpected side effects (Leong and Chan, 2006). Therefore, the desire for more predictable models, including cell culture models, is becoming stronger and stronger, and more and more is being invested into their development and research.

To best reflect the *in vivo* situation of the GI tract in a cell culture model, various parameters should be fulfilled as far as possible in any *in vitro* system. Some of these physiologically relevant parameters are listed in Table 3. The cell culture material needs to be flexible to provide cycle deformation to the cells around 8-10% strains at 0.15Hz. The stiffness should be around 0.5-1 kPa to simulate native lamina propria in terms of chemical composition and biochemical behaviour. And to mimic fluid shear stress to the cells around 0.0002- 0.009 Pa should be provided (Costa and Ahluwalia, 2019).

Table 3: Overview of the most important physiologically parameters of gastrointestinal cell culture models (Costa and Ahluwalia, 2019 modified).

Stiffness	Shear stress	Strain	Villi	Cell types
0.5-1 kPa	0.0002-0.008 Pa	8-10 % at 0.15 Hz	Density: 10-40 mm <sup>2</sup> Height: 0.5-1 mm	Goblet cells Stem cells Enterocytes Enteroendocrine cells Paneth cells M cells Tuft cells

---

In addition, a main need in such cell culture models is that they should be able to recapitulate the main function of the cells by for example secreting enzymes or signals and the interaction of cells with each other. Further needed characteristics are to include an extracellular matrix which forms a microenvironment for the different cell types, to add a flow which can mimic mechanical stress and stimulation to the cells.

Several *in vitro* models to study toxic effects of new drug candidates have been developed and are available. Unfortunately, not all these parameters are fulfilled in each cell culture system. One of the most widely used and accepted cell culture models for the intestinal is the use of Caco-2 cells, but not for the evaluation of toxic effects so far.

### **Caco-2 cell line**

The cell line Caco-2 (Cancer coli) was isolated from a human colon adenocarcinoma for the first time in the 70's (Figure 21). These cells express morphological and functional characteristics of the differentiated cytotypes of the intestinal mucosa (Sambruy *et al.*, 2001).

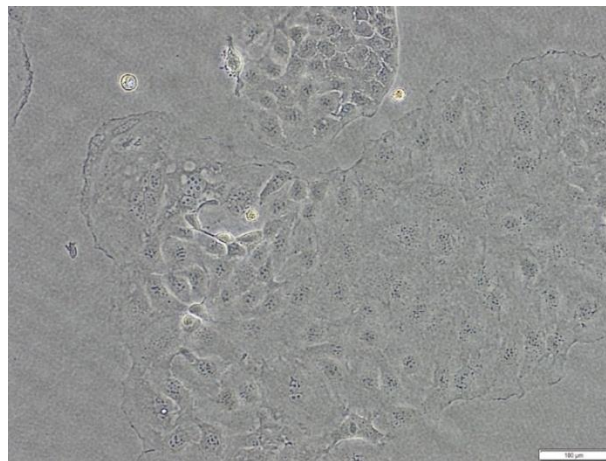


Figure 21: Caco-2 cell culture in cell culture flasks. Bar =100µm

After about three weeks in culture the cells spontaneously differentiate, build confluent monolayers with highly polarized cells, joined via tight junctions, and build apical and basolateral sides with organized microvilli on the apical membrane. Caco-2 cells are well established as an *in vitro* cell culture model of the GI tract, especially for the intestinal barrier (Sambuy *et al.*, 2005). Even though Caco-2 was originally generated from colon, they are physiologically /morphologically more like jejunum. They show typical characteristics of the small intestine, such as the formation of apical brush borders and microvilli on the enterocytes (Ölander *et al.*, 2016) but not all small intestinal functions have been demonstrated to be expressed (Sambruy *et al.*, 2001).

---

Frequent applications of the Caco-2 cells include drug permeability tests, metabolism studies (Hidalgo, Raub and Borchardt, 1989) and the investigation and prediction of intestinal drug absorption (Awortwe, Fasinu and Rosenkranz, 2014). For the investigation and prediction of intestinal drug absorption the Caco-2 cell line is the most common *in vitro* model (Hidalgo, Raub and Borchardt, 1989). Caco-2 cells in culture show intestine specific features. They differentiate to small intestine like enterocytes with well-formed apical brush borders. These cells produce brush border-associated hydrolases (sucrase-isomaltase (SI), lactase, aminopeptidase N, dipeptidyl peptidase IV) which are specific for small intestine and fetal colon and the presence of the Ca<sup>2+</sup> binding protein villin which is an important component of the microvillous in the brush border cytoskeleton (Chantret *et al.*, 1988; Sambuy *et al.*, 2005). Furthermore, it is known that the cells produce some phase I (cytochrome (CYP)) and phase II enzymes (Awortwe, Fasinu and Rosenkranz, 2014)

The benefits of cell lines are that they are immortalized (Maqsood *et al.*, 2013), cheap and easy to handle. The biggest advantage, however, is that they can replicate indefinitely and there are no ethical concerns when using cell lines originally derived from cancer (Kaur and Dufour, 2012). However, the use of cell lines has important limitations, such as lack of appropriate ratio of cell populations or altered expression of transporters and enzymes compared to *in vivo* (Kasendra *et al.*, 2019). In addition, the genetic manipulation of these cells often can have an effect on their phenotype, native functions or their responsiveness to stimuli (Kaur and Dufour, 2012). The cells cannot organize themselves in a 3D environment as it *in vivo*, they cannot interact with other cell types and they have been shown to be poor predictor of cellular toxicity and toxicogenic responses (Rezaee and Abdollahi, 2017). In addition, the cells are cultivated on optimized plastic surfaces. All these properties lead to the loss of physiological functions of the cells (Joseph, Malindisa and Ntwasa, 2019).

2D models do not completely recapitulate the *in vivo* complexity. To mimic better the 3D structure of the organs in the human body 3D cell culture models have been established, which are either spheroids or organoids. These 3D models capture the microarchitecture of the organ better and often include an extracellular matrix that better represents the complex *in vivo* environment and the tissue specific functions (Samy *et al.*, 2019).

## Organoids – *in vitro* mini tissues

The constant and fast renewal of the GI tract is controlled by adult stem cells in the crypts (Merker, Weitz and Stange, 2016). These stem cells can be used as a basis for generating intestinal organoids. The first *in vitro* organoid model was described by Sato et al in 2009. He described a mouse small intestinal organoid model (Sato *et al.*, 2009). Intestinal organoids are advanced *in vitro* models which recapitulate closely the crypt-villus like structures of the intestine and cell differentiation processes (Bardenbacher *et al.*, 2019). These organoids can be generated from induced pluripotent stem cells (iPSCs), which are pluripotent stem cells, and these cells can differentiate into the different cells from the human body (Yin et al., 2016). Three characteristics distinguish organoids from 2D models or 3D spheroids: self-organization, multi-cellularity, and functionality.

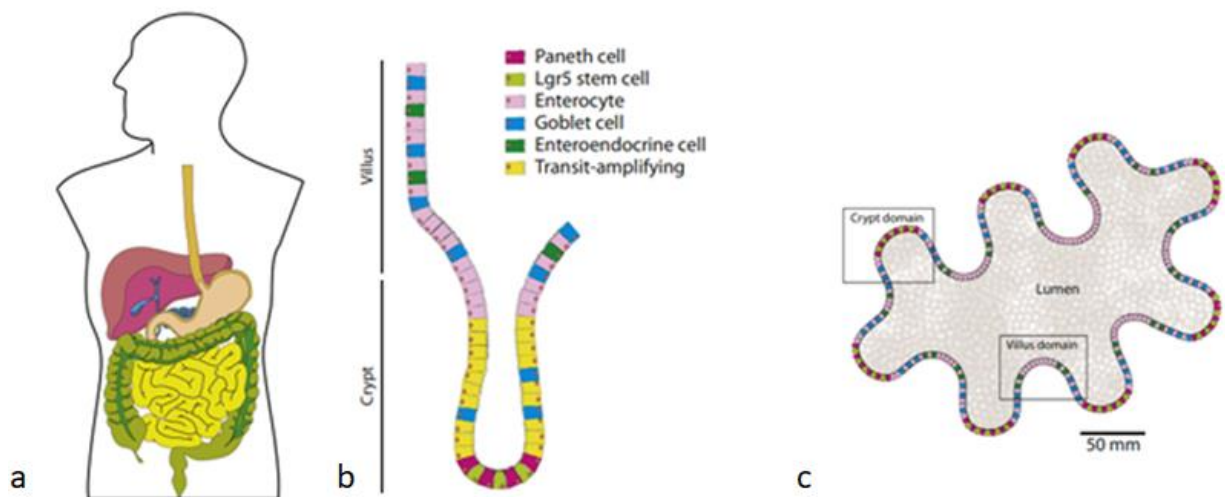


Figure 22: Overview of the GI tract, its cells, and the localization of intestinal cells in an organoid. a.) Schematic overview of the human GI tract and the localization in the body. b.) The functional unit of one crypt and villi structure of the intestinal epithelium. In the crypts base the stem cells are localized which differentiate along the villi axis to transit-amplifying cells (undifferentiated population of cells in transition between stem cells and differentiated cells) and further to goblet, Paneth, enteroendocrine cells and Enterocytes. c.) Schematic outline of an intestinal organoid with the lumen representing the intestine lumen and colored cells represent different cell types (Roeselers *et al.*, 2013).

Each organoid consists of a 3D-fold that encloses a cavity. Intestinal organoids reflect the intestinal crypts, which grow together around a lumen and contain proliferating components at the outside and with mature cells in the middle (Kuratnik and Giardina, 2013) (Figure 22). Beside the clear advantage that organoids can be human derived material they are very costly and time consuming to produce (Kim, Koo and Knoblich, 2020). The 3D structure offers only limited access to the lumen, which is indispensable for the observation of intestinal permeability or drug



---

absorption (Kasendra *et al.*, 2019). Also, heterogeneity of organoids (size, viability, and shape) can impact the reproducibility of results.

### **Organs-on-a-chip – The new promising tool for drug discovery**

Despite all the developments and improvements in testing strategies, experiments or improved cell culture models, there are still lots of medicines that come onto market and show significant side effects or even must be withdrawn from the market. The main problem with commercially available *in vitro* models is the difficulty of mimicking complex cell interactions (Polini *et al.*, 2014).

A promising new tool are the further improved and more complex OoC systems, small microfluidic cell culture systems that attempt to replicate the structure, function, pathology and physiology of human organs (Bein *et al.*, 2018). OoC systems are being developed to recapitulate the dynamics of human organs and their physiological architecture. *In vivo*, nutrients and oxygen get transported via blood flow to the cells and back. A static cultivation of cells in *in vitro* models often the reason for the loss of cellular function (Kimura, Sakai and Fujii, 2018). The most important improvement compared to 3D models is the change from static culture to a fluidic cultivation of cells. This is generated by the integration of microchannels to set up a flow of medium, which mimics the “blood flow”. This is often provided by passive medium transport by changing the inclination of the plate or by an active pumping of the medium through the chip platform.

Compared to commercial 2D models and 3D models the OoC systems can recapitulate the complex human structure of different tissues, by including an ECM, 3D structures, and flow. The big benefit of OoC models is that they can mimic better the complexity of animal or human models by adding a flow and thereby mimic the sheer stress of cells in the human body compared to 2D models. Compared to the animal models they are more controllable than animal models but less to 2D models (Figure 23) (Ma *et al.*, 2021). But the complexity and interaction between the different organs in the body cannot be completely recapitulated and therefore animal experiments will still be needed in the future.

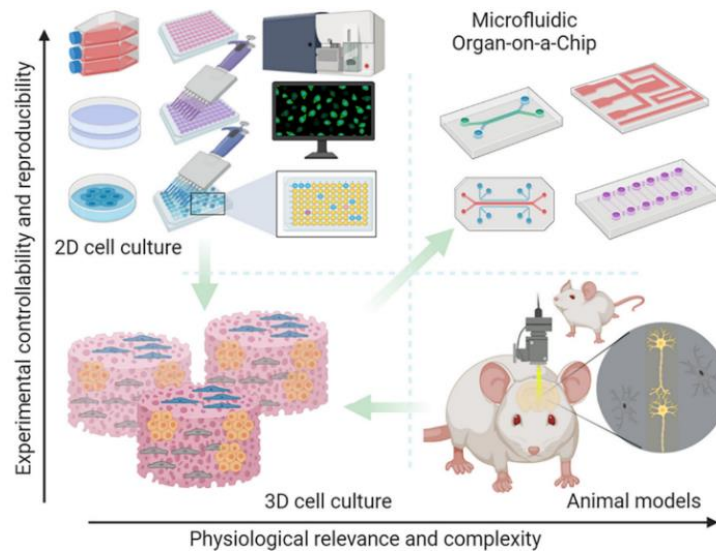


Figure 23: Compared complexity, relevance, controllability, and reproducibility of used in vitro and in vivo models (Ma *et al.*, 2021)

The first concept of OoC system was described in a publication about a “lung-on-a-chip” already in 2010 (Huh *et al.*, 2010; Quan *et al.*, 2020). The OoC systems are ideal to get better insights into mechanisms of drug toxicity and efficacy. They are most stem cell based and reduce the need, costs, time and ethical burden of animal experiments (Mastrangeli and van den Eijnden-van Raaij, 2021). For the intestine some companies, like Emulate and Mimetas, have established specific OoC systems and protocols. These systems work mostly with either stem cells, primary cells, or cell lines. The emulate system for example uses Caco-2 cells in an upper channel in which the cells are seeded on a permeable membrane. On the opposite of the membrane in a bottom channel another cell line (for example endothelial cells) can be added. The emulate system has an external pump and allows to simulate peristalsis by attaching mechanical pressure or traction to vacuum channels beside the cell channels (Bovard *et al.*, 2017; Kasendra *et al.*, 2018; Trantakis, 2018). To improve this system even more scientists developed a protocol which shows the possibility to seed human organoids within the emulate chips (Apostolou *et al.*, 2021). This enables an even more *in vivo* similar model due to the use of stem cell-based organoids compared to cells from a cancer cell line.

Another well-known company which has focused on gut models is Mimetas. They offer a pump and membrane free high throughput chip model based on a 384-well plate (Figure 26). It allows to generate a tubular structure of Caco-2 cells which mimics the tubular structure of the human intestine (Beaurivage *et al.*, 2019; Nicolas *et al.*, 2021). The main benefit of this system is the membrane-free culture of cells, this allows the interpretation of results without skewing the results by membrane characteristics like pore size or coatings (Nicolas *et al.*, 2021).

Nowadays, new companies are emerging every year to develop and marketed their complex cell culture models such as the OoC systems. Some of them are for example TissUse, AlevoliX, Hesperos and inSphero. However, these complex systems need often specific handling and specialized equipments. Together with the mostly high costs these models are at the moment not suitable for high-throughput screening studies of new drug candidates but more beneficial for the mechanistic understanding of biological processes.

### 1.7. The utility of biomarkers

It is not only the cell models that need to be more predictable, but the endpoints which are measured for the assessment of toxic effects need to be improved. In this context biomarkers play an important role. Biomarkers are used to measure biochemical, cellular or molecular alterations in cell culture media, cells, tissues or fluids (Mayeux, 2004). Biomarkers have two main functions, to measure a presence and status of a disease or to measure the response of a drug treatment or assess health risks and toxic potential (Timbrell, 1998). They can be used for diagnostic, monitoring, predictive, prognostic, pharmacodynamic/response, safety and susceptibility/risk of new drugs (Gromova *et al.*, 2020). In each phase of the drug development process biomarkers could help to understand the mechanism of action of drugs or help to select the right dose for clinical trials or even later after drug approval to monitor the therapeutic response (Figure 24).

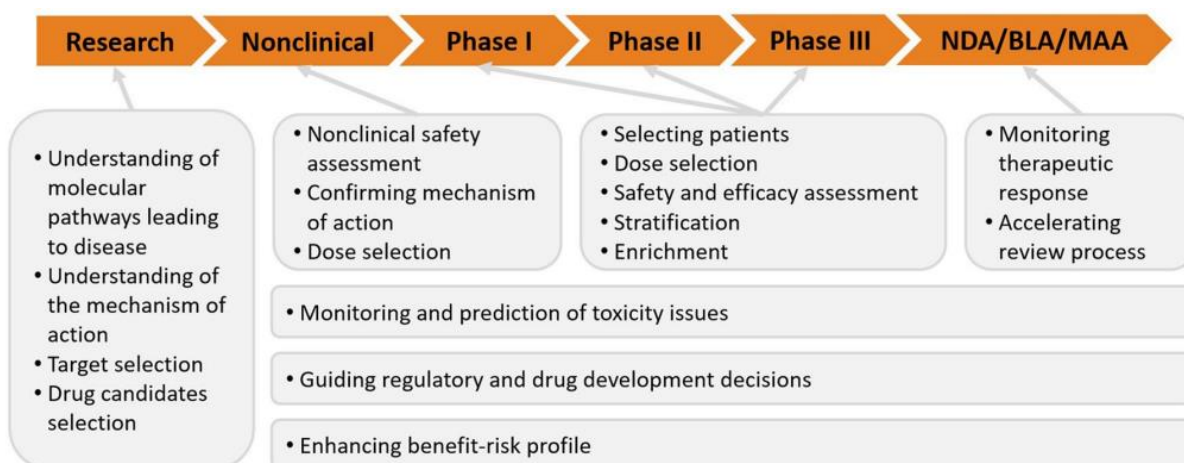


Figure 24: Possible benefits of biomarkers during drug discovery and development phases. (NDA (New drug application (FDA)), BLA (biological license application (FDA)), MAA (marketing authorisation application (EU)) (Gromova *et al.*, 2020).

Normally biomarkers are suitable tools for disease diagnosis or for monitoring for example the response to a specific therapy (Mayeux, 2004; Pletcher and Pignone, 2011). For each part of the human GI tract specific biomarkers are known and used for the diagnosis of specific diseases or injuries. Specifically in very ill patients plays the GI tract plays an important role, because a

dysfunction is often common (Li *et al.*, 2017). Almost 50% of patients in intensive care units show enterocyte damage (Piton *et al.*, 2013). Table 4 shows an overview of well-known and used biomarkers for the different parts of the GI tract. So is for example for the small intestine citrulline or diamine oxidase (DAO) a biomarker for the detection of enterocyte injury, calprotectin, CD64, C-reactive protein, lactoferrin can detect inflammatory processes and Ghrelin can be used to identify gastric acid secretion (Walker *et al.*, 2007, Crenn, Messing and Cynober, 2008, Tillinger *et al.*, 2009, Yang *et al.*, 2011; John-Baptiste *et al.*, 2012, Burri and Beglinger, 2014, Müller *et al.*, 2015, Dragoni, Innocenti and Galli, 2021).

Table 4: List of existing in vivo biomarkers for human intestinal tissues and potential in vitro biomarkers. \* = blood biomarker, ° = fecal biomarker.

<b>Biomarker</b>	<b>Marker of</b>	<b>Tissue specificity</b>	<b>References</b>
Gastrin-17 *	Epithelial mass/health	Esophagus	(Sipponen <i>et al.</i> , 2005)
Eosinophilic cationic protein *	Inflammation	Gastric mucosa	(Aydemir <i>et al.</i> , 2004)
Pepsinogen *	Epithelial mass/health	Gastric mucosa	(Huang <i>et al.</i> , 2015)
Prohepcidin *	Epithelial mass/health	Gastric mucosa	(Kim <i>et al.</i> , 2013)
Vitamin B12 *	Malabsorption	Gastric mucosa	(Schenk <i>et al.</i> , 1999)
Ghrelin *	Motility, gastric acid secretion, gastric emptying	Stomach/small intestine	(Müller <i>et al.</i> , 2015)
Diamine oxidase *	Epithelial mass/health	Small intestine	(Yang <i>et al.</i> , 2011; John-Baptiste <i>et al.</i> , 2012)
Citrulline *	Epithelial mass/health	Small intestine	(Crenn, Messing and Cynober, 2008; John-Baptiste <i>et al.</i> , 2012)
CD64 *	Inflammation	Small/large intestine	(Tillinger <i>et al.</i> , 2009)
C-reactive protein *	Inflammation	Small/large intestine	(Dragoni, Innocenti and Galli, 2021)
Calprotectin °	Neutrophil infiltration/inflammation	Small/large intestine	(Burri and Beglinger, 2014)
Lactoferrin °	Inflammation	Small/large intestine	(Walker <i>et al.</i> , 2007; Dragoni, Innocenti and Galli, 2021)
Bilde acids °	Dysbiosis of gut flora	Small/large intestine	(Duboc <i>et al.</i> , 2012)
<sup>13</sup> C Sucrose	Permeability	Small intestine	(Wardill, Bowen and Gibson, 2013)

Biomarkers show big potential to improve, understand and speed up the drug discovery and development phases (Figure 24) (Gromova *et al.*, 2020). In particular, scientists expect great potential for very early drug development and for translation into clinical application. But so far there is a lack of predictable, sensitive, reliable, and noninvasive biomarkers for the pre-clinical and clinical phases, mostly due to a lack of trustworthy, robust, predictable and *in vivo* similar *in vitro* models (John-Baptiste *et al.*, 2012; Carr *et al.*, 2017). Different potentially novel biomarkers for the assessment of toxic effects in *in vitro* experiments are named in several publications.

Table 5: Potentially novel biomarker for the prediction of drug-induced toxicity of the GI tract in *in vitro* models

Biomarker	Marker of	Tissue specificity	References
miR-194 °	Inflammation	Small intestine	(Wells <i>et al.</i> , 2017; Banerjee and Gupta, 2019; Dragoni, Innocenti and Galli, 2021)
<i>LCN-2</i>	Inflammation	Small/large intestine	(Chassaing <i>et al.</i> , 2012; Abella <i>et al.</i> , 2015; Wells <i>et al.</i> , 2017; Celi <i>et al.</i> , 2019)
<i>FABP-1</i>	Enterocyte injury	Small/large intestine, enterocytes	(Celi <i>et al.</i> , 2019)
<i>FABP-2/I-FABP</i>	Barrier function, intestinal obstruction, cellular damage	Small intestine	(Albala <i>et al.</i> , 2004; Wiercinska-Drapalo <i>et al.</i> , 2008; Banerjee and Gupta, 2019; Wu <i>et al.</i> , 2021)
MLCK	Barrier function	Small/large intestine	(Wells <i>et al.</i> , 2017)
<i>HDC</i>	Mucosal injury	Small/large intestine	(Yang <i>et al.</i> , 2011)
<i>CRP</i>	Inflammation	Small/large intestine	(Dragoni, Innocenti and Galli, 2021)

MicroRNAs are nowadays seen as potential novel biomarker for damage of specific tissues because they are enriched in serum after the damage of these tissues. Specifically, miR-194 is highly expressed in the small intestine. miRNAs are known to play a role in barrier function and can thereby potentially be a good predictive biomarker (Kalabat *et al.*, 2017; Wells *et al.*, 2017; Banerjee and Gupta, 2019). *LCN-2* is widely used as biomarker for kidney injury. Nevertheless, *LCN-2* shows as well potential to detect drug-induced GI inflammations (Chassaing *et al.*, 2012; Abella *et al.*, 2015). Intestinal fatty acid binding protein (*I-FABP* or *FABP-2*) is found without exception only in the enterocytes of the small intestine and is responsible for the absorption of fatty acids (Gajda and Storch, 2015).

---

During inflammation or cellular damage *I-FABP* is released into circulation and its plasma concentration increases, which can be measured and then used as biomarker (Albala *et al.*, 2004; Wiercinska-Drapalo *et al.*, 2008; Banerjee and Gupta, 2019; Wu *et al.*, 2021). Upregulated myosin light chain kinase (*MLCK*) leads to further destruction of the barrier function (Wells *et al.*, 2017) when the barrier is already affected by drugs. This fact leads to the assumption to use *MLCK* as *in vitro* biomarker for the evaluation of barrier function. In 2011 Yang *et al.*, showed that *HDC* can be used as sensitive and specific biomarker for intestinal mucosal injury. The serum level of *HDC* is elevated in patients with intestinal mucosal injury. *CRP* is a widely accepted biomarker for the detection of inflammation. During inflammation *CRP* levels increase (Dragoni, Innocenti and Galli, 2021).

---

## 1.8. Aim of the work

The overall aim of this thesis was to evaluate different cell culture systems (Caco-2 2D, Caco-2 OoC, iPSC derived colon organoids 3D and iPSC derived colon organoids in OoC) for their use in the pre-clinical drug discovery and development. The evaluation involved multiple endpoints for the prediction of potential drug induced gastrointestinal toxicity. This included experiments to characterize these models and evaluate their ability to predict intestinal toxicity.

Therefore, the first aim of this thesis was to focus on the characterization of the used cell culture models. This included experiments for the detection of intestine specific markers and the measurement of the basal expression of proteins and genes. Detection of these markers should be investigated using widefield microscopy, immunofluorescence stainings and gene expression and protein production.

As a second aim, the applicability of the cell culture models to detect toxic effects should be investigated. In order to get an insight into this the cells should be treated with cytotoxic reference compounds and their viability should be checked using a viability assay. To assess the effects of a compound on the intestinal barrier, two different assays should be compared and their relevance evaluated. On the one hand the measurement of Transepithelial electrical resistance (TEER) and on the other hand the permeability of the membrane using a fluorescent dye.

Currently no predictive, sensitive and reliable *in vitro* biomarkers for the prediction of drug-induced gastrointestinal toxicity exist. Which leads to the third aim and the main focus of this thesis which should deal with the research and evaluation of novel potential *in vitro* biomarkers for the prediction of drug-induced gastrointestinal toxicity. As most drug-induced injuries develop after a latency period, the treatment should be performed in a repeated-dose manner. The evaluation of potential biomarkers should be performed by the measurement of gene expression of potential novel genetic biomarkers after 48h of treatment. And beside this the measurement of *in vitro* used biomarkers should be investigated after repeated treatment for 7 days by using a citrulline and calprotectin assay. The statistical analysis should identify a biomarker or a set of biomarkers that differ significantly between cells treated with compounds that induce GI toxicity compared to cells without this treatment.

Finally, in the end it should be demonstrated how the different cell culture models can fit in the drug development process and which of the tested biomarkers demonstrate the suitability for predicting drug-induced GI toxicity.

---

## **1.9. Personal contribution**

This thesis was performed with the goal to establish and characterize different already used cell culture models (Caco-2 2D) and advanced cell culture models (Caco-2 OoC and iPSC derived colon organoids in 3D). To characterize these systems nine different pharmaceuticals (Alo, Gef, Dic, Irino, Flavo, Terf, Lop, 5-FU and Oxali) were used for this thesis. The work on the OrganoPlate® was supported by a cooperation with Mimetas and Millipore. In the following paragraphs a comprehensive overview on my personal contributions is given.

### **Cell culture**

I conducted all the cell culture work, which included coating, cell proliferation and seeding, by myself. Every experiment was prepared and processed by me.

### **Data generation in experiments**

The generated samples of experiments were processed by me. This includes everything except the analysis of the proteomic data. These samples were analyzed by Thomas Wild.

### **Statistical analysis**

Except for the evaluation of the gene expression experiments, which were statistically analyzed by Julian Kreis, I analyzed all other experiments by myself.

### **Biological interpretation of results**

My major task was the biological interpretation of all results of the, IF stainings, transcriptomics, proteomics, TEER and BI assay values, viability experiments and biomarker assays.

### **Further contributions**

I was responsible for data presentation during regular meetings within the cooperation and in inter-group meetings. I have also supported other research groups with questions related to extended cell culture models and performed specific experiments using my cell culture models. Help in writing application notes, preparing posters and presentations for the organoid model.



---

## 2. Material and methods

---

### 2.1. Materials

#### 2.1.1. Cells

<b>Name</b>	<b>Manufacturer, Corporate headquarters</b>	<b>Catalog number</b>
3dGRO™ Human iPSC derived colon organoids	Merck KGaA; Darmstadt, Germany	SCC300
Caco-2 cells	Merck KGaA; Darmstadt, Germany	86010202
SK-Hep-1	ATCC; Manassas (VA), USA	HB-52
Saos-2	ATCC; Manassas (VA), USA	HTB-85
SW480	ATCC; Manassas (VA), USA	CCL-228

#### 2.1.2. Compounds

<b>Name</b>	<b>Manufacturer, Corporate headquarters</b>	<b>Catalog number</b>
5-Fluouracil	Sigma Aldrich; St. Louis (MO), USA	F6627
Alosetron hydrochloride	Cayman Chemicals; Ann Arbor (MI), USA	22434
Diclofenac sodium	Calbiochem; St. Diego (CA), USA	287840
Flavopiridol hydrochloride	Cayman Chemicals; Ann Arbor (MI), USA	10009197
Gefitinib	Cayman Chemicals; Ann Arbor (MI), USA	13166
Irinotecan hydrochloride	Cayman Chemicals; Ann Arbor (MI), USA	14180
Loperamide hydrochloride	LKT Laboratories; St. Paul (MN), USA	L5660
Metformin hydrochloride	Sigma Aldrich; St. Louis (MO), USA	PHR1084
Oxaliplatin	Cayman Chemicals; Ann Arbor (MI), USA	13106
Staurosporine	LKT Laboratories; St. Paul (MN), USA	S7600
Terfenadine	Sigma Aldrich; St. Louis (MO), USA	T9652

---

### 2.1.3. Kits

<b>Name</b>	<b>Manufacturer, Corporate headquarters</b>	<b>Catalog number</b>
CellTiter-Glo® 3D Cell Viability Assay	Promega; Madison (WI), USA	G9681
CellTiter-Glo® Luminescent Cell Viability Assay	Promega; Madison (WI), USA	G7571
FlexMAP™ 3D™ Calibration Kit	Thermo Fisher Scientific; Waltham (MA), USA	F3DCALK25
FlexMAP™ 3D™ Performance Verification Kit	Thermo Fisher Scientific; Waltham (MA), USA	F3DPVERK25
QuantiGene™ human 48-plex kit	Thermo Fisher Scientific; Waltham (MA), USA	customized
QuantiGene™ human 17-plex kit	Thermo Fisher Scientific; Waltham (MA), USA	customized
QuantiGene™ Sample processing Kit, cultured cells	Thermo Fisher Scientific; Waltham (MA), USA	QS0100
QuantiGene™ SinglePlex miRNA	Thermo Fisher Scientific; Waltham (MA), USA	QGSM-200, customized
QuantiGene™ Assay Kit, 2 plate each	Thermo Fisher Scientific; Waltham (MA), USA	QS0008
Homocitrulline/Citrulline Assay Kit	Abcam; Cambridge, UK	ab242292
Human Calprotectin ELISA kit (S100A8/S100A9)	Abcam; Cambridge, UK	ab267628

### 2.1.4. Antibodies, conjugates, and dyes

<b>Name</b>	<b>Manufacturer, Corporate headquarters</b>	<b>Catalog number</b>
Alexa Fluor 488 goat anti-rabbit	Thermo Fisher Scientific; Waltham (MA), USA	A-11008
Alexa Fluor 647 goat anti-mouse	Thermo Fisher Scientific; Waltham (MA), USA	A-21241
Alexa fluor 555 goat anti-rat	Thermo Fisher Scientific; Waltham (MA), USA	A-21434

Alexa Fluor 488 donkey anti-goat	Thermo Fisher Scientific; Waltham (MA), USA	A-11055
Alexa Fluor 790 goat anti-mouse	Thermo Fisher Scientific; Waltham (MA), USA	A-11357
Alexa Fluor 488 Anti-alpha Tubulin	Abcam; Cambridge, UK	ab195887
Anti-BCRP /ABCG2	Abcam; Cambridge, UK	Ab130244
Anti-Claudin 7	Abcam; Cambridge, UK	ab27487
Anti-CDX2	Abcam; Cambridge, UK	ab195007
Anti-CYP2D6	Abcam; Cambridge, UK	ab62204
Anti-CYP3A4	Santa Cruz Biotechnology; Dallas (TX), USA	sc53850
Anti-CYP2C9	Abcam; Cambridge, UK	ab4236
Anti-E-cadherin	Abcam; Cambridge, UK	ab194982
Anti-Ezrin (3C12)	Santa Cruz Biotechnology; Dallas (TX), USA	sc-58758
Anti-GSTA1	Abcam; Cambridge, UK	Ab53940
Anti-LGR5	Abcam; Cambridge, UK	ab75732
Anti-Mucin 5B	Santa Cruz Biotechnology; Dallas (TX), USA	sc21768
Anti-NAT 1/2	Santa Cruz Biotechnology; Dallas (TX), USA	sc-393937
Anti-OATP1A2	Abcam; Cambridge, UK	ab221804
Anti-Occludin	Sigma Aldrich; St. Louis (MO), USA	SAB4200489
Anti-P Glycoprotein	Abcam; Cambridge, UK	Ab3366
Anti-SOX9	Abcam; Cambridge, UK	ab26414
Anti-ZO1 tight junction protein	Abcam; Cambridge, UK	ab96587
Anti-Chromogranin A	Thermo Fisher Scientific; Waltham (MA), USA	MA5-13096
Anti-Cleaved notch1	Cell Signaling; Danvers (MA), USA	4147
Anti-Defensin alpha 5	Novus Biologicals; Centennial (CO), USA	NB110-60002SS

Anti-EpCAM antibody	Thermo Fisher Scientific; Waltham (MA), USA	710524
Fluoresceinisothiocyanat-Dextran (FITC), average mol wt 150,000	Sigma Aldrich; St. Louis (MO), USA	46946
Anti-GATA-4	Santa Cruz Biotechnology; Dallas (TX), USA	sc-25310
Anti-Ki67, Clone MIB1	Dako (Agilent); Santa Clara (CA), USA	M7240
Anti-Lysozyme C	Santa Cruz Biotechnology; Dallas (TX), USA	sc-518012
Anti-MRP2	Thermo Fisher Scientific; Waltham (MA), USA	MA1-26536
Anti-Non-phospho (active) YAP	Cell Signaling; Danvers (MA), USA	29495
Anti-Non-phospho (active) $\beta$ -catenin	Cell Signaling; Danvers (MA), USA	8814
Rhodamine Phalloidin	Thermo Fisher Scientific; Waltham (MA), USA	R415
Anti-SULT1E1	Santa Cruz Biotechnology; Dallas (TX), USA	sc376009
Anti-SYP antibody (Synaptophysin)	Aviva Systems Biology; San Diego (CA), USA	ARP45435_P050
Tetramethylrhodaminisothiocyanat-dextran (TRITC), average mol wt 4,400	Sigma Aldrich; St. Louis (MO), USA	T1037

### 2.1.5. Consumables

Produkt	Manufacturer, Corporate headquarters	Catalog number
3-lane 400 $\mu$ m OrganoPlate®	Mimetas; Oesgstgeest, Netherland	9603-400-B
15 ml tubes	Greiner bioOne GmbH; Frickenhausen, Germany	391-3460
50 ml tubes	Greiner bioOne GmbH; Frickenhausen, Germany	391-3450
24-well cell culture plate, clear	Corning; New York (NY), USA	3524
96-well cell culture plate, black/clear	VWR International GmbH; Darmstadt, Germany	734-2480

96-well cell culture plate, white/clear	Thermo Fisher Scientific; Waltham (MA), USA	165306
Bottle Top Filters, 1000 ml Capacity	Thermo Fisher Scientific; Waltham (MA), USA	597-4520
Cell culture flasks, 75 cm <sup>2</sup> , Cellstar®	Greiner bioOne GmbH; Frickenhausen, Germany	658175
Cell culture flasks, 175 cm <sup>2</sup> , Cellstar®	Greiner bioOne GmbH; Frickenhausen, Germany	660175
Cell culture inserts for 24well culture plate, pore size 0.4µm	Corning; New York (NY), USA	353495
Cell Scrapers	Thermo Fisher Scientific; Waltham (MA), USA	179707
Cell Strainer, 40 µm	Corning; New York (NY), USA	431750
Multipette® tips 1 ml	Eppendorf AG; Hamburg, Germany	613-2061
Multipette® tips 2.5 ml	Eppendorf AG; Hamburg, Germany	613-2062
Multipette® tips 5 ml	Eppendorf AG; Hamburg, Germany	613-2063
Multipette® tips 10 ml	Eppendorf AG; Hamburg, Germany	613-2064
Optifit Tips 0.1-10 µl	Sartorius; Goettingen, Germany	790011
Parafilm® "M" Laboratory Film	Bemis® Company Inc.; Neenah (WI), USA	10018130
Pipette Tips 0.5-10 µl	VWR International GmbH; Darmstadt, Germany	732104
Pipette Tips 2-200 µl	Brand GmbH& Co. KG; Wertheim, Germany	732128
Pipette Tips 5-300 µl	Brand GmbH& Co. KG; Wertheim, Germany	732110
Pipette Tips 50-1000 µl	Brand GmbH& Co. KG; Wertheim, Germany	732112
Optifit Tips 0.1-10 µl	Sartorius AG, Goettingen Germany	790010
Pipette Tips 12.5 µl, sterile filter	Integra Biosciences AG; Zizers, Switzerland	4405

Pipette Tips 125 µl, sterile filter	Integra Biosciences AG; Zizers, Switzerland	4425
Pipette Tips 300 µl, sterile filter	Integra Biosciences AG; Zizers, Switzerland	4435
Pipette Tips 1250 µl, sterile filter	Integra Biosciences AG; Zizers, Switzerland	4445
Safe-lock tubes, 2 ml	Eppendorf AG; Hamburg, Germany	0030120094
Safe-lock tubes, 1.5 ml	Eppendorf AG; Hamburg, Germany	0030120086
Safe-lock tubes, 5 ml	Eppendorf AG; Hamburg, Germany	0030119401
Serological pipettes 1 ml	VWR International GmbH; Darmstadt, Germany	734-0305
Serological pipettes 5 ml	VWR International GmbH; Darmstadt, Germany	734-0313
Serological pipettes 10 ml	VWR International GmbH; Darmstadt, Germany	734-0315
Serological pipettes 25 ml	VWR International GmbH; Darmstadt, Germany	734-0307
Serological pipettes 50 ml	VWR International GmbH; Darmstadt, Germany	734-0314
Transparent Sealing Tape PCR (adhesive)	Biozym Scientific GmbH; Oldendorf, Germany	600228
Whatman 0.2 µm; 7 bar	GE Healthcare Life Science	10462200

### 2.1.6. Reagents and chemicals

<b>Name</b>	<b>Manufacturer, Corporate headquarters</b>	<b>Catalog number</b>
50X Rinse Solution	Zytomed Systems GmbH; Berlin, Germany	ZUC076-500
3dGRO™ Organoid Dissociation Reagent	Merck KGaA; Darmstadt, Germany	SCM300
Acetic acid 96 %	Sigma Aldrich; St. Louis (MO), USA	100062
Alcianblue solution, pH 2.5	Sigma Aldrich; St. Louis (MO), USA	101647

Antibody diluent	Zytomed Systems GmbH; Berlin, Germany	ZUC051-100
Citrat buffer (10x)	Zytomed Systems GmbH; Berlin, Germany	ZUC028-100
Cultrex® 3D Culture Matrix™ rat Collagen	R&D Systems; Minneapolis (MN), USA	3447-020-01
Collagen from rat tail tendon	Sigma Aldrich; St. Louis (MO), USA	11179179001
DEPC treated water	Thermo Fisher Scientific; Waltham (MA), USA	AM9906
Dimethyl Sulfoxide (DMSO)	Sigma Aldrich; St. Louis (MO), USA	D2650
DMEM 4.5 g/L glucose	Lonza; Basel, Switzerland	12-614F
DMEM high glucose W/L-Glutamine W/O Sodium Pyruvate	Biowest; Riverside (MO), USA	L0102-500
DMEM high glucose	Thermo Fisher Scientific; Waltham (MA), USA	41965039
DMEM, high glucose, GlutaMAX™ Supplement	Thermo Fisher Scientific; Waltham (MA), USA	10566016
DPBS, no calcium, no magnesium (DPBS-/-)	Thermo Fisher Scientific; Waltham (MA), USA	14190144
DPBS, calcium, magnesium (DPBS+/+)	Thermo Fisher Scientific; Waltham (MA), USA	14040141
EmbryoMax® 1X Dulbecco's Phosphate Buffered Saline w/o Ca++ & Mg++	Sigma Aldrich; St. Louis (MO), USA	BSS-1006-B
Eagle's Minimum Essential Medium (EMEM)	ATCC; Manassas (VA), USA	30-2003
Ethanol 96%	Merck KGaA; Darmstadt, Germany	159010
Fetal bovine serum (FBS)	Thermo Fisher Scientific; Waltham (MA), USA	10270-106
Formalin solution 4%	Merck KGaA; Darmstadt, Germany	1004960700
Formaldehyde 4%	Sigma Aldrich; St. Louis (MO), USA	100496
Haematoxylin solution Gil III	Sigma Aldrich; St. Louis (MO), USA	105174
Hanks Balanced Salt Solution (HBSS)	Lonza; Basel, Switzerland	10-527

Helipur®	B Braun; Melsungen, Germany	18894
HEPES 1 M	Thermo Fisher Scientific; Waltham (MA), USA	15630106
Hoechst 33342 trihydrochloride, trihydrate 10 mg/ml solution in water	Thermo Fisher Scientific; Waltham (MA), USA	H3570
Human Colon Organoid Expansion Medium	Sigma Aldrich; St. Louis (MO), USA	SCM304
Hydrochloric acid solution	Sigma Aldrich; St. Louis (MO), USA	H9892
Hydrochloric acid 1 mol/L	Sigma Aldrich; St. Louis (MO), USA	109057
Kernel red aluminium sulphate solution 0.1 %	Sigma Aldrich; St. Louis (MO), USA	100121
L-Glutamine	Thermo Fisher Scientific; Waltham (MA), USA	11539876
Laminin Mouse Protein	Thermo Fisher Scientific; Waltham (MA), USA	23017015
Matrigel® Growth Factor Reduced (GFR) Basement Membrane Matrix	Corning; New York (NY), USA	356231
Mc Coy's 5A Medium	ATCC; Manassas (VA), USA	30-2007
Nuclease-Free Water	Thermo Fisher Scientific; Waltham (MA), USA	10793837
PAS staining kit (periodic acid 0.5% aqueous & Schiff reagent)	Sigma Aldrich; St. Louis (MO), USA	1016460001
Permanent AP Red Kit	Zytomed Systems GmbH; Berlin, Germany	ZUC001-125
Probe Equilibrium Buffer pH 1.5 (10x)	Zytomed Systems GmbH; Berlin, Germany	ZUC092-500
Sodium bicarbonate	Sigma Aldrich; St. Louis (MO), USA	S5761
Sodium disulphite	Sigma Aldrich; St. Louis (MO), USA	106528
Sodium hypochloride	VWR International GmbH; Darmstadt, Germany	27896291
Sodium hydroxide solution	Sigma Aldrich; St. Louis (MO), USA	S2770



Penicillin-Streptomycin (10,000 units Penicillin, 10 mg Streptomycin per ml in 0.9 % NaCl)	Sigma Aldrich; St. Louis (MO), USA	P4333
Recovery™ Cell Culture Freezing Medium	Thermo Fisher Scientific; Waltham (MA), USA	12648010
Resazurin	Sigma Aldrich; St. Louis (MO), USA	R7017
Rhodamine Phalloidin	Thermo Fisher Scientific; Waltham (MA), USA	R415
RNAse away	Molecular BioProducts; San Diego (CA), USA	4AJ-6227799
ROCK inhibitor	Sigma Aldrich; St. Louis (MO), USA	Y-27632
Tris-Wash Buffer B, TBS (20x)	Zytomed Systems GmbH; Berlin, Germany	ZUC066-500
Trypanblue-solution	Sigma Aldrich; St. Louis (MO), USA	T8154
TrypLE™ Express Enzyme (1x), no phenol red	Thermo Fisher Scientific; Waltham (MA), USA	12604013
Trypsin-EDTA-solution	Sigma Aldrich; St. Louis (MO), USA	T3924
Triton X-100	Sigma Aldrich; St. Louis (MO), USA	X100
Tween-20 (Polysorbate 20)	MP Biomedicals; Santa Anna (CA), USA	194841
Universal Human Reference RNA	Thermo Fisher Scientific; Waltham (MA), USA	QS0639
Vitronectin Recombinant Human Protein	Thermo Fisher Scientific; Waltham (MA), USA	A14700
ZytoChem-plus AP Polymer-kit	Zytomed Systems GmbH; Berlin, Germany	POLAP-006

### 2.1.7. Instruments & Equipment

Name	Manufacturer, Corporate headquarters	Catalog number
CellInsight CX7 High-Content Screening (HCS) Platform	Thermo Fisher Scientific; Waltham (MA), USA	
Cell counting chamber (Fuchs Rosenthal)	LO-Laboroptik; Lancing, UK	
cellZscope	nanoAnalytics; Muenster, Germany	

Centrifuge 5415 R	Eppendorf AG; Hamburg, Germany	
Eppendorf Pipettes	Eppendorf AG; Hamburg, Germany	
Heraeus®HERAcell®CO <sub>2</sub> incubator	Thermo Fisher Scientific; Waltham (MA), USA	
Heraeus®HERAsafe® Sterile bench	Thermo Fisher Scientific; Waltham (MA), USA	
Heraeus® Megafuge 1.0 R	Thermo Fisher Scientific; Waltham (MA), USA	
IntelliPath FLX Automated Stainer	Zytomed Systems; Berlin, Germany	IPS0001INTL
Microscope Leica DM IL LED Fluo	Leica Microsystems GmbH, Germany	
Microscope camera	Leica Microsystems GmbH, Germany	
MilliQ H <sub>2</sub> O Anlage	Merck KGaA; Darmstadt, Germany	
LUMistar galaxy	BMG LABTECH GmbH; Ortenberg, Germany	
Luminex™ FLEXMAP 3D™ Instrument System	Thermo Fisher Scientific; Waltham (MA), USA	APX1342
Multipette® plus	Eppendorf AG; Hamburg, Germany	
MWG Discovery HT-R	Agilent (prior Bio-TEK Instruments); Santa Clara (CA), USA	
NanoZoomer S210	Hamamatsu Photonics Deutschland GmbH; Herrsching, Germany	
NxGen DC-Modul	Zytomed Systems; Berlin, Germany	DC2012-220V
OrganoTEER®	Mimetas; Oesgstgeest, Netherland	
Pipet boy	VWR International GmbH; Darmstadt, Germany	
QuantiGene™ temperature validation kit	Thermo Fisher Scientific; Waltham (MA), USA	QS0517
Rotary microtome	eica Camera AG, Wetzlar Germany	
Sartorius eLINE® electronic pipette	Sartorius AG, Goettingen Germany	735021
Tecan Infinity F500	Tecan Deutschland; Crailsheim, Germany	

Titramax 101 Shaker	Heidolph Instruments GmbH & Co. KG; Schwabach, Germany	
Ventana Symphony H&E	Roche Diagnostics GmbH; Mannheim, Germany	
VorTemp™ 56 Shaking Incubator	Labnet International Inc., Edison (NJ), US	
Water bath 1002	GFL Gesellschaft für Labortechnik mbH; Burgwedel, Germany	
Weighing machine, special accuracy	Sartorius AG; Goettingen, Germany	
Varoklav Typ 300E	HP-Labortechnik GmbH; Oberschleißheim, Germany	
Vortex mixer	VWR International GmbH; Darmstadt, Germany	444-0996

### 2.1.8. Software

<b>Name</b>	<b>Manufacturer, Corporate headquarters</b>	
GraphPad Prism version 8	GraphPad Software, Inc., La Jolla (CA), USA	
HCI software	Thermo Fisher Scientific; Waltham (MA), USA	
icontrol	Agilent (prior Bio-TEK Instruments); Santa Clara (CA), USA	
ImageJ 1.53c	Wayne Rasband	
LUMIstar Galaxy version 4.30-0	BMG LABTECH GmbH; Ortenberg, Germany	
Microsoft 365 E3	Microsoft; Redmond (WA), USA	
NanoZoomer Digital Pathology Image/ NDP.view2	Hamamatsu Photon is our business; Naka-ku, Japan	
QuantiGene™ Dashboard	Thermo Fisher Scientific; Waltham (MA), USA	
xPONENT® v3.1 Software	Thermo Fisher Scientific; Waltham (MA), USA	
KC4		

---

## 2.2. Methods

### 2.2.1. Cell culture techniques

In the present work different cell culture models of the intestine were used. 2D monolayer, 2D transwell systems, 3D iPSC derived organoids in Matrigel® hemispheres and a micro physiological system (3-lane OrganoPlate® from Mimetas). All the cell culture techniques described below were conducted under sterile conditions. Cell cultures were cultivated in an incubator maintained under a humidified atmosphere of 5 % CO<sub>2</sub> and 37 °C.

### 2.2.2. Caco-2

The Caco-2 cell line is frequently used in research due to its robustness and ease of use. The cells were purchased at ATCC and Sigma Millipore and a large stock was generated in-house to be able to use cells for the experiments with a low passage number. Cells from one vial can be proliferated and frozen again for continuous use. For all experiment's reported here cells between passage 4 and 20 were used.

#### 2.2.2.1. Used cell culture formats for cultivation of Caco-2 cells

The Caco-2 cells were cultivated in two different cell culture formats. On the one hand in transwell inserts (Figure 25a) which generate two compartments, an apical and basal. The cells were cultivated on inserts, which separate these compartments and mimic the intestinal barrier. On the other hand, the cultivation in 3lane OrganoPlates® (Figure 25b). In these plates the cells grow as 3D tubular structure (Figure 26g) through which the medium flows. This mimics the tube formation of the human intestine and the flow of nutrients and xenobiotics.

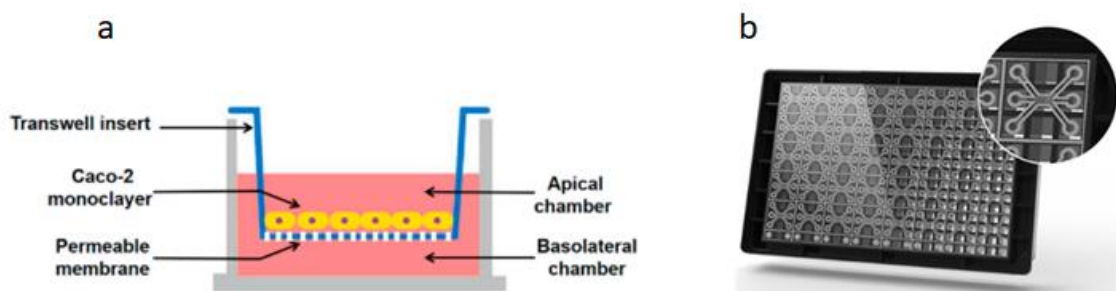


Figure 25: Used cell culture formats for the cultivation of Caco-2 cells. Cultivation of Caco-2 cells on transwell inserts as 2D model (a) and cultivation in 3lane OrganoPlates® as OoC model (b) (Naumovska *et al.*, 2020; Ding *et al.*, 2021).

---

### 2.2.2.2. Coating of 96-well plates, transwell inserts and OrganoPlate®

To obtain a complete differentiation of the Caco-2 cells an extracellular matrix is required (Kleinman *et al.*, 1987). All experiments with Caco-2 cells in 96-well plates and transwell inserts were collagen-coated. By reconstitution of collagen type IV (rat tail) with 0.2 % acetic acid (diluted in Milli-Q water) a stock concentration of 1mg/ml was generated. The collagen stock solution was further diluted to 50 µg/ml with 0.2 % acetic acid. For coating the surfaces, the described volumes in Table 6 were used.

Table 6: Overview of the used volumes of coating solution (50µg/ml collagen in 0.2% acetic acid) for the different cell culture formats

Cell culture surface types	Coating solution [µl]
96-well plates	100
24-well inserts	500

For the experiments in the OrganoPlate® the plates were coated with collagen-I at a concentration of 4 mg/ml. The collagen was prepared on ice by mixing 1 M HEPES, 37 g/L NaHCO<sub>3</sub> and 5 mg/ml collagen I (ratio 1:1:8). Each middle channel of one Mimetas OrganoPlate® chip was filled with 1.7 µl gel and then incubated for 15 min at 37 °C and 5 % CO<sub>2</sub>. After incubation 50 µl HBSS was added into each gel inlet to prevent the gel from drying out.

#### Determination of cell number and cell viability

For the determination of viable cells present in a cell suspension a Trypan blue exclusion assay was performed. Trypan blue cannot pass the cell membrane of vital cells, thus live cells appear white under the microscope and in contrast dead cells are stained blue due to their membrane permeability. 500 µl Trypan blue solution, 500 µl medium and 50 µl cell suspension were mixed. Afterwards, 20 µl of this solution was added to a Fuchs-Rosenthal counting chamber and live and dead cells of at least four of the 16 squares were counted to calculate a mean value. To seed the desired number of cells per well for each experiment, the number of cells per milliliter were calculated.

$$\text{viable cells} \times \frac{\text{dilution factor}}{\text{chamber depth} \times \text{counted area}} = \frac{\text{cells}}{\text{ml}}$$

$$\text{viable cells} \times \frac{21}{0.2\text{mm} \times (16 \times 0.0625\text{mm}^2)} = \frac{\text{cells}}{\text{ml}}$$

$$\text{viable cells} \times 21 \times 5000 = \frac{\text{cells}}{\text{ml}}$$

### 2.2.2.3. Media formulations

Caco-2 from ATCC were used for the cytotoxicity experiments, immunofluorescent stainings and for the TEER measurements. The Caco-2 WT from Sigma were used for all the experiments in the OrganoPlate®, for immunofluorescent stainings, genomics, and proteomics analysis. The formulation of the used media is shown in Table 7.

Table 7: Media compositions for the culture of Caco-2 cells

#### Caco-2 cells

500 ml DMEM 4.5 g/L Glucose

10 % FBS or (20 % FBS, for first 2 weeks after thawing)

1 % L-Glutamine (200 mM)

1 % Pen/Strep (100 U/100 µg/ml)

### 2.2.2.4. Thawing, culturing, and passaging of Caco-2

A cryovial containing 2-3 x10<sup>6</sup> viable Caco-2 cells was taken out of the liquid nitrogen storage tank and transferred into a water bath warmed to 37 °C to thaw the cells until some ice crystals were left. The cell suspension was transferred into 50 ml falcon tubes containing 50 ml prewarmed medium. To get the whole content out of the vial the vial was rinsed with 1ml prewarmed medium. To remove dead cells, cell debris and freezing medium, the cells were centrifuged for 5 min at RT at 260 xg. With 15 ml prewarmed Caco-2 medium the pellet was resuspended, and the solution was transferred into a T175 cm<sup>2</sup> culture flask. The cells were spread evenly by gently shaking of the flask a few times before placing it into the incubator. Cells were left to attach for at least 24 h before medium was renewed to remove unattached cells and residual DMSO from the freezing medium.

Once in culture, the medium was refreshed every 2-3 days. When the cells had reached a confluency of approximately 70-75 %, the cells were passaged by trypsinization. Here, the cells were washed with 10 ml Dulbecco's Phosphate buffered saline (calcium- and magnesium free) (DPBS -/-) and afterwards the growth area was covered with 2 ml of 0.5 g Trypsin/0.2 g EDTA solution. Excess trypsin was removed for a more controllable dissociation of the tight junctions between the cells. The cells were incubated for 8 min at 37 °C and 5 % CO<sub>2</sub> to achieve an optimal trypsinization. Detachment was controlled under a microscope and by knocking on the flask the cells completely detach from the plastic surface. The enzymatic reaction was stopped by adding 10 ml culture medium. To get all cells out of the flask the plastic surface was rinsed with the medium and then transferred via a cell strainer to a 50ml tube. 1.25ml cell suspension and 18.75 ml fresh culture medium were transferred to a new cell culture flask for further cultivation and proliferation of the cells. Generally, Caco-2 were passaged at a ratio 1:8.

#### 2.2.2.5. Seeding of Caco-2 cells

Caco-2 cell culture was conducted using 96-well plates and 24-transwell plates for 2D culture. Table 8 summarizes the cell seeding densities and pre-cultivation duration used for the different cell culture systems.

Table 8: Summary of the seeding densities and pre-cultivation times of caco-2 cells across all used cell culture models

Assay platform	Cell number/well or chip	Pre-culture time before experiment start
96-well plate	0.02x10 <sup>6</sup>	21 days
24-transwell plate	0.5x10 <sup>6</sup>	21 days
OrganoPlate®	0.02x10 <sup>6</sup>	4 days

For the 96-well plates, the calculated cell number was seeded in 100 µl medium per well and for the 24-well plates the cells were seeded in 500 µl medium per well.

For seeding into the OrganoPlate® 2 µl cell suspension was added into the top medium inlet (Figure 26 b, well A1) and afterwards 50 µl medium was added. The OrganoPlate® was placed on its side in the Mimetas plate stand (Figure 26 c) for 4 h in the incubator to allow cells to attach. After the attachment of the cells 50 µl medium was added to the top medium outlet and as well in the inlet and outlet of the bottom channel. Subsequently, the plate was placed on the rocker (Figure 26 d), which was stationed in the incubator. An inclination of 7 ° and an interval of 8 min was set on the rocker, which means that the plate stand moves from right to left every 8 min in an inclination of 7 °.

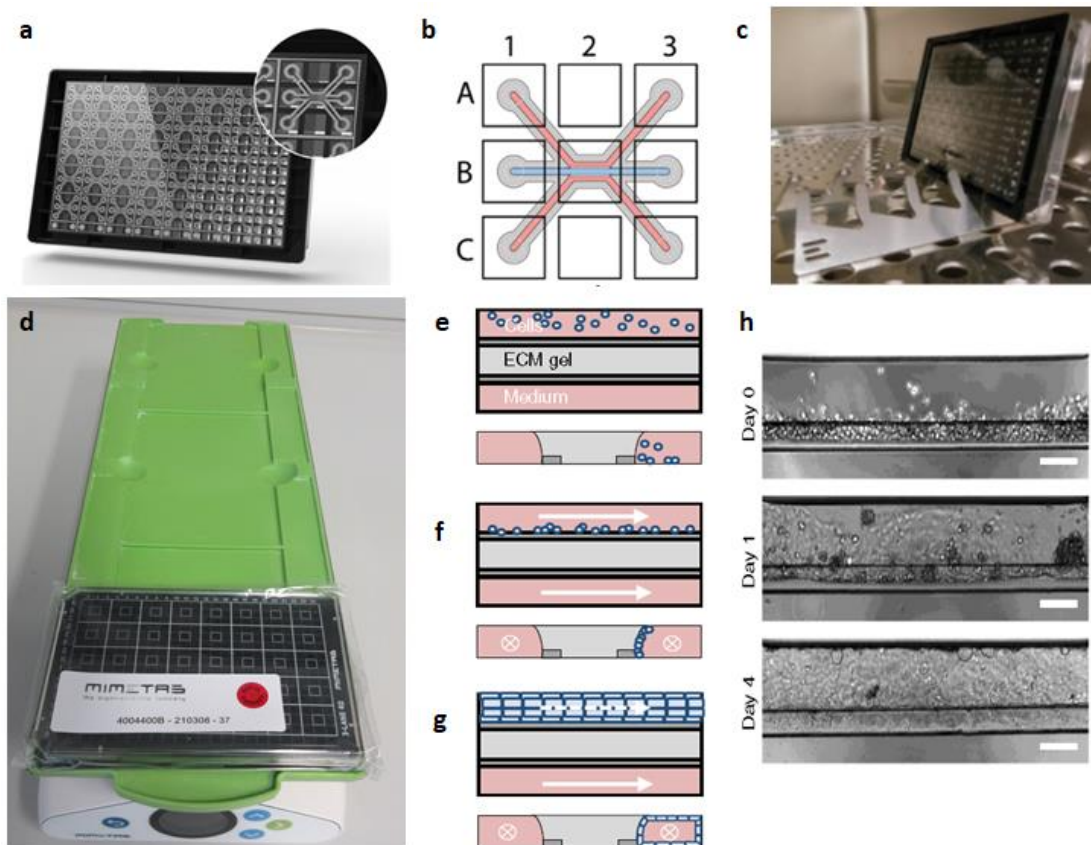


Figure 26: a.) Overview of the 3lane OrganoPlate® in the 384-well format. b.) One chip is composed of nine wells with two perfusion channels (red) and one ECM channel (blue) in the middle, c.) Plate position on a specific plate holder during cell attachment in the incubator, d.) Rocker platform for the cell cultivation, e.) Schematic overview of cell distribution in the perfusion channel directly after seeding, f.) Cell attachment against the ECM channel after, g.) After 4 days of cultivation on the rocker platform the cells are building a tubular structure where the medium flows through, & h.) Microscopic example of cell growing after different time points (Naumovska *et al.*, 2020).

Before starting any experiments each well or chip was checked for correct monolayer/ tube forming and approved as either “valid” or “invalid”. Invalid ones were not used for any experiments.

### 2.2.3. iPSC derived colon organoids

The iPSC derived colon organoids were provided by Millipore Sigma. Two different splitting procedures were performed. The first was used for the proliferation where the organoids stayed as organoids per se, and the second was used for dissociation of the organoids and the seeding as single cells for subsequent experiments.



---

### **2.2.3.1. Determination of cell number and cell viability**

The assessment of the cell culture of organoids was performed after dissociation of organoids into single cells. Therefore, a trypan blue exclusion was performed as already described in chapter (2.2.2.4).

### **2.2.3.2. Media formulations**

For culturing of organoids, a ready to use serum-free medium was used and provided from Sigma Aldrich (SCM304).

### **2.2.3.3. Thawing, culturing, and passaging of iPSC derived colon organoids**

A vial of cryopreserved human colon intestinal organoids contains  $\geq 200$  organoids. The vial was removed from liquid nitrogen and quickly thawed by submerging 3/5 of the vial in a 37 °C water bath. Culture medium was prepared by adding ROCKi Y-27632 at a final concentration of 10  $\mu\text{M}$  to colon expansion medium. ROCKi was added to permit survival of dissociated stem cells. The content of the cryovial was transferred into 4ml prewarmed culture medium and directly centrifugated at 4 °C and 1100 rpm for 5 min. The cell pellet was resuspended in 425  $\mu\text{l}$  Matrigel® Growth Factor Reduced. The solution was carefully pipetted up and down to evenly distribute the organoids. 25  $\mu\text{l}$  organoid-Matrigel® solution was seeded in each well of a 24-well plate and incubated for 10 min at 37 °C and 5 % CO<sub>2</sub> to harden the Matrigel® before 700  $\mu\text{l}$  medium with 10  $\mu\text{M}$  ROCKi was added to each well. One day after seeding the medium was changed with freshly added 10  $\mu\text{M}$  ROCKi. For the further cultivation ROCKi was not necessary.

### **2.2.3.4. Culturing and passaging of iPSC derived colon organoids**

Between 10-14 days after thawing the cells were ready for splitting and further proliferation. Since the organoids are growing in 24-well plates in 3D Matrigel® hemispheres, small Matrigel drops forming a hemisphere in which the organoids grow, (Figure 27) the medium exchanges every 2-3 days was performed by easily aspirating the medium and replacing it with fresh media.

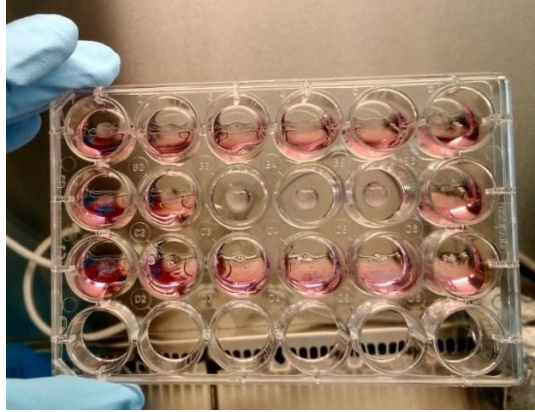


Figure 27: Cultivation format of colon organoids in Matrigel® hemispheres in 24-well plates.

After 10 days growing the organoids were split by aspirating the media and dispense 1 ml DPBS-/- in one well. By pipetting the DPBS-/- up and the down the Matrigel® was dissolved and the organoid-Matrigel®-DPBS-/- solution from 4 wells was combined and transferred into a 15 ml Falcon. After centrifugation at 4 °C and 1500 rpm for 5min the pellet was resuspended with 1ml dissociation reagent, mixed very briefly and an additional 4 ml dissociation reagent was added. The solution was incubated for 10min at RT on a shaker. Afterwards the solution was centrifuged again and followed by a washing step with 1 ml DPBS-/- and then a last centrifugation step. The organoid pellet was then resuspended in 425 µl ice cold Matrigel® and in each well of a 24-well plate 25 µl Matrigel®-organoid hemispheres were pipetted. During a 10 min incubation in the incubator the Matrigel® hardened and 700 µl medium with 1X ROCKi per well was added. One day after seeding the medium was changed with freshly added 10 µM ROCKi. For the further cultivation ROCKi was not necessary.

For the different experiments the organoids were dissociated into single cells, and this enabled accurate quantitative counting and seeding.

#### **2.2.3.5. Single cell passaging of organoids**

For organoid dissociation, which is needed to determinate the cell number for seeding, the medium was aspirated from each well containing the organoid-Matrigel® hemisphere. With 1 ml DPBS-/- the hemispheres were pipetted up and down to break them up and release the organoids. The organoid suspension from a maximum of 10 wells was combined in a 15 ml falcon tube and centrifugated at 1500 rpm for 5 min at 4°C. The centrifugation step with 1 ml fresh DPBS-/- was repeated several times until the supernatant was clear and the Matrigel® completely removed. Subsequently, the supernatant was carefully aspirated and 1ml TrypLE Express with 10 µM ROCKi

was added, and the pellet resuspended by pipetting up and down 10 times. An additional 2 ml of TrypLE express was added and then the solution was incubated for 15 min at 37 °C.

After 15 min the solution was checked to see if organoids were dissociated into single cells. If the organoids were not dissociated the solution was briefly mixed with a pipette and further 5 min of incubation. This step was repeated several times until the organoids could be observed under a hemocytometer as single cells. Immediately thereafter, 5 ml of medium containing 10 µM ROCKi was added twice and then centrifuged at 1500 rpm for 5 min at 4 °C to remove residual TrypLE Express. As a last step 5ml of medium with 10 mM ROCKi was added, and the cell number was determined by trypan blue exclusion under a hemocytometer. After counting the cells were centrifuged for a last time, the supernatant was discarded and an appropriate volume of thawed ice-cold Matrigel® + 10 µM ROCKi was added to the cell pellet. For the first 5days after single cell passaging the medium needs to be added with 10 µM ROCKi to avoid cell dedifferentiation. The cell densities for the different experiments are summarized in the Table 9.

Table 9: Seeding densities of single-cell organoids for the experiments in 96-well plates

Assay platform	Cell number	Pre-culture time before experiment start
96-well plate	0.02x10 <sup>6</sup> / 5 µl Matrigel® hemisphere	6 days

### 2.2.3.6. Implementation of organoids into OrganoPlate®

To obtain an even more complex and *in vivo* like cell culture model, an experiment was made to incorporate the colon organoids into the organ on a chip platform of Mimetas. Therefore, the organoids were dissociated to single cells according to the following protocol.

Before the cells were seeded as a first step the middle channel was coated with collagen I, as described in chapter 2.2.2.5. Before the cells were seeded, the cell channel (top channel) was coated. For this, different coatings were used. The different coatings, seeding densities and attachment times are listed in Table 10.

Table 10: Overview of the tested seeding densities, coating solutions and attachment times for the implementation of organoids into the OrganoPlate®

Attempt #	Coating middle channel	Coating top channel	Seeding density / chip	Attachment time
1	Collagen [4mg/ml]	Vitronectin [1.5µg/ml]	20.000, 40.000, 50.000	4h, 6h, 24h
2	Collagen [4mg/ml]	Laminin [1.5µg/ml]	20.000, 40.000, 50.000	4h, 6h, 24h
3	Collagen [4mg/ml]	Matrigel® [50µg/ml]	20.000, 40.000, 50.000	4h, 6h, 24h
4	Collagen [4mg/ml]	Collagen [25µg/ml]	30.000	4h, 24h
5	Collagen [4mg/ml]	Geltrex [100µg/ml]	30.000	4h, 24h

Different procedures were carried out for each coating. Vitronectin (5 µg/ml) was diluted with DPBS -/- to the desired concentration (1.5 µg/ml) and then 1.7 µl coating solution was added. The OrganoPlate® was then transferred in the incubator (37 °C) for 1h to let the vitronectin harden. For the coating with Matrigel®, Matrigel® (8 mg/ml) was diluted with DPBS -/- to 50 µg/ml and then incubated for 10 min at 37 °C. The laminin working solution (1.5 µg/ml) was prepared by adding DPBS-/- to the 1.2 mg/ml stock. For curing of the coating, the OrganoPlate® was stored at RT for 1 hour. For the coating with collagen the solution was prepared by adding 1 M HEPES, 37 g/L NaHCO<sub>3</sub> and Collagen I (ratio 1:1:8). The coating was added into the plate and then incubated for 15 min at 37 °C. After coating, the cells were dissociated (described in chapter 2.2.3.5.) and then seeded into the OrganoPlate®.

#### 2.2.4. Compound concentrations

In this study, nine well-known compounds at various concentrations, one positive control (Staurosporine) and one negative control (Metformin hydrochloride) were used. For the cell viability assessment, a dose range of each compound was used and is listed in Table 11. The compounds and concentrations for each experiment are listed in the respective subchapters of the results and discussion section. Compound concentrations for each experiment were defined depending on the compound specific EC<sub>50</sub> values and as well on experimental duration and setup.

Table 11: Overall compound concentrations that were used in this study.

Compound	Dose range [ $\mu\text{M}$ ]	Solvent
Alosetron hydrochloride	0.1-0.3-1-3-10-30-100- 200	Caco-2 medium
5-Fluorouracil	0.1-0.3-1-3-10-30-100-300	DMSO
Diclofenac sodium	0.1-0.3-1-3-10-30-100-300	DMSO
Flavopiridol	0.1-0.3-1-3-10-30-100-300	DMSO
hydrochloride		
Gefitinib	0.1-0.3-1-3-10-30-100-300	DMSO
Irinotecan hydrochloride	0.1-0.3-1-3-10-30-100-300	DMSO
Loperamide	0.1-0.3-1-3-10-30-100-300	DMSO
hydrochloride		
Metformin	750	Caco-2 medium
Oxaliplatin hydrochloride	0.1-0.3-1-3-10-30-100-300	DMSO
Staurosporine	0.1-0.3-1-3-10-30-100-300	DMSO
Terfenadine	0.1-0.3-1-3-10-30-100-300	DMSO

### 2.2.5. Widefield microscope

During the cultivation of cells, the morphology, tube formation, 3D structures and growth was visualized by a widefield microscope. In addition, potential contaminations could be detected.

### 2.2.6. Cell viability

For the evaluation of a potential cytotoxic effect of compounds, the cell viability was determined after exposing the cells to a range of concentrations of the test compounds. The cell viability of iPSC derived colon organoids was assessed by using the CellTiter-Glo® 3D assay and the viability of Caco-2 was determined with the CellTiter-Glo® assay and the Resazurin assay.

#### 2.2.6.1. CellTiter-Glo® assay

The concentration of adenosine triphosphate (ATP), an indicator for metabolic active cells, was determined by using the CellTiter-Glo® Luminescent Cell Viability assay. The assay is based on a luminescence reaction of beetle luciferin which is converted to light-emitting oxyluciferin by Ultra-Glo™ recombinant Luciferase in the presence of oxygen, magnesium, and ATP (Figure 28). The total amount of ATP in the cells is measured by a luminescent signal which is directly proportional to the ATP amount and consequently to the number of viable cells.

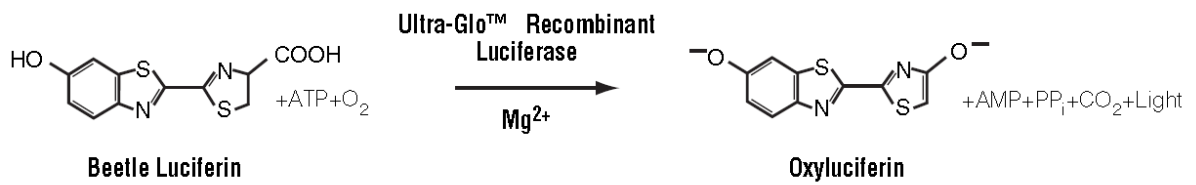


Figure 28: Principle of CellTiter-Glo® (Promega, 2015)

First the culture medium was removed from the cells then CellTiter-Glo® reagent was mixed 1:2 with fresh culture medium and added on top of the cells to lyse them. The respective volumes are recorded in the Table 12. According to the manufacture's protocol the plate was incubated for 2 min in the dark while shaking and afterwards for an additional 10 min without shaking. Luminescence signal was measured with a luminometer.

For the different cell culture models different volumes of CellTiter-Glo® was used (Table 12).

Table 12: Cell culture model specific differences for viability measurements using CellTiter-Glo®

Cell culture model	CellTiter-Glo® kit	Volume [µl]
Caco-2 (2D)	CellTiter-Glo®	50 (for one well of a 96well plate)
Organoid (3D)	CellTiter-Glo® 3D	100 (for one well of a 96well plate)
Caco-2 (OoC)	CellTiter-Glo® 3D	100 (for one chip of the OrganoPlate 3-lane)

### 2.2.6.2. Resazurin assay

A further method to measure viability was the Resazurin or Alamar blue assay. It is based on the reduction of the blue, non-fluorescent resazurin into pink and fluorescent resorufin in the reducing environment of viable cells (Figure 29).

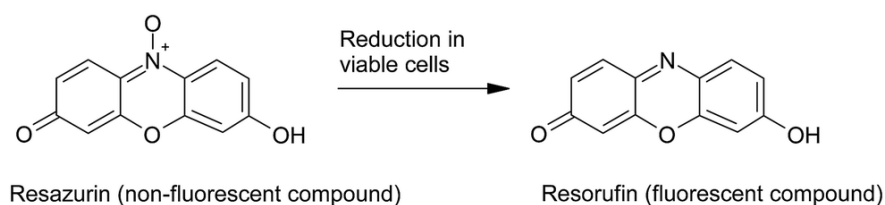


Figure 29: Principle of Resazurin. Viable cells reducing blue and weakly fluorescent Resazurin into pink and strongly fluorescent Resorufin (Aula *et al.*, 2015)

---

For the 4.5 mM resazurin solution, resazurin sodium salt was diluted with DPBS -/- and sterile filtered. To each well the resazurin solution was added as 10 % of total volume and incubated for 60-120 min at 37 °C and 5 % CO<sub>2</sub>. Afterwards, the supernatant was transferred into black 96-well plates with clear bottom and protected from light until measurement in the Tecan infinite F500 fluorescent reader ( $\lambda$  excitation: 535 nm;  $\lambda$  emission: 590 nm). If multiplexed, the cells were washed 2 times with DPBS-/- before performing a further assay.

## **2.2.7. Cell layer integrity**

### **2.2.7.1. Barrier Integrity (BI) Assay**

The BI assay was performed to assess the tightness of a barrier formed by Caco-2 cells in the OrganoPlate®. The cells were seeded in the cell channel and started growing against the ECM gel to establish tubular structures with adherens junctions and tight junctions, and which form a leak tight monolayer. The culture medium was replaced by medium containing a fluorescent dye and leakage of the dye from medium channel into ECM gel was monitored via pictures with a confocal microscope (HCS CellInsight CX7).

As first step, the microscope was set in such a way that the focus is directly on the top and middle channel of the chip. After adding the dye to the top channel, the plate only needs to be placed in the device and images can then be taken directly. For the BI two different fluorescent dyes (FITC-dextran 150 kDa and TRITC-dextran 4.4k Da) were used. The final concentration of the dyes was 0.5 mg/ml and were prepared in standard cell culture medium. Afterwards the medium from all inlets and outlets of a chip was aspirated and then 25  $\mu$ l medium was added to each inlet and outlet, including the gel channel for washing (Figure 30a). Therefore, the plate was placed at angle (7°) and perfused for 5min. After an aspiration of the whole medium from the chip the plate was ready for adding the dyes. Before adding the dyes into the chip 20  $\mu$ l medium was added to the gel inlet and outlet and as well to the bottom inlet and outlet. After that 40  $\mu$ l dye-medium solution was pipetted in each top inlet. To avoid premature flow of the dyes through the channel, the plate was held higher on the right than on the

left side. As a last step prior the imaging 30  $\mu$ l dye-medium solution was added to the top outlet (Figure 30 b). Afterwards the plate was directly imaged in the confocal microscope. For 16 mins a picture of each chip and each channel was taken.

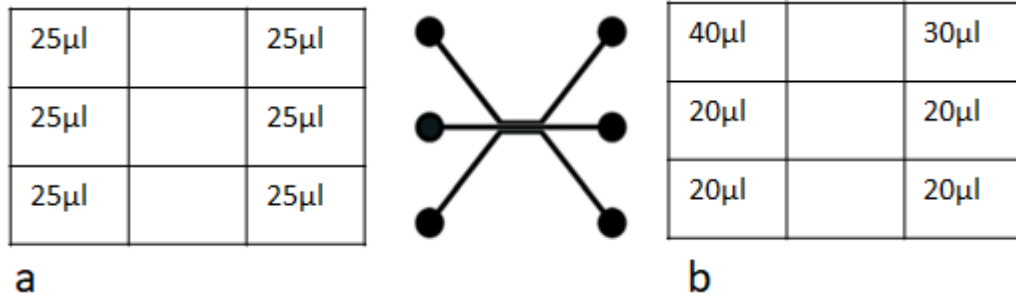


Figure 30: Volume scheme for immunofluorescence staining in OrganoPlate® a.) Volume scheme for washing step with medium, b.) Volume scheme for barrier integrity dyes

### 2.2.7.2. Data analysis for the Barrier Integrity Assay

The data analysis was performed with the ImageJ software. In the OrganoPlate® the separate channels (ECM and perfusion) are directly next to each other in the same focal plane. The images were analyzed by detecting fluorescent intensity in the perfusion and the ECM channel (Figure 31).

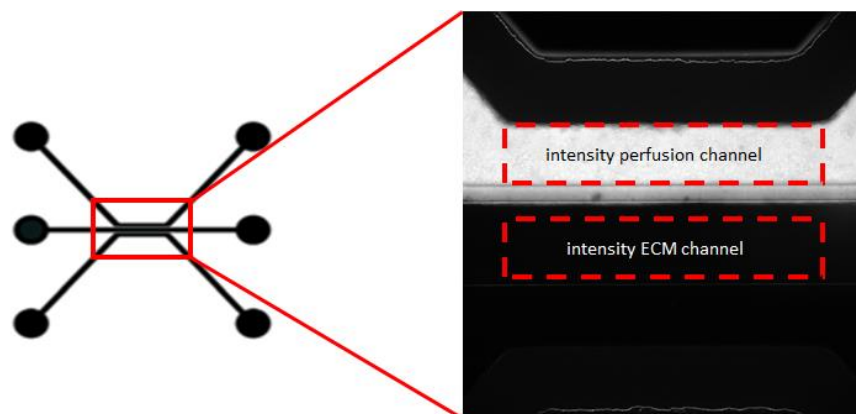


Figure 31: Imaging and selection of areas for the barrier integrity assay

The signal intensity of ECM channel was then divided by the signal intensity of perfusion channel. A ratio of 0 indicates a tight barrier. In case the barrier is leaky, the ratio increases over time, because the fluorescent signal in the ECM channel increases due to the dye leakage from the perfusion channel. Afterwards with these intensities and the specific dimensions of the channel the Papp (apparent permeability) value could be determined after the following formula:



$$Papp\ value = \frac{(I_{end} - I_{initial})}{(T_{end} - T_{initial})} * \frac{V_{gel}}{(A_{barrier})}$$

with:

$$V_{gel} = L_{gel} * W_{gel} * H_{gel} \quad (in\ cm^3)$$

and:

$$A_{barrier} = \frac{1}{2} * Pi * dh_{gel} * L_{gel} \quad (in\ cm^2)$$

(Calculation of the Papp value ( $I_{initial}$  = initial intensity;  $I_{end}$  = endpoint intensity;  $T_{initial}$  = time initial in seconds;  $T_{end}$  = time in end seconds))

The Papp based on the flux of a molecule across a barrier of known molecular weight is a measure of the integrity of the intestinal barrier.

The specifications of the used 3-lane OrganoPlate® are described in the appendix (appendix 1 in table 37). Formula for the calculation of Papp value is shown in appendix 9 in Figure 114

### 2.2.7.3. Measurement of the transepithelial electrical resistance

To measure the integrity of a cell culture model and its tight junctions a very widely accepted and used quantitative technique is the measurement of the transepithelial or transendothelial electrical resistance (TEER). The TEER value can be used as strong indicator for the barriers status of the gastrointestinal tract (Srinivasan *et al.*, 2015a). A tight cell layer exhibit high electrical resistance and vice versa.

The TEER measurement was performed with the Caco-2 cells in 2D and in the OrganoPlate®. Therefore, different cell densities and pre-cultivation times were needed and are described in Table 13.

Table 13: Cell densities and pre-cultivation times of Caco-2 cells for the TEER measurement experiments

Cell culture model	Cell density	Pre-cultivation time
Caco-2 2D (24well)	0.5x10 <sup>6</sup> / 500µl / well	21 days
Caco-2 OrganoPlate® (40chips)	0.02x10 <sup>6</sup> / 2µl /chip	4 days

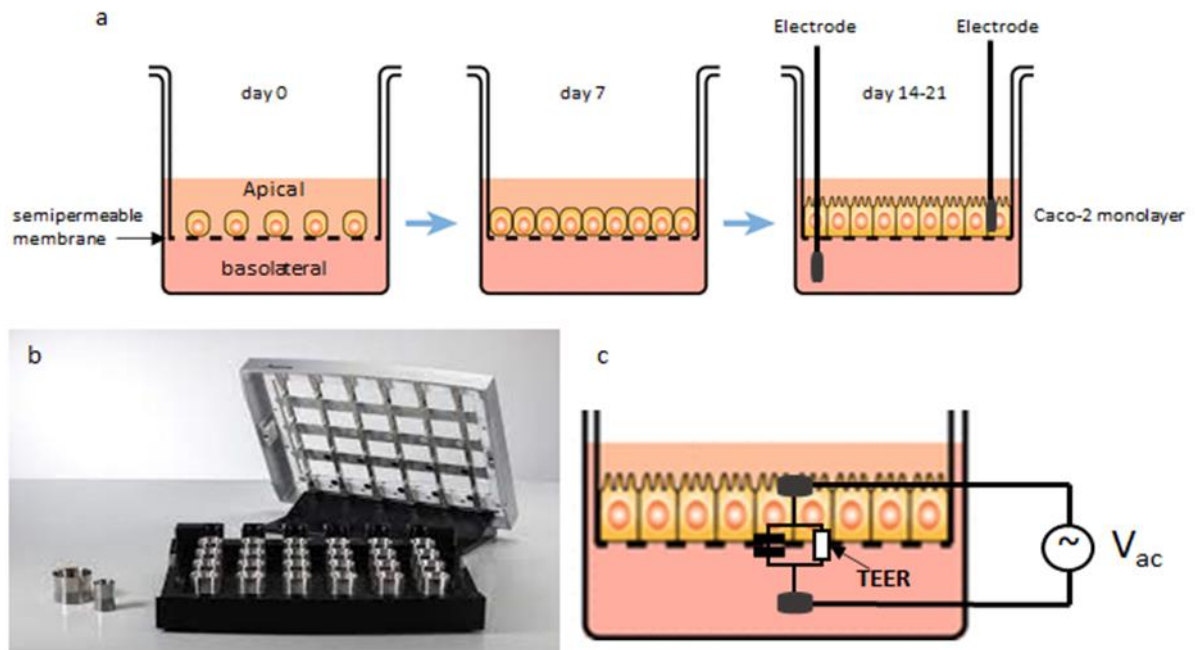


Figure 32: Experimental setup for TEER measurement in 2D. a.) Cells were seeded on semipermeable transwell inserts and transferred in 24-well plates for cultivation for 21 days to achieve two compartments (apical and basolateral). After a few days, the cells begin to stretch out and form a confluent tight monolayer which creates a resistance and that can be measured with two electrodes in the compartments. B.) Overview of the used TEER instrument. There are electrodes on the lid which dip into the pots on the bottom and thus measure the voltage, c.) Applied voltage between apical and basolateral compartments.

A classical setup for the Caco-2 cells was used and shown in Figure 32. The cells were seeded on semipermeable transwell filter inserts which generate two compartments, apical (or upper) and basolateral (or lower). For the measurement two electrodes were used. One is placed in the upper compartment and the other is placed in the lower compartment. Between both electrodes an ohmic resistance is setup by applying a direct current (DC) voltage. Since DC can damage the electrodes or the cells an altering current (AC) with a square waveform was applied. The resistance was calculated by the instrument based on Ohm's law (Srinivasan *et al.*, 2015a). The cells were cultivated for 21 days until a confluent and tight monolayer was achieved. This was verified as soon as the resistance was at least 300 ohms. Caco-2 cells form tight and dense monolayers, connected cells after 2-3 weeks in culture which can be detected by a generated TEER value between  $150\text{-}400 \Omega \cdot \text{cm}^2$  (Srinivasan *et al.*, 2015a). Afterwards the cells were treated with different compounds and every 6h a new measurement per well was performed for 24 h in total.

Compared to the 2D system the TEER measurement in the OrganoPlate® was conducted by using the OrganoTEER® instrument from Mimetas. It is an automated and fast impedance-based instrument which enables TEER measurements in the 3lane OrganoPlate® (Figure 33 b).

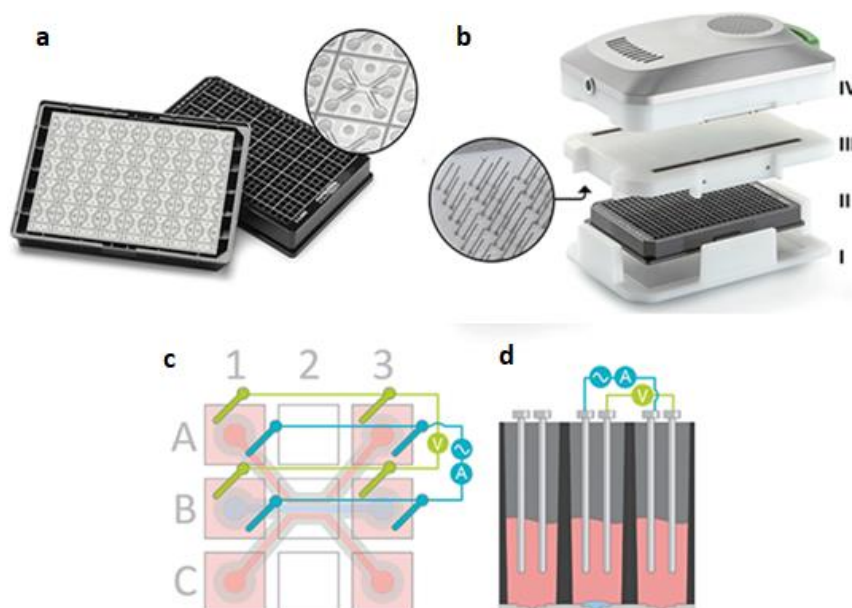


Figure 33: OrganoPlate® and OrganoTEER® instrument set up and measurement principle. a.) OrganoPlate® design with 40 chips in a 384-well format. Each chip has three channels, two perfusion channels and one ECM channel. b.) Exploded view of the setup of the OrganoTEER® instrument including (I) the plate holder, (II) the 3lane OrganoPlate®, (III) the electrode board and (IV) the measurement module. c.) Schematic design of the electrodes which addressing one chip. Eight electrodes dip in four wells of the upper perfusion channel and the ECM channel. Two electrodes build a current carrying pair (blue) and the other two a voltage sensing pair (green). Across the chip a controlled voltage was applied to impose a sinusoidal AC voltage of 100mV amplitude and to measure the resulting current. d.) Schematic overview of a cross-section of three access wells with inserted electrodes into the medium, which acts as contact to the tube at the luminal or basal side (Nicolas *et al.*, 2021, modified).

The seeding densities are shown in Table 13 and after seeding the cells were cultivated for around 4-5 days until a tubular structure was built and the measured TEER value was around 300 ohms. The system works with 480 electrodes which dip into the wells of the microtiter plate. In each chip four electrodes (a current carrying pair (blue) and a voltage sending pair (green)) dip in the medium of the upper channel / luminal side of the epithelium and in medium of the collagen channel / basal side of the epithelium (Figure 33 c). The medium works as an electrolyte. A sinusoidal AC voltage of 100 mV amplitude was set between the current carrying electrodes across the chip. The resulting voltage was then measured by the instrument (Figure 33 d) (Nicolas *et al.*, 2021).

The TEER was measured after treatment of the cells for 24h. The used compounds and concentrations are listed in Table 14.

Table 14: Used compounds and concentrations for the treatment of cells and then the measurement of the TEER

Compounds	Concentrations [ $\mu\text{M}$ ]
Gefitinib, 5-FU; Loperamide; Flavopiridol; Terfenadine; Diclofenac	300 - 30 - 3
Alosetron	200 - 30 - 3

### 2.2.8. Immunofluorescent staining

For the staining of cell specific markers different solutions and buffers were needed and are described in Table 15.

Table 15: Buffer compositions for immunofluorescent staining of cells in different cultivation systems

Buffer	Components for 2D	Components for 3D	Components OrganoPlate®
Fixative	4 % Formaldehyde	4 % Formaldehyde	4 % Formaldehyde
Wash buffer (after fixation)			DPBS +/+
Wash buffer	DPBS +/+ 0.2 % Triton X-100 0.04 % Tween 20	DPBS +/+ 0.2 % Triton X-100 0.04 % Tween 20	DPBS +/+ 4 % FBS
Permeabilization buffer	DPBS +/+ 0.1 % Triton X-100	DPBS +/+ 0.5 % Triton X-100 5 % BSA	DPBS +/+ 0.3 % Triton X-100
Blocking buffer	DPBS+ /+ 5 % BSA 0.04 % Tween 20 0.2 % Triton X-100	DPBS +/+ 2 % BSA 0.04 % Tween 20 0.2 % Triton X-100	DPBS +/+ 2 % BSA 0.1 % Tween 20 2 % FBS

#### 2.2.8.1. Immunofluorescent staining in the 2D model

The immunofluorescent staining in 2D culture was performed on two consecutive days. The procedure started with a fixation of the cells with 4 % formaldehyde (100 µl/well (96well plate)) for 30 min at RT. Afterwards the cells were washed two times with wash buffer (200 µl/well (96well plate)) and incubated for 5 min at RT with permeabilization buffer (100 µl/well (96well plate)) to permeabilize the membrane. Then the cells were washed two times and blocked with blocking buffer (100 µl/well (96well plate)) for 30 min at RT. Two further wash steps followed before the incubation of the primary antibodies (100 µl/well (96well plate)) was performed over night at 4 °C.

On the next day the primary antibodies were aspirated, and the cells were washed two times with wash buffer. The secondary antibodies (100 µl/well (96well plate)) and the nucleus stain were incubated for 1 h at RT and after that the cells were washed twice with wash buffer (200 µl/well (96well plate)). Before imaging fresh wash buffer (150 µl/well (96well plate)) was added.

---

### **2.2.8.2. Immunofluorescent staining in 3D organoid model**

The immunofluorescent stainings in 3D cell culture is a bit more complex compared to the staining in 2D. Four consecutive days were needed. On the first day the organoids were fixed with 4 % formaldehyde (1 ml for each well of a 24-well plate) and incubated for 1 h at RT. The Matrigel® hemispheres were carefully pipette up and down to break them up and then transferred with the fixative to a 50 ml falcon and the organoids allowed to settle down to the bottom of the falcon by gravity for around 15-20 min. The fixative was aspirated by trying to avoid aspirating the organoid pellet. 1 ml DPBS-/- was added to each well and the plates was swirled to get the last organoids out of the wells. Afterwards all was transferred to the 50 ml falcon containing the organoids. To remove the complete fixative, the organoids were washed with 5 ml DPBS-/. Then 1ml DPBS -/- was added and the organoid solution was transferred to a 1.5 ml tube. The organoids let settled down to the bottom and afterwards the DPBS-/- was aspirated. For permeabilization the organoids were mixed with 0.5 ml blocking buffer over night at 4 °C.

On the next day the blocking buffer was removed, and the primary antibodies were diluted in the desired concentrations and 300 µl was added in one tube and then incubated over night at 4 °C.

After the incubation the organoids were washed three times for 15 min each on a rotator. Afterwards 300 µl of diluted secondary antibodies including Hoechst for the nuclear staining was prepared and transferred into the tubes. The organoids were incubation at 4 °C overnight.

On day four the secondary antibodies were removed, and the organoids were washed three times with wash buffer. As a last step 300 µl Dulbecco's Phosphate buffered saline (with calcium and magnesium) (DPBS+/-) was added to the stained organoids and then 100 µl in one well of a u-bottom plate and were then imaged in the CellInsight CX7 Platform.

### **2.2.8.3. Immunofluorescent staining in OoC model**

The immunostaining of specific cellular biomolecules expressed on cells growing in the 3-lane OrganoPlate® was performed according to the following protocol and were performed at RT. To achieve successful binding of primary and secondary antibodies, the solutions were perfused through the OrganoPlate® during antibody incubation steps. Therefore, the flow was induced by placing the OrganoPlate® under an angle by positioning one end of the plate of a plate lid and regularly switching sides (Figure 34). This induction of flow could also be done by the rocker, but this was still in use in the incubator for cell culture.



Figure 34: Plate position during incubation and wash steps for Immunofluorescent stainings of the OrganoPlate®. Every 2 min the positions was changed to the other side, to achieve a flow.

After culturing the cells, the medium was aspirated from the chips and the fixative was added to inlets and outlets according to the volume scheme in Figure 35a and incubated for 15 min. After incubation the chips were washed twice with DPBS +/-.

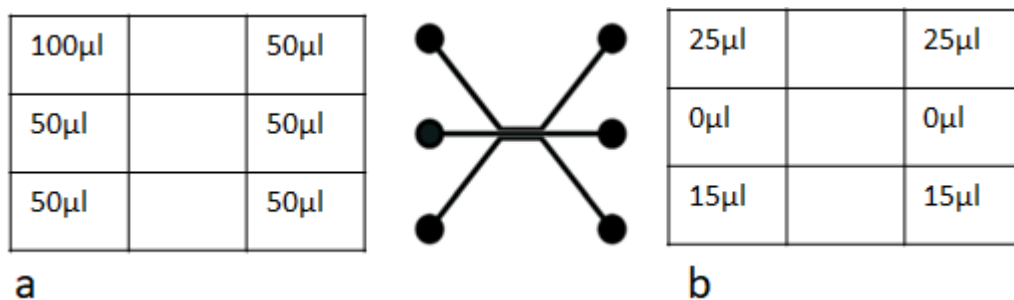


Figure 35: Overview of the used volumes for immunofluorescence stainings in the OrganoPlate®. a.) Volume scheme for the fixative, washing solution, blocking solution and permeabilization buffer. b.) Volume scheme for primary and secondary antibodies.

Before permeabilization the chips were washed with wash buffer for 5 min according to the scheme in (Figure 35 a). The same scheme was also used for adding the permeabilization buffer into the chip and incubated for 10 min. The chips were then washed again for 5 min with wash buffer and then blocked for 45 min at RT with blocking solution. Directly after the blocking the primary antibodies were dispensed into the chips according to the scheme in Figure 35b and incubated for 2 h at RT. Afterwards the chips were washed again two times with washing buffer (each 3 mins) and then the secondary antibodies were added and incubated for 30 min under perfusion at RT. The chips were washed again two times with washing buffer and afterwards once with DPBS +/- . As a last step in all inlets and outlets 50 µl DPBS +/- was dispensed and then the OrganoPlate® was ready for imaging.

---

## 2.2.9. Immunohistochemistry

For the detection of the different cell types included in the organoids immunohistochemistry was performed with antibodies against goblet cells, paneth cells, enteroendocrine cells, enterocytes as well for proliferating cells. The gold standard histologic staining method, the hematoxylin and eosin (H&E), was done to assess the histopathology of organoids. Tissue sections from rat and dog intestines were used as positive controls for the antibody staining, as it was not possible to obtain human tissue.

### 2.2.9.1. Preparation of paraffin blocks and alcohol serial

As much medium as possible was aspirated and then 2-4 organoid Matrigel® hemispheres were harvested by adding 1 ml DPBS/- per well and pipetting it up and down to break up the Matrigel® hemispheres. The organoid solution was transferred into 15 ml falcon tubes and centrifugated at 4 °C and 1100rpm for 5 min. The pellet was then washed again with 1 ml DPBS/- and directly transferred into 1.5 ml Eppendorf cups. After the organoids had dropped to the bottom of the cup, the DPBS was carefully aspirated and 400 µl of 4 % formaldehyde was pipetted and incubated for 30 min at RT. After the incubation with formaldehyde the organoids were processed through an ascending alcohol series by each adding 500 µl, incubating for 3 min (despite Xylene which was incubated for 5min) at RT and removing as much volume as possible. The alcohol series was performed as follows:

50% EtOH ->70% EtOH -> 96% EtOH -> Isopropanol -> Isopropanol : Xylene (1:1) -> Xylene

After the organoids settled down to the bottom of the eppendorf cup the xylene was aspirated. Before transferring the organoids into a biopsy cryomold a small volume of paraffine was pipetted onto the mold and then the organoids were added on top with a small spatula. More liquid paraffin was added on the side to fill the mold completely (Figure 36 a). Directly afterwards the section cassette was pressed on top (Figure 36 b), and the paraffin was left to harden.

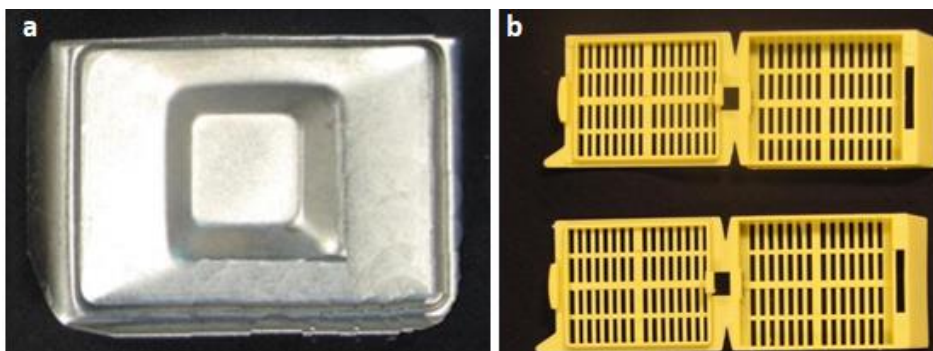


Figure 36: Example for a.) embedding molds and b.) plastic cassettes for the paraffin embedding of colon organoids (Yong, 2019)

Molds were placed for 20-30 min at -20 °C and then 1-1.5 µm thin sections were cut using a rotational microtome. The slices were transferred from cold to warm water (42 °C) for stretching and carefully transferred on glass slides. Sections were stored at RT until use for staining.

### 2.2.9.2. H&E staining

For the pathological assessment of tissue samples, the H&E staining is the gold standard histologic method. The organoids can be described as microtissues and can be handled in a modified form (described in 2.2.9.1) like histological tissue. H&E staining of paraffin-embedded organoids was performed to ensure general cell health, absence of necrotic cores and to check for the structure and distribution of cell nucleus and plasma content of the organoid. Similarly, to assess whether H&E stainings could be a possible endpoint for the detection of toxic effects of new drug candidates in the early safety assessment.

Staining was performed using the Ventana Symphony H&E automated stainer (Roche) with a specific staining program, which stained according to the protocol in Table 16.

Table 16: Staining procedure for H&E staining of paraffin sections of organoids

Order (step)	Reagent	Incubation time
1 (Deparaffinization)	Xylene	2x 2min
2 (Rehydration)	Isopropanol	3min
	96% EtOH	3min
	70% EtOH	3min
	50% EtOH	3min
	DI-H <sub>2</sub> O	3min
3 (Hematoxylin staining)	Hematoxylin	4min
4 (Washing)	Tap water	3x 2min
5 (Eosin staining)	Eosin	1min
6 (Dehydrate)	96% EtOH	2x 10sec
	Isopropanol	2x 1min
	Isopropanol / Xylene	2min
	Xylene	2x 2min
7 (Mount)	Entellan	-

The sections were evaluated with a light microscope and scanned with the NanoZoomer S210 (Hamamatsu Photonics) for further evaluations.



### 2.2.9.3. Antibody staining of different cell types in organoids

The staining was performed using the IntelliPath FLX automated stainer.

Before staining the prepared paraffin sections were deparaffinized and rehydrated with a descending alcohol series (Xylene -> Isopropanol : Xylene (1:1) -> Isopropanol -> 96 % EtOH -> 70 % EtOH). Subsequently the slides were pretreated in a pressure cooker with citrate buffer for 10 min at 110 °C. The Citrate buffer was prepared according to Table 17. After that the slices were cooled down under flowing DI-H<sub>2</sub>O.

Table 17: Buffer for immunofluorescent stainings of organoids paraffin sections

Buffer	Preparation
Citrate buffer	1:20 citrate buffer with DI-H <sub>2</sub> O

For antibody stainings the antibodies need specific concentrations which were determined in earlier experiments within Merck (experiments not reported here). The used dilutions of the antibodies are listed in Table 18.

Table 18: Antibody dilution for immunohistochemistry staining

Cell type	Antibody	Dilution
Paneth cells	Anti-Lysozyme C	1:75
Proliferating cells	Anti-Ki67	1:100
Enterocytes	Anti-Cytokeratin 20	1:50
Enteroendocrine cells	Anti-Synaptophysin	1:200

The antibodies were diluted with specific antibody diluent from Zytomed (ZUC051-100). All reagents, antibody solutions and the slices were transferred into the IntelliPath FLX automated stainer.

Cytokeratin (CK20), a major cellular protein of enterocytes is present in a high amount during differentiation of the mucosal epithelium and can therefore been used for the labeling of enterocytes (Moll *et al.*, 1993). Paneth cells are responsible for the defense against bacterial colonization in the intestine. This is mainly done with the help of the secretion of antibacterial substances such as lysozyme C (Bel *et al.*, 2017). Lysozyme C can therefore be used to stain paneth cells in the organoids. Synaptophysin, a membrane glycoprotein, can be found in secretory vesicles of enteroendocrine cells and is therefore well suited for the staining of enteroendocrine cells of the organoids (Gunawardene, Corfe and Staton, 2011). For the detection of proliferating

cells, the antibody Ki67 was used. Ki67 is a specific marker for staining proliferating cells (Villarreal, 2012). Ki67 is present during all active phases of cell cycle but is absent in resting cells. During mitosis is the protein located to the surface of chromosomes (Scholzen and Gerdes, 2000). The stained sections were evaluated microscopically and scanned with the NanoZoomer S210 (Hamamatsu Photonics) for further evaluations.

#### 2.2.9.4. Alcian blue staining

For the staining of the goblet cells in the iPSC derived colon organoids an Alcian blue staining was performed. It is a combined staining of Alcian blue and periodic acid Schiff. It stains neutral and acidic mucins secreted by the goblet cell (Osho *et al.*, 2017). For this staining paraffin sections were used and first deparaffinized and then rehydrated with a descending alcohol series (Xylene -> Xylene -> Isopropanol -> Isopropanol -> 96 % EtOH -> 80 % EtOH -> 70 % EtOH). The sections were incubated for 3 min in Xylene and in the other solutions in each case for 5 min. Until the staining processes the slides were stored in DI-H<sub>2</sub>O. The staining procedure was performed in glass cuvettes and according to the following protocol:

Table 19: Staining procedure for the Alcian blue staining of paraffin sections of organoids

Step	Reagent	Incubation time
1	Alcian blue solution	5min
2	Tap water	3min
3	DI-H <sub>2</sub> O	rinse
4	Core red	10min
5	Tap water	3min
6	DI-H <sub>2</sub> O	rinse
7	70 % EtOH	1min
8	80 % EtOH	1min
9	96 % EtOH	1min
10	96 % EtOH	1min
11	Isopropanol	1min
12	Isopropanol	1min
13	Isopropanol / Xylene	1min
14	(1:1)	5min
15	Xylene	5min

The stained sections were evaluated microscopically and scanned with the NanoZoomer S210 (Hamamatsu Photonics) for further evaluations.

---

### 2.2.10. Transcriptomics (QuantiGene™ Plex Assay Kit)

The QuantiGene™ Plex Assay was used for the quantification of different target mRNAs for the characterization of the cell culture systems and for the identification of potential biomarkers of drug-induced intestinal injury. The assay was measured with the FlexMap 3D® (Luminex multiplexing platform).

The kit allows the detection and quantification of multiple RNA targets in one sample. The method is based on two different approaches, namely the *branched DNA* (bDNA) signal amplification and the multi-analyte profiling beads® technology. The bDNA assay directly measures nucleic acid molecules and amplifies the reporter signal. This signal amplification uses labeled DNA probes hybridized to RNA of interest via extenders. One of these extenders is a so-called *capture extender*. This distinguishes between the different capture beads and hybridizes with a specific target RNA. This differentiation of different capture beads enables multiplexing with the multi-analyte profiling® technology. For bead identification, each capture bead has its own specific dye concentration detected by the Luminex™ FLEXMAP 3D™ instrument. The Luminex™ FLEXMAP 3D™ system is based on a flow cytometer. Each bead passes through two lasers measuring the specific bead signal and the amplified reporter signal resulting in a fluorescence signal, associated with each capture bead. A 532 nm green laser excites the probe bound to SAPE. The 635 nm red laser excites the dyes inside the beads and is also used to measure the light scatter for doublet discrimination. This signal is then reported as the *median fluorescence intensity* which is proportional to the number of target RNA molecules in the sample.

The simultaneous quantification of different target mRNAs was performed with a customized Plex Set for iPSC derived colon organoids and Caco-2 cells (QGP-148, M19083001 and QGP-213). It contained a target-specific mixture of Probe Set and Capture beads to detect different targets. The assay was based on hybridization of target sequences to magnetic multi-analyte profiling beads (xMAP®) and signal amplification via branched DNA (bDNA) (Affymetrix, 2014).

Before the mRNA's could be detected, the cells were treated twice with specific compounds in specific concentrations which are listed in Table 20. The concentrations used were according to the measured IC<sub>20</sub> values from prior viability experiments. After treatment and incubation, the cells were lysed and prepared for the mRNA measurement.

Table 20: Used compounds and concentrations for the gene expression experiment

Compound	Concentration range [ $\mu\text{M}$ ]
5 FU	50 – 5 - 0.5
Irinotecan	50 – 5 - 0.5
Oxaliplatin	5 – 0.5 – 0.05
Gefitinib	1 – 0.1 – 0.01
Flavopiridol	1 – 0.1 – 0.01
Loperamide	1 – 0.1 – 0.01
Terfenadine	1 – 0.1 – 0.01

The whole assay was divided in four parts: sample preparation, target hybridization, signal amplification and detection (Figure 37).

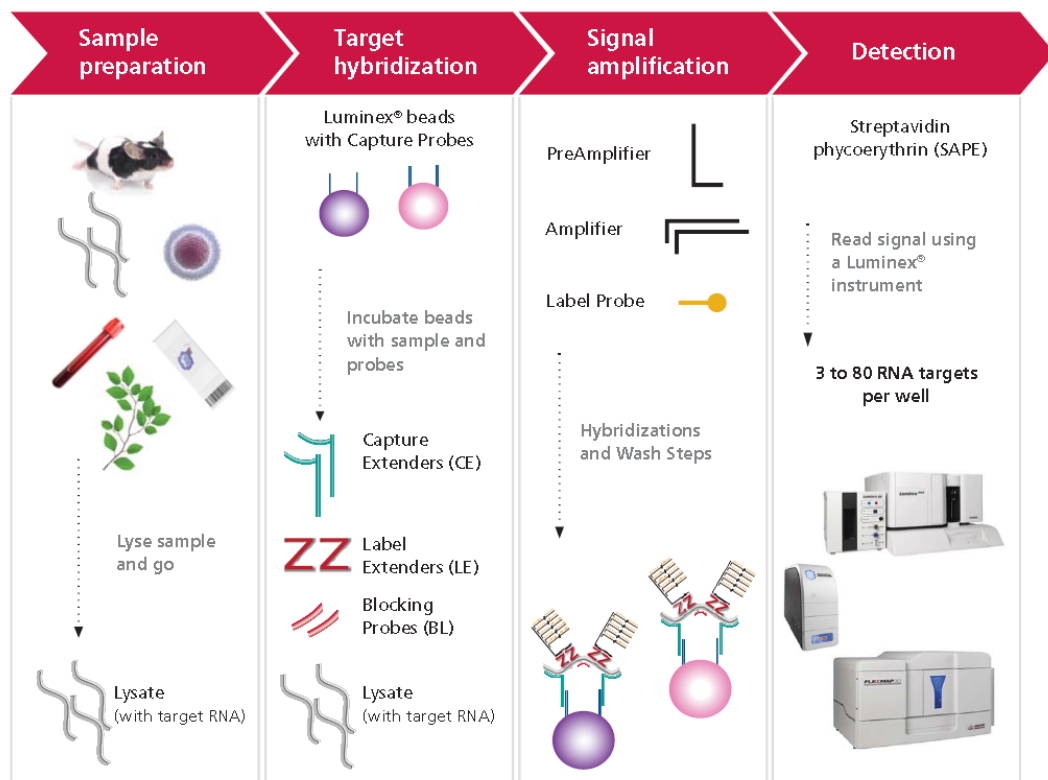


Figure 37: Principle for the QuantiGene™ Plex Assay (Affymetrix, 2014)

---

### 2.2.10.1. Sample preparation

After the cultivation and treatment of the cells or organoids they were lysed with a specific working lysis mixture. This mixture was prepared by diluting nysis mixture 1:3 with nuclease free water and adding 10 µl Proteinase K pro 1ml diluted lysis mixture. For the lysis the culture medium was aspirated and in each well the desired volume working lysis mixture was added. The volumes for each cell culture system are shown in (Table 21). The plates were then incubated for at least 30 min at 54 °C. Afterwards the cell lysates were transferred into deep well plates and either stored at -80 °C until hybridization or directly hybridized.

Table 21: Volumes for the working lysis mixture for the QuantiGene™ Plex Assay

<b>Cell culture system</b>	<b>Volume working lysis mixture [µl]</b>
Caco-2 2D	500 (for one well of a 24well plate)
Organoids 3D	250 (for one well of a 96well plate)
Caco-2 OrganoPlate®	50 (for inlet and outlet of one chip)

### 2.2.10.2. Target hybridization

Cell lysates were thawed at RT. The appropriate probe set, blocking reagent, proteinase K and universal human reference RNA (served as a quality control) were thawed on ice whereas the lysis mixture was prewarmed at 37 °C for 30 min. Capture beads were stored in the dark and vortexed thoroughly directly before using. For the hybridization of the target RNAs to the corresponding capture beads a working bead mix was prepared as described in Table 22 for samples and RNA control.

Table 22: Preparation of working bead mix for RNA samples and RNA control, each volume is calculated for one well

Reagent	Working bead mix RNA [ $\mu$ l]	Working bead mix samples & blank [ $\mu$ l]
Diluted lysis mixture	33.3	6.6
Nuclease free water	37.7	4.2
Proteinase K	-	0.2
Probe set	6	6
Capture beads	1	1
Blocking reagent	2	2

Table 23: Used dilutions of samples for different cell culture systems

Caco-2 2D (1well)	Caco-2 OoC (5 chips pooled)	Organoids 3D (1well)
1:5	1:2	1:6

The working bead mixes were vortexed and 80 $\mu$ l working bead mix for RNA and 20  $\mu$ l of reference RNA (50 ng/ $\mu$ l) as well as 20  $\mu$ l working bead mix for samples & blank and 80  $\mu$ l sample or blank were added in one well of a 96-well round bottom hybridization plate. The samples were diluted with diluted lysis mixture to an appropriated concentration (Table 23). Diluted lysis mixture (1 part lysis mixture to 2 parts nuclease free water) was used as blank. The plate was sealed with a pressure seal and incubated at 54 °C and 600 rpm for 18-22 h using a VorTemp 56 shaking incubator. The temperature was verified using QuantiGene™ temperature validation kit to ensure a maximum hybridization efficiency and minimal background from non-specific hybridization.

---

### **2.2.10.3. Signal amplification**

On day two of the assay, the Pre-Amplifier, Amplifier and Label Probe Solution were pre-warmed at 37 °C for at least 30 min to remove precipitates. Streptavidin-conjugated R-Phycoerythrin (SAPE) diluent was brought to RT. The wash buffer was prepared by adding wash buffer components 1 and 2 to Milli-Q® water. Before the measurement could be done the FlexMap® 3D was warmed up and a calibration was performed with the FlexMAP® 3D Calibration Kit and the Performance Verification Kit.

As a next step the hybridization plate was removed from the shaking incubator and centrifugated at 24 0xg for 3 min. Afterwards samples were pipetted up and down to mix and then transferred into the magnetic separation plate. The plate was then clamped in a hand-held magnetic plate and left for 1 min, so that the magnetic beads can settle down and were held by the magnet. The samples were washed three times with wash buffer. The wash buffer was tilted out over a sink and then the plate was tapped out 2-3 more times on disposable towels. Then 100 µl Pre-Amplifier was added to each well and the plate was sealed, shaken at 800 rpm for 1 min and incubated at 50 °C at 600 rpm for 1 h. After this the process was repeated using Amplifier and Label Probe Solution (washing, add 100 µl of specific solution into each well, shake 1 min at 800 rpm and incubate at 50 °C at 600 rpm for 1 h). After these steps the streptavidin-conjugated R-Phycoerythrin (SAPE) working reagent was prepared by diluting 36 µl SAPE with 15 ml SAPE diluent. A further washing step with wash buffer was done and an incubation with 100 µl SAPE working reagent in each well at RT for 30 min was followed. The plate was sealed and covered to protect from light. As a last step the plate was washed three times with SAPE wash buffer and 130 µl of this wash buffer was added to each well. The plate was shaken for 10 min at 800 rpm protected from light at RT to resuspend the beads. Immediately afterwards the plate was read using the FLEXMAP 3D instrument and xPONENT® v3.1 software. Analysis was done within excel.

## 2.2.11. Proteomics

### 2.2.11.1. Cell culture

To determine the basic expression of proteins in the different cell culture systems, the cells were cultivated for different times. The different cultivation times, cell numbers and cell culture systems used are shown in Table 24.

Table 24: Pre-cultivation times and seeding densities for the proteomics experiment

Cell culture system	Cultivation time	Cell number per sample
Caco-2 2D	24h	50,000
	21 days	50,000
Caco-2 OrganoPlate®	24h	50,000
	4 days	50,000
Organoids 3D	24h	50,000
	6 days	50,000
	10 days	50,000

After culturing the cells for the different times (Table 25), the culture medium was removed, and the cells were washed with DPBS -/-. Afterwards the cells were detached with trypsin for 8 min at 37 °C. With an appropriate volume of medium the trypsin reactions were stopped, and the cell suspension was transferred to 1.5 ml Eppendorf cups. The cell suspensions were centrifugated at 260 xg for 5 min at RT and then the pellet was washed with 500µl DPBS-/. This washing step was carried out twice in succession. Subsequently, the cell pellet was quickly transferred into liquid nitrogen for 30 sec and then stored until the measurement in -80 °C.

Table 25: Volumes for the detachment of cells for the proteomics experiment

Cell culture system	Volume DPBS -/- [µl]	Volume Trypsin [µl]	Volume Medium [µl]
Caco-2 (96-well)	200 (per well)	30 (per well)	300 (per well)
Caco-2 (Transwell)	500 (per well)	100 (per well)	1000 (per well)
Caco-2 OrganoPlate	100 (per top Inlet & Outlet)	25 (per top Inlet & Outlet)	75 (per top Inlet & Outlet)
Colon Organoids 3D	200 (per well)	30 (per well)	300 (per well)



---

### 2.2.11.2. Sample preparation

The cell pellets were lysed by resuspending the cells with 50 µl lysis buffer (Pierce Kinase Enrichment Kit #1862511, + Protease Inhibitor) and then incubated for 10 min on ice, followed by an incubation in an ultrasonic bath for 5min. The samples were transferred on ice for 5min and then centrifugated for 5 min at 16000 xg at RT. The supernatants (= lysates) were transferred into 1.5 ml eppendorf cups and resuspended into 50 mM Hepes / 1 M Urea by using 7kDa Zeba spin columns (Thermo Scientific, #89882; according to the manufacturer's guidelines). Afterwards the samples were reduced with 5 mM dithiothreitol for 30 min at 55 °C and then cooled down to RT. This was followed by an alkylation with 15 mM IAA for 30 min at RT in darkness. To each sample 0.2 µg trypsin (Promega, #V511A, solved in water) per 10 µl of lysate was added. The samples were incubated overnight (~14-16 h) at 37 °C with 700 rpm. On the next day, 25 µl of each sample was transferred into a new 1.5 ml Eppendorf cup. For the tandem mass tag (TMT) labelling, 9 TMT labels (126, 127N, 128N, 129N, 130N, 131N, 132N, 133N and 134N) of a TMT-16plex (Thermo Scientific, #A44521) were used. The TMT labeling is a chemical label method that allows multiplexing in mass spectrometry-based quantification and the identification of proteins. Of each TMT label 0.5 mg were dissolved in 60 µl acetonitrile (ACN) and 10 µl of the appropriate label was added to the samples. Then the samples were incubated for 60 min at RT. The TMT-labelling reaction was quenched by the addition of 4 µl 1 M Tris and a following incubation step of 15 min at RT. Samples were multiplexed by combining 34 µl of each appropriate sample into a new 1.5 ml Eppendorf cup. Then the samples were dried using a SpeedVac Vacuum Concentrator (eppendorf Concentrator plus) and afterwards dissolved in 200 µl 20 mM Hepes. The detergent (NP-40 present in the lysis buffer) was removed from the samples using a Detergent Removal Kit (Thermo Scientific, #87777; according to the manufacturer's guidelines). After that the samples were frozen overnight at -20 °C. On the next day, 10 µl of 10 % Trifluoroacetic acid (TFA) and 90 µl of 0.1 % TFA was added to the samples. The pH was confirmed to be < 3 using pH indicator strips (MQuant, Merck). Subsequently the samples were fractionated with the High pH Reversed-Phase Peptide Fractionation Kit (Thermo Scientific, #84868) according to the manufacturer's guidelines, except for using the following ACN concentrations for the 8 fractions: 7.5 %, 10 %, 12.5 %, 15 %, 17.5 %, 20 %, 30 % and 50 % ACN. The volume of the obtained fractions was reduced to 25 µl using a SpeedVac Vacuum Concentrator (0.1 % TFA was added to achieve a volume of 25 µl in case lower volumes were obtained after the SpeedVac Vacuum Concentrator). The 8 fractions were transferred into HPLC vials (Waters, # 186000385DV) and stored at -20 °C till analysis on the mass spectrometer.

### 2.2.11.1. Measurement of samples with Mass spectrometry

Samples were analyzed by coupling a nanoflow liquid chromatography (LC) system (nanoElute, Bruker Daltonics) to a trapped ion mobility spectrometry quadrupole time of flight spectrometer (timsTOF Pro, Bruker Daltonics). From each sample 2  $\mu$ l were injected for mass spectrometry (MS) analysis and peptides were separated on a reversed phase C18 column (25 cm x 75  $\mu$ m i.d., 1.6  $\mu$ M, IonOptics Odyssey) using a 100 min gradient of 2-37 % B (0.1 % formic acid in ACN) at a constant flow rate of 400 nL/min. The column temperature was controlled at 50°C and MS data were collected over an m/z range of 100 to 1700. All timsTOF parameters were documented.

### 2.2.11.2. Data analysis

The raw data was analyzed with Peaks Studio 10.6 with the following parameters listed in Table 26.

Table 26: Used parameters and their set up for the raw data analysis of the proteomics mass spectrometry data

Parameter	Set up
Parent Mass Error Tolerance	15.0 ppm
Fragment Mass Error Tolerance	0.1 Da
Precursor Mass Search Type	Monoisotopic
Enzyme	Trypsin
Max. Missed Cleavages	1
Digest Mode	Specific
Fixed Modifications	Carbamidomethylation 57.02 TMT 16plex 304.21
Variable Modifications	Oxidation (M) 15.99 Acetylation (N-term) 42.01
Max Variable PTM Per Peptide	3
Database	Human_2020_july (20199 entries)
FDR Estimation	Enabled (1%)
Quantification Type	TMT-16plex (CID/HCD)
Quantification Mass Tolerance	40.0 ppm
FDR Threshold (%):	1.0
Reporter Ion Type	MS2

## 2.2.12. Measurement of microRNA 194 (QuantiGene™2.0 miRNA Assay)

For the detection of microRNA (miRNA) 194 in the cell culture models the QuantiGene™2.0 miRNA Assay was used. This kit enables direct detection and quantification of miRNA's. The assay is based on direct quantification of miRNA by using novel oligonucleotide chemistry and probe design for the capturing of miRNA and a followed branched DNA signal amplification.

In this thesis the detection of miRNA 194 in all used cell culture models was performed. The assay was performed on two consecutive days and was divided into 4 steps (sample preparation, target hybridization, signal amplification and detection) which can be seen in Figure 38.

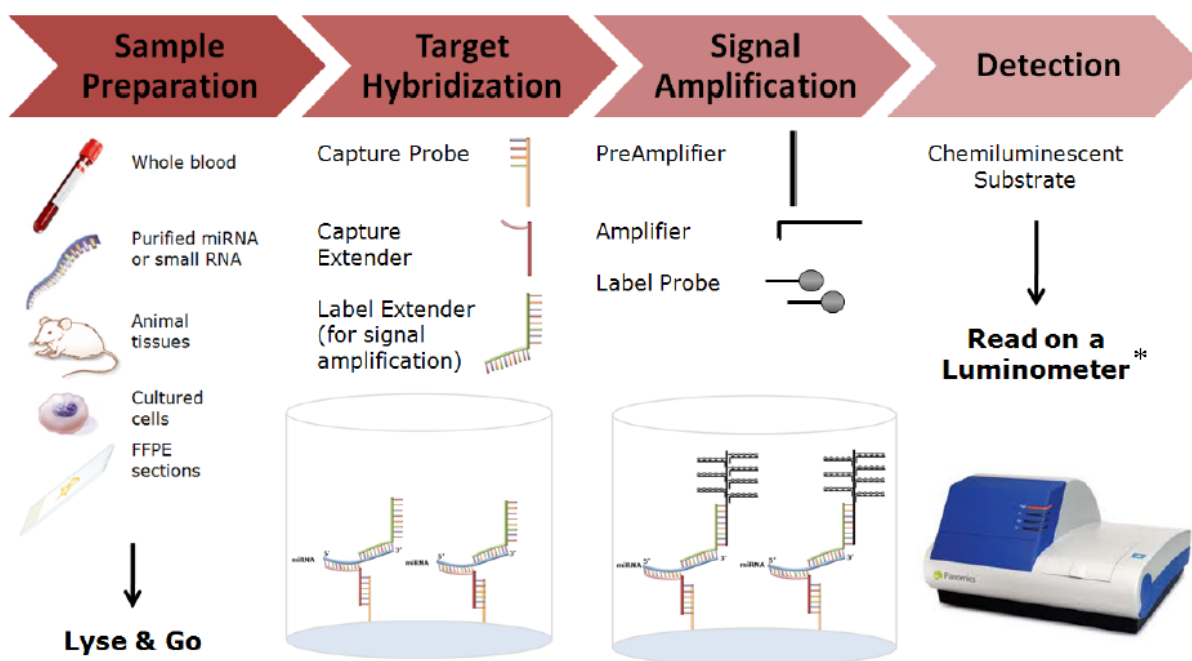


Figure 38: Assay workflow for the measurement of miRNA (Analysis and Manual, 2012)

### 2.2.12.1. Sample preparation and target hybridization (day 1)

On the first day, the samples were lysed to release the miRNAs which were incubated with the specific probe sets.

Before the detection of miRNA was performed the reagents were prepared and pre-warmed at different temperatures until use. As a first step a working probe set was prepared after the following scheme (Table 27).

Table 27: Preparation of working bead mix for the samples and standard serial, calculated volume is for one well of a 96-well plate

<b>Reagent</b>	<b>Volume [<math>\mu</math>l] for 1 well</b>
Nuclease-free water	11.7
Lysis mixture	6.7
Blocking reagent	1.0
Capture extenders	0.3
Label extenders	0.3

The working bead mix was vortexed and 20  $\mu$ l was added into one well of the capture plate. Afterwards the samples were first diluted, according to Table 28 with diluted lysis mixture (1:3 with nuclease free water).

Table 28: Dilutions of samples for miRNA Assay

<b>Caco-2 2D (1well/conc.)</b>	<b>Caco-2 OrganoPlate® (5chips/ conc.)</b>	<b>Organoids 3D (1 well/conc.)</b>
1:9	1:4	1:2

80 $\mu$ l of each diluted sample was added and then the plate was sealed with an adhesive plate seal. The plate was centrifugated for 240 xg for 20 sec. at RT. For the hybridization the plate was placed immediately in an incubator with 46 °C for 16-20 h.

### **2.2.12.2. Signal amplification and detection (day 2)**

The second day started with preparing of wash buffer and label probe working reagent. Wash buffer was prepared by mixing 1.5 ml wash buffer component 1, 2.5 ml wash buffer component 2 and 496 ml Milli-Q® water. Label probe working reagent was prepared by mixing 11  $\mu$ l label probe with 11 ml label probe diluent.

The capture plate was removed from the incubator and the plate seal was removed. 200  $\mu$ l wash buffer was added on top of the sample and then the plate was inverted over the sink to empty the wells. Subsequently, 300  $\mu$ l wash buffer was added and again the wells were emptied. This step was repeated twice. After washing, the plate was inverted centrifuged at 240 xg for 1 min at RT to remove the whole content out of the wells. Immediately afterwards 100  $\mu$ l Pre-Amplifier working reagent was added in to each well and the plate was sealed and incubated at 46 °C for 1 h.

After incubation the plate was taken out of the incubator and 200 µl wash buffer was added in each well to the pre-amplifier. The content was removed over a sink and the plate was washed twice with 300 µl wash buffer. To remove completely the content out from the wells the plate was inverted centrifuged at 240 xg for 1 min at RT. After centrifugation 100 µl amplifier working reagent was added in to each well and the sealed plate was incubated at 46 °c for 1h.

The next step was to add labelled probe to the samples. The plate was removed from the incubator and 200 µl wash buffer was added to the amplifier reagent. The content was removed by inverting the plate over a sink and tapping it on a paper towel. To wash the plate again, 300 µl wash buffer was added twice to the plate and removed again by tipping it over a sink. To remove any last content the plate was inverted centrifugated at 240 xg for 1 min at RT. Immediately after that 100µl substrate was added in to each well and then the plate was sealed and incubated for 5 min at RT. Afterwards the plate was placed in a luminometer and read (integration time 0.2 sec).

### 2.2.13. Citrulline measurement

The Homocitrulline/Citrulline Assay Kit from abcam (ab242292) was used for the measurement of citrulline and is based on a colorimetric method. Citrulline was measured in cell culture supernatants of all three cell culture models investigated in this thesis. The content of citrulline was compared to a predetermined standard curve. For each new measurement a fresh set of standards (Table 29) was prepared.

Table 29: Dilution series for citrulline standard

Standard #	Final citrulline conc. [µM]	Citrulline standard [µl]	DPBS +/- [µl]
1	2400	5	495
2	1200	250 of tube #1	250
3	600	250 of tube #2	250
4	300	250 of tube #3	250
5	150	250 of tube #4	250
6	75	250 of tube #5	250
7	37.5	250 of tube #6	250
8	0	0	250

Before the measurement the cell culture supernatant was centrifuged at 10,000 xg for 10 min at 4 °C to remove insoluble particles. Citrulline standards and unknown samples were transferred into 1.5ml screwcap tubes with an O-ring. In each tube 5 µl SDS solution and 5 µl Proteinase K was added, briefly mixed, and then incubated for 2 h at 37 °C. Afterwards 250 µl of assay reagent A and 50 µl assay reagent B was added in each tube and incubated for 30 min at 95 °C. Directly after the tubes were transferred into the fridge for 5min and the centrifugated at 18,000 xg for 10 min at RT. To read the absorbance at 540-560 nm with the MWG Discovery HT-R from Agilent, 200 µl of each sample was transferred into a clear 96-well plate. Each sample was run in duplicates.

#### 2.2.14. Calprotectin measurement

The human calprotectin ELISA kit (S100A8/S100A9) from abcam (ab267628) was used for the determination of calprotectin in the cell culture supernatant of all three cell culture models. This assay is based on an antibody specific for human calprotectin which is precoated on a 96-well plate.

Before the measurement could be performed several reagents needed to be prepared. The 5X Assay diluent was mixed with Milli-Q® water to prepare a 1X reagent. For the preparation of 1X biotinylated anti-human calprotectin detection antibody 100 µl 1X assay diluent was added to the antibody concentrate. 20X wash buffer was diluted with Milli-Q® water to prepare 1X reagent. As last preparation step 900X HRP-Streptavidin concentrate was diluted with 1X assay diluent to achieve a 1X solution. Beside the samples in each run a fresh standard was used (Table 30).

Table 30: Dilution series of calprotectin standard

Standard #	Final calprotectin conc. [pg/ml]	Volume calprotectin standard [µl]	Volume of assay diluent [µl]
1	8000	80 [50ng/ml stock]	420
2	3200	200	300
3	1280	200	300
4	512	200	300
5	204.8	200	300
6	81.92	200	300
7	32.77	200	300
8	0	-	300

---

As a first step 100  $\mu$ l standard or sample was added to the wells and incubated for 2.5 h at RT. Afterwards the wells were washed four times with 300  $\mu$ l 1X wash buffer. After the last washing step, the plate was inverted against a paper towel to remove the remaining content. Next step was to add 100  $\mu$ l of 1X prepared biotinylated antibody in each well and to incubate the plate at 300 rpm for 1 h at RT. Afterwards the solution was discarded and the plates were washed as described above. The next step was to add 100  $\mu$ l Streptavidin solution in each well and incubate the plate at 300 rpm for 45 min at RT. A final washing step followed and then 100  $\mu$ l TMB One-Step substrate reagent was added in each well and an incubation period for 30 min at RT in the dark with gentle shaking (300 rpm) was used. After the last incubation, 50  $\mu$ l stop solution was added in each well and the plate was read at 450 nm immediately.

The calprotectin concentrations were then calculated by an interpolation (Hyperbola) in GraphPad Prism 8.

---

### 3. Results and discussion

---

The work carried out for this thesis dealt with data from Caco-2 cells and iPSC derived colon organoids after short and long-term treatment with nine well known drugs. In this section the results from different endpoints, including morphology, immunofluorescent, immunohistological stainings, barrier integrity, viability, transcriptomics, and biomarker measurements are presented and discussed. Illustrations, data analysis and comprehensive interpretation of all results, beside the analysis of mass spectrometry results, which was performed by Thomas Wild, represent my own work.

In the following sections the Mimetas OrganoPlate® is referred to as “OoC”.

#### 3.1. Morphology assessment of the cell culture models

All cell culture models were investigated by different methods to assess morphology, presence of different cell types or specific intestinal markers for barrier function.

##### 3.1.1. Caco-2 2D

The very widely used cell line Caco-2 was used in this study in a 2D transwell model and in the OoC model from Mimetas. This cell line builds an epithelial barrier to molecular transport and is known to express functional and morphological characteristics of mature enterocytes of the human intestine (Hidalgo, Raub and Borchardt, 1989; Kim and Ingber, 2013).

With brightfield microscopy the morphology and formation of the cells during culture and after seeding the cells into the plates for experiments were observed.

The Caco-2 cell line has a doubling time of around 60 h, if cultivated in medium without amino acids. By adding L-glutamine the doubling time increases and the cells grow faster in cell culture flasks (Turowski *et al.*, 1994). The morphology changed from day two after seeding, where the cells were rounder in shape and have thin borders towards more thickened borders and angular cells after 21 days in culture (Figure 39). Visually it looked like a confluent and tight monolayer without any gaps between the cells after 21 days in culture.



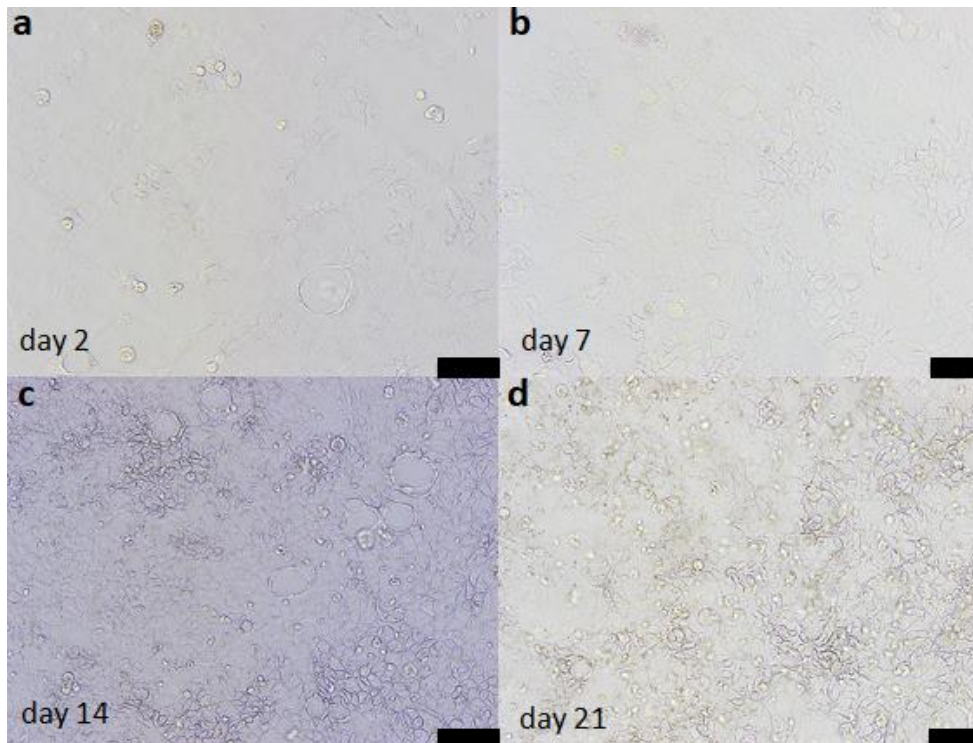


Figure 39: Caco-2 cells growing in cell culture plates. a.) Two days after seeding. b.) Seven days after seeding. c.) 14 days after seeding. d.) 21 days after seeding. bar = 100 $\mu$ m, 10x magnification.

To achieve a confluent monolayer with a tight barrier, Caco-2 cells need to be seeded on transwell inserts and cultivated for 21 days to differentiate a homogenous monolayer with polarized cells (Verhoeckx *et al.*, 2015). In order to estimate Caco-2 health on a molecular basis, the tightness of the Caco-2 cell monolayer was measured, by determine the TEER value for 24h after 19 days in culture (Figure 40a). In order to confirm the morphological results on a molecular level the ATP content was also measured after 21 days in culture every 24h for 8 days (Figure 40b).

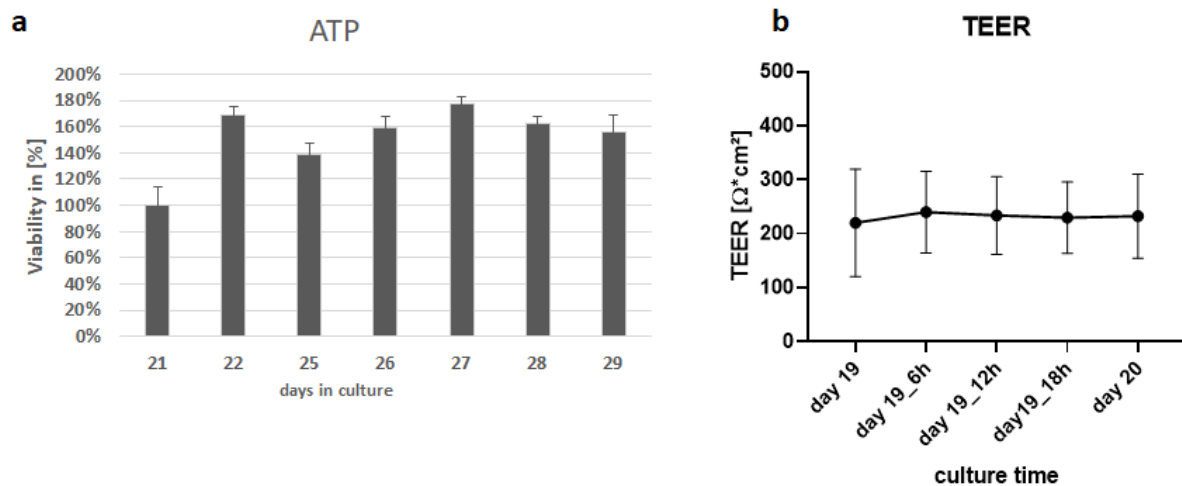


Figure 40: a.) ATP content over time in the Caco-2 2D model. ATP content was measured with the CellTiterGlo® Kit from Promega. Viability was measured on days 21, 22, 25, 26, 27, 28, 29, and 32 after seeding. Shown are the mean values and the corresponding standard deviations. N=5 (appendix 2, Table 40). b.) Measured TEER values after 19 days pre-cultivation and after 6, 12, 18 and 24h in Caco-2 cells. Shown are the mean values and the corresponding standard deviations. N= 10.

The ATP content in the Caco-2 cells in the transwell model was measured from day 21, as the cells were cultivated for experiments until this day. The ATP content stayed constant over 8 days, which confirms that cells were viable during a long culture period (Figure 40a). The increasing viability is due to the fact that the cells are still proliferating and day 21 was used as 100 % viability and the other viability values were referred to this.

An intact and dense monolayer in Caco-2 cells has been formed when the TEER values are between 150-400  $\Omega \cdot \text{cm}^2$  (Srinivasan *et al.*, 2015a). These tight junctions prevent the diffusion of substances through the cell barrier (Srinivasan *et al.*, 2015a). Figure 40b shows that the Caco-2 cells generated after 19 days TEER values between 100 and 350  $\Omega \cdot \text{cm}^2$ , which indicates a stable and tight monolayer and thereby a good imitation of the intestinal barrier.

### 3.1.2. Caco-2 OoC

The cultivation of Caco-2 cells in the OoC from Mimetis is based on a tube formation of cells against a collagen layer. The cells build a tubular structure after 4 days cultivation on the rocker. This tube formation resembles the tube structure of the intestine.

Figure 41a shows how the Caco-2 cells in one chip from the OoC initially distributed themselves directly after seeding. After the OoC had been stored at a 75 ° angle in the incubator, the cells attach themselves to the collagen layer in the middle (Figure 41b) and after the plate had been

cultivated on the rocker in the incubator for 4 days, uniform cell growth was seen within the chip channel (Figure 41c).

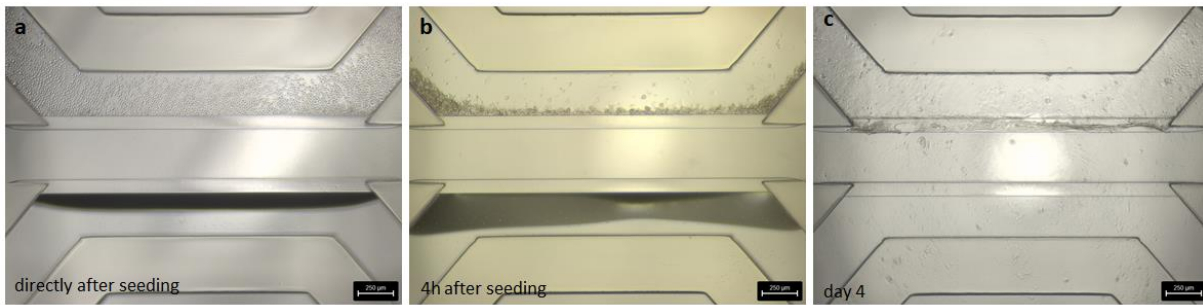


Figure 41: Cultivation of Caco-2 cells in chips of the OrganoPlate from Mimetas. a.) Cell distribution within the chip directly after seeding. b.) Cell sedimentation against the collagen layer after 4h of attachment time. c.) Confluent cell layer visible after 4 days cultivation on the rocker

For the estimation of cell health, the TEER value and ATP content was measured and determined for 8 days after tube formation (day 4 in culture) in order to confirm the morphological results on a molecular level (Figure 42).

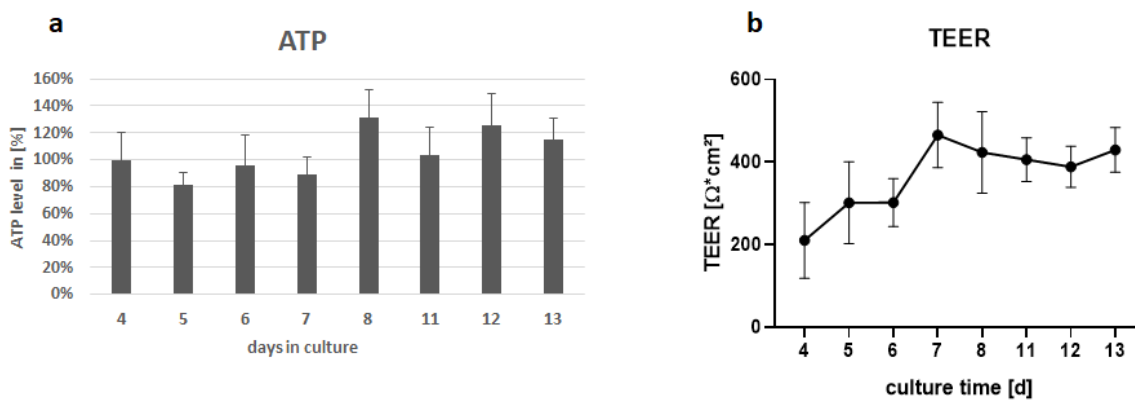


Figure 42.a.) ATP content over time in Caco-2 cells growing in the OrganoPlate®. Viability was measured with the CellTiter-Glo® Kit from Promega after 4, 5, 6, 7, 8, 11, 12 and 13 d. Shown are the mean values and the corresponding standard deviations. N=5 (Appendix 2, Table 38). b.) TEER values of Caco-2 cells growing in the OrganoPlate® from day 4 to day 13. Shown are the mean values and the corresponding standard deviations. N=34.

The viability of Caco-2 cells stayed constant for 8 days after forming a tubular structure (Figure 42a). For the estimation of an intact and tight monolayer the TEER values were used. A tight monolayer of Caco-2 cells is achieved when the TEER value reaches  $\sim 150-400 \Omega^*cm^2$  (Srinivasan *et al.*, 2015b). In the OoC the Caco-2 cells reached the minimum of  $150 \Omega^*cm^2$  already after 4 days.

---

After a further 3 days cultivation the TEER increased until it reached a plateau of approximate 400-600  $\Omega \cdot \text{cm}^2$ . These higher TEER values, compared to the 2D model were also reported in the publication of Beaurivage *et al.* 2019. They reported that TEER value increased until day 4 and then stabilized and led to TEER values between 500 and 700  $\Omega \cdot \text{cm}^2$ .

The OoC is a good opportunity to build up a Caco-2 model which is perfused, membrane free and grows against a collagen layer whereby a barrier function is enabled (Trietsch *et al.*, 2017). This model has the main advantage, of much quicker cultivation of Caco-2 cells to a polarized intestinal epithelial model (from 21 days in a transwell system to 4 days growing in the OoC model).

### 3.1.3. Colon organoids

After isolating cells from their tissues and transferring them to a monolayer as a 2D culture, cell culture models lose their phenotype and morphology. Due to these morphology changes the function can be affected (Kapałczyńska *et al.*, 2016). To culture the cells in more *in vivo* like conditions, the cells can be cultivated in a 3D structure. This greatly improves the morphology and has a positive effect on cell viability and physiological functions because of the more *in vivo* like conditions. One improved cultivation method is the generation of organoids. Organoids are advanced *in vitro* models which recapitulate closely the crypt-villus like structures of the intestine and cell differentiation processes (Bardenbacher *et al.*, 2019). Three characteristics distinguish organoids from 2D cell culture models and 3D spheroids: self-organization, multi-cellularity, and functionality. Intestinal organoids reflect the intestinal crypts, which grow together around a lumen and contain proliferating components at the outside and with mature cells in the middle (Kuratnik and Giardina, 2013).

Colon organoid morphology and formation were monitored by brightfield microscopy. Their formation is driven by self-assembly due multiple differentiation factors. The colon organoids generated here showed an increase in the diameter and as well in the area after each day in culture (Figure 43). The high standard deviations were due to the fact that every organoid is shaped and sized differently.

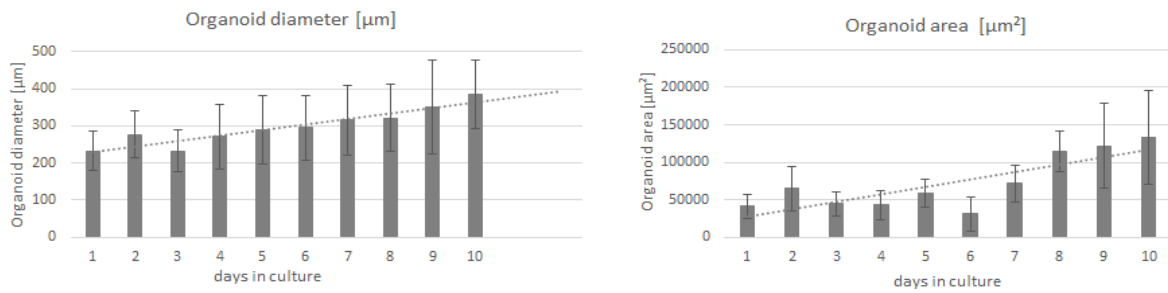


Figure 43: Increasing size and area of organoids during culture. Area and diameter were measured with Leica DM IL LED Fluo microscope. Shown are the mean values and the corresponding standard deviations. N=25.

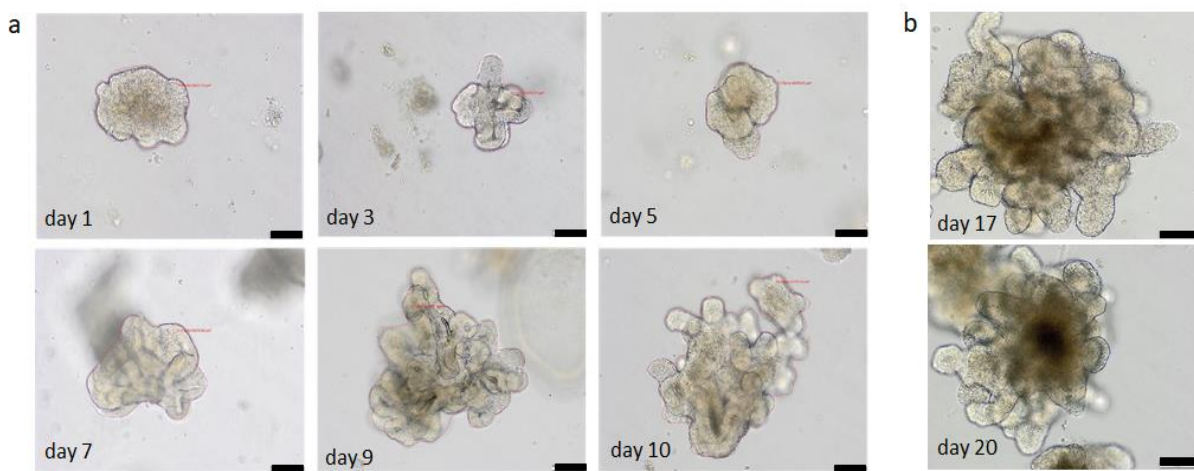


Figure 44: a.) Organoid growth and shape formation during cultivation. 10x magnification, bars = 100µm. b.) Formation of a necrotic lumen after prolonged cultivation without any splitting. 10x magnification, bars = 100µm.

The morphology of the organoids evolved every day to show more invaginations and folds (Figure 44). The microscopic observation of organoids over time showed that organoids stayed viable over a period of around 12-13 days, indicated by intact cell lining and absence of necrotic lumen. Therefore, to achieve viable organoids for the specific experiments the culture was performed for 10 days and after that the organoids were split and seeded for the experiments reported in this work. Organoids that were cultivated for longer became very large and showed a dark and dense lumen (Figure 44b). A long cultivation period can lead to a necrotic lumen due to excessive growth of the organoid, the switch from stem cell proliferating state to a non-proliferating, terminal differentiated state, as well as increased mortality of cells in the inner core. All this results from poor diffusion of oxygen, nutrients, and metabolites and limited waste removal (Yu, Hunziker and Choudhury, 2019; Hofer and Lutolf, 2021). To avoid premature differentiation of cells in the outer layer of the organoid (Grebenyuk and Ranga, 2019), the organoids were used for all further

---

experiments after a proliferation phase of 10 days, and also no necrotic lumen could be recognized.

In order to estimate organoid health on a molecular basis, organoids were stained for Ki67 and ATP content was measured for 8 days after seeding in order to confirm the morphological results (Figure 45 and Figure 46).

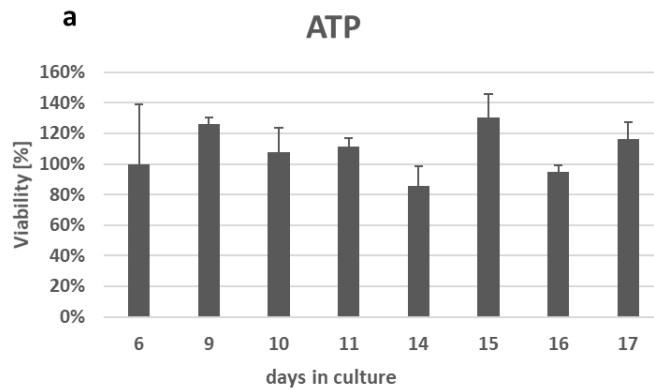


Figure 45: ATP content in colon organoids after several days in culture. Viability was measured with the CellTiter-Glo® 3D after 24h treatment. Shown are the mean values and the corresponding standard deviations. N=5 (appendix 2, Table 39)

The ATP level of colon organoids was constant over several days, without any significant differences reflecting living and healthy colon organoids. These results show the potential of these colon organoids for the use of short- and long-term toxic studies. The difference of  $\pm 20\%$  could be explained by the very different shapes and sizes of the organoids. This is indeed a very big issue for the reproducibility of experiments and for testing new drug candidates a big problem by evaluating drug response, for example normalizing the pharmacokinetic profile (Yu, Hunziker and Choudhury, 2019). However, culturing the organoids in extracellular matrices, like Matrigel™, immobilize the hemispheres on flat plastic surfaces, and does not allow for a culture scaffold to generate the organoids uniformly in shape and size and can result in physiological variations (Yu, Hunziker and Choudhury, 2019; Jung *et al.*, 2021).

---

### 3.2. Morphological characterization of organoids by using immunohistology stainings

Organoids are miniaturized self-organized mini tissue cultures which grow in 3D (Barbuzano, 2017) and are therefore well suited for histological applications. The H&E staining is the most widely used method and often used as the “gold standard method in pathology” (Dhurba, 2018).

Paraffin-embedded sections were prepared and stained with H&E (see section 2.2.9.2). Trained pathologist from Merck confirmed all observations that are described in the following. The organoids were cultivated for 10 days before H&E staining.

Various parameters were measured and exemplarily shown in and listed in Table 31.

Table 31: Characteristic parameters used for the evaluation of organoid health using H&E stained, paraffin embedded microdissections

<b>Parameter</b>	<b>Focus of observation</b>
General cell appearance	Shape & size
	Cell lining
	Villi and crypt structure
	Intact nuclei with included nucleoli
	Detection of diploid cells
Cell death	Fragmented and/or condensed cells
	Localization of necrosis/apoptosis

Active cell proliferation on day 10 was determined by using Ki67 antibody (Figure 46a) (Villarreal, 2012) which binds at the antigen located on the surface of chromosomes during mitosis (Scholzen and Gerdes, 2000). A positive staining of the Ki67 antigen in a microdissection of dog intestine tissue confirms correct staining and acted as a positive control (Figure 46b and c).



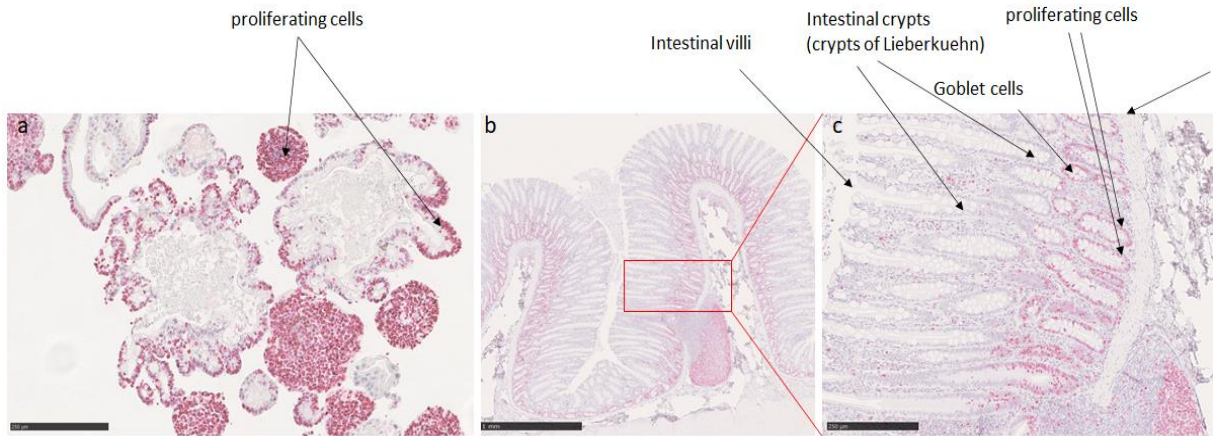


Figure 46: a.) Overview of Ki67 staining of iPSC derived colon organoids microdissection. 12x magnification, bar = 250  $\mu$ m. b.) Ki67 stained microdissection of colon dog, 2.5x magnification, bar = 100 $\mu$ m; c.) Higher magnification of Ki67 stained microdissection of dog colon, 10x magnification, bar = 250  $\mu$ m.

Figure 47 and Figure 48 shows representative images of H&E stained ipsc derived colon organoids after 10 days in culture. The organoids showed well organized cytoplasm and nuclei. This was visible by a defined purple staining and clearly visible nucleoli (Figure 48). No condensed or fragmented cells could be detected which means no signs of apoptotic or necrotic lumen. This indicates a sufficient nutrient transport into the middle of the organoids over 10 days in culture.

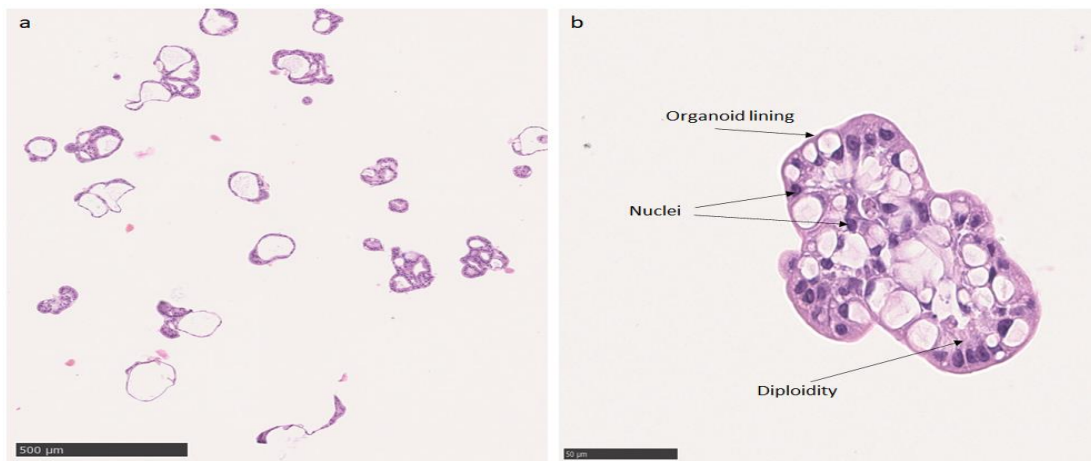


Figure 47: a.) Overview of H&E stained colon organoid microdissections showed different size and shape of organoids. 4x magnification, bar = 500  $\mu$ m. b.) Higher magnification and labelling of the H&E stained organoids, 40x magnification, bar = 50  $\mu$ m.



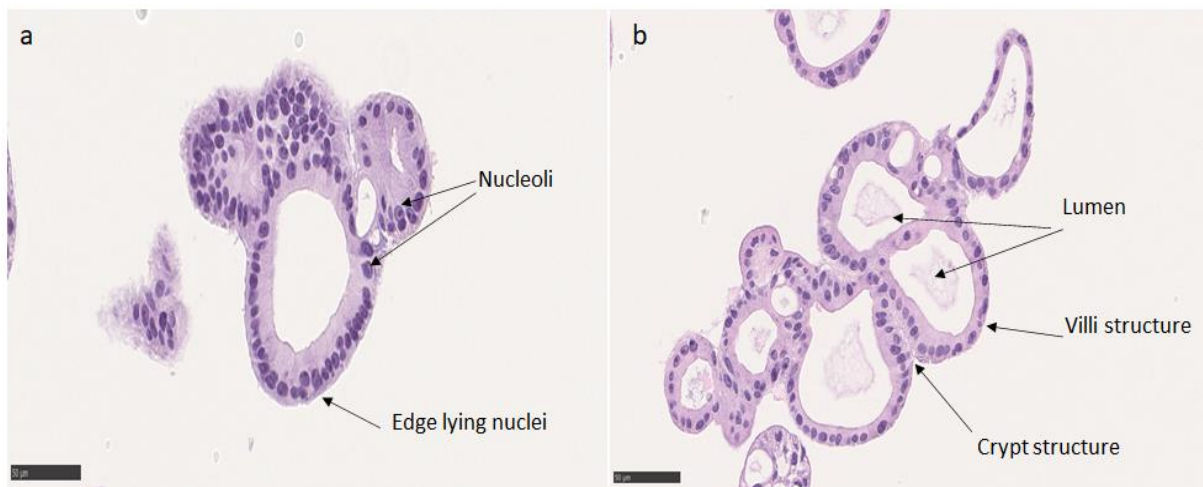


Figure 48: a.) & b.) H&E stained colon organoid microdissections showed specific intestine structures. 40x magnification, bars = 50µm.

The nucleus is usually located at the outer edge of the cells, facing away from the lumen. This is a typically arrangement of enterocytes in the intestine. The nucleus is usually located opposite the brush border, which protrudes into the lumen of the intestine. Villi and crypt like structure could be detected which are equally to this structure of the villis in the intestine. The simple H&E staining was an initial step to prove whether organoids could be cultured in Matrigel® hemispheres and then the organoid health could be monitored. But the generation of organized, viable cells in organoids, does not necessarily mean that the expression of DMETs (drug metabolizing enzymes and toxicologically relevant proteins) is enhanced in this cell culture format or that this model has a higher physiological relevance compared to the previously used 2D cell culture models.

Further antibody stainings were performed to confirm the presence of different cell types within the organoids. Therefore Cytokeratin 20 (CK20) was used for labeling enterocytes, Lysozyme C for paneth cells, synaptophysin A for enteroendocrine cells and to label goblet cells an Alcianblue staining was performed.

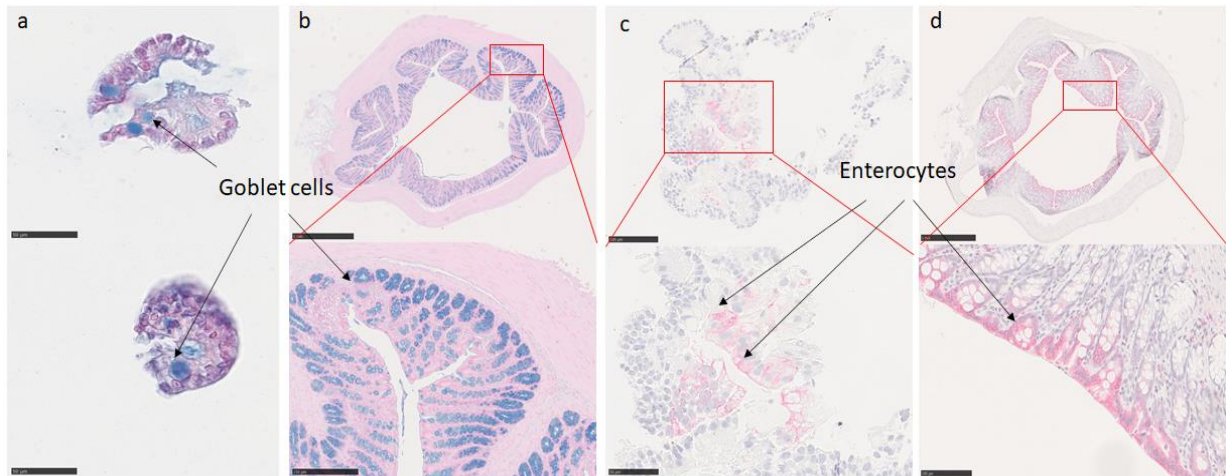


Figure 49: a.) With Alcian blue stained colon organoid microdissections showed presence of goblet cells within the organoids. 40x magnification, bar = 50  $\mu\text{m}$ . b.) Positive control for staining of goblet cells in rat colon tissue with Alcian blue staining, 2.5x magnification, bar = 1 mm (picture above) and 10x magnification, bar = 250 $\mu\text{m}$  (picture below). Staining of enterocytes in the organoids with CK20, 20x magnification, bar = 100  $\mu\text{m}$  (picture above) and 40x magnification, bar = 50  $\mu\text{m}$  (picture below). D.) Positive control for staining of enterocytes in dog colon with CK20, 2x magnification, bar = 1 mm (picture above) and 25x magnification, bar = 100  $\mu\text{m}$  (picture below).

Figure 49a shows clear Alcian blue staining, confirming the presence of goblet cells within the organoids. Alcian blue stains acidic mucins which were produced by goblet cells and is specific for the staining of cells with epithelial origin (Osho *et al.*, 2017). The staining of goblet cells of a rat colon tissue microdissections was used as a control (Figure 49b) and confirmed the correctly conducted and successful staining.

The identification of enterocytes in the organoids are shown in Figure 49c. The antibody CK20 was used since it reacts specifically with the cytokeratin intermediate filament of the villi of the human intestinal mucosa (Campbell and Herrington, 2001). A well-defined staining of enterocytes was observed in a microdissection of dog colon and thereby used as positive control (Figure 49d). In the dog colon tissue microdissection, the enterocytes are found at the top of the villis which means directed towards the intestinal lumen. The same localization was also seen in the organoids. The enterocytes are found in the middle of the organoid, which represents the lumen of the intestine. The CK20 stainings is clearly visible in the organoid sample and the dog colon sample as a thin colored border around the cells. This can be explained by the fact that cytokeratins are responsible for the formation of fibrous filaments of cells, which in turn build and influences the cytoskeleton of cells (Baum, 2019).

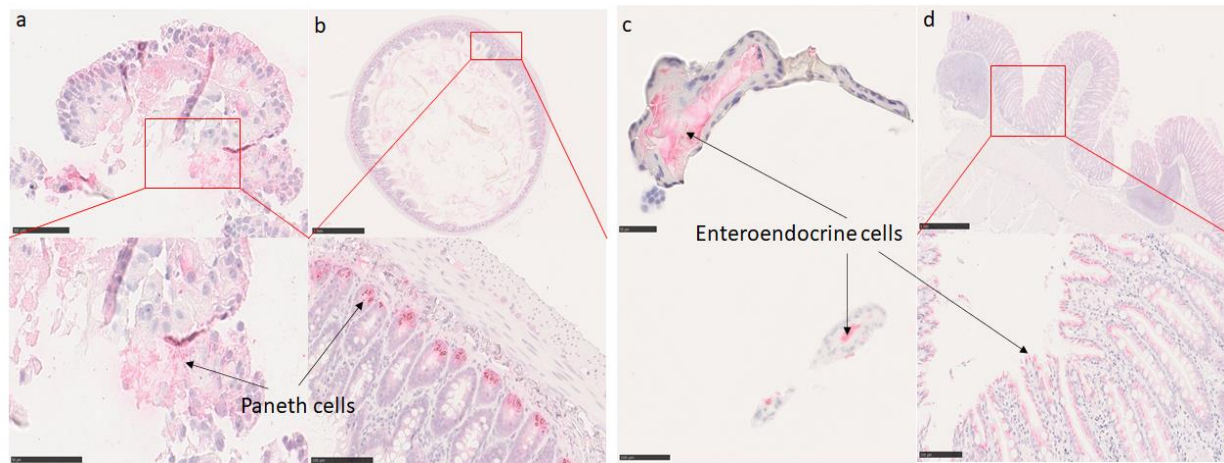


Figure 50: a.) With Lysozyme C stained colon organoid microdissections showed presence of Paneth cells within the organoids. 40x magnification, bar = 50  $\mu\text{m}$  (picture above) and 70x magnification, bar = 50  $\mu\text{m}$  (picture below). b.) Positive control for staining with Lysozyme C of Paneth cells in rat colon tissue, 2x magnification, bar = 1 mm (picture above) and 25x magnification, bar = 100  $\mu\text{m}$  (picture below). c.) Staining of enteroendocrine cells in the organoids with synaptophysin, 35x magnification, bar = 50  $\mu\text{m}$  (picture above) and 20x magnification, bar = 100  $\mu\text{m}$  (picture below). d.) Positive control for staining of enteroendocrine cells in dog colon with Synaptophysin, 2x magnification, bar = 1mm (picture above) and 25x magnification, bar = 100  $\mu\text{m}$  (picture below).

The presence of Paneth cells was determined by using Lysozyme C. In the dog colon control microdissection, the Paneth cells were located in the base of crypts of Lieberkuehn and can be seen as small dots of magenta color (Figure 50 b). The small dots are eosinophilic granules which were produced by Paneth cells and contain immunomodulating proteins and antimicrobial peptides to keep the composition of the intestinal flora in balance. This is a very important function in secondary controlling the maintenance of repair mechanisms of the intestinal epithelial layer or the status of intestinal inflammation (Lueschow and McElroy, 2020). The granules of Paneth cells within the organoids are also detectable as small pink dots (Figure 50 a). Synaptophysin is found in secretory vesicles of enteroendocrine cells (Gunawardene, Corfe and Staton, 2011) and is therefore perfectly applicable for the identification of enteroendocrine cells within the dog colon or organoid microdissections. Enteroendocrine cells are dispersed over the complete intestine and build around 1 % of the epithelium and secrete different hormones (Worthington, Reimann and Gribble, 2018). In both microdissections tested here enteroendocrine were identified. In the organoids the staining was visible within the lumen of the organoid (Figure 50 c). This suggested that the cells of the organoids were somewhat destroyed during cutting of the paraffin block or during transfer to the slide. In the microdissection of dog colon, the staining was visible on the complete surface of the villi (Figure 50 d).

---

In nearly all the microdissections no condensed cytoplasm and chromatin, characterized by an increased intensity of the staining, and nuclei fragments, which indicates poor health and often results in cell death, were observed. If such necrotic or apoptotic events were observed, however, then they were randomly distributed and only very rarely, which again indicates a normal physiological turnover.

### 3.3. Morphological characterization of all three cell culture models by using immunofluorescent (IF) stainings

The IF stainings were used to identify cell specific intestine markers or markers of intestinal function. In addition, markers for intact intestinal barrier were used to evaluate the tightness of the monolayers and therefore to estimate the cell health on a molecular basis.

Initially, the antibody LGR5 was used to identify the presence of stem cells within the organoids (Figure 51).

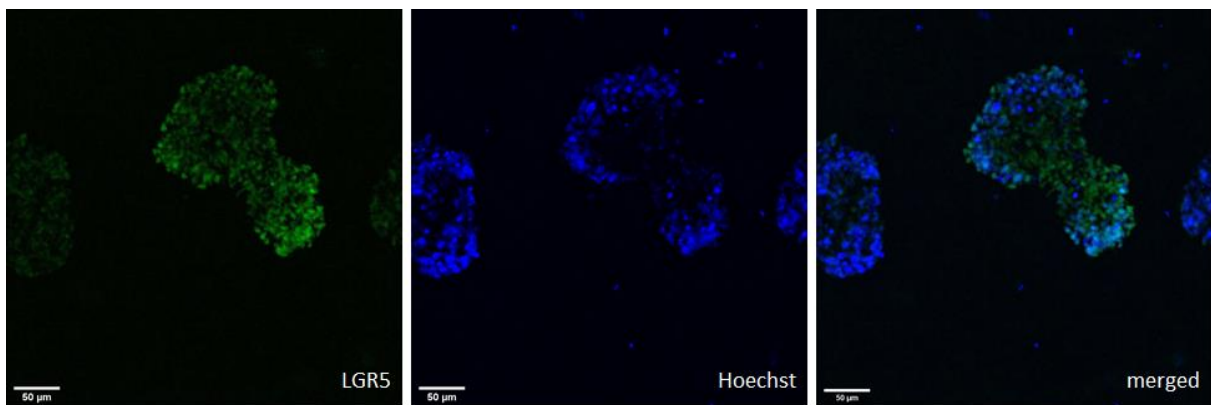


Figure 51: Staining of stem cells with the antibody LGR5 (green) within the organoids. Nuclei were counterstained with Hoechst (blue). 10x magnification, bar = 50 µm.

Stem cells in the intestine, also called crypt base columnar cells, are characterized by their expression of LGR5 receptor 1 on their cell surface. Under homeostatic conditions stem cells are jointly responsible for the rapid renewal of the epithelium. Beside the self-renewal function they are able to build transit-amplifying cells, which can differentiate along the villi structure to paneth cells, goblet cells, enteroendocrine cells, enterocytes and tuft cells (Haegbarth and Clevers, 2009; Fernandez Vallone *et al.*, 2020). The presence of the stem cells in the organoids suggests that the proliferating cells can differentiate into all other intestinal cell types.

With this staining and the immunohistochemistry stainings all five important cell types of the intestine could be determined, indicating a similar *in vivo* situation.



In addition to the assessment of organoids, the Caco-2 cells in 2D, the OoC system and the 3D system of organoids were side by side compared to be able to make a direct comparison of all models.

For the evaluation and further characterization of the cell culture models, the important components of the tight junctions and adherens junctions were stained. Both type of junctions play an essential role in the barrier function and protection (Takeichi, 1990; Zihni *et al.*, 2016).

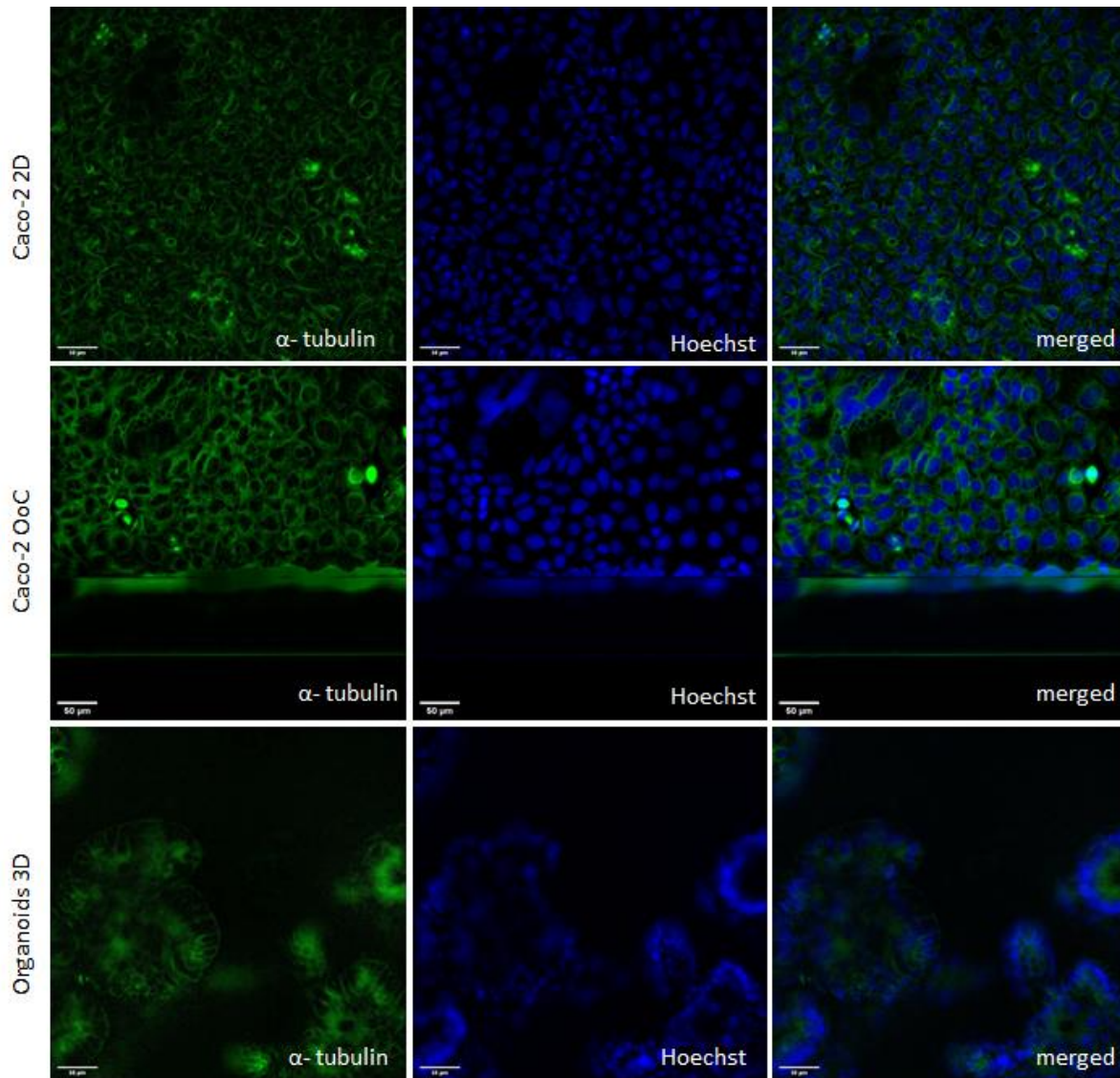


Figure 52: Immunofluorescent stainings with the antibody  $\alpha$ -tubulin to stain the structures of the cytoskeleton. Shown are the Caco-2 2D (pictures above), Caco-2 OoC (pictures in the middle) and Organoids 3D (pictures below) models with the antibody  $\alpha$ -tubulin (green). Nuclei were counterstained with Hoechst (blue). 20x magnification, bar = 50  $\mu$ m for 2D, OoC and 3D.

Figure 52 shows for each cell culture model the staining of microtubules, one out of three main components of the cytoskeleton (Horio, Murata and Murata, 2014) with the antibody  $\alpha$ -tubulin. Very small lines indicate the structure of microtubules, which are composed of  $\alpha$ - and  $\beta$ -tubulin dimers. Some of the main functions of microtubules are to determine the shape of the cell, provide intracellular transport pathways and they are involved in cell division (Avila, 1992; Vale, 2003). The staining shows an intact network of microtubules, which shows healthy cells capable for cell division and proliferation.

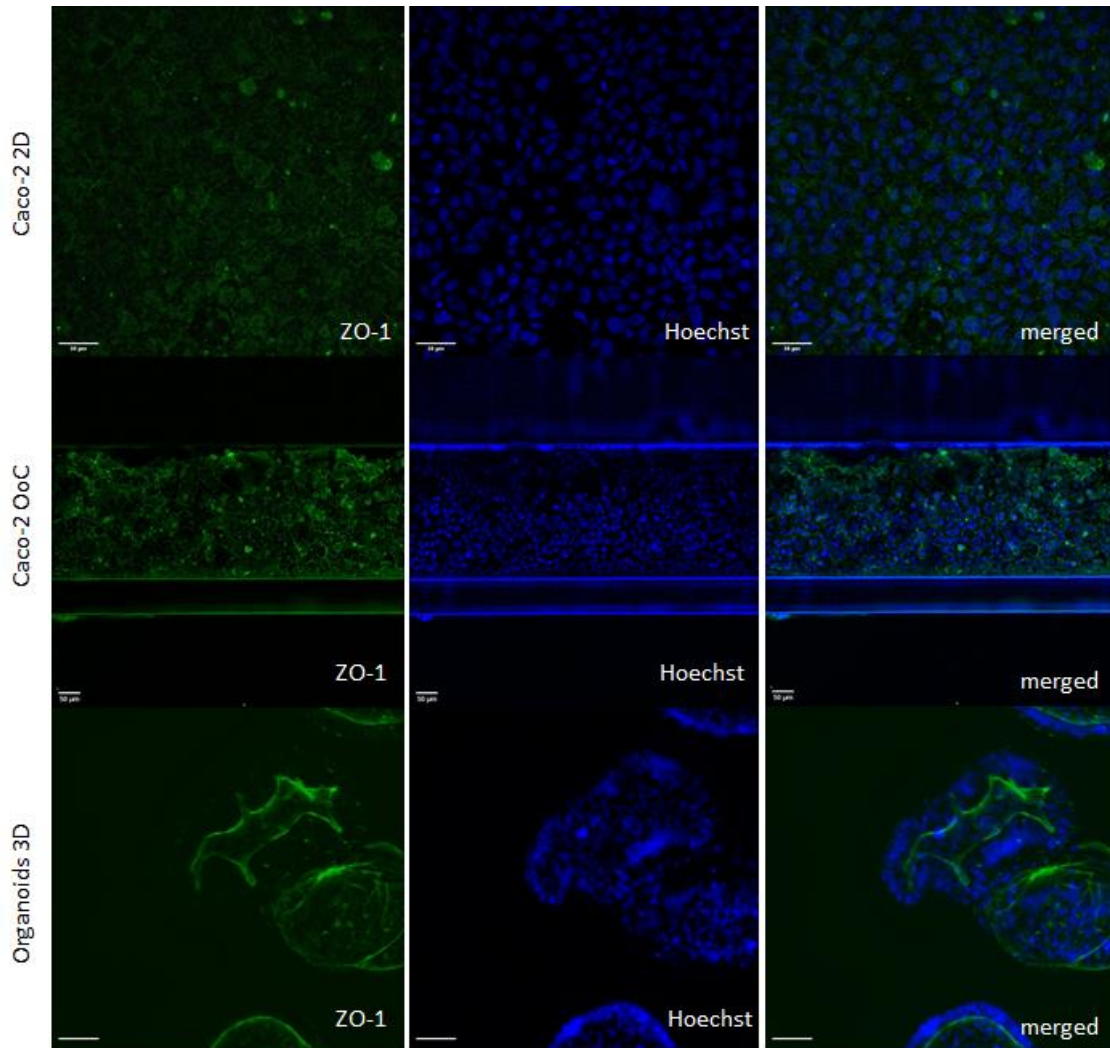


Figure 53: Immunofluorescent stainings with the antibody ZO-1 to stain specific proteins of the tight junctions. Shown are the Caco-2 2D (pictures above), Caco-2 OoC (pictures in the middle) and Organoids 3D (pictures below) models with the antibody ZO-1 (green). Nuclei were counterstained with Hoechst (blue). 20x magnification, bar = 50  $\mu$ m for 2D and 3D and 10x magnification, bar = 50  $\mu$ m for OoC.

---

A further staining was performed to detect specific tight junction proteins, to investigate the capability of the different cell culture systems to build a tight barrier due to a close cell-cell contact. Tight junctions are the most abundant connections between apical cells (Krause *et al.*, 2008), composed of approximately 40 different proteins (McNeil, Capaldo and Macara, 2006) and are responsible for the prevention of leakage of solutes from the gut lumen for example (Anderson *et al.*, 1989). ZO-1 is a peripheral scaffold protein of the cell membrane of epithelial and endothelial cells. It contains protein-binding domains for all major important transmembrane barrier proteins, like JAM-A (Martín-Padura *et al.*, 1998), occludin (Furuse *et al.*, 1998), claudin (Furuse *et al.*, 1998; Itoh *et al.*, 1999), and tricellulin (Ikenouchi *et al.*, 2005). Specifically, in the OoC system very small lines of stained ZO-1 around each cell was visible. The fact that only in the upper part of the picture the thin staining is visible is due to the 3D structure of the tube and it was not possible to document the different layers with the microscope. In the 2D system the staining was more broadly distributed, but it was still visible that the staining was around the cells indicating the building of tight junctions between the cells. Compared to the 2D and OoC system the staining of ZO-1 in the organoid system was completely different. It is clear that the staining surrounds the lumen in the middle of the organoids as well as around the complete organoid, but not between the cells. The annular coloring of ZO-1 in the organoids was on top of the cells and suggest that the inside of the organoids is the area of the brush border membrane, which is the side of drug absorption and first barrier against xenobiotics (Zhang *et al.*, 2014; Onozato *et al.*, 2018).

Claudins are tetraspan transmembrane proteins which are responsible for the complete closure of the gap between two cells (Krause *et al.*, 2008). Claudins are composed of an N- and C-termini which are orientated to the cytoplasm. The C-termini enables direct binding to the cytoplasmatic proteins, like ZO-1, ZO-2, or ZO-3, and thereby forming a link to the actin cytoskeleton, which stabilizes the tight junction complex and maintains the tightness (Findley and Koval, 2009). In all three models a defined staining of claudin7 protein was detected (Figure 54). Each cell showed a thin border staining. This staining demonstrated the capability of all three cell culture models to form a tight barrier with well-formed tight junctions. This is very useful for replicating the *in vivo* intestinal barrier, which obtains its barrier function mainly through these tight junctions. Thus, the three cell culture models represent a good *in vitro* method for evaluating the potential damaging effects of new drug candidates on the intestinal barrier – at least when direct toxicity against the barrier is observed.

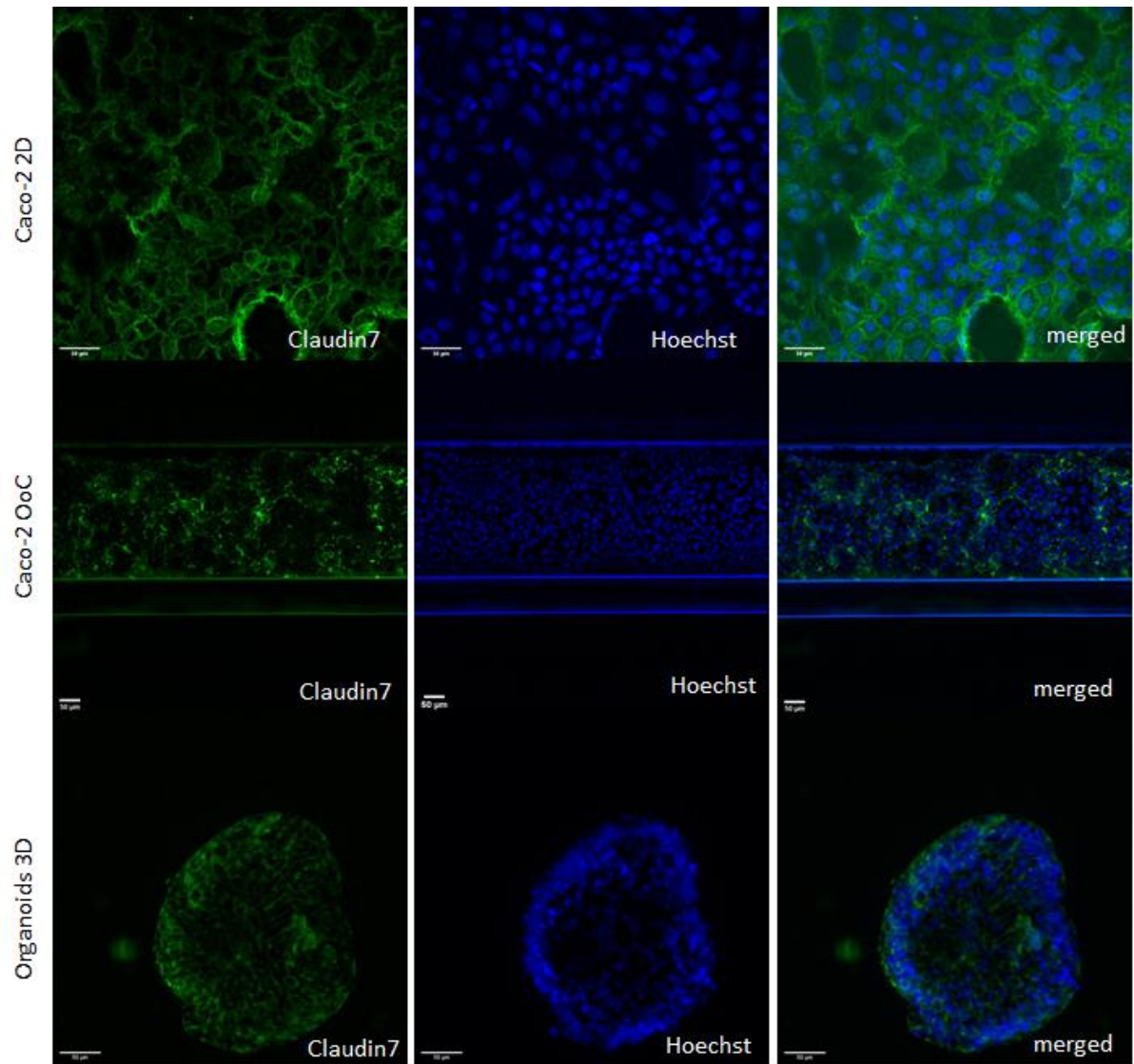


Figure 54: Immunofluorescent stainings with the antibody claudin 7 to stain for a specific tight junction protein. Shown are the pictures of Caco-2 2D (pictures above), Caco-2 OoC (pictures in the middle) and Organoids 3D (pictures below). Nuclei were counterstained with Hoechst (blue). 20x magnification, bar = 50 μm for 2D and 3D and 10x magnification, bar = 50 μm for OoC.

The staining of occludin, another important tight junction protein is shown in the appendix (appendix 3, Figure 107).



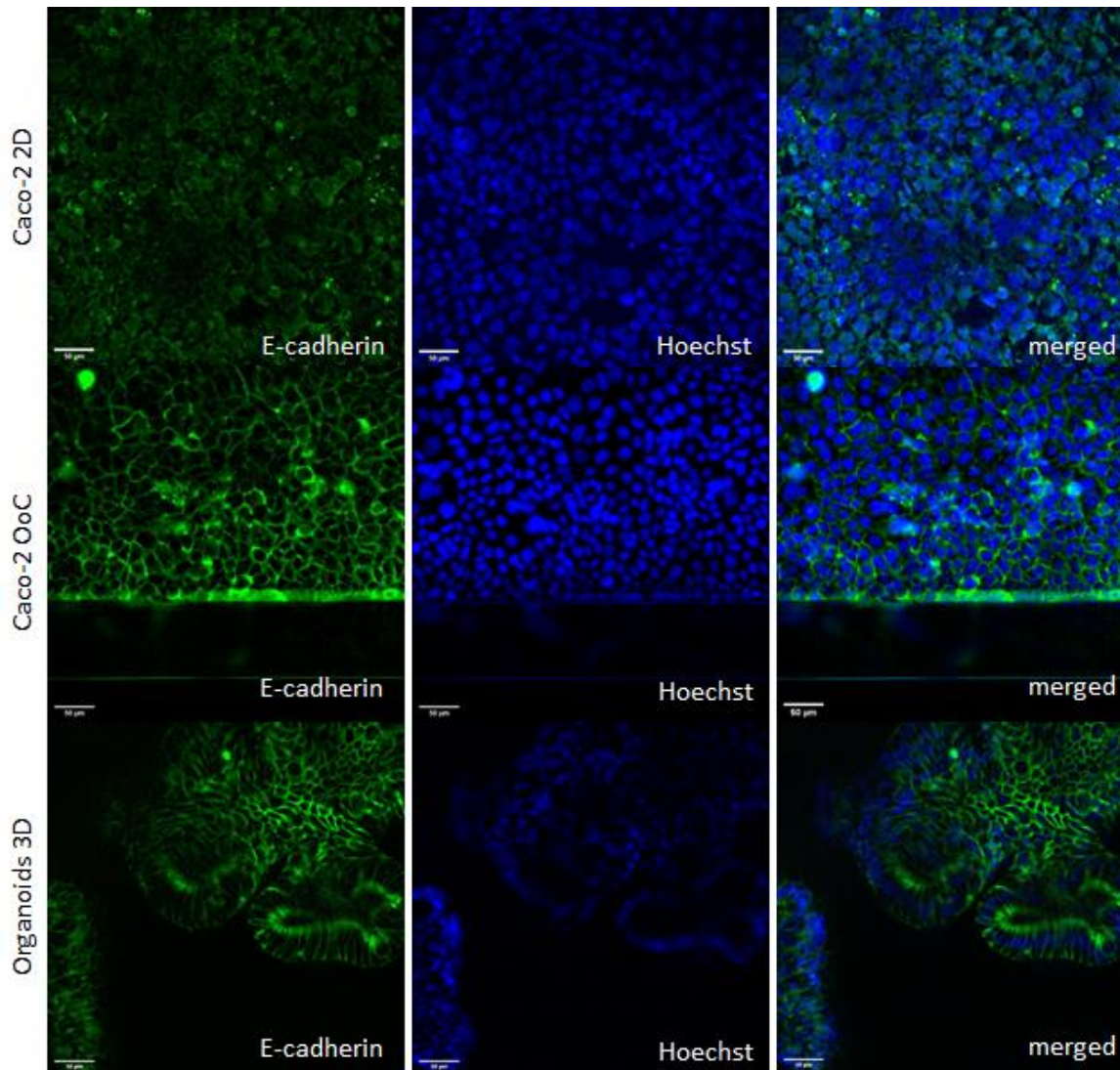


Figure 55: Immunofluorescent stainings with the antibody E-cadherin to stain for a specific protein of the adherens junctions. Shown are pictures of Caco-2 2D (pictures above), Caco-2 OoC (pictures in the middle) and colon organoids 3D (pictures below). Nuclei were counterstained with Hoechst (blue). 20x magnification, bar = 50 $\mu$ m for 2D, OoC and 3D and 10x magnification.

The adherens junctions between the cells play an important role for maintaining the intestinal barrier. Adherens junctions play a crucial role in the formation of tight junctions. It is assumed that the adherens junctions need to be formed prior to the tight junctions being built. The major component of adherens junctions is e-cadherin, which is a single transmembrane protein. It binds to similar dimers in neighbouring cells and leads to an interaction with the cytoplasm actin binding proteins. This shows its important function in maintaining the epithelial barrier function (Guo *et al.*, 2003). In the OoC system with Caco-2 cells and the organoid model a well-defined staining was shown around each cell. This indicates an intact building of adherens junctions in those two models. The 2D model did not show such thin and defined staining. The staining is more

widely and blurry, not only around the cells. This suggest that the Caco-2 cells in the 2D systems are not able to build a complete tight monolayer by forming adherens junctions. The picture of the organoids shows a defined and thin staining around each of the cells and a thicker staining against the lumen. The stainings in the Caco-2 OoC model and in the colon organoid model indicates that these models are able to maintain the intestinal barrier. E-cadherin is involved in the intestinal epithelial lining and helps to generate mechanical integrity. Likewise, it is responsible for the correct maturation of Paneth and goblet cells (Schneider *et al.*, 2010).

### 3.4. Functional characterization of all three cell culture models by using immunofluorescent (IF) stainings

Since the morphology and viability of the cells in the different cell culture models were determined in the first part of the characterization, using immunohistology stainings, it was important to further investigate whether organoids have an enhanced metabolic capacity. H&E and Ki67 staining of paraffin-embedded organoid sections is an attractive option to monitor organoid health and quality over the course of culture or to check whether certain cell types show increased damage after drug administration compared to other cell types. To assess the expression of drug metabolizing enzymes and transporters (DMETs), which play an important role in initiation of metabolite-related gastrointestinal toxicity immunofluorescent stainings were performed. For this purpose, a selection of representative members of each phase of xenobiotic metabolism were chosen (Table 32).

Table 32: Selected representative primary antibodies against phase I, II and III for the assessment of metabolic capacity of the different cell culture systems

	<b>Antigen</b>	<b>Host, clonality</b>	<b>Dilution</b>
Phase I	<i>CYP3A4</i>	Mouse, monoclonal	1:100
	<i>CYP2D6</i>	Rabbit, polyclonal	1:100
	<i>CYP2C9</i>	Rabbit, polyclonal	1:100
Phase II	<i>NAT 1/2</i>	Mouse, monoclonal	1:100
	<i>GSTA1</i>	Goat, polyclonal	1:100
	<i>SULT1E1</i>	Mouse, monoclonal	1:100
Phase III	<i>MRP2</i>	Mouse, monoclonal	1:50
	<i>MDR1</i>	Mouse, monoclonal	1:100
	<i>BCRP</i>	Mouse, monoclonal	1:200

IF stainings was done for the detection of intestine specific transporters, enzymes, or specific markers for the gut function. Gene expression experiments and protein expression were observed to detect differences between the cell culture models regarding their ability to resemble the *in vivo* intestine.

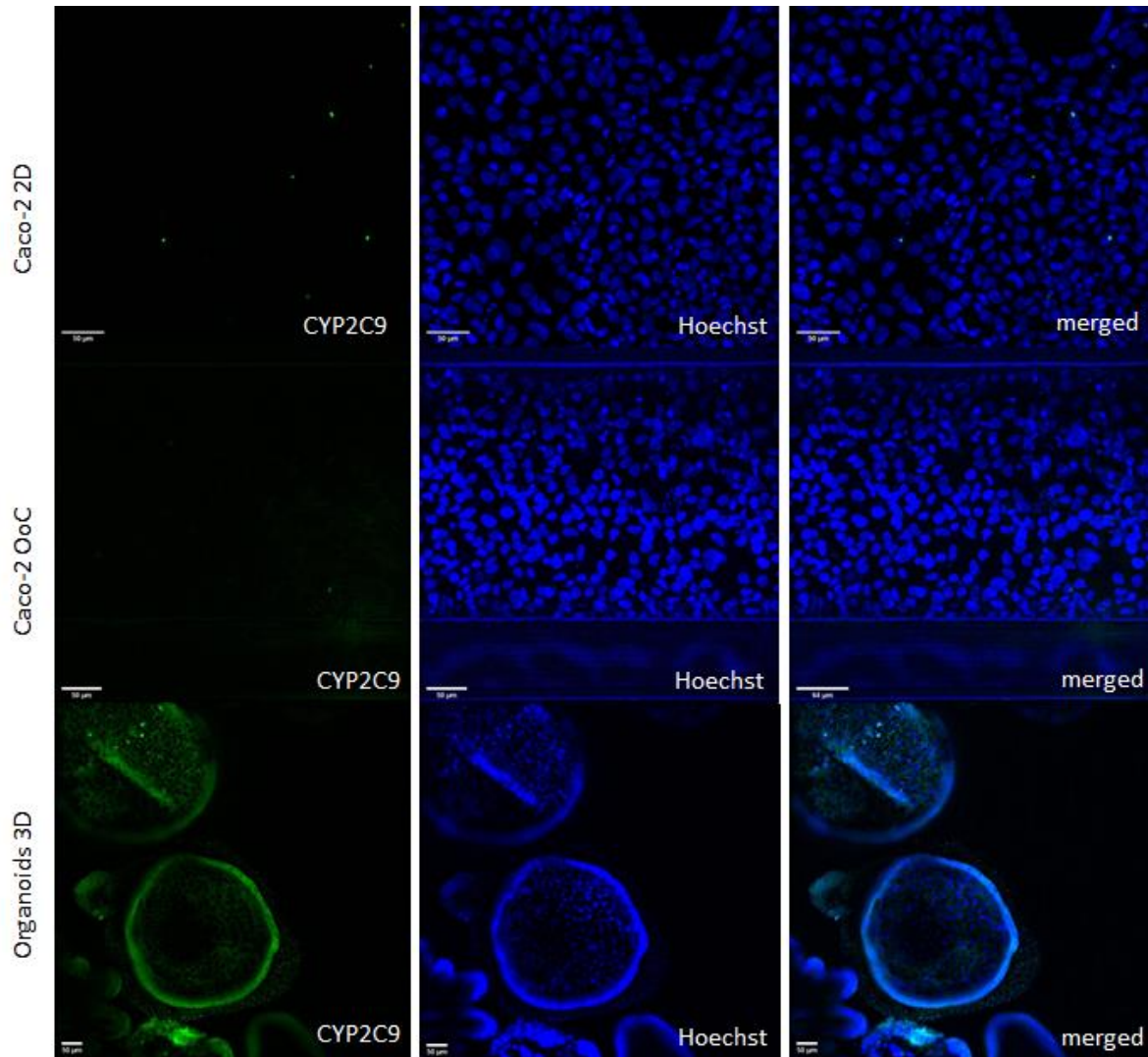


Figure 56: Immunofluorescent stainings with the antibody CYP2C9 to stain for a specific phase I enzyme. Shown are pictures of Caco-2 2D (pictures above), Caco-2 OoC (pictures in the middle) and colon organoids 3D (pictures below). Nuclei were counterstained with Hoechst (blue). 10x magnification, bar = 50 µm for 3D and 20x magnification, bar = 50 µm for 2D and OoC.

The enterocytes of the small intestine are the first site of xenobiotic metabolism, mostly through cytochrome P450 enzymes. The most abundant intestinal CYP's are: *CYP3A4*, *CYP3A5*, *CYP1A1*, *CYP2C9*, *CYP2C19*, *CYP2D6* and *CYP2J2* (Obach *et al.*, 2001; Galetin and Houston, 2006). However, interindividual variability in the expression of phase I and phase II metabolic enzymes in the human small intestine is a much discussed topic (Kaminsky and Zhang, 2003; Xie, Ding and Zhang,



2016). *CYP2C9* is an important phase I enzyme for drug metabolism, it contributes to approximately 15 % of all drug metabolism (Krogstad *et al.*, 2020). In Figure 56 it can be seen that only in the organoid cell culture model a staining for *CYP2C9* was detectable. The Caco-2 cells, whether cultured in 2D or in OoC, showed no staining, indicating that the enzyme *CYP2C9* is not expressed in the colon cancer cell line.

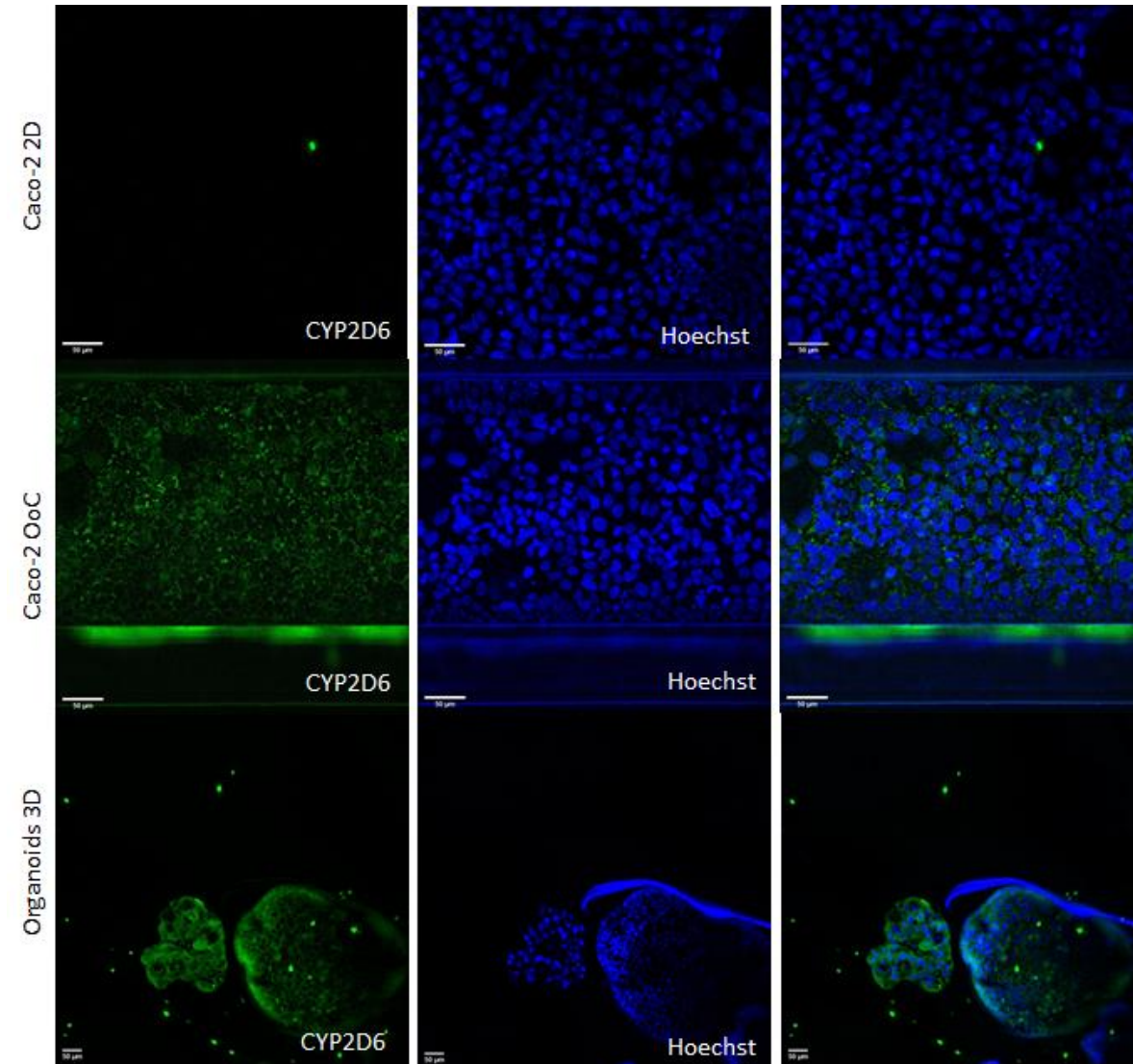


Figure 57: Immunofluorescent stainings with the antibody *CYP2D6* (green) to stain for a specific phase I enzyme of the intestine. Shown are pictures of Caco-2 2D (pictures above), Caco-2 OoC (pictures in the middle) and colon organoids 3D (pictures below). Nuclei were counterstained with Hoechst (blue). 10x magnification, bar = 50 µm for 3D and 20x magnification, bar = 50 µm for 2D and OoC.

Further stainings were done for *CYP3A4* and *CYP2D6*. Neither were detectable in the Caco-2 2D system. For *CYP2D6* a staining was seen in the 3D organoid system and in the OoC system (Figure 57). It is very surprising that the Caco-2 cells express *CYP2D6* when they were cultivated in the OoC system but not in 2D. This phenomenon was described and discussed before by other

---

scientists. Caco-2 cells alter their expression, when cultivated in a 3D structure compared to standard cultivation in a 2D monolayer. Some genes responsible for cell proliferation, differentiation and cell growth could be increased (e.g. JUN and BCL6) or decreased (EGFR, CMYC and MINA) in 3D cultures of Caco-2 cells (Luca *et al.*, 2013). The 3D model, and in the case of this thesis additionally the OoC model, helps to investigate experiments under more physiologically relevant conditions by implementing an extracellular matrix or 3D structure. Furthermore, the application of a medium flow, which exerts a stress on the cells, alters the morphology and gene expression of Caco-2 cells. The cells are more like *in vivo* after implementing flow to the cell culture system (Kulthong *et al.*, 2021).

The staining for *CYP3A4* is shown in the appendix. In all three models no specific staining of the enzyme *CYP3A4* was detectable, only a blurry undefined, unspecific staining (appendix 3, Figure 108). Caco-2 cells do not express *CYP3A4* at sufficient levels (Schmiedlin-Ren *et al.*, 1997), which may be problematic for staining and thus not visible. The small intestine and the liver have the highest *CYP3A4* expression in humans (MedSafe, 2015). Especially in the small intestine the *CYP3A4* enzymes plays an important role in the first pass metabolism of drugs and can extremely reduce the amount of orally taken drugs before they reach systemic circulation and there place of action (Kato *et al.*, 2003; Xie, Ding and Zhang, 2016).

Stainings for specific phase II enzymes were performed and the following antibodies were used: N-Acetyltransferase 1/2 (*NAT 1/2*), Sulfotransferase 1E1 (*SULT1E1*), and Glutathione-S-Transferase Alpha 1 (*GSTA1*).

An expression of *NAT 1/2* was only seen in the 3D organoid model (Figure 58). When looking at the overall distribution of *NAT 1/2* expressing cells within the organoid, it was clear that single cells expressed different enzyme levels, thus leading to a patchy appearance. It was also observed that the lining layers expressed no or very little levels of *NAT 1/2*.

In 2D and in the OoC system with Caco-2 cells no staining was detected. *NAT 1/2* catalyzes the conjugation of xenobiotics and has thereby an important role in detoxification and defense against chemicals and pollutants (Zhang, 2011). The expression of this enzyme in the organoid model suggests that the 3D model corresponds more closely to the physiological conditions of the human body, specifically the intestine, than the two models with the Caco-2 cells, since *NAT 1/2* is expressed in the small intestine and the colon (Windmill *et al.*, 2000).

Beside the staining with *NAT 1/2*, stainings with antibodies against *SULT1E1* and *GSTA1* were performed. *GSTA1* was not detectable in none of the three *in vitro* models whereas *SULT1E1* was observed in the 3D model as defined staining (appendix 3, Figure 109 and Figure 110).

*SULT1E1* was equally distributed within each cell and over the complete organoid. A very blurry staining was seen in the 2D model, but this was defined as unspecific staining. *SULT1E1* is expressed in the whole part of the human GI tract and is responsible for the conjugation of neutrophilic substrates and the formation of active intermediates (Teubner *et al.*, 2007). The fact that *SULT1E1* was not expressed in the Caco-2 cell line either in 2D nor OoC has also been reported (Meinl *et al.*, 2008).

In the case of *GSTA1* expression, all three *in vitro* models showed no specific staining. *GSTA1* and *GSTA2* is normally widely expressed in the human intestine, in high levels in duodenum and small intestine and in low level in colon (Coles *et al.*, 2002).

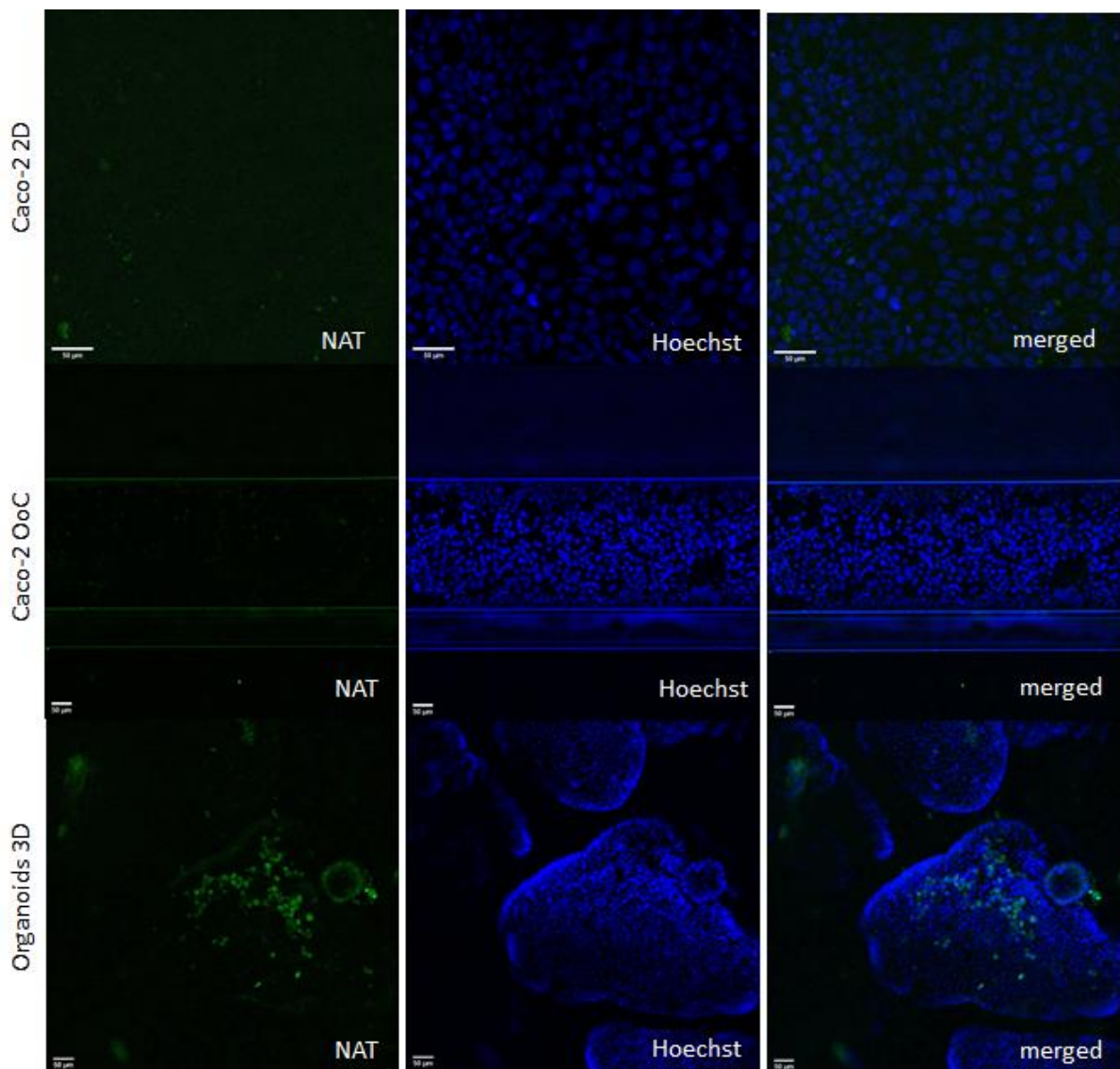


Figure 58: Immunofluorescent stainings with the antibody NAT 1/2 (green) to stain for a specific phase II enzyme of the intestine. Shown are pictures of Caco-2 2D (pictures above), Caco-2 OoC (pictures in the middle) and colon organoids 3D (pictures below). Nuclei were counterstained with Hoechst (blue). 10x magnification, bar = 50 µm for OoC and 3D and 20x magnification, bar = 50 µm for 2D.

---

The results obtained suggest that, regarding the expression of various phase I and II enzymes, the iPSC-derived colon organoids better reflect the physiological conditions of the human body than the Caco-2 cell line. The intestinal mucosa plays a major role in the metabolism of drugs via phase I and II reactions. Recent evidence has shown that the mucosal metabolism can also influence the bioavailability of orally administered drugs (Doherty and Charman, 2002). Therefore, it would be good to generate an *in vitro* model which combines several organs and most of the human abundant enzymes to better mimic clinical drug metabolism and pharmacokinetics.

One of the key functions of the small intestine is absorption. This involves the inclusion of nutrients, water, electrolytes, and drugs. The absorption is mainly possible due to the enlarged surface area and the presence of specific transporters (Doherty and Charman, 2002; Freeman and Thomson, 2005).

For the evaluation of transporter abundance different stainings against specific drug transporter and intestine transporters were performed. For this approach the following antibodies were used: *MRP2* (*ABCC2* or *cMOAT*), *MDR1* (*ABCB1* or *P-gp*), and *BCRP* (*ABCG2*).

The staining for *MRP2* showed a higher expression in the Caco-2 2D model compared to the OoC model with Caco-2 cells. The 2D model showed a very uniform and extensive coloration in each individual cell. In comparison, the OoC model showed only isolated circular staining around several cells. But the picture is a bit confusing, because of the 3D structure of the tubular structure and the different levels of the picture. In the lower level, which forms the lower straight part of the tube, an even distribution of *MRP2* expression can be seen. There was also a strong coloration on the lateral walls of the tube. In the 3D model a very thin lining around each cell of an organoid was observed. Some cells also showed a stronger, broader coloration, which indicates a higher expression of *MRP2* in these cells. In the human intestine the expression of *MRP2* is highest in jejunum and duodenum and decreases in the colon (Dietrich, Geier and Oude Elferink, 2003; Lemmens *et al.*, 2021). The localization of *MRP2* in the apical membrane of intestinal mucosal epithelial cells explains its role in drug transport, as well as its important role in drug metabolism and detoxification. The apical localization determines drug absorption and xenobiotic secretion (König *et al.*, 1999; Yang *et al.*, 2007). The singular and stronger staining of *MRP2* in the iPSC derived colon organoid model shows that the enterocytes are available in this model and that they are able to transport drugs similar to that in the human intestine.



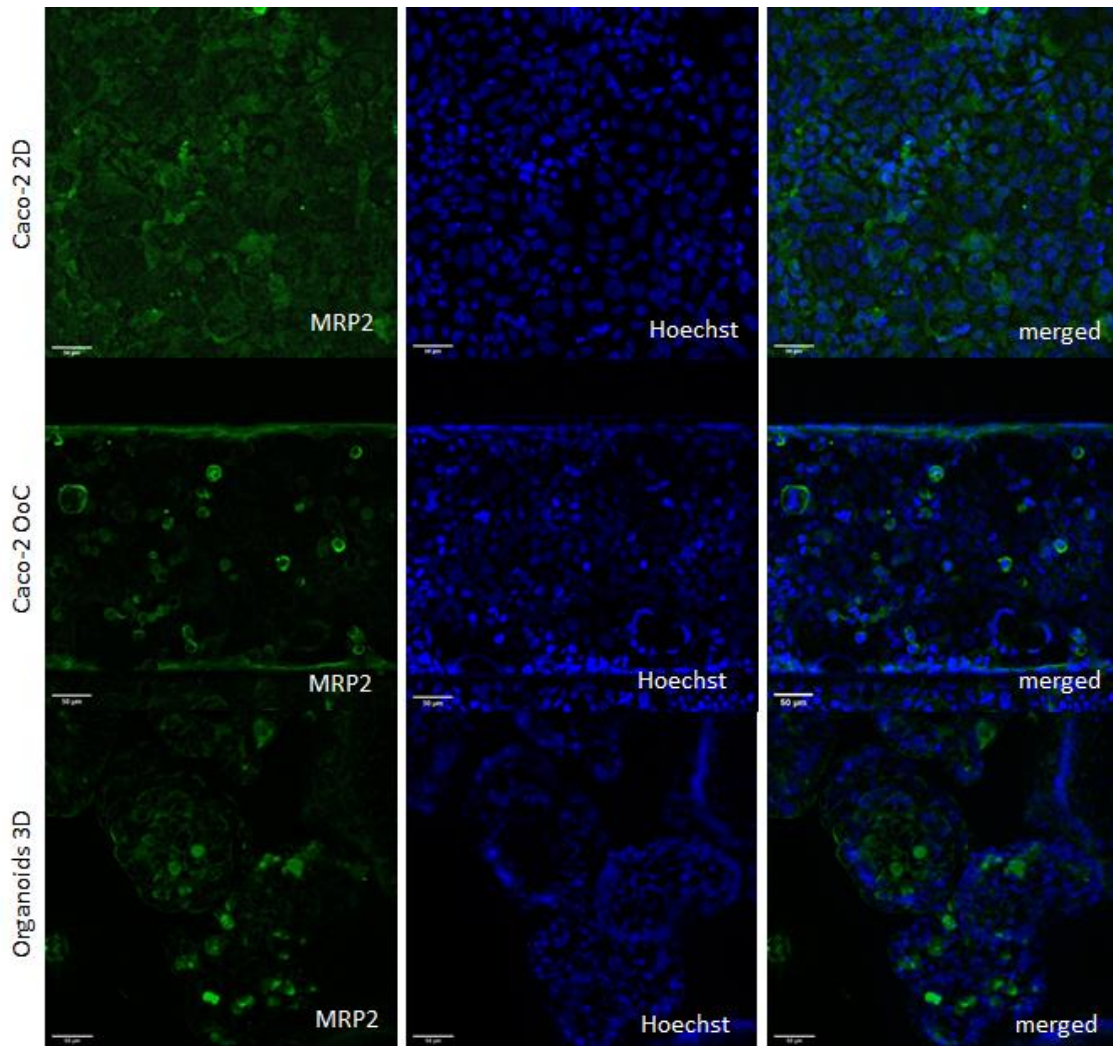


Figure 59: Immunofluorescent stainings with the antibody *MRP2* (green) to stain for a specific drug transporter of the intestine. Shown are pictures of Caco-2 2D (pictures above), Caco-2 OoC (pictures in the middle) and colon organoids 3D (pictures below). Nuclei were counterstained with Hoechst (blue). 20x magnification, bar = 50  $\mu\text{m}$  for 2D, OoC and 3D.

Beside the localization of *MRP2*, the presence of *BCRP* and *MDR1* was also investigated. For *MDR1* no expression was observed in either one of the three cell culture models (appendix 3, Figure 111). The integral membrane transport protein *MDR1* is located at the apical membrane of human intestinal enterocytes and is responsible for the efflux of drug substrates into the GI lumen. In the human intestine the expression of *MDR1* increases in the small intestine from duodenum to ileum (Mai *et al.*, 2021).

In Caco-2 cells *MDR1* gene expression changes during cultivation. It is highest on day 3 in culture and then decreases (Goto *et al.*, 2003). This discovery from Goto could explain the fact that no staining was observed in both Caco-2 cell culture models. The 2D model was cultivated for 21 days, to achieve a confluent and differentiated monolayer.



---

After that long cultivation period the cells were used for immunofluorescence staining. And the cells in the OoC system was cultivated for 4 days before staining. Both culture systems are known to develop differentiated, polarized Caco-2 cells after these cultivation time, which indicates that the expression of *MDR1* decreases. In human duodenum and colon tissue the *MDR1* expression is second only to *MRP3* (Zimmermann *et al.*, 2005). However, this cannot be depicted in the cell culture models used.

In terms of the detection of *BCRP* no clear staining was observed in all three culture models. Only the 2D system showed a broad, evenly distributed staining over the entire cell layer (appendix 3, Figure 112). This shows that the cell membrane had efflux transporter *BCRP* activity. The level of *BCRP* expression in Caco-2 cells is 100-fold lower than in human jejunum (Taipalensuu *et al.*, 2001). The amount of *BCRP* increased from jejunum to ileum and dropped again in the colon (Lemmens *et al.*, 2021).

Intestinal transporter and enzymes are important for the absorption and metabolism of orally taken drugs (Vaessen *et al.*, 2017). To assess the toxic effects of compounds on cell culture models and then transfer the results to humans, it is particularly important to have *in vitro* models that reflect the functional conditions, especially regarding enzymes and transporters for metabolism. In this context, especially the models with Caco-2 cells used in this thesis, need to be improved, e.g. by adding another cell type, which expresses the missing enzymes and transporters.

To determine whether the cell culture models form microvilli and a brush border, immunostaining with the antibody Ezrin was performed. Each enterocyte in the intestine has a brush border, which consists of thousands of uniform, closely packed microvilli that increase the surface area and are important for the absorption of nutrients. Each microvillus contains a polarized bundle of actin filaments. One of those filaments is Ezrin (McConnell *et al.*, 2009). Ezrin belongs to the ERM family (ezrin-radixin-moesin) and is a necessary cross-linker between the plasma membrane and the actin cytoskeleton (Gautreau *et al.*, 1999).

A visible staining with the antibody ezrin means that important components of the microvilli have been formed during the cultivation period of the cells. Figure 60 shows that in the OoC model and the organoid 3D model a clear staining was visible. A completely laminar staining, around each nucleus of a cell can be seen. Especially in the 3D model it is clear that at the outer end of the cells, i.e. away from the organoid, a stronger staining was detectable. During cell cultivation the cells in 2D could not form any brush border. This could be indicated by not successfully staining with ezrin.

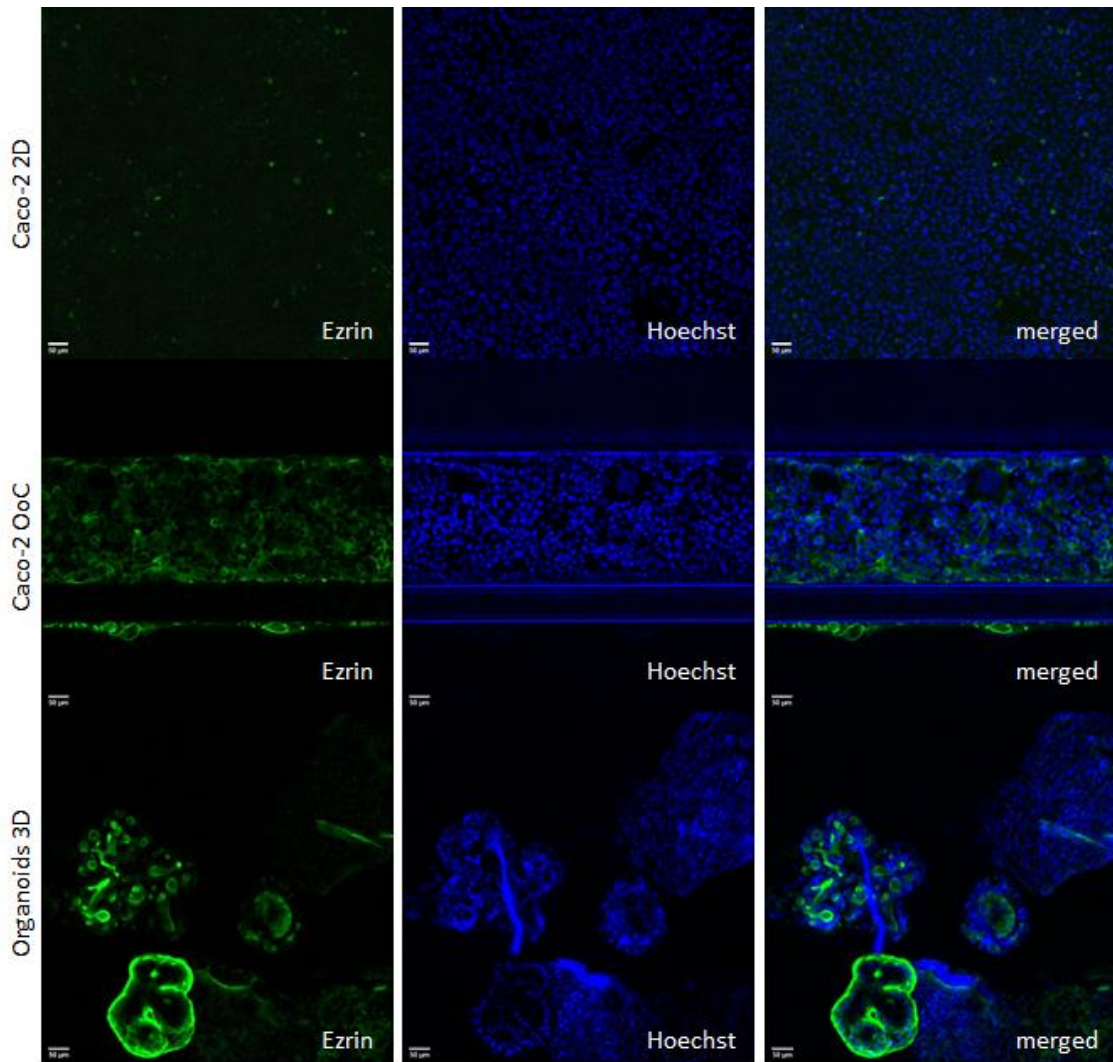


Figure 60: Immunofluorescent stainings with the antibody Ezrin (green) to stain for a specific component of the microvilli of the intestine. Shown are pictures of Caco-2 2D (pictures above), Caco-2 OoC (pictures in the middle) and colon organoids 3D (pictures below). Nuclei were counterstained with Hoechst (blue). 10x magnification, bar = 50 µm for 2D, OoC and 3D.

The formation of microvilli in the *in vitro* systems is a very important capability of the cells to mimic human-like absorption of drugs and nutrients. Both advanced cell culture models, OoC and 3D, are able to build such microvilli and potentially mimic the *in vivo* absorption to a higher amount than the 2D model.

To verify functionality, some immunostainings were performed against specific intestinal molecules with particular roles in the maintenance of homeostasis, cell differentiation or proliferation.

CDX2, the caudal-related homeobox transcription factor 2 is an important transcription factor, which is responsible for several functions in the human body. In enterocytes it specifically regulates intestinal cell proliferation, differentiation, adhesion, and apoptosis. CDX2 is

responsible for the stimulation of intestinal epithelium differentiation. It activates the transcription of mucin 2 (Muc2), SI and carbonic anhydrase I (CA I) which are specific intestinal proteins (Coskun, Troelsen and Nielsen, 2011; Saad, 2011). The successfully staining of CDX2 in all three cell culture models (Figure 61) show that the systems are capable for proliferation, differentiation, cell adhesion and apoptosis. This means that the systems are able to recapitulate this specific normal intestinal cell renewal.

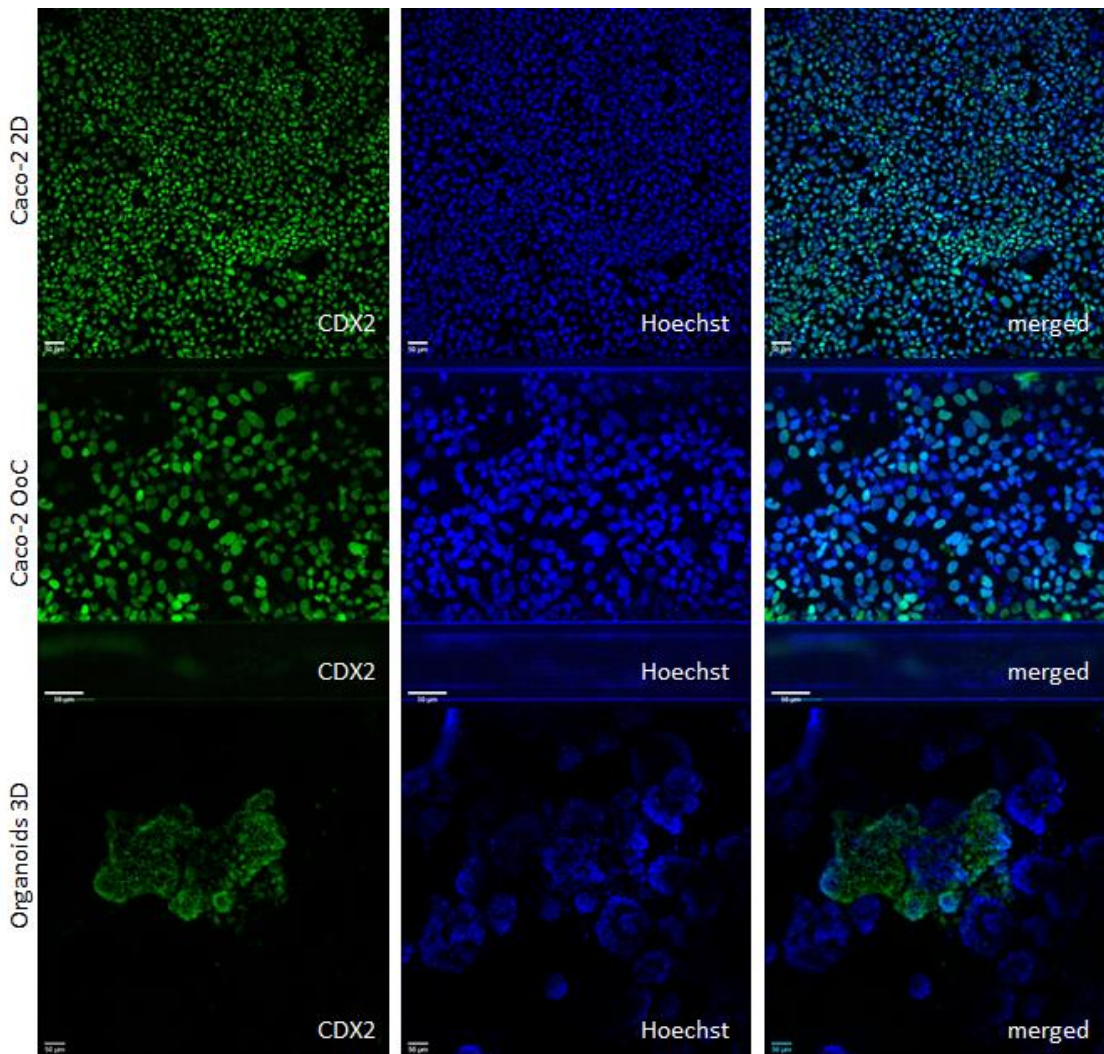


Figure 61: Immunofluorescent stainings with the antibody CDX2 (green) to stain for a specific intestinal transcription factor. Shown are pictures of Caco-2 2D (pictures above), Caco-2 OoC (pictures in the middle) and colon organoids 3D (pictures below). Nuclei were counterstained with Hoechst (blue). 10x magnification, bar = 50 µm for 2D and 3D, 20x magnification, bar = 50 µm for OoC.

With the use of the antibody EpCAM (epithelial cell adhesion molecule, also known as CD326 (cluster of differentiation 326)), we can verify whether the used *in vitro* models are able to regulate intestinal homeostasis and to help maintain the intestinal barrier. EpCAM is, among other things, responsible for the regulation of adherens junctions. Beside this function it is also known



that EpCAM is important for differentiation, cell signaling, proliferation, formation and maintenance of organ morphology. EpCAM regulates the intracellular localization and degradation of specific claudins, which modify tight junction function and adhesion (Wu *et al.*, 2013; Huang *et al.*, 2018; Chen *et al.*, 2021). Caco-2 cells are known for their very high expression of EpCAM (Vázquez-Iglesias *et al.*, 2019). A staining was observed in each of the three models used in this thesis. In the 2D and OoC model the staining looked very similar and is very diffuse within the whole cell but predominantly membrane localized. The organoid model showed a more precise staining around each cell. This corresponds exactly to the location of the tight and adherens junctions involved proteins and the cell-cell interaction.

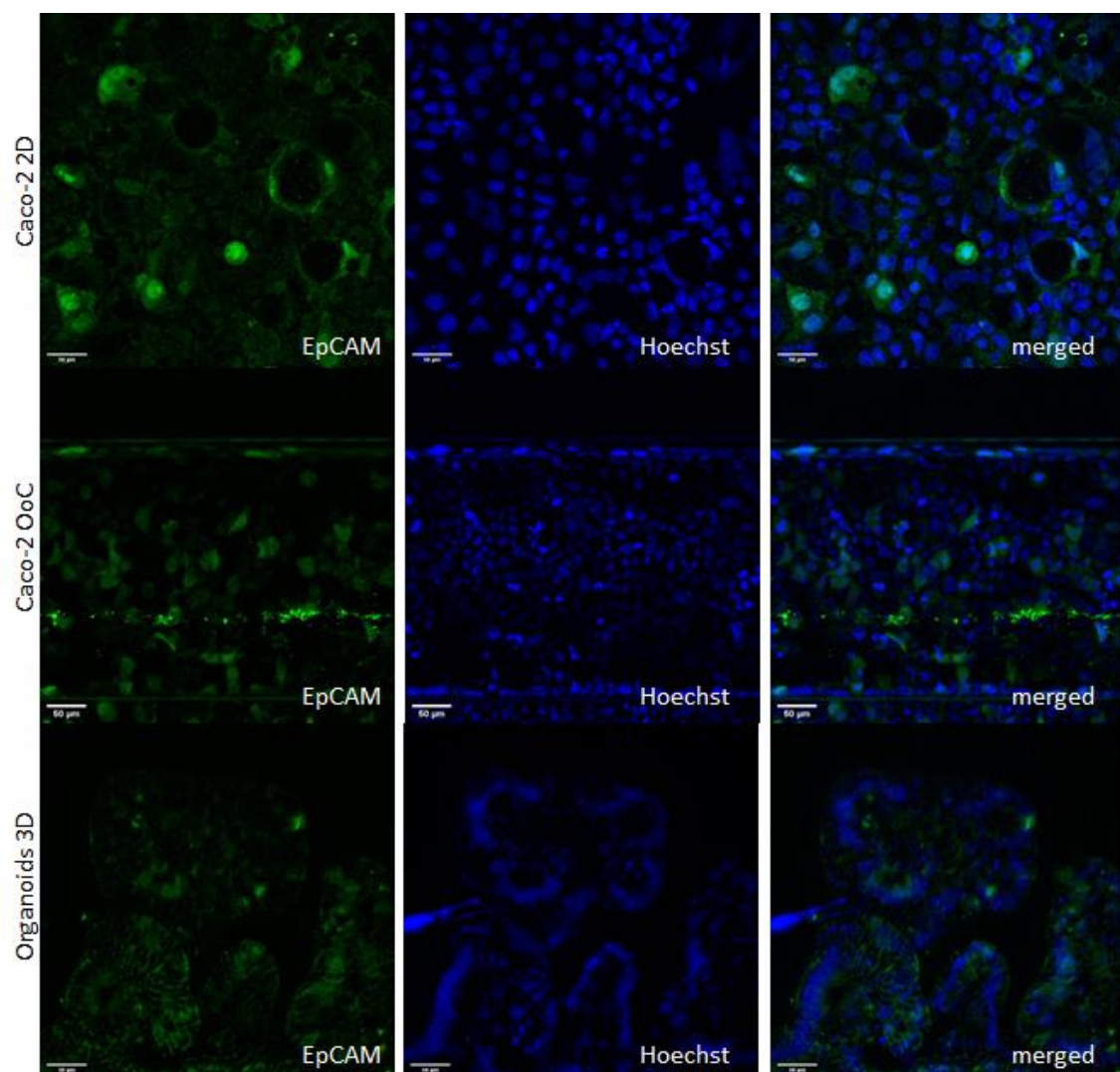


Figure 62: Immunofluorescent stainings with the antibody EpCAM (green) to stain for a specific intestinal molecule, responsible for maintenance of intestinal barrier and homeostasis. Shown are pictures of Caco-2 2D (pictures above), Caco-2 OoC (pictures in the middle) and colon organoids 3D (pictures below). Nuclei were counterstained with Hoechst (blue). 20x magnification, bar = 50µm for 2D, OoC and 3D.

---

Specifically, for the organoid *in vitro* model a staining for Mucin 5B (Muc5B) was performed to evaluate the functionality of mucin production. Muc5B is produced by goblet cells in the intestine (Pelaseyed *et al.*, 2014). These cells are only included in the organoid model, but not in the Caco-2 cell models.

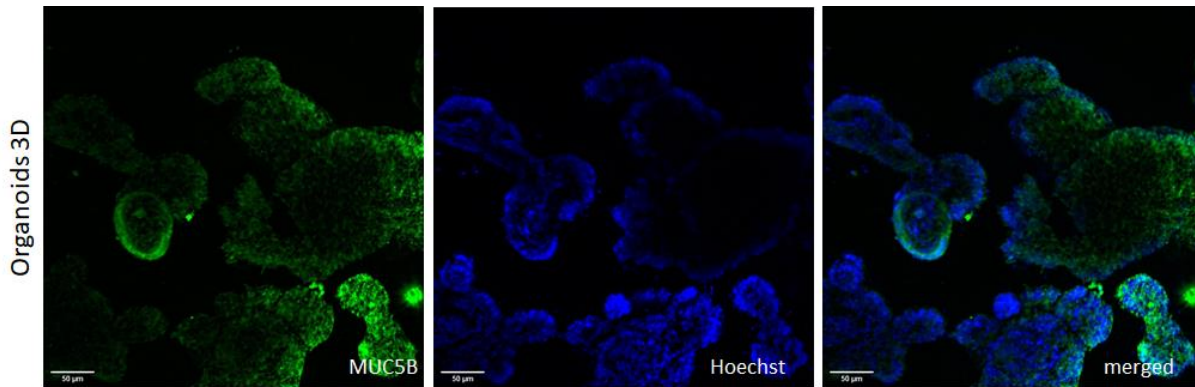


Figure 63: Immunofluorescent stainings of Organoids 3D with the antibody Muc5B (green) to stain for goblet cells and their capability to secrete mucin. Nuclei were counterstained with Hoechst (blue). 20x magnification, bar = 50µm.

Figure 63 shows the immunofluorescent staining of Muc5B, in colon organoids at day 10, which shows healthy colon organoids. Muc5B is one of the main mucins secreted by goblet cells in the colon (Walsh *et al.*, 2013). Mucins are composed of large and highly molecular mass glycoconjugates and are the main component of mucus (Paone and Cani, 2020). The main function of the mucus is to protect the human body from xenobiotics, toxins or other irritants and providing a lubricant within the intestine to help the passage of food or to clean the surface from bacteria and debris (Grondin *et al.*, 2020; Paone and Cani, 2020). This Muc5B staining showed that the organoids used for experiments are healthy and functional by producing mucin.

In summary, it was shown that the three models used in this thesis differ in their expression of intestinal enzymes and transporters. The expression of important intestinal markers for the maintenance of homeostasis or barrier function also differs between the models. The 3D organoid model shows the strongest similarity regarding the expression of intestinal markers compared to the *in vivo* situation. The organoid model is the more suitable model in terms of drug metabolism compared to the two Caco-2 cell based models, as it expresses more enzymes and transporters. Only the expression of important components of the tight and adherens junctions could be shown equally in all three models.

### 3.5. Functional characterization of all three cell culture models: Gene expression

After the successful and promising assessment using immunofluorescent staining, further characterization was carried out at the gene level. The evaluation was done by using an QuantiGene™ Plex assay (see section 2.2.10). A customized panel (QGP-248, Assay Design: M19083001, human) with specific intestinal markers was used. These targets are listed in Table 33.

Table 33: Used targets for the analysis of gene expression in the used cell culture models

Target class	Gen name	Function in human intestine
Phase I enzymes	<i>CYP 2C9, 2C19, 3A4</i>	xenobiotic metabolism
Phase II enzymes	<i>SULT 1A1, 1E1</i> <i>UGT 1A6, 2B7</i> <i>GSTA1</i>	xenobiotic metabolism
Phase III enzymes	<i>MDR1</i> <i>MRP-1 /-2 /-3</i> <i>BCRP</i>	efflux transporter of xenobiotics or xenobiotic metabolites
Phase III enzymes	<i>OCT-1 /-2</i> <i>GLUT-2</i> <i>SGLT-1 /-2</i> <i>OSTalpha</i> <i>OATP1A2</i> <i>ASBT</i> <i>MCT</i>	uptake transporter of xenobiotics or xenobiotic metabolites
Mucins	<i>Muc2</i> <i>Muc5Ac</i>	Mucins are fluids, secreted by goblet cells Helps by maintaining the defense against toxins Helps with transport of chyme

The cells were cultivated for 21 days (Caco-2 2D), 4 days (Caco-2 OoC) or for 6 days (Organoids 3D) and then the cells were lysed. The measurement of mRNA expression was conducted on two consecutive days with the Luminex instrument.

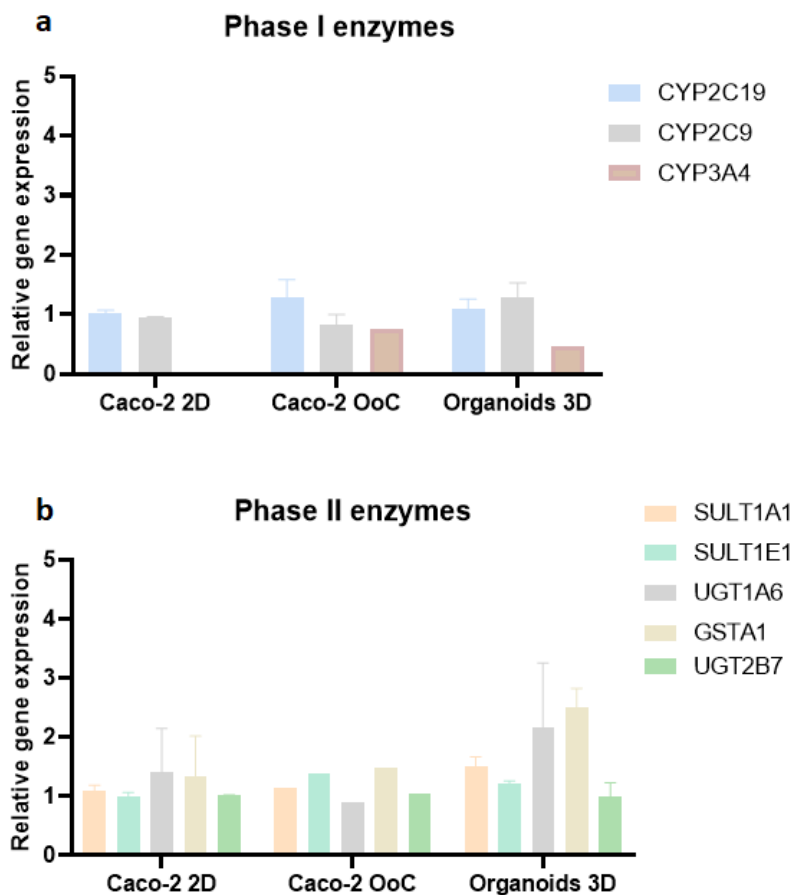


Figure 64: Column plots of basal gene expression of phase I (a.) and II (b.) enzymes in the three cell culture models. The gene expression was measured after several days in culture, for 2D after 21 days, for OoC after 4days and for 3D after 6 days. The relative gene expression was measured using the QuantiGene™ Plex method. Relative gene expression was normalized to the Housekeepers *PPIA*, *PIB*, *HPRT1* and *LDHA*. N=2. Shown is the relative gene expression and the corresponding standard deviations. The gene expression values are listed in appendix 5, Table 41 and Table 42.

Figure 64 summarizes the basal gene expression of three phase I enzymes (a.) and five phase II enzymes (b.) in the three cell culture models used. A further analysis of the transcriptomic profiling was performed to elucidate the underlying mechanisms of the cellular processes. Figure 64a shows the expression of the phase I enzymes *CYP2C19*, *2C9* and *3A4*. *CYP2C19* and *3A4* represent the main CYPs in the human intestine (Xie, Ding and Zhang, 2016). The expression level of *CYP2C19* and *2C9* in all three cell culture models was nearly identical. *CYP3A4* was not detectable in the colon organoid 3D model but in both Caco-2 models. Compared to immunofluorescence staining, where *CYP2C9* could not be detected in the Caco-2 2D and OoC model, the more sensitive method of determining gene expression showed detection in all three

systems. It was shown that the expression of phase II enzyme in Caco-2 cells depend on their differentiation status. In short-term, cultivated cells the mRNA expression was lower, for example for *GSTA1/2*, *GSTP1*, *SULT1A1/2* and *COMT* compared to long-term cultivated and completely differentiated Caco-2 cells. *UGT1A6* was not detected in undifferentiated (3d cultivated cells) and as well not in differentiated (21d in culture) cells (in line with that reported by Lněničková *et al.*, 2020).

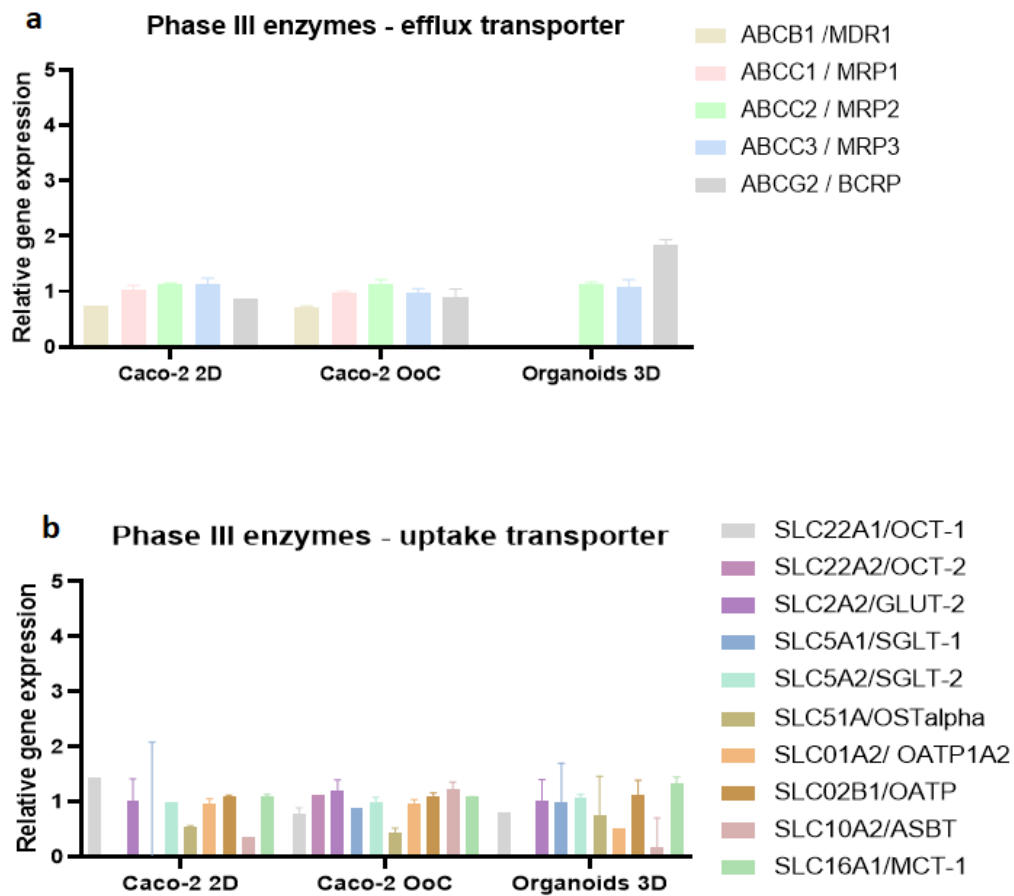


Figure 65: Column plots of basal gene expression of phase III efflux transporter (a.) and phase II uptake transporter (b.) enzymes in the three cell culture models. The gene expression was measured after several days in culture, for 2D after 21 days, for OoC after 4 days and for 3D after 6 days. The relative gene expression was measured using the QuantiGene™ Plex method. Relative gene expression was normalized to the Housekeepers *PPIA*, *PIB*, *HPRT1* and *LDHA*. N=2. Shown is the relative gene expression and the corresponding standard deviation.

Figure 65a shows the expression levels of different efflux transporters. The expression levels between the Caco-2 2D model and the OoC model are very similar. In each system mRNA expression levels of *MDR1*, *MRP1*, *MRP2*, *MRP3* and *BCRP* was measured. In the organoid samples, mRNA levels for *MDR1* and *MRP1* could not be detected.



The mRNA expression of *BCRP*, *MCT-1*, *OCT-2*, in the organoid sample was comparable to already measured mRNA levels of human colon samples by Englund (Englund *et al.*, 2006).

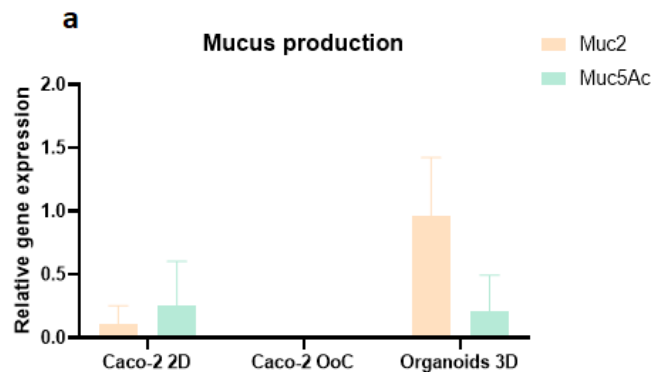


Figure 66: Column plots of basal gene expression of a.) *Muc2* and *Muc5Ac*. The gene expression was measured after several days in culture, for 2D after 21 days, for OoC after 4 days and for 3D after 6 days. The relative gene expression was measured using the QuantiGene™ Plex method. Relative gene expression was normalized to the Housekeepers *PPIA*, *PIB*, *HPRT1* and *LDHA*. N=2. Shown are the fold changes values and the corresponding standard deviations. Exact fold change values are shown in appendix 5, Table 45.

Figure 66 summarizes the basal gene expression of two genes which are responsible for the mucus production in the intestine. It is clear that the highest expression of *Muc2* was measured in the organoid model. In the Caco-2 2D model a very low expression was detectable whereas in the Caco-2 OoC model no expression could be measured. For *Muc5Ac* the expression was again not measurable in the OoC model but comparable in the 2D and organoid 3D model. Mucus is produced throughout the whole intestine but varies in its function depending on the location in the intestine. For secreting mucus, the goblet cells are responsible (Herath *et al.*, 2020). Only in the Organoid model goblet cells are present, which would be able to produce and to secrete mucus. *Muc2* is the major component of mucus in the colon (Hansson, 2012) and compared to the rest of the intestine, the mucus layer is thickest in the colon (Atuma *et al.*, 2001). This supports the observation of a higher expression in the organoid model compared to the Caco-2 models. Even though Caco-2 was originally generated from colon, they are more like jejunum. They show typical characteristics of the small intestine with regard to the structure of the epithelium during differentiation (Ölander *et al.*, 2016). To achieve a mucus production in the 2D or OoC model with Caco-2 cells a co-culture with HT29-MTX cells would be beneficial, because this cell line is capable for secreting mucus. This cell line was treated long term with methotrexate, and this leads to a differentiation to a goblet-cell like phenotype which are capable of secreting *Muc2* (Lesuffleur *et al.*, 1993). It was already shown that Caco-2 cells are capable of producing mucins in low amounts but the mucin amounts are significant higher when the Caco-2 cells were cultivated in a co-culture with HT29 cells (Akbari, Lavasanifar and Wu, 2017; Lian *et al.*, 2021).

---

The longer the Caco-2 cells are cultivated, the more mucin can be produced by the cells (Akbari, Lavasanifar and Wu, 2017). This may explain why the cells in the 2D model expressed *Muc2* and *Muc5Ac*, but not in the OoC model. Here, after 4 days in culture, the amount of mucins seems not to be detectable yet. It could be possible that the cells need some more days on the rocker and then they could be capable to produce higher amounts of *CDX2*. *CDX2* a transcription factor is important for the activation of *Muc2* (Coskun, Troelsen and Nielsen, 2011). The IF staining thereby leads to the suggestion that the cells in the OoC model could potentially be able to express *Muc2*.

The mucus which covers the complete intestinal epithelial surfaces is the first barrier in the intestine against xenobiotics or drugs. It has thereby a wide influence on drug absorption (MacAdam, 1993; Falavigna *et al.*, 2020) and is important for a more *in vivo* recapitulating cell model and for the better understanding and prediction of potential toxic effects of new drugs.

### **3.6. Comparative study on the evaluation of cytotoxic effects of compounds**

The detection of important pharmacological DMETs in the cell culture systems used indicated that the *in vitro* systems are suitable for the evaluation of drug toxicity. Many drugs or xenobiotics are detoxified or converted to toxic metabolites with the help of DMETs. To assess toxic effects, different well-known drugs with GI injury were used to compare the three model systems. With this the utility of organoid culture and the use of OoC systems was tested by a simple viability assay. Cells were treated with compounds to address whether one of those systems or both exhibit greater sensitivity to chemical insult compared to commonly used Caco-2 monolayer. Simple viability tests are carried out in *in vitro* toxicology to test the toxic effects of new drugs. For this purpose, short-term tests are usually carried out as routine investigations in the early drug discovery process.

Therefore, Caco-2 were cultured in 2D and in OoC format and organoids were culture in 3D in Matrigel® hemispheres. The cells were treated for 24h with nine different compounds (Table 34) which all have well-known toxic effects on the GI tract. As negative control Metformin hydrochloride (Met) at a concentration of 750  $\mu$ M and as positive control Staurosporine (Stauro) at 0.1-0.3-1-3-10-30-100-300  $\mu$ M was used.

Table 34: Selected test compounds and final concentration ranges for the cytotoxicity comparison of the three cell culture models.

<b>Test compound (Code)</b>	<b>Final concentration [<math>\mu</math>M]</b>
Alosetron hydrochloride (Alo)	0.1-0.3-1-3-10-30-100- 300
5-Fluorouracil (5-FU)	0.1-0.3-1-3-10-30-100-300
Diclofenac sodium (Dic)	0.1-0.3-1-3-10-30-100-300
Flavopiridol hydrochloride (Flav)	0.1-0.3-1-3-10-30-100-300
Gefitinib (Gef)	0.1-0.3-1-3-10-30-100-300
Irinotecan hydrochloride (Irino)	0.1-0.3-1-3-10-30-100-300
Loperamide hydrochloride (Lop)	0.1-0.3-1-3-10-30-100-300
Oxaliplatin hydrochloride (Oxali)	0.1-0.3-1-3-10-30-100-300
Terfenadine (Terf)	0.1-0.3-1-3-10-30-100-300

The IC<sub>50</sub> values (inhibition concentration 50%) for the response in ATP content to each test compound in the tested cell culture models are shown in Figure 67. All calculated viabilities are shown in appendix 6 in Table 46- Table 56 (Caco-2 2D), Table 57- Table 66 (Caco-2 OoC) and Table 67- Table 77 (colon organoids 3D).

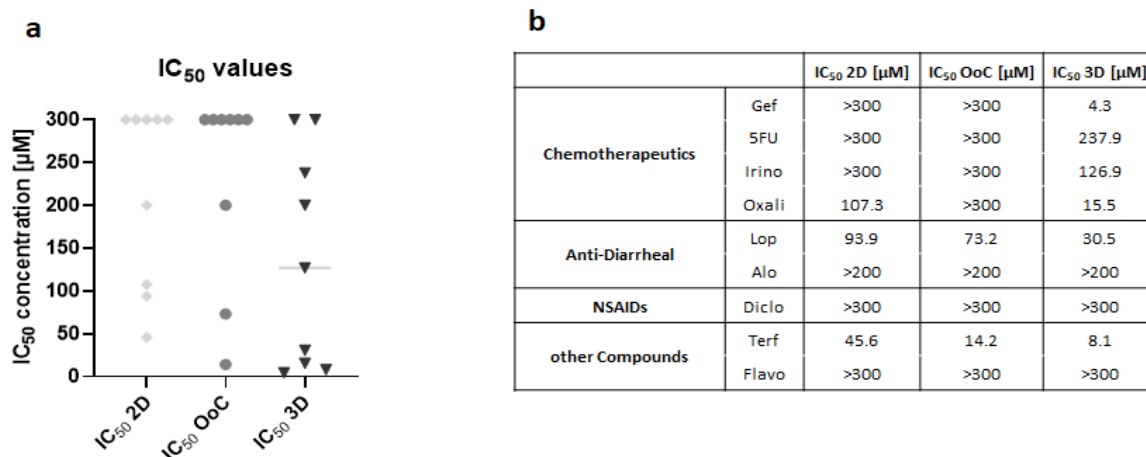


Figure 67: a.) Scatterplot of IC<sub>50</sub> values derived from ATP content measurements after exposure to the nine different test compounds for 24h. Visualized is each cell culture system. Data is expressed as mean from multiple measurements (N=3) across test sites for each compound. B.) Mean IC<sub>50</sub> values of cell models after 24h treatment with the GI compounds (N=3).

All tested compounds are known to either induce side effects in the GI tract, like diarrhea, vomiting, bleeding, constipation, inflammation or increase of intestinal barrier permeability. The scatterplot in Figure 67a shows that in the 2D cell culture model three out of nine test compounds had an effect on the Caco-2 cells, but the rest of the compounds showed no toxic reaction. Caco-2 cells in the OoC model showed a similar profile to the model in 2D. It showed a reaction against two out of nine test compounds. The 3D model with the organoids showed the most sensitive effect. Six out of nine test compounds were toxic for the cells and leads to cell death. The distribution of IC<sub>50</sub> values clearly shows that the 3D organoid model is the most sensitive compared to both models with Caco-2 cells. Four out of nine compounds were toxic for the organoids and lead to very low IC<sub>50</sub> values (below 50 μM). The detection of the presence of all five major intestinal cell types in the iPSC derived colon organoid models, the 3D arrangement of the cells and the cultivation in an ECM leads to a more similar *in vivo* condition than the 2D system. The toxic properties of the drugs on the human GI system can therefore be better mapped (Edmondson *et al.*, 2014).

In Figure 67b the table lists the mean IC<sub>50</sub> values, sorted by their mode of action into chemotherapeutics, Anti-Diarrheal, NSAIDs and other compounds. The highest concentration of Terfenadine was not used for the calculation of the IC<sub>50</sub> value due to precipitation in all the models. It is clear that the 3D model with the organoids can be best depict the toxic effects of the compounds. All four chemotherapeutic compounds lead to cell death of organoids. For 5-FU similar results could be shown by Rodrigues *et al.* by treating colon and small intestinal organoids with 5-FU, which leads to cell death, decreased organoid size, change in morphology and increased caspase 3/7 activity (Rodrigues *et al.*, 2021).

---

In the 2D models only Oxali could lead to cytotoxicity. Compared to this the Caco-2 cells in the OoC model was more resistance against the chemotherapeutic compounds and all of them stayed viable after 24h of treatment. The compounds Terf and Lop leads to cell death in all three tested cell culture models, whereby the 3D organoid model being the most sensitive, followed by the OoC model and then the 2D model. These chemotherapeutic drugs that have a direct effect on the activation of apoptosis which leads to cell death (Amjad, Chidharla and Kasi, 2021). The cytotoxic occurring after treatment with chemotherapeutics could only be observed in the organoid model. Cell morphology, gene expression, protein expression and the expression of specific biomarkers are more similar in 3D models than in 2D models (Reidy *et al.*, 2021). This is therefore a possible explanation for the fact that the 3D model is more similar to the GI tract of the human than the 2D model and thus can represent the effect of chemotherapeutics as they act in the human GI tract. Comparing the  $IC_{50}$  values of the two models with the Caco-2 cells, it becomes clear that for the two compounds that have a toxic effect (Loperamide and Terfenadine), a stronger effect was seen in the OoC model, which showed a lower  $IC_{50}$  value. Cultivation of cancer cells in 3D can lead to a less resistance against specific drugs (Breslin and O'Driscoll, 2016). Exactly the opposite has also been shown in other publications. One example is the higher sensitivity of cells in 2D against drugs due to their different organization of receptors on the cell surface compared to cells in a 3D structure (Lv *et al.*, 2017; Langhans, 2018). The arrangement of receptors on the surface effect the binding efficacy of drugs to the receptors (Lancaster and Knoblich, 2014; Langhans, 2018). Another example would be that cells growing in 3D often contain cells in different cell stages. Outlying cells are more proliferating than cells in the inner and many drugs act strongest against active proliferating cells (Langhans, 2018). And as a last example in the middle of a spheroid another pH level exists compared to the outside, which can as well lead to difference in drug activity (Lancaster and Knoblich, 2014).

These limitations are mainly for cells growing as spheroids and could not be completely transferred to the cells growing in the Mimetas OoC tubular structure. When the cells are growing as a tubular structure the cells build a dense monolayer but connected completely together around a lumen where the medium flows through. This avoids the problems of different pH values due to the thickness of cell models, different nutrient gradients and waste removal. Likewise, the receptors against some drugs are directed are still easily accessible.

---

MDR1 is located in the small intestine and the expression increases from duodenum to ileum (Mai *et al.*, 2021). These transporters are responsible for the limited absorption of certain drugs, e.g. loperamide (Naruhashi and Kamino, 2016). The fact that the cell culture models do not fully express MDR1 explains the fact that the drug could accumulate in the cells, and this leads to cell death. In Caco-2 cells MDR1 gene expression changes during cultivation. It is highest on day 3 in culture and then decreases (Goto *et al.*, 2003). In different cancer cell lines, e.g. one from the GI tract (SGC7901) it could be shown that loperamide is cytotoxic. Loperamide leads to decreased viability due to induction of apoptosis and G2/M-phase cell cycle arrest (Gong *et al.*, 2012).

The anti-diarrheal drug Alosetron was withdrawn from the market due to very strong occurring side effects, such as ischemic colitis and death (Hyman and Garvey, 2002). Constipation could also be seen in clinical phases (I, II and III) as a reported adverse effect (Camilleri, 2000). In none of the three cell culture models used here was a toxic response of Alosetron observed.

The need to generate cell culture models for the early identification of adverse effects of new drug candidates has led to the development of multiple OoC systems. These provide the additional advantage of flow compared to already established 3D models. The biggest disadvantage of spheroids, due to their spherical and very close arrangement of cells, often results in them being less sensitive to specific toxic substances than when cultured in 2D (Karlsson *et al.*, 2012; Imamura *et al.*, 2015). This problem was circumvented in the development of the Mimetas OrganoPlate®. Here, the cells were cultivated as 3D tubes. Thus, the cells have contact with neighbouring cells and to the ECM, in this case the collagen. An additional component, the flow, which exerts shear stress and supplies the cells with nutrient medium is an advantage (Trietsch *et al.*, 2017). In this form of cultivation, the problem of uneven substance distribution is circumvented, a problem often observed with spherical cell clusters. It also avoids the problem of insufficient oxygen, nutrients in the centre and the removal of harmful metabolites or waste (Barisam *et al.*, 2018; Mukomoto *et al.*, 2020). All these problems are not relevant when culturing the Caco-2 cells as tubular structure.

These cytotoxicity studies indicate that the organoid model is the most sensitive and can best predict the actual effect of different drug classes e.g., chemotherapeutics. However, it must be kept in mind that a 3D structure of cells grown in Matrigel® does not only have advantages like and *in vivo* similar microenvironment. There exist also certain limitations. The solidified Matrigel® results in different levels in which the individual organoids are distributed. This leads to an uneven temporal and spatial distribution of substances that are applied or distributed (Jung *et al.*, 2021).

---

In spheroids or organoids the gas transport is mediated by passive transport and the oxygen saturation in the surrounding media decreases in static conditions (Sutherland *et al.*, 1986). Further limitation with organoid culture includes the formation of very large organoids. In spheroids, it has been shown that the larger the diameter, the poorer the oxygen supply to the cells in the centre. Between 200-600  $\mu\text{m}$  diameter, the oxygen consumption decreases 3-fold (Freyer *et al.*, 1984; Mueller-Klieser, Freyer and Sutherland, 1986). In organoids a maximum diameter of 300  $\mu\text{m}$  is suggested to avoid necrotic cores (Zhang, Wan and Kamm, 2021). Additionally, it was observed that the organoids used for experiments here varied in their size, shape and structure within the wells and as well within the replicates. Despite the previous determination of the cell number this leads to differently growing organoids in one well and from these very large standard deviations can occur. A few sample images of the colon organoids, all from day 6 after seeding, can be seen in the appendix 4, Figure 113.

In addition to the evaluation of ATP content after drug treatment, another viability measurement was performed. For this purpose, the Alamar Blue assay was performed. It is based on the reduction of the blue, non-fluorescent resazurin into pink and fluorescent resorufin in the reducing environment of viable cells. The concept of assessing a second viability assay is that two different cellular processes can be evaluated. In the ATP assay, the extent to which the cells can still obtain their energy in the form of ATP was examined. Immediately after loss of membrane integrity, cells lose their ability to generate ATP. The amount of ATP is then proportional to the number of living cells. In comparison, in the resazurin/ Alamar Blue assay, resazurin is taken up through the cell membrane into the cell. Living cells can then reduce the non-fluorescent resazurin to resorufin, which fluoresces.

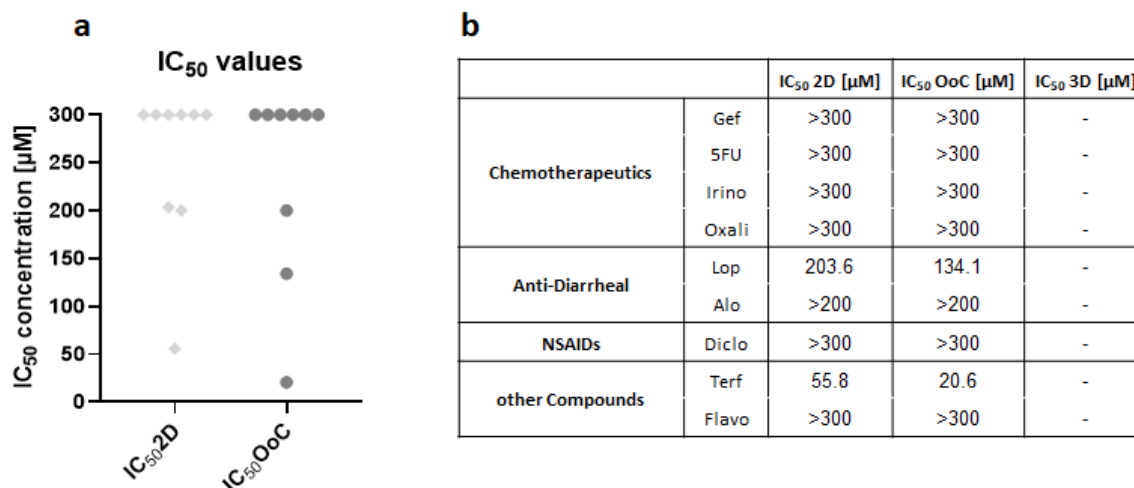


Figure 68:a.) Scatterplot of IC<sub>50</sub> values derived from Resazurin assay after exposure to the nine different test compounds for 24h. Visualized is both cell culture models with Caco-2 cells. Data is expressed as mean from multiple measurements (N=3) across test sites for each compound. b.) Mean IC<sub>50</sub> values of cell models after 24h treatment with the GI compounds (N=3).

Figure 68 a show a scatterplot of the distribution of IC<sub>50</sub> values from the Alamar Blue assay. IC<sub>50</sub> values for both models (2D and OoC) with Caco-2 cells are shown. In both models 2 out of 9 compounds had a toxic effect on the cells. The two dots representing the IC<sub>50</sub> at 200μM are from the compound Alosetron and do not represent a loss of viability of the cells but fully alive cells, as this was the highest tested concentration tested of Alosetron.

For the 3D model with organoids no reliable data was generated. The used solution for the assay was darkish blue and in some prior experiments was observed that the Matrigel® hemisphere absorbed the blue colour and then very unequal and untrustful results were generated. The Alamar Blue had a negative effect on the Matrigel® and the hemispheres began to dissolve, which in turn led to very variable results with very large standard deviations. Afterwards it was not possible to perform the viability assessment with the CellTiter Glo Kit from Promega.

Regarding the IC<sub>50</sub> values for both Caco-2 models it could be clearly seen that the cell viability analysis using the kit from Promega yielded much lower IC<sub>50</sub> values. For example, for Loperamide (Lop) the IC<sub>50</sub> value for the 2D model in the ATP assay was 93.9μM and in the Alamar blue assay it was 203.6μM. The same can be seen in the OoC model. Here the IC<sub>50</sub> values was calculated as 73.2μM in the ATP assay and in comparison, the IC<sub>50</sub> value was 134.1μM in the Alamar Blue assay. This phenomenon has already described by Valley *et al.*, in 2014. The CellTiterGlo 3D® assay allows the measurement of signals that are several times higher compared to the cell-free control. In contrast, a fluorescent, non-lytic assay such as the Alamar Blue assay is less sensitive and usually achieves signals just above those of the control (Valley, Zimprich and Lazar, 2014).



---

Thus, slight toxic effects of substances may be missed, since the signals are not significantly higher than those of the background and thus are not detectable. Additionally, the CellTiter Glo kit and the Alamar Blue assay measure different things. The Alamar blue assay measures a colour change in the surrounding medium (fluorescence) and with the CellTiter Glo kit ATP is used in vital cells to reduce luciferin to oxyluciferin. This produces light which can be measured (luminescence).

These results and the already published data from Valley, Zimprich and Lazar show that for evaluating toxic effects of compounds the CellTiter Glo kit from Promega allows the more sensitive and reliable determination.

Since not all of the used test compounds lead to toxic effects, a smaller number of compounds were used for the further experiments (TEER, BI assay, Biomarker evaluation). The Proteomics analysis was performed without any treatment.

### **3.7. Comparative study on the evaluation of barrier integrity effects of compounds**

#### **3.7.1. Evaluation of the TEER after treatment with test compounds in 2D and OoC**

A major component for the maintenance of the intestinal barrier function are the very tight connections between the enterocytes (Estudante *et al.*, 2013). These called tight junctions are responsible for the cell-cell adhesion and creating an intact barrier against toxins. This barrier is selective for specific molecules and ions (Assimakopoulos, 2011). The barrier has a specific electrical resistance which can be measured with the help of electrodes. For Caco-2 cells (2D) a TEER value between 150-400  $\Omega \cdot \text{cm}^2$  indicates a tight and dense barrier (Srinivasan *et al.*, 2015a).

So far no publication for the direct measurement of TEER in intestinal organoids has been published (Kim, Ginga and Takayama, 2018). The rounded structure of the organoids with an inner lying lumen makes it very difficult to measure directly TEER values, since two compartments for the electrodes are needed. One way to circumvent this problem would be to dissociate the organoids to individual cells and seed them onto transwell inserts. But this needs a lot of cell material and is very cost intensive when using iPSC derived organoids. Due to this fact and the problem of running out of consumables, due to covid-19, the attempt with the dissociation of organoids, seeding on transwell inserts and then try to generate an intact, confluent barrier was only repeated twice. During these approaches the cells were seeded at different densities onto the inserts and then transferred into the 2D TEER instrument CellZscope from nanoanalytics. In none of the attempts a dense monolayer with a stable TEER value was achieved (results are not shown) and therefore treatment with different compounds were not carried out.

Since 2021 a new method was established by Ahn and his group which allows the measurement of the expression status of tight junction proteins in human intestinal organoids. It's a specific pressure-controlled system with custom-designed microchannels. It measures the change in electrical resistance of organoids depending on the integrity of the organoid cell membrane (Ahn *et al.*, 2021). However, this realization was not possible for this thesis due to time constraints and the non-delivery of materials due to covid-19.

All measured TEER values are listed in the appendix 7 in Table 78-Table 84 for the Caco-2 2D model and in the appendix 8 in Table 85- Table 102 for the Caco-2 OoC model.

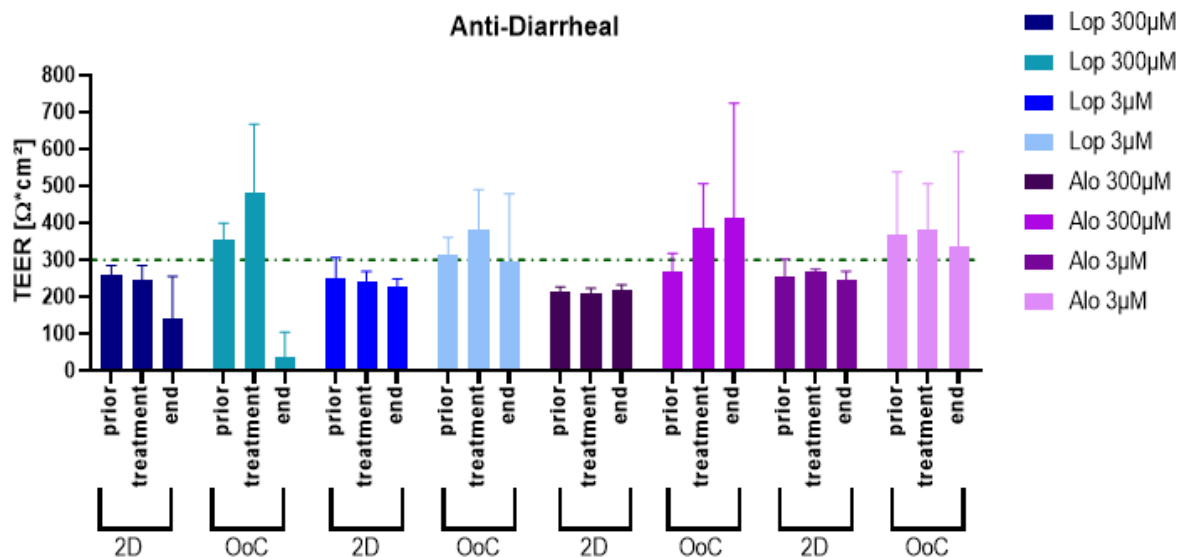


Figure 69: Measured TEER values after different time points in culture. Shown are the TEER values for (Caco-2 2D prior = 20days, Caco-2 OoC prior = 5 days, Caco-2 2D treatment = 21 days, Caco-2 OoC treatment= 6days, Caco-2 2D end= 22days (after 24h of treatment) and Caco-2 OoC end = 7days (after 24h of treatment)). An achieved value of about 300Ohm was used as a minimum value for the successful formation of an intact barrier (green broken line). Shown are the TEER values for Caco-2 2D and OoC bevor and after the treatment with two anti-diarrheal drugs, Loperamide (Lop) and Alosetron (Alo) in two different concentrations (300 and 3 µM) for 24h. (N=3)

Figure 69 shows the measured TEER values of Caco-2 cells before and after treatment (24h) of the cells in the 2D (dark blue and dark magenta) and OoC (light blue and light magenta) model. On the first view it's clear that overall, the TEER values were general higher in the OoC model than in the 2D model. The standard deviations are also higher in the OoC model compared to the 2D model. In both models, 3 independent replicates were performed. It can be seen that Alosetron had no negative or toxic effect on the Caco-2 cells, neither in the 2D nor in the OoC model. However, there is one difference between the models. In the 2D model, the TEER value remains relatively stable after Alosetron treatment and in the OoC model the TEER values continues to

increase. The increasing TEER in the OoC can be explained by the activity of proliferating cells. The cells are only few days in the chip until they build a complete tight tube, so they still have plenty of space and continue to proliferate. Compared to this the cells in the 2D system are growing for 21 days before the first TEER measurement is done. The monolayer is very, very dense and the cells are completely connected to each other. It is already known that cells inhibit their growth behaviour and proliferation when cultivated at high densities (Pavel *et al.*, 2018).

The compound loperamide at 300µM had a negative effect on the tight junctions and decreased the TEER values in both systems. In one publication from Gong *et al.*, from 2012 it could be shown that loperamide could have toxic influence on the cell viability of several cancer cell lines (Gong *et al.*, 2012).

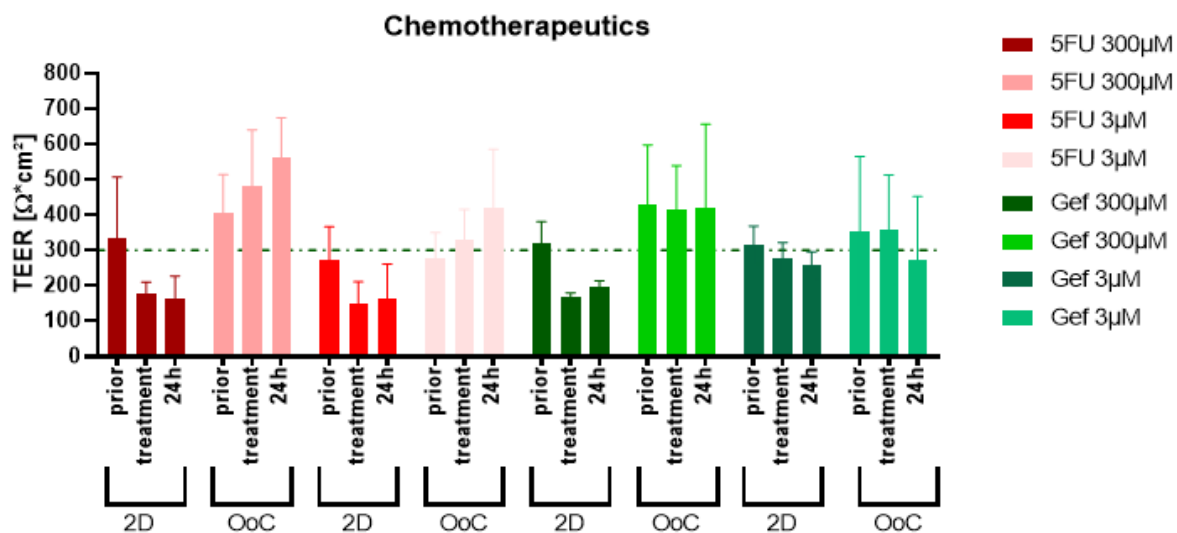


Figure 70: Measured TEER values after different time points in culture. Shown are the TEER values for (Caco-2 2D prior = 20days, Caco-2 OoC prior = 5 days, Caco-2 2D treatment = 21 days, Caco-2 OoC treatment= 6days, Caco-2 2D end= 22days (after 24h of treatment) and Caco-2 OoC end = 7days (after 24h of treatment)). An achieved value of about 300 Ohm was used as a minimum value for the successful formation of an intact barrier (green broken line). Shown are the TEER values for Caco-2 2D and OoC before and after the treatment with two chemotherapeutics, 5-FU and Gefitinib (Gef) in two different concentrations (300 and 3 µM ) and the corresponding standard deviations for 24h. (N=3)

In Figure 70 the change of TEER values of the 2D and OoC model before and after the treatment with two chemotherapeutic drugs (5-FU & Gefitinib (Gef)) at 300 & 3µM are shown. It is shown that after treatment with 5-FU the TEER value in 2D decreased at both concentrations to nearly to the same value. After treatment with 300µM and 3µM 5-FU the TEER value dropped in the 2D model to  $162 \pm 64 \Omega \cdot \text{cm}^2$  and  $161 \pm 99 \Omega \cdot \text{cm}^2$ , respectively. It has shown that 5-FU has a toxic effect on specific proteins of the tight junctions in immunodeficient mice, specifically on occludin and claudin-1 (Song, Park and Sung, 2013). Both proteins are also found in the human intestine

(Garcia-Hernandez, Quiros and Nusrat, 2017) and have also been detected in Caco-2 cells (Orlando *et al.*, 2014). In the OoC system both 5-FU concentrations lead to a slight increase of the TEER which means that the cells are still proliferative and viable.

The treatment with Gefitinib showed in the OoC system no toxic influence. The TEER values remained stable over time and after treatment, regardless of concentration.

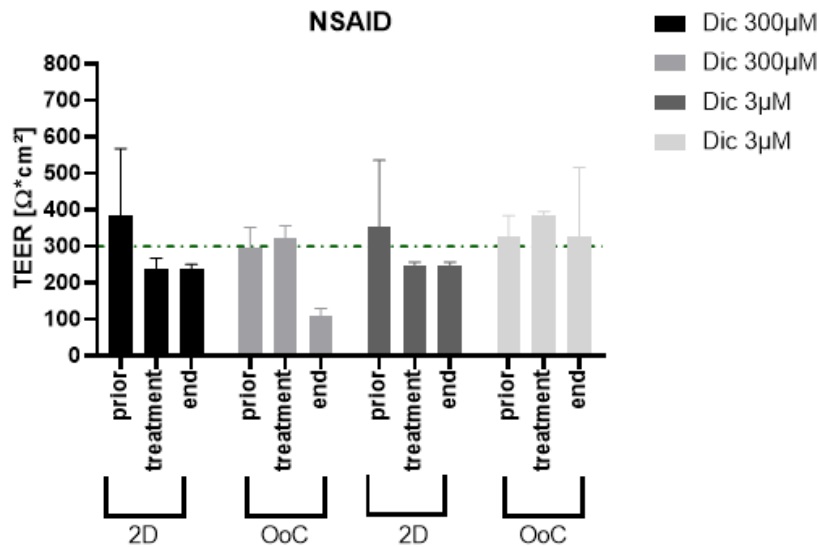


Figure 71: Measured TEER values after different time points in culture. Shown are the TEER values for (Caco-2 2D prior = 20days, Caco-2 OoC prior = 5 days, Caco-2 2D treatment = 21 days, Caco-2 OoC treatment= 6days, Caco-2 2D end= 22days (after 24h of treatment) and Caco-2 OoC end = 7days (after 24h of treatment)). An achieved value of about 300 Ohm was used as a minimum value for the successful formation of an intact barrier (green broken line). Shown are the TEER values for Caco-2 2D and OoC bevor and after the treatment with the NSAID Diclofenac (Dic) in two different concentrations (300 and 3 μM) and the corresponding standard deviations for 24h. (N=3)

Figure 71 shows the measured TEER values of Caco-2 cells before and after treatment with Diclofenac (24 h) in the 2D (black and darkish grey) and OoC (light gray tones) model. It is clear that Diclofenac at the higher concentration (300 μM) influenced the barrier of Caco-2 cells in the OoC system. The lower concentration of 3 μM showed no effect. In the 2D system the TEER value decreased a little but was stable at  $237 \pm 13 \Omega \cdot \text{cm}^2$  (300 μM) and at  $249 \pm 7 \Omega \cdot \text{cm}^2$  (3 μM). It is already known that NSAIDs can lead to intestinal toxicity and this toxicity is even less without enterohepatic circulation (Brett *et al.*, 1990; Leong and Chan, 2006). This often leads to a loss of intracellular ATP and can disrupt the tight junction integrity which is then followed by an unwanted barrier permeability (Somasundaram *et al.*, 2000). Diclofenac is more tolerated than other NSAIDs but still well known to be associated with toxic effects in the small intestine. In most cases, the dose of diclofenac is 50mg taken orally. This leads to a concentration of around 300-1600 μM within the intestinal lumen (Bhatt *et al.*, 2018). Already with the highest concentration of 300 μM used in this thesis, an effect in the OoC system could be detected. It is likely that this

effect is even more pronounced with increasing diclofenac concentration. Bhatt et al. has shown that a treatment with 500-1000  $\mu\text{M}$  of Diclofenac can cause adverse effects (Bhatt *et al.*, 2018).

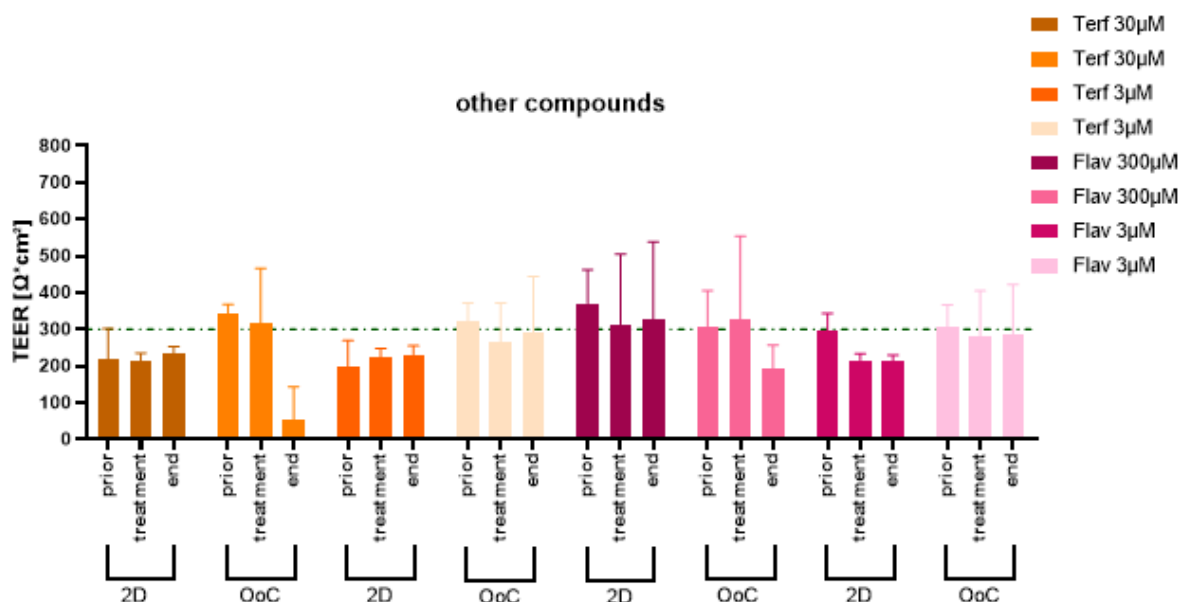


Figure 72: Measured TEER values after different time points in culture. Shown are the TEER values for (Caco-2 2D prior = 20days, Caco-2 OoC prior = 5 days, Caco-2 2D treatment = 21 days, Caco-2 OoC treatment= 6days, Caco-2 2D end = 22days (after 24h of treatment) and Caco-2 OoC end = 7days (after 24h of treatment). An achieved value of about 300Ohm was used as a minimum value for the successful formation of an intact barrier (green broken line). Shown are the TEER values for Caco-2 2D and OoC bevor and after the treatment with two compounds Terfenadine (Terf) and Flavopiridol (Flav) in two different concentrations (300 and 3  $\mu\text{M}$ ) and the corresponding standard deviations for 24h. (N=3).

Figure 72 shows the TEER values for the Caco-2 2D and OoC system before and after treatment with Terfenadine (Terf) und Flavopiridol (Flav) (at 300 and 3  $\mu\text{M}$  for Flav and 30 and 3  $\mu\text{M}$  for Terf). In both systems Flav did not have a toxic influence on the cells for both tested concentrations. TEER values in the 2D system remained above 300  $\Omega\cdot\text{cm}^2$  throughout the experiment (after treatment with the higher concentration of 300  $\mu\text{M}$ ) and with the lower concentration they decreased slightly and then remained at  $240\pm 45 \Omega\cdot\text{cm}^2$ , which remains in the range for a tight barrier of Caco-2 cells. The treatment with Terfenadine showed at 300  $\mu\text{M}$  in both systems a precipitation and was therefore left out for further analysis. For this purpose, the middle concentration (30  $\mu\text{M}$ ) was used. In 2D the 30  $\mu\text{M}$  showed no effect and the TEER values stayed stable after treatment. In the OoC model the TEER value dropped after treatment with Terfenadine (30  $\mu\text{M}$ ). The low concentration of 3  $\mu\text{M}$  showed no effect on TEER. Terfenadine is normally metabolized in the small intestine by CYP3A4 (Bauman, 2001) due to the fact that Caco-2 cells did not express CYP3A4 (results from IF stainings) it could be that the drug accumulated leading to cytotoxic effects at 30  $\mu\text{M}$ .

---

Overall, it is clear that after treatment with non-toxic compounds the TEER values stayed stable in the 2D system and in the OoC system the TEER value increased over time. This could be explained by the very short pre-cultivation of Caco-2 cells until the tube is build. After already 4-5 days in culture the tube is completely confluent, and a tight barrier is observable by TEER values around  $300 \Omega \cdot \text{cm}^2$ . As the cells continued to proliferate, the cell-cell connections strengthened and a stronger cell association was formed, which can also be represented by an increasing TEER value. In a previously published paper, it was shown that the cells can reach TEER values of about  $600\text{-}800 \Omega \cdot \text{cm}^2$ , which then end in a plateau (Beaurivage et al., 2019). Equal maximum TEER values were obtained in all experiments performed in the OoC system. It is interestingly to see that for NSAIDs only the OoC system was able to detect their influence on the tight junctions and for Chemotherapeutics only the 2D system was able. So far there is no literature evidence on this phenomenon.

In addition to the TEER measurement, another method for testing intestinal barrier integrity, the barrier integrity assay (BI assay), was performed in the OrganoPlates<sup>®</sup>. The aim was to determine whether one method was more sensitive than the other.

### **3.7.2. Evaluation of the BI assay after treatment with test compounds in the OrganoPlate<sup>®</sup>**

A further method to assess the barrier integrity is by using fluorescent dyes and then measure the diffusion of the dye through the cell membrane. This assay can be used before any endpoint assay because it does not destroy the cells. After the BI assay the cells can be washed and used for other experiments. The BI assay was performed in the OrganoPlate<sup>®</sup> since the TEER instrument for the OrganoPlate<sup>®</sup> was not available in the beginning of the experiments. The BI assay gives informations on the intactness of the intestinal barrier in cell culture models. That's why the BI assay works as a good alternative for assessment of barrier integrity compared to a TEER measurement. The BI assay, like the TEER assay, was used for the detection of compound induced barrier disruption.

Figure 73 shows the results for the barrier tightness after treatment with the test compounds, each at two concentrations (3 and 300  $\mu\text{M}$ , except Alo was tested at 3 and 200  $\mu\text{M}$ ). Shown are the percentage intactness of the intestinal barrier after treatment. For the calculation of percentage intactness of the barrier the start value (intensity for the BI assay and TEER value for the TEER assay) of both methods was set to 100 % and then the decrease in TEER (TEER assay) or in the intensity of the fluorescence dye (BI assay) was compared to this. The figure compares the results from the BI and TEER assay. It can be seen that for 5-FU, Alo and Lop the results of both methods

are very similar. 5FU and Alo showed no influence on the intestinal barrier in neither the BI assay nor the TEER assay. After the treatment with Diclo at 300  $\mu$ M the disrupted barrier was only detectable with the TEER assay. In the BI assay no damage on the barrier could be observed. Like that, showed the TEER assay after treatment with 300  $\mu$ M Terf a complete damage barrier compared to the BI assay. Compared to this showed the BI assay after treatment with 300  $\mu$ M Gef a slightly more damaged barrier than the TEER assay.

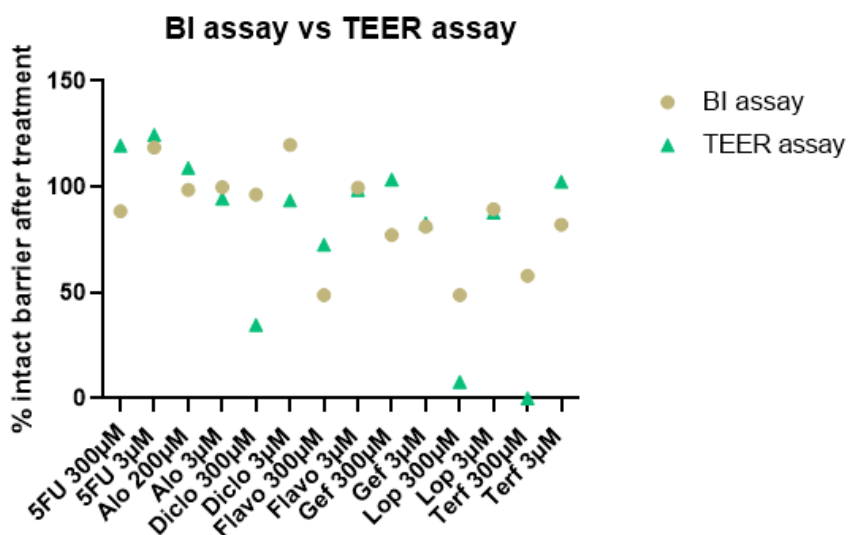


Figure 73: Comparison of the results of the BI and TEER assay. Shown are the mean percentage intactness of the barrier after treatment. 100 % would mean the barrier is still intact after treatment and if the barrier is damaged the percentage decreased. The percentage can increase over 100 % due to proliferating cells and thereby increased resistance or due to not complete perfectly similar formed tubes in the OoC system. N=3.

In summary it can be said that if the cell layer remained intact, both assays are able to show this. As soon as a substance has a strong effect on the barrier and thus the tight junctions are destroyed, this can be determined more sensitively with the TEER assay. Already Nicolas et al. showed that the fluorescence-based BI assay is less sensitive compared to the measurement of the TEER (Nicolas *et al.*, 2021). In addition to the higher sensitivity, the TEER assay is also easier and faster to perform compared to the BI assay and the evaluation also requires less effort. Finally, the TEER method is the more suitable method for screening compounds and their effect on the intestinal barrier in the early phase of drug development. This method is much faster, it is more sensitive, and it is more easily to analyze the generated data compared to the BI assay.

### 3.8. Evaluation of protein expression between the advanced cell culture models

Another step in the characterization of the different cell culture models was the measurement of the basal expression of proteins. For this approach, Caco-2 cells were seeded in 3 different models (96-well plate, transwell plate and OoC) and organoids were seeded in Matrigel® hemispheres in 96-well plates. Gene expression does not always mean that the corresponding protein is also present in the cell. Several studies showed that levels of mRNA not always correlate with protein levels (Greenbaum *et al.*, 2003; Fu *et al.*, 2007) . For this evaluation the protein content was analyzed via LC-MS. The comparison of the proteomic profiles will help to understand what each model is fit for and what each model is able to perform.

For better comparability of protein expression within the models, different amounts of chips or wells were pooled in each case to achieve a cell number of 50,000 cells per sample. Overall, it was possible to detect and measure many proteins in each system after several time points.

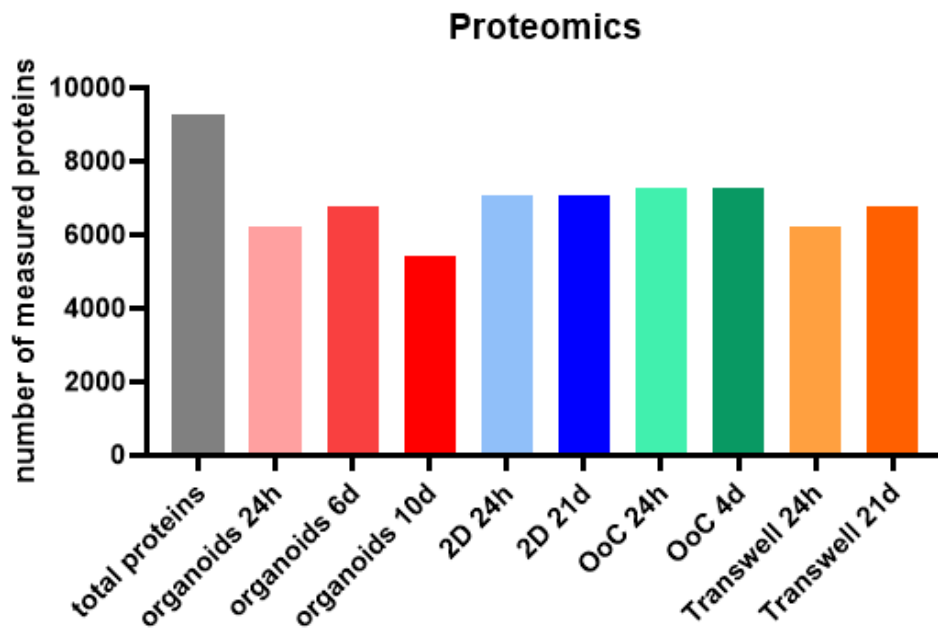


Figure 74: Number of all measured proteins in the different cell culture formats. The samples were analysed via LC-MS. N=1.



---

Protein profiles of the two different cell types (Caco-2 and colon organoids) in four different cell culture models (2D, 3D, OoC and Transwell) and after several time points were generated for a total of 9252 proteins. The different time points were chosen to check how protein expression changes during cell culture. Thus, the number of proteins was measured one day after cell seeding (24h), at the time point the cells were used for experiments (4d, 10d, 21d) and for the organoids additionally at the time of cell splitting (6d).

Figure 74 shows the total numbers of measured proteins, in each system after several time points. In total 9252 proteins were detected. In the organoid system, the measured number of proteins immediately after seeding was 6218. After 6 days in culture, which is the time when the organoids were used for all experiments, 6785 proteins could be measured, and after 10 days in culture, the number of detectable proteins was 5412. This lower number of proteins in the longer cultivated organoids was since in one of these replicates it was difficult to remove the complete Matrigel. Matrigel can influence the identification and quantification of proteins (Wang *et al.*, 2022).

In comparison, the measured number of proteins was slightly higher in the 2D and OoC systems. For the 2D system, 24h after seeding and 21days later, 7075 proteins were detected in each case. When Caco-2 cells were cultured in the OoC system, the number of proteins counted 7300 24h after seeding. Even after 4days in culture, there was no change in the number. In the transwell system the number of measured proteins increased over culture time. After 24h after seeding 6218 proteins could be measured and after 21days in culture 6783 proteins.

### 3.8.1. Global protein expression

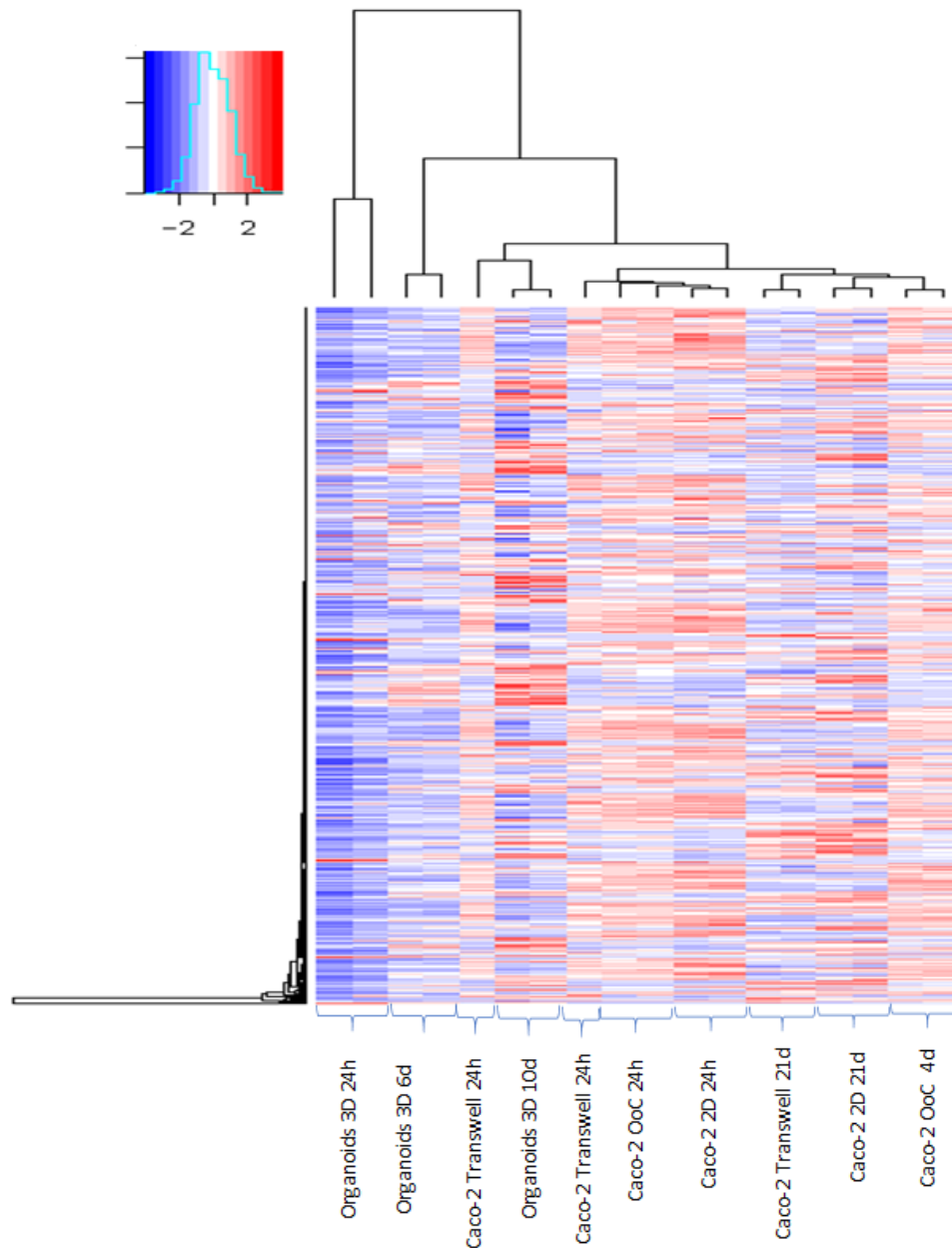


Figure 75: Heatmap representation of the 4070 overlapping proteins identified in all cell models including hierarchical clustering. Columns represent the different samples analysed and rows represent protein IDs. Values range from low (blue) to high (red).

Figure 75 shows a heatmap of the 4070 overlapping proteins identified across all cell culture models. Hierarchical clustering of the proteins indicates clearly that the samples from organoids after 24h and 6d separated from all other samples. This shows that different proteins are present in different amounts in the used cell culture models. The expression profile of Caco-2, cultured for 24h on transwell inserts showed the least differences compared to the organoids. Protein expression of Caco-2 in 2D after 24h was very similar to the expression of Caco-2 OoC and

Transwell after 24h in culture. Samples of Caco-2 cells at the respective starting point of the experiments (21d and 4d) showed the greatest differences compared to the shorter cultured organoids, with the OoC samples being the most different. The heatmap was generated to compare the overall profile of overlapping proteins of all models. A large number of proteins showed significantly lower expressions in the organoid model compared to the other models. However, some proteins showed the highest expression in the organoid model, which was cultured for 10d, compared to the other models. These differences in the protein expression between the used models showed the potential to use the Caco-2 models and the organoid models for different questions. The Caco-2 cells express morphological and functional characteristics of the differentiated cytotypes of the intestinal mucosa (Sambruy *et al.*, 2001) and are well established as an *in vitro* cell culture model of the GI tract, especially for the intestinal barrier (Sambuy *et al.*, 2005). They are physiologically and morphologically more like jejunum although they are derived from colon. They show typical characteristics of the small intestine with regard to the structure of the epithelium during differentiation (Ölander *et al.*, 2016). These properties are particularly suitable for the investigation of compound effects on the intestinal barrier in the small intestine. In comparison, the organoid 3D model contains more *in vivo*-like features such as different cell types, extracellular matrix, or a 3D structure, which allows better mechanistic understanding of drug side effects through the interplay of multiple cells with each other.

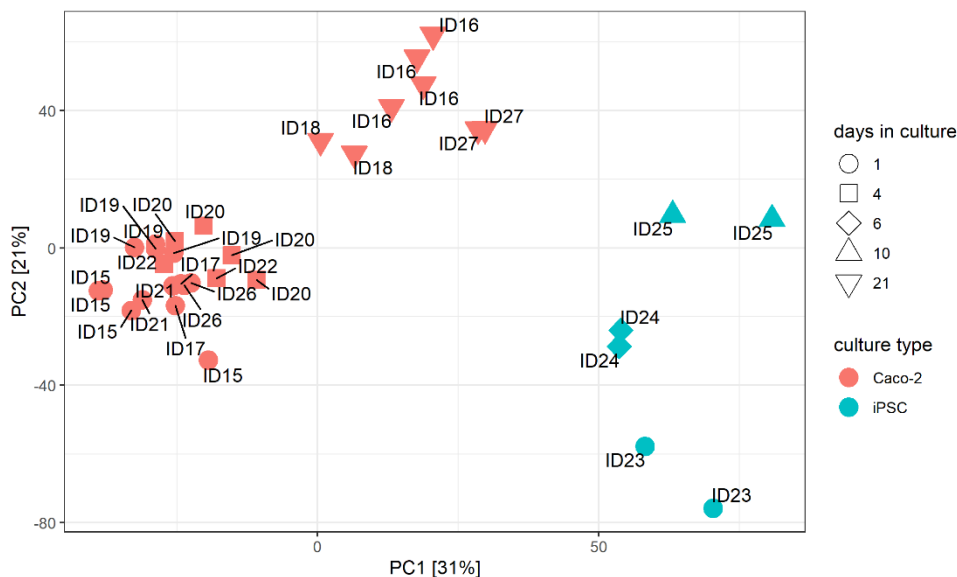


Figure 76: Principal component analysis (PCA) of all measured protein samples in the LC-MS. Shown are the samples of iPSC derived colon organoids in turquoise and for all Caco-2 models in orange. The shape of the objects divides in the cultivation time. ID numbers show the different samples. Same ID numbers stand for the replicates

---

Figure 76 shows a PCA analysis of all measured samples. PCA allows for grouping of samples with overall similar protein expression characteristics and it enables the identification of the proteins which are responsible for the main differences between the test groups. PC1 (principle component 1) and PC2 (principle component 2) explain 31% and 21% of the total variation, respectively. The PCA plot in Figure 76 captures the most (PC1) and the second most (PC2) important parameters that caused the variation in the data. Duplicates get clustered together which indicates that the protein expression is very similar and the biological variation is responsible for the clear separation of different groups. Along PC1 three distinct groups are visible, of which one corresponds to the organoids (turquoise), independent of cell culture time. The second corresponds to the Caco-2, which were fully differentiated (21d in culture) and the third corresponds to the short cultivated Caco-2 cells (1d and 4d). It can be clearly seen that the samples of organoids separate from the samples of Caco-2 cells, they are clustered according their model type. In the Caco-2 models, a distinction is clearly seen between the cells cultured for only a short time (1 and 4d in culture, circles and squares in orange) and the cells cultured for a longer time (21d in culture, downward triangle). The Caco-2 cells in the OoC system are the only cells that were sampled after 4d (squares in orange) in culture, because that was the start time of their experiments. It can be seen that this model, in terms of protein expression, is similar to the cells of the other Caco-2 models, which only grows for 1d (circles in orange). The samples of the organoid models shows clearly differences in protein expression between cultivation time (turquoise circles, lozenges and triangles). The most similar samples between the models are those, in which the Caco-2 cells were culture for 21d and the organoids for 10d.

### **3.8.2. Expression profiles of proteins for tight and adherens junction**

The determination of expression levels of proteins that are involved in the formation of tight and adherens junctions is of great importance in the context of forming tight barriers *in vitro* and helps to identify the suitability of the used models. It is well known that one of the common problems which occurs in the GI tract during treatment with specific drugs is the damage of the intestinal barrier and mucosa (mucositis) (Gibson and Bowen, 2011; Panarelli, 2014) by damage the junctional complexes. Tight junctions are responsible for the maintenance of homeostasis through their ability to regulate as gate keeper the diffusion of molecules (Zihni et al., 2016). Tight junctions are the most abundant connections between cells (Krause et al., 2008) and are responsible for the prevention of leakage of solutes (Anderson et al., 1989).

To assess the suitability of the models used in this work for the formation of an *in vivo* similar intestinal barrier, all detected proteins were subdivided.

In Figure 77 a heatmap of the tight junction protein expression levels is shown. It represents the hierarchical clustering of the samples of the different cell models. The expression levels were compared between Caco-2 and organoids. For the comparison, only one time point was used, which represents the timepoint of each start of the experiments of the individual models.

The protein set is composed of three claudins and one tight junction protein. As with the global expression profile results, the basal expression of tight junction proteins of organoids is very different compared to all other cell culture models used. In particular, the claudins are more highly expressed in the organoids model whereas the tight junction protein is more highly expressed in the OoC and 2D models. The expression of each replicate within a cell culture model is very similar to the other. For claudin -1 and -4 it is known that they are expressed in the human intestine. Among other areas, they are mainly localized in the duodenum and colon (Yang *et al.*, 2011; Lameris *et al.*, 2013; Lu *et al.*, 2013). Claudins play an important role in the maintenance of the colon mucosa. Claudins are therefore an important element in the assessment of changes of the mucosal function (Yang *et al.*, 2011) and can thereby work as indicator of intestinal barrier function.

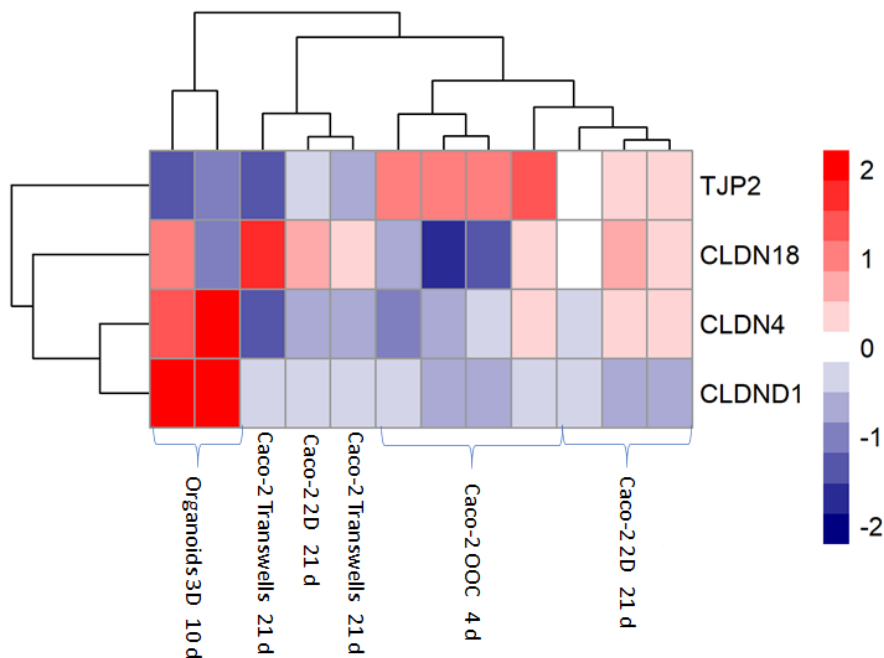


Figure 77: Heatmap representing the hierarchical clustering of the basal expression levels of tight junction formation involved proteins. Shown are the samples of different cell models at the time points of experiment start. Values range from high to low using colour increments of red and blue, respectively. The corresponding measured values of the proteins are shown in the appendix 10 in Table 106.

Figure 77 only shows those proteins which could be detected in each of the models. Red shows high expressed proteins and blue are low expressed proteins. In total other proteins were detected as well but only in the Caco-2 2D 21d and Caco-2 OoC 4d samples. Beside tight junction protein 2 (TJP2), Claudin -18, -4 and -1 the proteins claudin3, occludin, ZO-1, ZO-3 and tight junction associated protein (TJAP1) were measured as well in both above named Caco-2 models. ZO-1, ZO-2 and ZO-3 are present in the tight junctions of epithelial cells which were linked to the transmembrane proteins occludin and claudin (Itoh *et al.*, 1999). TJAP1 is involved in the formation of tight junctions and is present in late stages of formation (NCBI, 2022b). The main key determinates of the tight junctions in the intestinal barrier are the claudins. These transmembrane proteins work as paracellular channels or can plug the paracellular pathways. Claudin expression differs with respect to their localization in the GI tract. In humans, for example, RT- PCR has shown that claudin 4 is mainly present in the colon, sigmoid and rectum (Lu *et al.*, 2013). This also explains the results shown in Figure 77. The expression of claudin 4 is highest in the organoid system, which is very similar to the colon, whereas the protein expression is low in the Caco-2 models, which are more similar to the small intestine. The same is the case for *CLDND1*, which showed the highest expression in the organoid system. In human the expression increases from stomach to small intestine and has the highest expression in the colon (ProteinAtlas, 2020).

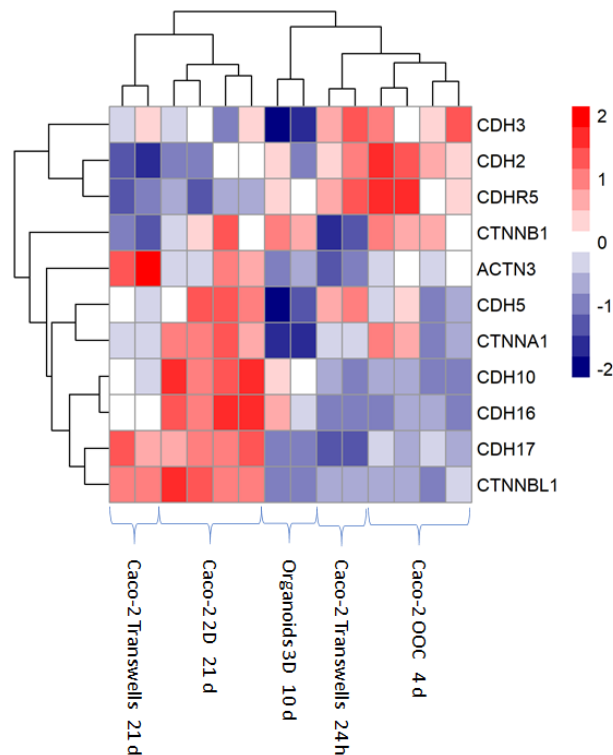


Figure 78: Heatmap representing the hierarchical clustering of the basal expression levels of adherens junction involved proteins. Shown are the samples of different cell models at the time points of experiment start. Values range from high to low using colour increments of red and blue, respectively. The corresponding measured values of the proteins are shown in the appendix 10 in Table 107.

---

Figure 78 shows a heatmap, which represent the different protein expression levels of adherens junctions, detectable in all used models. Shown are the results for each cell model on the day of experiment starts. In total 19 different proteins, which are involved in the building of adherens junctions, could be measured at least in one of the *in vitro* models. Figure 78 shows the expression profiles from 11 adherens junction proteins, which could be measured in each of the system. The heatmap shows, that the expression profile from Caco-2 in 2D and in transwell inserts are most different compared to the Caco-2 cells in the OoC system. The expression profile from Caco-2 in 2D is very similar to the cells growing in transwell. The proteins with the highest expression are contained in the Caco-2 2D system, whereas the organoid system shows the lowest expression levels.

Cadherins are the key elements for intercellular junctions. They are adhesive transmembrane proteins and are involved in tissue morphogenesis and important for the maintenance of homeostasis (Leckband and Prakasam, 2006; Leckband and Sivasankar, 2012). A wide number of cadherins could be measured within the cell systems. For example Cadherin 17 (*CDH17*, also named LI cadherin (liver-intestine)), it is a transmembrane protein which is responsible for the cell-cell adhesion in intestinal epithelium (Su *et al.*, 2008). *CDH17* is present in high amounts in the colon, duodenum and small intestine and plays an important role during the first step of oral absorption of peptide-based drugs (NCBI, 2022a). The heatmap showed that the expression of *CDH17* was higher in the Caco-2 2D and Transwell system compared to the organoid and OoC systems.

*CTNNA1* ( $\beta$ -catenin) and *CTNNA1* ( $\alpha$ -catenin) are the two main components which bind to *CDH1* (E-cadherin) and together they are the main components of adherens junctions (Kobielak and Fuchs, 2004). All three proteins were detected in the Caco-2 2D model. *CDH1* was measured within the Caco-2 2D, transwell and OoC system, but was not shown in the heatmap above due to less measured protein in the organoid samples.

Comparing the protein expressions of Caco-2 cells within a model (transwell) between different time points, in this case 24h after seeding and 21d later in culture. Between these two time points the basal protein expression completely changed. Caco-2 cells change during long cultivation from the proliferative state to a differentiated state. After differentiation a polarized monolayer of mature enterocytes with a brush border develops. This differentiation is associated with changes in expression levels of mRNA and proteins (Stierum *et al.*, 2003).

For the evaluation of the cell models with respect to their ability to form adherens junctions and the resulting maintenance of homeostasis, it becomes clear that the Caco-2 cells in 2D and transwells are better suited compared to the organoid model.

### 3.8.3. Expression profiles of drug metabolizing enzymes

The evaluation of the potential of xenobiotic metabolism and the identification of suitability of a cell model was done by determination of expression levels of proteins of phase I, II and III. It is widely known that not only a drug itself can have a toxic effect on the patient but also the metabolites. This often leads to reactive metabolites (Guengerich, 2006; Baillie, 2008) which can have toxic influences. Intestinal cytochrome P450 (CYP450)-mediated metabolism can be responsible for the elimination of some orally taken drugs. They are transformed to metabolites and then are excreted. These drugs cannot reach the systemic circulation and can therefore not act as they should (Xie, Ding and Zhang, 2016). This can then, for example, lead to incorrect interpretation of results in toxicity screenings in liver cells. The effect of intestinal xenobiotic metabolism can then not be covered correctly. One example that the gut wall contributes to first-pass metabolism is cyclosporin. Kolars et al., showed that cyclosporin metabolites accounted for 25% and 51% of total identifiable cyclosporin in portal blood of two patients (Kolars *et al.*, 1991).

In the following figures (79-81) protein expression profiles of a subset of different phase I, II and III enzymes are shown. In the appendix 10 in Table 108, Table 109 and Table 110 the measured proteins and their intensities are shown.

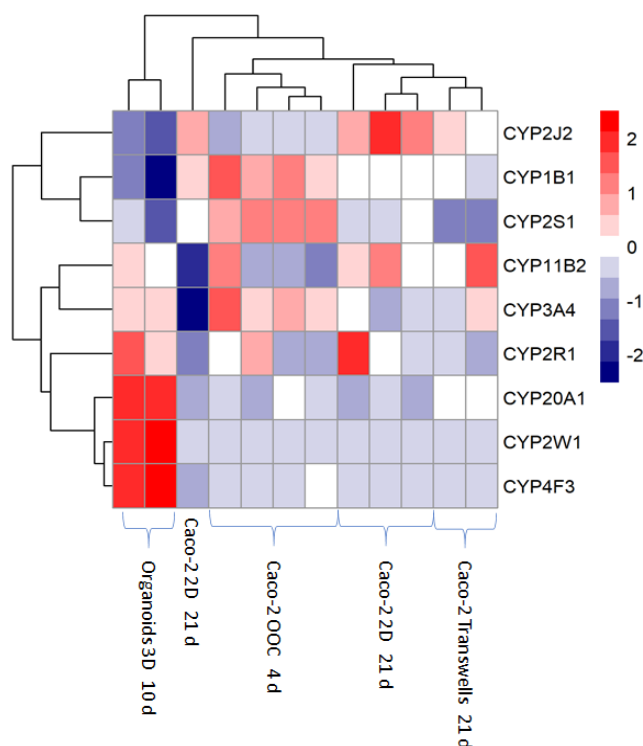


Figure 79: Heatmap representing the hierarchical clustering the basal expression levels of different CYP450 enzymes. Shown are the samples of different cell models at the time points of experiment start. Values range from high to low using colour increments of red and blue, respectively. The corresponding measured values of the proteins are shown in the appendix 10 in Table 108.



---

Figure 79 shows the different expression levels of several CYP450 enzymes (red represents a high expression and blue a low expression). In total a set of 19 different CYP450 enzymes was detected in at least one of the models. Shown in the heatmap are only nine different CYP450 enzymes due to not enough data for the other proteins. This is because for certain enzymes the expression was not detectable and thus leads too few data points which were then useable for the generation of the heatmap. The heatmap in Figure 79 shows that the expression from each model is different. The organoids showed the highest expression for *CYP20A1*, *CYP2W1* and *CYP4F3*. All these three CYP enzymes are expressed in the human intestine. *CYP20A1* is known to be expressed in the human ileum (Takayama *et al.*, 2021) and *CYP4F3* is weakly distributed in the GI tract (Christmas *et al.*, 2001). *CYP2W1* is expressed in the colon, exclusively in crypts (Choong *et al.*, 2015) and small intestine in the early stage of embryonic life. Later in life, the expression decreases completely. The colon organoids contain villi and crypt structures in which the different cell types of the intestine are found. Specifically in the base of the intestinal crypts stem cells reside which are also present in embryonic stages.

In comparison to this, all-other models with Caco-2 cells showed very low expressions for these proteins. In comparison to this *CYP2J2* and *CYP11B2* shows the highest expression level in the Caco-2 2D model and for the OoC system *CYP1B1*, *CYP2S1* and *CYP3A4* were higher expressed compared to all other systems. In already published articles could be shown that Caco-2 cells express *CYP1B1* (Buesen *et al.*, 2002), *CYP1A1* (Boulenc *et al.*, 1992), *CYP3A4* and *CYP3A5* (Engman *et al.*, 2001). Some publications show that the most abundant CYP's in the intestinal mucosa belong to the families of *CYP3A* and *CYP2C*, whereby about 80% of all present CYP's belong to the subfamily *CYP3A* and around 15-18% are *CYP2C9* (Dressman and Thelen, 2009; Janssen *et al.*, 2020; Krogstad *et al.*, 2020). Further present CYPS in the human intestine are *CYP1A1*, *2C19*, *2D6*, *2J2* (Galetin and Houston, 2006; Xie, Ding and Zhang, 2016). *CYP2C9*, *2C19* and *2D6* could not be measured in any of the systems tested.

In addition to the liver, the intestine is the next most important extrahepatic organ for drug metabolism, especially for all orally taken medications (Janssen *et al.*, 2020). Data on intestinal P450 metabolism is very important for the evaluation of drug-drug interactions, oral bioavailability, and drug disposition. To achieve a more complete CYP enzyme profile in an *in vitro* system it could be the idea to generate a co-culture system with cells which represent the missed enzymes. This could be performed by adding immune cells to the systems. CD14<sup>+</sup> cells which are present in the human intestine (Kamada *et al.*, 2009) expresses *CYP1B1*. Additionally, *CYP2D6*, *CYP2A6* and *CYP2E1* are expressed in all immune cell subtypes in the human intestine (Effner *et al.*, 2017).

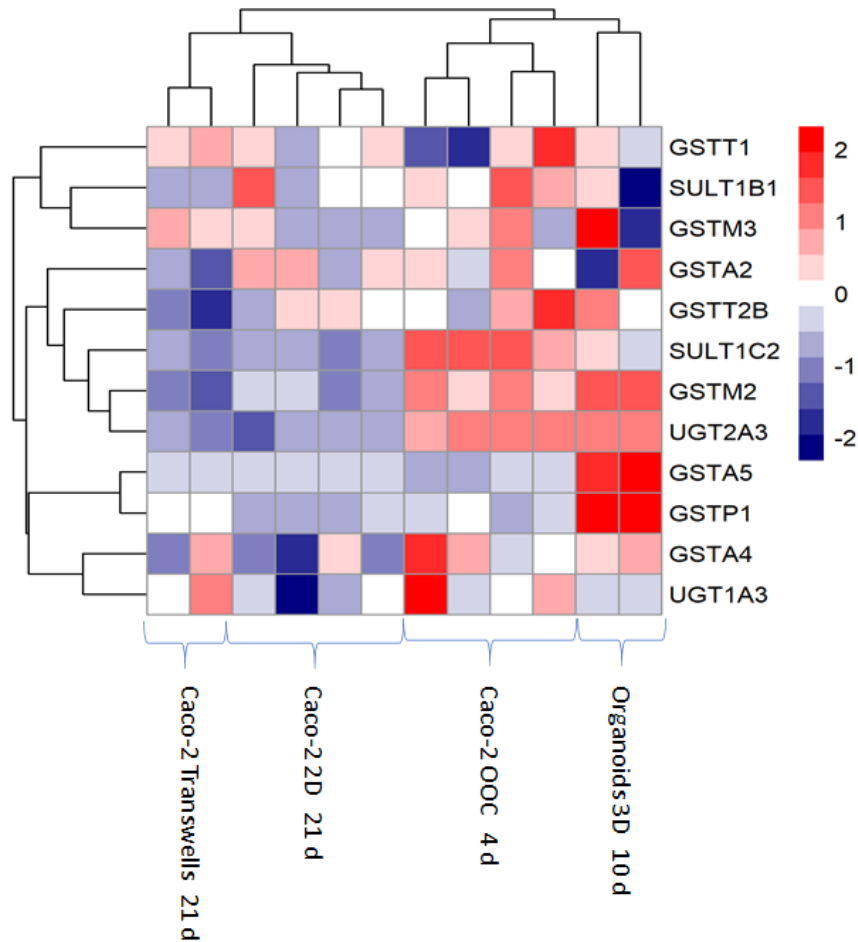


Figure 80: Heatmap representing the hierarchical clustering of the basal expression levels of different phase II enzymes. Shown are the samples of different cell models at the time points of experiment start. Values range from high to low using colour increments of red and blue, respectively. The corresponding measured values of the proteins are shown in the appendix 10 in Table 109.

Figure 80 shows a heatmap representing the expression levels of the phase II enzyme subset in the four cell models. The protein set is composed of 32 phase II enzymes, but only 12 are shown due to not enough measured proteins in each system. In line with the global expression profile and the detailed profiles for the tight and adherens junctions and the phase I enzymes the organoid model was clearly segregated from the other cell systems. The organoid system showed the highest expression for *GSTM2*, *GSTA5* and *GSTP1*. Overall, the Caco-2 2D and Transwell system had the lowest expression over all phase II enzymes in the heatmap. Beside the organoid system the Caco-2 OoC model showed the second highest expression of the different proteins.

---

In the publication of Peters et al., it was reported that the activity of several drug-metabolizing enzymes in human intestine decreases from duodenum over jejunum to ileum and has a clearly drop in the colon (Peters *et al.*, 1991). For Caco-2 cells several phase II enzymes were identified in earlier publications. *SULT1A1* (Baranczyk-Kuzma *et al.*, 1991) and *SULT1A3*, *UGT1A6* and *UGT1A9* (Münzel *et al.*, 1999) and  $\alpha$ - and  $\pi$ -GST (Peters and Roelofs, 1989) are expressed. Beside *UGT1A9* all other proteins were expressed in all the used Caco-2 models in this thesis. For the organoid system it is clear that fewer proteins were measured, which in turn supports the statement of Peters et al. from 1991.

Some of the main important functions of the enterocytes in the intestine is the uptake and efflux of xenobiotics or nutrients and the transport of fluidics through the cells. Specifically, the Caco-2 cells are known for their use as intestinal barrier model and for measuring cellular uptake and transport (Verhoeckx et al., 2015).

Figure 82 shows the basal expression levels of different phase III enzymes. In total 182 transporter proteins were detected in either one or more of the used cell culture models. Of these, 28 belong to the ABC transporters and 154 to the SLC family. Only 3 out of 28 ABC transporter and 69 out of 154 SLC transporter are shown in the heatmap due to low abundance in other systems.

In line with the other analysed protein expression levels, the organoid system differs from all other systems the most. The Caco-2 2D and Transwell models were more similar to each other than to the OoC System. The OoC system showed a higher protein expression level compared to the 2D and transwell models.

In the organoid system several proteins were highly expressed (SLC's 7A3, 7A11, 11A2, 17A5, 29A2, 29A3, 30A1, 35D2, 35A2, 35F2, 35B2, 38A9, 39A14 and 43A2).

All of these highly expressed proteins are present in the human intestinal tract. SLC7 family members can be divided in two subfamilies cationic amino acid transporters (CATs) and L-type amino acid transporters (LATs). LATs are the catalytic subunit or the heteromeric amino acid transporter (HATs). HATs are important in the intestine for reabsorption and cell redox balance (Fotiadis, Kanai and Palacín, 2013). *SLC11A2* is the only known transporter, which is required for the absorption of iron in the intestine (Gunshin *et al.*, 2005). Duncan et al., has published that *SLC17A5* is highly expressed during specific development stages in the colon and distal small intestine of humans (Duncan *et al.*, 2009). *SLC29A2* and *SLC29A3* is widely expressed in the human small intestine and colon (The Human Protein Atlas, 2021). *SLC39A14* and *SLC30A1* are both zinc transporters and are responsible for the zinc uptake and efflux in the human small intestine

(Hennigar *et al.*, 2022). The transporter *SLC43A2* is expressed in the human small intestine and is correlated with the plasma citrulline levels (Maric, Flüchter, *et al.*, 2021). *SLC35A2* transports UDP-galactose from the cytosol into the Golgi apparatus and is localized in the small intestine and colon (Nishimura *et al.*, 2009).

The Caco-2 OoC model showed the highest expression in *SLC16A10*, *SLC25A15*, *ABCB11* and *ABCG2*. *SLC16A10* is mainly expressed in the human duodenum, pancreas, kidney, small intestine, skin, and placenta and is an amino acid transporter and mediates the transport of aromatic amino acids across the plasma membrane (National Center for Biotechnology Information (NCBI), 2004; Mariotta *et al.*, 2012). *SLC25A15* is in human expressed in the large intestine, duodenum, kidney, liver, placenta and small intestine (National Center for Biotechnology Information, 2022b) and is responsible for the transport of cytosolic ornithine into the mitochondria and citrulline back (Ersoy Tunali *et al.*, 2014). *ABCB11* is a member of the *MDR* subfamily and is involved in multidrug resistance, is mainly expressed in the liver and the colon and is the main canalicular bile salt export pump (National Center for Biotechnology Information, 2022a). *ABCG2*, also called *BCRP* is expressed in human in the blood-brain barrier and the intestine and plays a major role in controlling the uptake of xenobiotics (Goebel, Chmielewski and Hrycyna, 2021).

Drug transporters from the ABC and SLC family play an important role in the bioavailability of all orally taken drugs (Liu and Liu, 2013).

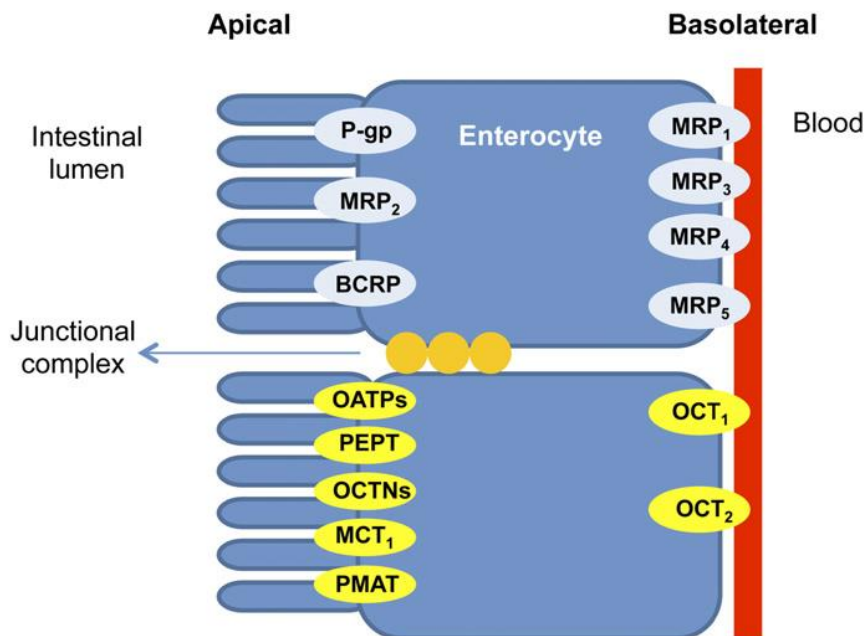


Figure 81: Major drug transporters proteins expressed in the intestinal epithelium (Estudante *et al.*, 2013).

---

The main important efflux transporter(Figure 81) in the intestine and there localization are *MDR1/P-gp* (*ABCB1*, apical), *BCRP/MXR* (*ABCG2*, apical), *MRP1* (*ABCC1*, basal), *MRP2* (*ABCC1*, apical) and as important efflux transporter *PEPT1* (*SLC15A*, apical), *OCTN1* (*SLC22A*, apical), *OCTN2* (*SLC22A*, apical), *OCT1/OCT2* (*SLC22A*, basal), *PMAT* (plasma membrane monoamine transporter/ *SLC29*, apical), *OATP2B1* (*SLCO*, apical), *OATP1A2* (*SLCO*, apical) and *MCT1* (*SLC16A*, apical) are identified. *PEPTs*, *OCTNs*, *OCTS*, *PMATs*, *OATPS* and *MCTs* are known for their important function in drug transport in the intestine (Estudante *et al.*, 2013).

From the important pharmacokinetic transporters, family members from *PMAT* (*SLC29A2* and *SLC29A3*) and *OATP2B1* (*SLC02B1*) were identified only in the 3D organoid model. From the *OCTN1* family, *SLC22A17* and *SLC22A18* were only identified in the 2D system. From the *OATP2B1* family, *SLC02B1* was identified in the organoid model. This transporter was shown to be equally distributed in small and large intestine (Müller *et al.*, 2017). *BCRP/ABCG2* was only measurable in the OoC model. It is normally expressed in the human intestine. A high expression of this transporter can be involved in the resistance to chemotherapeutic drugs. This could be seen in the viability experiment (Figure 67) in which all used chemotherapeutics showed no toxic effect on the cells in the OoC system. *MCT1* transporter was only measured in the OoC system. In the 2D and organoid model this transporter protein was not detectable. The expression of one *MCT1* family member, the *SLC16A3* was as well measurable in the Caco-2 2D system but at lower levels. *MCT1* family members are expressed in the Caco-2 cell line (Gill *et al.*, 2005), which supports the results from this thesis.

The Caco-2 models, which resembles enterocytes from the small intestine, showed more high expressed proteins compared to the 3D colon organoid model. This could be explained with the fact that the small intestine is the major side of the absorption of nutrients or drugs due to the large surface area and that's why more transporter for the uptake are present (Hua, 2020).

The results show that the Caco-2 models and the organoid model express different important DMETs. Overall, the Caco-2 models showed a higher expression profile of human important DMETs especially in the OoC model.

Each of the systems expressed different transporter, which correspond to the *OCTN1*, *OCTN2*, *OCT1/OCT2*, *PMAT*, *OATP2B1*, *OATP1A2* and *MCT1* families and thereby play important function in the metabolism of drugs. This leads to the fact that none of the system completely map the protein expression of the human intestine and must kept in mind when testing new drugs and their toxic potential to the cells.

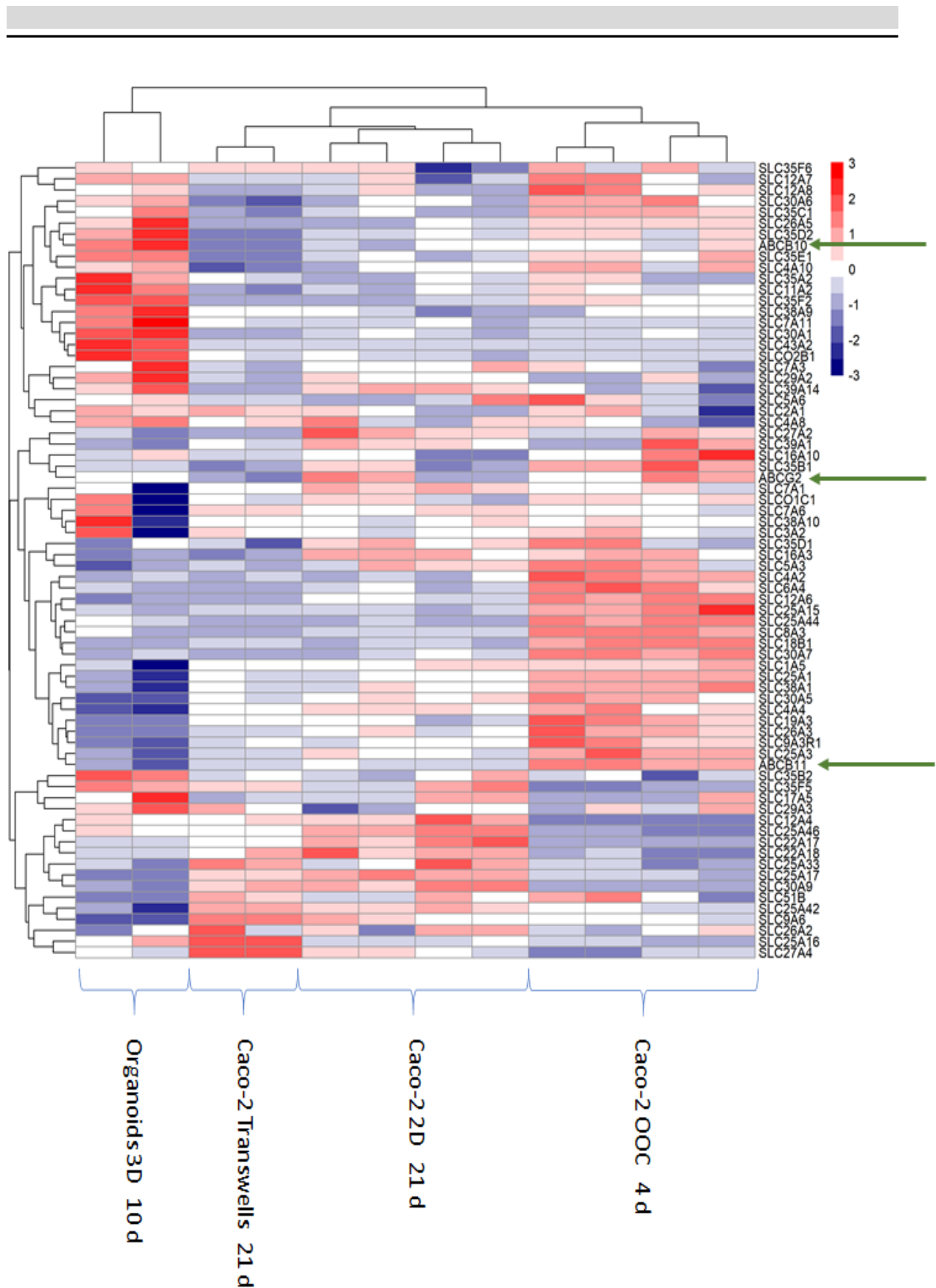


Figure 82: Heatmap representing the hierarchical clustering of the basal expression levels of different phase II enzymes. Shown are the samples of different cell models at the time points of experiment start. Values range from high to low using colour increments of red and blue, respectively. The corresponding measured values of the proteins are shown in the appendix 10 in Table 110.

---

In summary the protein expression of the two Caco-2 models (2D and Transwell) are very similar. In most cases the organoid model differed the most in the expression of proteins compared to the Caco-2 2D model and the OoC model was between the 2D and Transwell model and the organoid 3D model.

However, it must be mentioned that some problems were encountered in the measurement of the organoid samples, which made it difficult to measure a high number of proteins. It was assumed that more proteins could have been detected. A possible cause could be residues from the Matrigel®, which can cause problems in sample purification and generation. Complete removal of Matrigel® from the cells is a very important process. Matrigel® has an undefined composition and may affect protein identification and quantification. The better the Matrigel® is removed, the higher the peptide identification and better accuracy of quantification is ensured. Protein extraction and cell recovery is also improved (Wang *et al.*, 2022).

However, the intestinal metabolism plays an important role in the bioavailability of many orally taken drugs. The intra-individual variation of DMETs can influence the efficacy of the drug (Doherty and Charman, 2002). That's why it's more than important to try to find a model which mimics best the DMETs present *in vivo*.

---

### 3.9. Gene expression measurements for the detection of new biomarker for GI damage

To examine the expression of specific markers identified to be involved in GI damage, QuantiGene™ Plex assay was used after 48h treatment with the test compounds. Investigation of the gene expression profile is a widely used method to determine and understand cellular mechanism, including toxicity mechanisms. In this thesis, five published potential new biomarkers (Table 35) for GI damage were investigated in three independent experiments. The three different cell culture models (Caco-2 2D, Caco-2 OoC and 3D organoids) were treated with the test compounds, which showed in the early experiment's toxic effects on the cells. All calculated fold changes are listed in the appendix 11 in Table 111, Table 112 and Table 113.

Table 35: List of investigated potential genetic biomarkers for drug-induced GI damage.

Potential in vitro biomarker	Function (References)
<i>LCN-2</i>	Biomarker for inflammatory disease (Wells <i>et al.</i> , 2017; Celi <i>et al.</i> , 2019)
<i>FABP-2/I-FABP</i>	Specific marker for barrier function (Albala <i>et al.</i> , 2004), biomarker for intestinal obstruction (Wu <i>et al.</i> , 2021), specific marker of small intestine cellular damage (Banerjee and Gupta, 2019)
<i>MLCK</i>	upregulated myosin light chain kinase (MLCK) leads to further destruction of the barrier function (Wells <i>et al.</i> , 2017)
<i>CRP</i>	Indirect biomarker of inflammatory disease (Dragoni, Innocenti and Galli, 2021)
<i>HDC</i>	Potential biomarker of intestinal mucosal injury (Yang <i>et al.</i> , 2011)



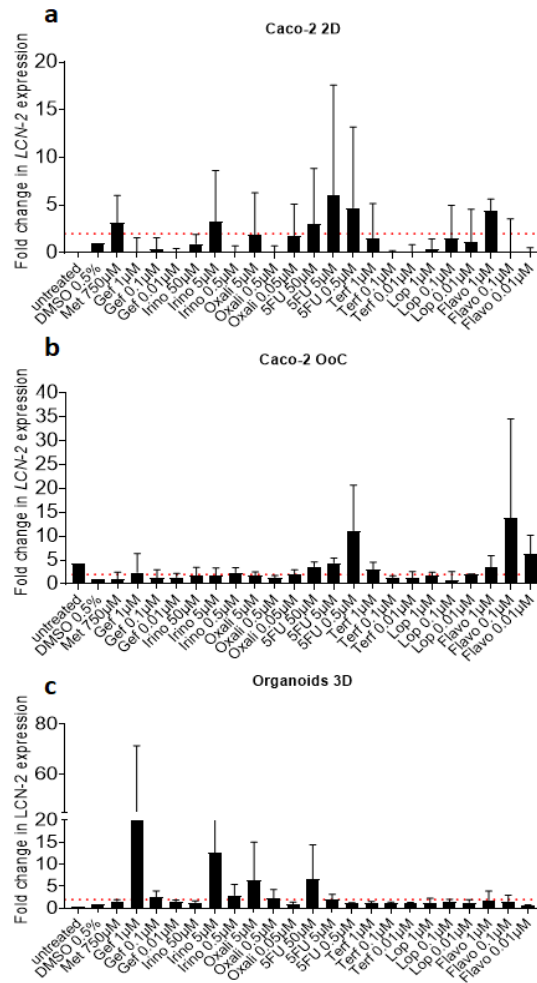


Figure 83: Caco-2 cells were cultivated in 2D for 21d, Caco-2 in the OoC were cultivated for 4d and organoids in 3D were cultivated for 6d. All cells were treated for 48h with test compounds in three different concentrations. After treatment the cells were lysed, and gene expression was analysed by the QuantiGene™ Plex assay. Graphs show the fold changes of a.-c.) *LCN-2* expression normalized to the vehicle control (DMSO 0.5%) in Caco-2 2D, Caco-2 OoC and Organoids 3D. The threshold value was set at 2. N= 3.

Figure 83 a-c showed the expression of *LCN-2* in all three used cell culture models. Overall, it was seen that in the Caco-2 2D model the expression was the lowest compared to the Caco-2 OoC and the organoid 3D models. In each of the models the threshold values (2-fold change) were reached after treatment with 5-FU in each of the tested concentration. Additionally, in the Caco-2 2D and OoC models the expression of *LCN-2* was increased after treatment with Flavo. In the organoid 3D model, the treatment with Gef increased the expression of *LCN-2* and showed a dose-dependent increased expression. *LCN-2* is mainly located in neutrophil granules and involved in metabolic homeostasis, infection, immune response, apoptosis, and inflammation (Chassaing *et al.*, 2012; Abella *et al.*, 2015; Toyonaga *et al.*, 2016; Celi *et al.*, 2019). It is reported to be a fecal biomarker for intestinal inflammation. It is a noninvasive and very sensitive biomarker (Wells *et al.*, 2017)

---

and can be detected in chronic and acute inflammation. In health biological matrices the *LCN-2* levels are low but were increased in inflammatory processes (Celi *et al.*, 2019). In mice it was shown that 5-FU decreased villi height and leads to blunted and fused villis (Chang *et al.*, 2012) and this can also lead to intestinal inflammation (Chang *et al.*, 2012). 5-FU and Irino are both drugs which lead to an inhibition of DNA synthesis (Song, Park and Sung, 2013) and this can lead to inflammation by DNA damage and thereby an inhibition of topoisomerase I which is involved in the activation of inflammatory pathways (Ribeiro *et al.*, 2016). *LCN-2* is therefore a good candidate biomarker to analyze the effect of drugs regarding their inflammation potential. However, the OoC and 3D model seem to be more suitable for this purpose due to the much higher gene expression of *LCN-2* compared to the 2D model.

The gene expression levels of *MLCK* (Figure 84a-c) showed only an increase in the organoid 3D model. In both Caco-2 models the gene expression level of *MLCK* remained very low. In addition, no treatment condition strongly induced an increase of *MLCK* in either Caco-2 models. In comparison *MLCK* was increased in the organoid 3D model after treatment with Med, Gef and 5-FU. *MLCK* is an enzyme which activates the myosin light chain and this leads to cytoskeleton contraction and tight junction regulation (Yao, Feng and Shen, 2020). The *MLCK* mediated pathway is one of the key factors in the regulation of intestinal permeability (Du *et al.*, 2016). Inflammatory diseases like inflammatory bowel disease (IBD) or celiac disease, are known to influence tight junction dysfunction and increased permeability. The released cytokines during inflammation then increase further intestinal permeability and can increase the expression of *MLCK* (Wells *et al.*, 2017). The only slight increase of expression could be seen in the 3D organoid model after treatment with Gef, a chemotherapeutic which is known for its ability to induce intestinal inflammation (Lee, Ryan and Doherty, 2014; Lian *et al.*, 2017).

In Figure 84 d-f the gene expression levels of *CRP* are shown. Again, it is clear that the colon organoids showed the highest elevated expression of this biomarker. The expression of *CRP* was increased after the treatment with Gef and Oxali in the Caco-2 2D model and a slight increase was detected after the treatment with Oxali and Terf. In the OoC model an increase in the gene expression of *CRP* was detected after treatment with 0.5 $\mu$ M 5-FU and 0.1 $\mu$ M Flavo. The organoid 3D model showed the highest expression after treatment with Gef, Irino, Oxali and Flavo. Especially after treatment with Gef and Oxali the expression elevated to a very high value (Gef: FC= 62.5 and Oxali: FC = 64.25). Gef, Oxali, Irino and 5-FU are all chemotherapeutics and induced a high expression of *CRP* in this study. Chemotherapeutics are known to be able to induce intestinal inflammation (Lee, Ryan and Doherty, 2014; Lian *et al.*, 2017).

*CRP* is beside calprotectin the most reliable and used biomarker for inflammatory disease in human (Dragoni, Innocenti and Galli, 2021). Especially in the 3D organoid model it seems to be a good *in vitro* biomarker for inflammation.

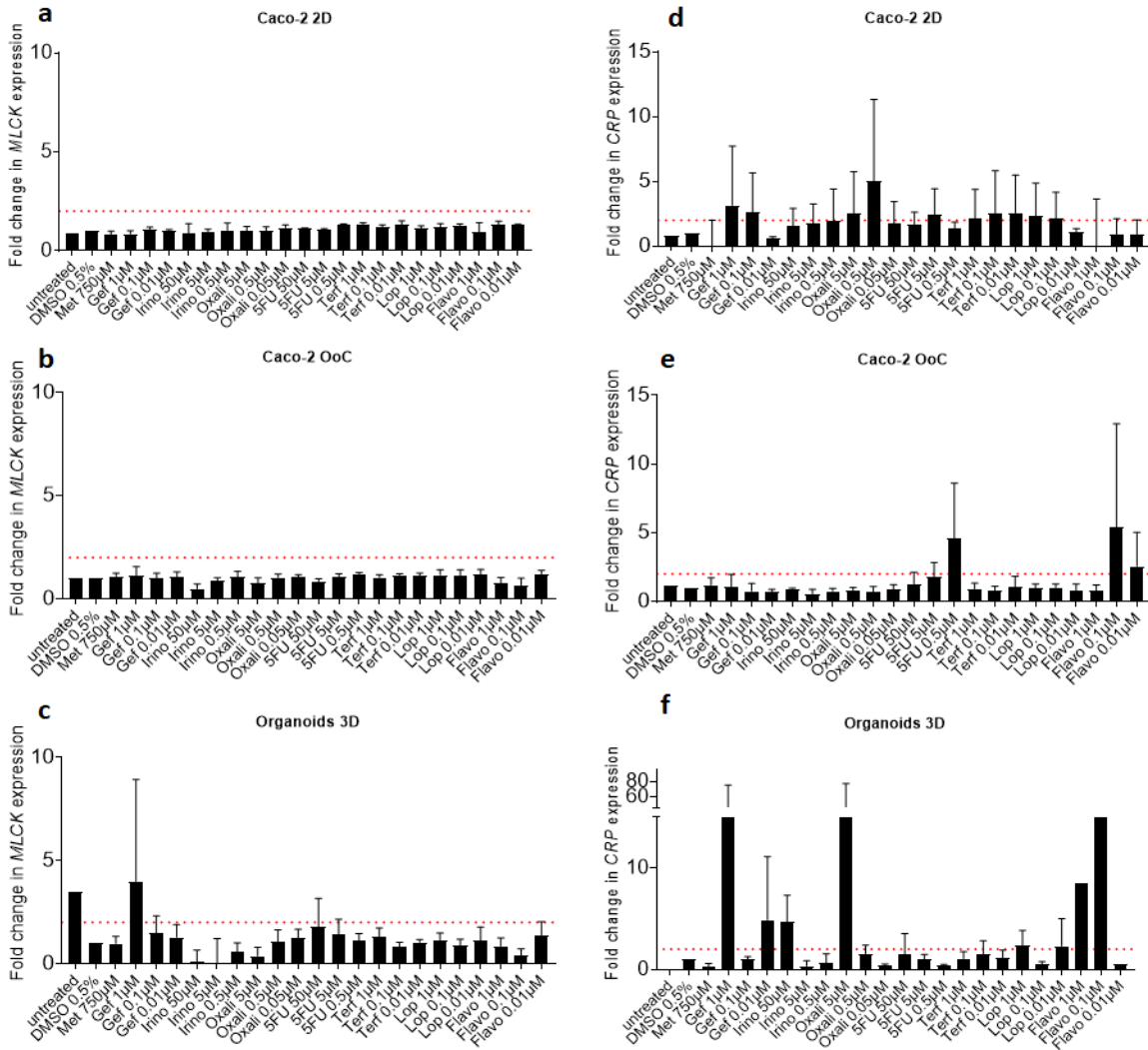


Figure 84: Fold change in gene expression of potential biomarkers *MLCK* and *CRP*. Caco-2 cells were cultivated in 2D for 21d, Caco-2 in the OoC were cultivated for 4d and organoids in 3D were cultivated for 6d. All cells were treated for 48h with test compounds in three different concentrations. After treatment the cells were lysed, and gene expression was analysed by the QuantiGene™ Plex assay. Graphs show the fold changes of a.-c. *MLCK* and d.- f. *CRP* expression normalized to the vehicle control (DMSO 0.5%) in Caco-2 2D, Caco-2 OoC and Organoids 3D. The threshold value was set at 2. N= 3.

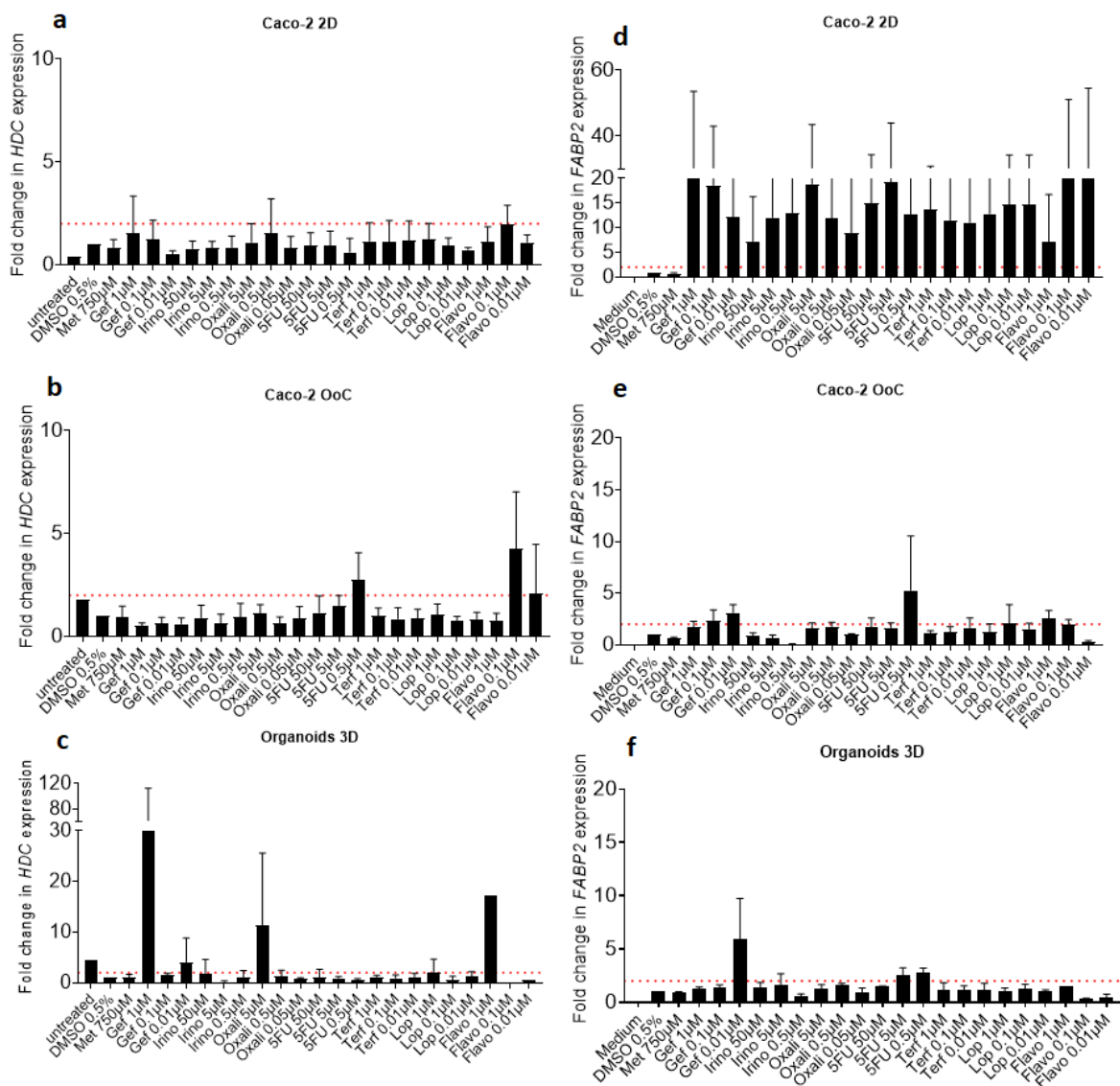


Figure 85: Fold change in gene expression of potential biomarkers *HDC* and *FABP-2*. Caco-2 cells were cultivated in 2D for 21d, Caco-2 in the OoC were cultivated for 4d and organoids in 3D were cultivated for 6d. All cells were treated for 48h with test compounds in three different concentrations. After treatment the cells were lysed, and gene expression was analysed by the QuantiGene™ Plex assay. Graphs show the fold changes of a.-c. *HDC* and d-f. *FABP-2* expression normalized to the vehicle control (DMSO 0.5 %) in Caco-2 2D, Caco-2 OoC and Organoids 3D. The threshold value was set at 2. N= 3

No treatment condition strongly induced an increase of *HDC* in the Caco-2 2D model (Figure 85a). In the Caco-2 OoC model the two-fold threshold was reached only after treatment with 5-FU and Flavo. In the organoid 3D model, the expression was increased after treatment with Gef, Oxali and Flavo (Figure 85a-c). *HDC* is known to be weakly expressed in normal, healthy serum plasma compared to serum plasma of patient with simple intestinal obstruction or simple appendicitis. It was clear that the relative gene expression is lower compared to patients with intestinal obstruction (Yang *et al.*, 2011). An intestinal obstruction is a mechanical blockade, in which food cannot move normally through the intestine (Schick and Meseha, 2018).

---

Several drugs like NSAIDs or topoisomerase inhibitor, like SN-38, the active metabolite from Irinotecan (Lee, Ryan and Doherty, 2014; Fujita *et al.*, 2016), can lead to a drug-induced gastrointestinal obstruction (Satake *et al.*, 2021). In this study the treatment with Irino did not influence the expression level of *HDC*. The main effects were seen with Gef, Oxali and Flavo. It is already known that several chemotherapeutics can lead to intestinal obstructions (Tebbutt *et al.*, 2003; Coward *et al.*, 2012). Both, Gef and Oxali, are chemotherapeutic drugs and can thereby lead to obstruction of the intestine. In one patient each, intestinal obstruction was detected after the administration of gefitinib (Liang *et al.*, 2015) or irinotecan (Van Ruth, Cats and Zoetmulder, 2002).

*HDC* can thereby play an important role in the prediction and identification of intestinal obstructions, already in a cell culture model. In particular, the very high gene expression of *HDC* in the organoid 3D model leads to the assumption that the organoid model can potentially represent chemotherapeutic-induced intestinal obstruction.

In Figure 85d-f the expression of *FABP-2* in the three used cell culture models are shown. *FABP-2* is expressed in high amounts in the small intestine and ileum. It is involved in lipid metabolism and inflammatory processes (Levy *et al.*, 2001; Ohmachi *et al.*, 2006). In patients with ischemia or reperfusion-induced intestinal barrier injury the *FABP-2* is down-regulated and plays an important role in barrier function (Albala *et al.*, 2004). *FABP-2* is specific for the intestine and is responsible for the uptake of fatty acids. In humans *FABP-2* is an effective biomarker for the early diagnosis of strangulated intestinal obstruction (Wu *et al.*, 2021) and it is also named as marker for inflammatory process in patients of ulcerative colitis (Wiercinska-Drapalo *et al.*, 2008).

In summary, iPSC derived colon organoids cultured in 3D Matrigel® hemispheres showed the highest gene expression of potential new genetic biomarkers for drug-induced intestinal toxicity. Lowest fold changes were detected for the Caco-2 2D culture model except for *FABP-2*, here the strongest gene expression was detected after treatment of the cells in the Caco-2 2D model. In this experiment, the OoC model did not show any advantages with regard to the expression of potential new biomarkers compared to the conventionally used 2D model.

### 3.9.1. Statistical comparison of gene expression of drug induced GI toxicity compounds and the DMSO control

Published potential new biomarkers for the prediction of drug induced GI toxicity were screened in all three used cell culture models. The cells were treated with test compounds which are known to cause GI side effects. In this section the gene expression data from chapter 3.9. was analysed statistically to identify if one or more biomarkers differed significantly between the DMSO control and the treated samples. For this approach all treated samples were combined and classified as "GI" and all none treated as "DMSO". Prior to the analysis, data normalisation was done by Julian Kreis and all calculated statistical p-values are listed in the appendix 11 in Table 114.

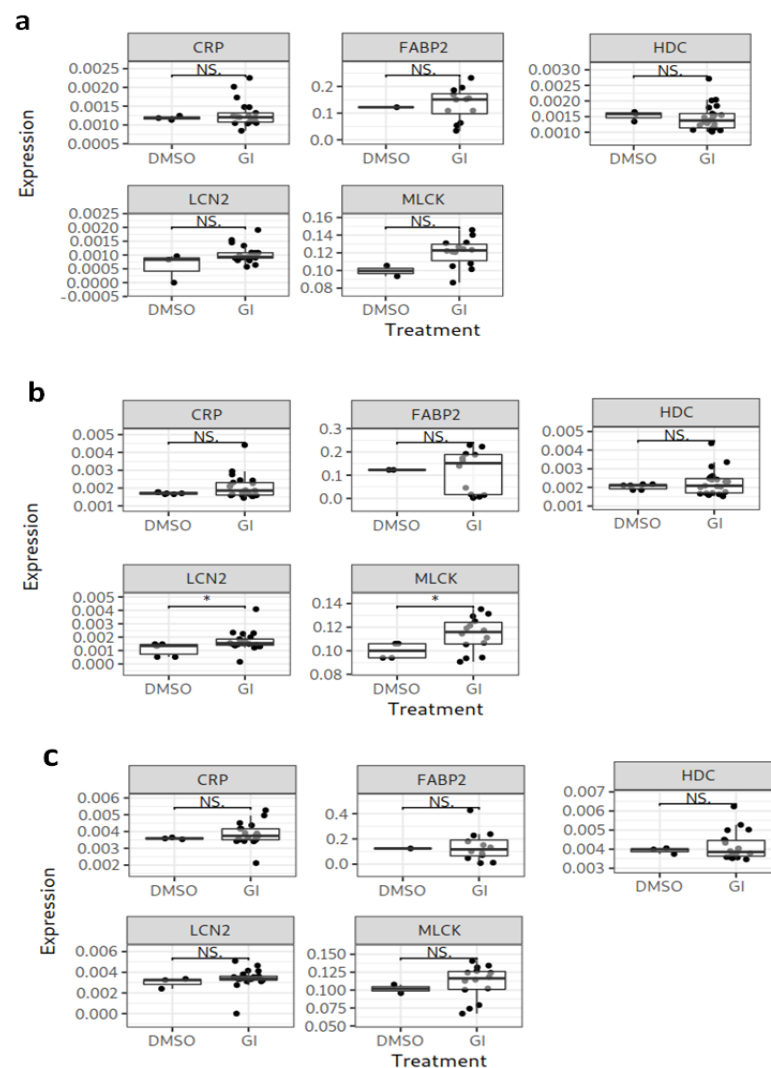


Figure 86: Statistically significant differences between GI toxicity drugs and DMSO control in the Caco-2 2D model. Cells were treated for 48h in the used cell culture models with GI toxicity compounds and with DMSO as control. After treatment the cells were lysed, and gene expression was analyzed with the QuantiGene™ Plex assay. Graphs show statistically significance in a.) Caco-2 2D low dose group, b.) Caco-2 2D mid dose group and c.) Caco-2 2D high dose group, normalized to the vehicle control. Statistical analysis was performed by Julian Kreis using one-sided Wilcoxon tests. Statistically significant \*p < 0.05. All calculated p-values are shown in the appendix 11 in Table 114. N = 3.

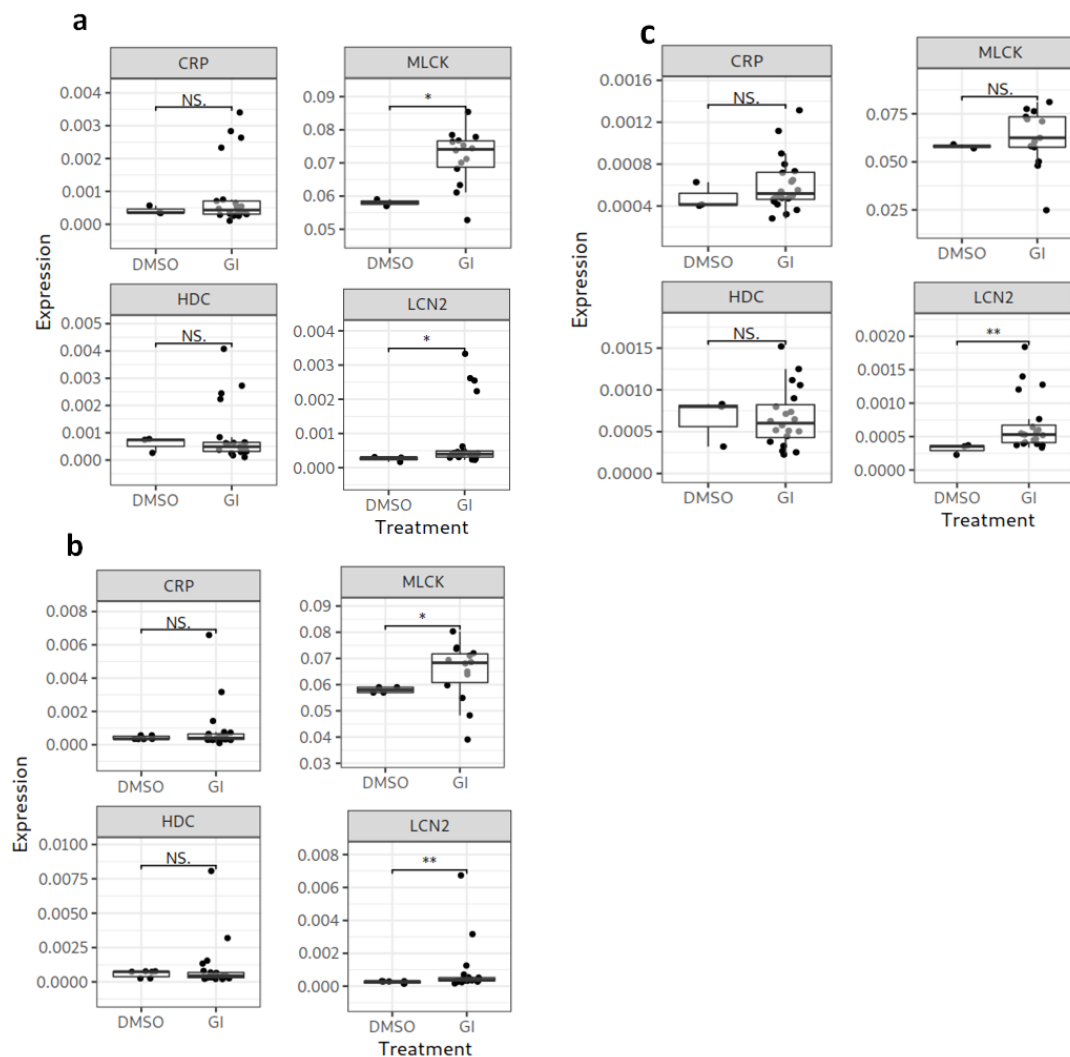


Figure 87: Statistically significant differences between GI toxicity drugs and DMSO control in the Caco-2 OoC model. Cells were treated for 48h in the used cell culture models with GI toxicity compounds and with DMSO as control. After treatment the cells were lysed, and gene expression was analyzed with the QuantiGene™ Plex assay. Graphs show statistically significance in a.) Caco-2 OoC low dose group, b.) Caco-2 OoC mid dose group and c.) Caco-2 OoC high dose group, normalized to the vehicle control. Statistical analysis was performed by Julian Kreis using one-sided Wilcoxon tests. Statistically significant \* $p < 0.05$ . All calculated p-values are shown in the appendix 11 in Table 114. N = 3.

Figure 86 shows the statistical significance in gene expression between GI damage inducing compounds (“GI”) and the DMSO control samples (“DMSO”) in the Caco-2 2D model. Figure 86a shows the differences after treatment with the compounds in the lowest concentration tested, Figure 86b the results for the mid-dose group and Figure 86c shows the results of the high doses. In the Caco-2 2D model a statistically significant difference p value ( $p=0.022$ ) was calculated for *LCN-2* and *MLCK* ( $p=0.049$ ) after treatment with the mid dose compounds. Likewise, *LCN-2* ( $p=0.041$  for low dose group,  $p=0.006$  for mid dose group and  $p=0.049$  for high dose group) was statistically significantly different in the Caco-2 OoC model (Figure 87) treated with all of the tested concentrations. Beside *LCN-2*, *MLCK* showed significantly different expressions, compared

to the DMSO group, in the low dose group ( $p=0.033$ ) and mid dose group ( $p=0.049$ ). All other examined potential biomarkers showed no statistically significant difference between the treated samples and DMSO samples Figure 87. Moreover, no significant change was found in the 3D organoid model due to very high deviations between the samples (Figure 88).

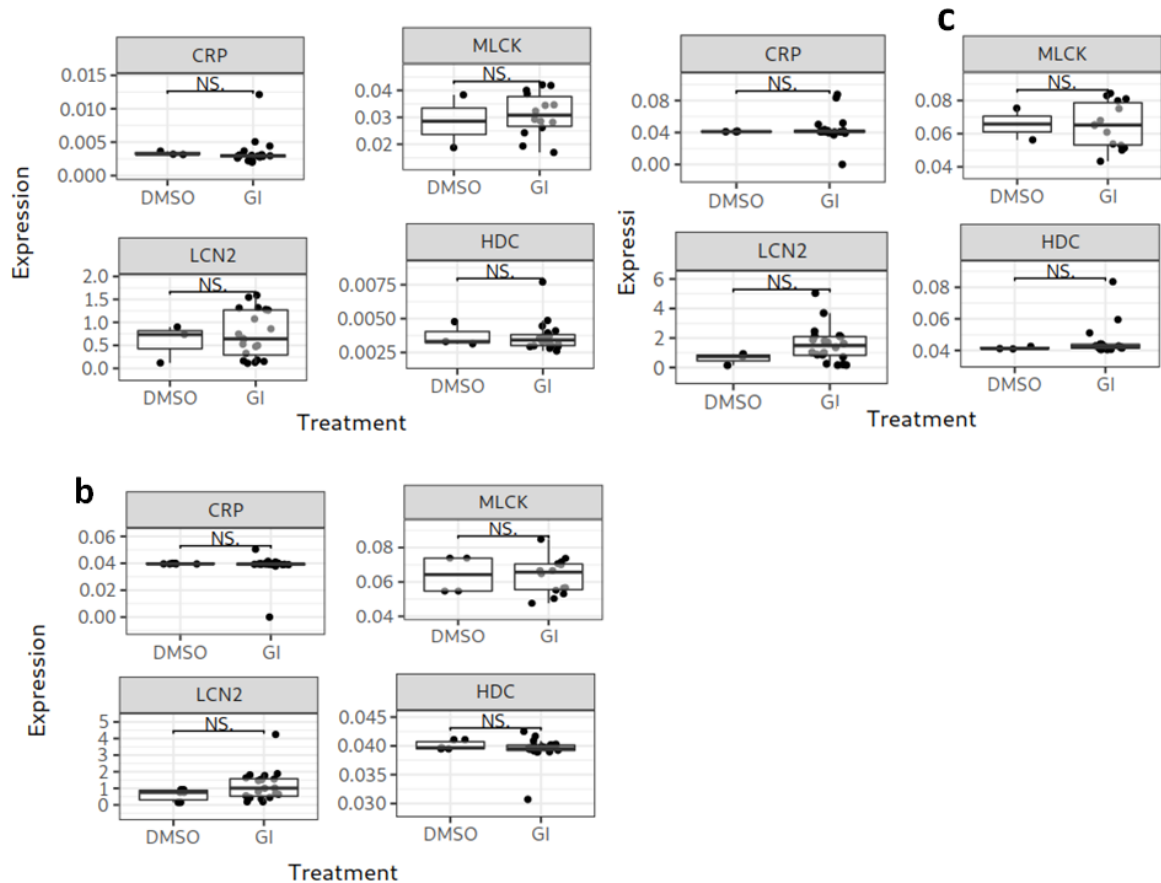


Figure 88: Statistically significant differences between GI toxicity drugs and DMSO control in the colon organoid 3D model. Cells were treated for 48h in the used cell culture models with GI toxicity compounds and with DMSO as control. After treatment the cells were lysed, and gene expression was analyzed with the QuantiGene™ Plex assay. Graphs show statistically significance in a.) Organoid 3D low dose group, b.) Organoid 3D mid dose group and c.) Organoid 3D high dose group, normalized to the vehicle control. Statistical analysis was performed by Julian Kreis using one-sided Wilcoxon tests. Statistical p-values are shown in the appendix 11 in Table 114. N = 3.

Overall, it is clear that the OoC model showed the most promising results for the use of *LCN-2* as biomarker. As well *MLCK* showed potential as in vitro biomarker in Caco-2 cells, when cultivated in the OoC system.



### 3.10. Expression levels of mir194 for the evaluation of drug-induced toxicity

It is already described that miRNAs have the potential to act as biomarkers for the detection of several drug induced organ toxicities (Kalabat *et al.*, 2017). Specifically for intestinal damage mir194 and mir215 (John-Baptiste *et al.*, 2012) are described. miRNAs are small non-coding RNA molecules and are post-transcriptional regulators of gene expression (John-Baptiste *et al.*, 2012; Rashid *et al.*, 2020). During drug-induced damage or disease conditions, miRNAs are expressed differently and act as negative regulators of gene expression (Rashid *et al.*, 2020). For example miR-155, miR-124 or miR-23b are upregulated in inflamed enterocytes (Neudecker *et al.*, 2017). This study attempted to detect mir 194 in the cell lysate and to compare the levels between control and treated samples to check for drug-induced intestinal damage.

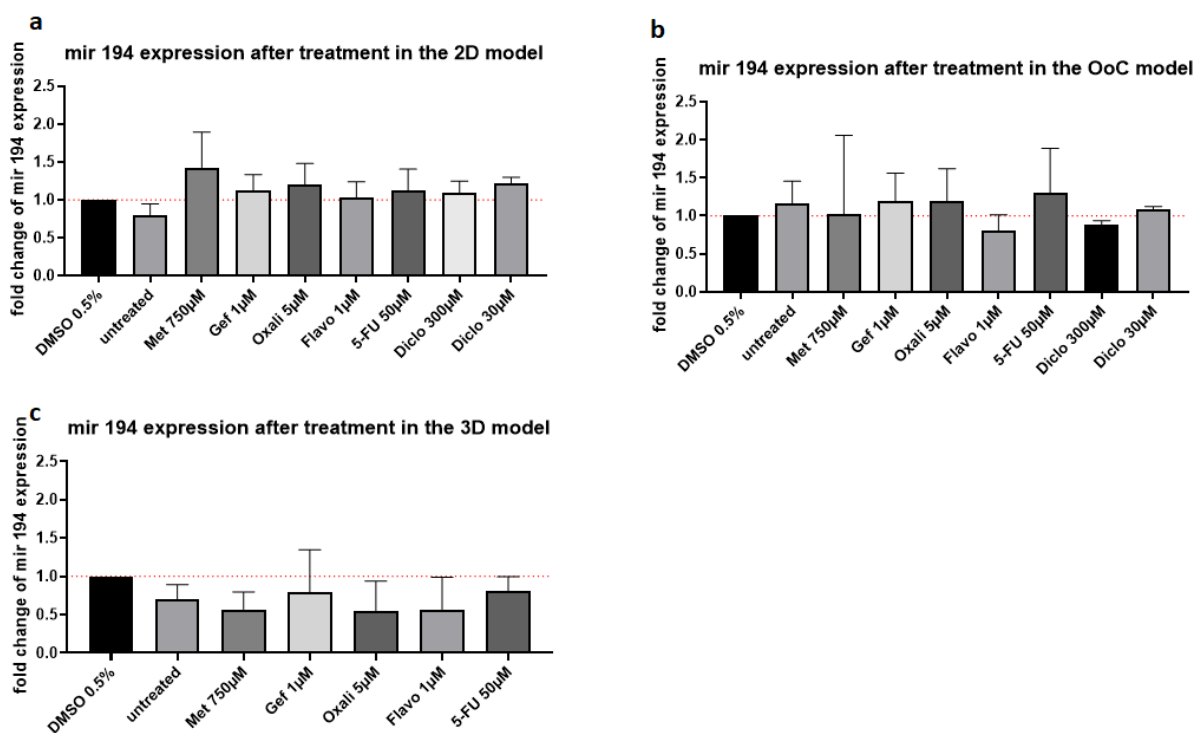


Figure 89: Fold change in mir194 expression. Advanced cell cultured models were treated with test compounds for 48h. The mir194 level was detected in the cell lysate using the QuantiGene™2.0 miRNA assay. Graphs show the fold change in mir194 expression after treatment in the different cell culture models. Calculated fold changes are shown in appendix 12 in Table 115 and statistical differences were calculated in all models with a one-way ANOVA and are shown in the appendix 12 in Table 116. N=3.

In the 2D model mir194 expression was decreased in all used test compounds and as well in the negative control Met (Figure 89a). The highest fold change was detectable in the Met sample. In the OoC (Figure 89b) model in two (Flavo 1µM and Diclo 300µM) of six test compounds a decreased expression was observed. All other test compounds showed a slightly increase in the expression of mir194. In the 3D model (Figure 89c) all tested compounds decreased the level of

---

mir194. Although none of the tested compounds showed a significant difference to the DMSO control. All statistical values were calculated in a one-way ANOVA for all models and are listed in appendix 12 in Table 116. Mir194 is highly expressed in differentiated Caco-2 cells (Hino *et al.*, 2008) and in the human intestine it is enriched and plays a role in the differentiation of intestinal epithelium (McKenna, Lindsay *et al.*, 2010). Kalabat et al. could show that the concentration of mir194 in rat feces increased after treatment with 50mg/kg Diclofenac (Kalabat *et al.*, 2017). Diclofenac inhibits COX's (cyclooxygenase), which is an enzyme that catalyse the production of prostaglandin or prostanoids and is a common target for NSAID's (Turini and DuBois, 2003). The inhibition suppresses the prostaglandin production which is necessary for the maintenance of homeostasis of the mucosa in rats (Tanaka *et al.*, 2002). COX's are widely expressed in the GI tract and the produced prostaglandins play important role in inflammation (Ferrer *et al.*, 2018). In this miRNA expression evaluation and in the prior viability experiments Diclofenac showed no toxic effects at the tested concentrations. Diclofenac is an NSAID and has been reported to lead to cell death in Caco-2 cells and in human small intestinal epithelium it can have an effect on the maintenance of homeostasis of the GI mucosa (Zhu and Zhang, 2012). In Caco-2 cells the cell viability decreased after treatment with 1000µM Diclofenac by 50% (Boonyong, Vardhanabhuti and Jianmongkol, 2020). In case of the treatment of diclofenac in this thesis the results from Boonyong 2020 suggest that the expression of mir194 was so low due to the low concentration of diclofenac. For all other compounds as well a low compound concentration could be the reason for the low expression of Mir194. As well a longer treatment time (more than 48h) could lead towards a clearer effect.

### **3.11. Measurement of *in vivo* used biomarkers for the prediction of GI damage *in vitro***

Drug-induced GI toxicity is a big issue for several drugs. It can occur in each part of the GI tract and can range from harmless but quality of life limiting diarrhea, nausea, or stomach cramps up to perforation of the intestine or hemorrhage (Pusztaszeri, Genta and Cryer, 2007). The prediction of different GI damages due to drugs is one of the important steps during drug development. Biomarkers measure biochemical, cellular or molecular alterations in cell culture media, cells, tissue or fluids (Mayeux, 2004). Biomarkers are standard tools used to measure the presence and status of a disease and the response of a drug treatment or assess health risks and toxic potential (Timbrell, 1998). To date there is a lack of noninvasive, sensitive, reliable and specific *in vitro* biomarkers exist (Carr *et al.*, 2017). Therefore, L-citrulline and calprotectin, both *in vivo* used biomarkers, were tested in this work for their applicability as biomarkers for the early detection of drug-induced damage in the GI tract in *in vitro* models.

### 3.11.1. L-Citrulline

One of the most facile tests of toxicity *in vivo* is the measurement of the change in specific biomarkers in blood, feces, or plasma. In the clinical phase of drug development or even in the screening of potential damage in the intestine in patients, specific biomarkers are used. Citrulline is one of the best known and used clinical biomarkers for the detection of GI damage (small intestine) and is based on a damage to the enterocytes. When damaged the non-essential amino acid L-Citrulline is released by enterocytes. During inflammation or damage of the intestinal barrier, the plasma levels are reduced and this leads to reduced citrulline concentration which can be measured and then used as a surrogate of the effects in the small intestine (Crenn *et al.*, 2003, 2009; Crenn, Messing and Cynober, 2008; Van Der Velden *et al.*, 2013; Fragkos and Forbes, 2018; Saitoh *et al.*, 2018).

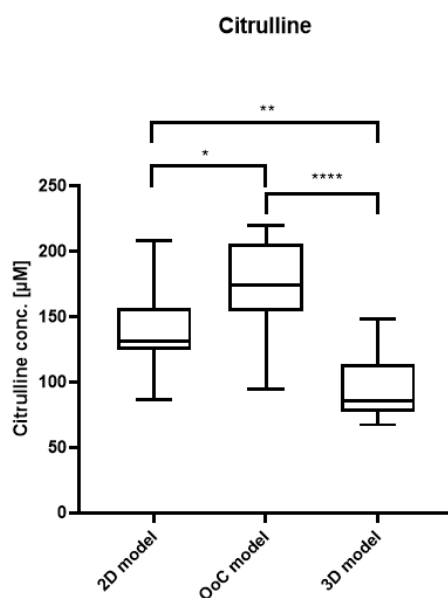


Figure 90: Boxplot chart of the L-citrulline concentrations in the cell culture systems. The L-citrulline concentrations were measured after treatment with different compounds. The samples were analysed in a one side Kruskal-Wallis Test with following Dunn's Test: \* indicates statistical significance ( $P=0.0193$ ), \*\* indicates statistical significance ( $p=0.0020$ ) and \*\*\*\* indicates statistical significance ( $p<0.0001$ ). All calculated p-values are shown in the appendix 13 in Table 117.

In the boxplot of Figure 90 it is shown that in each of the models tested L-citrulline could be detected. The Caco-2 OoC model has on average the highest measurable concentration, directly followed by the 2D model and the lowest concentration of L-citrulline was measured in the organoid 3D model. In healthy human plasma the L-citrulline concentration is about  $40 (\pm 10) \mu\text{mol/L}$  (Crenn, Messing and Cynober, 2008; Crenn *et al.*, 2011) but depends on the uptake of food and the absorption in the small intestine (Schoultz and Keita, 2020). In the human body the L-citrulline is released from damaged enterocytes in the bloodstream and gets

metabolized to arginine in the kidney (Crenn *et al.*, 2003). This metabolizing step can decrease the L-citrulline levels *in vivo* but is not present in the *in vitro* cell culture models. The higher concentration of L-citrulline in the cell culture models can be explained that the cell culture models do not contain kidney cells.

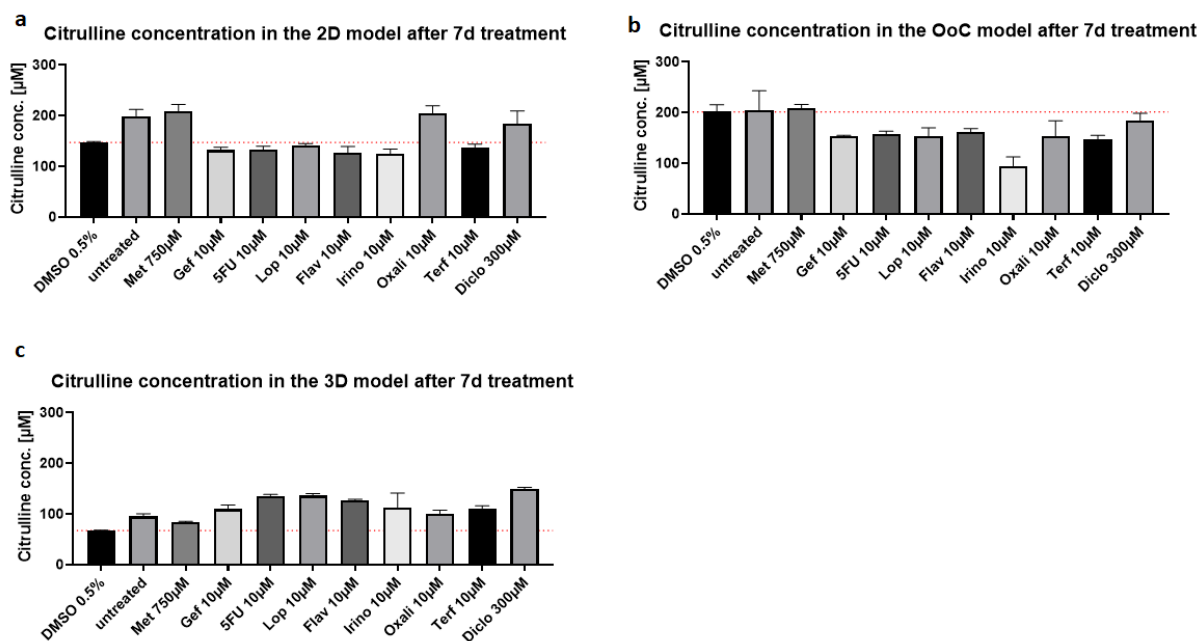


Figure 91: Bar graph of the L-citrulline concentration in the different models. The citrulline was measured after 7d treatment with different test compounds. Graphs show the citrulline concentration in the a.) 2D, b.) OoC and c.) organoid 3D models. Statistical differences were calculated for the 2D model in a Kruskal-Wallis Test with followed Dunn’s test and for the OoC and 3D model in an ANOVA with followed Dunnett’s test. Statistical values are shown in the appendix 13 in Table 119. N= 3.

Figure 91 shows the measured citrulline concentrations after 7d treatment with the test compounds in all three used cell culture formats. The concentration in the 2D and OoC models were very similar. In the Med and Met controls concentrations around 200µM were measured. In the Caco-2 2D (Figure 91a) model a small decrease was observed after treatment with Gef, 5-Fu, Flav, Irino and Terf, but all were not significantly different to the DMSO control. After treatment with Gef, 5-Fu, Lop and Terf and DMSO the concentrations decreased but were not significantly different to the Med control. In the OoC model (Figure 91b) the concentration of L-citrulline decreased after treatment for 7d with Gef, 5-FU, Lop, Irino, Oxali and Terf. The concentrations were significantly different to the DMSO control (Gef: p= 0.0232, 5-FU: p=0.0454, Lop: p=0.0240, Irino: p<0.0001, Oxali: p= 0.0238, Terf: p=0.0092). The small drop in the concentration of Diclo was not significantly different to the DMSO control. Similar to the not cytotoxic effect of Diclofenac in the viability screenings, this could be due to the too low concentration of diclofenac. The measured citrulline concentrations of each system are shown in the appendix 13 in Table 118.

---

The citrulline concentration in the organoid model (Figure 91c) increased after treatment with all the tested compounds. The concentrations were significantly different to the DMSO control (Gef:  $p=0.3028$ , 5-FU:  $p<0.0001$ , Lop:  $p<0.0001$ , Flav:  $p<0.0001$ , Irino:  $p<0.0001$ , Oxali:  $p=0.0034$ , Terf:  $p<0.0001$  and Diclo:  $p<0.0001$ ). In the human GI tract a decrease in citrulline is visible during several pathologies, for example villous atrophy with celiac disease, acute mucosal enteropathy, specifically mucositis after the treatment with chemotherapeutics, antineoplastics or after radiotherapy (Maric, Restin, *et al.*, 2021). After damage of the intestinal barrier this leads to reduced plasma citrulline concentration (Crenn *et al.*, 2003, 2009; Crenn, Messing and Cynober, 2008; Van Der Velden *et al.*, 2013; Fragkos and Forbes, 2018; Saitoh *et al.*, 2018). A decrease in citrulline was observed in the 2D and OoC model after treatment with the used chemotherapeutics which supports the statement of Maric *et al.* 2021. The Caco-2 models (2D and OoC) are both differentiated and resemble mature enterocytes and are capable of producing citrulline which suggests that these models together with citrulline are potentially suitable for the early assessment of biomarker for chemotherapeutic induced intestinal damage. The higher amount of citrulline in the organoid 3D model could be due to the organoids not completely containing only enterocytes. It's the same case as in humans in which the enterocytes are more abundant in the small intestine, due to the higher absorption function, than in the large intestine (*Cell types Enterocytes*, 2021). The fact that mainly enterocytes of the small intestine release citrulline after damage (Crenn, Messing and Cynober, 2008) supports the results that the colon organoids did not show a decrease in citrulline concentration .

### 3.11.2. Calprotectin

For detecting intestinal inflammation, the current gold standard is endoscopy with biopsies (Ponce de León-Rodríguez, Guyot and Laurent-Babot, 2019). A further method to measure inflammatory bowel disease is the measurement of calprotectin in feces, which is used as a biomarker in patients (Konikoff and Denson, 2000; Burri and Beglinger, 2014; Kopi *et al.*, 2019).

Calprotectin is a protein which binds calcium and zinc and is mainly found in neutrophils. It is also found in monocytes and macrophages but in lower amounts (Pathirana *et al.*, 2018). It is present throughout the whole human body in various fluids and is proportionate to the degree of any existing inflammation. The concentration in feces is six times higher than in the plasma in healthy humans (Ayling and Kok, 2018).

In this study the calprotectin concentration was measured in cell culture supernatant of treated cells of the three cell culture models. Every second day the cells were treated three times and the calprotectin concentration were detected on day 7.

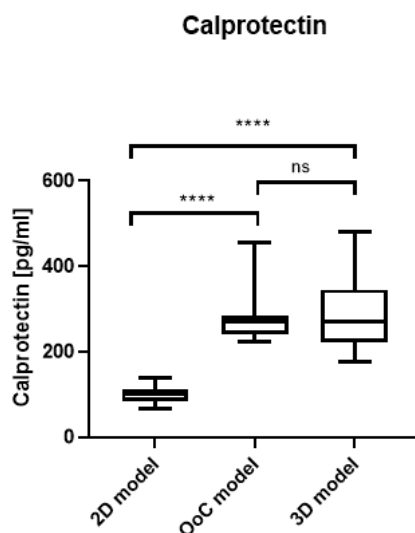


Figure 92: Boxplot chart of the calprotectin concentrations in the cell culture systems. The calprotectin concentrations were measured after treatment with different compounds. The samples were analysed in an one side Kruskal-Wallis Test with following Dunn's test \*\*\*\* indicates statistical significance ( $p < 0.0001$ ).

Figure 92 shows a boxplot of the baseline calprotectin concentrations in the different cell culture models. The lowest concentrations which were detected was in the Caco-2 2D model (51.33pg/ml). The boxplot shows that overall measurements the 2D model was the one in which the cells generated the lowest calprotectin concentrations. The Caco-2 OoC and organoid 3D model were similar in their concentration ranges. The concentrations in the 2D model were significantly different to the 3D and OoC models ( $p < 0.001$ ). Only the concentrations of calprotectin between the OoC and 3D model showed no significant difference ( $p = 0.8016$ ). Calculated p-values are shown in the appendix 14 in Table 120.

Figure 93 shows bar graphs of the calprotectin concentration after treatment for 7d with test compounds. It is shown that the concentration of calprotectin decreased after the treatment with two of the eight test compounds in the Caco-2 2D model. An increase in the concentration was observed in seven of the eight tested compounds. Only after treatment with Lop the calprotectin concentration decreased.

In the OoC model an increase in calprotectin concentration was detected after the treatment with all test compounds, whereby the highest levels were reached with Met and Gef. In the 3D model

the cells increased their calprotectin level after treatment with Met, 5-FU, Irino, Oxali and Diclo. The levels decreased with Gef, Lop, Flavo and Terf. No significant differences were calculated for any of the samples. All measured calprotectin levels are shown in the appendix 14 in Table 121 and all calculated p-values are listed in the appendix 14 in Table 122.

Calprotectin is known as a fecal biomarker in clinic for inflammatory disease (Konikoff and Denson, 2000; Burri and Beglinger, 2014; Kopi *et al.*, 2019). In a healthy humans the plasma concentration of calprotectin ranges from 28-205 ng/ml (Cikot *et al.*, 2016). In inflammatory processes the calprotectin is released and increased in plasma, urine, stool and synovial fluid (Tøn *et al.*, 2000; Konikoff and Denson, 2006). In the results a very slight increase of calprotectin was detected but in total the concentrations observed *in vitro* are many times lower compared to *in vivo*. One explanation could be that too few cells were present in *in vitro* models which leads to too low calprotectin levels. Another explanation could be that the used *in vitro* models not completely recapitulate the *in vivo* intestine system, which for example means that the immune cells are not present and that's why the inflammation process could not complete covered. Additionally in all three models no neutrophils, macrophages and monocytes are present, which are the main localization areas of calprotectin (Pathirana *et al.*, 2018). And in order to measure a change in cell metabolites induced by drugs, a longer treatment period is often required. Some drugs show potentially toxic effects only after long-term use.

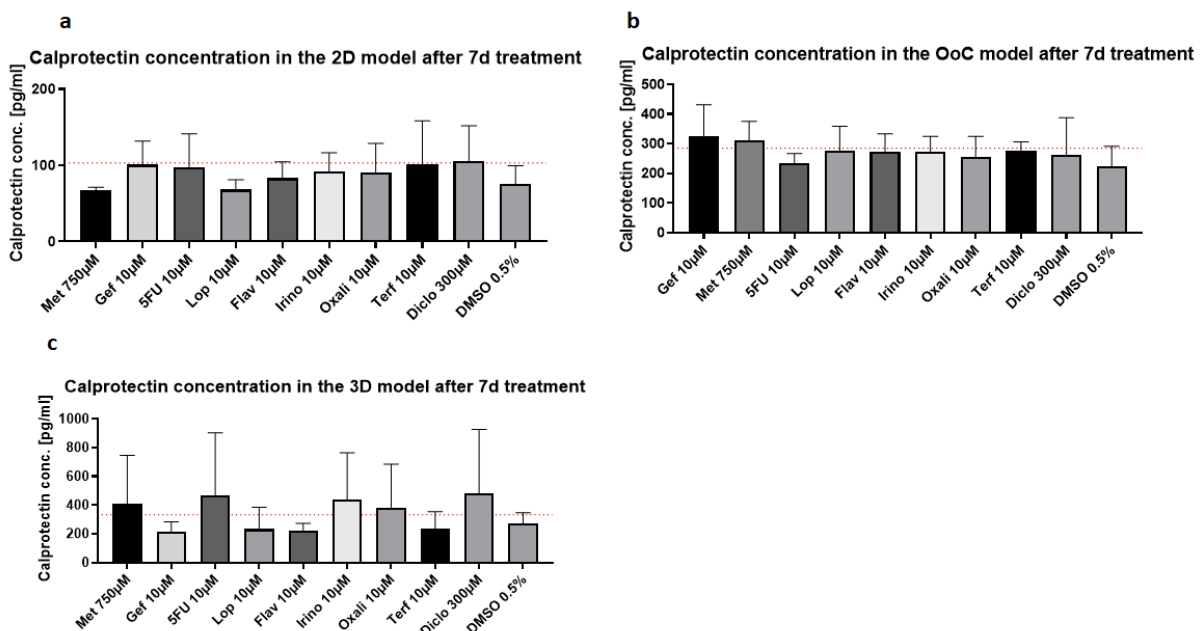


Figure 93: Bar graph of the calprotectin concentration in the different models. The calprotectin was measured after 7d treatment with different test compounds. Graphs show the calprotectin concentration in the a.) 2D, b.) OoC and c.) organoid3D models. Statistic was calculated for the 2D model in an ANOVA with followed Dunnett's test and for the OoC and 3D model in a Kruskal-Wallis Test with followed Dunn's test. Statistical values are shown in the appendix 14 Table 122 . N= 3.

### 3.12. Evaluation of human intestine specific pathways

For the evaluation of *in vivo* like function, it is necessary to assess relevant intestinal pathways which are important within the intestinal development. Several molecular pathways, like the Wnt/ $\beta$ -catenin, Notch, Hippo, transforming growth factor- $\beta$  (TGF- $\beta$ )/bone morphogenetic protein (BMP) and Hedgehog pathways, are known to be involved in the regulation of intestinal homeostasis (Jeon, 2013). The major intestinal pathways for the regulation of stem cell population proliferation are the Wnt/  $\beta$ -catenin and Notch pathways (Ternet and Kiel, 2021). Hippo, notch and Wnt/  $\beta$ -catenin pathways are very crucial and together they regulate intestinal tissue homeostasis and regeneration (Hong, Meng and Guan, 2016). The Wnt/  $\beta$ -catenin pathway plays an important role in the homeostasis of the intestinal epithelium and the embryogenesis (Fevr *et al.*, 2007; Komiya and Habas, 2008; Mah, Yan and Kuo, 2016).

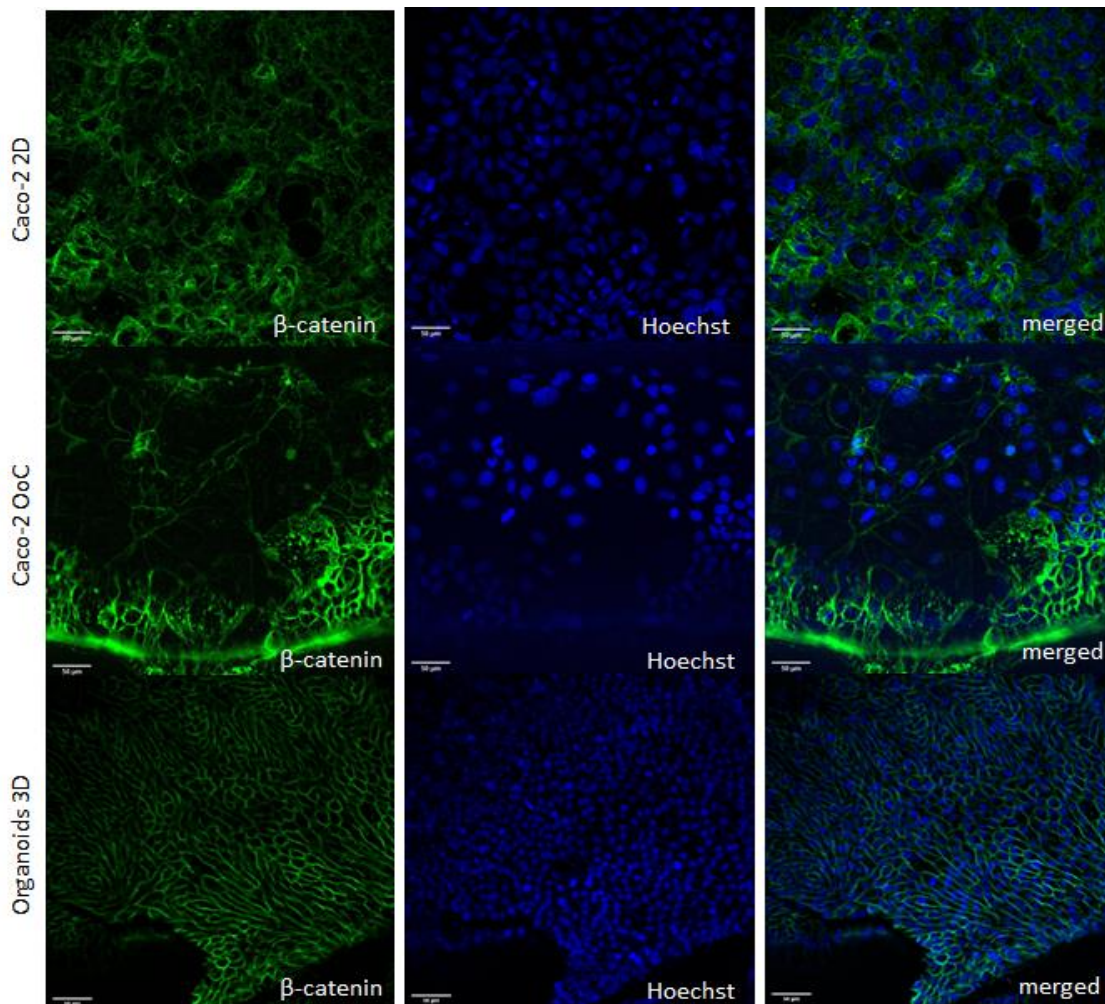


Figure 94: Immunofluorescent stainings with the antibody  $\beta$ -catenin to stain a major component of the Wnt-signaling pathway. Shown are the Caco-2 2D (pictures above), Caco-2 OoC (pictures in the middle) and Organoids 3D (pictures below) models with the antibody  $\beta$ -catenin (green). Nuclei were counterstained with Hoechst (blue). 20x magnification, bar = 50  $\mu$ m for 2D, OoC and 3D.



The Wnt/  $\beta$ -catenin pathway (Figure 16) contains a canonical and non-canonical route. In the canonical pathway the  $\beta$ -catenin play a central role (Jeon, 2013). When Wnt proteins are present, they bind to the frizzled and LRP co receptors. This inactivates the glycogen synthase kinase 3 $\beta$  and thus prevents phosphorylation of downstream molecules which leads to an accumulation of  $\beta$ -catenin. Accumulated  $\beta$ -catenin interact with Tef/Lef in the nucleus which triggers the transcription of genes for cell proliferation. Figure 94 shows the immunofluorescence stainings of all three used cell culture models with the antibody  $\beta$ -catenin. This antibody was chosen due to the main role of  $\beta$ -catenin in the Wnt pathway  $\beta$ -catenin is a major component of the cadherin complex, which is necessary for the activation of the Wnt/  $\beta$ -catenin pathway (Pai *et al.*, 2017). As a control staining the staining of SW480 cells were performed. These cells are from a colon carcinoma and express in low density nuclear  $\beta$ -catenin. In higher densities, after longer cultivation, the cells change to an epithelial like phenotype which switches the nuclear  $\beta$ -catenin to the cytoplasm and membrane (Brabletz *et al.*, 2001). Both densities of SW480 are shown in Figure 95.

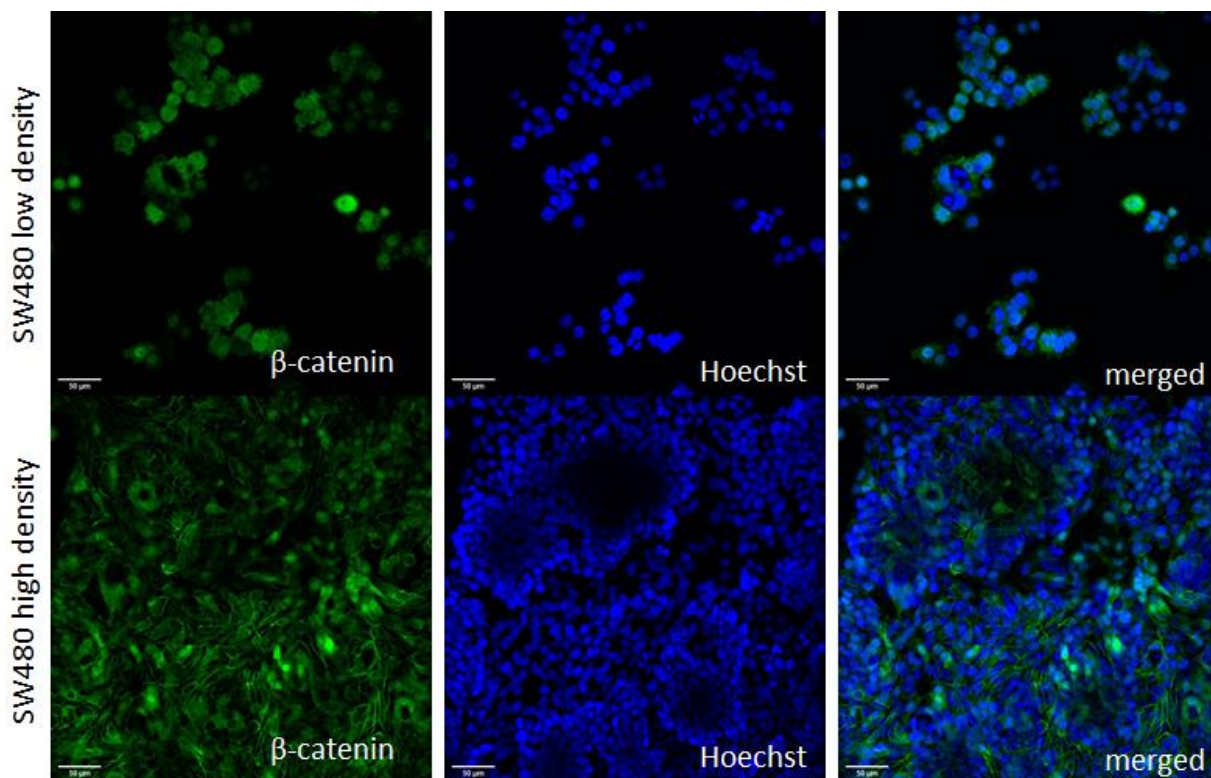


Figure 95: Immunofluorescent stainings with the antibody  $\beta$ -catenin to stain a major component of the Wnt-signaling pathway. Shown are SW480 cells in low density, which means 1day after seeding (top pictures) and in high density, which means 7days after seeding (bottom pictures) as positive control for the Wnt-pathway with the antibody  $\beta$ -catenin (green). Nuclei were counterstained with Hoechst (blue). 20x magnification, bar = 50 $\mu$ m.

The control staining in SW480 cells and the staining in the cell culture models (Figure 94) showed that  $\beta$ -catenin is present in cytoplasm and the membrane of the cell culture models (Figure 95), but not in the nucleus. This means that in these models the Wnt signaling pathway is present but not active due to the membrane localized staining.  $\beta$ -catenin is mainly localized in normal cells in cell-cell junctions (Park *et al.*, 2005). After ligand binding to a Frizzled receptor which leads to an accumulation of  $\beta$ -catenin. Accumulated  $\beta$ -catenin interact with Tef/Lef in the nucleus which triggers then the transcription of genes for cell proliferation (Pai *et al.*, 2017).

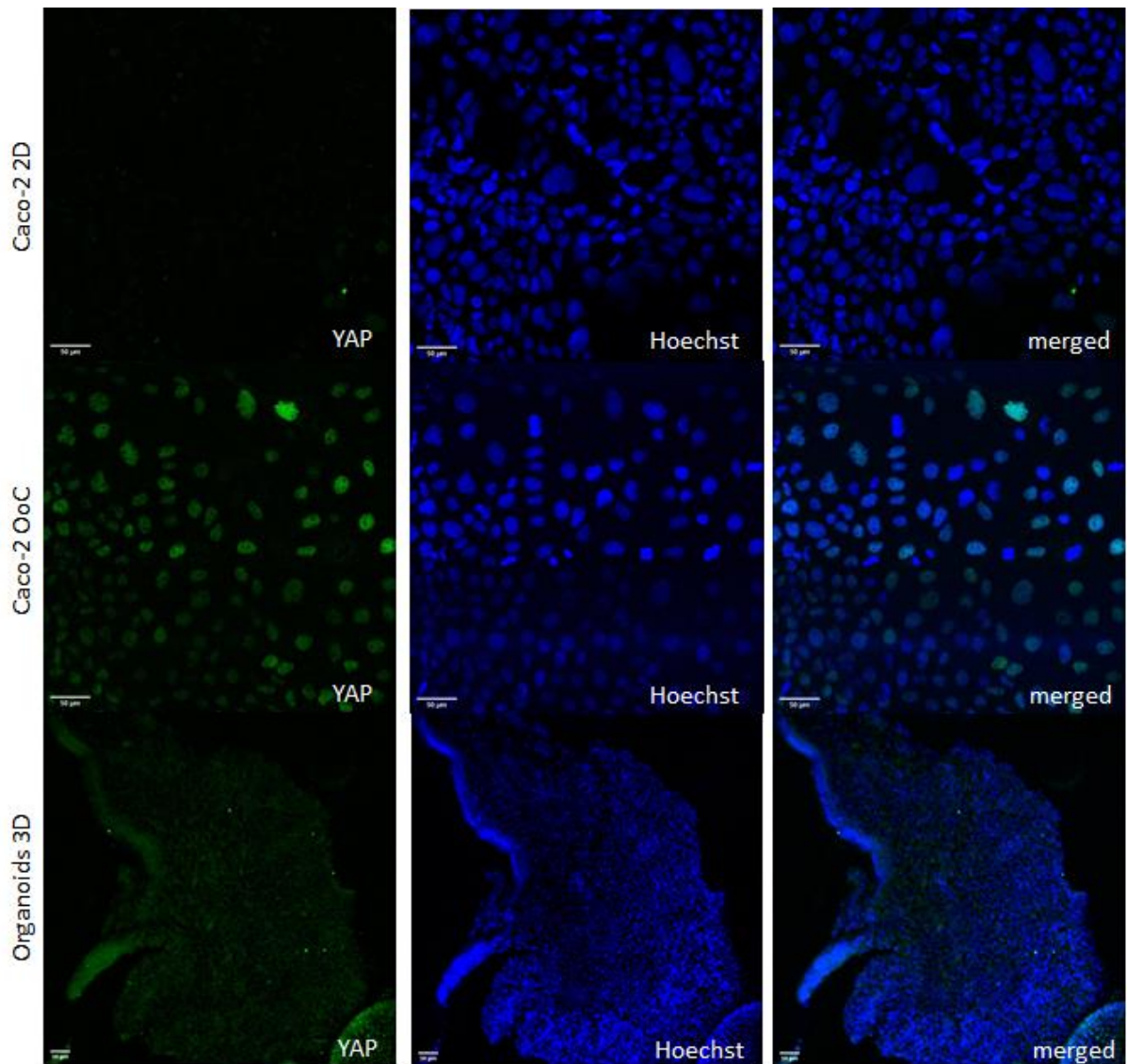


Figure 96: Immunofluorescent stainings with the antibody YAP to stain a major component of the Hippo-signaling pathway. Shown are the Caco-2 2D (pictures above), Caco-2 OoC (pictures in the middle) and Organoids 3D (pictures below) models with the antibody YAP (green). Nuclei were counterstained with Hoechst (blue). 20x magnification, bar = 50 µm for 2D and OoC. 10x magnification, bar=50 µm for 3D.

---

Figure 96 shows the staining with the antibody YAP in the three cell culture models. YAP is clearly detectable in the nuclei of the Caco-2 cells in the OoC model. In the Caco-2 2D model no staining was not existent in the cells. In the 3D organoid model, a staining within the cytoplasm is visible. The Hippo signaling pathway (Appendix 16, Figure 116) plays an important role in the maintenance of intestinal homeostasis (Hong, Meng and Guan, 2016; Ma and Shah, 2018), cell growth (Xie *et al.*, 2021) and is responsible for organ size, which is regulated by tissue-specific stem cells (Mo, Park and Guan, 2014). Activated LATS1/2 (large tumor suppressor 1 and 2) phosphorylates YAP1 (yes-associated protein) and TAZ (PDZ-binding domain). Both are transcriptional coactivators of the Hippo signaling pathway (Hong, Meng and Guan, 2016; Ma and Shah, 2018). Both coactivators are of critical importance for tissue regeneration after injury (Hong, Meng and Guan, 2016). When the coactivators are phosphorylated, this leads to an accumulation of YAP1/TAZ in the cytoplasm and this leads to proteolytic degradation. Unphosphorylated YAP1/TAZ does not remain in the cytoplasm, this gets transported into the nucleus and after binding with TEAD1-4 (TEA domain DNA-binding transcription factors 1-4) cell proliferation and differentiation are induced (Kang *et al.*, 2016). The staining in the nucleus in the OoC model showed that YAP was located into the nucleus, and this indicates that the Hippo pathway is not active. When YAP is not phosphorylated it gets transported in the nucleus where it builds a complex with TEADs and this then regulates genes which are responsible for cell proliferation, migration and survival (Boopathy and Hong, 2019). Compared to the results in the OoC the staining of YAP in the organoid model showed a clear staining in the cytoplasm. This indicates that YAP was phosphorylated, and this leads to the proteolytic degradation and stops the pathway (Zhao *et al.*, 2007; Oka, Mazack and Sudol, 2008).

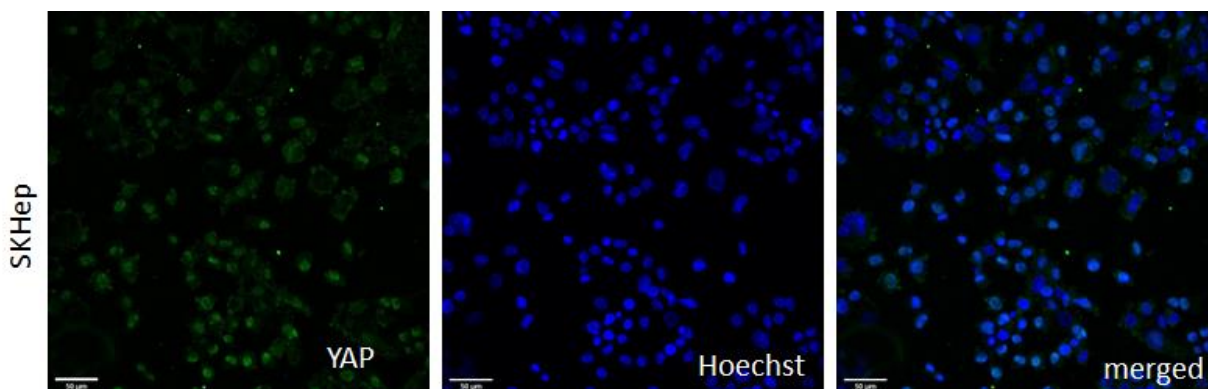


Figure 97: Immunofluorescent stainings with the antibody YAP to stain a major component of the Hippo-signaling pathway. Shown are SK-Hep-1 cells as positive control for the Hippo-pathway with the antibody YAP (green). Nuclei were counterstained with Hoechst (blue). 20x magnification, bar = 50 µm.



The staining of YAP, in the control (SK-Hep-1 cells) showed a clear staining in the cytoplasm (Figure 97). SK-Hep 1 cells were originally isolated from a liver adenocarcinoma (Eun et al., 2014) and YAP is localized in the nucleus when the cells are cultured in low density. In high density the cells express YAP in the cytoplasm (Qin *et al.*, 2021).

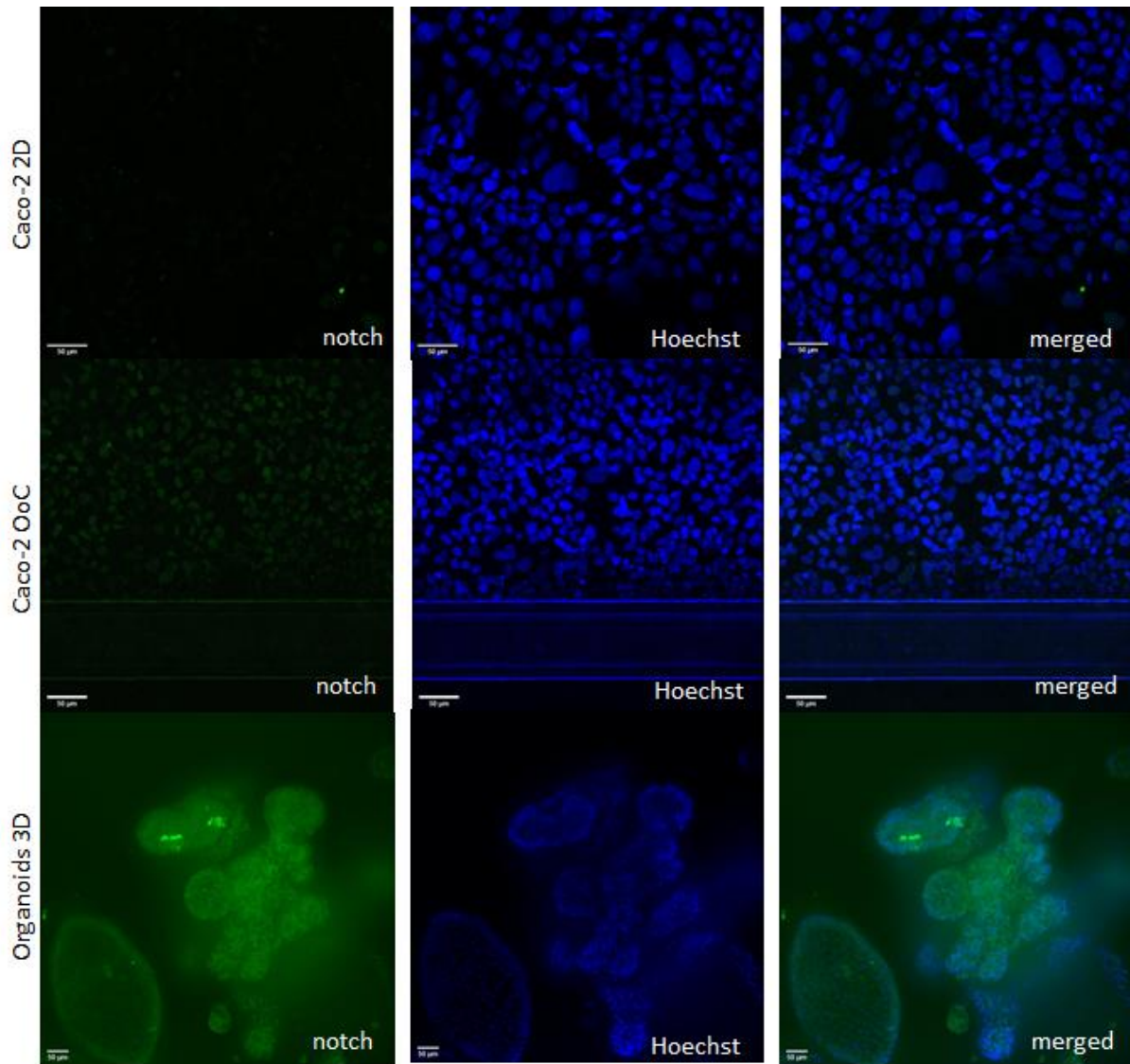


Figure 98: Immunofluorescent stainings with the antibody notch to stain a major component of the Notch-signaling pathway. Shown are the Caco-2 2D (pictures above), Caco-2 OoC (pictures in the middle) and Organoids 3D (pictures below) models with the antibody notch (green). Nuclei were counterstained with Hoechst (blue). 20x magnification, bar = 50 µm for 2D and OoC. 10x magnification, bar=50 µm for 3D.

---

Figure 98 shows the immunofluorescence staining with the antibody notch in the three cell culture models. It is visible that in the 2D model no staining was visible, in the Caco-2 OoC and organoid 3D model a staining of notch in the nucleus was detectable. The notch pathway plays an important role in the stem cell maintenance, progenitor cell proliferation and cell fate determination and is thereby a key regulator of the intestinal epithelium. It controls several functions in the developing intestine, helps in maintaining the homeostasis and regulates proliferation and differentiation of cells (Bray, 2006; Katoh and Katoh, 2007; Demitrack and Samuelson, 2016).

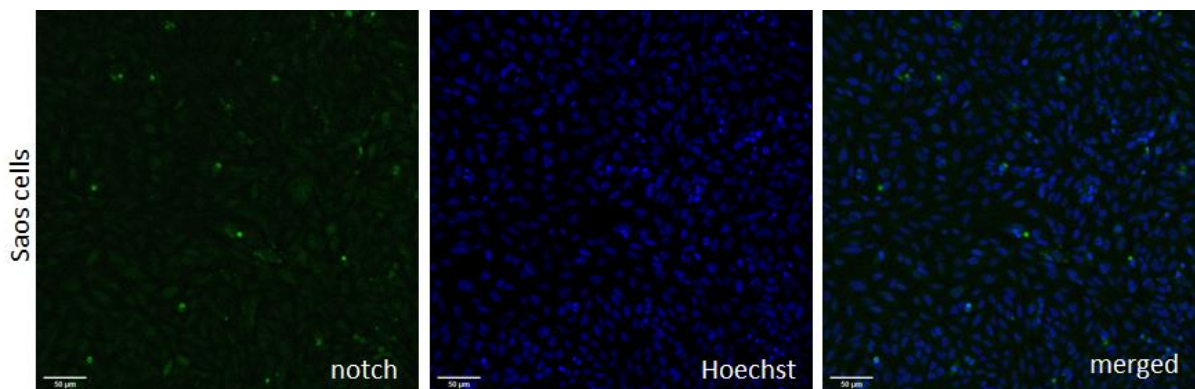


Figure 99: Immunofluorescent stainings with the antibody notch to stain a major component of the Notch-signaling pathway. Shown are SK-Hep-1 cells as positive control for the Notch-pathway with the antibody (green). Nuclei were counterstained with Hoechst (blue). 20x magnification, bar = 50µm.

The cell line Saos (Sarcoma osteogenic) originally comes from a primary osteosarcoma of an 11-year-old caucasian girl (Fogh, Fogh and Orfeo, 1977) and is an adherent, epithelial cell line which grows as a monolayer (Rhode, 2018). The Saos 2 cell line was used as positive control for the staining of notch, because it express notch 1 (Bio-technie, 2021). The staining of notch in the Saos cell lines showed a localization in the nuclei (Figure 99).

In the notch pathway a cleavage of notch results after ligand binding to the notch receptor which results in a notch intracellular domain (NICD). NICD can then be transported into the nucleus and this leads to transcriptional regulation (Kopan, 2012). To stain only the NICD a cleaved-notch antibody was used. Both staining of NICD / cleaved notch in the nuclei of the cells in the OoC and 3D organoid model showed that the notch signaling pathway could be mapped with these systems and is active.

---

### 3.12.1. Impact of drugs targeting intestinal major pathways

In conclusion, these findings show that not each of the systems can map the main important intestinal pathways involved in cell proliferation, regeneration, stem cell maintenance, maintenance of intestinal homeostasis, cell growth or organ size. For testing toxic effects of new drug candidates, the Wnt-pathway do not have any impact on the effect of the drug or on its toxicity. The Wnt signaling pathway is mainly responsible for the embryo growth and tissue repair, which means it has no strong activity in an adult human (Liu, Takada and Zhu, 2020). Compared to this, is the notch pathway involved in drug-resistance of tumor cells (Wang *et al.*, 2010; Allen and Maillard, 2021). This shows its great application possibility in the treatment of tumors in cancer diseases. For this research area this needs as good as possible *in vitro* models for detecting the effect and toxicity of new cancer drug candidates. The Caco-2 OoC model and the colon organoid 3D model have expressed notch, the key mediator of the notch pathway.

The Hippo pathway was detected by expressed YAP in the Caco-2 OoC model and in the colon organoid 3D model. The Hippo pathway is similar like the notch pathway involved in tumor cells and their resistance against anti-cancer treatments (Zeng and Dong, 2021). Both models lead to the suggestion that they can be used to detect possible drug targets in the notch pathway and to evaluate their effect and toxicity.

### 3.13. Assessment of iPSC derived colon organoids into the OrganoPlate®

To obtain an even more complex and *in vivo* like cell culture model, an experiment was made to incorporate the colon organoids into the organ on a chip platform of Mimetas. The organoids include a 3D structure and all available cell types of the colon which is much more *in vivo* like than a standardized cell line like the Caco-2 cells. The main benefit of this approach would be to generate a more *in vivo* like model for the application of drugs to the intestinal lumen, like it is in the *in vivo* intestine. The disadvantage of the 3D organoids is that the actual drug uptake cannot be perfectly mimicked. *In vivo*, the drug uptake is via the inner epithelial cell layer, which, however, is located inside the organoids. With the tube formation of organoid cells however, this limitation can be circumvented.

For cell seeding the organoids were dissociated to single cells. Thereby it was tried to remove the Matrigel as much as possible in several washing steps to achieve a Matrigel free cell suspension. Different coatings (vitronectin, laminin, collagen I, geltrex and Matrigel®) applied to the top channel were tested. Specific concentrations of the coating solutions, seeding densities and attachment times for the implementation of organoids are found in Table 10.

---

Figure 100 shows vitronectin (2.5  $\mu\text{g}$ ) coating into the top channel of the OoC system with subsequent seeding of the single cells into the chips. In all four experiments it can be seen that after 4h of attachment (plate stands upright on the plate stand for this time, as shown in Figure 26c) the cells were still floating in the channel. After 4h the plates were transferred onto the rocker. Some of the cells remained in the channel and started to spread out and attach. The plate was left on the rocker for further 48h, and it was visible that some cells flowed back to the inlet and a lower cell count was observed in the channel after 48h and 72h (Appendix 15 Figure 115).

Figure 101 shows sample images for the establishment of the organoids in the OoC system. The top channels were coated with Laminin 1.5  $\mu\text{g}/\text{ml}$ . It is shown that the seeding seemed successfully. In the experiment with the 40,000 & 50,000 cells, the cells slip into the channel and after 4h appeared to have attached. However, 24h after the transfer to the rocker, the majority of cells flowed out of the channel again. In the picture with 50,000 seeded cells/dissociated organoids it is clear that the cells were not completely dissociated (Figure 101a). There was one complex bubble in the channel and the rest of the cells flowed back to the inlet and outlet. In all other experiments the cells either did not flow in the channel (with 20,000 cells) or flowed back to the in-and outlets after putting the plate on the rocker (Figure 101b-d).

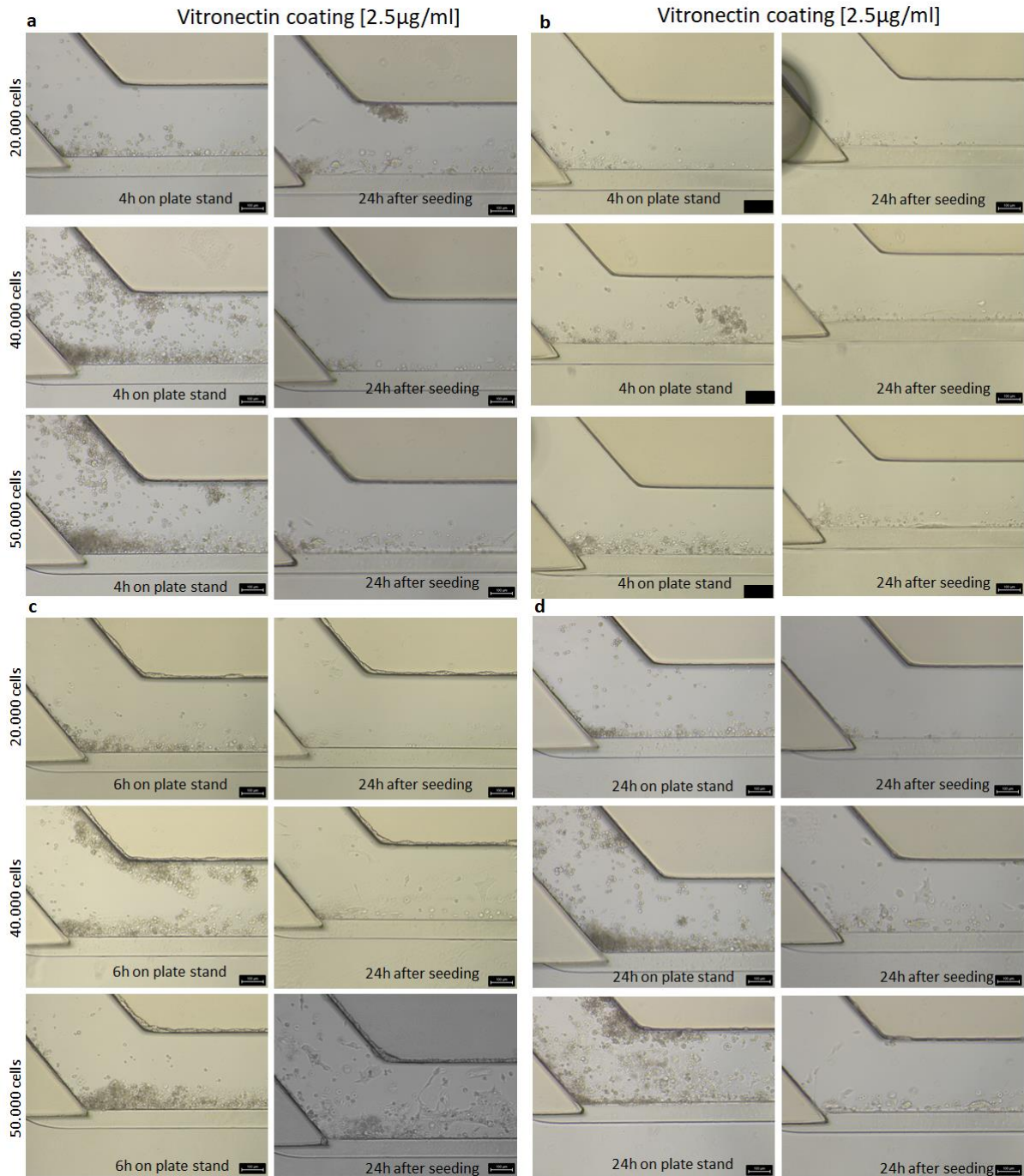


Figure 100: Overview of the implementation of organoids into the OoC system after coating the top channel with vitronectin. a.+b) Shows pictures of the first experiment of the different seeding densities (20,000; 40,000 and 50,000 cells) and after 4h on the plate stand and then transferring the plate on the rocker and taking pictures after 24h C.) shows the pictures for the third attempt in which the cells remained on the plate holder for 6h and were then transferred to the rocker and d.) for the fourth approach in which the cells remained on the plate stand for 24h before transferring them to the rocker. 10x magnification and scale bar 100µm.



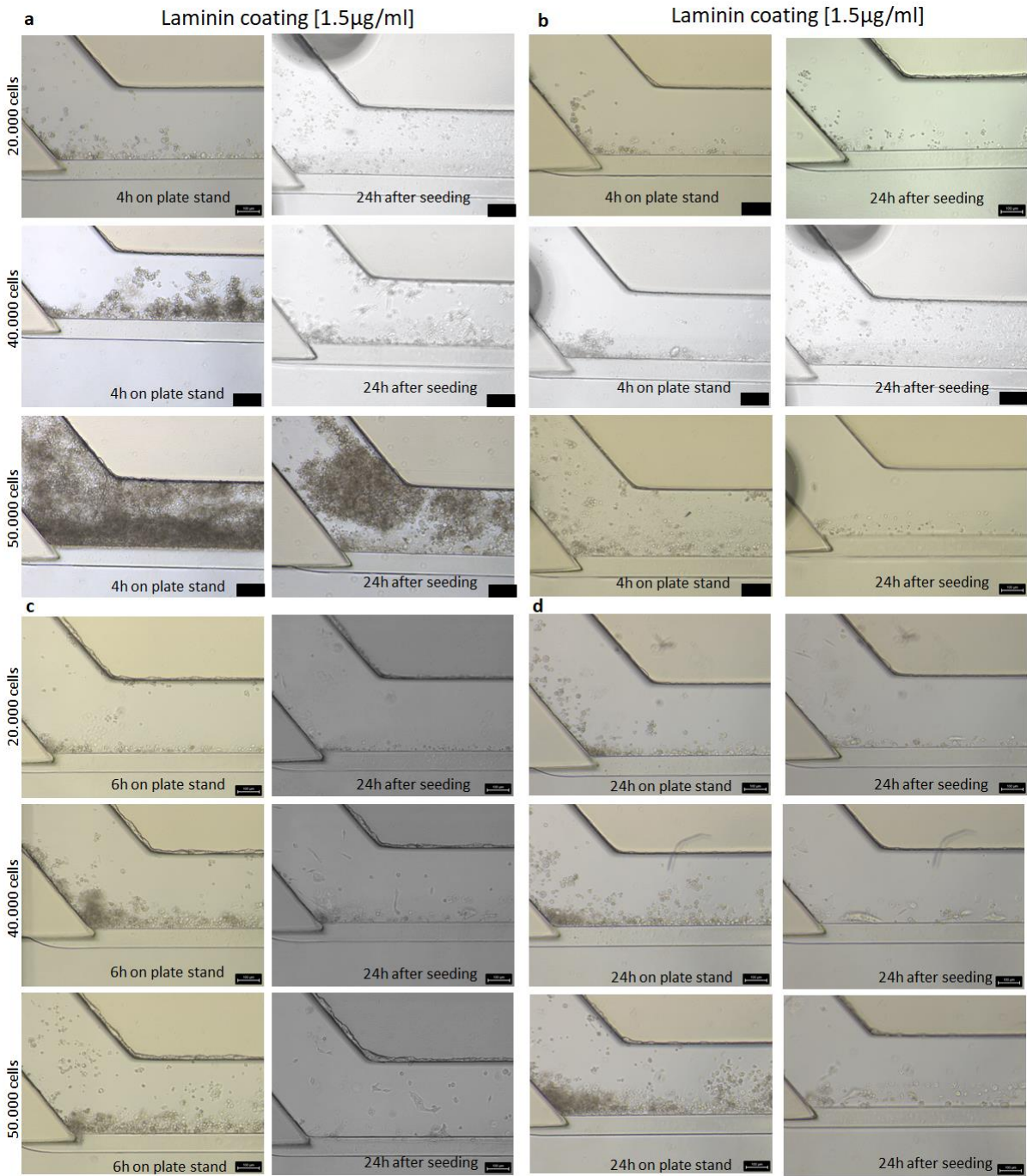


Figure 101: Overview of the implementation of organoids into the OoC system after coating the top channel with Laminin. a. +b) Shows pictures of the first experiment of the different seeding densities (20,000; 40,000 and 50,000 cells) and after 4h on the plate stand and then transferring the plate on the rocker and taking pictures after 24h C.) shows the pictures for the third attempt in which the cells remained on the plate holder for 6h and were then transferred to the rocker and d.) for the fourth approach in which the cells remained on the plate stand for 24h before transferring them to the rocker. 10x magnification and scale bar 100µm.

---

Figure 102 shows pictures of the seeding of dissociated organoids into the OrganoPlate® after coating the top channel with 50 µg/ml Matrigel®. It is shown that after 4h on the plate stand the cell attachment was not successful. After transferring the OrganoPlate® to the rocker the cells flowed back to the in-and outlet. After storing the plate for 6h on its side, on the plate holder, the attachment appeared more successful than after 4h. However, the images showed that the cells again exited the top channel after being transferred to the rocker and flowed back into the in-and outlets. In the first experiment it was visible that in the approach with 40,000 cells a clump of cells flowed into the channel after transferring the plate on the rocker. This is a Matrigel®-cell clump and clarifies that the Matrigel® could not be completely removed in the cell suspension. But in each experiment, it was visible that the cell density in this approach with Matrigel® coating plays no role. It doesn't matter how many cells were seeded, in each experiment the cells could not successfully attach against the middle channel's collagen layer.

Figure 103 shows images of the attempt to seed the dissociated organoids into the 25 µg/ml collagen I coated top channel of the OrganoPlate®. Only one 4h and one 24h attachment experiment was performed with collagen coating due to COVID 19 supply issues. It was clear that in both approaches it was not possible to bring the cells in the channels and seed the single cell organoids into the channel. Figure 103c & d show that the cells remained in the top inlet of the channel.

Figure 104 shows the images of trying to coat the top channel with 100 µg/ml geltrex. Due to the COVID 19 delivery problems for laboratory material, unfortunately only 1 attempt could be made for the 4h and one for the 24h attachment. It was clear to see that the cells flowed into the channel, and it looked like that the cells attached successfully against the collagen layer, but after transferring the plate to the rocker the cells flowed back to the in-and outlets of the top channel (Figure 104c&d).

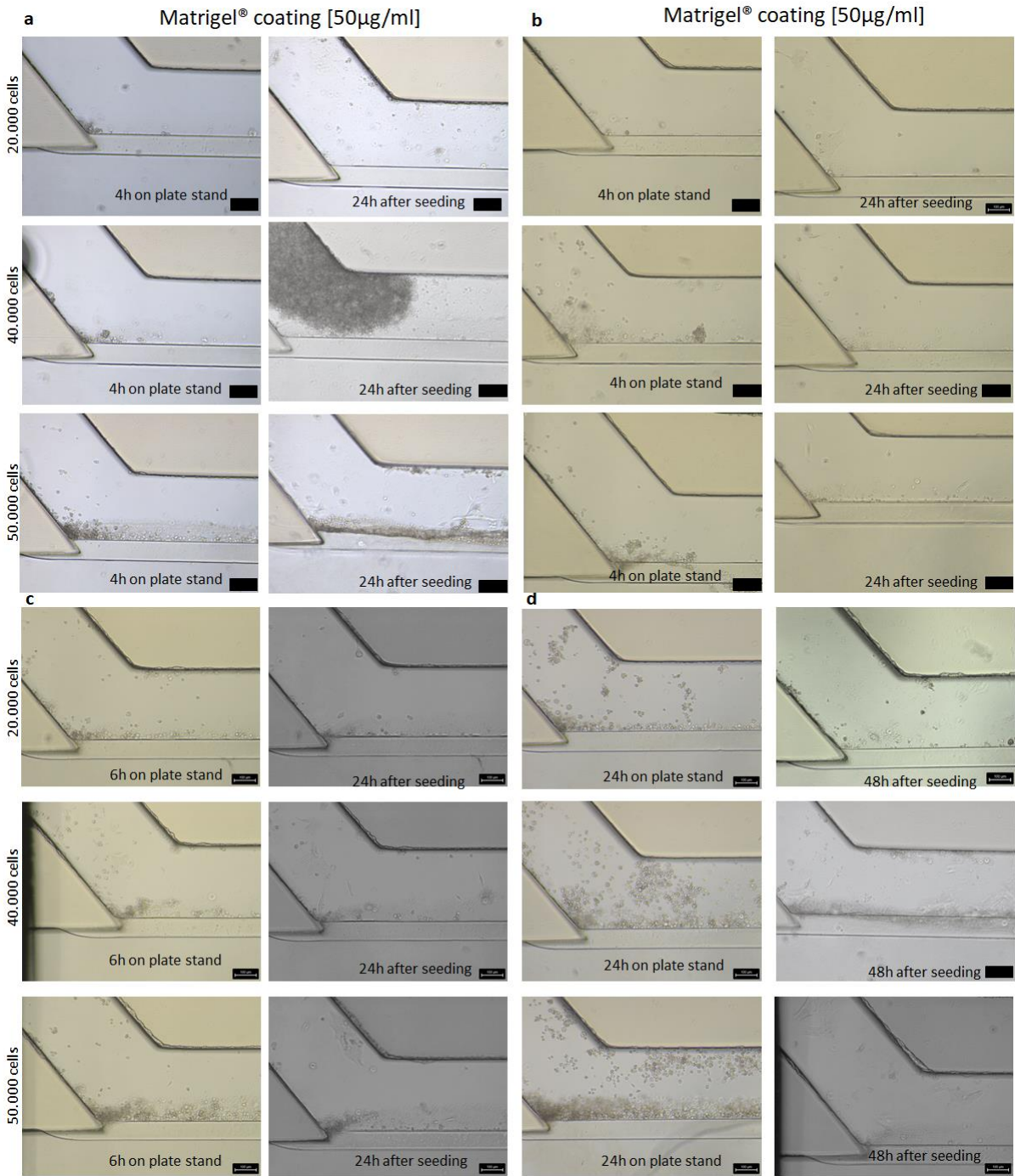


Figure 102: Overview of the implementation of organoids into the OrganoPlate® after coating the top channel with Matrigel®. a.-b) Shows pictures of the first experiment of the different seeding densities (20,000; 40,000 and 50,000 cells) and after 4h on the plate stand and then transferring the plate on the rocker and taking pictures after 24h C.) shows the pictures for the third attempt in which the cells remained on the plate holder for 6h and were then transferred to the rocker and d.) for the fourth approach in which the cells remained on the plate stand for 24h before transferring them to the rocker. 10x

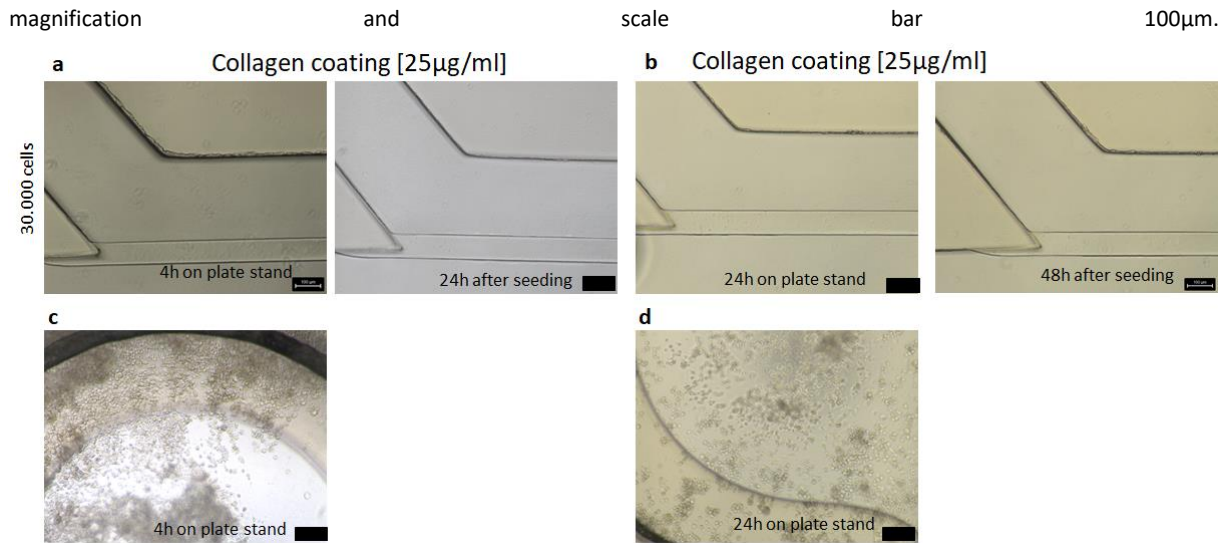


Figure 103: Overview of the implementation of organoids into the OrganoPlate® after coating the top channel with collagen. a.) Shows pictures of the first experiment of collagen coated top channels of the OrganoPlate® and seeding organoids (30.000cells). The cells were left on the plate stand for 4h and then transferred on the rocker. B.) Shows pictures for the attachment time of 14h on the plate stand and then 48h later the rocker. 10x magnification and scale bar 100µm.c.+d.) Shows a picture after 4h on the plate stand and after 24h on the plate stand (d). The pictures show the inlets of the top channel. 4x magnification and scale bar 250µm.

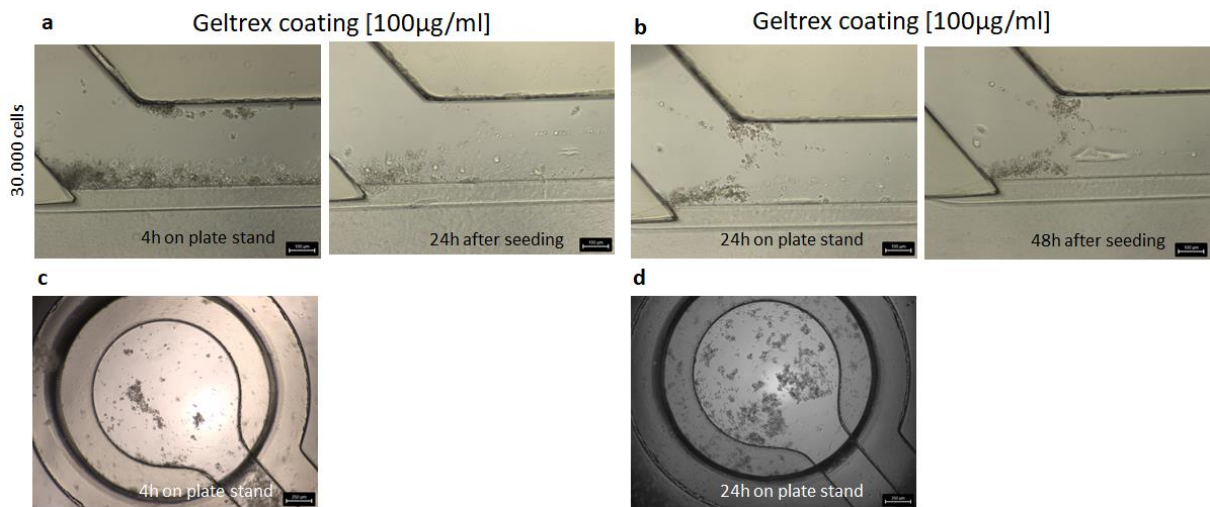


Figure 104: Overview of the implementation of organoids into the OrganoPlate® after coating the top channel with geltrex. a.) Shows pictures of the first experiment of collagen coated top channels of the OrganoPlate® and seeding organoids (30.000cells). The cells were left on the plate stand for 4h and then transferred on the rocker. B.) Shows pictures for the attachment time of 14h on the plate stand and then 48h later the rocker. 10x magnification and scale bar 100µm.c.+d.) Shows a picture after 4h on the plate stand and after 24h on the plate stand (d). The pictures show the inlets of the top channel. 4x magnification and scale bar 250µm.

In summary, it could be seen that in some experiments the dissociation process of the organoids needs some improvement. In the channel still some rounded 3D structured organoids were visible (Figure 101a). After each experiment, the dissociation process and the washing step were refined to obtain single cells without Matrigel®.

None of the tested coating solutions and concentrations (Table 36) could lead to a successful attachment of the cells and the formation of a tube in the top channel of the OrganoPlate®.

Table 36: Tested coating solutions and concentrations for the assessment of seeding single cell

Attempt #	Coating middle channel	Coating top channel	Seeding density / chip	Attachment time
1	Collagen [4mg/ml]	Vitronectin [1.5µg/ml]	20.000, 40.000, 50.000	4h, 6h, 24h
2	Collagen [4mg/ml]	Laminin [1.5µg/ml]	20.000, 40.000, 50.000	4h, 6h, 24h
3	Collagen [4mg/ml]	Matrigel® [50µg/ml]	20.000, 40.000, 50.000	4h, 6h, 24h
4	Collagen [4mg/ml]	Collagen [25µg/ml]	30.000	4h, 24h
5	Collagen [4mg/ml]	Geltrex [100µg/ml]	30.000	4h, 24h

A bit similar experiment, but not with iPSC derived colon organoids, with iPSC cells was performed by Naumovska et al. They seeded iPSC cells in the coated top channel of the OrganoPlate® and could then start to cultivate them to tubes. The cells successfully attached to the channel and then the researcher started to differentiate these cells to intestinal-like cells (Naumovska *et al.*, 2020).



---

## 4. Conclusion

---

Since most drugs are taken orally and absorbed through the GI tract, this organ plays an important role in drug uptake, transport, and metabolism. Orally taken drugs can lead to moderate to severe side effects in the GI tract (Zentler-Munro and Northfield, 1979; Makins and Ballinger, 2003b). For example, when taking chemotherapeutic agents, a major problem is still the frequent side effects, which reduce the patient's quality of life. Between 2013 and 2015 of all 174 clinical trials 76% of all drug candidates failed due to efficacy or safety issues. The increasing trend of cancer diagnoses or central nervous system (CNS) disease leads to an increased research focus in these areas which results in the higher proportion of failed drug developments for oncology and CNS (Harrison, 2016).

Beside this, the actual inefficiency of current cell culture models for predicting toxic effects of new drugs is one of the main reasons why so many side effects in human are being observed. To predict the toxic effects of new drug candidates these preclinical safety models need further improvement, including the development of novel more advanced cell systems.

In case of the GI tract, the intestinal epithelium is with around 4-5 days the fastest self-renewing tissue in the human body. It is a very complex and multicellular 3D structure with an multiparametric and dynamic microenvironment. This complexity makes it difficult to recreate it in an *in vitro* system (Van Der Flier and Clevers, 2009; Creff, Malaquin and Besson, 2021).

In this thesis, different cell culture models (Caco-2 2D, Caco-2 OoC and organoids 3D) and their applicability in the drug development process were investigated. For this purpose, the different cell culture models were first established and characterized. The 3D organoid system reflects the best the *in vivo* situation of the intestinal colon barrier and the intestinal colon tissue. The presence of the 5 major cell types of the intestine (enteroendocrine cells, stem cells, enterocytes, Paneth cells and goblet cells) was confirmed by immunohistochemical and immunofluorescent staining in the organoids.

One of the aims of this thesis was to characterize the cell models by immunofluorescent stainings, histochemical stainings and gene and protein expression. A further goal was to determine the functionality of the intestinal barrier by measuring the TEER. The staining with the antibodies claudin 7 and ZO-1, to evaluate the presence of the important proteins for building a tight barrier with tight junctions, were confirmed in all the used culture models. The formation of adherens junctions was additionally proven in all three used cell culture models by using the antibody e-cadherin.

---

The presence of intestine specific DMEs (CYP2D6, CYP2C9, NAT, SULT1E1) could be shown with immunofluorescence stainings specifically for the 3D organoid model. This was to be expected, since these enzymes are also expressed in the human intestine-. The most CYP enzymes are present in the small intestine and in smaller amounts in colon. Only CYP2D6 could be detected in the Caco-2 OoC model. In the small intestinal mucosa the major present enzymes are belonging to the CYP3A and CYP2C families (Xie, Ding and Zhang, 2016) and play important roles in the metabolism of drugs and chemicals (Kato *et al.*, 2003). Especially the expression of CYP2D6 and CYP2C9 could be shown in the 3D organoid model which better mimic the *in vivo* situation of the human intestine than the two models with Caco-2 cells. With respect to intestine-specific transporters, only MRP2 could be detected with immunofluorescence staining, but in all 3 models. The other two transporters BCRP and MDR1 could not be detected by stainings.

By treating the cells for 24 hours with various test compounds, the applicability of the models was tested to determine the extent to which they can reproduce the toxic properties of drugs. It was shown that the 3D organoid model showed the best predictivity. On the one hand, this is not surprising, since the 3D organoid model most closely represents the *in vivo* situation of the intestine (colon). On the other hand, the large intestine is not the area of drug absorption.

Nevertheless, does the 3D model showed the best possibility to represent the cytotoxic effect of chemotherapeutics. For compounds that showed cytotoxic effects in each model (loperamide, terfenadine), the 3D organoid model responded most sensitively. The IC<sub>50</sub> value was much lower than in the Caco-2 2D and OoC models suggesting that these models are less suitable than the organoid 3D model for testing the toxic effect of drugs on the cell viability.

Evaluation of tight and adherent junction formation and verification of the associated intestinal barrier is one of the most important tools in screening potential toxic effects of new drugs. A damage of the intestinal barrier function has consequences which can lead to chronic disorders, inflammation or malnutrition (Ponce de León-Rodríguez, Guyot and Laurent-Babot, 2019). A damaged intestinal barrier can impair or increase the effect of drugs. Since, for example, the protective mucus layer is no longer present drugs can be absorbed unhindered and thus enter the bloodstream. The comparison of the TEER and BI assay showed that both performed similarly, but for some compounds the TEER measurement was more sensitive. Additionally, is the TEER method the more suitable method due to the faster measurement, the simpler and less error-prone evaluation and the more sensitive data generation.

---

Identifying potential new biomarkers for early detection of drug-induced damage in the gut remains challenging. The use of transcriptomic, genomics and proteomics datasets are nowadays well established technologies and are becoming increasingly important in identifying biomarkers for evaluating toxic effects from drugs (Synnergren and Dönnnes, 2018). A specific genomics methodology, a QuantiGene Plex assay, was used in this thesis for the identification of potential new biomarkers of drug-induced GI toxicity. Overall, the 3D organoid model seems to be the most promising model. After treatment with different drugs, especially chemotherapeutics, it showed an increased expression of *LCN-2*, *CRP* and *HDC*. However, no statistically significant differences were calculated. In comparison in the Caco-2 models both *LCN-2* and *MLCK* were significantly increased after treatment. This leads to the assumption to use these markers as biomarker for the prediction of drug-induced GI toxicity. However, this needs confirmation. The mechanisms of drug induced GI toxicity are still poorly understood, and manifests as different facets in human. That's why it is more than important to study the pathomechanism which can help to understand the development of disease, drug-induced GI toxicity and to identify reliable biomarkers. This suggests that the simpler 2D and OoC model with Caco-2 cells are better in terms of studying drug-induced GI toxicity than the 3D organoid model. The results of this work support the already discussed potential of *LCN-2* as biomarker for the detection of drug-induced GI inflammations (Chassaing *et al.*, 2012; Abella *et al.*, 2015; Wells *et al.*, 2017; Celi *et al.*, 2019) and the potential of *MLCK* as biomarker for drug-induced barrier damage (Wells *et al.*, 2017)

To determine whether the cell culture models used are also capable of detecting plasma or fecal biomarkers applied *in vivo*, measurements of citrulline and calprotectin levels were performed after treatment with Gefitinib, Loperamide, 5-FU, Flavopiridol, Irinotecan, Oxaliplatin, Terfenadine and Diclofenac. These compounds showed cytotoxic effects after treatment. The measurement of citrulline showed that the concentrations decreased after treatment with chemotherapeutic compounds in the Caco-2 2D and OoC model. Both models are based on enterocyte-like cells. *In vivo* enterocytes release citrulline when they were damaged and this lowers the concentration of citrulline, which can be measured. The fact that mainly enterocytes of the small intestine release citrulline after damage (Crenn, Messing and Cynober, 2008) supports the results that the colon organoids did not show a decrease in citrulline concentration. In summary, the organoid 3D model is the least suitable of the three cell culture models tested for the measurement of citrulline and the application of it as biomarker.



---

The measurement of calprotectin in the used cell culture models showed that this *in vivo* used fecal biomarker is not suitable as a predictive *in vitro* biomarker. In all of the three models the concentrations increased slightly after treatment with test compounds, but in none of the models was a significant difference detected in the calprotectin concentration compared to the control.

YAP, notch and  $\beta$ -catenin stainings was used to understand how these gut pathways (Hippo, notch and Wnt) are recapitulated in the cell culture models. It could be shown that the main key part in the Wnt-pathway,  $\beta$ -catenin, could be observed in all of the three cell culture models as a defined staining of the cell membrane. This shows that the key member of the Wnt-pathway is present in each model but not active. Is  $\beta$ -catenin not transported in the nucleus due to phosphorylation this leads to ubiquitin-mediated proteolysis and stopped transcription of genes (like cyclin D1 or MYC) involved in cell proliferation (Fevr *et al.*, 2007; Komiya and Habas, 2008; Van Der Flier and Clevers, 2009; Mah, Yan and Kuo, 2016).

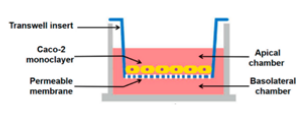
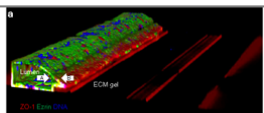

The staining of YAP showed an active Hippo-pathway in the Caco-2 OoC model due to a clear staining within the nucleus and a defined staining in the cytoplasm in the organoid model. This indicates YAP is phosphorylated, leading to the inactivation of the pathway. Is YAP phosphorylated this leads to protein degradation and results in reduced expression of genes involved in cell growth and survival (CTGF, MYC and BIRC5) of the intestinal cells. Inactive pathways can influence in for example long term treatment experiments the overall survival of cells and thereby the results of drug testing on the cell viability. The staining with cleaved-notch showed in the Caco-2 OoC and organoid 3D model a clear staining in the nuclei. This indicates that the notch pathway could be active in these two models. The notch pathway was confirmed by using notch as antibody and a resulting staining in the nucleus in the OoC and 3D organoid model.

The implementation of organoids into the OrganoPlate<sup>®</sup> was unfortunately not successfully. All tested cell densities (20,000; 40,000; and 50,000) and all tested attachment times (4h, 6h, 24h) could not result in the attachment of the cells into the channels. Additionally, all tested coating solutions (vitronectin, laminin, Matrigel, collagen and geltrex) did not lead to successful attachment of the cells and growing against the collagen matrix. The cells always flowed back towards the inlet and outlet of the upper channel after transferring the OrganoPlate<sup>®</sup> to the rocker. One possible reason could be that the coating concentrations needs to be adapted or maybe the shape of the collagen coating, which is like a meniscus, could be problematic for cell attachment of iPSC derived colon organoids. To date no data is published which shows successfully seeding and attachment of iPSC derived colon organoids as single cells in the OrganoPlate<sup>®</sup>.

One of the main problems in drug testing is that often the very complex human body needs to be mapped in a simplified *in vitro* model. Mostly, cell culture models are presented in a very simplified way. In this case, the physiological functions, and properties of the organs actually under consideration are lost. In general, the Caco-2 cells only include one cell type and does not have a mucus and unstirred water layer present which can have an influence on the absorption of drugs (Verhoeckx *et al.*, 2015).

Compared to this a multicellular intestinal organoid model, which includes all important major cell types of the intestine, especially the goblet cells, which better mimic the *in vivo* process of drug absorption through the mucus layer which builds a first barrier against xenobiotics. The main components of the mucus are the mucins (Paone and Cani, 2020) secreted by goblet cells in the colon (Walsh *et al.*, 2013) and one of the main mucins is Muc5B, which was proven by an immunofluorescence staining in the colon organoid 3D model.

The used cell culture models in this thesis have all shown different complexities and different relevance related to the human body and the use in drug discovery (Figure 105). The Caco-2 2D model is the cheapest model but as well the model that takes the longest time to pre-cultivate cells for experiments. The benefit of the Caco-2 OoC model compared to the 2D model is definitely the presence of a flow and the ECM. The ECM can have an effect on cellular functions (Teti, 1992) and the flow can have a positive effect on the drug transport and absorption (Kulthong *et al.*, 2020).

	<b>Caco-2 2D</b>	<b>Caco-2 OoC</b>	<b>Organoid 3D</b>
Model	 (Ding <i>et al.</i> , 2021)	 (Trietsch <i>et al.</i> , 2017)	 (Conder <i>et al.</i> , 2015)
Costs	low	mid	mid
Time consuming	long	short	short
Multicellular	no	no	yes
ECM	no	yes	yes
Flow	no	yes	no
Expression of DMETs	low	moderate	high
Predictivity of compound toxicity	low	low	high
Complexity	low	moderate	high

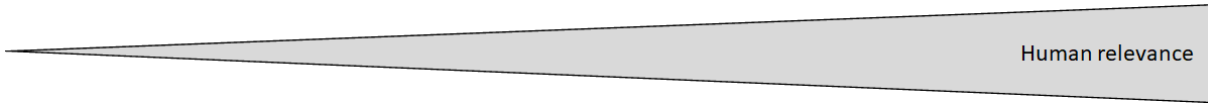


Figure 105: Summary of the used cell culture models and their advantages and limitations.

---

The main benefits of the colon organoid 3D model are the short cultivation time before experiments can be done, the multicellularity, the expression of gut specific markers and gut specific DMET's and the cultivation includes an ECM.

But to further test and map the absorption and metabolization of drug candidates, it would be advisable to use small intestinal organoids. The small intestine is the major site of drug absorption due to the longer transit time of drugs and the larger surface compared to the colon (Austin *et al.*, 2017). Further impact on the absorption of drugs can have the food intake (Welling, 1977) or the pH in the stomach (Mitra and Kesisoglou, 2013), but both could not be mapped with *in vitro* cell culture models. This needs still investigation studies in animals.

The results of this work assume that functional advanced *in vitro* models, especially like the iPSC derived colon organoids, can be a suitable tool to evaluate potential toxic effects of new drug candidates better than the widely used 2D models. They have a more physiologically relevant environment and most system can reflect better the complexity of the human body. Each model per se has its advantages and as well some limitations. But, here in this work in the end the organoid model needs some further improvements to achieve more reliable data. Regarding the drug development process, it could be conceivable that the Caco-2 OoC model could be used as screening tool in the early pre-clinical development to screen drug candidates. For example, by using it for testing the effect in the intestinal barrier by measuring the TEER or by measuring the released citrulline, which indicates enterocyte damage.

Especially for drugs for the treatment of cancer because they often show adverse side effects in the GI tract. The OoC model could be used to screen the effect of drugs on the intestinal barrier by measuring the viability or the TEER. Compared to this, the organoid model seems to be more applicable in the later stages of drug development due to its much stronger similarity to the human organ. It could be a useful tool for more mechanistic approaches due to the high expression of gut specific DMET's and the presence and cooperation of all important cell types of the intestine. But overall, the advanced cell culture models can bridge the gap between simplified and mostly unpredictable 2D *in vitro* models and the animal models (Fitzgerald *et al.*, 2015) and can thereby support the 3R principle (Figure 106).

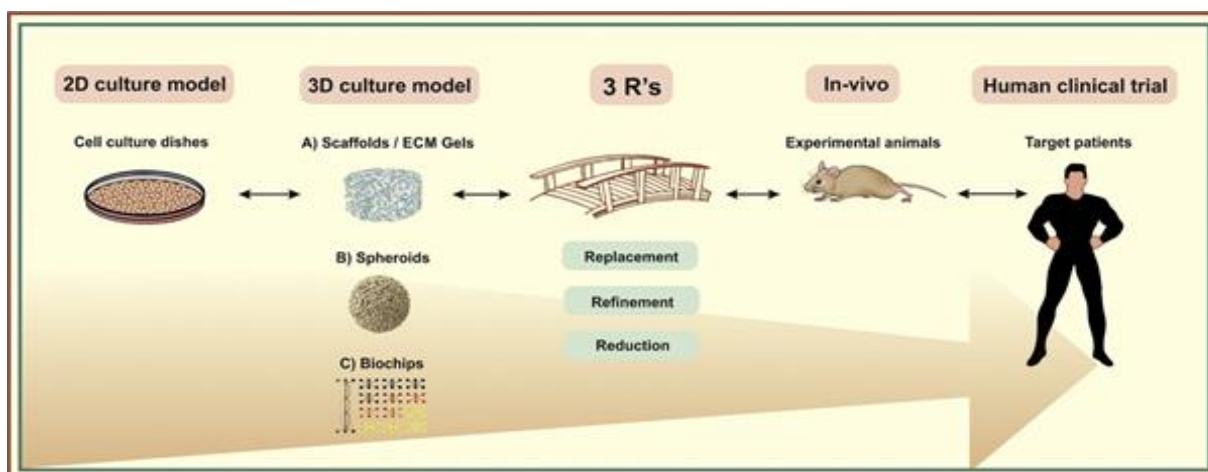


Figure 106: 3D models can bridge the gap between simple 2D models and animal experiments and can thereby help to support the 3R principle (Fitzgerald *et al.*, 2015).

The FDA (US Food and Drug Administration, 2021) and the EMA (Broms-Thie, 2021) have already noticed the promising positive aspects of the OoC systems and established working groups, focusing on alternative and innovative test methods and models by the 3R principles. But to include these novel models in the pipeline for drug testing different criteria needs to be fulfilled: relevance, reliability, validity, and sensitivity. Since 2010 many companies are developing complex microfluidic devices which try to mimic the physiological processes of the human body. At least for the gut eleven different OoC tissue/organ models were established since 2001 and commercially available (Busek *et al.*, 2022). In addition to the advantage of more similarity to the *in vivo* situation of the complex human body, the OoC systems can significantly reduce the costs in the R&D area of the pharmaceutical industries. Researchers have calculated estimated cost reduction of 10-26% in R&D for one drug when using OoC technology (Franzen *et al.*, 2019). Finally, however, much research is still needed to finally apply the new innovative methods of organoid cultivation or OoC systems as routine screening methods for the development of new drugs.

---

## 5. Further perspectives

---

Since still many drugs fail during development, especially in the late clinical phase, a need for better predictive, translatable cell culture models and more reliable and efficient biomarkers which can detect drug-induced GI toxicity is high. The need for advanced cell culture models which recapitulate more the *in vivo* situation of the complex human body gets more and more important. This thesis dealt with two new approaches of advanced cell culture models, compared to a widely used 2D model. Used was an iPSC derived 3D colon organoid system and a OoC system with a widely used colon cancer cell line, the Caco-2 cells.

Advance cell culture models, which include OoC systems and 3D cultures are increasingly being developed and can contribute to a better understanding of the complex body structures and the interactions between the organs. These models often use human tissue as a cell basis and therefore make it easier to bridge to the clinical phases. There is no longer the problem of using animal cell material and then having to consider species-specific differences when transferring to humans. The new models allow to recapitulate better the complex human *in vivo* body compared to the widely used 2D models so far.

Several quantitative GI biomarkers to detect GI toxicity already exist for animal experiments and in clinical development. For cell culture a lack of sensitive, specific, and non-degrading biomarker exists. To evaluate the used potential new biomarker in this thesis additional studies are required. Above all, it would be important to test other potential biomarkers such as DAO, CD64, Gastrin and lactoferrin which could not be delivered in time during this work, due to covid-19 supply issues.

Regarding the implementation of dissociated colon organoids into the OrganoPlate® it needs further improvements. Ideas would be to change the concentrations of the coating solutions, further improve the Matrigel® removal and the dissociation step or to test more coating solutions. After discussion with another researcher (Inga Hensel, BioMed X GmbH) about the problems of implementing iPSC derived colon organoids into the OrganoPlate® it seemed to be a general problem with the attachment of iPSC-based cell models into the OrganoPlate® from Mimetas. Inga is working with iPSC-derived organoids from animals and could as well not implement the cells in the OrganoPlate® (data unpublished). An additional step which could improve the attachment of cells could be to add a fluorescent activated cell sorting (FACS) step to select the cell population based on the epithelial adhesion molecule (EpCAM). Workman et al., could show when performing FACS prior to seeding of iPSC cells into a chip this improves the success for cell attachment and viable culturing (Workman *et al.*, 2018).

---

Another idea would be to seed iPSC cells into the chip and differentiate these cells directly in the chip system to intestinal-like cells. Such a work was done by Naumovska et al. by successfully adding iPSC cells in the OrganoPlate®. They directly differentiate these cells to intestinal-like tubules in the top channel of the OrganoPlate® (Naumovska *et al.*, 2020).

Overall, however, it must be kept in mind that the actual main organ for the absorption of nutrients, drugs or xenobiotics is the small intestine. The small intestine includes the main important cells, goblet cells, paneth cells, stem cells, enterocytes and enteroendocrine cells. But compared to the large intestine the mucosae of the small intestine is covered with villi's which include epithelial cells with microvilli, which maximize the surface and enables the absorption (Mühlemann, 2018). Especially for drug absorption and drug metabolism the small intestine plays an important role.

Therefore, the generation of small intestinal organoids could be one of the next steps and then to compare those with the colon organoids from this thesis.

---

## 6. References

---

- Abella, V. *et al.* (2015) 'The potential of lipocalin-2/NGAL as biomarker for inflammatory and metabolic diseases', *Biomarkers*, 20(8), pp. 565–571. doi: 10.3109/1354750X.2015.1123354.
- Affymetrix (2014) 'User Manual QuantiGene Plex Assay', *Technical Bulletin*, pp. 1–24.
- Ahn, J. *et al.* (2021) 'Impedance measurement system for assessing the barrier integrity of three-dimensional human intestinal organoids', *Analytical Chemistry*. doi: 10.1021/acs.analchem.1c00655.
- Akbari, A., Lavasanifar, A. and Wu, J. (2017) 'Interaction of cruciferin-based nanoparticles with Caco-2 cells and Caco-2/HT29-MTX co-cultures', *Acta Biomaterialia*, 64, pp. 249–258. doi: 10.1016/j.actbio.2017.10.017.
- Albala, C. *et al.* (2004) 'Intestinal FABP2 A54T polymorphism: Association with insulin resistance and obesity in women', *Obesity Research*, 12(2), pp. 340–345. doi: 10.1038/oby.2004.42.
- Alimonti, A. *et al.* (2004) 'New approaches to prevent intestinal toxicity of irinotecan-based regimens', *Cancer Treatment Reviews*, 30(6), pp. 555–562. doi: 10.1016/j.ctrv.2004.05.002.
- Allen, F. and Maillard, I. (2021) 'Therapeutic Targeting of Notch Signaling: From Cancer to Inflammatory Disorders', *Frontiers in Cell and Developmental Biology*, 9, p. 1262. doi: 10.3389/fcell.2021.649205/BIBTEX.
- Amjad, M. T., Chidharla, A. and Kasi, A. (2021) 'Cancer Chemotherapy', *Fundamentals of Pharmaceutical Nanoscience*, pp. 401–427. Available at: <https://www.ncbi.nlm.nih.gov/books/NBK564367/> (Accessed: 2 November 2021).
- Analysis, A. and Manual, U. (2012) 'User Manual User Manual', *Data Base*, 3304(January), pp. 1–148.
- Anderson, J. M. *et al.* (1989) 'ZO-1 mRNA and protein expression during tight junction assembly in Caco-2 cells', *Journal of Cell Biology*, 109(3), pp. 1047–1056. doi: 10.1083/jcb.109.3.1047.
- Angst, B. D., Marcozzi, C. and Magee, A. I. (2001) 'The cadherin superfamily: Diversity in form and function', *Journal of Cell Science*, 114(4), pp. 629–641. doi: 10.1242/jcs.114.4.629.
- Apostolou, A. *et al.* (2021) 'A Novel Microphysiological Colon Platform to Decipher Mechanisms Driving Human Intestinal Permeability', *Cmgh*, 12(5), pp. 1719–1741. doi: 10.1016/j.jcmgh.2021.07.004.
- Artavanis-Tsakonas, S., Rand, M. D. and Lake, R. J. (1999) 'Notch signaling: Cell fate control and signal integration in development', *Science*, 284(5415), pp. 770–776. doi: 10.1126/science.284.5415.770.
- Assimakopoulos, S. F. (2011) 'Enterocytes' tight junctions: From molecules to diseases', *World Journal of Gastrointestinal Pathophysiology*, 2(6), p. 123. doi: 10.4291/wjgp.v2.i6.123.
- Attarwala, H. (2010) 'TGN1412: From discovery to disaster', *Journal of Young Pharmacists*, 2(3), pp. 332–336. doi: 10.4103/0975-1483.66810.
- Atuma, C. *et al.* (2001) 'The adherent gastrointestinal mucus gel layer: Thickness and physical state in vivo', *American Journal of Physiology - Gastrointestinal and Liver Physiology*, 280(5 43-5), pp. 922–929. doi: 10.1152/ajpgi.2001.280.5.g922.

---

Aula, S. *et al.* (2015) 'Biophysical, biopharmaceutical and toxicological significance of biomedical nanoparticles', *RSC Advances*, 5(59), pp. 47830–47859. doi: 10.1039/c5ra05889a.

Austin, D. *et al.* (2017) *Drug absorption in the small intestine | Deranged Physiology, College of Intensive Care Medicine(CICM)*. Available at: <https://derangedphysiology.com/main/cicm-primary-exam/required-reading/pharmacokinetics/Chapter 1.3.4/drug-absorption-small-intestine> (Accessed: 17 July 2022).

Avila, J. (1992) 'Microtubule functions', *Life Sciences*, 50(5), pp. 327–334. doi: 10.1016/0024-3205(92)90433-P.

Awortwe, C., Fasinu, P. S. and Rosenkranz, B. (2014) 'Application of Caco-2 cell line in herb-drug interaction studies: Current approaches and challenges', *Journal of Pharmacy and Pharmaceutical Sciences*, 17(1). doi: 10.18433/j30k63.

Aydemir, S. *et al.* (2004) 'Eosinophil infiltration, gastric juice and serum eosinophil cationic protein levels in Helicobacter pylori-associated chronic gastritis and gastric ulcer', *Mediators of Inflammation*, 13(5–6), pp. 369–372. doi: 10.1080/09629350400014115.

Ayling, R. M. and Kok, K. (2018) 'Fecal Calprotectin', *Advances in Clinical Chemistry*, 87, pp. 161–190. doi: 10.1016/bs.acc.2018.07.005.

Azzouz, L. L. and Sharma, S. (2018) 'Physiology, Large Intestine', *StatPearls*. Available at: <http://europepmc.org/books/NBK507857> (Accessed: 8 August 2021).

Baigent, C. *et al.* (2013) 'Vascular and upper gastrointestinal effects of non-steroidal anti-inflammatory drugs: Meta-analyses of individual participant data from randomised trials', *The Lancet*, 382(9894), pp. 769–779. doi: 10.1016/S0140-6736(13)60900-9.

Baillie, T. A. (2008) 'Metabolism and toxicity of drugs. Two decades of progress in industrial drug metabolism', *Chemical Research in Toxicology*, 21(1), pp. 129–137. doi: 10.1021/tx7002273.

Balfour, J. A. B., Goa, K. L. and Perry, C. M. (2000) 'Alosetron', 59(3), pp. 511–518.

Banerjee, A. and Gupta, R. C. (2019) 'Gastrointestinal Toxicity Biomarkers', *Biomarkers in Toxicology*, pp. 277–285. doi: 10.1016/b978-0-12-814655-2.00016-5.

Baranczyk-Kuzma, A. *et al.* (1991) 'Substrate specificity and some properties of phenol sulfotransferase from human intestinal Caco-2 cells', *Life Sciences*, 49(16), pp. 1197–1206. doi: 10.1016/0024-3205(91)90568-V.

Barbuzano, J. (2017) *Organoids: A new window into disease, development and discovery | Harvard Stem Cell Institute (HSCI), Harvard Stem Cell Institute*. Available at: <https://hsci.harvard.edu/organoids> (Accessed: 27 July 2021).

Bardenbacher, M. *et al.* (2019) 'Permeability analyses and three dimensional imaging of interferon gamma-induced barrier disintegration in intestinal organoids', *Stem Cell Research*, 35(June 2018), p. 101383. doi: 10.1016/j.scr.2019.101383.

Barisam, M. *et al.* (2018) 'Prediction of necrotic core and hypoxic zone of multicellular spheroids in a microbio-reactor with a U-shaped barrier', *Micromachines*, 9(3), pp. 1–19. doi: 10.3390/mi9030094.

Barker, N. (2014) 'Adult intestinal stem cells: Critical drivers of epithelial homeostasis and regeneration', *Nature Reviews Molecular Cell Biology*, 15(1), pp. 19–33. doi: 10.1038/nrm3721.



- 
- Basuroy, S. *et al.* (2006) 'MAPK interacts with occludin and mediates EGF-induced prevention of tight junction disruption by hydrogen peroxide', *Biochemical Journal*, 393(1), pp. 69–77. doi: 10.1042/BJ20050959.
- Baum, H. (2019) 'Zytokeratin', in: Springer, Berlin, Heidelberg, pp. 2553–2553. doi: 10.1007/978-3-662-48986-4\_3383.
- Bauman, J. L. (2001) 'The role of pharmacokinetics, drug interactions and pharmacogenetics in the acquired long QT syndrome', *European Heart Journal, Supplement*, 3(K), pp. 93–100. doi: 10.1016/S1520-765X(01)90012-4.
- Beaurivage, C. *et al.* (2019) 'Development of a gut-on-a-chip model for high throughput disease modeling and drug discovery', *International Journal of Molecular Sciences*, 20(22). doi: 10.3390/ijms20225661.
- Bedford, A. *et al.* (2015) 'Epidermal growth factor containing culture supernatant enhances intestine development of early-weaned pigs in vivo: Potential mechanisms involved', *Journal of Biotechnology*, 196–197, pp. 9–19. doi: 10.1016/j.jbiotec.2015.01.007.
- Bein, A. *et al.* (2018) 'Microfluidic Organ-on-a-Chip Models of Human Intestine', *Cmgh*, 5(4), pp. 659–668. doi: 10.1016/j.jcmgh.2017.12.010.
- Bel, S. *et al.* (2017) 'Paneth cells secrete lysozyme via secretory autophagy during bacterial infection of the intestine', *Science*, 357(6355), pp. 1047–1052. doi: 10.1126/science.aal4677.
- Bevins, C. L. and Salzman, N. H. (2011) 'Paneth cells, antimicrobial peptides and maintenance of intestinal homeostasis', *Nature Reviews Microbiology*, 9(5), pp. 356–368. doi: 10.1038/nrmicro2546.
- Bhatt, A. P. *et al.* (2018) 'NSAID-Induced Leaky Gut Modeled Using Polarized Monolayers of Primary Human Intestinal Epithelial Cells', *ACS Infectious Diseases*, 4(1), pp. 46–52. doi: 10.1021/acsinfecdis.7b00139.NSAID-Induced.
- Bio-techne (2021) *Human Notch-1 Intracellular Domain Antibody (AF3647) | Bio-Techne*. Available at: [https://www.bio-techne.com/p/antibodies/human-notch-1-intracellular-domain-antibody\\_af3647](https://www.bio-techne.com/p/antibodies/human-notch-1-intracellular-domain-antibody_af3647) (Accessed: 20 October 2021).
- Blagosklonny, M. V. (2004) 'Flavopiridol, an inhibitor of transcription: Implications, problems and solutions', *Cell Cycle*, 3(12), pp. 1537–1542. doi: 10.4161/cc.3.12.1278.
- Boonyong, C., Vardhanabhuti, N. and Jianmongkol, S. (2020) 'Natural polyphenols prevent indomethacin-induced and diclofenac-induced Caco-2 cell death by reducing endoplasmic reticulum stress regardless of their direct reactive oxygen species scavenging capacity', *Journal of Pharmacy and Pharmacology*, 72(4), pp. 583–591. doi: 10.1111/jphp.13227.
- Boopathy, G. T. K. and Hong, W. (2019) 'Role of Hippo Pathway-YAP/TAZ signaling in angiogenesis', *Frontiers in Cell and Developmental Biology*, 7(APR), pp. 1–12. doi: 10.3389/fcell.2019.00049.
- Borggreffe, T. and Oswald, F. (2009) 'The Notch signaling pathway: Transcriptional regulation at Notch target genes', *Cellular and Molecular Life Sciences*, 66(10), pp. 1631–1646. doi: 10.1007/s00018-009-8668-7.
- Boulenc, X. *et al.* (1992) 'Regulation of cytochrome P450IA1 gene expression in a human intestinal cell line, CACO-2', *Journal of Pharmacology and Experimental Therapeutics*, 263(3), pp. 1471–1478.

- 
- Bovard, D. *et al.* (2017) 'Organs-on-a-chip', *Toxicology Research and Application*, 1, p. 239784731772635. doi: 10.1177/2397847317726351.
- Brabletz, T. *et al.* (2001) 'Variable  $\beta$ -catenin expression in colorectal cancers indicates tumor progression driven by the tumor environment', *Proceedings of the National Academy of Sciences of the United States of America*, 98(18), pp. 10356–10361. doi: 10.1073/pnas.171610498.
- Bray, S. J. (2006) 'Notch signalling: A simple pathway becomes complex', *Nature Reviews Molecular Cell Biology*, 7(9), pp. 678–689. doi: 10.1038/nrm2009.
- Breslin, S. and O'Driscoll, L. (2016) 'The relevance of using 3D cell cultures, in addition to 2D monolayer cultures, when evaluating breast cancer drug sensitivity and resistance', *Oncotarget*, 7(29), pp. 45745–45756. doi: 10.18632/oncotarget.9935.
- Brett, M. A. *et al.* (1990) 'Nabumetone: Evidence for the Lack of Enterohepatic Circulation of the Active Metabolite 6-MNA in Humans', *Drugs*, 40(5), pp. 67–70. doi: 10.2165/00003495-199000405-00017.
- Broms-Thie, L. (2021) *EMA implements new measures to minimise animal testing during medicines development*, EMA Press Office. Available at: <https://www.ema.europa.eu/en/news/ema-implements-new-measures-minimise-animal-testing-during-medicines-development> (Accessed: 15 July 2022).
- Buesen, R. *et al.* (2002) 'Interaction between metabolism and transport of benzo[a]pyrene and its metabolites in enterocytes', *Toxicology and Applied Pharmacology*, 183(3), pp. 168–178. doi: 10.1006/taap.2002.9484.
- Bundesinstitut für Risikobewertung (2020) *3R Prinzip - BfR*. Available at: [https://www.bfr.bund.de/de/3r\\_prinzip-193970.html](https://www.bfr.bund.de/de/3r_prinzip-193970.html) (Accessed: 15 October 2021).
- Burri, E. and Beglinger, C. (2014) 'The use of fecal calprotectin as a biomarker in gastrointestinal disease', *Expert Review of Gastroenterology and Hepatology*, 8(2), pp. 197–210. doi: 10.1586/17474124.2014.869476.
- Busek, M. *et al.* (2022) 'Academic User View: Organ-on-a-Chip Technology', *Biosensors*, 12(2). doi: 10.3390/bios12020126.
- Buur, A. *et al.* (1996) 'Permeability of 5-fluorouracil and prodrugs in Caco-2 cell monolayers', *International Journal of Pharmaceutics*, 129(1–2), pp. 223–231. doi: 10.1016/0378-5173(95)04331-4.
- Camilleri, M. *et al.* (1999) 'Improvement in pain and bowel function in female irritable bowel patients with alosetron, a 5-HT<sub>3</sub> receptor antagonist'.
- Camilleri, M. (2000) 'Pharmacology and clinical experience with alosetron', *Expert Opinion on Investigational Drugs*, 9(1), pp. 147–159. doi: 10.1517/13543784.9.1.147.
- Camilleri, M. *et al.* (2001) 'A randomized controlled clinical trial of the serotonin type 3 receptor antagonist alosetron in women with diarrhea-predominant irritable bowel syndrome', *Archives of Internal Medicine*, 161(14), pp. 1733–1740. doi: 10.1001/archinte.161.14.1733.
- Campbell, F. and Herrington, C. S. (2001) 'Application of cytokeratin 7 and 20 immunohistochemistry to diagnostic pathology', *Current Diagnostic Pathology*, 7(2), pp. 113–122. doi: 10.1054/cdip.2001.0063.
- Carr, D. F. *et al.* (2017) 'Towards better models and mechanistic biomarkers for drug-induced gastrointestinal injury', *Pharmacology and Therapeutics*, 172(December 2016), pp. 181–194. doi:

---

10.1016/j.pharmthera.2017.01.002.

Carr, D. F. and Pirmohamed, M. (2018) 'Biomarkers of adverse drug reactions', *Experimental Biology and Medicine*, 243(3), pp. 291–299. doi: 10.1177/1535370217733425.

Carulli, A. J., Samuelson, L. C. and Schnell, S. (2014) 'Unraveling intestinal stem cell behavior with models of crypt dynamics', *Integrative Biology*, 6(3), pp. 243–257. doi: 10.1039/c3ib40163d.Unraveling.

Cassidy, J. and Misset, J.-L. (2002) 'Oxaliplatin-related side effects: Characteristics and management', *Seminars in Oncology*, 29(5 Suppl 15), pp. 11–20. doi: 10.1053/sonc.2002.35524.

Celi, P. *et al.* (2019) 'Biomarkers of gastrointestinal functionality in animal nutrition and health', *Animal Feed Science and Technology*, 250(July), pp. 9–31. doi: 10.1016/j.anifeedsci.2018.07.012.

*Cell types Enterocytes* (2021) *Atlas of plant and animal histology*. Available at: <http://mmegias.webs.uvigo.es/02-english/8-tipos-celulares/enterocito.php> (Accessed: 26 February 2022).

Chang, C. T. *et al.* (2012) '5-fluorouracil induced intestinal mucositis via nuclear factor- $\kappa$ B activation by transcriptomic analysis and in vivo bioluminescence imaging', *PLoS ONE*, 7(3), p. e31808. doi: 10.1371/journal.pone.0031808.

Chantret, I. *et al.* (1988) 'Epithelial Polarity, Villin Expression, and Enterocytic Differentiation of Cultured Human Colon Carcinoma Cells: A Survey of Twenty Cell Lines', *Cancer Research*, 48(7), pp. 1936–1942.

Chassaing, B. *et al.* (2012) 'Fecal Lipocalin 2, a Sensitive and Broadly Dynamic Non-Invasive Biomarker for Intestinal Inflammation', *PLoS ONE*, 7(9), pp. 3–10. doi: 10.1371/journal.pone.0044328.

Chelakkot, C., Ghim, J. and Ryu, S. H. (2018) 'Mechanisms regulating intestinal barrier integrity and its pathological implications', *Experimental and Molecular Medicine*, 50(8). doi: 10.1038/s12276-018-0126-x.

Chen, G. *et al.* (2021) 'EpCAM is essential for maintenance of the small intestinal epithelium architecture via regulation of the expression and localization of proteins that compose adherens junctions', *International Journal of Molecular Medicine*, 47(2), pp. 621–632. doi: 10.3892/ijmm.2020.4815.

Choong, E. *et al.* (2015) 'Developmental regulation and induction of cytochrome P450 2W1, an enzyme expressed in colon tumors', *PLoS ONE*, 10(4), pp. 1–17. doi: 10.1371/journal.pone.0122820.

Christiansen, S. (2020) *Small Intestine: Anatomy, Function, and Treatment*. Available at: <https://www.verywellhealth.com/small-intestine-anatomy-4788350> (Accessed: 5 August 2021).

Christmas, P. *et al.* (2001) 'Alternative Splicing Determines the Function of CYP4F3 by Switching Substrate Specificity', *Journal of Biological Chemistry*, 276(41), pp. 38166–38172. doi: 10.1074/jbc.m104818200.

Cikot, M. *et al.* (2016) 'Plasma calprotectin level: Usage in distinction of uncomplicated from complicated acute appendicitis', *World Journal of Emergency Surgery*, 11(1), pp. 7–12. doi: 10.1186/s13017-016-0062-9.

Cimini, A. *et al.* (2017) 'Flavopiridol: An Old Drug With New Perspectives? Implication for

---

Development of New Drugs', *Journal of Cellular Physiology*, 232(2), pp. 312–322. doi: 10.1002/jcp.25421.

Cohen, M. M. (1988) 'Mechanism of Injury to Gastric Mucosa by Non-Steroidal Anti-Inflammatory Drugs and the Protective Role of Prostaglandins', in *Prostaglandins and Leukotrienes in Gastrointestinal Diseases*. Springer, Berlin, Heidelberg, pp. 148–151. doi: 10.1007/978-3-642-73316-1\_31.

Coles, B. F. *et al.* (2002) 'Interindividual variation and organ-specific patterns of glutathione S-transferase alpha, mu, and pi expression in gastrointestinal tract mucosa of normal individuals', *Archives of Biochemistry and Biophysics*, 403(2), pp. 270–276. doi: 10.1016/S0003-9861(02)00226-6.

Collins, J., Nguyen, A. and Badireddy, M. (2017) 'Anatomy, Abdomen and Pelvis, Small Intestine', *StatPearls*. Available at: <http://europepmc.org/books/NBK459366> (Accessed: 21 July 2021).

Corr, S.C.; Gahan, C. C.G. M. and Hill, C. (2008) 'M-cells: origin, morphology and role mucosal immunity and microbial pathogenesis' *FEMS Immunology & Medical Microbiology*, 52(1), pp.2-12. doi.org/10.1111/j.1574-695X.2007.00359.x

Coskun, M., Troelsen, J. T. and Nielsen, O. H. (2011) 'The role of CDX2 in intestinal homeostasis and inflammation', *Biochimica et Biophysica Acta - Molecular Basis of Disease*, 1812(3), pp. 283–289. doi: 10.1016/j.bbadis.2010.11.008.

Costa, J. and Ahluwalia, A. (2019) 'Advances and Current Challenges in Intestinal in vitro Model Engineering: A Digest', *Frontiers in Bioengineering and Biotechnology*, 7(JUN), pp. 1–14. doi: 10.3389/fbioe.2019.00144.

Coward, J. I. G. *et al.* (2012) 'Chemotherapy-induced bowel obstruction in small cell lung cancer: A case report', *Medical Oncology*, 29(4), pp. 2623–2625. doi: 10.1007/s12032-011-0150-3.

Creff, J., Malaquin, L. and Besson, A. (2021) 'In vitro models of intestinal epithelium: Toward bioengineered systems', *Journal of Tissue Engineering*, 12. doi: 10.1177/2041731420985202.

Crenn, P. *et al.* (2003) 'Plasma citrulline: A marker of enterocyte mass in villous atrophy-associated small bowel disease', *Gastroenterology*, 124(5), pp. 1210–1219. doi: 10.1016/S0016-5085(03)00170-7.

Crenn, P. *et al.* (2009) 'Plasma citrulline is a biomarker of enterocyte mass and an indicator of parenteral nutrition in HIV-infected patients', *American Journal of Clinical Nutrition*, 90(3), pp. 587–594. doi: 10.3945/ajcn.2009.27448.

Crenn, P. *et al.* (2011) 'La citrullinémie : Un biomarqueur de la fonctionnalité intestinale', *Annales de Biologie Clinique*, 69(5), pp. 513–521. doi: 10.1684/abc.2011.0609.

Crenn, P., Messing, B. and Cynober, L. (2008) 'Citrulline as a biomarker of intestinal failure due to enterocyte mass reduction', *Clinical Nutrition*, 27(3), pp. 328–339. doi: 10.1016/j.clnu.2008.02.005.

Daly, A. K. (2013) 'Pharmacogenomics of adverse drug reactions', *Daly Genome Medicine*, 5(5), pp. 1–12.

Demitrack, E. S. and Samuelson, L. C. (2016) 'Notch regulation of gastrointestinal stem cells', *Journal of Physiology*, 594(17), pp. 4791–4803. doi: 10.1113/JP271667.

Derek Lowe (2019) *The Latest on Drug Failure and Approval Rates | In the Pipeline*, *Science Translational Medicine*. Available at: [https://www.science.org/content/blog-post/latest-drug-](https://www.science.org/content/blog-post/latest-drug)

---

failure-and-approval-rates (Accessed: 15 October 2021).

Desager, J.-P. and Horsmans, Y. (2012) 'Pharmacokinetic-Pharmacodynamic Relationships of H1-Antihistamines', *Clinical Pharmacokinetics* 1995 28:5, 28(5), pp. 419–432. doi: 10.2165/00003088-199528050-00006.

Dhurba, G. (2018) *Hematoxylin and Eosin (H&E) Staining : Principle, Procedure and Interpretation*, *Laboratorytest.org*. Available at: <http://laboratorytests.org/hematoxylin-and-eosin-staining/> (Accessed: 3 August 2021).

Dietrich, C. G., Geier, A. and Oude Elferink, R. P. J. (2003) 'ABC of oral bioavailability: Transporters as gatekeepers in the gut', *Gut*, 52(12), pp. 1788–1795. doi: 10.1136/gut.52.12.1788.

DiMasi, J. A., Grabowski, H. G. and Hansen, R. W. (2016) 'Innovation in the pharmaceutical industry: New estimates of R&D costs', *Journal of Health Economics*, 47, pp. 20–33. doi: 10.1016/j.jhealeco.2016.01.012.

Ding, X. *et al.* (2021) 'Differentiated Caco-2 cell models in food-intestine interaction study: Current applications and future trends', *Trends in Food Science and Technology*, 107(May 2020), pp. 455–465. doi: 10.1016/j.tifs.2020.11.015.

Doherty, M. M. and Charman, W. N. (2002) 'The mucosa of the small intestine', *Clinical Pharmacokinetics*, 41(4), pp. 235–253. doi: 10.1136/pgmj.37.434.717.

Dragoni, G., Innocenti, T. and Galli, A. (2021) 'Biomarkers of Inflammation in Inflammatory Bowel Disease: How Long before Abandoning Single-Marker Approaches?', *Digestive Diseases*, 39(3), pp. 190–203. doi: 10.1159/000511641.

Drancourt, M. (2017) *Acute Diarrhea*. Fourth Edi, *Infectious Diseases*. Fourth Edi. Elsevier Ltd. doi: 10.1016/B978-0-7020-6285-8.00038-1.

Dressman, J. B. and Thelen, K. (2009) 'Cytochrome P450-mediated metabolism in the human gut wall', *Journal of Pharmacy and Pharmacology*, 61(5), pp. 541–558. doi: 10.1211/jpp/61.05.0002.

Du, L. *et al.* (2016) 'Crosstalk between Inflammation and ROCK/MLCK Signaling Pathways in Gastrointestinal Disorders with Intestinal Hyperpermeability', *Gastroenterology Research and Practice*, 2016(Nm Ii). doi: 10.1155/2016/7374197.

Duboc, H. *et al.* (2012) 'Increase in fecal primary bile acids and dysbiosis in patients with diarrhea-predominant irritable bowel syndrome', *Neurogastroenterology and Motility*, 24(6). doi: 10.1111/j.1365-2982.2012.01893.x.

DuBuske, L. M. (1999) 'Second-generation antihistamines: The risk of ventricular arrhythmias', *Clinical Therapeutics*, 21(2), pp. 281–295. doi: 10.1016/S0149-2918(00)88286-7.

Duncan, P. I. *et al.* (2009) 'Sialic acid utilisation and synthesis in the neonatal rat revisited', *PLoS ONE*, 4(12). doi: 10.1371/journal.pone.0008241.

Edmondson, R. *et al.* (2014) 'Three-dimensional cell culture systems and their applications in drug discovery and cell-based biosensors', *Assay and Drug Development Technologies*, 12(4), pp. 207–218. doi: 10.1089/adt.2014.573.

Effner, R. *et al.* (2017) 'Cytochrome P450s in human immune cells regulate IL-22 and c-Kit via an AHR feedback loop', *Scientific Reports*, 7(July 2016), pp. 1–13. doi: 10.1038/srep44005.

Eisenbrand, G. *et al.* (2002) 'Methods of in vitro toxicology', *Food and Chemical Toxicology*, 40(2–

---

3), pp. 193–236. doi: 10.1016/S0278-6915(01)00118-1.

Emc (2018) 'Irinotecan Hydrochloride 20 mg/ml Concentrate for Solution for Infusion - Summary of Product Characteristics (SmPC) - (eMC)', *Hospira*. Available at: <https://www.medicines.org.uk/emc/product/6506/smpc> (Accessed: 5 May 2022).

Emc (2019) *Oxaliplatin 5mg/ml concentrate for Solution for Infusion - Summary of Product Characteristics (SmPC) - (emc)*, *medicines.org.uk*. Available at: [https://www.medicines.org.uk/emc/product/6088/smpc#PRECLINICAL\\_SAFETY](https://www.medicines.org.uk/emc/product/6088/smpc#PRECLINICAL_SAFETY) (Accessed: 5 May 2022).

Emc (2020) *Diclofenac Sodium 50mg Gastro-Resistant Tablets - Summary of Product Characteristics (SmPC) - (emc)*. Available at: [https://www.medicines.org.uk/emc/product/2660/smpc#UNDESIRABLE\\_EFFECTS](https://www.medicines.org.uk/emc/product/2660/smpc#UNDESIRABLE_EFFECTS) (Accessed: 5 May 2022).

Emc (2021) *Gefitinib 250 mg Tablets - Summary of Product Characteristics (SmPC) - (emc)*. Available at: [https://www.medicines.org.uk/emc/product/10456/smpc#PRECLINICAL\\_SAFETY](https://www.medicines.org.uk/emc/product/10456/smpc#PRECLINICAL_SAFETY) (Accessed: 5 May 2022).

Emc (2022) *Loperamide (P) 2mg Caps - Summary of Product Characteristics (SmPC) - (emc)*. Available at: <https://www.medicines.org.uk/emc/product/11853/smpc> (Accessed: 5 May 2022).

Englund, G. *et al.* (2006) 'Regional levels of drug transporters along the human intestinal tract: Co-expression of ABC and SLC transporters and comparison with Caco-2 cells', *European Journal of Pharmaceutical Sciences*, 29(3–4 SPEC. ISS.), pp. 269–277. doi: 10.1016/j.ejps.2006.04.010.

Engman, H. A. *et al.* (2001) 'CYP3A4, CYP3A5, and MDR1 in human small and large intestinal cell lines suitable for drug transport studies', *Journal of Pharmaceutical Sciences*, 90(11), pp. 1736–1751. doi: 10.1002/jps.1123.

Ersoy Tunali, N. *et al.* (2014) 'A novel mutation in the SLC25A15 gene in a Turkish patient with HHH syndrome: Functional analysis of the mutant protein', *Molecular Genetics and Metabolism*, 112(1), pp. 25–29. doi: 10.1016/J.YMGME.2014.03.002.

Estudante, M. *et al.* (2013) 'Intestinal drug transporters: An overview', *Advanced Drug Delivery Reviews*, 65(10), pp. 1340–1356. doi: 10.1016/j.addr.2012.09.042.

Eun, J. R. *et al.* (2014) 'Hepatoma SK Hep-1 cells exhibit characteristics of oncogenic mesenchymal stem cells with highly metastatic capacity', *PLoS ONE*, 9(10). doi: 10.1371/journal.pone.0110744.

Evans, W. H. and Martin, P. E. M. (2002) 'Gap junctions: Structure and function (review)', *Molecular Membrane Biology*, 19(2), pp. 121–136. doi: 10.1080/09687680210139839.

Falavigna, M. *et al.* (2020) 'Impact of mucin on drug diffusion: Development of a straightforward in vitro method for the determination of drug diffusivity in the presence of mucin', *Pharmaceutics*, 12(2). doi: 10.3390/pharmaceutics12020168.

Fernandez Vallone, V. *et al.* (2020) 'LGR 5 controls extracellular matrix production by stem cells in the developing intestine', *EMBO reports*, 21(7). doi: 10.15252/embr.201949224.

Ferrer, M. D. *et al.* (2018) 'Cyclooxygenase-2 Inhibitors as a Therapeutic Target in Inflammatory Diseases', *Current Medicinal Chemistry*, 26(18), pp. 3225–3241. doi: 10.2174/0929867325666180514112124.

- 
- Ferry, D. R. and Kerr, D. J. (2002) *Mechanistic Approaches To Phase I Clinical Trials, Anticancer Drug Development*. ACADEMIC PRESS. doi: 10.1016/b978-012072651-6/50021-8.
- Fevr, T. *et al.* (2007) 'Wnt/ $\beta$ -Catenin Is Essential for Intestinal Homeostasis and Maintenance of Intestinal Stem Cells', *Molecular and Cellular Biology*, 27(21), pp. 7551–7559. doi: 10.1128/mcb.01034-07.
- Findley, M. K. and Koval, M. (2009) 'Regulation and roles for claudin-family tight junction proteins', *IUBMB Life*, 61(4), pp. 431–437. doi: 10.1002/iub.175.Regulation.
- Fitzgerald, K. A. *et al.* (2015) 'Life in 3D is never flat: 3D models to optimise drug delivery', *Journal of Controlled Release*, 215, pp. 39–54. doi: 10.1016/j.jconrel.2015.07.020.
- Fleetwood, G. *et al.* (2015) 'Making progress and gaining momentum in global 3Rs efforts: How the European pharmaceutical industry is contributing', *Journal of the American Association for Laboratory Animal Science*, 54(2), pp. 192–197.
- Van Der Flier, L. G. and Clevers, H. (2009) 'Stem cells, self-renewal, and differentiation in the intestinal epithelium', *Annual Review of Physiology*, 71, pp. 241–260. doi: 10.1146/annurev.physiol.010908.163145.
- Fogh, J., Fogh, J. M. and Orfeo, T. (1977) 'One hundred and twenty seven cultured human tumor cell lines producing tumors in nude mice', *Journal of the National Cancer Institute*. Oxford Academic, pp. 221–226. doi: 10.1093/jnci/59.1.221.
- Forsgård, R. A. *et al.* (2017) 'Chemotherapy-induced gastrointestinal toxicity is associated with changes in serum and urine metabolome and fecal microbiota in male Sprague–Dawley rats', *Cancer Chemotherapy and Pharmacology*, 80(2), pp. 317–332. doi: 10.1007/s00280-017-3364-z.
- Fotiadis, D., Kanai, Y. and Palacín, M. (2013) 'The SLC3 and SLC7 families of amino acid transporters', *Molecular Aspects of Medicine*, 34(2–3), pp. 139–158. doi: 10.1016/j.mam.2012.10.007.
- Fragkos, K. C. and Forbes, A. (2018) 'Citrulline as a marker of intestinal function and absorption in clinical settings: A systematic review and meta-analysis', *United European Gastroenterology Journal*, 6(2), pp. 181–191. doi: 10.1177/2050640617737632.
- Frampton, J. E. *et al.* (2004) *ADIS DRUG EVALUATION Gefitinib A Review of its Use in the Management of Advanced Non-Small-Cell Lung Cancer, Drugs*.
- Franzen, N. *et al.* (2019) 'Impact of organ-on-a-chip technology on pharmaceutical R&D costs', *Drug Discovery Today*, 24(9), pp. 1720–1724. doi: 10.1016/J.DRUDIS.2019.06.003.
- Freeman, H. J. and Thomson, A. B. R. (2005) 'The small intestine', in Thomson, A. B. R. and A., S. E. (eds) *First Principles of Gastroenterology*, pp. 175–257. doi: 10.1097/00000441-196608000-00027.
- Freyer, J. P. *et al.* (1984) 'In situ oxygen consumption rates of cells in V-79 multicellular spheroids during growth', *Journal of Cellular Physiology*, 118(1), pp. 53–61. doi: 10.1002/jcp.1041180111.
- Friedel, D., Thomas, R. and Fisher, R. S. (2001) 'Ischemic colitis during treatment with alosetron', *Gastroenterology*, 120(2), pp. 557–560. doi: 10.1053/gast.2001.21177.
- Fu, N. *et al.* (2007) 'Comparison of protein and mRNA expression evolution in humans and chimpanzees', *PLoS ONE*, 2(2), pp. 1–5. doi: 10.1371/journal.pone.0000216.

- 
- Fujita, D. *et al.* (2016) 'Organic anion transporting polypeptide (OATP)2b1 contributes to gastrointestinal toxicity of anticancer drug sn-38, active metabolite of irinotecan hydrochloride', *Drug Metabolism and Disposition*, 44(1), pp. 1–7. doi: 10.1124/dmd.115.066712.
- Fujita, K. I. *et al.* (2015) 'Irinotecan, a key chemotherapeutic drug for metastatic colorectal cancer', *World Journal of Gastroenterology*, pp. 12234–12248. doi: 10.3748/wjg.v21.i43.12234.
- Furuse, M. *et al.* (1998) 'Claudin-1 and -2: Novel integral membrane proteins localizing at tight junctions with no sequence similarity to occludin', *Journal of Cell Biology*, 141(7), pp. 1539–1550. doi: 10.1083/jcb.141.7.1539.
- Gajda, A. M. and nStorch, J. (2015) 'Enterocyte fatty acid-binding proteins (FABPs): Different functions of liver and intestinal FABPS in the intestine', *Prostaglandins, Leukotrienes and essential Fatty Acids*, 93, pp. 9-16. doi.org/10.1016/j.plefa.2014.10.001
- Galeano, D. *et al.* (2020) 'Predicting the frequencies of drug side effects', *Nature Communications*, 11(1). doi: 10.1038/s41467-020-18305-y.
- Galetin, A. and Houston, J. B. (2006) 'Intestinal and hepatic metabolic activity of five cytochrome P450 enzymes: Impact on prediction of first-pass metabolism', *Journal of Pharmacology and Experimental Therapeutics*, 318(3), pp. 1220–1229. doi: 10.1124/jpet.106.106013.
- Gan, T. J. (2010) 'Diclofenac: An update on its mechanism of action and safety profile', *Current Medical Research and Opinion*, 26(7), pp. 1715–1731. doi: 10.1185/03007995.2010.486301.
- García-Gutiérrez, L., Delgado, M. D. and León, J. (2019) 'Myc oncogene contributions to release of cell cycle brakes', *Genes*, 10(3). doi: 10.3390/genes10030244.
- Garcia-Hernandez, V., Quiros, M. and Nusrat, A. (2017) 'Intestinal epithelial claudins: expression and regulation in homeostasis and inflammation', *Annals of the New York Academy of Sciences*, 1397(1), pp. 66–79. doi: 10.1111/nyas.13360. Intestinal.
- Gautreau, A. *et al.* (1999) 'Ezrin, a plasma membrane – microfilament linker, signals cell survival through the phosphatidylinositol 3-kinase<sup>-</sup>Akt pathway', *Proceedings of the National Academy of Sciences of the United States of America*, 96(June), pp. 7300–7305.
- Gelberg, H. (2018) 'Pathophysiological Mechanisms of Gastrointestinal Toxicity', in *Comprehensive Toxicology: Third Edition*, pp. 139–178. doi: 10.1016/B978-0-12-801238-3.10923-7.
- Gerbe, F. *et al.* (2011) 'Distinct ATOH1 and Neurog3 requirements define tuft cells as a new secretory cell type in the intestinal epithelium', *Journal of Cell Biology*, 192(5), pp. 767–780. doi: 10.1083/jcb.201010127.
- Gerbe, F., Legrauerend, C. and Jay, P. (2012) 'The intestinal epithelium tuft cells: Specification and function', *Cellular and Molecular Life Sciences*, 69(17), pp. 2907–2917. doi: 10.1007/s00018-012-0984-7.
- Gibson, J. P., Huffmann, K. W. and Newberne, J. W. (1982) 'Preclinical safety studies with terfenadine', *Arzneimittel-Forschung/Drug Research*, 32(9 A), pp. 1179–1184. Available at: <https://pubmed.ncbi.nlm.nih.gov/6129864/> (Accessed: 5 May 2022).
- Gibson, R. J. and Bowen, J. M. (2011) 'Biomarkers of regimen-related mucosal injury', *Cancer Treatment Reviews*, 37(6), pp. 487–493. doi: 10.1016/j.ctrv.2011.05.007.
- Gill, R. K. *et al.* (2005) 'Expression and membrane localization of MCT isoforms along the length of the human intestine', *American Journal of Physiology - Cell Physiology*, 289(4 58-4), pp. 846–



---

852. doi: 10.1152/ajpcell.00112.2005.

Goebel, J., Chmielewski, J. and Hrycyna, C. A. (2021) 'The roles of the human ATP-binding cassette transporters P-glycoprotein and ABCG2 in multidrug resistance in cancer and at endogenous sites: Future opportunities for structure-based drug design of inhibitors', *Cancer Drug Resistance*. OAE Publishing Inc., pp. 784–804. doi: 10.20517/cdr.2021.19.

Goh, J. Y. *et al.* (2015) 'Development and use of in vitro alternatives to animal testing by the pharmaceutical industry 1980-2013', *Toxicology Research*, 4(5), pp. 1297–1307. doi: 10.1039/c5tx00123d.

Gong, X. W. *et al.* (2012) 'Loperamide, an antidiarrhea drug, has antitumor activity by inducing cell apoptosis', *Pharmacological Research*, 65(3), pp. 372–378. doi: 10.1016/j.phrs.2011.11.007.

Goodenough, D. A. and Paul, D. L. (2009) 'Gap junctions.', *Cold Spring Harbor perspectives in biology*, 1(1). doi: 10.1101/cshperspect.a002576.

Goto, M. *et al.* (2003) 'Decreased expression of P-glycoprotein during differentiation in the human intestinal cell line Caco-2', *Biochemical Pharmacology*, 66(1), pp. 163–170. doi: 10.1016/S0006-2952(03)00242-9.

Grabinger, T. *et al.* (2014) 'Ex vivo culture of intestinal crypt organoids as a model system for assessing cell death induction in intestinal epithelial cells and enteropathy', *Cell Death and Disease*, 5(5), pp. e1228-10. doi: 10.1038/cddis.2014.183.

Graham, J., Muhsin, M. and Kirkpatrick, P. (2004) 'Oxaliplatin. Market analysis', *Nature Reviews Drug Discovery*, 3(1), pp. 11–12. doi: 10.1038/nrd1287.

Grebenyuk, S. and Ranga, A. (2019) 'Engineering organoid vascularization', *Frontiers in Bioengineering and Biotechnology*, 7(MAR), pp. 1–12. doi: 10.3389/fbioe.2019.00039.

Greenbaum, D. *et al.* (2003) 'Comparing protein abundance and mRNA expression levels on a genomic scale', *Genome Biology*, 4(9). doi: 10.1186/gb-2003-4-9-117.

Gribble, F. M. and Reimann, F. (2019) 'Function and mechanisms of enteroendocrine cells and gut hormones in metabolism', *Nature Reviews Endocrinology*, 15(4), pp. 226–237. doi: 10.1038/s41574-019-0168-8.

Guzman-Aranguez, A. and Argüeso P. (2010) 'Structure and biological roles of mucin-type O-glycans at the ocular surface', *The Ocular surface*, 8(1), pp 8-17. doi: .org/10.1016/S1542-0124(12)70213-6

Gromova, M. *et al.* (2020) 'Biomarkers: Opportunities and Challenges for Drug Development in the Current Regulatory Landscape', *Biomarker Insights*, 15. doi: 10.1177/1177271920974652.

Grondin, J. A. *et al.* (2020) 'Mucins in Intestinal Mucosal Defense and Inflammation: Learning From Clinical and Experimental Studies', *Frontiers in Immunology*, 11(September), pp. 1–19. doi: 10.3389/fimmu.2020.02054.

Groschwitz, K. R. and Hogan, S. P. (2009) 'Intestinal Barrier Function: Molecular Regulation and Disease Pathogenesis', *Journal of Allergy and Clinical Immunology*, 124(1), pp. 3–22. doi: 10.1016/j.jaci.2009.05.038.Intestinal.

Gross, A. *et al.* (2018) 'Desmoglein 2, but not desmocollin 2, protects intestinal epithelia from injury', *Mucosal Immunology*, 11(6), pp. 1630–1639. doi: 10.1038/s41385-018-0062-z.

Guengerich, F. P. (2006) 'Cytochrome P450s and other enzymes in drug metabolism and

---

toxicity', *AAPS Journal*, 8(1), pp. E101–E111. doi: 10.1208/aapsj080112.

Gunawardene, A. R., Corfe, B. M. and Staton, C. A. (2011) 'Classification and functions of enteroendocrine cells of the lower gastrointestinal tract', *International Journal of Experimental Pathology*, 92(4), pp. 219–231. doi: 10.1111/j.1365-2613.2011.00767.x.

Gunaydin, C. and Bilge, S. S. (2018) 'Effects of nonsteroidal anti-inflammatory drugs at the molecular level', *Eurasian Journal of Medicine*, 50(2), pp. 116–121. doi: 10.5152/eurasianjmed.2018.0010.

Gunshin, H. *et al.* (2005) 'Slc11a2 is required for intestinal iron absorption and erythropoiesis but dispensable in placenta and liver', *Journal of Clinical Investigation*, 115(5), pp. 1258–1266. doi: 10.1172/JCI24356.

Guo, X. *et al.* (2003) 'Regulation of adherens junctions and epithelial paracellular permeability: A novel function for polyamines', *American Journal of Physiology - Cell Physiology*, 285(5 54-5), pp. 1174–1187. doi: 10.1152/ajpcell.00015.2003.

Gupta, A. *et al.* (2015) 'Risk correlates of diarrhea in children under 5 years of age in slums of Bankura, West Bengal', *Journal of Global Infectious Diseases*, 7(1), pp. 23–29. doi: 10.4103/0974-777X.150887.

Haegbarth, A. and Clevers, H. (2009) 'Wnt Signaling, LGR5, and stem cells in the intestine and skin', *The American Journal of Pathology*, 174(3).

Hansson, G. C. (2012) 'Role of mucus layers in gut infection and inflammation', *Current Opinion in Microbiology*, 15(1), pp. 57–62. doi: 10.1016/j.mib.2011.11.002.

Harrison, O. J. *et al.* (2016) 'Structural basis of adhesive binding by desmocollins and desmogleins', *Proceedings of the National Academy of Sciences of the United States of America*, 113(26), pp. 7160–7165. doi: 10.1073/pnas.1606272113.

Harrison, R. K. (2016) 'Phase II and phase III failures: 2013-2015', *Nature Reviews Drug Discovery*, 15(12), pp. 817–818. doi: 10.1038/nrd.2016.184.

Harwood, M. D. *et al.* (2007) 'Absolute abundance and function of intestinal drug transporters: a prerequisite for fully mechanistic in vitro-in vivo extrapolation of oral drug absorption', *Biopharmaceutics & drug disposition*, 28(3), pp. 135–143. doi: 10.1002/bdd.

Hayes, A. N. and Gilbert, S. G. (2009) *Historical milestones and discoveries that shaped the toxicology sciences., Exs.* doi: 10.1007/978-3-7643-8336-7\_1.

Henderson, R. (no date) *What does the pancreas do? | Abdomen Anatomy | Patient.* Available at: <https://patient.info/news-and-features/what-does-the-pancreas-do> (Accessed: 17 April 2022).

Hennigar, S. R. *et al.* (2022) 'Slc39a4 in the small intestine predicts zinc absorption and utilization: a comprehensive analysis of zinc transporter expression in response to diets of varied zinc content in young mice', *Journal of Nutritional Biochemistry*, 101, p. 108927. doi: 10.1016/j.jnutbio.2021.108927.

Herath, M. *et al.* (2020) 'The Role of the Gastrointestinal Mucus System in Intestinal Homeostasis: Implications for Neurological Disorders', *Frontiers in Cellular and Infection Microbiology*, 10(May). doi: 10.3389/fcimb.2020.00248.

Hidalgo, I. J., Raub, T. J. and Borchardt, R. T. (1989) 'Characterization of the Human Colon Carcinoma Cell Line (Caco-2) as a Model System for Intestinal Epithelial Permeability', *Gastroenterology*, 96(2), pp. 736–749. doi: 10.1016/S0016-5085(89)80072-1.

- 
- Hino, K. *et al.* (2008) 'Inducible expression of microRNA-194 is regulated by HNF-1 $\alpha$  during intestinal epithelial cell differentiation', *Rna*, 14(7), pp. 1433–1442. doi: 10.1261/rna.810208.
- Hodgson, E. (2004) 'INTRODUCTION', in Hodgson, E. (ed.) *A Textbook of Modern Toxicology*. 3rd edn. John Wiley & Sons, Inc., p. 557. doi: <https://doi.org/10.1002/0471646776.ch1>.
- Hofer, M. and Lutolf, M. P. (2021) 'Engineering organoids', *Nature Reviews Materials*. Nature Research, pp. 402–420. doi: 10.1038/s41578-021-00279-y.
- Hong, A. W., Meng, Z. and Guan, K. L. (2016) 'The Hippo pathway in intestinal regeneration and disease', *Nature Reviews Gastroenterology and Hepatology*, 13(6), pp. 324–337. doi: 10.1038/nrgastro.2016.59.
- Horio, T., Murata, T. and Murata, T. (2014) 'The role of dynamic instability in microtubule organization', *Frontiers in Plant Science*, 5(OCT), pp. 1–10. doi: 10.3389/fpls.2014.00511.
- Hua, S. (2020) 'Advances in Oral Drug Delivery for Regional Targeting in the Gastrointestinal Tract - Influence of Physiological, Pathophysiological and Pharmaceutical Factors', *Frontiers in Pharmacology*, 11(April), pp. 1–22. doi: 10.3389/fphar.2020.00524.
- Huang, L. *et al.* (2018) 'Functions of EpCAM in physiological processes and diseases (Review)', *International Journal of Molecular Medicine*, 42(4), pp. 1771–1785. doi: 10.3892/ijmm.2018.3764.
- Huang, Y. K. *et al.* (2015) 'Significance of Serum Pepsinogens as a Biomarker for Gastric Cancer and Atrophic Gastritis Screening: A Systematic Review and Meta-Analysis', *PLOS ONE*, 10(11), p. e0142080. doi: 10.1371/JOURNAL.PONE.0142080.
- Huh, D. *et al.* (2010) 'Reconstituting organ-level lung functions on a chip', *Science*, 328(5986), pp. 1662–1668. doi: 10.1126/science.1188302.
- Hyman, P. E. and Garvey, T. Q. (2002) *Return of alosetron, Expert Opinion on Drug Safety*. doi: 10.1517/14740338.1.1.1.
- Hynds, R. E. and Giangreco, A. (2013) 'Concise review: The relevance of human stem cell-derived organoid models for epithelial translational medicine', *Stem Cells*, 31(3), pp. 417–422. doi: 10.1002/stem.1290.
- Ikenouchi, J. *et al.* (2005) 'Tricellulin constitutes a novel barrier at tricellular contacts of epithelial cells', *Journal of Cell Biology*, 171(6), pp. 939–945. doi: 10.1083/jcb.200510043.
- Imamura, Y. *et al.* (2015) 'Comparison of 2D- and 3D-culture models as drug-testing platforms in breast cancer', *Oncology Reports*, 33(4), pp. 1837–1843. doi: 10.3892/or.2015.3767.
- Inc., P. L. (2008) 'FULL PRESCRIBING INFORMATION WARNING : SERIOUS GASTROINTESTINAL ADVERSE REACTIONS Infrequent but serious gastrointestinal adverse reactions have been reported with the use of LOTRONEX . These events , including ischemic colitis and serious complications o', *Pharmacology*, pp. 1–28.
- Innocenti, F. *et al.* (2000) 'Flavopiridol metabolism in cancer patients is associated with the occurrence of diarrhea', *Clinical Cancer Research*, 6(9), pp. 3400–3405.
- Itoh, M. *et al.* (1999) 'Direct binding of three tight junction-associated MAGUKs, ZO-1, ZO-2, and ZO-3, with the COOH termini of claudins', *Journal of Cell Biology*, 147(6), pp. 1351–1363. doi: 10.1083/jcb.147.6.1351.
- Ivey, K. J. (1988) 'Mechanisms of nonsteroidal anti-inflammatory drug-induced gastric damage:

---

Actions of therapeutic agents', *The American Journal of Medicine*, 84(2), pp. 41–48. doi: 10.1016/0002-9343(88)90253-7.

Janssen, A. W. F. *et al.* (2020) 'Cytochrome P450 expression, induction and activity in human induced pluripotent stem cell-derived intestinal organoids and comparison with primary human intestinal epithelial cells and Caco-2 cells', *Archives of Toxicology*, 95(3), pp. 907–922. doi: 10.1007/s00204-020-02953-6.

Jeon, M. K. (2013) 'Intestinal barrier: Molecular pathways and modifiers', *World Journal of Gastrointestinal Pathophysiology*, 4(4), p. 94. doi: 10.4291/wjgp.v4.i4.94.

John-Baptiste, A. *et al.* (2012) 'Evaluation of Potential Gastrointestinal Biomarkers in a PAK4 Inhibitor-treated Preclinical Toxicity Model to Address Unmonitorable Gastrointestinal Toxicity', *Toxicologic Pathology*, 40(3), pp. 482–490. doi: 10.1177/0192623311432289.

Joseph, J. S., Malindisa, S. and Ntwasa, M. (2019) 'Two-Dimensional (2D) and Three-Dimensional (3D) Cell Culturing in Drug Discovery', *Cell culture, i(tourism)*, p. 23.

Jung, Y. H. *et al.* (2021) 'Drug screening by uniform patient derived colorectal cancer hydro-organoids', *Biomaterials*, 276(June), p. 121004. doi: 10.1016/j.biomaterials.2021.121004.

Kalabat, D. Y. *et al.* (2017) 'Identification and Evaluation of Novel MicroRNA Biomarkers in Plasma and Feces Associated with Drug-induced Intestinal Toxicity', *Toxicologic Pathology*, 45(2), pp. 302–320. doi: 10.1177/0192623316644992.

Kamada, N. *et al.* (2009) 'Human CD14 + Macrophages in Intestinal Lamina Propria Exhibit Potent Antigen-Presenting Ability', *The Journal of Immunology*, 183(3), pp. 1724–1731. doi: 10.4049/jimmunol.0804369.

Kaminsky, L. S. and Zhang, Q. Y. (2003) 'The small intestine as a xenobiotic-metabolizing organ', *Drug Metabolism and Disposition*, 31(12), pp. 1520–1525. doi: 10.1124/dmd.31.12.1520.

Kang, W. *et al.* (2016) 'Emerging role of Hippo pathway in gastric and other gastrointestinal cancers', *World Journal of Gastroenterology*, 22(3), pp. 1279–1288. doi: 10.3748/wjg.v22.i3.1279.

Kapałczyńska, M. *et al.* (2016) '2D and 3D cell cultures – a comparison of different', *Archives of Medical Science*, 14(4), pp. 910–919.

Karlsson, H. *et al.* (2012) 'Loss of cancer drug activity in colon cancer HCT-116 cells during spheroid formation in a new 3-D spheroid cell culture system', *Experimental Cell Research*, 318(13), pp. 1577–1585. doi: 10.1016/j.yexcr.2012.03.026.

Karunahatamoorthy, A. (2021) *Duodenum: Anatomy, histology, composition, functions | Kenhub*. Available at: <https://www.kenhub.com/en/library/anatomy/the-duodenum> (Accessed: 5 August 2021).

Kasendra, M. *et al.* (2018) 'Development of a primary human Small Intestine-on-a-Chip using biopsy-derived organoids', *Scientific Reports*, 8(1). doi: 10.1038/s41598-018-21201-7.

Kasendra, M. *et al.* (2019) 'Organoid-derived Duodenum Intestine-Chip for preclinical drug assessment in a human relevant system', *bioRxiv*, pp. 1–34. doi: 10.1101/723015.

Kato, M. *et al.* (2003) 'The Intestinal First-pass Metabolism of Substrates of CYP3A4 and P-glycoprotein-Quantitative Analysis Based on Information from the Literature', *Drug Metabolism and Pharmacokinetics*, 18(6), pp. 365–372. doi: 10.2133/dmpk.18.365.

- 
- Katoh, M. and Katoh, M. (2007) 'Notch signaling in gastrointestinal tract (Review)', *International Journal of Oncology*, 30(1), pp. 247–251. doi: 10.3892/ijo.30.1.247.
- Kaur, G. and Dufour, J. M. (2012) 'Cell lines', *Spermatogenesis*, 2(1), pp. 1–5. doi: 10.4161/spmg.19885.
- Kelland, L. R. (2005) 'Flavopiridol, the first cyclin-dependent kinase inhibitor to enter the clinic: current status', <http://dx.doi.org/10.1517/13543784.9.12.2903>, 9(12), pp. 2903–2911. doi: 10.1517/13543784.9.12.2903.
- Kim, G. A., Ginga, N. J. and Takayama, S. (2018) 'Integration of Sensors in Gastrointestinal Organoid Culture for Biological Analysis', *Cmgh*, 6(1), p. 123–131.e1. doi: 10.1016/j.jcmgh.2018.03.002.
- Kim, H. J. and Ingber, D. E. (2013) 'Gut-on-a-Chip microenvironment induces human intestinal cells to undergo villus differentiation', *Integrative Biology (United Kingdom)*, 5(9), pp. 1130–1140. doi: 10.1039/c3ib40126j.
- Kim, H. K. *et al.* (2013) 'Serum prohepcidin levels are lower in patients with atrophic gastritis', *Gastroenterology Research and Practice*, 2013. doi: 10.1155/2013/201810.
- Kim, J., Koo, B. K. and Knoblich, J. A. (2020) 'Human organoids: model systems for human biology and medicine', *Nature Reviews Molecular Cell Biology*, 21(10), pp. 571–584. doi: 10.1038/s41580-020-0259-3.
- Kimura, H., Sakai, Y. and Fujii, T. (2018) 'Organ/body-on-a-chip based on microfluidic technology for drug discovery', *Drug Metabolism and Pharmacokinetics*, 33(1), pp. 43–48. doi: 10.1016/j.dmpk.2017.11.003.
- Kleinman, H. K. *et al.* (1987) 'Use of extracellular matrix components for cell culture', *Analytical Biochemistry*, 166(1), pp. 1–13. doi: 10.1016/0003-2697(87)90538-0.
- Knight, L. A. *et al.* (2004) 'The in vitro effect of gefitinib ('Iressa') alone and in combination with cytotoxic chemotherapy on human solid tumours', *BMC Cancer*, 4, pp. 1–8. doi: 10.1186/1471-2407-4-83.
- Kobielak, A. and Fuchs, E. (2004) 'α-catenin: At the junction of intercellular adhesion and actin dynamics', *Nature Reviews Molecular Cell Biology*, 5(8), pp. 614–625. doi: 10.1038/nrm1433.
- Kola, I. and Landis, J. (2004) 'Can the pharmaceutical industry reduce attrition rates?', *Nature Reviews Drug Discovery*, 3(8), pp. 711–715. doi: 10.1038/nrd1470.
- Kolars, J. C. *et al.* (1991) 'First-pass metabolism of cyclosporin by the gut', *The Lancet*, 338(8781), pp. 1488–1490. doi: 10.1016/0140-6736(91)92302-I.
- Komiya, Y. and Habas, R. (2008) 'Wnt Secretion and Extra-Cellular Regulators', 4(2), pp. 68–75. Available at: [www.landesbioscience.com](http://www.landesbioscience.com).
- König, J. *et al.* (1999) 'Conjugate export pumps of the multidrug resistance protein (MRP) family: Localization, substrate specificity, and MRP2-mediated drug resistance', *Biochimica et Biophysica Acta - Biomembranes*, 1461(2), pp. 377–394. doi: 10.1016/S0005-2736(99)00169-8.
- Konikoff, M. R. and Denson, L. A. (2000) *Role of Fecal Calprotectin as a Biomarker of Intestinal Inflammation in Inflammatory Bowel Disease*. Available at: <https://academic.oup.com/ibdjournal/article/12/6/524/4682696>.
- Konikoff, M. R. and Denson, L. A. (2006) 'Role of fecal calprotectin as a biomarker of intestinal

---

inflammation in inflammatory bowel disease', *Inflammatory Bowel Diseases*, 12(6), pp. 524–534. doi: 10.1097/00054725-200606000-00013.

Kopan, R. (2012) 'Notch signaling', *Cold Spring Harbor Perspectives in Biology*, 4(10), pp. 1–4. doi: 10.1111/dgd.12642.

Kopi, T. A. *et al.* (2019) 'The role of serum calprotectin as a novel biomarker in inflammatory bowel diseases: A review study', *Gastroenterology and Hepatology from Bed to Bench*, 12(3), pp. 183–189. doi: 10.22037/ghfbb.v12i3.1591.

Krause, G. *et al.* (2008) 'Structure and function of claudins', *Biochimica et Biophysica Acta - Biomembranes*, 1778(3), pp. 631–645. doi: 10.1016/j.bbame.2007.10.018.

Krogstad, V. *et al.* (2020) 'A comparative analysis of cytochrome P450 activities in paired liver and small intestinal samples from patients with obesity S', *Drug Metabolism and Disposition*, 48(1), pp. 8–17. doi: 10.1124/DMD.119.087940.

Kulshrestha, V. *et al.* (1978) 'Some clinical pharmacological studies with terfenadine, a new antihistamine drug.', *British Journal of Clinical Pharmacology*, 6(1), pp. 25–29. doi: 10.1111/j.1365-2125.1978.tb01677.x.

Kulthong, K. *et al.* (2020) 'Microfluidic chip for culturing intestinal epithelial cell layers: Characterization and comparison of drug transport between dynamic and static models', *Toxicology in Vitro*, 65(February), p. 104815. doi: 10.1016/j.tiv.2020.104815.

Kulthong, K. *et al.* (2021) 'Transcriptome comparisons of in vitro intestinal epithelia grown under static and microfluidic gut-on-chip conditions with in vivo human epithelia', *Scientific Reports*, 11(1), pp. 1–13. doi: 10.1038/s41598-021-82853-6.

Kuratnik, A. and Giardina, C. (2013) 'Intestinal organoids as tissue surrogates for toxicological and pharmacological studies', *Biochemical Pharmacology*, 85(12), pp. 1721–1726. doi: 10.1016/j.bcp.2013.04.016.

Lameris, A. L. *et al.* (2013) 'Expression profiling of claudins in the human gastrointestinal tract in health and during inflammatory bowel disease', *Scandinavian Journal of Gastroenterology*, 48(1), pp. 58–69. doi: 10.3109/00365521.2012.741616.

Lancaster, M. A. and Knoblich, J. A. (2014) 'Organogenesis in a dish: Modeling development and disease using organoid technologies', *Science*, 345(6194). doi: 10.1126/science.1247125.

Langhans, S. A. (2018) 'Three-dimensional in vitro cell culture models in drug discovery and drug repositioning', *Frontiers in Pharmacology*, 9(JAN), pp. 1–14. doi: 10.3389/fphar.2018.00006.

Leckband, D. and Prakasam, A. (2006) 'Mechanism and dynamics of cadherin adhesion', *Annual Review of Biomedical Engineering*, 8, pp. 259–287. doi: 10.1146/annurev.bioeng.8.061505.095753.

Leckband, D. and Sivasankar, S. (2012) 'Cadherin recognition and adhesion', *Current Opinion in Cell Biology*, 24(5), pp. 620–627. doi: 10.1016/j.ceb.2012.05.014.

Lee, B., Moon, K. M. and Kim, C. Y. (2018) 'Tight junction in the intestinal epithelium: Its association with diseases and regulation by phytochemicals', *Journal of Immunology Research*, 2018(Figure 2). doi: 10.1155/2018/2645465.

Lee, C. S., Ryan, E. J. and Doherty, G. A. (2014) 'Gastro-intestinal toxicity of chemotherapeutics in colorectal cancer: The role of inflammation', *World Journal of Gastroenterology*, 20(14), pp.

---

3751–3761. doi: 10.3748/wjg.v20.i14.3751.

Lemmens, G. *et al.* (2021) 'Drug disposition in the lower gastrointestinal tract: Targeting and monitoring', *Pharmaceutics*, 13(2). doi: 10.3390/pharmaceutics13020161.

Leong, R. W. L. and Chan, F. K. L. (2006) 'Drug-induced side effects affecting the gastrointestinal tract', *Expert Opinion on Drug Safety*, 5(4), pp. 585–592. doi: 10.1517/14740338.5.4.585.

Lesuffleur, T. *et al.* (1993) 'Differential expression of the human mucin genes MUC1 to MUC5 in relation to growth and differentiation of different mucus-secreting HT-29 cell subpopulations', *Journal of Cell Science*, 106(3), pp. 771–783. doi: 10.1242/jcs.106.3.771.

Levy, E. *et al.* (2001) 'The Polymorphism at Codon 54 of the FABP2 Gene Increases Fat Absorption in Human Intestinal Explants', *Journal of Biological Chemistry*, 276(43), pp. 39679–39684. doi: 10.1074/jbc.M105713200.

Li, H. *et al.* (2017) 'Association between acute gastrointestinal injury and biomarkers of intestinal barrier function in critically ill patients', *BMC Gastroenterology*, 17(1), pp. 1–8. doi: 10.1186/s12876-017-0603-z.

Lian, P. *et al.* (2021) 'Hypoxia and heat stress affect epithelial integrity in a Caco-2/HT-29 co-culture', *Scientific Reports*, 11(1), pp. 1–14. doi: 10.1038/s41598-021-92574-5.

Lian, Q. *et al.* (2017) 'Chemotherapy-induced intestinal inflammatory responses are mediated by exosome secretion of double-strand DNA via AIM2 inflammasome activation', *Cell Research*, 27(6), pp. 784–800. doi: 10.1038/cr.2017.54.

Liang, Y. C. *et al.* (2015) 'Gefitinib-induced intestinal obstruction in advanced non-small cell lung carcinoma: A case report', *Oncology Letters*, 10(3), pp. 1277–1280. doi: 10.3892/ol.2015.3463.

Lim, Y. J. and Yang, C. H. (2012) 'Non-steroidal anti-inflammatory drug-induced enteropathy', *Clinical Endoscopy*, 45(2), pp. 138–144. doi: 10.5946/ce.2012.45.2.138.

Liu, C., Takada, K. and Zhu, D. (2020) 'Targeting Wnt/ $\beta$ -Catenin Pathway for Drug Therapy', *Medicine in Drug Discovery*, 8, p. 100066. doi: 10.1016/j.medidd.2020.100066.

Liu, Z. and Liu, K. (2013) 'The transporters of intestinal tract and techniques applied to evaluate interactions between drugs and transporters', *Asian Journal of Pharmaceutical Sciences*, 8(3), pp. 151–158. doi: 10.1016/j.ajps.2013.07.020.

Lněničková, K. *et al.* (2020) 'The modulation of phase ii drug-metabolizing enzymes in proliferating and differentiated caco-2 cells by hop-derived prenylflavonoids', *Nutrients*, 12(7), pp. 1–14. doi: 10.3390/nu12072138.

Longley, D. B., Harkin, D. P. and Johnston, P. G. (2003) '5-Fluorouracil: Mechanisms of action and clinical strategies', *Nature Reviews Cancer*, 3(5), pp. 330–338. doi: 10.1038/nrc1074.

Lu, Z. *et al.* (2013) 'Claudins in intestines', *Tissue Barriers*, 1(3), p. e24978. doi: 10.4161/tisb.24978.

Luca, A. C. *et al.* (2013) 'Impact of the 3D Microenvironment on Phenotype, Gene Expression, and EGFR Inhibition of Colorectal Cancer Cell Lines', *PLoS ONE*, 8(3). doi: 10.1371/journal.pone.0059689.

Lucak, S. L. (2010) 'Optimizing outcomes with alosetron hydrochloride in severe diarrhea-predominant irritable bowel syndrome', *Therapeutic Advances in Gastroenterology*, 3(3), pp. 165–172. doi: 10.1177/1756283X10362277.

- 
- Lueschow, S. R. and McElroy, S. J. (2020) 'The Paneth Cell: The Curator and Defender of the Immature Small Intestine', *Frontiers in Immunology*, p. 587. doi: 10.3389/fimmu.2020.00587.
- Lurje, G. and Lenz, H. J. (2010) 'EGFR signaling and drug discovery', *Oncology*, 77(6), pp. 400–410. doi: 10.1159/000279388.
- Lv, D. *et al.* (2017) 'Three-dimensional cell culture: A powerful tool in tumor research and drug discovery', *Oncology Letters*, 14(6), pp. 6999–7010. doi: 10.3892/ol.2017.7134.
- Ma, C. *et al.* (2021) 'Organ-on-a-Chip: A new paradigm for drug development', *Trends in Pharmacological Sciences*, 42(2), pp. 119–133. doi: 10.1016/j.tips.2020.11.009.Organ-on-a-Chip.
- Ma, X. and Shah, Y. M. (2018) *The Role of Hippo Signaling in Intestinal Homeostasis*. Sixth Edit, *Physiology of the Gastrointestinal Tract: Sixth Edition*. Sixth Edit. Elsevier Inc. doi: 10.1016/B978-0-12-809954-4.00005-0.
- MacAdam, A. (1993) 'The effect of gastro-intestinal mucus on drug absorption', *Advanced Drug Delivery Reviews*. Elsevier, pp. 201–220. doi: 10.1016/0169-409X(93)90010-2.
- Mah, A. T., Yan, K. S. and Kuo, C. J. (2016) 'Wnt pathway regulation of intestinal stem cells', *Journal of Physiology*, 594(17), pp. 4837–4847. doi: 10.1113/JP271754.
- Mai, Y. *et al.* (2021) 'Quantification of P-Glycoprotein in the Gastrointestinal Tract of Humans and Rodents: Methodology, Gut Region, Sex, and Species Matter', *Molecular Pharmaceutics*, 18(5), pp. 1895–1904. doi: 10.1021/acs.molpharmaceut.0c00574.
- Makins, R. and Ballinger, A. (2003a) 'Gastrointestinal side effects of drugs', *Expert Opinion on Drug Safety*, 2(4), pp. 421–429. doi: 10.1517/14740338.2.4.421.
- Makins, R. and Ballinger, A. (2003b) 'Gastrointestinal side effects of drugs', *Expert Opinion on Drug Safety*. *Expert Opin Drug Saf*, pp. 421–429. doi: 10.1517/14740338.2.4.421.
- Man, Y. *et al.* (2000) 'Loss of epithelial integrity resulting from E-cadherin dysfunction predisposes airway epithelial cells to adenoviral infection', *American Journal of Respiratory Cell and Molecular Biology*, 23(5), pp. 610–617. doi: 10.1165/ajrcmb.23.5.4046.
- Maqsood, M. I. *et al.* (2013) 'Immortality of cell lines: Challenges and advantages of establishment', *Cell Biology International*, 37(10), pp. 1038–1045. doi: 10.1002/cbin.10137.
- Maric, S., Restin, T., *et al.* (2021) 'Citrulline, Biomarker of Enterocyte Functional Mass and Dietary Supplement. Metabolism, Transport, and Current Evidence for Clinical Use Stefano', *Nutrients*, 13(8), p. 2794. doi: <https://doi.org/10.3390/nu13082794> Academic.
- Maric, S., Flüchter, P., *et al.* (2021) 'Plasma citrulline correlates with basolateral amino acid transporter LAT4 expression in human small intestine', *Clinical Nutrition*, 40(4), pp. 2244–2251. doi: 10.1016/j.clnu.2020.10.003.
- Mariotta, L. *et al.* (2012) 'T-type amino acid transporter TAT1 (Slc16a10) is essential for extracellular aromatic amino acid homeostasis control', *The Journal of physiology*, 590(24), pp. 6413–6424. doi: 10.1113/JPHYSIOL.2012.239574.
- Martignoni, M., Groothuis, G. M. M. and de Kanter, R. (2006) 'Species differences between mouse, rat, dog, monkey and human CYP-mediated drug metabolism, inhibition and induction', *Expert Opinion on Drug Metabolism and Toxicology*, 2(6), pp. 875–894. doi: 10.1517/17425255.2.6.875.
- Martín-Padura, I. *et al.* (1998) 'Junctional adhesion molecule, a novel member of the immunoglobulin superfamily that distributes at intercellular junctions and modulates monocyte



- 
- transmigration', *Journal of Cell Biology*, 142(1), pp. 117–127. doi: 10.1083/jcb.142.1.117.
- Mastrangeli, M. and van den Eijnden-van Raaij, J. (2021) 'Organs-on-chip: The way forward', *Stem Cell Reports*. ElsevierCompany., pp. 2037–2043. doi: 10.1016/j.stemcr.2021.06.015.
- Mayeux, R. (2004) 'Biomarkers: Potential Uses and Limitations', *NeuroRx*, 1(2), pp. 182–188. doi: 10.1602/neurorx.1.2.182.
- Maynard, A. A. *et al.* (2010) 'Epidermal growth factor reduces autophagy in intestinal epithelium and in the rat model of necrotizing enterocolitis', *American Journal of Physiology - Gastrointestinal and Liver Physiology*, 299(3), pp. 614–622. doi: 10.1152/ajpgi.00076.2010.
- McConnell, R. E. *et al.* (2009) 'The enterocyte microvillus is a vesicle-generating organelle', *Journal of Cell Biology*, 185(7), pp. 1285–1298. doi: 10.1083/jcb.200902147.
- McKenna, Lindsay, B. *et al.* (2010) 'MicroRNAs Control Intestinal Epithelial Differentiation, Architecture, and Barrier Function', *Gastroenterology*, 139(5), pp. 1654–1664. doi: 10.1053/j.gastro.2010.07.040.MicroRNAs.
- McNeil, E., Capaldo, C. T. and Macara, I. G. (2006) 'Zonula Occludens-1 Function in the Assembly of Tight Junctions in Madin-Darby Canine Kidney Epithelial Cells', *Molecular Biology of the Cell*, 17, pp. 1922–1932. doi: 10.1091/mbc.E05.
- McQuade, R. M. *et al.* (2016) 'Chemotherapy-induced constipation and diarrhea: Pathophysiology, current and emerging treatments', *Frontiers in Pharmacology*, 7(NOV), pp. 1–14. doi: 10.3389/fphar.2016.00414.
- McTavish, D., Goa, K. L. and Ferrill, M. (1990) 'Terfenadine: An Updated Review of its Pharmacological Properties and Therapeutic Efficacy', *Drugs*, 39(4), pp. 552–574. doi: 10.2165/00003495-199039040-00006.
- MDC Berlin (2020) *The 3R principles*. Available at: <https://www.mdc-berlin.de/research-animal-experiments-3r/3r-principles> (Accessed: 20 October 2021).
- MedSafe (2015) *Drug Metabolism - The Importance of Cytochrome P450*. Available at: <https://www.medsafe.govt.nz/profs/puarticles/march2014drugmetabolismcytochromep4503a4.htm> (Accessed: 5 September 2022).
- Meinl, W. *et al.* (2008) 'Sulfotransferase forms expressed in human intestinal Caco-2 and TC7 cells at varying stages of differentiation and role in benzo[a]pyrene metabolism', *Drug Metabolism and Disposition*, 36(2), pp. 276–283. doi: 10.1124/dmd.107.018036.
- Merker, S. R., Weitz, J. and Stange, D. E. (2016) 'Gastrointestinal organoids: How they gut it out', *Developmental Biology*, 420(2), pp. 239–250. doi: 10.1016/j.ydbio.2016.08.010.
- Miller, H. *et al.* (2017) 'Loperamide misuse and abuse', *Journal of the American Pharmacists Association*, 57(2), pp. S45–S50. doi: 10.1016/j.japh.2016.12.079.
- Mitchell, E. P. (2006) 'Gastrointestinal toxicity of chemotherapeutic agents', *Seminars in Oncology*, 33(1), pp. 106–120. doi: 10.1053/j.seminoncol.2005.12.001.
- Mitra, A. and Kesisoglou, F. (2013) 'Impaired drug absorption due to high stomach pH: A review of strategies for mitigation of such effect to enable pharmaceutical product development', *Molecular Pharmaceutics*, 10(11), pp. 3970–3979. doi: 10.1021/MP400256H.
- Mo, J.-S., Park, J. W. and Guan, K.-L. (2014) 'The hippo signaling pathway and cancer', *EMB reports*, 15(6), pp. 624–656. doi: 10.1007/978-1-4614-6220-0.

- 
- Mohs, R. C. and Greig, N. H. (2017) 'Drug discovery and development: Role of basic biological research', *Alzheimer's and Dementia: Translational Research and Clinical Interventions*, 3(4), pp. 651–657. doi: 10.1016/j.trci.2017.10.005.
- Moll, R. *et al.* (1993) 'The human gene encoding cytokeratin 20 and its expression during fetal development and in gastrointestinal carcinomas', *Differentiation; research in biological diversity*, 53(2), pp. 75–93. doi: 10.1111/J.1432-0436.1993.TB00648.X.
- Mueller-Klieser, W., Freyer, J. P. and Sutherland, R. M. (1986) 'Influence of glucose and oxygen supply conditions on the oxygenation of multicellular spheroids', *British Journal of Cancer*, 53(3), pp. 345–353. doi: 10.1038/bjc.1986.58.
- Mühlemann, M. (2018) *Intestinal stem cells and the Na<sup>+</sup>-D-Glucose Transporter SGLT1: potential targets regarding future therapeutic strategies for diabetes* *Intestinale Stammzellen und der Na<sup>+</sup>-D-Glukose Transporter SGLT1: potentielle Ansatzpunkte neuartiger Therapien für Diab.* Available at: [https://www.researchgate.net/publication/328475917\\_Intestinal\\_stem\\_cells\\_and\\_the\\_Na-D-Glucose\\_Transporter\\_SGLT1\\_potential\\_targets\\_regarding\\_future\\_therapeutic\\_strategies\\_for\\_diabetes](https://www.researchgate.net/publication/328475917_Intestinal_stem_cells_and_the_Na-D-Glucose_Transporter_SGLT1_potential_targets_regarding_future_therapeutic_strategies_for_diabetes) (Accessed: 4 November 2021).
- Muhsin, M., Graham, J. and Kirkpatrick, P. (2003) 'Gefitinib. Market analysis', *Nature Reviews Drug Discovery*, 2(7), pp. 515–516. doi: 10.1038/nrd1136.
- Mukomoto, R. *et al.* (2020) 'Oxygen consumption rate of tumour spheroids during necrotic-like core formation', *Analyst*, 145(19), pp. 6342–6348. doi: 10.1039/d0an00979b.
- Müller, J. *et al.* (2017) 'Expression, regulation and function of intestinal drug transporters: An update', *Biological Chemistry*, 398(2), pp. 175–192. doi: 10.1515/hsz-2016-0259.
- Müller, T. D. *et al.* (2015) 'Ghrelin', *Molecular Metabolism*, 4(6), pp. 437–460. doi: 10.1016/J.MOLMET.2015.03.005.
- Münzel, P. A. *et al.* (1999) 'Induction of human UDP glucuronosyltransferases (UGT1A6, UGT1A9, and UGT2B7) by t-butylhydroquinone and 2,3,7,8-tetrachlorodibenzo-p-dioxin in Caco-2 cells', *Drug Metabolism and Disposition*, 27(5), pp. 569–573.
- Naruhashi, K. and Kamino, A. (2016) 'Transport Mechanism of Intestinal Absorption of  $\mu$  Opioid Recept or Agonists and Contribution of P-Glycoprotein in Rats and Human Intestinal Epithelial Caco-2', *Clinical Pharmacology & Biopharmaceutics*, 5(2). doi: 10.4172/2167-065x.1000154.
- National Center for Biotechnology Information, (NCBI) (2022a) *ABCB11 ATP binding cassette subfamily B member 11*. Available at: <https://www.ncbi.nlm.nih.gov/gene/8647> (Accessed: 11 September 2022).
- National Center for Biotechnology Information, (NCBI) (2022b) *Slc25a15 solute carrier family 25 (mitochondrial carrier ornithine transporter), member 15 [Mus musculus (house mouse)]* - Gene - NCBI. Available at: <https://www.ncbi.nlm.nih.gov/gene?Db=gene&Cmd=DetailsSearch&Term=18408> (Accessed: 11 September 2022).
- National Center for Biotechnology Information (NCBI) (2004) *SLC16A10 - solute carrier family 16 member 10, USA: Genes and Expression-Gene*. Available at: <https://www.ncbi.nlm.nih.gov/gene/117247> (Accessed: 11 September 2022).
- Naumovska, E. *et al.* (2020) 'Direct on-chip differentiation of intestinal tubules from induced pluripotent stem cells', *International Journal of Molecular Sciences*, 21(14), pp. 1–15. doi: 10.3390/ijms21144964.

- 
- NCBI (2022a) *CDH17 cadherin 17 [Homo sapiens (human)] - Gene - NCBI*. Available at: <https://www.ncbi.nlm.nih.gov/gene?Db=gene&Cmd=ShowDetailView&TermToSearch=1015> (Accessed: 28 January 2022).
- NCBI (2022b) *TJAP1 tight junction associated protein 1 [Homo sapiens (human)] - Gene - NCBI*. Available at: <https://www.ncbi.nlm.nih.gov/gene?Db=gene&Cmd=ShowDetailView&TermToSearch=93643> (Accessed: 26 January 2022).
- Neudecker, V. *et al.* (2017) 'MicroRNAs in mucosal inflammation', *Journal of Molecular Medicine*, 95(9), pp. 935–949. doi: 10.1007/s00109-017-1568-7. MicroRNAs.
- Nicolas, A. *et al.* (2021) 'High throughput transepithelial electrical resistance (TEER) measurements on perfused membrane-free epithelia', *Lab on a Chip*, 21(9), pp. 1676–1685. doi: 10.1039/d0lc00770f.
- Nielsen, M. S. *et al.* (2012) 'Gap junctions', *Comprehensive Physiology*, 2(3), pp. 1981–2035. doi: 10.1002/cphy.c110051.
- Nigam Y, Knight J, W. (2019) 'Gastrointestinal tract 5: the anatomy and functions of the large intestine', *Nursing Times*, 115(10), pp. 50–53.
- Nishimura, M. *et al.* (2009) 'Tissue-specific mRNA expression profiles of human solute carrier 35 transporters', *Drug Metabolism and Pharmacokinetics*, 24(1), pp. 91–99. doi: 10.2133/dmpk.24.91.
- Nonnenmacher (2021) *Terfenadin - Wirkung, Anwendung & Risiken | MedLexi.de*. Available at: <https://medlexi.de/Terfenadin> (Accessed: 26 October 2021).
- Noordhuis, P. *et al.* (2004) '5-Fluorouracil incorporation into RNA and DNA in relation to thymidylate synthase inhibition of human colorectal cancers', *Annals of Oncology*, 15(7), pp. 1025–1032. doi: 10.1093/annonc/mdh264.
- Obach, R. S. *et al.* (2001) 'METABOLIC CHARACTERIZATION OF THE MAJOR HUMAN SMALL INTESTINAL CYTOCHROME P450S', *The American Society of pharmacology and experimental therapeutics*, 29(3), pp. 347–352.
- Oda, K. *et al.* (2005) 'A comprehensive pathway map of epidermal growth factor receptor signaling', *Molecular systems biology*, 1. doi: 10.1038/msb4100014.
- Ohmachi, T. *et al.* (2006) 'Fatty acid binding protein 6 is overexpressed in colorectal cancer', *Clinical Cancer Research*, 12(17), pp. 5090–5095. doi: 10.1158/1078-0432.CCR-05-2045.
- Oka, T., Mazack, V. and Sudol, M. (2008) 'Mst2 and Lats kinases regulate apoptotic function of Yes kinase-associated protein (YAP)', *Journal of Biological Chemistry*, 283(41), pp. 27534–27546. doi: 10.1074/jbc.M804380200.
- Okumura, R. and Takeda, K. (2017) 'Roles of intestinal epithelial cells in the maintenance of gut homeostasis', *Experimental and Molecular Medicine*, 49(5), pp. e338-8. doi: 10.1038/emm.2017.20.
- Ölander, M. *et al.* (2016) 'The Proteome of Filter-Grown Caco-2 Cells with a Focus on Proteins Involved in Drug Disposition', *Journal of Pharmaceutical Sciences*, 105(2), pp. 817–827. doi: 10.1016/j.xphs.2015.10.030.
- Onozato, D. *et al.* (2018) 'Generation of intestinal organoids suitable for pharmacokinetic studies from human induced pluripotent stem cells', *Drug Metabolism and Disposition*, 46(11), pp. 1572–

---

1580. doi: 10.1124/dmd.118.080374.

Oostendorp, R. L. *et al.* (2010) *Dose-finding and pharmacokinetic study of orally administered indibulin (D-24851) to patients with advanced solid tumors*, *Investigational New Drugs*. doi: 10.1007/s10637-009-9244-6.

Orlando, A. *et al.* (2014) 'Lactobacillus GG restoration of the gliadin induced epithelial barrier disruption: The role of cellular polyamines', *BMC Microbiology*, 14(1), pp. 1–12. doi: 10.1186/1471-2180-14-19.

Osho, S. O. *et al.* (2017) 'Research Note: Comparison of goblet cell staining methods in jejunal mucosa of Turkey poult', *Poultry Science*, 96(3), pp. 556–559. doi: 10.3382/ps/pew324.

Owen, D. A. (no date) 'Drug Induced Injury of the G . I . Tract', *American Journal of Gastroenterology*.

Pai, S. G. *et al.* (2017) 'Wnt/beta-catenin pathway: Modulating anticancer immune response', *Journal of Hematology and Oncology*, 10(1), pp. 1–12. doi: 10.1186/s13045-017-0471-6.

Pammolli, F. *et al.* (2020) 'The endless frontier? The recent increase of R&D productivity in pharmaceuticals', *Journal of Translational Medicine*, 18(1), pp. 1–15. doi: 10.1186/s12967-020-02313-z.

Panarelli, N. C. (2014) 'Drug-induced injury in the gastrointestinal tract', *Seminars in Diagnostic Pathology*, 31(2), pp. 165–175. doi: 10.1053/j.semmp.2014.02.007.

Paone, P. and Cani, P. D. (2020) 'Mucus barrier, mucins and gut microbiota: The expected slimy partners?', *Gut*, 69(12), pp. 2232–2243. doi: 10.1136/gutjnl-2020-322260.

Park, C. H. *et al.* (2005) 'Quercetin, a potent inhibitor against  $\beta$ -catenin/Tcf signaling in SW480 colon cancer cells', *Biochemical and Biophysical Research Communications*, 328(1), pp. 227–234. doi: 10.1016/j.bbrc.2004.12.151.

Pathirana, W. P. N. G. W. *et al.* (2018) 'Faecal calprotectin', *Clinical Biochemist Reviews*, 39(3), pp. 77–90. doi: 10.1097/mcg.0b013e318250e34e.

Paul, S. M. *et al.* (2010) 'How to improve RD productivity: The pharmaceutical industry's grand challenge', *Nature Reviews Drug Discovery*, 9(3), pp. 203–214. doi: 10.1038/nrd3078.

Pavel, M. *et al.* (2018) 'Contact inhibition controls cell survival and proliferation via YAP/TAZ-autophagy axis', *Nature Communications*, 9(1). doi: 10.1038/s41467-018-05388-x.

Pelaseyed, T. *et al.* (2014) 'The mucus and mucins of the goblet cells and enterocytes provide the first defense line of the gastrointestinal tract and interact with the immune system', *Immunology Review*, 260(1), pp. 8–20. doi: 10.1111/imr.12182.The.

Penton, A. L., Leonard, L. D. and Spinner, N. B. (2013) 'Notch signaling in human development and disease', 23(4), pp. 450–457. doi: 10.1016/j.semcd.2012.01.010.Notch.

Peters, W. H. . *et al.* (1991) 'Biotransformation enzymes in human Intestine: Critical Low Levels in the Colon?', *Small*, 32, pp. 408–412.

Peters, W. H. N. and Roelofs, H. M. J. (1989) 'Time-dependent activity and expression of glutathione S-transferases in the human colon adenocarcinoma cell line Caco-2', *Biochemical Journal*, 264(2), pp. 613–616. doi: 10.1042/bj2640613.

Peterson, L. W. and Artis, D. (2014) 'Intestinal epithelial cells: Regulators of barrier function and immune homeostasis', *Nature Reviews Immunology*, pp. 141–153. doi: 10.1038/nri3608.

- 
- Philpott, H. L. *et al.* (2014) 'Drug-induced gastrointestinal disorders.', *Frontline gastroenterology*, 5(1), pp. 49–57. doi: 10.1136/flgastro-2013-100316.
- Pirmohamed, M. *et al.* (1998) 'Adverse drug reactions', *British Medical Journal*, 316.
- Piton, G. *et al.* (2013) 'Enterocyte damage in critically ill patients is associated with shock condition and 28-day mortality', *Critical Care Medicine*, 41(9), pp. 2169–2176. doi: 10.1097/CCM.0b013e31828c26b5.
- Pletcher, M. J. and Pignone, M. (2011) 'Evaluating the clinical utility of a biomarker: A review of methods for estimating health impact', *Circulation*, 123(10), pp. 1116–1124. doi: 10.1161/CIRCULATIONAHA.110.943860.
- Polini, A. *et al.* (2014) 'Organs-on-a-chip: A new tool for drug discovery', *Expert Opinion on Drug Discovery*, 9(4), pp. 335–352. doi: 10.1517/17460441.2014.886562.
- Ponce de León-Rodríguez, M. del C., Guyot, J. P. and Laurent-Babot, C. (2019) 'Intestinal in vitro cell culture models and their potential to study the effect of food components on intestinal inflammation', *Critical Reviews in Food Science and Nutrition*, 59(22), pp. 3648–3666. doi: 10.1080/10408398.2018.1506734.
- Promega (2015) *CellTiter-Glo® Luminescent Cell Viability Assay, Instructions for Use of Products G7570, G7571, G7572 and G7573, Technical Bulletin*. Available at: [www.promega.com](http://www.promega.com) (Accessed: 25 November 2021).
- ProteinAtlas (2020) 'Tissue expression of CLDND1'. Available at: <https://www.proteinatlas.org/ENSG00000080822-CLDND1/tissue> (Accessed: 31 January 2022).
- Pusztaszeri, M. P., Genta, R. M. and Cryer, B. L. (2007) 'Drug-induced injury in the gastrointestinal tract: Clinical and pathologic considerations', *Nature Clinical Practice Gastroenterology and Hepatology*, 4(8), pp. 442–453. doi: 10.1038/ncpgasthep0896.
- Qin, Y. *et al.* (2021) 'Oncogenic Activation of YAP Signaling Sensitizes Ferroptosis of Hepatocellular Carcinoma via ALOXE3-Mediated Lipid Peroxidation Accumulation', *Frontiers in Cell and Developmental Biology*, 9(December), pp. 1–16. doi: 10.3389/fcell.2021.751593.
- Quan, Y. *et al.* (2020) 'Organ-on-a-chip: The next generation platform for risk assessment of radiobiology', *RSC Advances*, 10(65), pp. 39521–39530. doi: 10.1039/d0ra05173j.
- Radtke, R. (2022) *Verwendete Tiere in der Grundlagenforschung nach Forschungszweck 2020 | Statista*. Available at: <https://de.statista.com/statistik/daten/studie/646825/umfrage/anzahl-der-in-der-grundlagenforschung-verwendeten-tiere-nach-therapiebereich/> (Accessed: 5 April 2022).
- Ramirez-alcantara, V., Loguidice, A. and Boelsterli, U. A. (2021) 'Protection from diclofenac-induced small intestinal injury by the JNK inhibitor SP600125 in a mouse model of NSAID-associated enteropathy', (28), pp. 990–998. doi: 10.1152/ajpgi.00219.2009.
- Rashid, H. *et al.* (2020) 'Fecal MicroRNAs as Potential Biomarkers for Screening and Diagnosis of Intestinal Diseases', *Frontiers in Molecular Biosciences*, 7(August), pp. 1–11. doi: 10.3389/fmolb.2020.00181.
- Rees, W. D. *et al.* (2020) 'Regenerative Intestinal Stem Cells Induced by Acute and Chronic Injury: The Saving Grace of the Epithelium?', *Frontiers in Cell and Developmental Biology*, 8(November), pp. 1–15. doi: 10.3389/fcell.2020.583919.

- 
- Regnard, C. *et al.* (2011) 'Loperamide', *Journal of Pain and Symptom Management*, 42(2), pp. 319–323. doi: 10.1016/j.jpainsymman.2011.06.001.
- Reidy, E. *et al.* (2021) 'A 3D view of colorectal cancer models in predicting therapeutic responses and resistance', *Cancers*, 13(2), pp. 1–22. doi: 10.3390/cancers13020227.
- Rezaee, R. and Abdollahi, M. (2017) 'The importance of translatability in drug discovery', *Expert Opinion on Drug Discovery*, 12(3), pp. 237–239. doi: 10.1080/17460441.2017.1281245.
- Rhode, C. (2018) *German Collection of Microorganisms and Cell Cultures, 1st German Phage Symposium*. Available at: <https://www.dsmz.de/collection/catalogue/details/culture/ACC-243> (Accessed: 19 October 2021).
- Ribeiro, R. A. *et al.* (2016) 'Irinotecan- and 5-fluorouracil-induced intestinal mucositis: insights into pathogenesis and therapeutic perspectives', *Cancer Chemotherapy and Pharmacology*, 78(5), pp. 881–893. doi: 10.1007/s00280-016-3139-y.
- Rodrigues, D. *et al.* (2019) 'Drug-induced gene expression profile changes in relation to intestinal toxicity: State-of-the-art and new approaches', *Cancer Treatment Reviews*, 77(June), pp. 57–66. doi: 10.1016/j.ctrv.2019.06.004.
- Rodrigues, D. *et al.* (2021) 'New insights into the mechanisms underlying 5-fluorouracil-induced intestinal toxicity based on transcriptomic and metabolomic responses in human intestinal organoids', *Archives of Toxicology*, 95(8), pp. 2691–2718. doi: 10.1007/s00204-021-03092-2.
- Roeselers, G. *et al.* (2013) 'Ex vivo systems to study host-microbiota interactions in the gastrointestinal tract', *Best Practice and Research: Clinical Gastroenterology*, 27(1), pp. 101–113. doi: 10.1016/j.bpg.2013.03.018.
- Van Ruth, S., Cats, A. and Zoetmulder, F. A. N. (2002) 'Gastrointestinal toxicity caused by irinotecan in the case of preexistent passaged problems', *Nederlands Tijdschrift voor Geneeskunde*, 146(43), pp. 2036–2039. Available at: <https://europepmc.org/article/med/12428464> (Accessed: 15 February 2022).
- Saad, R. S. (2011) 'CDX2 as a marker for intestinal differentiation: Its utility and limitations', *World Journal of Gastrointestinal Surgery*, 3(11), p. 159. doi: 10.4240/wjgs.v3.i11.159.
- Saitoh, W. *et al.* (2018) 'Plasma citrulline is a sensitive safety biomarker for small intestinal injury in rats', *Toxicology Letters*, 295(March), pp. 416–423. doi: 10.1016/j.toxlet.2018.07.009.
- Sambruy, Y. *et al.* (2001) 'Chapter 7 Intestinal Cell Culture Models', *Cell Biology and Toxicology*, 17, pp. 301–317.
- Sambuy, Y. *et al.* (2005) 'The Caco-2 cell line as a model of the intestinal barrier: Influence of cell and culture-related factors on Caco-2 cell functional characteristics', *Cell Biology and Toxicology*, 21(1), pp. 1–26. doi: 10.1007/s10565-005-0085-6.
- Samy, K. E. *et al.* (2019) 'Human intestinal spheroids cultured using Sacrificial Micromolding as a model system for studying drug transport', *Scientific Reports*, 9, p. 12.
- Satake, R. *et al.* (2021) 'Analysis of Drug-Induced Gastrointestinal Obstruction and Perforation Using the Japanese Adverse Drug Event Report Database', *Frontiers in Pharmacology*, 12(July). doi: 10.3389/fphar.2021.692292.
- Sato, A. (2007) 'Tuft cells' *Anatomical science international*, 82, pp. 187–199.
- Sato, T. *et al.* (2009) 'Single Lgr5 stem cells build crypt-villus structures in vitro without a

- 
- mesenchymal niche', *Nature*, 459(7244), pp. 262–265. doi: 10.1038/nature07935.
- Scarpignato, C. (1995) 'Nonsteroidal Anti-Inflammatory Drugs: How Do They Damage Gastrointestinal Mucosa?', *Digestive Diseases*, 13(Suppl. 1), pp. 9–39. doi: 10.1159/000171523.
- Schenk, B. E. *et al.* (1999) 'Atrophic gastritis during long-term omeprazole therapy affects serum vitamin B12 levels', *Alimentary Pharmacology and Therapeutics*, 13(10), pp. 1343–1346. doi: 10.1046/j.1365-2036.1999.00616.x.
- Schick, M. A. and Meseha, M. (2018) *Bowel, Obstruction Small, StatPearls*. StatPearls Publishing. Available at: <https://www.ncbi.nlm.nih.gov/books/NBK448079/> (Accessed: 15 February 2022).
- Schiller, L. R. (2017) 'Antidiarrheal Drug Therapy', *Current Gastroenterology Reports*, 19(5). doi: 10.1007/s11894-017-0557-x.
- Schmiedlin-Ren, P. *et al.* (1997) 'Expression of enzymatically active CYP3A4 by Caco-2 cells grown on extracellular matrix-coated permeable supports in the presence of 1 $\alpha$ ,25-dihydroxyvitamin D3', *Molecular Pharmacology*, 51(5), pp. 741–754. doi: 10.1124/mol.51.5.741.
- Schneider, M. R. *et al.* (2010) 'A key role for E-cadherin in intestinal homeostasis and paneth cell maturation', *PLoS ONE*, 5(12). doi: 10.1371/journal.pone.0014325.
- Scholzen, T. and Gerdes, J. (2000) 'The Ki-67 protein: From the known and the unknown', *Journal of Cellular Physiology*, 182(3), pp. 311–322. doi: 10.1002/(SICI)1097-4652(200003)182:3<311::AID-JCP1>3.0.CO;2-9.
- Schultz, I. and Keita, A. V. (2020) 'The Intestinal Barrier and Current Techniques for the Assessment of Gut Permeability', *Cells*, 9(8), pp. 1–30. doi: 10.3390/cells9081909.
- Shobha Rani, K. N., Goundalkar, A. G. and Prakasam, K. (1994) 'Preparation and evaluation of microspheres of diclofenac sodium', *Indian Journal of Pharmaceutical Sciences*, 56(2), pp. 45–50. Available at: <https://www.pharmatutor.org/articles/preparation-evaluation-biodegradable-albumin-microspheres-diclofenac-sodium?page=1%2C0> (Accessed: 5 September 2022).
- Siegel, J. (no date) *Use of Biomarkers in Drug Development*.
- Simon-Hettich, B., Rothfuss, A. and Steger-Hartmann, T. (2006) 'Use of computer-assisted prediction of toxic effects of chemical substances', *Toxicology*, 224(1–2), pp. 156–162. doi: 10.1016/j.tox.2006.04.032.
- Sipponen, P. *et al.* (2005) 'Low circulating levels of gastrin-17 in patients with Barrett's esophagus', *World Journal of Gastroenterology*, 11(38), pp. 5988–5992. doi: 10.3748/wjg.v11.i38.5988.
- Snoeck, V., Goddeeris, B. and Cox, E. (2005) 'The role of enterocytes in the intestinal barrier function and antigen uptake', *Microbes and Infection*, 7(7–8), pp. 997–1004. doi: 10.1016/j.micinf.2005.04.003.
- Soares, P. M. G. *et al.* (2013) 'Cytokine Inflammatory intestinal damage induced by 5-fluorouracil requires IL-4', *Cytokine*, 61(1), pp. 46–49. doi: 10.1016/j.cyto.2012.10.003.
- Somasundaram, S. *et al.* (2000) 'Uncoupling of intestinal mitochondrial oxidative phosphorylation and inhibition of cyclooxygenase are required for the development of NSAID-enteropathy in the rat', *Alimentary Pharmacology and Therapeutics*, 14(5), pp. 639–650. doi: 10.1046/j.1365-2036.2000.00723.x.
- Song, M.-K., Park, M.-Y. and Sung, M.-K. (2013) '5-Fluorouracil-Induced Changes of Intestinal

---

Integrity Biomarkers in BALB/C Mice', *Journal of Cancer Prevention*, 18(4), pp. 322–329. doi: 10.15430/jcp.2013.18.4.322.

Srinivasan, B. *et al.* (2015a) 'TEER Measurement Techniques for In Vitro Barrier Model Systems', *Journal of Laboratory Automation*, 20(2), pp. 107–126. doi: 10.1177/2211068214561025.

Srinivasan, B. *et al.* (2015b) 'TEER Measurement Techniques for In Vitro Barrier Model Systems', *Journal of Laboratory Automation*. SAGE Publications Inc., pp. 107–126. doi: 10.1177/2211068214561025.

*Statistiken zu Tierversuchen* (2022). Available at: <https://www.tierschutzbund.de/information/hintergrund/tierversuche/statistiken-zu-tierversuchen/> (Accessed: 23 July 2021).

Stewart, B. W. and Wild, C. P. (eds) (2016) *World Cancer Report 2014. Geneva, Switzerland: World Health Organization, International Agency for Research on Cancer, WHO Press, 2015, Advances in Nutrition*. doi: 10.3945/an.116.012211.

Stierum, R. *et al.* (2003) 'Proteome analysis reveals novel proteins associated with proliferation and differentiation of the colorectal cancer cell line Caco-2', *Biochimica et Biophysica Acta - Proteins and Proteomics*, 1650(1–2), pp. 73–91. doi: 10.1016/S1570-9639(03)00204-8.

Su, M. C. *et al.* (2008) 'Cadherin-17 is a useful diagnostic marker for adenocarcinomas of the digestive system', *Modern Pathology*, 21(11), pp. 1379–1386. doi: 10.1038/modpathol.2008.107.

Sundler, F. *et al.*, (1989) 'The Neuroendocrine system of the Gut. *Acta Oncologica*, 28 (3), pp. 303-314.

Sutherland, R. M. *et al.* (1986) 'Oxygenation and Differentiation in Multicellular Spheroids of Human Colon Carcinoma', *Cancer Research*, 46(10), pp. 5320–5329.

Synnergren, J. and Dönnes, P. (2018) 'Current Perspectives on Multi-Omics Data Integration With Application on Toxicity Biomarkers Discovery', *Open Access Journal of Toxicology*, 2(5), pp. 1–2. doi: 10.19080/oajt.2018.02.555597.

Taipalensuu, J. *et al.* (2001) 'Correlation of gene expression of ten drug efflux proteins of the atp-binding cassette transporter family in normal human jejunum and in human intestinal epithelial Caco-2 cell monolayers', *Journal of Pharmacology and Experimental Therapeutics*, 299(1), pp. 164–170.

Tajima, A. (2013) 'Non-Steroidal Anti-Inflammatory Drug (NSAID)-Induced Small Intestinal Injury', *Pharmaceutica Analytica Acta*, 5(1), pp. 1–5. doi: 10.4172/2153-2435.1000282.

Takahashi, T. and Shiraishi, A. (2020) 'Stem cell signaling pathways in the small intestine', *International Journal of Molecular Sciences*, 21(6), pp. 1–18. doi: 10.3390/ijms21062032.

Takayama, K. *et al.* (2021) 'In vivo gene expression profile of human intestinal epithelial cells: From the viewpoint of drug metabolism and pharmacokinetics', *Drug Metabolism and Disposition*, 49(3), pp. 221–232. doi: 10.1124/DMD.120.000283.

Takeichi, M. (1990) 'Cadherins: A molecular family important in selective cell-cell adhesion', *Annual Review of Biochemistry*, 59(March), pp. 237–252. doi: 10.1146/annurev.bi.59.070190.001321.

Tanaka, A. *et al.* (2002) 'Up-regulation of COX-2 by inhibition of COX-1 in the rat: A key to NSAID-induced gastric injury', *Alimentary Pharmacology and Therapeutics, Supplement*, 16(2), pp. 90–101. doi: 10.1046/j.1365-2036.16.s2.22.x.



- 
- Tang, X. *et al.* (2016) 'Epidermal Growth Factor and Intestinal Barrier Function', *Mediators of Inflammation*, 2016, pp. 27–30. doi: 10.1155/2016/1927348.
- Tebbutt, N. C. *et al.* (2003) 'Intestinal complications after chemotherapy for patients with unresected primary colorectal cancer and synchronous metastases', *Gut*, 52(4), pp. 568–573. doi: 10.1136/gut.52.4.568.
- Terada, T. and Hira, D. (2015) 'Intestinal and hepatic drug transporters: pharmacokinetic, pathophysiological, and pharmacogenetic roles', *Journal of Gastroenterology*, 50(5), pp. 508–519. doi: 10.1007/s00535-015-1061-4.
- Ternet, C. and Kiel, C. (2021) 'Signaling pathways in intestinal homeostasis and colorectal cancer: KRAS at centre stage', *Cell Communication and Signaling*, 19(1), pp. 1–22. doi: 10.1186/s12964-021-00712-3.
- Teti, A. (1992) 'Regulation of cellular functions by extracellular matrix', *Journal of the american society of nephrology*, 2, pp. 83–87.
- Teubner, W. *et al.* (2007) 'Identification and localization of soluble sulfotransferases in the human gastrointestinal tract', *Biochemical Journal*, 404(2), pp. 207–215. doi: 10.1042/BJ20061431.
- The Editors of Encyclopaedia Britannica (1998) *Small intestine | anatomy | Britannica*. Available at: <https://www.britannica.com/science/small-intestine> (Accessed: 20 July 2021).
- The Editors of Encyclopaedia Britannica (2020) *large intestine | Definition, Location, Anatomy, Length, Function, & Facts | Britannica*. Available at: <https://www.britannica.com/science/large-intestine> (Accessed: 20 July 2021).
- The Human Protein Atlas (2021) *Tissue expression of SLC29A2*. Available at: <https://www.proteinatlas.org/ENSG00000174669-SLC29A2/tissue> (Accessed: 16 July 2022).
- Tillinger, W. *et al.* (2009) 'Expression of the High-Affinity IgG Receptor FcRI (CD64) in patients with inflammatory bowel disease', *American Journal of Ga*, 104(1), pp. 102–109. Available at: [https://journals.lww.com/ajg/Abstract/2009/01000/Expression\\_of\\_the\\_High\\_Affinity\\_IgG\\_Receptor\\_FcRI.21.aspx](https://journals.lww.com/ajg/Abstract/2009/01000/Expression_of_the_High_Affinity_IgG_Receptor_FcRI.21.aspx) (Accessed: 29 April 2022).
- Timbrell, J. A. (1998) 'Biomarkers in Toxicology', *Toxicology*, 129, pp. 1–12.
- Todd, P. A. and Sorokin, E. M. (1988) 'Diclofenac Sodium: A Reappraisal of its Pharmacodynamic and Pharmacokinetic Properties, and Therapeutic Efficacy', *Drugs*, 35(3), pp. 244–285. doi: 10.2165/00003495-198835030-00004.
- Tomaszewski, J. E. *et al.* (2002) *Relevance of Preclinical Pharmacology and Toxicology To Phase I Trial Extrapolation Techniques: Relevance of Animal Toxicology, Anticancer Drug Development*. ACADEMIC PRESS. doi: 10.1016/b978-012072651-6/50018-8.
- Tøn, H. *et al.* (2000) 'Improved assay for fecal calprotectin', *Clinica Chimica Acta*, 292(1–2), pp. 41–54. doi: 10.1016/S0009-8981(99)00206-5.
- Toyonaga, T. *et al.* (2016) 'Lipocalin 2 prevents intestinal inflammation by enhancing phagocytic bacterial clearance in macrophages', *Scientific Reports*, 6(June), pp. 1–13. doi: 10.1038/srep35014.
- Trantakis, I. (2018) 'In vitro Models for Testing Toxicity in the Gastrointestinal Tract', *Functional Foods and Beverages*, pp. 201–218. doi: 10.1002/9781118823309.ch7.

- 
- Trietsch, S. J. *et al.* (2017) 'Membrane-free culture and real-time barrier integrity assessment of perfused intestinal epithelium tubes', *Nature Communications*, 8(1), pp. 1–7. doi: 10.1038/s41467-017-00259-3.
- Troxell, M. L. *et al.* (1999) 'Cadherin function in junctional complex rearrangement and posttranslational control of cadherin expression', *American Journal of Physiology - Cell Physiology*, 276(2 45-2). doi: 10.1152/ajpcell.1999.276.2.c404.
- Turini, M. E. and DuBois, R. N. (2003) 'Cyclooxygenase-2: A Therapeutic Target', <https://doi.org/10.1146/annurev.med.53.082901.103952>, 53, pp. 35–57. doi: 10.1146/ANNUREV.MED.53.082901.103952.
- Turowski, G. A. *et al.* (1994) 'Glutamine Modulates Phenotype and Stimulates Proliferation in Human Colon Cancer Cell Lines', *Cancer Research*, 54(22), pp. 5974–5980.
- Ungewiß, H. (2019) *Adhesive and signaling properties of Dsg2 in intestinal epithelial barrier regulation*.
- US Food and Drug Administration (2021) *Advancing Alternative Methods at FDA, FDA Website*. Available at: <https://www.fda.gov/science-research/about-science-research-fda/advancing-alternative-methods-fda> (Accessed: 15 July 2022).
- Vaessen, S. F. C. *et al.* (2017) 'Regional expression levels of drug transporters and metabolizing enzymes along the pig and human intestinal tract and comparison with Caco-2 cells', *Drug Metabolism and Disposition*, 45(4), pp. 353–360. doi: 10.1124/dmd.116.072231.
- Vale, R. D. (2003) 'The molecular motor toolbox for intracellular transport', *Cell*, 112(4), pp. 467–480. doi: 10.1016/S0092-8674(03)00111-9.
- Valley, M. P., Zimprich, C. A. and Lazar, D. F. (2014) 'CellTiter-Glo® 3D: A Sensitive, Accurate Viability Assay for 3D Cell Cultures', *Promega Corporation*, (May 2014), pp. 1–6. Available at: <https://www.promega.de/resources/pubhub/a-cell-viability-assay-for-3d-cultures/> (Accessed: 14 January 2022).
- Vandenbossche, J. *et al.* (2010) 'Loperamide and P-glycoprotein inhibition: assessment of the clinical relevance', *Journal of Pharmacy and Pharmacology*, 62(4), pp. 401–412. doi: 10.1211/jpp.62.04.0001.
- Vane, J. R. and Botting, R. M. (1998a) 'Anti-inflammatory drugs and their mechanism of action', *Inflammation Research*, 47(SUPPL. 2), pp. 78–87. doi: 10.1007/s000110050284.
- Vane, J. R. and Botting, R. M. (1998b) 'Mechanism of action of antiinflammatory drugs', *International Journal of Tissue Reactions*. Taylor & Francis, pp. 3–15. doi: 10.3109/03009749609097226.
- Vargesson, N. (2015) 'Thalidomide-induced teratogenesis: History and mechanisms', *Birth Defects Research Part C - Embryo Today: Reviews*, 105(2), pp. 140–156. doi: 10.1002/bdrc.21096.
- Vasković, J. (2021) *Small intestine: Anatomy, location and function* / Kenhub. Available at: <https://www.kenhub.com/en/library/anatomy/the-small-intestine> (Accessed: 20 July 2021).
- Vázquez-Iglesias, L. *et al.* (2019) 'Surface expression marker profile in colon cancer cell lines and sphere-derived cells suggests complexity in CD26+ cancer stem cells subsets', *Biology Open*, 8(7), pp. 1–10. doi: 10.1242/bio.041673.
- Van Der Velden, W. J. F. M. *et al.* (2013) 'Citrulline and albumin as biomarkers for gastrointestinal mucositis in recipients of hematopoietic SCT', *Bone Marrow Transplantation*,

---

48(7), pp. 977–981. doi: 10.1038/bmt.2012.278.

Verhoeckx, K. *et al.* (2015) *The impact of food bioactives on health: In vitro and Ex Vivo models, The Impact of Food Bioactives on Health: In Vitro and Ex Vivo Models*. doi: 10.1007/978-3-319-16104-4.

Villarreal, B. (2012) 'Ki-67 immunohistochemical staining with heat-induced epitope retrieval in rat tibial and femoral growth plates', *Journal of Histotechnology*, 35(4), pp. 171–174. doi: 10.1179/2046023612Y.0000000014.

Vinken, M. (2020) '3rs toxicity testing and disease modeling projects in the European horizon 2020 research and innovation program', *EXCLI Journal*, 19, pp. 775–784. doi: 10.17179/excli2020-2450.

Walker, T. R. *et al.* (2007) 'Fecal lactoferrin is a sensitive and specific marker of disease activity in children and young adults with inflammatory bowel disease', *Journal of Pediatric Gastroenterology and Nutrition*, 44(4), pp. 414–422. doi: 10.1097/MPG.0B013E3180308D8E.

Walsh, M. D. *et al.* (2013) 'Expression of MUC2, MUC5AC, MUC5B, and MUC6 mucins in colorectal cancers and their association with the CpG island methylator phenotype', *Modern Pathology*, 26(12), pp. 1642–1656. doi: 10.1038/modpathol.2013.101.

Wang, M. *et al.* (2022) 'In-Depth Comparison of Matrigel Dissolving Methods on Proteomic Profiling of Organoids', *Molecular and Cellular Proteomics*, 21(1), p. 100181. doi: 10.1016/j.mcpro.2021.100181.

Wang, Z. *et al.* (2010) 'Targeting Notch signaling pathway to overcome drug resistance for cancer therapy', *Biochimica et Biophysica Acta (BBA) - Reviews on Cancer*, 1806(2), pp. 258–267. doi: 10.1016/J.BBCAN.2010.06.001.

Wardill, H. R., Bowen, J. M. and Gibson, R. J. (2013) 'Biomarkers of small intestinal mucosal damage induced by chemotherapy: An emerging role for the 13C sucrose breath test', *Journal of Supportive Oncology*, 11(2), pp. 61–67. doi: 10.1016/J.SUPONC.2012.06.004.

Welcome, M. O. (2018) *Gastrointestinal physiology: Development, principles and mechanisms of regulation, Gastrointestinal Physiology: Development, Principles and Mechanisms of Regulation*. doi: 10.1007/978-3-319-91056-7.

Welling, P. G. (1977) 'Influence of food and diet on gastrointestinal drug absorption: A review', *Journal of Pharmacokinetics and Biopharmaceutics*, 5(4), pp. 291–334. doi: 10.1007/BF01061694.

Wells, J. M. *et al.* (2017) 'Homeostasis of the gut barrier and potential biomarkers', *American Journal of Physiology - Gastrointestinal and Liver Physiology*, 312(3), pp. G171–G193. doi: 10.1152/ajpgi.00048.2015.

Wiercinska-Drapalo, A. *et al.* (2008) 'Intestinal fatty acid binding protein (I-FABP) as a possible biomarker of ileitis in patients with ulcerative colitis', *Regulatory Peptides*, 147(1–3), pp. 25–28. doi: 10.1016/j.regpep.2007.12.002.

Windmill, K. F. *et al.* (2000) 'Localization of N-acetyltransferases NAT1 and NAT2 in human tissues', *Toxicological Sciences*, 54(1), pp. 19–29. doi: 10.1093/toxsci/54.1.19.

Wong, J. *et al.* (2019) 'The Role of Connexins in Gastrointestinal Diseases', *Journal of Molecular Biology*, 431(4), pp. 643–652. doi: 10.1016/j.jmb.2019.01.007.

Workman, M. J. *et al.* (2018) 'Enhanced Utilization of Induced Pluripotent Stem Cell-Derived

---

Human Intestinal Organoids Using Microengineered Chips', *Cmgh*, 5(4), p. 669–677.e2. doi: 10.1016/j.jcmgh.2017.12.008.

World Health Organization (1997) 'Terfenadine (Seldane\*): Proposed Withdrawal - Safe Alternative Available', p. 1. Available at: [http://www.who.int/medicines/publications/drugalerts/drug\\_alert54terfenadine\\_proposed\\_withdrawal.pdf?ua=1](http://www.who.int/medicines/publications/drugalerts/drug_alert54terfenadine_proposed_withdrawal.pdf?ua=1).

Worthington, J. J., Reimann, F. and Gribble, F. M. (2018) 'Enteroendocrine cells-sensory sentinels of the intestinal environment and orchestrators of mucosal immunity', *Mucosal Immunology*, pp. 3–20. doi: 10.1038/mi.2017.73.

Wu, C. *et al.* (2021) 'Intestinal fatty acid-binding protein as a biomarker for the diagnosis of strangulated intestinal obstruction: A meta-analysis', *Open Medicine (Poland)*, 16(1), pp. 264–273. doi: 10.1515/med-2021-0214.

Wu, C. J. *et al.* (2013) 'Epithelial cell adhesion molecule (EpCAM) regulates claudin dynamics and tight junctions', *Journal of Biological Chemistry*, 288(17), pp. 12253–12268. doi: 10.1074/jbc.M113.457499.

Wu, C. Q. *et al.* (2019) 'Modulation of intestinal epithelial permeability and mucin mRNA (MUC2, MUC5AC, and MUC5B) expression and protein secretion in Caco-2/HT29-MTX co-cultures exposed to aflatoxin M1, ochratoxin A, and zearalenone individually or collectively', *Toxicology Letters*, 309(February), pp. 1–9. doi: 10.1016/j.toxlet.2019.03.010.

Wu, P. E. and Juurlink, D. N. (2017) 'Clinical Review: Loperamide Toxicity', *Annals of Emergency Medicine*, 70(2), pp. 245–252. doi: 10.1016/j.annemergmed.2017.04.008.

Xie, F., Ding, X. and Zhang, Q. Y. (2016) 'An update on the role of intestinal cytochrome P450 enzymes in drug disposition', *Acta Pharmaceutica Sinica B*, 6(5), pp. 374–383. doi: 10.1016/j.apsb.2016.07.012.

Xie, Z. *et al.* (2021) 'The role of the Hippo pathway in the pathogenesis of inflammatory bowel disease', *Cell Death and Disease*, 12(1). doi: 10.1038/s41419-021-03395-3.

Yang, J. J. *et al.* (2011) 'Histidine decarboxylase is identified as a potential biomarker of intestinal mucosal injury in patients with acute intestinal obstruction', *Molecular Medicine*, 17(11), pp. 1323–1337. doi: 10.2119/molmed.2011.00107.

Yang, Q. *et al.* (2007) 'Ezrin and radixin both regulate the apical membrane localization of ABCC2 (MRP2) in human intestinal epithelial Caco-2 cells', *Experimental Cell Research*, 313(16), pp. 3517–3525. doi: 10.1016/j.yexcr.2007.07.033.

Yang, S. and Yu, M. (2021) 'Role of goblet cells in intestinal barrier and mucosal immunity', *Journal of Inflammation Research*, 14, pp. 3171–3183. doi: 10.2147/JIR.S318327.

Yao, Y., Feng, Q. and Shen, J. (2020) 'Myosin light chain kinase regulates intestinal permeability of mucosal homeostasis in Crohn's disease', *Expert Review of Clinical Immunology*, 16(12), pp. 1127–1141. doi: 10.1080/1744666X.2021.1850269.

Yin, X.; Mead, B. E.; Safaei, H.; Langer, R.; Karp, J. M. and Levy, O. (2016) 'Engineering stem cell organoids', *Cell Stem Cell*, 18 (1), pp-25-38.

Yong, W. H. (2019) *Biobanking. Methods and Protocols, Anticancer research*.

Yoshida, K., Maeda, K. and Sugiyama, Y. (2013) 'Hepatic and intestinal drug transporters: Prediction of pharmacokinetic effects caused by drug-drug interactions and genetic

- 
- polymorphisms', *Annual Review of Pharmacology and Toxicology*, 53, pp. 581–612. doi: 10.1146/annurev-pharmtox-011112-140309.
- Yu, F., Hunziker, W. and Choudhury, D. (2019) 'Engineering microfluidic organoid-on-a-chip platforms', *Micromachines*, 10(3), pp. 1–12. doi: 10.3390/mi10030165.
- Zeino, Z., Sisson, G. and Bjarnason, I. (2010) 'Adverse effects of drugs on small intestine and colon', *Best Practice and Research: Clinical Gastroenterology*, 24(2), pp. 133–141. doi: 10.1016/j.bpg.2010.02.008.
- Zeng, R. and Dong, J. (2021) 'The Hippo Signaling Pathway in Drug Resistance in Cancer', *Cancers*, 13(2), pp. 1–23. doi: 10.3390/CANCERS13020318.
- Zentler-Munro, P. L. and Northfield, T. C. (1979) 'Drug induced gastrointestinal diseases', *British Medical Journal*, 1(10), pp. 1263–1265. doi: 10.1136/bmj.1.6173.1263.
- Zhang, N. *et al.* (2008) '5-Fluorouracil: Mechanisms of resistance and reversal strategies', *Molecules*, 13(8), pp. 1551–1569. doi: 10.3390/molecules13081551.
- Zhang, S., Wan, Z. and Kamm, R. D. (2021) 'Vascularized organoids on a chip: Strategies for engineering organoids with functional vasculature', *Lab on a Chip*, 21(3), pp. 473–488. doi: 10.1039/d0lc01186j.Vascularized.
- Zhang, Y. (2011) 'Phase II Enzymes', in *Encyclopedia of Cancer*. Springer, Berlin, Heidelberg, pp. 2853–2855. doi: 10.1007/978-3-642-16483-5\_4510.
- Zhang, Y. G. *et al.* (2014) 'Salmonella-infected crypt-derived intestinal organoid culture system for host–bacterial interactions', *Physiological Reports*, 2(9). doi: 10.14814/phy2.12147.
- Zhao, B. *et al.* (2007) 'Inactivation of YAP oncoprotein by the Hippo pathway is involved in cell contact inhibition and tissue growth control', *Genes and Development*, 21(21), pp. 2747–2761. doi: 10.1101/gad.1602907.
- Zhu, Y. and Zhang, Q. Y. (2012) 'Role of intestinal cytochrome P450 enzymes in diclofenac-induced toxicity in the small intestine', *Journal of Pharmacology and Experimental Therapeutics*, 343(2), pp. 362–370. doi: 10.1124/jpet.112.198077.
- Zihni, C. *et al.* (2016) 'Tight junctions: From simple barriers to multifunctional molecular gates', *Nature Reviews Molecular Cell Biology*, 17(9), pp. 564–580. doi: 10.1038/nrm.2016.80.
- Zimmermann, C. *et al.* (2005) 'Mapping of multidrug resistance gene 1 and multidrug resistance-associated protein isoform 1 to 5 mRNA expression along the human intestinal tract', *Drug Metabolism and Disposition*, 33(2), pp. 219–224. doi: 10.1124/dmd.104.001354.
- Zorn, A. M. and Wells, J. M. (2009) 'Vertebrate endoderm development', *Annu Rev Cell Biol*, 25, pp. 221–251. doi: 10.1146/annurev.cellbio.042308.113344.Vertebrate.

## 7. Appendix

### Appendix 1: Specification of one chip of the Mimetas OrganoPlate®

Table 37: Specifications of one chip of the Mimetas OrganoPlate®

Constants	values	units
Vgel	0.00010381	cm <sup>3</sup>
Abarrier	0.00570199	cm <sup>2</sup>
dhgel	0.0165	cm
Lgel	0.22	cm
Hgel	0.022	cm
Wgel	0.02048	cm

### Appendix 2: Luminescence signals of the ATP measurements for morphological assessment of the cell culture models

Table 38: Luminescence signals of the ATP measurement for the morphological assessment of Caco-2 cells growing in the OrganoPlate® (OoC)

day	Luminescence signal OoC								Viability	
	Replicate	Replicate	Replicate	Replicate	Replicate	Mean	Mean-MW_Blank	SD	% Control	%SD
4	10579	18840	15615	16931	15207	15434	15431	3061.7	100.0%	19.8%
5	11037	12756	14282	12467	12226	12554	12551	1166.5	81.3%	9.3%
6	11400	15685	19880	14610	12533	14822	14822	3291.0	96.0%	22.2%
7	12899	12164	16738	13805	12930	13707	13705	1791.2	88.8%	13.1%
8	19182	22521	21376	24529	13874	20296	20296	4077.9	131.5%	20.1%
11	958	11383	18793	17931	16019	16032	16032	3308.7	103.9%	20.6%
12	12998	17349	23025	24382	18882	19327	19327	4566.0	125.2%	23.6%
13	6	13	20507	18473	15037	18006	17803	2764.8	115.4%	15.4%

Table 39: Luminescence signals of the ATP measurement for the morphological assessment of iPSC derived colon organoids in 3D.

day	Luminescence signal organoids 3D								Viability	
	Replicate	Replicate	Replicate	Replicate	Replicate	Mean	Mean-MW_Blank	SD	% Control	%SD
6	20257	2723	20117	22624	19694	20673	20641	8108.8	100.0%	39.2%
9	26899	24735	25065	27348	26178	26045	26016	1131.5	126.0%	4.3%
10	27333	24717	19090	19793	20087	22204	22191	3626.8	107.5%	16.3%
11	23038	22925	24341	20890	23820	23003	22961	1316.2	111.2%	5.7%
14	15854	19803	19829	18361	14741	17718	17691	2321.3	85.7%	13.1%
15	31547	30346	27072	22389	23623	26995	26956	4016.9	130.6%	14.9%
16	18673	19207	19863	19474	21049	19653	19573	892.2	94.8%	4.5%
17	28299	24828	23414	22188	21472	24040	24010	2700.8	116.3%	11.2%

Table 40: Luminescence signals of the ATP measurement for the morphological assessment of Caco-2 cells growing in 2D.

day	Luminescence signal 2D								Viability	
	Replicate	Replicate	Replicate	Replicate	Replicate	Mean	Mean-MW_Blank	SD	% Control	%SD
21	34062	24761	29674	27035	24231	28751	28705	4036.3	100.0%	14.0%
22	59443	52451	47367	48765	45748	48583	48561	2858.3	169.2%	5.9%
25	24596	34755	40072	41572	42428	39707	39700	3441.8	138.3%	8.7%
26	51188	42549	42039	46116	47253	45829	45818	3740.0	159.6%	8.2%
27	48885	50155	54397	52631	47883	50790	50790	2687.1	176.9%	5.3%
28	44283	47297	44371	50317	47266	46707	46704	2501.3	162.7%	5.4%
29	54329	45885	42222	40767	41290	44899	44897	5638.3	156.4%	12.6%

### Appendix 3: IF staining's for specific intestinal markers

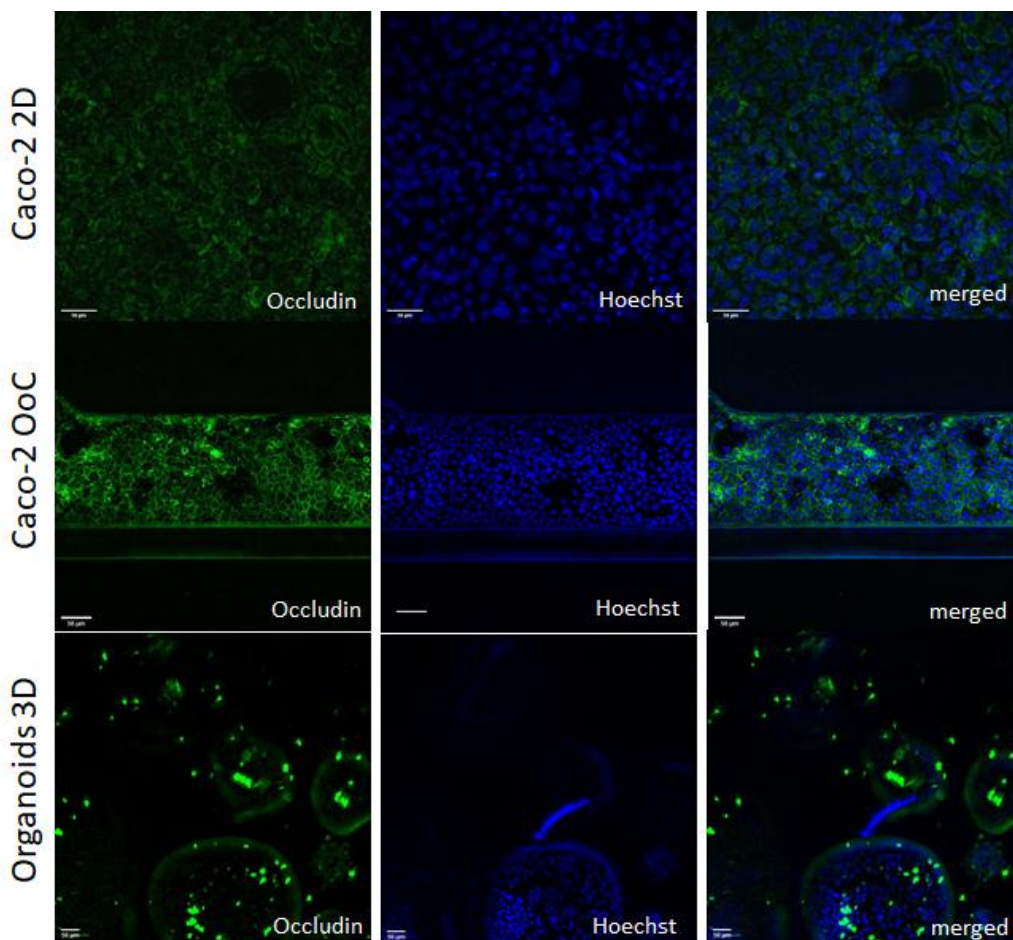


Figure 107: Immunofluorescent stainings with the antibody occludin to stain for a specific claudin family member to build tight junctions. Shown are the pictures of Caco-2 2D (pictures above), Caco-2 OoC (pictures in the middle) and colon organoids 3D (pictures below). Nuclei were counterstained with Hoechst (blue). 10x magnification, bar = 50µm for 3D and 20x magnification, bar = 50µm for 2D and OoC.



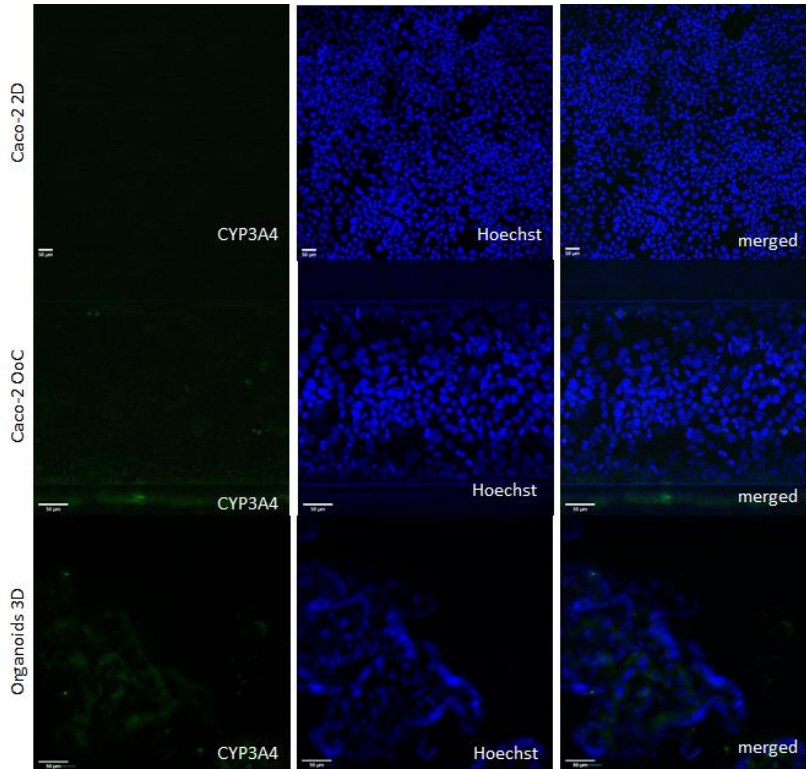


Figure 108: Immunofluorescent stainings with the antibody occludin to stain for a specific claudin family member to build tight junctions. Shown are pictures of Caco-2 2D (pictures above), Caco-2 OoC (pictures in the middle) and colon organoids 3D (pictures below) c. Nuclei were counterstained with Hoechst (blue). 10x magnification, bar = 50 $\mu$ m for 2D, 20x magnification, bar = 50 $\mu$ m for OoC and 3D.

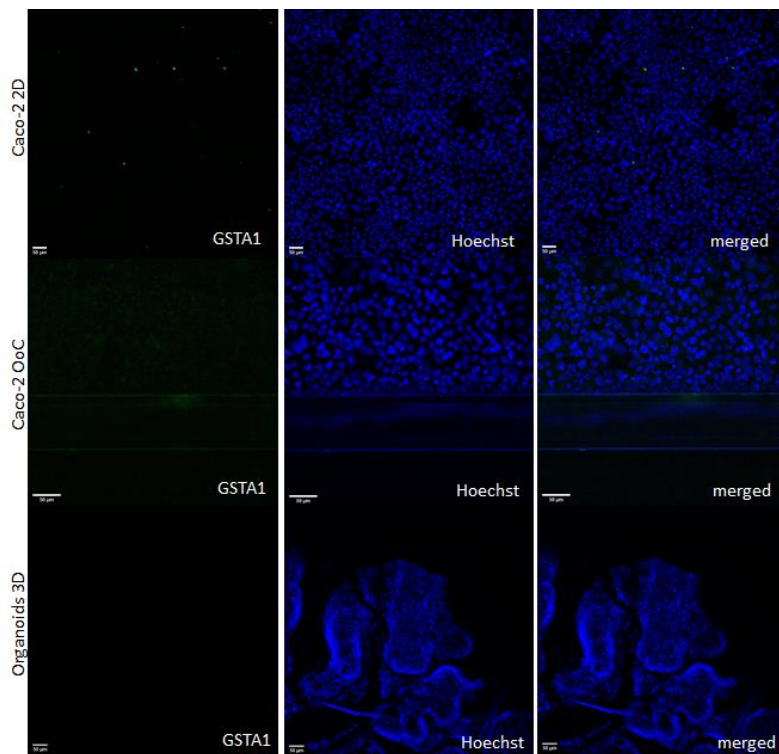


Figure 109: Immunofluorescent stainings with the antibody *GSTA1* to stain for a specific phase II enzyme. Shown are pictures of Caco-2 2D (pictures above), Caco-2 OoC (pictures in the middle) and colon organoids 3D (pictures below). Nuclei were counterstained with Hoechst (blue). 10x magnification, bar = 50 $\mu$ m for 2D and 3D, 20x magnification, bar = 50 $\mu$ m for OoC.



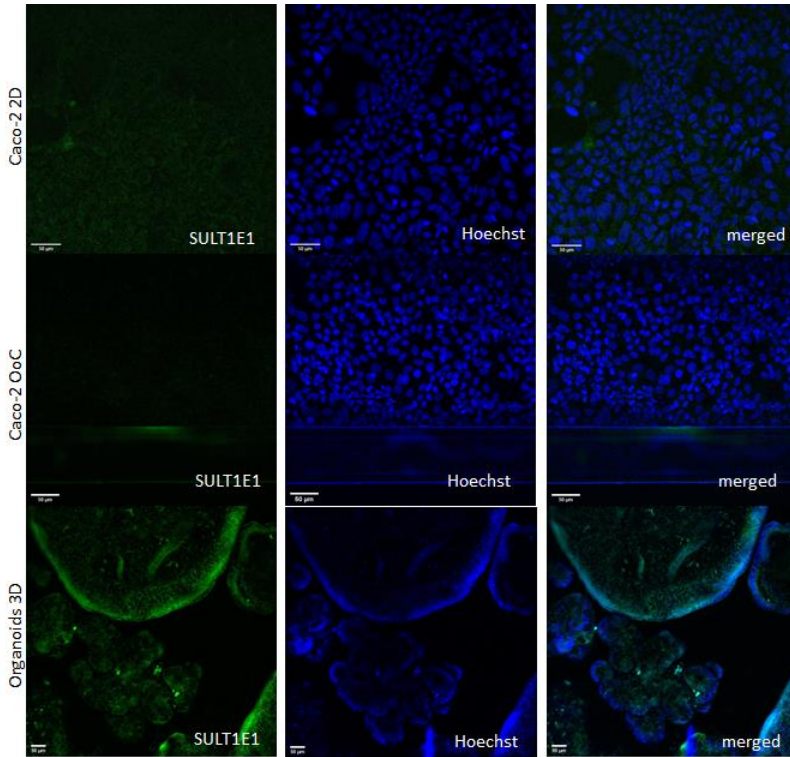


Figure 110: Immunofluorescent stainings with the the antibody *SULT1E1* to stain for a specific phase II enzyme. Shown are pictures of Caco-2 2D (pictures above), Caco-2 OoC (pictures in the middle) and colon organoids 3D (pictures below). Nuclei were counterstained with Hoechst (blue). 10x magnification, bar = 50µm for 3D, 20x magnification, bar = 50µm for 2D and OoC.

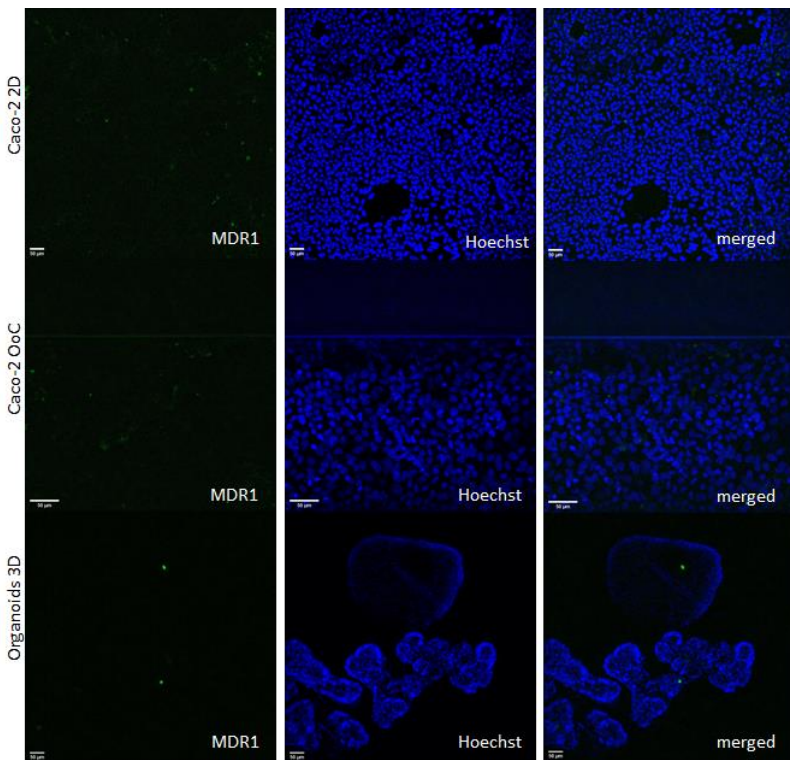


Figure 111: Immunofluorescent stainings with the antibody *MDR1* to stain for a specific phase III enzyme. Shown are pictures of Caco-2 2D (pictures above), Caco-2 OoC (pictures in the middle) and colon organoids 3D (pictures below). Nuclei were counterstained with Hoechst (blue). 10x magnification, bar = 50µm for 2D and 3D, 20x magnification, bar = 50µm for OoC.

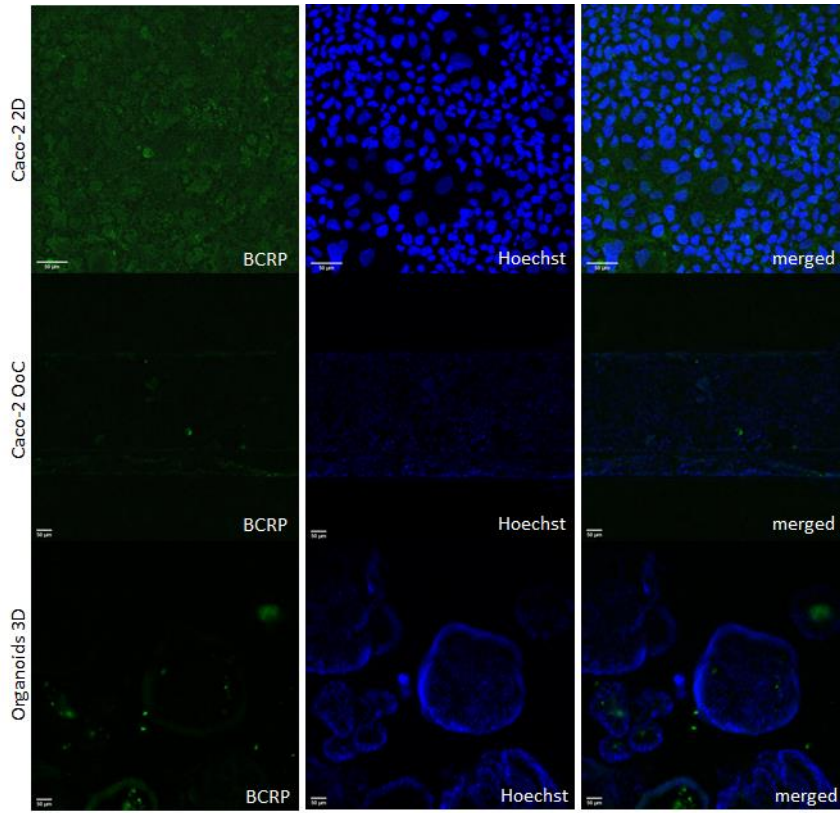


Figure 112: Immunofluorescent stainings with the antibody *BCRP* to stain for a specific phase III enzyme. Shown are pictures of Caco-2 2D (pictures above), Caco-2 OoC (pictures in the middle) and colon organoids 3D (pictures below). Nuclei were counterstained with Hoechst (blue). 10x magnification, bar = 50 $\mu$ m for 3D and OoC, 20x magnification, bar = 50 $\mu$ m for 2D.

#### Appendix 4: Overview of the differences in shape, size and structure of the organoids

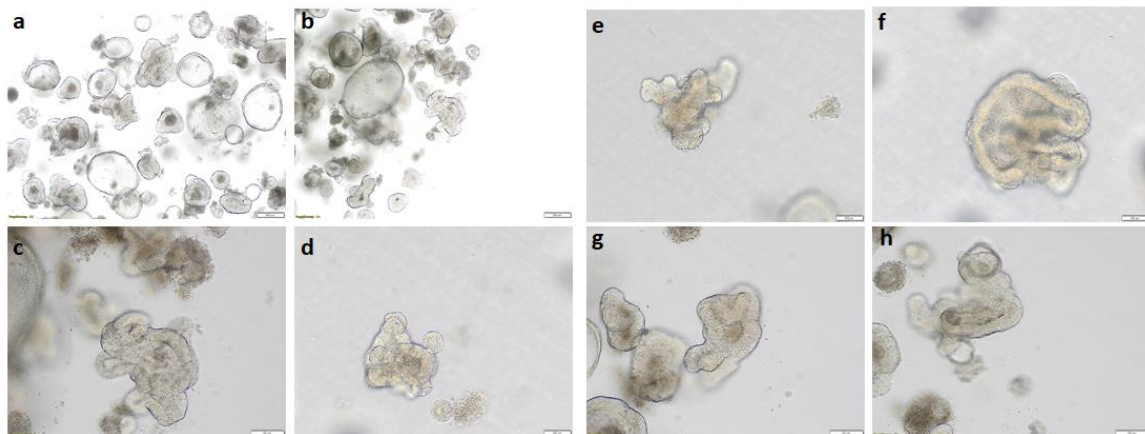


Figure 113: Overview of differences in size, shape and structure of iPSC derived colon organoids. All images were taken at day 6 after seeding. a-b) 4x magnification and bar = 200 $\mu$ m. c-h) 10x magnification and bar = 100 $\mu$ m.

## Appendix 5: Fold changes in gene expression for functional characterization of the used cell culture models

Table 41: Results from two replicates of the gene expression of phase I enzymes for the functional characterization of the three cell culture models. Values are normalized to the gene expression of the housekeepers *PPIA*, *PIB*, *HPRT1* and *LDHA* and given as fold changes towards the vehicle control.

		Caco-2 2D	Caco-2 OoC	Organoids 3D
CYP2C19	N=1	0.99	1.50	0.97
	N=2	1.06	1.08	1.21
CYP2C9	N=1	0.93	0.70	1.09
	N=2	0.96	0.95	1.46
CYP3A4	N=1	NA	0.75	0.46
	N=2	NA	NA	NA

Table 42: Results from two replicates of the gene expression phase II enzymes for the functional characterization of the three cell culture models. Values are normalized to the gene expression of the housekeepers *PPIA*, *PIB*, *HPRT1* and *LDHA* and given as fold changes towards the vehicle control.

		Caco-2 2D	Caco-2 OoC	Organoids 3D
SULT1A1	N=1	1.16	NA	1.38
	N=2	1.01	1.15	1.62
SULT1E1	N=1	1.04	NA	1.19
	N=2	0.93	1.38	1.25
UGT1A6	N=1	1.93	NA	2.94
	N=2	0.88	0.9	1.4
GSTA1	N=1	0.86	NA	2.26
	N=2	1.82	1.49	2.73
UGT2B7	N=1	1.02	NA	0.83
	N=2	1	1.04	1.16

Table 43: Results from two replicates of the gene expression of efflux transporter for the functional characterization of the three cell culture models. Values are normalized to the gene expression of the housekeepers *PPIA*, *PIB*, *HPRT1* and *LDHA* and given as fold changes towards the vehicle control.

		Caco-2 2D	Caco-2 OoC	Organoids 3D
ABCB1 /MDR1	N=1	NA	0.68	NA
	N=2	0.75	0.73	NA
ABCC1 /MRP1	N=1	1.09	0.97	NA
	N=2	0.97	1	NA
ABCC2 /MRP2	N=1	1.15	1.06	1.1
	N=2	1.11	1.19	1.16
ABCC3 /MRP3	N=1	1.06	0.92	1
	N=2	1.21	1.03	1.18
ABCG2 /BCRP	N=1	NA	0.78	1.76
	N=2	0.86	1	1.91

Table 44: Results from two replicates of the gene expression of uptake transporter for the functional characterization of the three cell culture models. Values are normalized to the gene expression of the housekeepers *PPIA*, *PIB*, *HPRT1* and *LDHA* and given as fold changes towards the vehicle control.

		Caco-2 2D	Caco-2 OoC	Organoids 3D
SLC22A1/OCT-1	N=1	NA	0.86	0.8
	N=2	1.45	0.71	NA
SLC22A2/OCT-2	N=1	NA	1.13	NA
	N=2	NA	NA	NA
SLC2A2/GLUT-2	N=1	0.73	1.34	1.29
	N=2	1.3	1.09	0.72
SLC5A1/SGLT-1	N=1	1.11	0.88	0.49
	N=2	-3.59	NA	1.49
SLC5A2/SGLT-2	N=1	0.99	0.91	1.04
	N=2	0.99	1.05	1.12
SLC51A/OSTalpha	N=1	0.56	0.39	0.27
	N=2	0.52	0.5	1.26
SLC01A2/ OATP1A2	N=1	0.91	1.02	0.52
	N=2	1.03	0.91	NA
SLC02B1/OATP	N=1	1.07	1.05	0.93
	N=2	1.11	1.14	1.31
SLC10A2/ASBT	N=1	NA	1.13	0.55
	N=2	0.35	1.32	-0.19
SLC16A1/MCT-1	N=1	1.06	1.08	1.26
	N=2	1.12	1.09	1.42

Table 45: Results from two replicates of the gene expression of two mucins for the functional characterization of the three cell culture models. Values are normalized to the gene expression of the housekeepers *PPIA*, *PIB*, *HPRT1* and *LDHA* and given as fold changes towards the vehicle control.

		Caco-2 2D	Caco-2 OoC	Organoids 3D
Muc2	N=1	0	0	0.64
	N=2	0.1	0	1.29
Muc5Ac	N=1	0	0	0.41
	N=2	0.9	0	0

## Appendix 6: Luminescence signals of the ATP measurements for the comparative study on the evaluation of cytotoxic effects of compounds

Table 46: Luminescence signals of the ATP measurements after the treatment with Gefitinib for 24h in the Caco-2 2D model

N=1 Luminescence signal Caco-2 2D after treatment with <b>Gefitinib</b>							
	Replicate	Replicate	Replicate	Mean	Mean-Mean_Blank	SD	% Viability
0.1µM	45877	40856	41423	42719	42272	2750	104.5
0.3µM	47601	47675	42718	45998	45551	2841	112.6
1µM	35113	44608	41178	40300	39853	4808	98.5
3µM	40576	39633	38445	39551	39104	1068	96.7
10µM	36333	39343	36503	37393	36946	1691	91.3
30µM	39834	40079	42862	40925	40478	1682	100.1
100µM	43318	46243	36649	42070	41623	4917	102.9
300µM	580	447	708	578	131	131	0.3

N=2 Luminescence signal Caco-2 2D after treatment with <b>Gefitinib</b>							
	Replicate	Replicate	Replicate	Mean	Mean-Mean_Blank	SD	% Viability
0.1µM	35411	29468	31360	32080	31500	3036	73.3
0.3µM	30822	34595	29716	31711	31131	2558	72.5
1µM	30563	28229	29040	29277	28697	1185	66.8
3µM	30661	28627	27251	28846	28266	1716	65.8
10µM	27738	29833	29459	29010	28430	1117	66.2
30µM	30855	25532	27532	27973	27393	2689	63.8
100µM	18391	21567	28277	22745	22165	5047	51.7
300µM	167	241	247	218	-362	45	-0.4

N=3 Luminescence signal Caco-2 2D after treatment with <b>Gefitinib</b>							
	Replicate	Replicate	Replicate	Mean	Mean-Mean_Blank	SD	% Viability
0.1µM	20763	18420	24983	21389	20809	3326	62.5
0.3µM	8909	708	25675	11764	11184	12726	34.0
1µM	10468	829	22087	11128	10548	10644	32.1
3µM	31216	22256	28749	27407	26827	4628	80.3
10µM	28527	4253	17847	16876	16296	12166	49.1
30µM	19870	23256	10090	17739	17159	6837	51.7
100µM	36517	22708	33095	30773	30193	7191	90.3
300µM	21283	23484	21324	22030	21450	1259	64.4

Table 47: Luminescence signals of the ATP measurements after treatment with Alosetron for 24h in the Caco-2 2D model

N=1 Luminescence signal Caco-2 2D after treatment with <b>Alosetron</b>							
	Replicate	Replicate	Replicate	Mean	Mean-Mean_Blank	SD	% Viability
0.1µM	42142	39698	50283	44041	43461	5542	104.5
0.3µM	45520	46694	49991	47402	46822	2318	112.6
1µM	43751	46691	47576	46006	45426	2002	98.5
3µM	49780	42978	46985	46581	46001	3419	96.7
10µM	47547	46252	45926	46575	45995	857	91.3
30µM	52013	45008	49231	48751	48171	3527	100.1
100µM	48787	44220	57508	50172	49592	6751	102.9
300µM	54827	45992	48686	49835	49255	4528	0.3

N=2 Luminescence signal Caco-2 2D after treatment with <b>Alosetron</b>							
	Replicate	Replicate	Replicate	Mean	Mean-Mean_Blank	SD	% Viability
0.1µM	42145	40229	42258	41544	40964	1140	95.2
0.3µM	35719	38398	37867	37328	36748	1419	85.5
1µM	41234	36055	40045	39111	38531	2713	89.6
3µM	41083	39127	39700	39970	39390	1006	91.6
10µM	40022	41603	40664	40763	40183	795	93.4
30µM	41944	37925	40899	40256	39676	2085	92.2
100µM	42681	36558	41502	40247	39667	3249	92.2
300µM	36075	36850	35896	36274	35694	507	83.0

N=3 Luminescence signal Caco-2 2D after treatment with <b>Alosetron</b>							
	Replicate	Replicate	Replicate	Mean	Mean-Mean_Blank	SD	% Viability
0.1µM	24103	2588	4943	10545	9965	11801	30.3
0.3µM	20127	25549	37412	27696	27116	8840	81.1
1µM	24075	30183	31730	28663	28083	4048	84.0
3µM	32559	38546	31514	34206	33626	3794	100.4
10µM	27199	11564	20238	19667	19087	7833	57.4
30µM	34135	994	13789	16306	15726	16713	47.4
100µM	29356	9643	32547	23849	23269	12405	69.7
300µM	31224	12250	39251	27575	26995	13865	80.8

Table 48: Luminescence signals of the ATP measurements after treatment with 5-FU for 24h in the Caco-2 2D model

Luminescence signal Caco-2 2D after treatment with 5-FU							
N=1					Mean-	SD	% Viability
	Replicate	Replicate	Replicate	Mean	Mean_Blank		
0.1µM	44354	44370	47136	45287	44707	1602	110.9
0.3µM	44755	47879	46538	46391	45811	1567	113.6
1µM	54808	44305	48958	49357	48777	5263	120.9
3µM	44499	50554	49297	48117	47537	3195	117.9
10µM	46676	51302	46836	48271	47691	2626	118.2
30µM	50215	49644	49050	49636	49056	583	121.6
100µM	59908	43472	54313	52564	51984	8356	128.9
300µM	65474	51312	54454	57080	56500	7437	140.0

Luminescence signal Caco-2 2D after treatment with 5-FU							
N=2					Mean-	SD	% Viability
	Replicate	Replicate	Replicate	Mean	Mean_Blank		
0.1µM	37094	40339	45149	40861	40281	4053	93.6
0.3µM	38567	42206	37602	39458	38878	2428	90.4
1µM	38524	40006	40894	39808	39228	1197	91.2
3µM	42437	40587	39469	40831	40251	1499	93.6
10µM	39938	42181	42072	41397	40817	1265	94.9
30µM	41381	48350	44211	44647	44067	3505	102.4
100µM	46343	48897	48559	47933	47353	1387	110.0
300µM	47312	53092	48971	49792	49212	2976	114.3

Luminescence signal Caco-2 2D after treatment with 5-FU							
N=3					Mean-	SD	% Viability
	Replicate	Replicate	Replicate	Mean	Mean_Blank		
0.1µM	40542	39361	357	26753	26173	22868	78.3
0.3µM	35353	31692	9507	25517	24937	13986	74.7
1µM	38167	8638	2279	16361	15781	19150	47.6
3µM	26626	35256	29187	30356	29776	4432	89.0
10µM	25134	27574	30332	27680	27100	2601	81.1
30µM	3007	9931	9395	7444	6864	3852	21.2
100µM	3007	9931	9395	7444	6864	3852	21.2
300µM	8570	1614	413	3532	2952	4404	9.6

Table 49: Luminescence signals of the ATP measurements after treatment with Diclofenac for 24h in the Caco-2 2D model

Luminescence signal Caco-2 2D after treatment with Diclofenac							
N=1					Mean-	SD	% Viability
	Replicate	Replicate	Replicate	Mean	Mean_Blank		
0.1µM	28889	41273	39830	36664	36084	6772	89.5
0.3µM	36669	43170	42899	40913	40333	3678	100.1
1µM	38636	37090	41187	38971	38391	2069	95.3
3µM	37806	41171	39468	39482	38902	1683	96.5
10µM	38332	44110	37282	39908	39328	3677	97.6
30µM	43283	46130	42569	43994	43414	1884	107.7
100µM	40163	48996	46186	45115	44535	4513	110.4
300µM	43569	52206	48972	48249	47669	4364	118.2

Luminescence signal Caco-2 2D after treatment with Diclofenac							
N=2					Mean-	SD	% Viability
	Replicate	Replicate	Replicate	Mean	Mean_Blank		
0.1µM	31646	29529	29730	30302	29722	1169	69.2
0.3µM	30086	29096	29856	29679	29099	518	67.8
1µM	32283	29967	31999	31416	30836	1263	71.8
3µM	33135	30441	29242	30939	30359	1994	70.7
10µM	31661	29537	29442	30213	29633	1255	69.0
30µM	31067	30714	30623	30801	30221	235	70.4
100µM	34610	31447	34411	33489	32909	1772	76.6
300µM	32648	31096	33698	32481	31901	1309	74.2

Luminescence signal Caco-2 2D after treatment with Diclofenac							
N=3					Mean-	SD	% Viability
	Replicate	Replicate	Replicate	Mean	Mean_Blank		
0.1µM	13676	23898	39864	25813	25233	13199	75.6
0.3µM	29203	8981	21889	20024	19444	10239	58.4
1µM	33061	12361	27376	24266	23686	10695	71.0
3µM	4089	12981	39659	18910	18330	18511	55.1
10µM	34055	32196	38664	34972	34392	3330	102.7
30µM	26355	25047	23177	24860	24280	1597	72.7
100µM	1202	1421	604	1076	496	423	2.3
300µM	6763	261	9408	5477	4897	4707	15.3

Table 50: Luminescence signals of the ATP measurements after treatment with Flavopiridol for 24h in the Caco-2 2D model

Luminescence signal Caco-2 2D after treatment with <b>Flavopiridol</b>							
N=1	Replicate	Replicate	Replicate	Mean	Mean- Mean_Blank	SD	% Viability
0.1µM	39432	50855	48170	46152	45572	5973	113.0
0.3µM	53169	49255	55080	52501	51921	2969	128.7
1µM	44834	47581	49083	47166	46586	2155	115.5
3µM	50514	43728	35858	43367	42787	7335	106.1
10µM	50851	50238	42162	47750	47170	4849	117.0
30µM	46523	54026	52094	50881	50301	3896	124.7
100µM	49506	48858	50255	49540	48960	699	121.4
300µM	38945	52281	33686	41637	41057	9585	101.8

Luminescence signal Caco-2 2D after treatment with <b>Flavopiridol</b>							
N=2	Replicate	Replicate	Replicate	Mean	Mean- Mean_Blank	SD	% Viability
0.1µM	40239	40523	39426	40063	39483	569	91.8
0.3µM	44099	43293	48754	45382	44802	2948	104.1
1µM	41091	42110	45692	42964	42384	2417	98.5
3µM	42982	42678	44742	43467	42887	1114	99.7
10µM	39851	47580	43412	43614	43034	3868	100.0
30µM	48683	48089	43491	46754	46174	2842	107.3
100µM	42069	54866	42738	46558	45978	7203	106.8
300µM	44492	49053	44960	46168	45588	2509	105.9

Luminescence signal Caco-2 2D after treatment with <b>Flavopiridol</b>							
N=3	Replicate	Replicate	Replicate	Mean	Mean- Mean_Blank	SD	% Viability
0.1µM	42342	36058	25145	34515	33935	8702	101.3
0.3µM	42842	31122	24548	32837	32257	9267	96.4
1µM	45353	31238	23927	33506	32926	10892	98.3
3µM	41979	35535	30829	36114	35534	5598	106.1
10µM	36926	32784	3774	24495	23915	18064	71.7
30µM	48821	33275	25222	35773	35193	11996	105.1
100µM	47776	36276	42679	42244	41664	5762	124.2
300µM	41799	39128	36675	39201	38621	2563	115.2

Table 51: Luminescence signals of the ATP measurements after treatment with Irinotecan for 24h in the Caco-2 2D model

Luminescence signal Caco-2 2D after treatment with <b>Irinotecan</b>							
N=1	Replicate	Replicate	Replicate	Mean	Mean- Mean_Blank	SD	% Viability
0.1µM	38219	44848	41650	41572	40992	3315	101.7
0.3µM	28230	35997	39770	34666	34086	5884	84.6
1µM	35151	36219	39066	36812	36232	2024	89.9
3µM	36032	38492	41324	38616	38036	2648	94.4
10µM	34014	39435	36406	36618	36038	2717	89.4
30µM	37943	38966	39053	38654	38074	617	94.5
100µM	38060	40416	43165	40547	39967	2555	99.1
300µM	37617	40252	40226	39365	38785	1514	96.2

Luminescence signal Caco-2 2D after treatment with <b>Irinotecan</b>							
N=2	Replicate	Replicate	Replicate	Mean	Mean- Mean_Blank	SD	% Viability
0.1µM	35517	40843	41247	39202	38622	3198	89.8
0.3µM	32986	40560	38779	37442	36862	3960	85.7
1µM	40624	39504	36619	38916	38336	2066	89.1
3µM	32931	42809	36097	37279	36699	5044	85.4
10µM	33560	40265	38089	37305	36725	3421	85.4
30µM	35996	42560	38275	38944	38364	3333	89.2
100µM	31057	40257	32993	34769	34189	4850	79.5
300µM	36008	43171	40384	39854	39274	3611	91.3

Luminescence signal Caco-2 2D after treatment with <b>irinotecan</b>							
N=3	Replicate	Replicate	Replicate	Mean	Mean- Mean_Blank	SD	% Viability
0.1µM	18546	12221	9808	13525	12945	4513	39.2
0.3µM	7940	19576	20310	15942	15362	6940	46.3
1µM	20628	24673	3788	16363	15783	11076	47.6
3µM	31449	30734	27053	29745	29165	2359	87.2
10µM	22666	28232	23440	24779	24199	3015	72.5
30µM	9594	26948	10052	15531	14951	9890	45.1
100µM	30391	26551	25923	27622	27042	2419	80.9
300µM	26216	30391	30163	28923	28343	2347	84.8



Table 52: Luminescence signals of the ATP measurements after treatment with Loperamide for 24h in the Caco-2 2D model

Luminescence signal Caco-2 2D after treatment with <b>Loperamide</b>							
	Replicate	Replicate	Replicate	Mean	Mean- Mean_Blank	SD	% Viability
0.1µM	40974	42490	42467	41977	41397	869	102.7
0.3µM	34273	34932	40034	36413	35833	3153	88.9
1µM	37040	33912	34016	34989	34409	1777	85.4
3µM	38441	35930	32762	35711	35131	2846	87.2
10µM	37548	35247	28575	33790	33210	4661	82.4
30µM	34192	33770	32964	33642	33062	624	82.1
100µM	16007	12760	13203	13990	13410	1761	33.5
300µM	415	349	422	395	-185	40	-0.1

Luminescence signal Caco-2 2D after treatment with <b>Loperamide</b>							
	Replicate	Replicate	Replicate	Mean	Mean- Mean_Blank	SD	% Viability
0.1µM	28913	32609	30986	30836	30256	1853	70.4
0.3µM	30005	30969	28549	29841	29261	1218	68.1
1µM	28284	32286	28228	29599	29019	2327	67.6
3µM	26769	31675	28299	28914	28334	2510	66.0
10µM	27525	31164	33300	30663	30083	2920	70.0
30µM	27399	25936	23661	25665	25085	1884	58.5
100µM	12638	7204	5732	8525	7945	3637	18.8
300µM	278	199	168	215	-365	57	-0.4

Luminescence signal Caco-2 2D after treatment with <b>Loperamide</b>							
	Replicate	Replicate	Replicate	Mean	Mean- Mean_Blank	SD	% Viability
0.1µM	26245	14525	31880	24217	23637	8854	70.8
0.3µM	22350	29225	30556	27377	26797	4404	80.2
1µM	24860	26257	29360	26826	26246	2303	78.6
3µM	22255	15239	25955	21150	20570	5443	61.8
10µM	19765	23475	24418	22553	21973	2460	65.9
30µM	18219	22836	26277	22444	21864	4043	65.6
100µM	16955	9656	17893	14835	14255	4509	43.1
300µM	471	288	224	328	-252	128	0.1

Table 53: Luminescence signals of the ATP measurements after treatment with Oxaliplatin for 24h in the Caco-2 2D model

Luminescence signal Caco-2 2D after treatment with <b>Oxaliplatin</b>							
	Replicate	Replicate	Replicate	Mean	Mean- Mean_Blank	SD	% Viability
0.1µM	38977	30510	27692	32393	31813	5873	95.0
0.3µM	28647	28923	28023	28531	27951	461	83.6
1µM	30848	30642	20459	27316	26736	5940	80.0
3µM	30441	30217	29204	29954	29374	659	87.8
10µM	29001	31426	30199	30209	29629	1213	88.6
30µM	28846	24911	27339	27032	26452	1985	79.2
100µM	37237	34987	26210	32811	32231	5827	96.3
300µM	44766	35887	37375	39343	38763	4755	115.6

Luminescence signal Caco-2 2D after treatment with <b>Oxaliplatin</b>							
	Replicate	Replicate	Replicate	Mean	Mean- Mean_Blank	SD	% Viability
0.1µM	44141	35641	47661	42481	41901	6180	93.7
0.3µM	31613	10679	38255	26849	26269	14392	58.9
1µM	45052	52247	45623	47641	47061	3999	105.1
3µM	28242	52510	5098	28617	28037	23708	62.9
10µM	51580	55530	3577	36896	36316	28922	81.3
30µM	54176	55927	5586	38563	37983	28572	85.0
100µM	20708	63102	66223	50011	49431	25425	110.4
300µM	57989	66513	72178	65560	64980	7142	145.0

Luminescence signal Caco-2 2D after treatment with <b>Oxaliplatin</b>							
	Replicate	Replicate	Replicate	Mean	Mean- Mean_Blank	SD	% Viability
0.1µM	38977	30510	27692	32393	31813	5873	95.0
0.3µM	28647	28923	28023	28531	27951	461	83.6
1µM	30848	30642	20459	27316	26736	5940	80.0
3µM	30441	30217	29204	29954	29374	659	87.8
10µM	29001	31426	30199	30209	29629	1213	88.6
30µM	28846	24911	27339	27032	26452	1985	79.2
100µM	37237	34987	26210	32811	32231	5827	96.3
300µM	44766	35887	37375	39343	38763	4755	115.6



Table 54: Luminescence signals of the ATP measurements after treatment with Terfenadine for 24h in the Caco-2 2D model

N=1 Luminescence signal Caco-2 2D after treatment with <b>Terfenadine</b>							
	Replicate	Replicate	Replicate	Mean	Mean-Mean_Blank	SD	% Viability
0.1µM	36732	35388	39605	37242	36662	2154	91.0
0.3µM	43799	39040	46259	43033	42453	3670	105.3
1µM	35672	43009	41934	40205	39625	3962	98.3
3µM	43850	37887	41732	41156	40576	3023	100.7
10µM	36867	38518	42200	39195	38615	2730	95.8
30µM	37511	38149	37734	37798	37218	324	92.4
100µM	571	465	568	535	-45	60	0.2
300µM	385	275	347	336	-244	56	-0.3

N=2 Luminescence signal Caco-2 2D after treatment with <b>Terfenadine</b>							
	Replicate	Replicate	Replicate	Mean	Mean-Mean_Blank	SD	% Viability
0.1µM	32021	27993	32980	30998	30418	2646	70.8
0.3µM	27746	30754	39462	32654	32074	6085	74.6
1µM	30402	28132	31893	30142	29562	1894	68.8
3µM	28915	27280	28144	28113	27533	818	64.1
10µM	30187	28656	30531	29791	29211	998	68.0
30µM	28329	26183	22618	25710	25130	2885	58.6
100µM	264	217	211	231	-349	29	-0.4
300µM	123	104	87	105	-475	18	-0.7

N=3 Luminescence signal Caco-2 2D after treatment with <b>Terfenadine</b>							
	Replicate	Replicate	Replicate	Mean	Mean-Mean_Blank	SD	% Viability
0.1µM	33302	32769	4965	23679	23099	16209	69.2
0.3µM	26368	15388	27072	22943	22363	6552	67.1
1µM	27805	21178	20561	23181	22601	4016	67.8
3µM	25720	2332	28070	18707	18127	14230	54.5
10µM	19844	16049	27635	21176	20596	5907	61.8
30µM	27369	22056	20145	23190	22610	3743	67.8
100µM	257	272	259	263	-317	8	-0.1
300µM	131	116	142	130	-450	13	-0.5

Table 55: Luminescence signals of the ATP measurements after treatment with Staurosporine for 24h in the Caco-2 2D model

N=1 Luminescence signal Caco-2 2D after treatment with <b>Staurosporine</b>							
	Replicate	Replicate	Replicate	Mean	Mean-Mean_Blank	SD	% Viability
0.1µM	37079	55380	45548	46002	45422	9159	101.5
0.3µM	15035	37242	29326	27201	26621	11255	59.7
1µM	25370	21291	14193	20285	19705	5656	44.3
3µM	8946	10552	14990	11496	10916	3131	24.8
10µM	808	530	5109	2149	1569	2567	4.0
30µM	4178	3041	2893	3371	2791	703	6.7
100µM	629	594	664	629	49	35	0.6
300µM	616	533	948	699	119	220	0.8

N=2 Luminescence signal Caco-2 2D after treatment with <b>Staurosporine</b>							
	Replicate	Replicate	Replicate	Mean	Mean-Mean_Blank	SD	% Viability
0.1µM	20563	27023	26635	24740	24160	3623	72.4
0.3µM	5249	11798	6147	7731	7151	3550	22.0
1µM	330	649	6302	2427	1847	3360	6.3
3µM	630	2788	11446	4955	4375	5724	13.8
10µM	7875	3245	2629	4583	4003	2868	12.7
30µM	1141	2188	1175	1501	921	595	3.6
100µM	398	189	189	259	-321	121	-0.1
300µM	355	151	142	216	-364	120	-0.2

N=3 Luminescence signal Caco-2 2D after treatment with <b>Staurosporine</b>							
	Replicate	Replicate	Replicate	Mean	Mean-Mean_Blank	SD	% Viability
0.1µM	14012	6899	27562	16158	15578	10497	29.7
0.3µM	2043	19613	21192	14283	13703	10629	26.2
1µM	918	455	7179	2851	2271	3756	4.8
3µM	555	2957	1707	1740	1160	1201	2.7
10µM	1595	579	6197	2790	2210	2994	4.7
30µM	1803	4705	7628	4712	4132	2913	8.3
100µM	371	201	142	238	-342	119	-0.1
300µM	528	174	113	272	-308	224	-0.1

Table 56. Luminescence signals of the ATP measurements after treatment with Metformin 750µM (a) and 0.5% DMSO (b) for 24h in the Caco-2 2D model

**a**

Luminescence signal Caco-2 2D after treatment with <b>Metformin 750µM</b>							
	Replicate	Replicate	Replicate	Mean	Mean-Mean_Blank	SD	% Viability
Metformin 750µM	39304	32639	31376	34439.7	34159	4259.71	104.3
Metformin 750µM	2767	99984	82362	61704.3	61403	51796.1	162.0
Metformin 750µM	36694	12097	41959	30250	29910	15939.8	66.5
Metformin 750µM	39304	32639	31376	34439.7	34141.9	4259.71	104.3
Metformin 750µM	45549	49125	43920	46198	45792.8	2662.5	106.2
Metformin 750µM	43742	45964	42291	43999	43548.7	1849.94	107.7

**b**

Luminescence signal Caco-2 2D after treatment with <b>DMSO 0.5%</b>							
	Replicate	Replicate	Replicate	Mean	Mean-Mean_Blank	SD	% Viability
DMSO 0.5%	33789	33246	32090	33041.7	32761	867.735	100.0
DMSO 0.5%	3253	99984	11394	38210.3	37909	53652.2	100.0
DMSO 0.5%	46853	38118	51014	45328.3	44988.3	6581.81	100.0
DMSO 0.5%	33789	33246	32090	33041.7	32743.9	867.735	100.0
DMSO 0.5%	46278	43684	40563	43508.3	43103.1	2861.55	100.0
DMSO 0.5%	39603	41462	41609	40891.3	40441	1118.15	100.0

Table 57: Luminescence signals of the ATP measurements after treatment with Gefitinib for 24h in the Caco-2 OoC model

Luminescence signal Caco-2 OoC after treatment with <b>Gefitinib</b>							
N=1	Replicate	Replicate	Replicate	Mean	Mean-Mean_Blank	SD	% Viability
0.1µM	42902	48580	39031	43504	39819	4803	102.4%
0.3µM	48436	39777	38467	42227	38541	5417	99.1%
1µM	42172	46654	47907	45578	41892	3015	107.7%
3µM	44197	45861	49192	46417	42731	2543	109.9%
10µM	35930	34374	48521	39608	35923	7758	92.4%
30µM	40830	41373	38283	40162	36477	1650	93.8%
100µM	39131	46376	41229	42245	38560	3728	99.2%
300µM	39490	34666	39766	37974	34289	2868	88.2%

Luminescence signal Caco-2 OoC after treatment with <b>Gefitinib</b>							
N=2	Replicate	Replicate	Replicate	Mean	Mean-Mean_Blank	SD	% Viability
0.1µM	56826	55510	62928	58421	58421	3958	105.0%
0.3µM	58276	43427	53693	51799	51799	7604	93.1%
1µM	51481	56183	49247	52304	52304	3540	94.0%
3µM	44623	41422	50659	45568	45568	4690	81.9%
10µM	47594	29255	38991	38613	38613	9175	69.4%
30µM	19514	28326	21642	23161	23161	4598	41.6%
100µM	5259	13105	1659	6674	6674	5853	12.0%
300µM	772	19	39	277	277	429	0.5%

Luminescence signal Caco-2 OoC after treatment with <b>Gefitinib</b>							
N=3	Replicate	Replicate	Replicate	Mean	Mean-Mean_Blank	SD	% Viability
0.1µM	10327	8769	12063	10386	10376	1648	71.3%
0.3µM	12591	13621	14629	13614	13603	1019	93.5%
1µM	12688	11816	22327	15610	15600	5833	107.2%
3µM	13381	15153	15604	14713	14702	1175	101.0%
10µM	14858	10562	12657	12692	12682	2148	87.2%
30µM	12216	10390	12297	11634	11624	1078	79.9%
100µM	13108	10910	12321	12113	12102	1114	83.2%
300µM	10589	3986	5906	6827	6816	3396	46.8%

Table 58: Luminescence signals of the ATP measurements after treatment with Alosetron for 24h in the Caco-2 OoC model

N=1	Luminescence signal Caco-2 OoC after treatment with <b>Alosetron</b>						
	Replicate	Replicate	Replicate	Mean	Mean-Mean_Blank	SD	% Viability
0.1µM	37812	36549	38366	37576	37576	931	102.1%
0.3µM	30517	38489	28484	32497	32497	5288	88.3%
1µM	36234	36978	28007	33740	33740	4979	91.7%
3µM	42557	46568	32665	40597	40597	7156	110.3%
10µM	34964	34527	36904	35465	35465	1265	96.3%
30µM	45576	38211	30636	38141	38141	7470	103.6%
100µM	35362	39778	36768	37303	37303	2256	101.3%
300µM	32209	40916	34734	35953	35953	4480	97.7%

N=2	Luminescence signal Caco-2 OoC after treatment with <b>Alosetron</b>						
	Replicate	Replicate	Replicate	Mean	Mean-Mean_Blank	SD	% Viability
0.1µM	8709	10334	9849	9631	9626	834	76.8%
0.3µM	13125	11618	13466	12736	12731	983	101.6%
1µM	13902	11175	15342	13473	13468	2116	107.5%
3µM	14419	12595	15726	14247	14242	1573	113.6%
10µM	13906	11952	14379	13412	13407	1287	107.0%
30µM	16185	12321	13812	14106	14101	1949	112.5%
100µM	16620	13404	13764	14596	14591	1762	116.4%
300µM	5477	12886	17017	11793	11788	5847	94.1%

N=3	Luminescence signal Caco-2 OoC after treatment with <b>Alosetron</b>						
	Replicate	Replicate	Replicate	Mean	Mean-Mean_Blank	SD	% Viability
0.1µM	11470	27579	4196	14415	14161	11966	57.9%
0.3µM	17473	39797	40805	32692	32438	13189	132.6%
1µM	34707	7512	8428	16882	16629	15443	68.0%
3µM	35016	41628	35784	37476	37222	3616	152.1%
10µM	10004	23564	37799	23789	23535	13899	96.2%
30µM	23634	22493	23551	23226	22972	636	93.9%
100µM	40714	36923	29745	35794	35540	5571	145.2%
300µM	19674	33778	40297	31250	30996	10541	126.7%

Table 59: Luminescence signals of the ATP measurements after treatment with 5-FU for 24h in the Caco-2 OoC model

N=1	Luminescence signal Caco-2 OoC after treatment with <b>5-FU</b>						
	Replicate	Replicate	Replicate	Mean	Mean-Mean_Blank	SD	% Viability
0.1µM	14315	15286	4592	9939	9858	7562	75.5%
0.3µM	11283	14548	7782	11165	11085	4784	84.8%
1µM	15075	17517	17207	17362	17282	219	132.3%
3µM	11963	15003	10385	12694	12614	3265	96.6%
10µM	10915	15339	13837	14588	14508	1062	111.1%
30µM	15211	15609	14293	14951	14871	931	113.8%
100µM	18083	16307	14616	15462	15381	1196	117.7%
300µM	14226	15187	15575	15381	15301	274	117.1%

N=2	Luminescence signal Caco-2 OoC after treatment with <b>5-FU</b>						
	Replicate	Replicate	Replicate	Mean	Mean-Mean_Blank	SD	% Viability
0.1µM	44503	53318	57747	51856	51856	6742	93.2%
0.3µM	47078	63555	64617	58417	58417	9834	105.0%
1µM	65857	62187	63340	63795	63795	1877	114.7%
3µM	43014	54804	59694	52504	52504	8575	94.4%
10µM	21241	37851	62169	40420	40420	20585	72.7%
30µM	12595	60511	32117	35074	35074	24095	63.1%
100µM	59613	54590	61601	58601	58601	3613	105.4%
300µM	53526	59115	52895	55179	55179	3424	99.2%

N=3	Luminescence signal Caco-2 OoC after treatment with <b>5-FU</b>						
	Replicate	Replicate	Replicate	Mean	Mean-Mean_Blank	SD	% Viability
0.1µM	9435	16760	18299	14831	14810	4736	89.6%
0.3µM	18830	18259	18294	18461	18439	320	111.6%
1µM	20351	17456	18571	18793	18771	1460	113.6%
3µM	19131	18479	20644	19418	19396	1111	117.4%
10µM	20473	21592	23938	22001	21979	1768	133.0%
30µM	21869	20960	21089	21306	21284	492	128.8%
100µM	21246	19294	22393	20978	20956	1567	126.8%
300µM	14773	17065	15569	15802	15781	1164	95.5%

Table 60: Luminescence signals of the ATP measurements after treatment with Diclofenac for 24h in the Caco-2 OoC model

Luminescence signal Caco-2 OoC after treatment with <b>Diclofenac</b>							
N=1	Replicate	Replicate	Replicate	Mean	Mean- Mean_Blank	SD	% Viability
0.1µM	12356	15473	14000	13943	13943	1559	109.6%
0.3µM	14848	15292	15570	15237	15237	364	119.8%
1µM	14022	15504	16140	15222	15222	1087	119.6%
3µM	14794	15627	18322	16248	16248	1844	127.7%
10µM	13913	14601	11727	13414	13414	1501	105.4%
30µM	15310	15994	16815	16040	16040	754	126.1%
100µM	13396	15044	15290	14577	14577	1030	114.6%
300µM	10470	14038	8134	10881	10881	2973	85.5%

Luminescence signal Caco-2 OoC after treatment with <b>Diclofenac</b>							
N=2	Replicate	Replicate	Replicate	Mean	Mean- Mean_Blank	SD	% Viability
0.1µM	12183	17194	14971	14783	14778	2511	117.9%
0.3µM	15461	15887	15146	15498	15493	372	123.6%
1µM	13300	15490	13380	14057	14052	1242	112.1%
3µM	15282	16675	15267	15741	15736	809	125.6%
10µM	14728	17073	14714	15505	15500	1358	123.7%
30µM	14376	17397	15070	15614	15609	1582	124.5%
100µM	13974	19155	15987	16372	16367	2612	130.6%
300µM	14618	14905	15824	15116	15111	630	120.6%

Luminescence signal Caco-2 OoC after treatment with <b>Diclofenac</b>							
N=3	Replicate	Replicate	Replicate	Mean	Mean- Mean_Blank	SD	% Viability
0.1µM	37441	48738	20514	35564	35311	14205	144.3%
0.3µM	41776	51992	50152	47973	47720	5445	195.0%
1µM	43034	44633	40522	42730	42476	2072	173.6%
3µM	46577	35262	40384	40741	40487	5666	165.5%
10µM	39006	33535	24832	32458	32204	7148	131.6%
30µM	19771	42040	54810	38874	38620	17733	157.8%
100µM	42176	48895	44576	45216	44962	3405	183.7%
300µM	38705	46202	46729	43879	43625	4488	178.3%

Table 61: Luminescence signals of the ATP measurements after treatment with Flavopiridol for 24h in the Caco-2 OoC model

Luminescence signal Caco-2 OoC after treatment with <b>Flavopiridol</b>							
N=1	Replicate	Replicate	Replicate	Mean	Mean- Mean_Blank	SD	% Viability
0.1µM	50469	48762	71317	56849	53164	12558	214.4%
0.3µM	46433	65714	81626	64591	60906	17623	245.6%
1µM	58662	68187	49531	58793	55108	9329	222.2%
3µM	55338	56465	54888	55564	51878	812	209.2%
10µM	62967	49002	61742	57904	54218	7733	218.6%
30µM	60275	54502	72388	62388	58703	9128	236.7%
100µM	49232	67112	65002	60449	56763	9771	228.9%
300µM	79180	58600	72394	70058	66373	10487	267.6%

Luminescence signal Caco-2 OoC after treatment with <b>Flavopiridol</b>							
N=2	Replicate	Replicate	Replicate	Mean	Mean- Mean_Blank	SD	% Viability
0.1µM	11023	6972	10501	9499	9494	2204	75.8%
0.3µM	13273	18411	15724	15803	15798	2570	126.1%
1µM	15732	17794	14635	16054	16049	1604	128.1%
3µM	16410	18158	13675	16081	16076	2260	128.3%
10µM	16968	14006	18015	16330	16325	2079	130.3%
30µM	19262	16884	16698	17608	17603	1435	140.5%
100µM	25152	19702	17101	20652	20647	4109	164.7%
300µM	7926	18951	16316	14398	14393	5757	114.8%

Luminescence signal Caco-2 OoC after treatment with <b>Flavopiridol</b>							
N=3	Replicate	Replicate	Replicate	Mean	Mean- Mean_Blank	SD	% Viability
0.1µM	24351	4762	8590	12568	12314	10383	50.3%
0.3µM	24578	25308	16918	22268	22014	4648	90.0%
1µM	23456	27320	23785	24854	24600	2142	100.5%
3µM	18499	17329	14779	16869	16615	1902	67.9%
10µM	39500	28986	53807	40764	40511	12459	165.5%
30µM	45030	40840	61086	48985	48732	10687	199.1%
100µM	46765	51119	44158	47347	47094	3517	192.4%
300µM	18627	48329	35778	34245	33991	14910	138.9%

Table 62: Luminescence signals of the ATP measurements after treatment with Irinotecan for 24h in the Caco-2 OoC model

N=1 Luminescence signal Caco-2 OoC after treatment with <b>Irinotecan</b>							
	Replicate	Replicate	Replicate	Mean	Mean-Mean_Blank	SD	% Viability
0.1µM	11442	14063	13465	12990	12990	1374	102.1%
0.3µM	15023	14003	12964	13997	13997	1030	110.0%
1µM	14725	14590	13457	14257	14257	696	112.1%
3µM	15024	16032	15059	15372	15372	572	120.8%
10µM	15096	15943	14680	15240	15240	644	119.8%
30µM	12663	14415	14153	13744	13744	945	108.0%
100µM	10069	13691	13780	12513	12513	2117	98.4%
300µM	10008	6892	10077	8992	8992	1819	70.7%

N=2 Luminescence signal Caco-2 OoC after treatment with <b>Irinotecan</b>							
	Replicate	Replicate	Replicate	Mean	Mean-Mean_Blank	SD	% Viability
0.1µM	10683	12558	14405	12549	12544	1861	100.1%
0.3µM	11105	13444	12241	12263	12258	1170	97.8%
1µM	11996	14163	13550	13236	13231	1117	105.6%
3µM	10590	13094	15160	12948	12943	2288	103.3%
10µM	11886	15120	15074	14027	14022	1854	111.9%
30µM	12323	15948	14665	14312	14307	1838	114.2%
100µM	13272	14355	15650	14426	14421	1191	115.1%
300µM	9824	13715	13380	12306	12301	2156	98.2%

N=3 Luminescence signal Caco-2 OoC after treatment with <b>irinotecan</b>							
	Replicate	Replicate	Replicate	Mean	Mean-Mean_Blank	SD	% Viability
0.1µM	34758	39619	40542	38306	38053	3107	155.5%
0.3µM	41411	41956	52319	45229	44975	6146	183.8%
1µM	40371	45763	52467	46200	45947	6060	187.8%
3µM	38636	42929	22904	34823	34569	10543	141.3%
10µM	37241	44505	17411	33052	32799	14024	134.0%
30µM	38004	45735	41168	41636	41382	3887	169.1%
100µM	37144	35328	38230	36901	36647	1466	149.8%
300µM	18615	29180	28096	25297	25043	5812	102.3%

Table 63: Luminescence signals of the ATP measurements after treatment with Loperamide for 24h in the Caco-2 OoC model

N=1 Luminescence signal Caco-2 OoC after treatment with <b>Loperamide</b>							
	Replicate	Replicate	Replicate	Mean	Mean-Mean_Blank	SD	% Viability
0.1µM	46798	46156	44190	45715	44123	1359	134.1%
0.3µM	46437	46689	45691	46272	44680	519	135.8%
1µM	49444	45356	35588	43463	41871	7119	127.2%
3µM	42358	38829	36503	39230	37638	2948	114.4%
10µM	42358	42035	42876	42423	40831	424	124.1%
30µM	47690	37333	40686	41903	40311	5285	122.5%
100µM	10975	9181	10208	10121	8529	900	25.9%
300µM	142	164	98	135	-1457	34	-4.4%

N=2 Luminescence signal Caco-2 OoC after treatment with <b>Loperamide</b>							
	Replicate	Replicate	Replicate	Mean	Mean-Mean_Blank	SD	% Viability
0.1µM	14814	14814	11794	13807	13797	1744	94.8%
0.3µM	18687	18913	20901	19500	19490	1218	134.0%
1µM	16209	19771	20040	18673	18663	2138	128.3%
3µM	16278	17331	16648	16752	16742	534	115.1%
10µM	16990	16558	16733	16760	16750	217	115.1%
30µM	11156	16477	16626	14753	14742	3116	101.3%
100µM	8087	9019	9008	8705	8694	535	59.8%
300µM	97	68	27	64	53	35	0.4%

N=3 Luminescence signal Caco-2 OoC after treatment with <b>Loperamide</b>							
	Replicate	Replicate	Replicate	Mean	Mean-Mean_Blank	SD	% Viability
0.1µM	16786	17604	16668	17019	17009	510	103.0%
0.3µM	24052	22114	20214	22127	22116	1919	133.9%
1µM	24973	24855	22326	24051	24041	1495	145.5%
3µM	24458	19980	23479	22639	22628	2354	137.0%
10µM	21940	20889	22118	21649	21638	664	131.0%
30µM	21759	18127	19269	19718	19708	1857	119.3%
100µM	2735	2715	3987	3146	3135	729	19.0%
300µM	30	36	47	38	27	9	0.2%

Table 64: Luminescence signals of the ATP measurements after treatment with Oxaliplatin for 24h in the Caco-2 OoC model

Luminescence signal Caco-2 OoC after treatment with <b>Terfenadine</b>							
	Replicate	Replicate	Replicate	Mean	Mean-Mean_Blank	SD	% Viability
0.1µM	53222	247	49681	34383	34383	29616	138.6%
0.3µM	45425	61066	53021	53171	53171	7822	214.4%
1µM	53558	46174	62131	53954	53954	7986	217.6%
3µM	143	42305	53321	31923	31923	28068	128.7%
10µM	194	225	32742	11054	11054	18783	44.6%
30µM	311	40	209	187	187	137	0.8%
100µM	374	818	178	457	457	328	1.8%
300µM	480	405	189	358	358	151	1.4%

Luminescence signal Caco-2 OoC after treatment with <b>Terfenadine</b>							
	Replicate	Replicate	Replicate	Mean	Mean-Mean_Blank	SD	% Viability
0.1µM	10681	12747	10429	11286	11275	1272	77.5%
0.3µM	15072	17201	16609	16294	16283	1099	111.9%
1µM	17559	17742	19406	18236	18225	1018	125.3%
3µM	16641	17638	17146	17142	17131	499	117.7%
10µM	16938	18528	16957	17474	17464	913	120.0%
30µM	1505	10938	6010	6151	6140	4718	42.2%
100µM	10	42	60	37	27	25	0.2%
300µM	5	14	10	10	-1	5	0.0%

Luminescence signal Caco-2 OoC after treatment with <b>Terfenadine</b>							
	Replicate	Replicate	Replicate	Mean	Mean-Mean_Blank	SD	% Viability
0.1µM	34822	8930	12908	18887	18633	13943	76.1%
0.3µM	47443	28612	10891	28982	28728	18279	117.4%
1µM	45712	44714	15655	35360	35107	17073	143.5%
3µM	45216	44688	34398	41434	41180	6099	168.3%
10µM	21591	51333	4430	25785	25531	23731	104.3%
30µM	8133	18516	2832	9827	9573	7978	39.1%
100µM	757	149	38	315	61	387	0.2%
300µM	122	88	21	77	-177	51	-0.7%

Table 65: Luminescence signals of the ATP measurements after treatment with 0.5% DMSO (a) and Metformin 750µM (b) for 24h in the Caco-2 OoC model

Luminescence signal Caco-2 3D after treatment with <b>DMSO 0.5%</b>							
	Replicate	Replicate	Replicate	Mean	Mean-Mean_Blank	SD	% Viability
DMSO 0.5%	46304	38837	315	28485.3	24800	24680.3	100.0%
DMSO 0.5%	12836	15671	10926	13144.3	13064	2387.48	100.0%
DMSO 0.5%	38644	35225	36560	36809.7	36809.7	1723.12	100.0%
DMSO 0.5%	15272	42308	45919	34499.7	32907.6	16749.2	100.0%
DMSO 0.5%	52801	60788	53263	55617.3	55617.3	4483.88	100.0%
DMSO 0.5%	11877	13323	12968	12722.7	12722.7	753.572	100.0%
DMSO 0.5%	15710	13003	14968	14560.3	14549.7	1398.79	100.0%
DMSO 0.5%	13202	12963	11448	12537.7	12532.7	951.215	100.0%
DMSO 0.5%	17582	16038	16026	16548.7	16527	894.913	100.0%
DMSO 0.5%	39455	17864	16854	24724.3	24470.7	12767.1	100.0%
DMSO 0.5%	29394	35196	45486	36692	36663.3	8149.64	100.0%
DMSO 0.5%	25542	27070	34031	28881	28862.7	4524.99	100.0%
DMSO 0.5%	15463	14915	19206	16528	16517.3	2335.35	100.0%

**b**

Luminescence signal Caco-2 3D after treatment with <b>Metformin 750µM</b>							
	Replicate	Replicate	Replicate	Mean	Mean-Mean_Blank	SD	% Viability
Metformin 750µM	39460	29216	45205	37960	34275	8099.31	138.2%
Metformin 750µM	12137	13508	13359	13001.3	12921	752.233	98.9%
Metformin 750µM	1714	31249	33090	22017.7	22017.7	17607.6	59.8%
Metformin 750µM	16678	28166	42231	29025	27433	12798.1	83.4%
Metformin 750µM	35126	70216	65223	56855	56855	18982.7	102.2%
Metformin 750µM	10638	12660	13241	12179.7	12179.7	1366.36	95.7%
Metformin 750µM	10681	12747	10429	11285.7	11275	1271.81	77.5%
Metformin 750µM	12246	14896	16319	14487	14482	2067.07	115.6%
Metformin 750µM	12159	17353	16381	15297.7	15276	2761.27	92.4%
Metformin 750µM	36527	32780	13108	27471.7	27218	12579.6	111.2%
Metformin 750µM	32840	34528	37163	34843.7	34815	2178.72	95.0%
Metformin 750µM	28346	28679	32575	29866.7	29848.3	2351.39	103.4%
Metformin 750µM	14861	19091	17254	17068.7	17058	2121.08	103.3%

Table 66: Luminescence signals of the ATP measurements after treatment with Staurosporine for 24h in the Caco-2 OoC model

N=1	Luminescence signal Caco-2 OoC after treatment with <b>Staurosporine</b>						
	Replicate	Replicate	Replicate	Mean	Mean-Mean_Blank	SD	% Viability
0.1µM	29738	32089	306	30914	27228	17710	70.0%
0.3µM	26666	35460	124	31063	27378	18396	70.4%
1µM	27593	28450	27194	27746	24060	642	61.9%
3µM	8189	101	6081	4790	1105	4196	2.8%
10µM	8189	31	4623	6406	2721	4090	7.0%
30µM	611	1966	17	865	-2821	999	-9.0%
100µM	312	177	15	168	-3517	149	-9.0%
300µM	492	65	263	273	-3412	214	-8.8%

N=2	Luminescence signal Caco-2 OoC after treatment with <b>Staurosporine</b>						
	Replicate	Replicate	Replicate	Mean	Mean-Mean_Blank	SD	% Viability
0.1µM	11122	10129	13286	11512	11432	1614	87.5%
0.3µM	9733	8746	412	9240	9159	698	70.1%
1µM	10	10633	10026	10330	10249	429	78.5%
3µM	6473	8844	7973	7763	7683	1199	58.8%
10µM	5463	4481	5178	5041	4960	505	38.0%
30µM	699	645	409	584	504	154	3.9%
100µM	139	184	173	165	85	23	0.7%
300µM	0	340	214	277	197	89	1.5%

N=3	Luminescence signal Caco-2 OoC after treatment with <b>Staurosporine</b>						
	Replicate	Replicate	Replicate	Mean	Mean-Mean_Blank	SD	% Viability
0.1µM	1714	31249	33090	22018	22018	17608	59.8%
0.3µM	38463	14388	38205	30352	30352	13826	82.5%
1µM	19951	18903	22641	20498	20498	1928	55.7%
3µM	18860	14544	4531	12645	12645	7351	34.4%
10µM	15085	12486	22762	16778	16778	5343	45.6%
30µM	11053	11050	11157	11087	11087	61	30.1%
100µM	721	885	806	804	804	82	2.2%
300µM	319	418	394	377	377	52	1.0%

N=4	Luminescence signal Caco-2 OoC after treatment with <b>Staurosporine</b>						
	Replicate	Replicate	Replicate	Mean	Mean-Mean_Blank	SD	% Viability
0.1µM	30735	51993	50306	44345	42753	11816	129.9%
0.3µM	18934	25024	23088	22349	20757	3112	63.1%
1µM	22229	22293	14180	19567	17975	4666	54.6%
3µM	664	18510	15873	11682	10090	9633	30.7%
10µM	7258	6174	10508	7980	6388	2255	19.4%
30µM	337	330	657	441	-1151	187	-3.5%
100µM	321	313	233	289	-1303	49	-4.0%
300µM	137	7258	210	2535	943	4090	2.9%

N=5	Luminescence signal Caco-2 OoC after treatment with <b>Staurosporine</b>						
	Replicate	Replicate	Replicate	Mean	Mean-Mean_Blank	SD	% Viability
0.1µM	66428	71434	23442	53768	53768	26382	96.7%
0.3µM	75684	59602	49510	61599	61599	13201	110.8%
1µM	68580	68173	62444	66399	66399	3431	119.4%
3µM	61553	68754	64057	64788	64788	3656	116.5%
10µM	63668	55256	64932	61285	61285	5260	110.2%
30µM	42748	39587	30823	37719	37719	6178	67.8%
100µM	16318	20506	4438	13754	13754	8335	24.7%
300µM	16015	15686	16639	16113	16113	16113	29.0%

N=6	Luminescence signal Caco-2 OoC after treatment with <b>Staurosporine</b>						
	Replicate	Replicate	Replicate	Mean	Mean-Mean_Blank	SD	% Viability
0.1µM	15133	17960	20503	17865	17865	2686	140.4%
0.3µM	2890	15826	14950	11222	11222	7229	88.2%
1µM	7733	7704	4525	6654	6654	1844	52.3%
3µM	2392	3905	1787	2695	2695	1091	21.2%
10µM	1832	7210	179	3074	3074	3676	24.2%
30µM	883	955	724	854	854	118	6.7%
100µM	78	152	129	120	120	38	0.9%
300µM	42	112	76	77	77	35	0.6%

N=7	Luminescence signal Caco-2 OoC after treatment with <b>Staurosporine</b>						
	Replicate	Replicate	Replicate	Mean	Mean-Mean_Blank	SD	% Viability
0.1µM	14279	14040	11145	13155	13144	1745	90.3%
0.3µM	14551	16091	14284	14975	14965	975	102.9%
1µM	4670	9819	6483	6991	6980	2612	48.0%
3µM	1067	13459	2056	5527	5517	6887	37.9%
10µM	7624	5477	2912	5338	5327	2359	36.6%
30µM	414	202	694	437	426	247	2.9%
100µM	166	169	122	152	142	26	1.0%
300µM	46	38	40	41	31	4	0.2%

Table 67: Luminescence signals of the ATP measurements after treatment with Gefitinib for 24h in the organoid 3D model

N=1	Luminescence signal Caco-2 3D after treatment with <b>Gefitinib</b>						
	Replicate	Replicate	Replicate	Mean	Mean-Mean_Blank	SD	% Viability
0.1µM	30331	37414	34788	34178	33946	3581	86.4%
0.3µM	39343	37727	30072	35714	35482	4952	90.3%
1µM	21423	28961	25708	25364	25132	3781	64.0%
3µM	23651	25632	26768	25350	25118	1577	63.9%
10µM	23320	20508	18602	20810	20578	2373	52.4%
30µM	4374	8992	16473	9946	9714	6106	24.7%
100µM	691	805	716	737	505	60	1.3%
300µM	1225	1012	740	992	760	243	1.9%

N=2	Luminescence signal Caco-2 3D after treatment with <b>Gefitinib</b>						
	Replicate	Replicate	Replicate	Mean	Mean-Mean_Blank	SD	% Viability
0.1µM	21980	27972	23090	24347	24146	3188	109.5%
0.3µM	13820	14614	17813	15416	15214	2114	69.0%
1µM	8895	15789	11794	12159	11958	3461	54.2%
3µM	6507	10666	7531	8235	8033	2167	36.4%
10µM	2663	3398	2802	2954	2753	390	12.5%
30µM	357	247	271	292	90	58	0.4%
100µM	264	150	147	187	-14	67	-0.1%
300µM	704	668	579	650	449	64	2.0%

N=3	Luminescence signal Caco-2 3D after treatment with <b>Gefitinib</b>						
	Replicate	Replicate	Replicate	Mean	Mean-Mean_Blank	SD	% Viability
0.1µM	8736	9352	10996	9695	9615	1168	74.0%
0.3µM	10698	11242	10170	10703	10624	536	81.7%
1µM	9612	10532	6546	8897	8817	2087	67.8%
3µM	9045	7593	8572	8403	8324	741	64.0%
10µM	3922	6081	3367	4457	4377	1434	33.7%
30µM	340	222	321	294	215	63	1.7%
100µM	225	181	222	209	130	25	1.0%
300µM	240	383	251	291	212	80	1.6%

Table 68: Luminescence signals of the ATP measurements after treatment with Alosetron for 24h in the organoid 3D model

N=1	Luminescence signal Caco-2 3D after treatment with <b>Alosetron</b>						
	Replicate	Replicate	Replicate	Mean	Mean-Mean_Blank	SD	% Viability
0.1µM	37826	38584	43415	39942	39592	3032	129.9%
0.3µM	59581	54316	56997	56965	56615	2633	185.8%
1µM	65397	62552	61641	63197	62847	1959	206.2%
3µM	55707	60235	58636	58193	57843	2296	189.8%
10µM	60905	45047	48683	51545	51196	8307	168.0%
30µM	64512	37757	48845	50371	50022	13443	164.1%
100µM	50626	63386	52380	55464	55115	6916	180.8%
300µM	36324	36657	45305	39429	39079	5092	128.2%

N=2	Luminescence signal Caco-2 3D after treatment with <b>Alosetron</b>						
	Replicate	Replicate	Replicate	Mean	Mean-Mean_Blank	SD	% Viability
0.1µM	29419	46188	34314	36640	36439	8623	165.2%
0.3µM	36386	34771	34080	35079	34878	1183	158.1%
1µM	41615	34602	60109	45442	45241	13177	205.1%
3µM	43084	30353	34972	32663	32461	6445	147.2%
10µM	38802	44678	36497	40588	40386	4218	183.1%
30µM	41227	32171	22955	27563	27362	9136	124.0%
100µM	31694	30434	35099	32409	32208	2413	146.0%
300µM	12936	14110	16308	14451	14250	1712	64.6%

N=3	Luminescence signal Caco-2 3D after treatment with <b>Alosetron</b>						
	Replicate	Replicate	Replicate	Mean	Mean-Mean_Blank	SD	% Viability
0.1µM	8181	1364	13912	7819	7740	6282	59.5%
0.3µM	12309	16044	10040	12798	12718	3032	97.8%
1µM	11143	13099	16311	13518	13438	2609	103.4%
3µM	15397	14570	20118	16695	16616	2993	127.8%
10µM	15476	16009	17925	16470	16391	1288	126.1%
30µM	14989	12709	13057	13585	13506	1228	103.9%
100µM	11004	13593	20979	15192	15113	5176	116.3%
300µM	7655	9057	8251	8321	8242	704	63.4%



Table 69: Luminescence signals of the ATP measurements after treatment with 5-FU for 24h in the organoid 3D model

Luminescence signal Caco-2 3D after treatment with 5-FU							
	Replicate	Replicate	Replicate	Mean	Mean-Mean_Blank	SD	% Viability
0.1µM	46778	32760	34708	39769	39537	9912	100.6%
0.3µM	55383	60724	55702	55543	55311	226	140.8%
1µM	60752	66417	60389	63585	63353	4006	161.2%
3µM	52986	57110	52210	54102	53870	2634	137.1%
10µM	60516	63780	64452	62148	61916	2308	157.6%
30µM	36693	61020	58945	48857	48625	17202	123.8%
100µM	33071	50125	42694	41963	41731	8550	106.2%
300µM	26130	36937	30747	31534	31302	7642	79.7%

Luminescence signal Caco-2 3D after treatment with 5-FU							
	Replicate	Replicate	Replicate	Mean	Mean-Mean_Blank	SD	% Viability
0.1µM	42453	38406	70212	50357	50008	17314	164.1%
0.3µM	39408	51203	61678	50763	50414	11142	165.4%
1µM	59013	56870	54259	56714	56365	2381	184.9%
3µM	52952	60337	50211	54500	54151	5237	177.7%
10µM	49343	65884	59746	58324	57975	8362	190.2%
30µM	57273	53272	37390	49312	48962	10516	160.6%
100µM	35534	54334	48090	45986	45637	9575	149.7%
300µM	29248	35120	36458	33609	33259	3835	109.1%

Luminescence signal Caco-2 3D after treatment with 5-FU							
	Replicate	Replicate	Replicate	Mean	Mean-Mean_Blank	SD	% Viability
0.1µM	43855	42872	43445	43391	43091	494	131.6%
0.3µM	53876	48485	47345	49902	49603	3488	151.4%
1µM	52643	49138	49287	50356	50057	1982	152.8%
3µM	58604	48222	45190	50672	50373	7035	153.8%
10µM	57642	48236	55016	53631	53332	4853	162.8%
30µM	54752	43758	52562	50357	50058	5819	152.8%
100µM	52796	52899	50061	51919	51619	1610	157.6%
300µM	37052	37118	37712	37294	36995	363	113.0%

Table 70 Luminescence signals of the ATP measurements after treatment with Diclofenac for 24h in the organoid 3D model

Luminescence signal Caco-2 3D after treatment with Diclofenac							
	Replicate	Replicate	Replicate	Mean	Mean-Mean_Blank	SD	% Viability
0.1µM	35538	36142	16432	29371	29021	11209	95.2%
0.3µM	34415	49000	41800	41738	41389	7293	135.8%
1µM	72669	45613	22015	46766	46416	25347	152.3%
3µM	65640	34907	32469	44339	43989	18488	144.3%
10µM	63187	23929	24481	37199	36850	22508	120.9%
30µM	58947	28804	27094	38282	37932	17917	124.5%
100µM	49482	27674	19930	32362	32013	15324	105.0%
300µM	35942	31890	13320	27051	26701	12062	87.6%

Luminescence signal Caco-2 3D after treatment with Diclofenac							
	Replicate	Replicate	Replicate	Mean	Mean-Mean_Blank	SD	% Viability
0.1µM	44181	32899	33423	36834	36633	6368	166.1%
0.3µM	51547	33495	36995	40679	40478	9573	183.5%
1µM	22766	45872	33596	34078	33877	11561	153.6%
3µM	33148	26488	31073	30236	30035	3408	136.2%
10µM	38405	26139	35108	33217	33016	6348	149.7%
30µM	47576	50578	53342	50499	50297	2884	228.0%
100µM	42819	34299	27322	34813.3	34612	7761	156.9%
300µM	11098	10563	13884	11848	11647	1783	52.8%

Luminescence signal Caco-2 3D after treatment with Diclofenac							
	Replicate	Replicate	Replicate	Mean	Mean-Mean_Blank	SD	% Viability
0.1µM	13106	8656	10054	10605	10526	2276	81.0%
0.3µM	14082	11035	10288	11802	11722	2010	90.2%
1µM	17505	11665	8109	12426	12347	4744	95.0%
3µM	14810	10970	7275	11018	10939	3768	84.1%
10µM	9762	13513	10243	11173	11093	2041	85.3%
30µM	12645	11405	6635	10228	10149	3173	78.1%
100µM	10622	11845	7747	10071	9992	2104	76.9%
300µM	5447	7464	7782	6898	6818	1266	52.4%

Table 71 Luminescence signals of the ATP measurements after treatment with Flavopiridol for 24h in the organoid 3D model

Luminescence signal Caco-2 3D after treatment with <b>Flavopiridol</b>							
	Replicate	Replicate	Replicate	Mean	Mean-Mean_Blank	SD	% Viability
0.1µM	22075	24870	18313	21753	21403	3290	70.2%
0.3µM	25950	42296	51604	39950	39601	12987	129.9%
1µM	27882	38081	34050	33338	32988	5137	108.2%
3µM	24832	44849	30225	33302	32953	10357	108.1%
10µM	26447	47499	37970	37305	36956	10542	121.3%
30µM	25318	47492	54822	42544	42195	15362	138.4%
100µM	19949	46097	46744	37597	37247	15287	122.2%
300µM	16071	29523	33200	26265	25915	9017	85.0%

Luminescence signal Caco-2 3D after treatment with <b>Flavopiridol</b>							
	Replicate	Replicate	Replicate	Mean	Mean-Mean_Blank	SD	% Viability
0.1µM	15831	19648	18567	18015	17814	1967	80.8%
0.3µM	6955	23042	28357	19451	19250	11144	87.3%
1µM	14306	21989	20076	18790	18589	4000	84.3%
3µM	15915	18153	16925	16998	16796	1121	76.1%
10µM	17868	21257	18575	19233	19032	1788	86.3%
30µM	16995	24913	18584	20164	19963	4189	90.5%
100µM	13733	13092	24400	17075	16874	6352	76.5%
300µM	9205	10055	9408	9556	9355	444	42.4%

Luminescence signal Caco-2 3D after treatment with <b>Flavopiridol</b>							
	Replicate	Replicate	Replicate	Mean	Mean-Mean_Blank	SD	% Viability
0.1µM	6069	7317	5387	6258	6178	979	47.5%
0.3µM	9894	10552	9504	9983	9904	530	76.2%
1µM	9633	10695	13141	11156	11077	1799	85.2%
3µM	9692	5593	8859	8048	7969	2167	61.3%
10µM	5362	7324	8605	7097	7018	1633	54.0%
30µM	8358	7187	6735	7427	7347	838	56.5%
100µM	8053	9081	11767	9634	9554	1918	73.5%
300µM	5869	3941	7621	5810	5731	1841	44.1%

Table 72: Luminescence signals of the ATP measurements after treatment with Irinotecan for 24h in the organoid 3D model

Luminescence signal Caco-2 3D after treatment with <b>Irinotecan</b>							
	Replicate	Replicate	Replicate	Mean	Mean-Mean_Blank	SD	% Viability
0.1µM	45974	36751	53823	45516	45167	8545	148.2%
0.3µM	56905	58606	66012	60508	60158	4842	197.4%
1µM	61781	61403	62719	61968	61618	678	202.2%
3µM	57462	49019	51915	52799	52449	4290	172.1%
10µM	58008	51975	51381	53788	53439	3667	175.3%
30µM	38195	56337	54556	49696	49347	10000	161.9%
100µM	33152	33401	37076	34543	34194	2197	112.2%
300µM	8585	17244	14404	13411	13062	4414	42.9%

Luminescence signal Caco-2 3D after treatment with <b>Irinotecan</b>							
	Replicate	Replicate	Replicate	Mean	Mean-Mean_Blank	SD	% Viability
0.1µM	29027	37888	29903	32273	31923	4883	104.7%
0.3µM	40148	42100	35993	39414	39064	3119	128.2%
1µM	37691	52732	41077	43833	43484	7890	142.7%
3µM	31088	57124	38208	42140	41791	13456	137.1%
10µM	41210	48369	33785	41121	40772	7292	133.8%
30µM	45658	46221	24261	38713	38364	12519	125.9%
100µM	17627	31396	18681	22568	22219	7663	72.9%
300µM	10393	12552	7927	10291	9941	2314	32.6%

Luminescence signal Caco-2 3D after treatment with <b>Irinotecan</b>							
	Replicate	Replicate	Replicate	Mean	Mean-Mean_Blank	SD	% Viability
0.1µM	30574	18592	17730	22299	22097	7180	100.2%
0.3µM	29520	22715	20342	24192	23991	4764	108.8%
1µM	17919	18509	14963	17130	16929	1900	76.7%
3µM	13392	18981	13981	15451	15250	3071	69.1%
10µM	12217	14570	10793	12527	12325	1907	55.9%
30µM	8853	9431	9564	9283	9081	378	41.2%
100µM	2912	4036	4166	3705	3503	690	15.9%
300µM	137	86	64	96	-106	37	-0.5%

Table 73 Luminescence signals of the ATP measurements after treatment with Loperamide for 24h in the organoid 3D model

N=1 Luminescence signal Caco-2 3D after treatment with <b>Loperamide</b>							
	Replicate	Replicate	Replicate	Mean	Mean-Mean_Blank	SD	% Viability
0.1µM	34512	35827	47453	39264	38915	7122	127.7%
0.3µM	44366	49148	51808	48441	48091	3771	157.8%
1µM	42856	54557	61899	53104	52755	9604	173.1%
3µM	33718	48045	62889	48217	47868	14586	157.1%
10µM	36835	50828	58392	48685	48336	10937	158.6%
30µM	22272	40538	46926	36579	36229	12795	118.9%
100µM	632	654	986	757	408	198	1.3%
300µM	244	320	474	346	-3	117	0.0%

N=2 Luminescence signal Caco-2 3D after treatment with <b>Loperamide</b>							
	Replicate	Replicate	Replicate	Mean	Mean-Mean_Blank	SD	% Viability
0.1µM	33523	39784	48060	40456	40185	7292	150.3%
0.3µM	59455	63250	71510	64738	64468	6164	241.2%
1µM	66913	60202	83480	70198	69928	11982	261.6%
3µM	55596	94767	55741	68701	68431	22574	256.0%
10µM	56669	73105	55871	61882	61611	9728	230.5%
30µM	11935	37222	17673	22277	22006	13257	82.3%
100µM	377	419	357	384	114	32	0.4%
300µM	196	185	193	191	-79	6	-0.3%

N=3 Luminescence signal Caco-2 3D after treatment with <b>Loperamide</b>							
	Replicate	Replicate	Replicate	Mean	Mean-Mean_Blank	SD	% Viability
0.1µM	15415	12622	8484	12174	12094	3487	93.0%
0.3µM	11837	9837	13016	11563	11484	1607	88.3%
1µM	17072	12036	12665	13924	13845	2744	106.5%
3µM	12622	9452	14162	12079	11999	2402	92.3%
10µM	10549	11777	8941	10422	10343	1422	79.6%
30µM	5136	4197	8143	5825	5746	2061	44.2%
100µM	209	174	206	196	117	19	0.9%
300µM	134	112	128	125	45	11	0.3%

Table 74: Luminescence signals of the ATP measurements after treatment with Oxaliplatin for 24h in the organoid 3D model

N=1 Luminescence signal Caco-2 3D after treatment with <b>Oxaliplatin</b>							
	Replicate	Replicate	Replicate	Mean	Mean-Mean_Blank	SD	% Viability
0.1µM	31864	49522	29023	36803	36454	11106	119.6%
0.3µM	50415	41803	38224	43481	43131	6266	141.5%
1µM	44241	50412	49560	48071	47722	3344	156.6%
3µM	50578	63733	48849	54387	54037	8140	177.3%
10µM	41006	48810	45331	45049	44700	3910	146.7%
30µM	23468	29918	21426	24937	24588	4433	80.7%
100µM	3858	3265	3500	3541	3192	299	10.5%
300µM	548	487	604	546	197	59	0.6%

N=2 Luminescence signal Caco-2 3D after treatment with <b>Oxaliplatin</b>							
	Replicate	Replicate	Replicate	Mean	Mean-Mean_Blank	SD	% Viability
0.1µM	35161	21271	28331	28254	28053	6945	127.2%
0.3µM	38843	17649	34029	30174	29972	11111	135.9%
1µM	26909	23273	26011	25398	25196	1894	114.2%
3µM	23267	29717	22256	25080	24879	4047	112.8%
10µM	12943	11937	14536	13139	12937	1311	58.6%
30µM	2583	2719	1995	2432	2231	385	10.1%
100µM	910	920	776	869	667	80	3.0%
300µM	1852	2157	1760	1923	1722	208	7.8%

N=3 Luminescence signal Caco-2 3D after treatment with <b>Oxaliplatin</b>							
	Replicate	Replicate	Replicate	Mean	Mean-Mean_Blank	SD	% Viability
0.1µM	43022	45800	44623	44482	44211	1394	165.4%
0.3µM	49865	66199	55564	57209	56939	8290	213.0%
1µM	40206	63570	69028	57601	57331	15310	214.5%
3µM	46245	57501	63448	55731	55461	8737	207.5%
10µM	20496	40937	36819	32751	32480	10811	121.5%
30µM	8374	5271	4977	6207	5937	1882	22.2%
100µM	740	1132	1045	972	702	206	2.6%
300µM	278	665	460	468	197	194	0.7%

Table 75: Luminescence signals of the ATP measurements after treatment with Terfenadine for 24h in the organoid 3D model

Luminescence signal Caco-2 3D after treatment with <b>Terfenadine</b>							
	Replicate	Replicate	Replicate	Mean	Mean-Mean_Blank	SD	% Viability
0.1µM	61485	58464	37925	52625	52275	12820	171.5%
0.3µM	61600	55459	55023	57361	57011	3678	187.1%
1µM	29969	60408	55400	48592	48243	16322	158.3%
3µM	64590	45388	60755	56911	56562	10162	185.6%
10µM	80277	59495	56998	65590	65241	12780	214.1%
30µM	7121	756	515	2797	2448	3746	8.0%
100µM	291	277	211	260	-90	43	-0.3%
300µM	231	183	145	186	-163	43	-0.5%

Luminescence signal Caco-2 3D after treatment with <b>Terfenadine</b>							
	Replicate	Replicate	Replicate	Mean	Mean-Mean_Blank	SD	% Viability
0.1µM	53193	37379	24488	38353	38152	14377	172.9%
0.3µM	35437	49450	44765	43217	43016	7134	195.0%
1µM	37331	42675	32974	37660	37459	4859	169.8%
3µM	27769	35124	25423	29439	29237	5061	132.5%
10µM	553	381	333	422	221	116	1.0%
30µM	439	242	214	298	97	123	0.4%
100µM	325	176	141	214	13	98	0.1%
300µM	214	140	107	154	-48	55	-0.2%

Luminescence signal Caco-2 3D after treatment with <b>Terfenadine</b>							
	Replicate	Replicate	Replicate	Mean	Mean-Mean_Blank	SD	% Viability
0.1µM	14760	61562	44414	40245	39975	23678	149.5%
0.3µM	38570	68281	26936	44596	44325	21321	165.8%
1µM	68538	83152	40828	64173	63902	21497	239.0%
3µM	50329	17990	35229	34516	34245	16181	128.1%
10µM	878	441	335	551	281	288	1.0%
30µM	336	244	727	436	165	256	0.6%
100µM	173	174	437	261	-9	152	0.0%
300µM	111	92	74	92	-178	19	-0.7%

Table 76: Luminescence signals of the ATP measurements after treatment with 0.5% DMSO (a) and Metformin 750µM (b) for 24h in the organoid 3D model

**a**

Luminescence signal Caco-2 3D after treatment with <b>DMSO 0.5%</b>							
	Replicate	Replicate	Replicate	Mean	Mean-Mean_Blank	SD	% Viability
DMSO 0.5%	27346	43095	40765	37069	36837	8500	100.0%
DMSO 0.5%	34811	32512	34651	33991	30608	1284	100.0%
DMSO 0.5%	24890	33875	36519	31761	31412	6096	100.0%
DMSO 0.5%	16910	18402	24002	19771	19570	3739	100.0%
DMSO 0.5%	22060	27469	31479	27003	26732	4727	100.0%
DMSO 0.5%	34007	39878	25272	33052	32753	7350	100.0%
DMSO 0.5%	13756	10954	14528	13079	13000	1881	100.0%

**b**

Luminescence signal Caco-2 3D after treatment with <b>Metformin 750µM</b>							
	Replicate	Replicate	Replicate	Mean	Mean-Mean_Blank	SD	% Viability
Metformin 750µM	36904	35793	35020	35906	35674	947	96.8%
Metformin 750µM	29217	28447	37568	31744	28360	5058	92.7%
Metformin 750µM	48423	64061	38139	50208	49858	13053	158.7%
Metformin 750µM	31322	28304	25668	28431	28230	2829	144.3%
Metformin 750µM	41405	41534	27038	36659	36388	8332	136.1%
Metformin 750µM	42194	35733	44337	40755	40455	4479	123.5%
Metformin 750µM	13847	14402	12751	13667	13587	840	104.5%

Table 77: Luminescence signals of the ATP measurements after treatment with Staurosporine for 24h in the organoid 3D model

N=1 Luminescence signal Caco-2 3D after treatment with <b>Staurosporine</b>							
	Replicate	Replicate	Replicate	Mean	Mean-Mean_Blank	SD	% Viability
0.1µM	11518	13094	13050	12554	12322	897	31.4%
0.3µM	14028	13059	10540	12542	12310	1800	31.3%
1µM	11917	11797	8201	10638	10406	2112	26.5%
3µM	10132	6964	7068	7016	6784	1800	17.3%
10µM	2455	1705	1920	1813	1581	386	4.0%
30µM	4522	3181	3603	3392	3160	686	8.0%
100µM	3374	4591	4125	4030	3798	614	9.7%
300µM	3646	3331	3685	3554	3322	194	8.5%

N=2 Luminescence signal Caco-2 3D after treatment with <b>Staurosporine</b>							
	Replicate	Replicate	Replicate	Mean	Mean-Mean_Blank	SD	% Viability
0.1µM	49040	50901	15424	38455	35071	19967	114.6%
0.3µM	52637	55327	65574	57846	54462	6826	177.9%
1µM	37341	49854	44864	44020	40636	6299	132.8%
3µM	41395	38005	28311	35904	32520	6790	106.2%
10µM	18957	29154	12442	20184	16801	8423	54.9%
30µM	646	344	717	569	-2815	198	-9.2%
100µM	421	162	502	362	-3022	178	-9.9%
300µM	289	189	228	235	-3148	50	-10.3%

N=3 Luminescence signal Caco-2 3D after treatment with <b>Staurosporine</b>							
	Replicate	Replicate	Replicate	Mean	Mean-Mean_Blank	SD	% Viability
0.1µM	39208	43278	34122	38869	38520	4587	126.4%
0.3µM	43929	32409	39644	38661	38311	5823	125.7%
1µM	22772	20094	22605	21824	21474	1500	70.5%
3µM	20906	22633	23322	22287	21938	1245	72.0%
10µM	11020	11084	13997	12034	11684	1701	38.3%
30µM	714	523	552	596	247	103	0.8%
100µM	809	632	633	691	342	102	1.1%
300µM	1060	1007	908	992	642	77	2.1%

N=4 Luminescence signal Caco-2 3D after treatment with <b>Staurosporine</b>							
	Replicate	Replicate	Replicate	Mean	Mean-Mean_Blank	SD	% Viability
0.1µM	20897	18271	14646	17938	17639	3139	53.9%
0.3µM	22462	20282	16964	19903	19603	2769	59.9%
1µM	7827	7781	7555	7721	7422	146	22.7%
3µM	7296	4612	6098	6002	5703	1345	17.4%
10µM	1476	1423	2200	1700	1400	434	4.3%
30µM	714	488	550	584	285	117	0.9%
100µM	593	407	449	483	184	97.55	0.6%
300µM	458	304	340	367	68	81	0.2%

## Appendix 7: TEER values after treatment with test compounds for the evaluation of the intestinal barrier in Caco-2 2D model

Table 78: TEER values of the Caco-2 2D model after the treatment on day 21 with the controls (DMSO, Metformin, Staurosporine) and 5-FU

N=1	TEER values [ $\Omega\text{-cm}^2$ ] Caco-2 2D							
	Metformin 750 $\mu\text{M}$	DMSO 0.3%	Staurosporine 0.1 $\mu\text{M}$	Staurosporine 1 $\mu\text{M}$	Staurosporine 10 $\mu\text{M}$	5-FU 3 $\mu\text{M}$	5-FU 30 $\mu\text{M}$	5-FU 300 $\mu\text{M}$
day 19	161.34	199.73	191.41	228.05	200.49	200.57	230.16	221.34
day 19_6h	221.93	206.90	238.92	262.18	218.76	234.92	239.30	241.62
day 19_12h	196.76	188.64	222.18	241.55	199.47	211.25	223.86	214.73
day19_18h	196.78	193.34	227.23	242.51	195.21	187.31	199.96	199.54
day 20	177.48	179.26	233.27	225.71	193.22	177.43	189.75	191.33
day 20_6h	168.37	179.70	238.20	206.92	197.88	176.57	183.10	187.39
day20_12h	165.56	187.89	240.77	204.38	204.90	177.33	175.85	194.16
day20_18h	169.42	195.60	250.97	205.24	218.29	173.76	186.98	201.25
day 21	160.99	196.64	196.97	24.91	14.25	183.29	176.05	179.66
day 21_6h	197.36	210.91	197.57	5.37	-0.12	202.16	196.65	184.22
day 21_12h	224.34	212.57	182.50	-0.30	-0.61	198.07	203.94	182.01
day21-18h	246.46	225.86	181.23	-1.53	-1.96	195.46	208.22	184.26
Day 22 end	252.39	221.63	182.71	-1.84	-1.65	197.28	213.66	182.04

N=2	TEER values [ $\Omega\text{-cm}^2$ ] Caco-2 2D							
	Metformin 750 $\mu\text{M}$	DMSO 0.3%	Staurosporine 0.1 $\mu\text{M}$	Staurosporine 1 $\mu\text{M}$	Staurosporine 10 $\mu\text{M}$	5FU 3 $\mu\text{M}$	5FU 30 $\mu\text{M}$	5FU 300 $\mu\text{M}$
day 19	469.49	189.23	235.82	208.21	230.34	241.89	309.06	242.88
day 19_6h	296.28	166.85	222.01	176.49	208.43	219.42	268.39	224.92
day 19_12h	223.43	161.06	218.69	164.96	207.9	203.78	254.69	209.84
day 19_18h	149.18	169.26	229.21	164.83	223.94	192.3	259.65	190.51
day 20	157.28	177.27	230.3	164.55	221.46	189.75	254.93	200.41
day 20_6h	133.85	206.13	204.62	22.97	8.37	246.7	262.04	240.64
day 20_12h	138.79	217.87	199.21	9.88	2.38	258.54	281.04	247.01
day 20_18h	144.84	194.36	204.95	4.42	3.34	267.62	297.6	230.81
Day21	39.45	208.29	212.77	2.24	0.31	248.12	288.65	216.93
day 21_6h	101.87	203.13	214.26	1.32	0.27	240.78	283.73	196.32
day 21_12h	88.21	225.56	218.94	0.94	0.26	234.9	284.71	172.57
day 21_18h	73.01	232.37	221.95	4.99	0.27	231.44	293.72	152.18
day 22	69.59	237.79	223.33	0.53	0.25	237.99	291.25	137.29

N=3	TEER values [ $\Omega\text{-cm}^2$ ] Caco-2 2D							
	Metformin 750 $\mu\text{M}$	DMSO 0.3%	Staurosporine 0.1 $\mu\text{M}$	Staurosporine 1 $\mu\text{M}$	Staurosporine 10 $\mu\text{M}$	5FU 3 $\mu\text{M}$	5Fu 30 $\mu\text{M}$	5Fu 300 $\mu\text{M}$
day 19	469.49	141.15	408.1	421.34	455.15	378.04	285.47	532.61
day 19_6h	296.28	71	179.99	227.88	298.13	200.98	221.4	286.76
day 19_12h	223.43	60.28	107.19	176.77	210.57	117.94	166.73	177.71
day 19_18h	149.18	45.68	93.99	129.17	169.51	93.91	138.21	134.67
day 20	157.28	47.94	84.57	109.52	156.33	72.91	131.87	139.05
day 20_6h	133.85	40.13	91.8	99.33	138.66	48.51	150.28	124.5
day 20_12h	138.79	37.59	96.99	108.29	136.35	65.54	149.93	129.94
day 20_18h	144.84	37.3	100.03	121.84	166.33	75.45	164.94	138.85
Day21	39.45	32.06	114.68	25.48	6.91	52.83	132.3	91.99
day 21_6h	101.87	37.37	26.75	0	0	84.98	180.29	148.31
day 21_12h	88.21	28.26	25.83	0	0	60.33	162.97	124.03
day 21_18h	73.01	20.26	26.24	0	0	50.05	144.43	73.78
day 22	69.59	19.09	27.29	0	0	42.46	132.21	42.48

Table 79: TEER values of the Caco-2 2D model after the treatment on day 21 with the controls (DMSO, Metformin, Staurosporine) and Alosetron

N=1									
TEER values [ $\Omega \cdot \text{cm}^2$ ] Caco-2 2D									
	Metformin 750 $\mu\text{M}$	DMSO 0.3%	Staurosporin 0.1 $\mu\text{M}$	Staurosporin 1 $\mu\text{M}$	Staurosporin 10 $\mu\text{M}$	Alosetron 3 $\mu\text{M}$	Alosetron 30 $\mu\text{M}$	Alosetron 300 $\mu\text{M}$	
day 19	229.70	227.26	216.38	193.67	173.19	220.84	228.63	204.40	
day 19_6h	267.55	220.84	242.24	213.04	193.07	236.36	299.03	239.75	
day 19_12h	264.98	222.20	239.75	198.59	182.08	234.38	297.33	220.91	
day19_18h	251.32	207.83	265.31	212.27	198.19	254.08	278.41	228.56	
day 20	270.90	202.32	273.18	226.44	195.31	272.15	278.89	219.48	
day 20_6h	265.77	201.30	276.69	224.68	196.52	273.51	284.63	215.97	
day20_12h	258.76	186.02	261.07	228.27	207.79	272.40	274.25	205.96	
day20_18h	269.20	189.15	242.83	240.98	216.96	276.56	295.14	209.72	
day 21	258.22	205.98	267.83	234.50	214.66	267.23	290.40	205.33	
day 21_6h	278.60	219.69	251.64	23.46	8.94	316.76	337.33	325.96	
day 21_12h	287.87	212.78	253.63	4.42	0.07	316.34	350.50	357.07	
day21-18h	301.17	213.31	231.60	0.90	0.19	303.50	352.50	405.27	
Day 22 end	NA	NA	NA	NA	NA	NA	NA	NA	

N=2									
TEER values [ $\Omega \cdot \text{cm}^2$ ] Caco-2 2D									
	Metformin 750 $\mu\text{M}$	DMSO 0.3%	Staurosporin 0.1 $\mu\text{M}$	Staurosporin 1 $\mu\text{M}$	Staurosporin 10 $\mu\text{M}$	Alosetron 3 $\mu\text{M}$	Alosetron 30 $\mu\text{M}$	Alosetron 300 $\mu\text{M}$	
day 20_6h	316.56	276.58	299.3	466.98	287.13	283.7	282.92	283.7	
day20_12h	259.42	243.41	255.17	370.45	234	219.6	242.74	219.6	
day20_18h	251.48	234.88	248.42	364.01	214.45	227.51	243.34	227.51	
day 21	236.82	233.77	232.39	358.13	214.59	215.62	222.08	215.62	
day 21_6h	228.95	222.24	229.64	349.01	206.85	210.4	218.51	210.4	
day 21_12h	217.76	240	183.72	58.09	27.9	199.92	189.39	199.92	
day21-18h	217.34	238.78	187.22	36.65	14.11	198.9	192.98	198.9	
Day 22 end	214.72	240.42	204.83	23.52	13.2	191.96	192.46	191.96	

N=3									
TEER values [ $\Omega \cdot \text{cm}^2$ ] Caco-2 2D									
	Metformin 750 $\mu\text{M}$	DMSO 0.3%	Staurosporine 0.1 $\mu\text{M}$	Staurosporine 1 $\mu\text{M}$	Staurosporine 10 $\mu\text{M}$	Alosetron 3 $\mu\text{M}$	Alosetron 30 $\mu\text{M}$	Alosetron 300 $\mu\text{M}$	
day 19	248.85	300.94	263.79	344.67	315.05	287.62	344.89	223.81	
day 19_6h	180.52	245.51	217.05	272.61	256.44	253.72	264.53	189.97	
day 19_12h	177.97	244.02	223.44	266.57	258.18	257.13	274.26	186.59	
day 19_18h	177.14	251.87	223.58	272.88	269.72	259.74	262.06	195.80	
day 20	180.09	252.92	223.62	257.73	275.41	261.44	264.16	199.65	
day 20_6h	176.09	258.74	222.16	271.72	290.72	261.41	269.90	216.76	
day 20_12h	174.49	264.23	228.27	276.00	289.84	260.46	266.15	220.21	
day 20_18h	178.20	262.93	221.98	270.70	286.94	261.79	267.21	225.53	
Day21	173.43	232.13	192.78	149.92	103.22	247.23	254.05	233.06	
day 21_6h	173.25	249.07	203.54	28.60	14.64	243.26	255.29	342.56	
day 21_12h	179.13	258.62	225.61	17.07	13.13	239.60	252.75	357.36	
day 21_18h	168.20	263.26	248.43	15.84	13.18	236.52	244.70	358.97	
day 22 end	168.21	248.68	246.86	14.49	14.34	222.76	242.45	351.92	

Table 80: TEER values of the Caco-2 2D model after the treatment on day 21 with the controls (DMSO, Metformin, Staurosporine) and Diclofenac

N=1	TEER values ( $\Omega\text{-cm}^2$ ) Caco-2 2D							
	Metformin 750 $\mu\text{M}$	DMSO 0.3%	Staurosporin 0.1 $\mu\text{M}$	Staurosporin 1 $\mu\text{M}$	Staurosporin 10 $\mu\text{M}$	Diclofenac 3 $\mu\text{M}$	Diclofenac 30 $\mu\text{M}$	Diclofenac 300 $\mu\text{M}$
day 19	647.98	427.15	603.73	634.70	543.13	560.78	568.66	595.17
day 19_6h	307.27	215.81	332.76	292.22	270.31	288.34	285.21	305.82
day 19_12h	250.73	181.35	298.05	251.07	234.01	252.41	239.74	284.14
day19_18h	250.60	181.48	264.17	229.07	215.72	238.05	221.13	258.78
day 20	243.88	159.88	251.55	220.05	211.09	235.44	211.18	226.18
day 20_6h	224.41	170.43	233.05	201.43	196.53	229.11	200.53	239.80
day20_12h	231.48	175.41	238.62	200.50	202.15	230.96	213.77	240.31
day20_18h	224.39	170.42	246.47	196.07	191.98	228.87	203.38	253.33
day 21	260.78	204.41	272.80	88.26	74.73	258.17	240.56	249.75
day 21_6h	258.70	204.87	254.80	20.78	2.42	276.97	250.63	249.21
day 21_12h	271.15	209.34	250.90	6.68	1.84	269.41	225.78	259.70
day21-18h	269.21	203.20	248.14	2.66	1.47	274.76	216.24	258.39
Day 22 end	275.90	200.89	244.39	2.10	1.77	249.90	209.43	241.33

N=2	TEER values ( $\Omega\text{-cm}^2$ ) Caco-2 2D							
	Metformin 750 $\mu\text{M}$	DMSO 0.3 %	Staurosporine 0.1 $\mu\text{M}$	Staurosporine 1 $\mu\text{M}$	Staurosporine 10 $\mu\text{M}$	Diclofenac 3 $\mu\text{M}$	Diclofenac 30 $\mu\text{M}$	Diclofenac 300 $\mu\text{M}$
day19	247.05	257.22	340.06	265.97	280.01	218.55	220.96	251.92
day19_6h	252.11	264.02	323.55	270.58	259.99	231.73	221.82	271.81
day19_12h	269.68	261.55	304.80	265.75	278.34	232.17	215.29	259.97
day19_18h	269.85	277.02	316.10	269.01	283.92	248.95	211.62	255.31
day20	279.03	263.06	305.11	272.91	289.52	245.75	226.20	272.29
day 20_6h	273.13	262.13	291.61	271.24	280.14	236.00	214.56	261.77
day20_12h	277.84	272.12	289.27	279.55	282.33	237.58	214.59	256.16
day20_18h	263.89	263.08	279.41	268.80	282.71	237.50	214.52	247.42
day 21	264.48	271.11	256.49	186.99	189.56	245.63	223.58	239.35
day 21_6h	259.76	242.47	89.08	42.23	17.00	217.42	212.78	234.80
day 21_12h	257.24	239.25	81.91	30.30	13.74	211.00	202.56	241.17
day121-18h	249.45	227.74	95.37	24.31	13.09	205.95	190.68	227.77
Day 22 end	236.33	214.89	106.00	20.32	12.79	206.50	179.97	236.56

N=3	TEER values ( $\Omega\text{-cm}^2$ ) Caco-2 2D							
	Metformin 750 $\mu\text{M}$	DMSO 0.3 %	Staurosporine 0.1 $\mu\text{M}$	Staurosporine 1 $\mu\text{M}$	Staurosporine 10 $\mu\text{M}$	Diclofenac 3 $\mu\text{M}$	Diclofenac 30 $\mu\text{M}$	Diclofenac 300 $\mu\text{M}$
day19	217.62	253.83	246.19	281.64	241.69	286.40	300.09	302.91
day19_6h	220.35	237.75	205.27	220.83	202.35	225.47	239.64	235.61
day19_12h	214.92	237.27	198.39	215.19	208.40	231.95	231.12	220.63
day19_18h	215.01	241.92	202.24	216.78	212.58	237.41	216.72	220.63
day20	215.77	229.31	208.72	229.75	216.97	257.52	238.76	222.43
day20_6h	226.51	235.22	221.04	239.05	216.75	259.71	231.64	224.22
day20_12h	227.68	251.57	224.88	249.12	213.15	271.99	229.65	232.98
day20_18h	218.91	223.52	229.39	256.03	222.74	269.62	228.01	236.64
day 21	210.40	245.61	160.33	61.00	35.26	244.15	221.82	222.88
day 21_6h	215.34	246.43	119.75	39.81	15.59	247.77	226.83	220.16
day 21_12h	215.50	247.27	116.50	32.46	14.33	252.85	220.46	219.50
day121-18h	210.25	240.36	118.58	28.11	13.92	249.69	220.42	221.79
Day 22 end	211.00	241.90	122.92	25.62	13.96	251.52	224.08	219.52



Table 81: TEER values of the Caco-2 2D model after the treatment on day 21 with the controls (DMSO, Metformin, Staurosporine) and Flavopiridol

N=1	TEER values [ $\Omega\cdot\text{cm}^2$ ] Caco-2 2D								
	Metformin 750 $\mu\text{M}$	DMSO 0.3%	Staurosporine 0.1 $\mu\text{M}$	Staurosporine 1 $\mu\text{M}$	Staurosporine 10 $\mu\text{M}$	Flavopiridol 3 $\mu\text{M}$	Flavopiridol 30 $\mu\text{M}$	Flavopiridol 300 $\mu\text{M}$	
day 19	293.35	354.31	249.25	297.04	339.33	323.65	358.35	317.33	
day 19 6h	262.59	302.53	230.38	272.43	263.35	289.82	308.07	234.84	
day 19 12h	247.22	255.79	206.88	258.39	248.56	265.56	269.16	205.97	
day19 18h	232.87	240.12	186.34	244.42	241.12	247.24	240.63	208.25	
day 20	214.22	224.72	167.61	220.61	226.12	213.56	226.58	184.97	
day 20 6h	216.94	232.36	168.72	217.24	225.43	207.58	215.96	191.06	
day20 12h	210.64	235.84	178.53	214.16	230.06	197.09	217.94	191.75	
day20 18h	202.91	236.21	180.01	202.84	229.51	199.55	219.08	197.11	
day 21	216.77	243.71	182.65	208.13	231.58	193.16	217.54	204.06	
day 21 6h	252.53	255.52	107.62	21.42	1.84	225.21	213.03	92.54	
day 21 12h	262.29	253.99	85.55	0.66	-1.68	170.63	158.84	71.79	
day21-18h	292.43	245.76	83.70	-2.69	-2.93	144.28	126.30	54.67	
day 22 end	NA	NA	NA	NA	NA	NA	NA	NA	

N=2	TEER values [ $\Omega\cdot\text{cm}^2$ ] Caco-2 2D								
	Metformin 750 $\mu\text{M}$	DMSO 0.3%	Staurosporine 0.1 $\mu\text{M}$	Staurosporine 1 $\mu\text{M}$	Staurosporine 10 $\mu\text{M}$	Flavopiridol 3 $\mu\text{M}$	Flavopiridol 30 $\mu\text{M}$	Flavopiridol 300 $\mu\text{M}$	
day 19	357.59	364.06	398.81	368.53	380.40	321.26	343.06	318.49	
day 19 6h	251.72	263.72	278.05	265.38	543.98	254.38	249.10	264.94	
day 19 12h	252.12	252.52	263.3	265.6	533.36	247.27	241.15	239.07	
day19 18h	242.51	252.12	258.53	256.32	534.41	242.44	249.24	238.35	
day 20	255.85	246.90	245.43	243.96	518.25	235.29	247.05	221.95	
day 20 6h	261.63	249.77	235.30	237.39	517.15	226.94	247.71	218.47	
day20 12h	259.85	252.14	223.11	232.52	515.8	226.51	248.17	210.36	
day20 18h	275.61	249.54	223.74	228.47	496.79	224.7	247.35	208.48	
day 21	263.77	262.65	207.62	94.95	393.71	227.34	269.25	199.19	
day 21 6h	268.23	260.18	225.22	48.01	344.29	214.72	258.02	200.14	
day 21 12h	282.32	265.18	259.10	37.05	345.54	213.88	239.75	183.63	
day21-18h	284.05	275.13	275.53	29.49	343.76	207.48	212.03	151.75	
day 22 end	273.96	269.03	293.96	23.82	345.24	201.73	179.45	151.90	

N=3	TEER values [ $\Omega\cdot\text{cm}^2$ ] Caco-2 2D								
	Metformin 750 $\mu\text{M}$	DMSO 0.3%	Staurosporine 0.1 $\mu\text{M}$	Staurosporine 1 $\mu\text{M}$	Staurosporine 10 $\mu\text{M}$	Flavopiridol 3 $\mu\text{M}$	Flavopiridol 30 $\mu\text{M}$	Flavopiridol 300 $\mu\text{M}$	
day 19	313.38	251.14	259.26	275.20	285.10	231.30	236.16	476.50	
day 19 6h	253.33	198.92	227.11	224.13	233.34	195.73	207.62	501.28	
day 19 12h	233.33	190.82	220.30	221.47	168.15	199.42	208.14	517.66	
day19 18h	228.37	195.27	219.72	232.57	166.12	188.69	207.23	525.79	
day 20	221.43	188.67	211.10	232.17	163.10	182.77	199.63	533.18	
day 20 6h	210.97	194.35	196.59	229.76	163.07	172.58	189.61	545.49	
day20 12h	214.39	193.57	194.76	230.95	164.33	176.92	196.51	538.19	
day20 18h	214.55	203.70	197.15	229.03	167.90	176.07	201.82	542.26	
day 21	224.58	211.86	197.29	160.42	117.59	190.77	216.12	571.73	
day 21 6h	233.08	223.41	197.59	69.45	40.56	189.68	222.87	589.30	
day 21 12h	234.87	220.52	205.64	60.25	35.90	174.45	225.33	579.57	
day21-18h	244.28	232.00	209.65	52.49	35.24	163.22	220.05	573.92	
day 22 end	226.40	220.02	211.67	42.47	36.60	154.34	203.25	539.54	
day 22 18h	248.02	229.77	258.84	33.08	48.59	137.84	205.95	515.71	

Table 82: TEER values of the Caco-2 2D model after the treatment on day 21 with the controls (DMSO, Metformin, Staurosporine) and Gefitinib

N=1	TEER values [ $\Omega\text{-cm}^2$ ] Caco-2 2D							
	Metformin 750 $\mu\text{M}$	DMSO 0.3%	Staurosporin 0.1 $\mu\text{M}$	Staurosporine 1 $\mu\text{M}$	Staurosporine 10 $\mu\text{M}$	Gefitinib 3 $\mu\text{M}$	Gefitinib 30 $\mu\text{M}$	Gefitinib 300 $\mu\text{M}$
day 19	257,24	274,76	263,44	278,65	301,08	273,51	193,47	277,42
day 19_6h	216,36	213,89	211,97	172,40	263,53	238,64	197,16	192,30
day 19_12h	229,83	194,52	217,18	151,17	243,46	231,26	208,11	179,12
day19_18h	224,76	191,85	203,19	130,31	243,13	252,35	213,98	162,48
day 20	210,11	180,39	206,40	121,30	248,30	248,18	215,74	157,10
day 20_6h	205,47	188,67	194,19	131,58	252,47	237,29	200,72	167,32
day20_12h	206,32	181,52	195,34	134,51	264,68	230,30	198,93	172,16
day20_18h	210,88	192,89	202,43	138,67	271,41	229,86	198,89	179,82
day 21	211,29	192,22	202,50	137,44	275,09	234,39	205,30	176,91
day 21_6h	220,21	192,17	205,35	133,91	282,09	232,32	206,67	178,68
day 21_12h	226,88	195,92	201,53	129,31	278,63	250,83	211,18	176,99
day21-18h	235,34	202,91	202,46	122,16	281,11	249,60	214,18	183,07
Day 22 end	192,98	182,58	172,61	46,80	151,94	246,48	212,08	-4,56

N=2	TEER values [ $\Omega\text{-cm}^2$ ] Caco-2 2D							
	Metformin 750 $\mu\text{M}$	DMSO 0.3%	Staurosporin 0.1 $\mu\text{M}$	Staurosporine 1 $\mu\text{M}$	Staurosporine 10 $\mu\text{M}$	Gefitinib 3 $\mu\text{M}$	Gefitinib 30 $\mu\text{M}$	Gefitinib 300 $\mu\text{M}$
day 20_6h	292,53	276,71	195,79	220,14	211,60	229,10	202,59	198,28
day20_12h	311,97	273,00	201,42	212,26	207,86	233,84	193,60	198,90
day20_18h	294,10	278,72	203,77	212,87	204,80	229,49	204,25	199,71
day 21	303,01	276,90	208,24	213,22	205,74	233,77	192,90	207,35
day 21_6h	272,89	287,50	150,22	20,26	4,44	239,99	218,89	227,50
day 21_12h	249,25	277,92	127,81	5,16	-2,05	231,52	202,95	219,70
day21-18h	244,90	267,78	117,16	-0,07	-1,78	219,26	207,89	212,36
Day 22 end	280,40	275,27	113,27	-1,64	-2,48	215,85	202,98	210,28

N=3	TEER values [ $\Omega\text{-cm}^2$ ] Caco-2 2D							
	Metformin 750 $\mu\text{M}$	DMSO 0.3%	Staurosporine 0.1 $\mu\text{M}$	Staurosporine 1 $\mu\text{M}$	Staurosporine 10 $\mu\text{M}$	Gefitinib 3 $\mu\text{M}$	Gefitinib 30 $\mu\text{M}$	Gefitinib 300 $\mu\text{M}$
day 19	326,15	361,98	330,89	360,56	372,16	351,99	228,52	363,32
day 19_6h	264,07	260,83	252,82	195,24	307,00	288,70	223,39	221,23
day 19_12h	286,39	237,18	263,67	167,50	272,20	281,40	242,50	206,64
day19_18h	279,85	234,13	248,12	140,09	266,95	309,31	250,81	184,31
day 20	262,51	220,39	255,74	128,99	273,09	309,12	259,63	176,00
day 20_6h	257,19	227,49	238,50	139,16	278,43	297,16	237,92	189,21
day20_12h	257,64	217,42	241,73	141,47	293,29	290,09	239,28	194,80
day20_18h	264,26	234,86	253,57	145,09	300,58	292,20	243,50	205,87
day 21	266,38	234,45	256,52	142,83	306,62	300,98	255,34	204,79
day 21_6h	276,85	233,26	261,73	138,51	313,86	298,96	263,65	207,09
day 21_12h	285,73	239,12	257,58	133,20	310,30	323,67	273,50	207,28
day21-18h	300,05	249,08	260,15	125,29	315,69	325,25	279,17	215,52
Day 22 end	254,14	232,26	227,80	47,86	152,58	330,88	273,11	3,16

Table 83: TEER values of the Caco-2 2D model after the treatment on day 21 with the controls (DMSO, Metformin, Staurosporine) and Loperamide

N=1	TEER values [ $\Omega \cdot \text{cm}^2$ ] Caco-2 2D							
	Metformin 750 $\mu\text{M}$	DMSO 0.3%	Staurosporine 0.1 $\mu\text{M}$	Staurosporine 1 $\mu\text{M}$	Staurosporine 10 $\mu\text{M}$	Loperamide 3 $\mu\text{M}$	Loperamide 30 $\mu\text{M}$	Loperamide 300 $\mu\text{M}$
day 19	210.94	261.48	207.84	183.05	188.27	210.48	254.64	242.24
day 19_6h	200.76	246.63	183.24	162.02	201.85	206.88	244.88	221.68
day 19_12h	192.30	195.44	171.58	157.07	183.83	193.91	229.67	211.73
day19_18h	204.76	212.89	198.34	170.59	185.07	197.68	240.86	224.31
day 20	217.19	221.87	213.47	188.95	187.11	212.54	251.75	238.38
day 20_6h	218.95	241.98	225.25	212.60	188.10	221.11	253.55	234.58
day20_12h	204.76	240.60	224.24	225.44	195.17	230.89	260.01	220.97
day20_18h	202.32	247.16	223.21	237.09	199.53	229.37	253.37	230.46
day 21	187.40	223.95	217.12	43.94	25.82	242.53	280.20	11.43
day 21_6h	220.83	225.59	223.48	24.21	13.43	265.89	243.65	10.85
day 21_12h	238.05	253.60	210.22	17.05	12.88	251.57	215.38	10.43
day21-18h	258.78	266.03	206.46	14.13	12.62	246.40	202.87	10.48
Day 22 end	286.61	272.81	218.89	13.02	12.87	248.48	193.14	10.42

N=2	TEER values [ $\Omega \cdot \text{cm}^2$ ] Caco-2 2D							
	Metformin 750 $\mu\text{M}$	DMSO 0.3%	Staurosporin 0.1 $\mu\text{M}$	Staurosporin 1 $\mu\text{M}$	Staurosporin 10 $\mu\text{M}$	Loperamide 3 $\mu\text{M}$	Loperamide 30 $\mu\text{M}$	Loperamide 300 $\mu\text{M}$
day 20	402.27	318.85	309.25	279.92	377.54	261.98	316.69	287.88
day 20_6h	446.00	279.11	258.91	309.63	258.09	229.52	279.49	250.61
day20_12h	451.48	269.77	263.54	298.00	246.60	212.86	262.72	232.77
day20_18h	462.64	261.68	254.07	286.61	231.45	208.62	262.72	227.45
day 21	462.99	249.49	249.07	270.91	228.34	203.92	250.55	220.46
day 21_6h	243.17	227.40	246.37	71.41	22.85	200.83	280.20	12.45
day 21_12h	231.34	239.86	263.95	65.32	12.96	196.21	274.07	12.35
day121-18h	228.77	230.24	290.27	58.72	12.02	201.58	264.44	11.93
Day 22 end	229.63	231.66	310.32	49.27	12.22	195.02	258.01	12.35

N=3	TEER values [ $\Omega \cdot \text{cm}^2$ ] Caco-2 2D							
	Metformin 750 $\mu\text{M}$	DMSO 0.3%	Staurosporin 0.1 $\mu\text{M}$	Staurosporin 1 $\mu\text{M}$	Staurosporin 10 $\mu\text{M}$	Loperamide 3 $\mu\text{M}$	Loperamide 30 $\mu\text{M}$	Loperamide 300 $\mu\text{M}$
day 19	333.53	266.48	248.60	362.59	312.92	290.14	335.60	277.50
day 19_6h	326.81	233.14	242.00	326.72	286.74	253.19	299.88	236.86
day 19_12h	306.92	196.05	233.13	326.06	286.73	250.61	274.26	219.54
day 19_18h	314.82	190.15	248.28	304.96	296.90	252.90	259.19	221.23
day 20	295.71	200.54	247.05	312.77	274.94	253.63	276.47	210.41
day 20_6h	275.73	185.23	242.10	307.43	267.11	237.18	264.78	193.04
day 20_12h	270.32	177.73	237.24	293.75	271.28	232.80	254.21	185.74
day 20_18h	271.16	183.31	243.11	305.84	262.88	232.26	267.36	186.45
Day21	270.97	184.35	245.68	295.23	263.84	235.73	270.98	194.02
day 21_6h	295.58	199.53	229.61	47.18	20.07	285.96	264.79	17.21
day 21_12h	296.19	192.45	233.51	25.84	11.44	266.70	226.27	17.32
day 21_18h	302.27	195.25	234.34	15.72	10.76	257.95	211.93	17.25
day 22 end	311.68	203.80	237.17	12.89	11.21	246.88	184.06	17.20

Table 84: TEER values of the Caco-2 2D model after the treatment on day 21 with the controls (DMSO, Metformin, Staurosporine) and Terfenadine

N=1	TEER values [ $\Omega \cdot \text{cm}^2$ ] Caco-2 2D							
	Metformin 750 $\mu\text{M}$	DMSO 0.3%	Staurosporin 0.1 $\mu\text{M}$	Staurosporin 1 $\mu\text{M}$	Staurosporin 10 $\mu\text{M}$	Terfenadine 3 $\mu\text{M}$	Terfenadine 30 $\mu\text{M}$	Terfenadine 300 $\mu\text{M}$
day 19	126.35	109.69	154.76	155.23	153.89	148.47	159.39	145.80
day 19_6h	157.19	126.53	163.81	198.69	160.06	165.46	167.55	160.69
day 19_12h	179.84	142.02	177.95	191.81	162.03	173.99	162.21	146.36
day19_18h	185.71	162.86	208.14	211.69	179.07	190.56	170.75	183.37
day 20	196.74	165.91	222.06	218.08	197.93	217.27	188.32	197.09
day 20_6h	194.09	168.09	227.69	216.55	198.54	226.33	182.46	204.07
day20_12h	197.63	175.68	217.82	204.30	214.70	217.12	190.88	214.62
day20_18h	206.26	183.74	219.69	208.43	217.30	222.41	201.79	208.77
day 21	209.06	197.65	223.26	201.15	165.69	226.94	224.78	36.59
day 21_6h	224.60	215.85	219.55	27.52	15.11	233.58	34.00	12.10
day 21_12h	248.42	214.91	195.37	15.77	13.07	239.72	12.11	14.15
day21-18h	258.31	215.01	189.62	13.41	12.23	238.99	13.74	14.61
Day 22 end	270.03	215.46	192.87	12.71	12.51	230.26	17.98	13.90

N=2	TEER values [ $\Omega \cdot \text{cm}^2$ ] Caco-2 2D							
	Metformin 750 $\mu\text{M}$	DMSO 0.3%	Staurosporin 0.1 $\mu\text{M}$	Staurosporin 1 $\mu\text{M}$	Staurosporin 10 $\mu\text{M}$	Terfenadine 3 $\mu\text{M}$	Terfenadine 30 $\mu\text{M}$	Terfenadine 300 $\mu\text{M}$
day 19	338.55	294.43	279.40	346.19	322.30	279.78	313.85	282.12
day 19_6h	271.72	247.44	229.41	255.86	285.37	219.96	251.64	252.35
day 19_12h	257.66	228.32	206.13	245.88	279.04	207.63	245.30	241.57
day19_18h	250.96	220.04	206.91	233.22	262.08	204.57	234.03	240.39
day 20	243.57	215.89	210.64	232.76	259.97	200.13	233.09	225.16
day 20_6h	237.46	215.81	214.20	226.10	258.21	199.24	225.11	218.93
day20_12h	230.14	211.91	219.74	224.52	249.30	198.31	224.72	216.56
day20_18h	226.23	202.56	224.76	221.69	247.09	197.95	213.15	214.11
day 21	212.64	195.70	213.59	63.62	53.22	209.99	218.18	14.26
day 21_6h	225.82	200.30	231.70	20.40	15.36	214.58	238.78	14.00
day 21_12h	221.17	205.23	253.90	14.72	13.51	209.63	188.43	13.82
Day 21-18h	221.50	211.87	269.10	13.83	14.10	207.63	107.66	14.53
Day 22 end	224.60	203.22	281.41	13.01	13.89	207.06	85.96	14.36

N=3	TEER values [ $\Omega \cdot \text{cm}^2$ ] Caco-2 2D							
	Metformin 750 $\mu\text{M}$	DMSO 0.3%	Staurosporine 0.1 $\mu\text{M}$	Staurosporine 1 $\mu\text{M}$	Staurosporine 10 $\mu\text{M}$	Terfenadine 3 $\mu\text{M}$	Terfenadine 30 $\mu\text{M}$	Terfenadine 300 $\mu\text{M}$
day 19	135.30	116.26	170.88	174.46	169.93	164.25	179.43	162.90
day 19_6h	170.54	135.19	178.65	227.44	174.41	180.06	184.06	177.39
day 19_12h	197.90	152.46	195.90	218.57	176.71	189.95	177.52	160.18
day 19_18h	207.76	179.28	239.03	250.80	198.99	213.22	192.16	208.65
day 20	223.27	183.79	257.73	263.05	225.78	249.19	216.70	224.99
day 20_6h	219.28	186.01	268.98	264.38	227.77	266.66	206.48	237.01
day 20_12h	223.80	197.11	256.37	249.74	250.55	252.47	218.79	253.60
day 20_18h	235.68	208.60	260.40	258.85	259.85	264.45	238.48	251.47
Day21	223.54	214.35	251.83	230.43	171.86	256.79	255.88	25.63
day 21_6h	246.99	240.62	241.99	17.07	6.69	270.20	24.47	1.02
day 21_12h	280.64	241.25	205.74	7.31	1.90	281.61	1.16	NA
day 21_18h	297.40	241.11	196.07	3.85	1.10	282.82	NA	NA
day 22 end	314.64	247.48	197.77	2.46	1.11	273.59	NA	NA



Table 86: TEER values of the Caco-2 OoC model. Shown are the TEER values of the experiment with Lop, Terf, Flav, Dic and Met. TEER values before treatment on day 6 (a.), on day 6 (1h after treatment) (b.), on day 6 (4h after treatment) (c.) and on day 7 (24h of treatment) (d.)

**a**

Caco2 OoC Teer  
1 day6  
Plate ID blue  
Date 27-May-2021  
Time 09:10:02  
Area 0,0057

RTEER	1	2	3	4	5	6	7	8	9	10	11	12	13	14	15	16	17	18	19	20	21	22	23	24	
A	693,019	667,838	667,838	667,838	667,838	667,838	638,775616	714,531388	512,783112	721,205264	677,833194	704,463231													
B																									
C	No Data	No Data	No Data	No Data	No Data	No Data	No Data	No Data	No Data	No Data	No Data	No Data	No Data	No Data	No Data	No Data	No Data	No Data	No Data	No Data	No Data	No Data	No Data	No Data	
D	594,348	377,341	377,341	377,341	377,341	377,341	370,169092	413,897491	488,739757	499,685735	523,577539	431,75019													
E																									
F	No Data	No Data	No Data	No Data	No Data	No Data	No Data	No Data	No Data	No Data	No Data	No Data	No Data	No Data	No Data	No Data	No Data	No Data	No Data	No Data	No Data	No Data	No Data	No Data	
G	427,861	347,935	347,935	347,935	347,935	347,935	322,02124	329,26198	304,312319	461,63589	535,873195	427,27729													
H																									
I	No Data	No Data	No Data	No Data	No Data	No Data	No Data	No Data	No Data	No Data	No Data	No Data	No Data	No Data	No Data	No Data	No Data	No Data	No Data	No Data	No Data	No Data	No Data	No Data	
J	414,613	258	258	258	258	258	309,095346	403,797753	528,32398	240,134748	548,140953	433,265257													
K																									
L	No Data	No Data	No Data	No Data	No Data	No Data	No Data	No Data	No Data	No Data	No Data	No Data	No Data	No Data	No Data	No Data	No Data	No Data	No Data	No Data	No Data	No Data	No Data	No Data	
M	356,889	358,154	358,154	358,154	358,154	358,154	346,177291	413,784856	389,616747	387,290474	440,020046	357,102582													
N																									
O	No Data	No Data	No Data	No Data	No Data	No Data	No Data	No Data	No Data	No Data	No Data	No Data	No Data	No Data	No Data	No Data	No Data	No Data	No Data	No Data	No Data	No Data	No Data	No Data	
P																									

**b**

Caco2 OoC Teer 1  
day6  
Plate ID blue\_1h  
Date 27-May-2021  
Time 10:40:22  
Area 0,0057

RTEER	1	2	3	4	5	6	7	8	9	10	11	12	13	14	15	16	17	18	19	20	21	22	23	24
A	0	0	0	0	0	0	0	0	0	0	0	0	0	0	0	0	0	0	258,63044	344,524516				
B																								
C	No Data	No Data	No Data	No Data	No Data	No Data	No Data	No Data	No Data	No Data	No Data	No Data	No Data	No Data	No Data	No Data	No Data	No Data	No Data	No Data	No Data	No Data	No Data	No Data
D	303,2343	319,2464	319,2464	319,2464	319,2464	319,2464	316,431611	327,059873	429,382047	461,86733	355,064981	320,287263												
E																								
F	No Data	No Data	No Data	No Data	No Data	No Data	No Data	No Data	No Data	No Data	No Data	No Data	No Data	No Data	No Data	No Data	No Data	No Data	No Data	No Data	No Data	No Data	No Data	No Data
G	305,7581	255,8849	255,8849	255,8849	255,8849	255,8849	251,182014	283,283236	244,777983	482,470272	306,141412	262,351927												
H																								
I	No Data	No Data	No Data	No Data	No Data	No Data	No Data	No Data	No Data	No Data	No Data	No Data	No Data	No Data	No Data	No Data	No Data	No Data	No Data	No Data	No Data	No Data	No Data	No Data
J	238,9730	41	41	41	41	41	256,574386	394,657132	557,493043	274,56372	547,268964	317,687335												
K																								
L	No Data	No Data	No Data	No Data	No Data	No Data	No Data	No Data	No Data	No Data	No Data	No Data	No Data	No Data	No Data	No Data	No Data	No Data	No Data	No Data	No Data	No Data	No Data	No Data
M	296,9206	308,0160	308,0160	308,0160	308,0160	308,0160	294,323956	331,095184	305,759083	316,207841	395,03804	No Fit												
N																								
O	No Data	No Data	No Data	No Data	No Data	No Data	No Data	No Data	No Data	No Data	No Data	0	No Data	No Data	No Data	No Data	No Data	No Data	No Data	No Data	No Data	No Data	No Data	No Data
P																								

**c**

Caco2 OoC Teer 1  
day6  
Plate ID blue\_4h  
Date 27-May-2021  
Time 13:38:44  
Area 0,0057

RTEER	1	2	3	4	5	6	7	8	9	10	11	12	13	14	15	16	17	18	19	20	21	22	23	24
A	0	0	0	0	0	0	0	0	0	0	0	0	0	0	0	0	0	0	404,22072	353,846241				
B																								
C	No Data	No Data	No Data	No Data	No Data	No Data	No Data	No Data	No Data	No Data	No Data	No Data	No Data	No Data	No Data	No Data	No Data	No Data	No Data	No Data	No Data	No Data	No Data	No Data
D	398,5424	253,7222	253,7222	253,7222	253,7222	253,7222	239,603882	381,678004	389,029461	377,809486	480,944601	604,839235												
E																								
F	No Data	No Data	No Data	No Data	No Data	No Data	No Data	No Data	No Data	No Data	No Data	No Data	No Data	No Data	No Data	No Data	No Data	No Data	No Data	No Data	No Data	No Data	No Data	No Data
G	402,5254	272,2682	272,2682	272,2682	272,2682	272,2682	245,843817	261,662014	230,750279	493,087939	440,490606	271,284283												
H																								
I	No Data	No Data	No Data	No Data	No Data	No Data	No Data	No Data	No Data	No Data	No Data	No Data	No Data	No Data	No Data	No Data	No Data	No Data	No Data	No Data	No Data	No Data	No Data	No Data
J	168,7446	93,19699	93,19699	93,19699	93,19699	93,19699	168,466054	371,3589	497,97302	270,293709	589,047991	339,774117												
K																								
L	No Data	No Data	No Data	No Data	No Data	No Data	No Data	No Data	No Data	No Data	No Data	No Data	No Data	No Data	No Data	No Data	No Data	No Data	No Data	No Data	No Data	No Data	No Data	No Data
M	313,9051	282,2768	282,2768	282,2768	282,2768	282,2768	228,748603	418,474308	354,231654	469,765115	708,877282	No Fit												
N																								
O	No Data	No Data	No Data	No Data	No Data	No Data	No Data	No Data	No Data	No Data	No Data	0	No Data	No Data	No Data	No Data	No Data	No Data	No Data	No Data	No Data	No Data	No Data	No Data
P																								

**d**

Caco2 OoC TEER1  
Plate ID blue24h  
Date 28-May-2021  
Time 10:11:41  
Area 0,0057

RTEER	1	2	3	4	5	6	7	8	9	10	11	12	13	14	15	16	17	18	19	20	21	22	23	24
A	0	0	0	0	0	0	0	0	0	0	0	0	0	0	0	0	0	0	421,593416	72,3795333				
B																								
C	No Data	No Data	No Data	No Data	No Data	No Data	No Data	No Data	No Data	No Data	No Data	No Data	No Data	No Data	No Data	No Data	No Data	No Data	No Data	No Data	No Data	No Data	No Data	No Data
D	402,2608	348,5799	348,5799	348,5799	348,5799	348,5799	368,55688	0	0	0	117,158137	618,538013												
E																								
F	No Data	No Data	No Data	No Data	No Data	No Data	No Data	No Data	No Data	No Data	No Data	No Data	No Data	No Data	No Data	No Data	No Data	No Data	No Data	No Data	No Data	No Data	No Data	No Data
G	433,6793	472,9885	472,9885	472,9885	472,9885	472,9885	490,996862	435,895104	345,789211	472,491635	138,796001	407,052162												
H																								
I	No Data	No Data	No Data	No Data	No Data	No Data	No Data	No Data	No Data	No Data	No Data	No Data	No Data	No Data	No Data	No Data	No Data	No Data	No Data	No Data	No Data	No Data	No Data	No Data
J	93,74562	77,19817	77,19817	77,19817	77,19817	77,19817	85,4515922	460,21141	477,810325	435,745689	529,359651	535,194966												
K																								
L	No Data	No Data	No Data	No Data																				

Table 87: TEER values of the Caco-2 OoC model after treatment with 5-FU, Med and Stau. Shown are the TEER values of the experiment with 5-FU, Med and Stau. Platelayout (a.), TEER values before treatment on day 3 (b.), day 4 (c.) and day 5 (d.)

a

	1	2	3	4	5	6	7	8	9	10	11	12	13	14	15	16	17	18	19	20	21	22	23	24
A	x			x			x			x			x			x			5FU HD		5FU MD			
B																								
C	No Data	No Data	No Data	No Data	No Data	No Data	No Data	No Data	No Data	No Data	No Data	No Data	No Data	No Data	No Data	No Data	No Data	No Data	No Data	No Data	No Data	No Data	No Data	No Data
D	x			x			x			x			x			x			5FU HD		5FU MD			
E																								
F	No Data	No Data	No Data	No Data	No Data	No Data	No Data	No Data	No Data	No Data	No Data	No Data	No Data	No Data	No Data	No Data	No Data	No Data	No Data	No Data	No Data	No Data	No Data	No Data
G	x			x			x			x			x			x			5FU HD		5FU MD			
H																								
I	No Data	No Data	No Data	No Data	No Data	No Data	No Data	No Data	No Data	No Data	No Data	No Data	No Data	No Data	No Data	No Data	No Data	No Data	No Data	No Data	No Data	No Data	No Data	No Data
J	Stau HD	Stau HD	Stau HD	Stau HD	Stau HD	Stau HD	Stau HD	Stau HD	Stau HD	Stau LD	Stau LD	Stau LD	Stau LD	Stau LD	Stau LD	Stau LD	Stau LD	Stau LD	Med		Med			
K																								
L	No Data	No Data	No Data	No Data	No Data	No Data	No Data	No Data	No Data	No Data	No Data	No Data	No Data	No Data	No Data	No Data	No Data	No Data	No Data	No Data	No Data	No Data	No Data	No Data
M	Stau MD	Stau MD	Stau MD	Stau MD	Stau MD	Stau MD	Stau MD	Stau MD	Stau MD	SFU LD	SFU LD	SFU LD	SFU LD	SFU LD	SFU LD	SFU LD	SFU LD	SFU LD	Med					
N																								
O																								

b

Caco-2 OoC day 3 No1\_2

Plate ID green  
Date 24-May-2021  
Time 09:06:38  
Area 0,0057

	1	2	3	4	5	6	7	8	9	10	11	12	13	14	15	16	17	18	19	20	21	22	23	24
A	103,093039	287,387966	32,0309622	59,0387168	206,450981	104,544553	86,0569612	55,5872365																
B																								
C	No Data	No Data	No Data	No Data	No Data	No Data	No Data	No Data	No Data	No Data	No Data	No Data	No Data	No Data	No Data	No Data	No Data	No Data	No Data	No Data	No Data	No Data	No Data	No Data
D	55,3890153	155,37373	85,6760259	87,1761458	208,954754	92,2498721	185,355755	122,494176																
E																								
F	No Data	No Data	No Data	No Data	No Data	No Data	No Data	No Data	No Data	No Data	No Data	No Data	No Data	No Data	No Data	No Data	No Data	No Data	No Data	No Data	No Data	No Data	No Data	No Data
G	67,0642483	155,037987	131,265697	29,3086388	118,170704	261,945352	203,178958	168,097446																
H																								
I	No Data	No Data	No Data	No Data	No Data	No Data	No Data	No Data	No Data	No Data	No Data	No Data	No Data	No Data	No Data	No Data	No Data	No Data	No Data	No Data	No Data	No Data	No Data	No Data
J	159,760865	182,851955	136,93664	170,213764	284,281553	58,3658576	55,320062	144,005329																
K																								
L	No Data	No Data	No Data	No Data	No Data	No Data	No Data	No Data	No Data	No Data	No Data	No Data	No Data	No Data	No Data	No Data	No Data	No Data	No Data	No Data	No Data	No Data	No Data	No Data
M	4,52453966	122,420969	264,979643	227,467616	112,391288	184,954494	259,514016	98,0746909																
N																								
O	No Data	No Data	No Data	No Data	No Data	No Data	No Data	No Data	No Data	No Data	No Data	No Data	No Data	No Data	No Data	No Data	No Data	No Data	No Data	No Data	No Data	No Data	No Data	No Data

c

Caco-2 OoC TEER No1 day 4

Plate ID green  
Date 25-May-2021  
Time 08:19:16  
Area 0,0057

	1	2	3	4	5	6	7	8	9	10	11	12	13	14	15	16	17	18	19	20	21	22	23	24
A	491,418732	454,601764	1428,198599	279,67687	177,883734	430,037995	348,470647	85,1710173																
B																								
C	No Data	No Data	No Data	No Data	No Data	No Data	No Data	No Data	No Data	No Data	No Data	No Data	No Data	No Data	No Data	No Data	No Data	No Data	No Data	No Data	No Data	No Data	No Data	No Data
D	330,871867	281,824611	150,370281	181,260312	341,134622	312,995554	316,311465	321,833589																
E																								
F	No Data	No Data	No Data	No Data	No Data	No Data	No Data	No Data	No Data	No Data	No Data	No Data	No Data	No Data	No Data	No Data	No Data	No Data	No Data	No Data	No Data	No Data	No Data	No Data
G	286,421709	264,360385	188,691249	No Fit	245,229453	287,544457	328,700868	147,915344																
H																								
I	No Data	No Data	No Data	No Data	No Data	No Data	No Data	No Data	No Data	No Data	No Data	No Data	No Data	No Data	No Data	No Data	No Data	No Data	No Data	No Data	No Data	No Data	No Data	No Data
J	297,698649	261,471816	303,475066	357,558662	269,678296	347,012632	319,352606	126,955004																
K																								
L	No Data	No Data	No Data	No Data	No Data	No Data	No Data	No Data	No Data	No Data	No Data	No Data	No Data	No Data	No Data	No Data	No Data	No Data	No Data	No Data	No Data	No Data	No Data	No Data
M	8,44770292	311,142008	210,919548	315,839394	225,388467	343,933809	351,698655	156,269484																
N																								
O	No Data	No Data	No Data	No Data	No Data	No Data	No Data	No Data	No Data	No Data	No Data	No Data	No Data	No Data	No Data	No Data	No Data	No Data	No Data	No Data	No Data	No Data	No Data	No Data
P																								

d

Caco-2 day 5 TEER No1

Plate ID green  
Date 26-May-2021  
Time 09:16:28  
Area 0,0057

	1	2	3	4	5	6	7	8	9	10	11	12	13	14	15	16	17	18	19	20	21	22	23	24
A	506,998884	399,968297	379,524422	339,359512	332,806523	363,712345	344,105588	137,005828																
B																								
C	No Data	No Data	No Data	No Data	No Data	No Data	No Data	No Data	No Data	No Data	No Data	No Data	No Data	No Data	No Data	No Data	No Data	No Data	No Data	No Data	No Data	No Data	No Data	No Data
D	327,845155	273,377074	302,066736	282,730656	339,475809	320,150231	311,014627	352,746896																
E																								
F	No Data	No Data	No Data	No Data	No Data	No Data	No Data	No Data	No Data	No Data	No Data	No Data	No Data	No Data	No Data	No Data	No Data	No Data	No Data	No Data	No Data	No Data	No Data	No Data
G	334,962563	265,752006	285,235816	No Fit	211,698011	280,523092	298,931676	283,91574																
H																								
I	No Data	No Data	No Data	No Data	No Data	No Data	No Data	No Data	No Data	No Data	No Data	No Data	No Data	No Data	No Data	No Data	No Data	No Data	No Data	No Data	No Data	No Data	No Data	No Data
J	286,963132	286,968749	264,594875	379,573074	290,051762	308,967245	283,82643	307,017756																
K																								
L	No Data	No Data	No Data	No Data	No Data	No Data	No Data	No Data	No Data	No Data	No Data	No Data	No Data	No Data	No Data	No Data	No Data	No Data	No Data	No Data	No Data	No Data	No Data	No Data
M	15,7195211	290,393248	291,706597	278,115619	226,510255	334,428014	324,007773	160,803336																
N																								
O	No Data	No Data	No Data	No Data	No Data	No Data	No Data	No Data	No Data	No Data	No Data	No Data	No Data	No Data	No Data	No Data	No Data	No Data	No Data	No Data	No Data	No Data	No Data	No Data
P																								

Table 88: TEER values of the Caco-2 OoC model. Shown are the TEER values of the experiment with 5-FU, Med and Stau. TEER values before treatment on day 6 (a.), on day 6 (1h after treatment) (b.), on day 6 (4h after treatment) (c.) and on day 7 (24h of treatment) (d.)

**a**

Caco2 OoC Teer 1  
day 6  
Plate ID green  
Date 27-May-2021  
Time 09:03:01  
Area 0,0057

RTEER																								
	1	2	3	4	5	6	7	8	9	10	11	12	13	14	15	16	17	18	19	20	21	22	23	24
A	635,652391			504,487213			504,751097			419,266197			395,35636			608,555366			583,535083			502,931711		
B																								
C	No Data	No Data	No Data	No Data	No Data	No Data	No Data	No Data	No Data	No Data	No Data	No Data	No Data	No Data	No Data	No Data	No Data	No Data	No Data	No Data	No Data	No Data	No Data	No Data
D	414,475765			337,885058			408,863805			404,780101			453,517226			400,177376			418,720694			453,32179		
E																								
F	No Data	No Data	No Data	No Data	No Data	No Data	No Data	No Data	No Data	No Data	No Data	No Data	No Data	No Data	No Data	No Data	No Data	No Data	No Data	No Data	No Data	No Data	No Data	No Data
G	379,331935			330,589365			341,777358			No Fit			261,284718			334,540203			370,652294			391,464598		
H																								
I	No Data	No Data	No Data	No Data	No Data	No Data	No Data	No Data	No Data	No Data	No Data	No Data	No Data	No Data	No Data	No Data	No Data	No Data	No Data	No Data	No Data	No Data	No Data	No Data
J	319,642877			354,388044			301,404993			415,070597			348,191832			377,924716			368,842796			360,698106		
K																								
L	No Data	No Data	No Data	No Data	No Data	No Data	No Data	No Data	No Data	No Data	No Data	No Data	No Data	No Data	No Data	No Data	No Data	No Data	No Data	No Data	No Data	No Data	No Data	No Data
M	57,6820827			312,094599			331,419463			318,903924			247,121598			354,958362			337,433414			193,340775		
N																								
O	No Data	No Data	No Data	No Data	No Data	No Data	No Data	No Data	No Data	No Data	No Data	No Data	No Data	No Data	No Data	No Data	No Data	No Data	No Data	No Data	No Data	0	No Data	No Data
P																								

**b**

Caco2 OoC Teer 1  
day 6  
Plate ID green\_1h  
Date 27-May-2021  
Time 10:38:46  
Area 0,0057

RTEER																								
	1	2	3	4	5	6	7	8	9	10	11	12	13	14	15	16	17	18	19	20	21	22	23	24
A	296,663816			284,440532			263,444453			223,906482			198,097107			245,365814			306,03426			223,482202		
B																								
C	No Data	No Data	No Data	No Data	No Data	No Data	No Data	No Data	No Data	No Data	No Data	No Data	No Data	No Data	No Data	No Data	No Data	No Data	No Data	No Data	No Data	No Data	No Data	No Data
D	283,606323			226,888789			294,747148			303,385559			335,161777			325,32149			423,607706			284,394369		
E																								
F	No Data	No Data	No Data	No Data	No Data	No Data	No Data	No Data	No Data	No Data	No Data	No Data	No Data	No Data	No Data	No Data	No Data	No Data	No Data	No Data	No Data	No Data	No Data	No Data
G	275,682312			250,565815			262,12598			49,6685608			207,72542			258,79936			376,720033			270,453492		
H																								
I	No Data	No Data	No Data	No Data	No Data	No Data	No Data	No Data	No Data	No Data	No Data	No Data	No Data	No Data	No Data	No Data	No Data	No Data	No Data	No Data	No Data	No Data	No Data	No Data
J	56,8204319			No Data			66,8469383			247,158368			202,223164			222,660939			369,470615			257,294996		
K																								
L	No Data	No Data	No Data	No Data	No Data	No Data	No Data	No Data	No Data	No Data	No Data	No Data	No Data	No Data	No Data	No Data	No Data	No Data	No Data	No Data	No Data	No Data	No Data	No Data
M	26,1172602			82,6587059			93,3584			181,198178			185,758658			297,928717			237,725313			131,524205		
N																								
O	No Data	No Data	No Data	No Data	No Data	No Data	No Data	No Data	No Data	No Data	No Data	No Data	No Data	No Data	No Data	No Data	No Data	No Data	No Data	No Data	No Data	0	No Data	No Data
P																								

**c**

Caco2 OoC Teer 1  
day 6  
Plate ID green\_4h  
Date 27-May-2021  
Time 13:42:38  
Area 0,0057

RTEER																								
	1	2	3	4	5	6	7	8	9	10	11	12	13	14	15	16	17	18	19	20	21	22	23	24
A	510,655613			478,639719			373,013848			292,339487			391,092126			519,161353			548,222758			431,038136		
B																								
C	No Data	No Data	No Data	No Data	No Data	No Data	No Data	No Data	No Data	No Data	No Data	No Data	No Data	No Data	No Data	No Data	No Data	No Data	No Data	No Data	No Data	No Data	No Data	No Data
D	461,88626			390,94401			465,503195			482,731524			530,077137			547,860266			532,373894			544,007687		
E																								
F	No Data	No Data	No Data	No Data	No Data	No Data	No Data	No Data	No Data	No Data	No Data	No Data	No Data	No Data	No Data	No Data	No Data	No Data	No Data	No Data	No Data	No Data	No Data	No Data
G	429,287925			355,230893			395,980116			46,5946976			347,525715			313,716737			477,004606			509,16236		
H																								
I	No Data	No Data	No Data	No Data	No Data	No Data	No Data	No Data	No Data	No Data	No Data	No Data	No Data	No Data	No Data	No Data	No Data	No Data	No Data	No Data	No Data	No Data	No Data	No Data
J	5,58604456			7,8687525			7,13524285			137,418048			96,1666119			125,627995			549,14585			649,319909		
K																								
L	No Data	No Data	No Data	No Data	No Data	No Data	No Data	No Data	No Data	No Data	No Data	No Data	No Data	No Data	No Data	No Data	No Data	No Data	No Data	No Data	No Data	No Data	No Data	No Data
M	8,69078898			22,916139			12,7472739			314,782554			379,558647			728,30278			366,063891			264,538579		
N																								
O	No Data	No Data	No Data	No Data	No Data	No Data	No Data	No Data	No Data	No Data	No Data	No Data	No Data	No Data	No Data	No Data	No Data	No Data	No Data	No Data	No Data	0	No Data	No Data
P																								

**d**

Caco2 OoC  
TEER1  
Plate ID green  
Date 28-May-2021  
Time 10:10:30  
Area 0,0057

RTEER																								
	1	2	3	4	5	6	7	8	9	10	11	12	13	14	15	16	17	18	19	20	21	22	23	24
A	572,169942			647,534539			459,689999			337,125552			633,070822			703,520068			564,534745			524,939779		
B																								
C	No Data	No Data	No Data	No Data	No Data	No Data	No Data	No Data	No Data	No Data	No Data	No Data	No Data	No Data	No Data	No Data	No Data	No Data	No Data	No Data	No Data	No Data	No Data	No Data
D	213,145738			465,707263			394,317695			391,853927			425,323013			436,249746			513,171599			532,733068		
E																								
F	No Data	No Data	No Data	No Data	No Data	No Data	No Data	No Data	No Data	No Data	No Data	No Data	No Data	No Data	No Data	No Data	No Data	No Data	No Data	No Data	No Data	No Data	No Data	No Data
G	438,836555			444,509381			465,391989			46,4977223			427,345686			451,282767			561,98427			593,879823		
H																								
I	No Data	No Data	No Data	No Data	No Data	No Data	No Data	No Data	No Data	No Data	No Data	No Data	No Data	No Data	No Data	No Data	No Data	No Data	No Data	No Data	No Data	No Data	No Data	No Data
J	1,73212034			2,06419545			0,84288109			65,6277611			74,3072409			56,6772197			478,373046			487,572642		
K																								
L	No Data	No Data	No Data	No Data	No Data	No Data	No Data	No Data	No Data	No Data	No Data	No Data	No Data	No Data	No Data	No Data	No Data	No Data	No Data	No Data	No Data	No Data	No Data	No Data
M	0			1,08691605			0,76987955			402,128673			311,748369											





Table 90: TEER values of the Caco-2 OoC model. Shown are the TEER values of the experiment with 5-FU, Alo, Gef and DMSO. TEER values before treatment on day 6 (a.), on day 6 (1h after treatment) (b.), on day 6 (4h after treatment) (c.) and on day 7 (24h of treatment) (d.)

**a**

Caco2 OoaCTeer 1 day 6  
 Plate ID red  
 Date 27-May-2021  
 Time 09:11:53  
 Area 0,0057

RTEER	1	2	3	4	5	6	7	8	9	10	11	12	13	14	15	16	17	18	19	20	21	22	23	24
A	633,095108	662,648717	659,115916	183,084333	616,822518	715,490834	747,242937	719,80412																
B																								
C	No Data	No Data	No Data	No Data	No Data	No Data	No Data	No Data																
D	463,252062	394,899525	434,701971	447,911931	419,299075	444,640828	462,178259	404,616252																
E																								
F	No Data	No Data	No Data	No Data	No Data	No Data	No Data	No Data																
G	423,021495	413,981534	438,026019	424,322026	425,004142	349,323378	400,428354	415,705179																
H																								
I	No Data	No Data	No Data	No Data	No Data	No Data	No Data	No Data																
J	414,491241	No Data	443,301163	437,461001	327,516818	395,585213	445,031169	423,379476																
K																								
L	No Data	No Data	No Data	No Data	No Data	No Data	No Data	No Data																
M	351,671085	357,640548	430,741597	358,909507	340,134268	367,861812	205,989239	351,814641																
N																								
O	No Data	No Data	No Data	No Data	No Data	No Data	No Data	No Data																
P																								

**b**

Caco2 OoaCTeer 1 day 6  
 Plate ID red\_1h  
 Date 27-May-2021  
 Time 10:37:08  
 Area 0,0057

RTEER	1	2	3	4	5	6	7	8	9	10	11	12	13	14	15	16	17	18	19	20	21	22	23	24
A	276,666753	233,528962	248,839986	118,513757	280,726856	264,465172	231,858193	291,112413																
B																								
C	No Data	No Data	No Data	No Data	No Data	No Data	No Data	No Data																
D	292,596755	270,22565	307,210677	270,746098	243,411391	321,990259	292,810374	301,013833																
E																								
F	No Data	No Data	No Data	No Data	No Data	No Data	No Data	No Data																
G	271,103101	279,219832	327,314631	313,12822	275,421596	236,19919	268,781639	248,333774																
H																								
I	No Data	No Data	No Data	No Data	No Data	No Data	No Data	No Data																
J	252,954871	No Data	380,752109	360,390106	227,171494	332,647432	337,913655	264,499952																
K																								
L	No Data	No Data	No Data	No Data	No Data	No Data	No Data	No Data																
M	268,309826	290,139995	321,097883	271,184543	232,957565	264,678745	No Fit	284,945435																
N																								
O	No Data	No Data	No Data	No Data	No Data	No Data	No Data	0																
P																								

**c**

Caco2 OoaCTeer 1 day 6  
 Plate ID red\_4h  
 Date 27-May-2021  
 Time 13:40:03  
 Area 0,0057

RTEER	1	2	3	4	5	6	7	8	9	10	11	12	13	14	15	16	17	18	19	20	21	22	23	24
A	444,182097	428,462316	494,530697	188,195254	460,177626	533,833308	491,675059	513,211704																
B																								
C	No Data	No Data	No Data	No Data	No Data	No Data	No Data	No Data																
D	452,380833	457,211937	470,68116	499,418426	450,899373	536,215796	504,914233	436,057162																
E																								
F	No Data	No Data	No Data	No Data	No Data	No Data	No Data	No Data																
G	399,685876	420,012512	444,582977	527,487428	490,501264	415,67725	417,579023	413,91209																
H																								
I	No Data	No Data	No Data	No Data	No Data	No Data	No Data	No Data																
J	441,655052	512,068024	567,899352	480,265251	330,708728	475,74807	520,426978	484,87352																
K																								
L	No Data	No Data	No Data	No Data	No Data	No Data	No Data	No Data																
M	366,766153	381,556686	434,291599	436,315785	413,503199	479,511887	No Fit	381,09077																
N																								
O	No Data	No Data	No Data	No Data	No Data	No Data	No Data	0																
P																								

**d**

Caco2 OoaCTEER1  
 Plate ID red 24h  
 Date 28-May-2021  
 Time 10:19:45  
 Area 0,0057

RTEER	1	2	3	4	5	6	7	8	9	10	11	12	13	14	15	16	17	18	19	20	21	22	23	24
A	748,508246	615,839512	679,706369	639,089387	692,750794	843,38968	766,787536	133,372995																
B																								
C	No Data	No Data	No Data	No Data	No Data	No Data	No Data	No Data																
D	696,665835	657,578925	654,521798	667,586681	550,467568	644,351487	716,850388	249,960088																
E																								
F	No Data	No Data	No Data	No Data	No Data	No Data	No Data	No Data																
G	592,943219	592,69961	589,468522	619,655471	598,120232	654,080596	527,212281	330,539874																
H																								
I	No Data	No Data	No Data	No Data	No Data	No Data	No Data	No Data																
J	431,113808	520,541599	562,831432	572,646957	472,275126	594,758315	668,650646	659,169623																
K																								
L	No Data	No Data	No Data	No Data	No Data	No Data	No Data	No Data																
M	513,499674	539,037206	572,822257	385,153754	478,979063	571,737724	No Fit	536,831117																
N																								
O	No Data	No Data	No Data	No Data	No Data	No Data	No Data	No Data																
P																								

Table 91: TEER values of the Caco-2 OoC model. Shown are the TEER values of the experiment with Terf, Flav and DMSO. Platelayout (a.), TEER values before treatment on day 4 (b.), day 5 (c.) and day 5 (1h after treatment) (d.)

**a**

	1	2	3	4	5	6	7	8	9	10	11	12	13	14	15	16	17	18	19	20	21	22	23	24
A	x	x		x			x			x			TerfHD	TerfHD	TerfHD							x		
B																								
C	No Data	No Data	No Data	No Data	No Data	No Data	No Data	No Data	No Data	No Data	No Data	No Data	No Data	No Data	No Data	No Data	No Data	No Data	No Data	No Data	No Data	No Data	No Data	No Data
D	DMSO	x		x			x			TerfMD	TerfMD	TerfMD										x		
E																								
F	No Data	No Data	No Data	No Data	No Data	No Data	No Data	No Data	No Data	No Data	No Data	No Data	No Data	No Data	No Data	No Data	No Data	No Data	No Data	No Data	No Data	No Data	No Data	No Data
G	DMSO	x		x			x			TerfLD	TerfLD	TerfLD										x		
H																								
I	No Data	No Data	No Data	No Data	No Data	No Data	No Data	No Data	No Data	No Data	No Data	No Data	No Data	No Data	No Data	No Data	No Data	No Data	No Data	No Data	No Data	No Data	No Data	No Data
J	x		DMSO	x			Flav MD	Flav MD	Flav MD												x		x	
K																								
L	No Data	No Data	No Data	No Data	No Data	No Data	No Data	No Data	No Data	No Data	No Data	No Data	No Data	No Data	No Data	No Data	No Data	No Data	No Data	No Data	No Data	No Data	No Data	No Data
M	x		Flav HD	Flav HD	Flav HD	Flav HD	Flav LD	Flav LD	Flav LD													x		
N																								
O																								

**b**

Caco-2 OoC TEER No 2

Plate ID green day 4  
Date 31-May-2021  
Time 11:13:38  
Area 0,0057

	1	2	3	4	5	6	7	8	9	10	11	12	13	14	15	16	17	18	19	20	21	22	23	24
A	36,9741356	122,395922	151,208577	160,198644	176,083592	189,561721	211,251457	180,038825																
B																								
C	No Data	No Data	No Data	No Data	No Data	No Data	No Data	No Data	No Data	No Data	No Data	No Data	No Data	No Data	No Data	No Data	No Data	No Data	No Data	No Data	No Data	No Data	No Data	No Data
D	49,8917346	188,422072	258,749266	254,465089	216,948417	221,477005	288,765921	186,451601																
E																								
F	No Data	No Data	No Data	No Data	No Data	No Data	No Data	No Data	No Data	No Data	No Data	No Data	No Data	No Data	No Data	No Data	No Data	No Data	No Data	No Data	No Data	No Data	No Data	No Data
G	15,813703	260,220676	271,002928	273,827052	263,210628	232,723244	244,44463	207,892912																
H																								
I	No Data	No Data	No Data	No Data	No Data	No Data	No Data	No Data	No Data	No Data	No Data	No Data	No Data	No Data	No Data	No Data	No Data	No Data	No Data	No Data	No Data	No Data	No Data	No Data
J	73,4569803	262,116809	281,405284	276,66731	251,504369	177,854618	237,524597	166,485389																
K																								
L	No Data	No Data	No Data	No Data	No Data	No Data	No Data	No Data	No Data	No Data	No Data	No Data	No Data	No Data	No Data	No Data	No Data	No Data	No Data	No Data	No Data	No Data	No Data	No Data
M	10,0814088	129,225464	141,291995	95,6888577	151,550238	134,551103	104,66654	92,1737381																
N																								
O	No Data	No Data	No Data	No Data	No Data	No Data	No Data	No Data	No Data	No Data	No Data	No Data	No Data	No Data	No Data	No Data	No Data	No Data	No Data	No Data	No Data	No Data	No Data	No Data
P																								

**c**

Caco-2 OoC TEER No 2

Plate ID day5 green  
Date 01-Jun-2021  
Time 08:27:20  
Area 0,0057

	1	2	3	4	5	6	7	8	9	10	11	12	13	14	15	16	17	18	19	20	21	22	23	24
A	299,804348	559,99493		466,161202			533,258034	555,146212	599,489016	551,62864	534,406917													
B																								
C	No Data	No Data	No Data	No Data	No Data	No Data	No Data	No Data	No Data	No Data	No Data	No Data	No Data	No Data	No Data	No Data	No Data	No Data	No Data	No Data	No Data	No Data	No Data	No Data
D	327,758445	356,390002		392,121129			395,812475	375,36844	364,465253	362,024559	429,687417													
E																								
F	No Data	No Data	No Data	No Data	No Data	No Data	No Data	No Data	No Data	No Data	No Data	No Data	No Data	No Data	No Data	No Data	No Data	No Data	No Data	No Data	No Data	No Data	No Data	No Data
G	327,236525	383,43976		274,042159			352,589154	392,217203	366,023898	371,505212	537,284004													
H																								
I	No Data	No Data	No Data	No Data	No Data	No Data	No Data	No Data	No Data	No Data	No Data	No Data	No Data	No Data	No Data	No Data	No Data	No Data	No Data	No Data	No Data	No Data	No Data	No Data
J	263,305761	349,50771		273,453368			349,172318	347,426958	341,99266	384,483306	460,568722													
K																								
L	No Data	No Data	No Data	No Data	No Data	No Data	No Data	No Data	No Data	No Data	No Data	No Data	No Data	No Data	No Data	No Data	No Data	No Data	No Data	No Data	No Data	No Data	No Data	No Data
M	No Fit	368,387359		279,592021			315,014763	305,701804	387,890011	417,768256	461,984435													
N																								
O	No Data	No Data	No Data	No Data	No Data	No Data	No Data	No Data	No Data	No Data	No Data	No Data	No Data	No Data	No Data	No Data	No Data	No Data	No Data	No Data	No Data	No Data	No Data	No Data
P																								

**d**

Caco-2 OoC TEER No 2

Plate ID day5 green\_1  
Date 01-Jun-2021  
Time 11:20:48  
Area 0,0057

	1	2	3	4	5	6	7	8	9	10	11	12	13	14	15	16	17	18	19	20	21	22	23	24
A	No Fit	177,690652		158,016272			158,364605	0	0	0,54237	145,660852													
B																								
C	No Data	No Data	No Data	No Data	No Data	No Data	No Data	No Data	No Data	No Data	No Data	No Data	No Data	No Data	No Data	No Data	No Data	No Data	No Data	No Data	No Data	No Data	No Data	No Data
D	137,8807003	161,212226		148,645045			160,985808	158,962902	172,066796	159,403583	162,412354													
E																								
F	No Data	No Data	No Data	No Data	No Data	No Data	No Data	No Data	No Data	No Data	No Data	No Data	No Data	No Data	No Data	No Data	No Data	No Data	No Data	No Data	No Data	No Data	No Data	No Data
G	139,1966454	161,469052		151,212652			155,627169	156,647338	158,886102	155,88594	169,14116													
H																								
I	No Data	No Data	No Data	No Data	No Data	No Data	No Data	No Data	No Data	No Data	No Data	No Data	No Data	No Data	No Data	No Data	No Data	No Data	No Data	No Data	No Data	No Data	No Data	No Data
J	No Fit	172,779327		No Fit			135,56364	152,238955	141,37288	173,87944	167,652216													
K																								
L	No Data	No Data	No Data	No Data	No Data	No Data	No Data	No Data	No Data	No Data	No Data	No Data	No Data	No Data	No Data	No Data	No Data	No Data	No Data	No Data	No Data	No Data	No Data	No Data
M	No Fit	153,83175		149,395627			135,69604	145,78541	163,396934	152,639877	135,727989													
N																								
O	No Data	No Data	No Data	No Data	No Data	No Data	No Data	No Data	No Data	No Data	No Data	No Data	No Data	No Data	No Data	No Data	No Data	No Data	No Data	No Data	No Data	No Data	No Data	No Data
P																								

Table 92: TEER values of the Caco-2 OoC model. Shown are the TEER values of the experiment with Terf, Flav and DMSO. TEER values on day 5 (4h after treatment) (a.), on day 5 (6h after treatment) (b.) and on day 6 (24h after treatment) (c.).

a

Caco-2 OoC TEER  
No 2  
Plate ID day5 green\_1 day5 4h  
Date 01-Jun-2021  
Time 14:15:12  
Area 0,0057

RTEER	1	2	3	4	5	6	7	8	9	10	11	12	13	14	15	16	17	18	19	20	21	22	23	24
A	No Fit			484,897095			429,520796			474,17667			0			0			0					388,368251
B																								
C	No Data			No Data			No Data			No Data			No Data			No Data			No Data				No Data	
D	225,4750943			335,492088			343,483652			337,71035			390,533483			358,249179			389,420497				449,99602	
E																								
F	No Data			No Data			No Data			No Data			No Data			No Data			No Data				No Data	
G	214,5068367			332,456973			329,028462			330,720102			367,039749			334,17233			397,542487				480,774329	
H																								
I	No Data			No Data			No Data			No Data			No Data			No Data			No Data				No Data	
J	No Fit			362,657447			No Fit			140,802447			230,608646			198,686268			377,162536				373,936788	
K																								
L	No Data			No Data			No Data			No Data			No Data			No Data			No Data				No Data	
M	No Fit			238,622123			66,1348757			192,748408			239,961245			297,073767			319,175402				382,013985	
N																								
O	No Data			No Data			No Data			No Data			No Data			No Data			No Data				No Data	
P																								

c

Caco2 OoC Teer No 2  
Plate ID green 24h  
Date 02-Jun-2021  
Time 10:26:07  
Area 0,0057

RTEER	1	2	3	4	5	6	7	8	9	10	11	12	13	14	15	16	17	18	19	20	21	22	23	24
A	127,474633			166,392582			152,095046			160,573448			0,73394625			0			0					66,0000171
B																								
C	No Data			No Data			No Data			No Data			No Data			No Data			No Data				No Data	
D	113,178269			114,212886			131,26393			130,615559			157,721064			155,019507			158,235425				168,49752	
E																								
F	No Data			No Data			No Data			No Data			No Data			No Data			No Data				No Data	
G	109,507466			119,441897			110,598689			118,934614			106,617886			120,422454			119,545304				97,7555944	
H																								
I	No Data			No Data			No Data			No Data			No Data			No Data			No Data				No Data	
J	No Fit			127,963855			124,367469			109,92261			92,8619948			130,211213			141,978189				133,63652	
K																								
L	No Data			No Data			No Data			No Data			No Data			No Data			No Data				No Data	
M	No Fit			126,267387			114,163055			122,460343			135,317522			134,146952			127,78084				105,855697	
N																								
O	No Data			No Data			No Data			No Data			No Data			No Data			No Data				No Data	
P																								

b

Caco-2 OoC TEER  
No 2  
Plate ID day5 green\_1 day5 6h  
Date 01-Jun-2021  
Time 16:13:15  
Area 0,0057

RTEER	1	2	3	4	5	6	7	8	9	10	11	12	13	14	15	16	17	18	19	20	21	22	23	24
A	No Fit			169,944218			154,980644			152,518776			0,65822362			0			0					147,411469
B																								
C	No Data			No Data			No Data			No Data			No Data			No Data			No Data				No Data	
D	102,8073444			132,512809			124,8156			136,104681			157,113917			153,90762			147,132675				161,540504	
E																								
F	No Data			No Data			No Data			No Data			No Data			No Data			No Data				No Data	
G	98,51403853			135,206479			117,782691			123,604564			128,442896			133,219744			130,979021				166,584264	
H																								
I	No Data			No Data			No Data			No Data			No Data			No Data			No Data				No Data	
J	No Fit			134,037944			No Fit			88,4510866			102,20583			93,3211099			139,983488				133,86101	
K																								
L	No Data			No Data			No Data			No Data			No Data			No Data			No Data				No Data	
M	No Fit			111,366331			111,194531			96,5981207			111,475239			126,04466			129,38414				111,466766	
N																								
O	No Data			No Data			No Data			No Data			No Data			No Data			No Data				No Data	
P																								



Table 94: TEER values of the Caco-2 OoC model. Shown are the TEER values of the experiment with Gef, Alo, Met, Lop and Med. TEER values on day 5 (4h after treatment) (a.), on day 5 (6h after treatment) (b.) and on day 6 (24h after treatment) (c.).

**a**

Caco-2 OoC TEER  
No 2  
Plate ID day5yellow\_1  
Date 01-Jun-2021 day5 4h  
Time 14:26:17  
Area 0,0057

RTEER	1	2	3	4	5	6	7	8	9	10	11	12	13	14	15	16	17	18	19	20	21	22	23	24
A	No Fit			417,707631	563,011886	524,489415	473,314094	559,458341	504,029813	555,624537														
B																								
C	No Data	No Data	No Data	No Data	No Data	No Data	No Data	No Data	No Data	No Data	No Data	No Data	No Data	No Data	No Data	No Data	No Data	No Data	No Data	No Data	No Data	No Data	No Data	No Data
D	425,5834847	340,402541	363,276756	322,1478	389,676256	413,670896	507,450032	507,298449																
E																								
F	No Data	No Data	No Data	No Data	No Data	No Data	No Data	No Data	No Data	No Data	No Data	No Data	No Data	No Data	No Data	No Data	No Data	No Data	No Data	No Data	No Data	No Data	No Data	No Data
G	418,1659768	439,15325	No Fit	No Fit	340,182261	469,894081	479,947762	531,392063																
H																								
I	No Data	No Data	No Data	No Data	No Data	No Data	No Data	No Data	No Data	No Data	No Data	No Data	No Data	No Data	No Data	No Data	No Data	No Data	No Data	No Data	No Data	No Data	No Data	No Data
J	No Fit	No Fit	No Fit	441,619289	360,817249	417,912258	488,480486	134,002944																
K																								
L	No Data	No Data	No Data	No Data	No Data	No Data	No Data	No Data	No Data	No Data	No Data	No Data	No Data	No Data	No Data	No Data	No Data	No Data	No Data	No Data	No Data	No Data	No Data	No Data
M	No Fit	423,551851	453,804853	316,252945	344,659558	148,462311	464,316297	No Fit																
N																								
O	No Data	No Data	No Data	No Data	No Data	No Data	No Data	No Data	No Data	No Data	No Data	No Data	No Data	No Data	No Data	No Data	No Data	No Data	No Data	No Data	No Data	No Data	No Data	No Data
P																								

**b**

Caco-2 OoC TEER  
No 2  
Plate ID day5yellow\_1 day5 6h  
Date 01-Jun-2021  
Time 16:18:10  
Area 0,0057

RTEER	1	2	3	4	5	6	7	8	9	10	11	12	13	14	15	16	17	18	19	20	21	22	23	24
A	No Fit			161,319181	178,915354	192,261182	165,417072	192,903163	174,884412	188,894962														
B																								
C	No Data	No Data	No Data	No Data	No Data	No Data	No Data	No Data	No Data	No Data	No Data	No Data	No Data	No Data	No Data	No Data	No Data	No Data	No Data	No Data	No Data	No Data	No Data	No Data
D	155,6717078	142,032243	147,606488	141,303688	119,69945	122,611132	144,406739	150,998332																
E																								
F	No Data	No Data	No Data	No Data	No Data	No Data	No Data	No Data	No Data	No Data	No Data	No Data	No Data	No Data	No Data	No Data	No Data	No Data	No Data	No Data	No Data	No Data	No Data	No Data
G	137,7747995	124,252555	No Fit	0	110,166707	135,688734	129,388366	148,492384																
H																								
I	No Data	No Data	No Data	No Data	No Data	No Data	No Data	No Data	No Data	No Data	No Data	No Data	No Data	No Data	No Data	No Data	No Data	No Data	No Data	No Data	No Data	No Data	No Data	No Data
J	No Fit	No Fit	No Fit	120,824908	116,119548	123,999202	133,160531	57,0210703																
K																								
L	No Data	No Data	No Data	No Data	No Data	No Data	No Data	No Data	No Data	No Data	No Data	No Data	No Data	No Data	No Data	No Data	No Data	No Data	No Data	No Data	No Data	No Data	No Data	No Data
M	No Fit	134,129016	139,889664	132,097934	133,068354	67,546403	169,842145	No Fit																
N																								
O	No Data	No Data	No Data	No Data	No Data	No Data	No Data	No Data	No Data	No Data	No Data	No Data	No Data	No Data	No Data	No Data	No Data	No Data	No Data	No Data	No Data	No Data	No Data	No Data
P																								

**c**

Caco2 OoC Teer No 2  
Plate ID yellow 24h  
Date 02-Jun-2021  
Time 10:07:20  
Area 0,0057

RTEER	1	2	3	4	5	6	7	8	9	10	11	12	13	14	15	16	17	18	19	20	21	22	23	24
A	104,181645	192,469833	192,566052	218,790322	168,322773	217,058514	177,186966	168,991435																
B																								
C	No Data	No Data	No Data	No Data	No Data	No Data	No Data	No Data	No Data	No Data	No Data	No Data	No Data	No Data	No Data	No Data	No Data	No Data	No Data	No Data	No Data	No Data	No Data	No Data
D	123,986557	138,198226	140,631154	141,411043	111,849744	110,152289	120,823949	134,208993																
E																								
F	No Data	No Data	No Data	No Data	No Data	No Data	No Data	No Data	No Data	No Data	No Data	No Data	No Data	No Data	No Data	No Data	No Data	No Data	No Data	No Data	No Data	No Data	No Data	No Data
G	120,638715	114,456526	No Fit	0	97,8433877	116,901791	118,367806	115,856725																
H																								
I	No Data	No Data	No Data	No Data	No Data	No Data	No Data	No Data	No Data	No Data	No Data	No Data	No Data	No Data	No Data	No Data	No Data	No Data	No Data	No Data	No Data	No Data	No Data	No Data
J	No Fit	No Fit	No Fit	112,438722	95,088405	104,822681	115,660082	29,6668704																
K																								
L	No Data	No Data	No Data	No Data	No Data	No Data	No Data	No Data	No Data	No Data	No Data	No Data	No Data	No Data	No Data	No Data	No Data	No Data	No Data	No Data	No Data	No Data	No Data	No Data
M	41,6598188	107,995965	111,428687	99,0248939	104,314292	42,6746091	141,456062	109,844465																
N																								
O	No Data	No Data	No Data	No Data	No Data	No Data	No Data	No Data	No Data	No Data	No Data	No Data	No Data	No Data	No Data	No Data	No Data	No Data	No Data	No Data	No Data	No Data	No Data	No Data
P																								

Table 95: TEER values of the Caco-2 OoC model. Shown are the TEER values of the experiment with Dic, Stau and Med. Platelayout (a.), TEER values before treatment on day 4 (b.), day 5 (c.) and day 5 (1h after treatment) (d.)

**a**

	1	2	3	4	5	6	7	8	9	10	11	12	13	14	15	16	17	18	19	20	21	22	23	24
A	x			x			x			x			Medium			Stau LD			x			x		
B																								
C	No Data	No Data	No Data	No Data	No Data	No Data	No Data	No Data	No Data	No Data	No Data	No Data	No Data	No Data	No Data	No Data	No Data	No Data	No Data	No Data	No Data	No Data	No Data	No Data
D	Dic HD	Dic HD					x			Dic LD	Dic LD	Dic LD	Dic LD						X			x		
E																								
F	No Data	No Data	No Data	No Data	No Data	No Data	No Data	No Data	No Data	No Data	No Data	No Data	No Data	No Data	No Data	No Data	No Data	No Data	No Data	No Data	No Data	No Data	No Data	No Data
G	Dic HD	Dic MD	Dic MD	Dic MD	Dic MD	Dic MD				Dic MD	Dic MD	Dic MD				x		x	X			X		
H																								
I	No Data	No Data	No Data	No Data	No Data	No Data	No Data	No Data	No Data	No Data	No Data	No Data	No Data	No Data	No Data	No Data	No Data	No Data	No Data	No Data	No Data	No Data	No Data	No Data
J	x		x				x			Stau LD			x			x			x					Stau HD
K																								
L	No Data	No Data	No Data	No Data	No Data	No Data	No Data	No Data	No Data	No Data	No Data	No Data	No Data	No Data	No Data	No Data	No Data	No Data	No Data	No Data	No Data	No Data	No Data	No Data
M	x						x			Stau MD	Stau MD	Stau MD	Stau MD	Stau MD	Stau MD	Stau HD			x					Stau HD
N																								
O																								

**b**

Caco-2 Ooac Teer No2

Plate ID blue day 4  
Date 31-May-2021  
Time 11:11:20  
Area 0,0057

	1	2	3	4	5	6	7	8	9	10	11	12	13	14	15	16	17	18	19	20	21	22	23	24
A	41,4707435			32,9450178			76,5170637			79,8028534			88,3605881			51,8722883			32,673916			17,1260272		
B																								
C	No Data	No Data	No Data	No Data	No Data	No Data	No Data	No Data	No Data	No Data	No Data	No Data	No Data	No Data	No Data	No Data	No Data	No Data	No Data	No Data	No Data	No Data	No Data	No Data
D	75,7588604	137,88394					0			150,19939			153,35934			139,876561			161,132641			57,0067093		
E																								
F	No Data	No Data	No Data	No Data	No Data	No Data	No Data	No Data	No Data	No Data	No Data	No Data	No Data	No Data	No Data	No Data	No Data	No Data	No Data	No Data	No Data	No Data	No Data	No Data
G	76,9239414			191,801419			162,442836			207,548732			205,295259			204,786263			129,183703			105,973715		
H																								
I	No Data	No Data	No Data	No Data	No Data	No Data	No Data	No Data	No Data	No Data	No Data	No Data	No Data	No Data	No Data	No Data	No Data	No Data	No Data	No Data	No Data	No Data	No Data	No Data
J	84,5660372	202,156807		184,189697			186,535203			189,973669			208,56629			207,135526			139,549413					
K																								
L	No Data	No Data	No Data	No Data	No Data	No Data	No Data	No Data	No Data	No Data	No Data	No Data	No Data	No Data	No Data	No Data	No Data	No Data	No Data	No Data	No Data	No Data	No Data	No Data
M	76,9890208	41,7187819		42,0682152			36,7643197			39,9106585			81,1928487			45,8154316			90,5964432					
N																								
O	No Data	No Data	No Data	No Data	No Data	No Data	No Data	No Data	No Data	No Data	No Data	No Data	No Data	No Data	No Data	No Data	No Data	No Data	No Data	No Data	No Data	No Data	No Data	No Data
P																								

**c**

Caco-2 Ooac TEER No 2

Plate ID day5 blue day 5  
Date 01-Jun-2021  
Time 08:28:43  
Area 0,0057

	1	2	3	4	5	6	7	8	9	10	11	12	13	14	15	16	17	18	19	20	21	22	23	24
A	95,7291224			368,625709			328,452413			423,00659			414,25479			339,227765			112,017218			38,1988773		
B																								
C	No Data	No Data	No Data	No Data	No Data	No Data	No Data	No Data	No Data	No Data	No Data	No Data	No Data	No Data	No Data	No Data	No Data	No Data	No Data	No Data	No Data	No Data	No Data	No Data
D	337,928626			349,043447			0			377,906913			371,603144			413,135354			433,103357			446,405323		
E																								
F	No Data	No Data	No Data	No Data	No Data	No Data	No Data	No Data	No Data	No Data	No Data	No Data	No Data	No Data	No Data	No Data	No Data	No Data	No Data	No Data	No Data	No Data	No Data	No Data
G	374,218411			357,114687			278,611199			364,282684			372,603896			324,39024			400,183204			439,030177		
H																								
I	No Data	No Data	No Data	No Data	No Data	No Data	No Data	No Data	No Data	No Data	No Data	No Data	No Data	No Data	No Data	No Data	No Data	No Data	No Data	No Data	No Data	No Data	No Data	No Data
J	272,154788			281,490179			242,07886			324,855027			337,759146			321,576323			343,802817			322,102368		
K																								
L	No Data	No Data	No Data	No Data	No Data	No Data	No Data	No Data	No Data	No Data	No Data	No Data	No Data	No Data	No Data	No Data	No Data	No Data	No Data	No Data	No Data	No Data	No Data	No Data
M	No Fit			326,077218			272,348858			385,662258			346,440856			372,216904			283,039729			381,800609		
N																								
O	No Data	No Data	No Data	No Data	No Data	No Data	No Data	No Data	No Data	No Data	No Data	No Data	No Data	No Data	No Data	No Data	No Data	No Data	No Data	No Data	No Data	No Data	No Data	No Data
P																								

**d**

Caco-2 Ooac TEER No 2

Plate ID day5 blue\_1 day 5 1h  
Date 01-Jun-2021  
Time 11:26:48  
Area 0,0057

	1	2	3	4	5	6	7	8	9	10	11	12	13	14	15	16	17	18	19	20	21	22	23	24
A	No Fit			330,451923			321,935631			331,801834			310,946382			206,762965			No Fit			No Fit		
B																								
C	No Data	No Data	No Data	No Data	No Data	No Data	No Data	No Data	No Data	No Data	No Data	No Data	No Data	No Data	No Data	No Data	No Data	No Data	No Data	No Data	No Data	No Data	No Data	No Data
D	304,6616535			341,059325			No Fit			367,426015			382,24879			419,264672			483,728985			370,31196		
E																								
F	No Data	No Data	No Data	No Data	No Data	No Data	No Data	No Data	No Data	No Data	No Data	No Data	No Data	No Data	No Data	No Data	No Data	No Data	No Data	No Data	No Data	No Data	No Data	No Data
G	280,7025026			332,414087			404,930148			480,313789			474,92002			449,578156			513,271089			462,05842		
H																								
I	No Data	No Data	No Data	No Data	No Data	No Data	No Data	No Data	No Data	No Data	No Data	No Data	No Data	No Data	No Data	No Data	No Data	No Data	No Data	No Data	No Data	No Data	No Data	No Data
J	No Fit			No Fit			243,910997			287,599688			379,563546			416,132957			256,860813			61,5866676		
K																								
L	No Data	No Data	No Data	No Data	No Data	No Data	No Data	No Data	No Data	No Data	No Data	No Data	No Data	No Data	No Data	No Data	No Data	No Data	No Data	No Data	No Data	No Data	No Data	No Data
M	No Fit			200,338701			270,883421			106,922782			113,812527			82,3568498			243,027384			34,5542153		
N																								
O	No Data	No Data	No Data	No Data	No Data	No Data	No Data	No Data	No Data	No Data	No Data	No Data	No Data	No Data	No Data	No Data	No Data	No Data	No Data	No Data	No Data	No Data	No Data	No Data
P																								

Table 96: TEER values of the Caco-2 OoC model. Shown are the TEER values of the experiment with Dic, Stau and Med. TEER values on day 5 (4h after treatment) (a.), on day 5 (6h after treatment) (b.) and on day 6 (24h after treatment) (c.).

**a**

Caco-2 OoC  
TEER No 2  
Plate ID day5blue\_1 day 5 4h  
Date 01-Jun-2021  
Time 14:22:14  
Area 0,0057

RTEER	1	2	3	4	5	6	7	8	9	10	11	12	13	14	15	16	17	18	19	20	21	22	23	24
A	No Fit			387,427827			380,628177			375,089232			469,861305			102,31894			No Fit				58,3598725	
B																								
C	No Data			No Data			No Data			No Data			No Data			No Data			No Data				No Data	
D	303,3448721			274,384965			No Fit			341,125917			397,695726			430,438152			410,475965				345,840203	
E																								
F	No Data			No Data			No Data			No Data			No Data			No Data			No Data				No Data	
G	269,5005606			371,097562			425,316347			376,884526			423,833998			387,73861			441,479181				440,662034	
H																								
I	No Data			No Data			No Data			No Data			No Data			No Data			No Data				No Data	
J	No Fit			No Fit			241,583188			110,999687			326,200133			356,50756			375,830618				10,6927145	
K																								
L	No Data			No Data			No Data			No Data			No Data			No Data			No Data				No Data	
M	No Fit			90,0165074			250,05594			9,95954536			15,4909896			9,23385436			304,388237				8,07471695	
N																								
O	No Data			No Data			No Data			No Data			No Data			No Data			No Data				No Data	
P																								

**b**

Caco-2 OoC  
TEER No 2  
Plate ID day5blue\_1 day 5 6h  
Date 01-Jun-2021  
Time 16:24:04  
Area 0,0057

RTEER	1	2	3	4	5	6	7	8	9	10	11	12	13	14	15	16	17	18	19	20	21	22	23	24
A	No Fit			383,855554			389,92564			408,036141			479,535371			104,280779			102,921817			52,4343992		
B																								
C	No Data			No Data			No Data			No Data			No Data			No Data			No Data				No Data	
D	307,3798995			295,380514			No Fit			356,473342			404,934324			423,710228			433,781558				348,686706	
E																								
F	No Data			No Data			No Data			No Data			No Data			No Data			No Data				No Data	
G	319,577417			430,4774			449,287693			384,548885			437,236457			409,267			455,796902				449,235861	
H																								
I	No Data			No Data			No Data			No Data			No Data			No Data			No Data				No Data	
J	No Fit			No Fit			287,45871			74,9569566			333,497405			367,123024			381,458876				5,26897875	
K																								
L	No Data			No Data			No Data			No Data			No Data			No Data			No Data				No Data	
M	No Fit			92,0999896			No Fit			6,74740323			10,8548415			4,8390142			293,531944				5,51293574	
N																								
O	No Data			No Data			No Data			No Data			No Data			No Data			No Data				No Data	
P																								

**c**

Caco2 OoC Teer No 2  
Plate ID blue24h day6 24h  
Date 02-Jun-2021  
Time 10:11:09  
Area 0,0057

RTEER	1	2	3	4	5	6	7	8	9	10	11	12	13	14	15	16	17	18	19	20	21	22	23	24
A	No Fit			151,721584			121,618778			133,76258			135,41427			66,3720222			101,063483				40,358533	
B																								
C	No Data			No Data			No Data			No Data			No Data			No Data			No Data				No Data	
D	120,151472			105,825456			0			107,623465			94,9769393			117,603487			86,9708475				142,568545	
E																								
F	No Data			No Data			No Data			No Data			No Data			No Data			No Data				No Data	
G	121,087754			109,2718			108,29456			117,100567			105,10262			103,903663			107,840635				152,147739	
H																								
I	No Data			No Data			No Data			No Data			No Data			No Data			No Data				No Data	
J	No Fit			No Fit			87,8587139			10,7600782			109,844545			105,618194			104,860568				0	
K																								
L	No Data			No Data			No Data			No Data			No Data			No Data			No Data				No Data	
M	No Fit			30,2610993			75,8566557			0			0,79942633			0,92582523			93,2510419				0	
N																								
O	No Data			No Data			No Data			No Data			No Data			No Data			No Data				No Data	
P																								



Table 97: TEER values of the Caco-2 OoC model. Shown are the TEER values of the experiment with Flav, Gef, Terf, Lop, Dic and Med. Platelayout (a.), TEER values before treatment on day 3 (b.), day 4 (c.) and day 5 (d.)

a

	1	2	3	4	5	6	7	8	9	10	11	12	13	14	15	16	17	18	19	20	21	22	23	24
A																								
B	FlavLD			FlavLD			FlavLD			GefHD			GefHD			GefHD			Med			Med		
C																								
D																								
E	TerfHD			TerfHD			TerfHD			GefMD			GefMD			GefMD			Med			x		
F																								
G																								
H	TerfMD			TerfMD			TerfMD			GefLD			GefLD			GefLD			DicHD			DicMD		
I																								
J																								
K	TerfLD			TerfLD			TerfLD			LopMD			LopMD			LopMD			DicHD			DicMD		
L																								
M																								
N	LopHD			LopHD			LopHD			LopLD			LopLD			LopLD			DicHD			DicMD		
O																								
P																								

b

Caco 2 OoC No3 TEER day3  
 Plate ID green  
 16-Jun-2021  
 Date 10:17:15  
 Time 0,0057  
 Area

TimePoint 1 of 1

	1	2	3	4	5	6	7	8	9	10	11	12	13	14	15	16	17	18	19	20	21	22	23	24
A	423,393275			389,202213			205,860992			383,95022			356,979746			182,943771			325,580988			297,766187		
B																								
C	No Data			No Data			No Data			No Data			No Data			No Data			No Data			No Data		
D	142,670353			403,355612			268,530819			223,840961			236,962489			62,3413513			196,617256			11,8855106		
E																								
F	No Data			No Data			No Data			No Data			No Data			No Data			No Data			No Data		
G	391,827168			314,966254			318,483819			121,201605			151,245419			361,061498			311,485231			314,188892		
H																								
I	No Data			No Data			No Data			No Data			No Data			No Data			No Data			No Data		
J	301,296761			353,19186			331,305189			380,008167			378,022911			140,744793			333,421284			402,053928		
K																								
L	No Data			No Data			No Data			No Data			No Data			No Data			No Data			No Data		
M	297,230942			351,028559			311,235439			392,284613			369,021798			132,569594			307,667121			372,525366		
N																								
O	No Data			No Data			No Data			No Data			No Data			No Data			No Data			No Data		
P																								

c

Caco 2 OoC No3 TEER day4  
 Plate ID green  
 Date 15-Jun-2021  
 Time 11:46:06  
 Area 0,0057

	1	2	3	4	5	6	7	8	9	10	11	12	13	14	15	16	17	18	19	20	21	22	23	24
A	352,02322			304,134266			313,719967			312,693666			321,926699			147,778055			80,6712201			143,159702		
B																								
C	No Data			No Data			No Data			No Data			No Data			No Data			No Data			No Data		
D	277,270894			287,149294			283,941669			263,103031			277,205943			291,25737			296,136317			10,7643222		
E																								
F	No Data			No Data			No Data			No Data			No Data			No Data			No Data			No Data		
G	321,059441			199,368821			164,342555			129,097424			287,902202			172,705885			276,895542			227,574604		
H																								
I	No Data			No Data			No Data			No Data			No Data			No Data			No Data			No Data		
J	267,162833			236,400485			260,964086			292,146698			271,235156			267,426875			260,523642			292,448192		
K																								
L	No Data			No Data			No Data			No Data			No Data			No Data			No Data			No Data		
M	342,114225			243,449954			247,631553			267,734178			249,713324			268,211155			268,164456			263,134193		
N																								
O	No Data			No Data			No Data			No Data			No Data			No Data			No Data			No Data		
P																								

d

Caco-2 OoC Teer No 3 day 5  
 Plate ID green  
 Date 16-Jun-2021  
 Time 08:10:34  
 Area 0,0057

	1	2	3	4	5	6	7	8	9	10	11	12	13	14	15	16	17	18	19	20	21	22	23	24
A	349,881354			319,221661			328,990703			327,352701			317,851472			328,409021			352,037368			353,917855		
B																								
C	No Data			No Data			No Data			No Data			No Data			No Data			No Data			No Data		
D	145,494771			240,889872			247,644054			248,904491			264,868123			259,690868			285,537926			10,9461212		
E																								
F	No Data			No Data			No Data			No Data			No Data			No Data			No Data			No Data		
G	266,940769			250,746404			222,961988			217,246882			259,372207			249,783904			245,974449			219,997081		
H																								
I	No Data			No Data			No Data			No Data			No Data			No Data			No Data			No Data		
J	247,319429			223,883131			251,677535			205,800485			241,300302			231,211716			236,215812			263,247782		
K																								
L	No Data			No Data			No Data			No Data			No Data			No Data			No Data			No Data		
M	193,928818			181,348906			196,222102			192,952412			191,438273			204,712015			226,548454			207,811183		
N																								
O	No Data			No Data			No Data			No Data			No Data			No Data			No Data			No Data		
P																								



Table 99: TEER values of the Caco-2 OoC model. Shown are the TEER values of the experiment with Dic, Stau and DMSO. Platelayout (a.), TEER values before treatment on day 3 (b.), day 4 (c.) and day 5 (d.)

a

	1	2	3	4	5	6	7	8	9	10	11	12	13	14	15	16	17	18	19	20	21	22	23	24
A										x			X			X					Stau MD			Stau MD
B		Dic LD		Dic LD																				
C																								
D																								
E		x		Stau HD		Stau HD		Stau HD					X		x						Stau MD			
F																								
G																								
H		x		Stau MD		Stau MD		Stau MD		Stau MD		Stau HD		Stau HD		Stau HD								x
I																								
J																								
K				Stau LD		Stau LD		Stau LD		Stau MD		Stau MD		Stau MD		Stau MD								x
L																								
M																								
N													Stau LD		Stau LD		Stau LD							DMSO
O																								
P																								

b

Caco 2 OoC No3 TEER day3  
 Plate ID yellow  
 Date 14-Jun-2021  
 Time 10:18:43  
 Area 0,0057

	1	2	3	4	5	6	7	8	9	10	11	12	13	14	15	16	17	18	19	20	21	22	23	24
A	56,2720623	429,254721	355,552807	21,066068	56,2289798	205,912167	223,056136	42,342144																
B																								
C	No Data	No Data	No Data	No Data	No Data	No Data	No Data	No Data	No Data	No Data	No Data	No Data	No Data	No Data	No Data	No Data	No Data	No Data	No Data	No Data	No Data	No Data	No Data	No Data
D	24,5680743	362,355463	220,678696	153,752321	406,458269	20,1684145	46,6311196	34,1851973																
E																								
F	No Data	No Data	No Data	No Data	No Data	No Data	No Data	No Data	No Data	No Data	No Data	No Data	No Data	No Data	No Data	No Data	No Data	No Data	No Data	No Data	No Data	No Data	No Data	No Data
G	59,3479202	346,98558	237,090709	404,597878	125,988841	120,842948	96,5097766	11,4643769																
H																								
I	No Data	No Data	No Data	No Data	No Data	No Data	No Data	No Data	No Data	No Data	No Data	No Data	No Data	No Data	No Data	No Data	No Data	No Data	No Data	No Data	No Data	No Data	No Data	No Data
J	372,50695	250,594472	322,934881	351,371792	376,446667	388,104068	407,191357	121,388052																
K																								
L	No Data	No Data	No Data	No Data	No Data	No Data	No Data	No Data	No Data	No Data	No Data	No Data	No Data	No Data	No Data	No Data	No Data	No Data	No Data	No Data	No Data	No Data	No Data	No Data
M	30,4000884	368,227178	57,1034804	322,302621	345,636347	305,202844	88,332522	79,6284239																
N																								
O	No Data	No Data	No Data	No Data	No Data	No Data	No Data	No Data	No Data	No Data	No Data	No Data	No Data	No Data	No Data	No Data	No Data	No Data	No Data	No Data	No Data	No Data	No Data	No Data
P																								

c

Caco 2 OoC No3 TEER day4  
 Plate ID yellow  
 Date 15-Jun-2021  
 Time 11:39:09  
 Area 0,0057

	1	2	3	4	5	6	7	8	9	10	11	12	13	14	15	16	17	18	19	20	21	22	23	24
A	130,74948	271,742842	272,258464	30,3963717	321,196357	305,224752	267,085994	52,3856018																
B																								
C	No Data	No Data	No Data	No Data	No Data	No Data	No Data	No Data	No Data	No Data	No Data	No Data	No Data	No Data	No Data	No Data	No Data	No Data	No Data	No Data	No Data	No Data	No Data	No Data
D	16,584367	259,096917	246,774029	268,16735	279,591547	19,1037937	251,88891	270,631434																
E																								
F	No Data	No Data	No Data	No Data	No Data	No Data	No Data	No Data	No Data	No Data	No Data	No Data	No Data	No Data	No Data	No Data	No Data	No Data	No Data	No Data	No Data	No Data	No Data	No Data
G	26,2063381	235,375614	217,578263	249,679187	285,205663	278,074637	234,45323	11,5193413																
H																								
I	No Data	No Data	No Data	No Data	No Data	No Data	No Data	No Data	No Data	No Data	No Data	No Data	No Data	No Data	No Data	No Data	No Data	No Data	No Data	No Data	No Data	No Data	No Data	No Data
J	194,67751	254,181426	232,131881	223,124612	262,177966	280,443414	258,61221	275,70688																
K																								
L	No Data	No Data	No Data	No Data	No Data	No Data	No Data	No Data	No Data	No Data	No Data	No Data	No Data	No Data	No Data	No Data	No Data	No Data	No Data	No Data	No Data	No Data	No Data	No Data
M	116,944716	226,267472	266,518611	230,183858	245,337466	190,188771	237,39273	244,183224																
N																								
O	No Data	No Data	No Data	No Data	No Data	No Data	No Data	No Data	No Data	No Data	No Data	No Data	No Data	No Data	No Data	No Data	No Data	No Data	No Data	No Data	No Data	No Data	No Data	No Data
P																								

d

Caco-2 OoC Teer No 3 day5  
 Plate ID yellow  
 Date 16-Jun-2021  
 Time 08:09:28  
 Area 0,0057

	1	2	3	4	5	6	7	8	9	10	11	12	13	14	15	16	17	18	19	20	21	22	23	24
A	307,625669	295,566031	355,791899	58,7867308	404,302501	373,728111	317,214123	52,9209117																
B																								
C	No Data	No Data	No Data	No Data	No Data	No Data	No Data	No Data	No Data	No Data	No Data	No Data	No Data	No Data	No Data	No Data	No Data	No Data	No Data	No Data	No Data	No Data	No Data	No Data
D	15,8189148	99,6740788	246,379017	294,831957	274,295406	43,4911528	247,859608	291,699469																
E																								
F	No Data	No Data	No Data	No Data	No Data	No Data	No Data	No Data	No Data	No Data	No Data	No Data	No Data	No Data	No Data	No Data	No Data	No Data	No Data	No Data	No Data	No Data	No Data	No Data
G	24,3344839	215,284862	202,991733	221,181226	272,876814	256,608819	290,158921	12,985709																
H																								
I	No Data	No Data	No Data	No Data	No Data	No Data	No Data	No Data	No Data	No Data	No Data	No Data	No Data	No Data	No Data	No Data	No Data	No Data	No Data	No Data	No Data	No Data	No Data	No Data
J	221,501026	250,484123	222,43474	217,132887	261,376631	267,110842	255,370218	272,616889																
K																								
L	No Data	No Data	No Data	No Data	No Data	No Data	No Data	No Data	No Data	No Data	No Data	No Data	No Data	No Data	No Data	No Data	No Data	No Data	No Data	No Data	No Data	No Data	No Data	No Data
M	174,047512	191,86652	219,392795	192,99529	215,556959	222,044861	216,617239	221,916457																
N																								
O	No Data	No Data	No Data	No Data	No Data	No Data	No Data	No Data	No Data	No Data	No Data	No Data	No Data	No Data	No Data	No Data	No Data	No Data	No Data	No Data	No Data	No Data	No Data	No Data
P																								

Table 100: TEER values of the Caco-2 OoC model. Shown are the TEER values of the experiment with Dic, Stau and DMSO. TEER values on day 6 (a.), on day 6 (1h after treatment) (b.) and on day 6 (4h after treatment) (c.) and on day 7 (24h after treatment).

**a**

Caco-2 OoacTeer No 3 day6  
 Plate ID yellow  
 Date 17-Jun-2021  
 Time 08:12:20  
 Area 0,0057

RTEER	1	2	3	4	5	6	7	8	9	10	11	12	13	14	15	16	17	18	19	20	21	22	23	24
A	348,3652	355,6800	399,3269	327,562397	452,492758	508,297562	428,556554	510,845061																
B																								
C	No Data	No Data	No Data	No Data	No Data	No Data	No Data	No Data																
D	14,39594	325,2832	311,3998	374,291841	367,840927	40,0880506	329,260787	396,283731																
E																								
F	No Data	No Data	No Data	No Data	No Data	No Data	No Data	No Data																
G	24,88917	283,4731	305,4907	277,032408	343,157597	327,985968	368,374579	25,8838217																
H																								
I	No Data	No Data	No Data	No Data	No Data	No Data	No Data	No Data																
J	320,4473	318,4092	297,8358	314,080316	330,492267	373,276212	357,0557	367,255513																
K																								
L	No Data	No Data	No Data	No Data	No Data	No Data	No Data	No Data																
M	231,4391	283,3345	294,0417	287,02943	312,429476	331,902509	326,612165	325,564267																
N																								
O	No Data	No Data	No Data	No Data	No Data	No Data	No Data	No Data																

**c**

Caco-2 OoacTeer No 3 day6  
 Plate ID yellow 4h  
 Date 17-Jun-2021  
 Time 12:36:50  
 Area 0,0057

RTEER	1	2	3	4	5	6	7	8	9	10	11	12	13	14	15	16	17	18	19	20	21	22	23	24
A	306,5181	357,9300	397,1322	10,7437417	14,0282891	8,93930413	20,0727854	11,8092821																
B																								
C	No Data	No Data	No Data	No Data	No Data	No Data	No Data	No Data																
D	14,22802	8,527272	7,552671	8,45495875	557,115482	36,7026447	15,9489349	No Fit																
E																								
F	No Data	No Data	No Data	No Data	No Data	No Data	No Data	No Data																
G	24,67230	12,20985	11,53898	13,5480799	12,9703921	10,6732595	9,55603103	26,0144807																
H																								
I	No Data	No Data	No Data	No Data	No Data	No Data	No Data	No Data																
J	370,2148	77,29885	73,11592	96,6763159	21,2113954	18,8691368	21,0133264	No Fit																
K																								
L	No Data	No Data	No Data	No Data	No Data	No Data	No Data	No Data																
M	293,2055	184,0297	221,0976	177,348324	40,8554068	52,4689185	7,77355705	391,934148																
N																								
O	No Data	No Data	No Data	No Data	No Data	No Data	No Data	No Data																

**b**

Caco-2 OoacTeer No 3 day6  
 Plate ID yellow 1h  
 Date 17-Jun-2021  
 Time 09:40:30  
 Area 0,0057

RTEER	1	2	3	4	5	6	7	8	9	10	11	12	13	14	15	16	17	18	19	20	21	22	23	24
A	270,2454	280,2894	326,1025	95,0388054	131,489627	120,26445	120,96799	108,314252																
B																								
C	No Data	No Data	No Data	No Data	No Data	No Data	No Data	No Data																
D	No Fit	105,3181	95,77109	124,355995	587,454844	23,8470779	128,229269	No Fit																
E																								
F	No Data	No Data	No Data	No Data	No Data	No Data	No Data	No Data																
G	No Fit	93,60321	101,9934	134,510904	147,472834	148,769562	132,165158	29,6743762																
H																								
I	No Data	No Data	No Data	No Data	No Data	No Data	No Data	No Data																
J	313,1488	328,4466	245,8561	289,618993	170,427965	185,329834	127,999171	No Fit																
K																								
L	No Data	No Data	No Data	No Data	No Data	No Data	No Data	No Data																
M	229,3728	234,9392	248,0652	238,131596	174,171654	223,208887	125,949475	336,808111																
N																								
O	No Data	No Data	No Data	No Data	No Data	No Data	No Data	No Data																

**d**

Caco-2 OoacTeer No 3 day6  
 Plate ID yellow  
 Date 18-Jun-2021  
 Time 08:35:25  
 Area 0,0057

RTEER	1	2	3	4	5	6	7	8	9	10	11	12	13	14	15	16	17	18	19	20	21	22	23	24
A	387,4764	410,7075	441,5294	0	13,6567885	1,36147918	0	No Fit																
B																								
C	No Data	No Data	No Data	No Data	No Data	No Data	No Data	No Data																
D	20,29910	0	0	0	593,375253	57,7610261	0	No Fit																
E																								
F	No Data	No Data	No Data	No Data	No Data	No Data	No Data	No Data																
G	31,20409	0	No Fit	1,30379258	0	0	0	33,602589																
H																								
I	No Data	No Data	No Data	No Data	No Data	No Data	No Data	No Data																
J	384,2059	39,56038	No Fit	63,9250594	0	0	0	No Fit																
K																								
L	No Data	No Data	No Data	No Data	No Data	No Data	No Data	No Data																
M	121,8140	183,2964	148,0510	38,4157313	0	1,78263627	0	438,10218																
N																								
O	No Data	No Data	No Data	No Data	No Data	No Data	No Data	No Data																

Table 101: TEER values of the Caco-2 OoC model. Shown are the TEER values of the experiment with 5-FU, Alo, Flavo, Met and DMSO. Platelayout (a.), TEER values before treatment on day 3 (b.), day 4 (c.) and day 5 (d.)

**a**

	1	2	3	4	5	6	7	8	9	10	11	12	13	14	15	16	17	18	19	20	21	22	23	24	
A																									
B	x			5FU HD			5FU HD			5FU HD			X			x				x					
C																									
D																									
E	x			5FU MD			5FU MD			5FU MD			x			x				Met					
F																									
G																									
H	DMSO			5FU LD			5FU LD			5FU LD			x			x				Flav MD					
I																									
J																									
K	Alo HD			Alo HD			Alo HD			Alo LD			Alo LD			Alo LD				Flav MD					Met
L																									
M																									
N	Alo MD			Alo MD			Alo MD			Flav HD			Flav HD			Flav HD				Flav MD					Met
O																									
P																									

**b** Caco 2 OoC No3 TEER day3  
 Plate ID red  
 Date 14-Jun-2021  
 Time 10:15:12  
 Area 0,0057

RTEER	1	2	3	4	5	6	7	8	9	10	11	12	13	14	15	16	17	18	19	20	21	22	23	24	
A	102,785496	395,248437	395,248437	150,964552	68,0600097					190,940327	465,588108	22,7672064													
B																									
C	No Data	No Data	No Data	No Data	No Data	No Data	No Data	No Data	No Data	No Data	No Data	No Data	No Data	No Data	No Data	No Data	No Data	No Data	No Data	No Data	No Data	No Data	No Data	No Data	
D	97,420484	337,15081	328,090359	134,474877	241,789502	253,504786	330,620899	182,485576																	
E																									
F	No Data	No Data	No Data	No Data	No Data	No Data	No Data	No Data	No Data	No Data	No Data	No Data	No Data	No Data	No Data	No Data	No Data	No Data	No Data	No Data	No Data	No Data	No Data	No Data	
G	355,001701	259,99048	265,492627	163,281641	338,199256	223,79227	170,221962	121,083755																	
H																									
I	No Data	No Data	No Data	No Data	No Data	No Data	No Data	No Data	No Data	No Data	No Data	No Data	No Data	No Data	No Data	No Data	No Data	No Data	No Data	No Data	No Data	No Data	No Data	No Data	
J	230,25123	267,576178	241,018373	299,973376	244,619151	333,977196	166,840785	331,873786																	
K																									
L	No Data	No Data	No Data	No Data	No Data	No Data	No Data	No Data	No Data	No Data	No Data	No Data	No Data	No Data	No Data	No Data	No Data	No Data	No Data	No Data	No Data	No Data	No Data	No Data	
M	61,5477209	85,0188805	360,80006	308,613923	70,9504846	311,14793	253,099148	379,419417																	
N																									
O	No Data	No Data	No Data	No Data	No Data	No Data	No Data	No Data	No Data	No Data	No Data	No Data	No Data	No Data	No Data	No Data	No Data	No Data	No Data	No Data	No Data	No Data	No Data	No Data	
P																									

**c**

Caco 2 OoC No3 TEER day4  
 Plate ID red  
 Date 15-Jun-2021  
 Time 11:44:46  
 Area 0,0057

RTEER	1	2	3	4	5	6	7	8	9	10	11	12	13	14	15	16	17	18	19	20	21	22	23	24
A	356,002139	373,346029	395,384422	403,566582	352,844999	409,300625	37,7534811	60,9050962																
B																								
C	No Data	No Data	No Data	No Data	No Data	No Data	No Data	No Data	No Data	No Data	No Data	No Data	No Data	No Data	No Data	No Data	No Data	No Data	No Data	No Data	No Data	No Data	No Data	No Data
D	238,183731	271,011847	254,678882	268,5192	250,429428	239,632676	248,721378	307,10306																
E																								
F	No Data	No Data	No Data	No Data	No Data	No Data	No Data	No Data	No Data	No Data	No Data	No Data	No Data	No Data	No Data	No Data	No Data	No Data	No Data	No Data	No Data	No Data	No Data	No Data
G	288,352307	258,051573	255,260951	265,344691	184,837539	271,690029	269,313736	297,400056																
H																								
I	No Data	No Data	No Data	No Data	No Data	No Data	No Data	No Data	No Data	No Data	No Data	No Data	No Data	No Data	No Data	No Data	No Data	No Data	No Data	No Data	No Data	No Data	No Data	No Data
J	219,554659	232,172683	207,252974	231,073704	242,997252	251,491489	245,983606	259,478154																
K																								
L	No Data	No Data	No Data	No Data	No Data	No Data	No Data	No Data	No Data	No Data	No Data	No Data	No Data	No Data	No Data	No Data	No Data	No Data	No Data	No Data	No Data	No Data	No Data	No Data
M	345,878064	243,643732	296,829221	269,718126	291,373533	258,704937	265,105418	273,315776																
N																								
O	No Data	No Data	No Data	No Data	No Data	No Data	No Data	No Data	No Data	No Data	No Data	No Data	No Data	No Data	No Data	No Data	No Data	No Data	No Data	No Data	No Data	No Data	No Data	No Data
P																								

**d**

Caco-2 OoC Teer No 3 day5  
 Plate ID red  
 Date 16-Jun-2021  
 Time 08:07:16  
 Area 0,0057

RTEER	1	2	3	4	5	6	7	8	9	10	11	12	13	14	15	16	17	18	19	20	21	22	23	24
A	430,526209	335,923594	336,484001	433,161825	402,905716	382,041559	38,1509694	390,714364																
B																								
C	No Data	No Data	No Data	No Data	No Data	No Data	No Data	No Data	No Data	No Data	No Data	No Data	No Data	No Data	No Data	No Data	No Data	No Data	No Data	No Data	No Data	No Data	No Data	No Data
D	233,206326	234,735842	233,791126	234,458009	214,23102	225,098388	224,705604	270,979305																
E																								
F	No Data	No Data	No Data	No Data	No Data	No Data	No Data	No Data	No Data	No Data	No Data	No Data	No Data	No Data	No Data	No Data	No Data	No Data	No Data	No Data	No Data	No Data	No Data	No Data
G	243,567025	208,042399	204,557254	209,678189	223,517335	247,124225	230,306163	251,608414																
H																								
I	No Data	No Data	No Data	No Data	No Data	No Data	No Data	No Data	No Data	No Data	No Data	No Data	No Data	No Data	No Data	No Data	No Data	No Data	No Data	No Data	No Data	No Data	No Data	No Data
J	222,798654	229,870634	199,682054	201,561753	204,55051	246,454107	220,431756	228,425456																
K																								
L	No Data	No Data	No Data	No Data	No Data	No Data	No Data	No Data	No Data	No Data	No Data	No Data	No Data	No Data	No Data	No Data	No Data	No Data	No Data	No Data	No Data	No Data	No Data	No Data
M	94,8011911	204,854172	216,982288	208,521785	208,525252	200,156096	204,702433	211,867958																
N																								
O	No Data	No Data	No Data	No Data	No Data	No Data	No Data	No Data	No Data	No Data	No Data	No Data	No Data	No Data	No Data	No Data	No Data	No Data	No Data	No Data	No Data	No Data	No Data	No Data
P																								

Table 102: TEER values of the Caco-2 OoC model. Shown are the TEER values of the experiment with 5-FU, Alo, Flav, Met and DMSO. TEER values on day 6 (a.), on day 6 (1h after treatment) (b.) and on day 6 (4h after treatment) (c.) and on day 7 (24h after treatment).

a										c																																							
Caco-2 OoC Teer No 3 day 6										Caco-2 OoC Teer No 3 day 6																																							
Plate ID	red									Plate ID	red 4h																																						
Date	17-Jun-2021									Date	17-Jun-2021																																						
Time	08:07:20									Time	12:37:54																																						
Area	0,0057									Area	0,0057																																						
RTTEER	1	2	3	4	5	6	7	8	9	10	11	12	13	14	15	16	17	18	19	20	21	22	23	24	RTTEER	1	2	3	4	5	6	7	8	9	10	11	12	13	14	15	16	17	18	19	20	21	22	23	24
A	344,823864			328,436488			324,731653			368,3426			388,56046			371,729			43,4652025			461,030751			A	461,774415			416,519593			424,139199			515,324686			552,437334			508,974382			47,4386259			535,751864		
B										B																B																							
C	No Data	No Data	No Data	No Data	No Data	No Data	No Data	No Data	No Data	C	No Data	No Data	No Data	No Data	No Data	No Data	No Data	No Data	No Data	No Data	No Data	No Data	No Data	No Data	C	No Data	No Data	No Data	No Data	No Data	No Data	No Data	No Data	No Data	No Data	No Data	No Data	No Data	No Data	No Data	No Data	No Data	No Data	No Data	No Data	No Data			
D	159,635789			271,655831			256,435427			286,788302			260,256555			249,275477			271,34481			299,185801			D	No Fit			410,341886			387,980305			423,128976			380,229203			388,539134			439,638042			427,334773		
E										E															E																								
F	No Data	No Data	No Data	No Data	No Data	No Data	No Data	No Data	No Data	F	No Data	No Data	No Data	No Data	No Data	No Data	No Data	No Data	No Data	No Data	No Data	No Data	No Data	F	No Data	No Data	No Data	No Data	No Data	No Data	No Data	No Data	No Data	No Data	No Data	No Data	No Data	No Data	No Data	No Data	No Data	No Data	No Data	No Data	No Data	No Data			
G	269,920305			262,46084			246,426725			274,675939			271,676247			295,165421			277,931089			291,557627			G	348,50874			395,99046			369,961837			435,733977			455,771681			475,589622			320,123723			519,49841		
H										H														H																									
I	No Data	No Data	No Data	No Data	No Data	No Data	No Data	No Data	No Data	I	No Data	No Data	No Data	No Data	No Data	No Data	No Data	No Data	No Data	No Data	No Data	No Data	No Data	I	No Data	No Data	No Data	No Data	No Data	No Data	No Data	No Data	No Data	No Data	No Data	No Data	No Data	No Data	No Data	No Data	No Data	No Data	No Data	No Data	No Data	No Data			
J	276,084119			273,78784			245,558751			266,316724			224,30237			273,706116			258,890947			269,228025			J	420,594836			452,900297			408,056011			389,114991			311,925379			371,830282			341,791956			381,814485		
K										K														K																									
L	No Data	No Data	No Data	No Data	No Data	No Data	No Data	No Data	No Data	L	No Data	No Data	No Data	No Data	No Data	No Data	No Data	No Data	No Data	No Data	No Data	No Data	No Data	L	No Data	No Data	No Data	No Data	No Data	No Data	No Data	No Data	No Data	No Data	No Data	No Data	No Data	No Data	No Data	No Data	No Data	No Data	No Data	No Data	No Data	No Data			
M	238,287703			263,668881			281,580273			261,296945			268,595525			250,848643			253,093471			268,481027			M	332,217944			375,210831			462,647533			305,392077			294,231085			220,812143			371,606438			400,902806		
N										N														N																									
O	No Data	No Data	No Data	No Data	No Data	No Data	No Data	No Data	No Data	O	No Data	No Data	No Data	No Data	No Data	No Data	No Data	No Data	No Data	No Data	No Data	No Data	No Data	O	No Data	No Data	No Data	No Data	No Data	No Data	No Data	No Data	No Data	No Data	No Data	No Data	No Data	No Data	No Data	No Data	No Data	No Data	No Data	No Data	No Data	No Data			

b										d																																							
Caco-2 OoC Teer No 3 day 6										Caco-2 OoC Teer No 3 day 6																																							
Plate ID	red 1h									Plate ID	red 24h																																						
Date	17-Jun-2021									Date	18-Jun-2021																																						
Time	09:39:08									Time	08:38:12																																						
Area	0,0057									Area	0,0057																																						
RTTEER	1	2	3	4	5	6	7	8	9	10	11	12	13	14	15	16	17	18	19	20	21	22	23	24	RTTEER	1	2	3	4	5	6	7	8	9	10	11	12	13	14	15	16	17	18	19	20	21	22	23	24
A	391,677002			344,583136			336,890941			380,005444			483,753424			398,846772			No Fit			320,065172			A	508,146517			483,835945			474,094438			418,504456			No Fit			359,168295			46,6197369			409,722996		
B										B															B																								
C	No Data	No Data	No Data	No Data	No Data	No Data	No Data	No Data	No Data	C	No Data	No Data	No Data	No Data	No Data	No Data	No Data	No Data	No Data	No Data	No Data	No Data	No Data	C	No Data	No Data	No Data	No Data	No Data	No Data	No Data	No Data	No Data	No Data	No Data	No Data	No Data	No Data	No Data	No Data	No Data	No Data	No Data	No Data	No Data				
D	No Fit			406,586071			373,032526			396,30535			335,688142			355,531867			426,198206			355,228224			D	No Fit			94,3186806			89,9080189			125,250573			217,172098			220,958797			342,362204			396,518017		
E										E														E																									
F	No Data	No Data	No Data	No Data	No Data	No Data	No Data	No Data	No Data	F	No Data	No Data	No Data	No Data	No Data	No Data	No Data	No Data	No Data	No Data	No Data	No Data	No Data	F	No Data	No Data	No Data	No Data	No Data	No Data	No Data	No Data	No Data	No Data	No Data	No Data	No Data	No Data	No Data	No Data	No Data	No Data	No Data	No Data	No Data	No Data			
G	347,945282			390,591612			367,087327			380,764877			447,079632			462,575717			393,127388			384,923779			G	407,467933			266,487231			239,522591			292,501236			300,361074			80,1919217			0			447,276725		
H										H														H																									
I	No Data	No Data	No Data	No Data	No Data	No Data	No Data	No Data	No Data	I	No Data	No Data	No Data	No Data	No Data	No Data	No Data	No Data	No Data	No Data	No Data	No Data	No Data	I	No Data	No Data	No Data	No Data	No Data	No Data	No Data	No Data	No Data	No Data	No Data	No Data	No Data	No Data	No Data	No Data	No Data	No Data	No Data	No Data	No Data	No Data			
J	346,595348			406,021126			380,21998			344,760935			305,667005			346,795554			346,091987			320,889584			J	428,385385			458,711019			553,211059			274,913274			225,618581			256,359118			244,381794			412,154299		
K										K														K																									
L	No Data	No Data	No Data	No Data	No Data	No Data	No Data	No Data	No Data	L	No Data	No Data	No Data	No Data	No Data	No Data	No Data	No Data	No Data	No Data	No Data	No Data	No Data	L	No Data	No Data	No Data	No Data	No Data	No Data	No Data	No Data	No Data	No Data	No Data	No Data	No Data	No Data	No Data	No Data	No Data	No Data	No Data	No Data	No Data	No Data			
M	294,873126			322,799532			352,438468			247,649307			238,327775			180,133652			284,268669			310,522568			M	409,305973			411,047994			336,508573			244,16833			250,778713			206,348255			273,891185			420,570286		
N										N														N																									
O	No Data	No Data	No Data	No Data	No Data	No Data	No Data	No Data	No Data	O	No Data	No Data	No Data	No Data	No Data	No Data	No Data	No Data	No Data	No Data	No Data	No Data	No Data	O	No Data	No Data	No Data	No Data	No Data	No Data	No Data	No Data	No Data	No Data	No Data	No Data	No Data	No Data	No Data	No Data	No Data	No Data	No Data	No Data	No Data	No Data			

**Appendix 9: Calculated Papp values of the Caco-2 cells in the OrganoPlate® after treatment with test compounds. Papp values are calculated with the formula seen in Figure 114.**

$$Papp = \frac{(I_{end} - I_{initial}) * V_{gel}}{(T_{end} - T_{initial}) (A_{barrier})}$$

- I\_end = initial fluorescent intensity
- I\_end = endpoint fluorescent intensity
- T\_initial = Time initial in seconds
- T\_end = Time end in seconds
- V\_gel = Volume of the gel
- A\_barrier = area of the barrier

Figure 114: Formula for the calculation of the Papp values. Values are calculated after treating the Caco-2 cells in the OrganoPlate® and performing the BI-assay.

Table 103: Papp values of the BI assay after treatment with 5-FU (a), Alo (b) and Diclo (c) in the Caco-2 OoC model.

**a**

#1	Papp values [cm/s]			#2	Papp values [cm/s]			#3	Papp values [cm/s]		
Compounds	FITC 150 kDa	TRITC 4.4 kDa		Compounds	FITC 150 kDa	TRITC 4.4 kDa		Compounds	FITC 150 kDa	TRITC 4.4 kDa	
5-FU 300µM	4.21352E-07	8.26679E-07		5-FU 300µM	-5.36696E-07	-3.31902E-07		5-FU 300µM	1.6435E-07	3.53608E-07	
5-FU 100 µM	4.90148E-07	5.79134E-07		5-FU 100 µM	-5.8366E-07	-3.77211E-07		5-FU 100 µM	9.08332E-08	8.76864E-08	
5-FU 30µM	4.18035E-07	7.75884E-07		5-FU 30µM	-4.83109E-05	-4.19405E-05		5-FU 30µM	-1.59756E-07	-1.40114E-07	
5-FU 10µM	-7.36817E-08	-4.98996E-08		5-FU 10µM	5.2421E-07	4.08677E-06		5-FU 10µM	-3.8344E-08	-1.59356E-08	
5-FU 3µM	-2.53247E-07	-4.22022E-07		5-FU 3µM	-1.68794E-07	-3.65494E-07		5-FU 3µM	-1.99139E-07	-2.66134E-07	
5-FU 1µM	2.14481E-08	-2.32118E-07		5-FU 1µM	-2.98438E-07	-2.42554E-06		5-FU 1µM	1.72611E-08	-6.27435E-09	
5-FU 0.3µM	1.035E-08	-2.98008E-07		5-FU 0.3µM	-6.83296E-07	-4.57701E-06		5-FU 0.3µM	-2.07057E-07	-3.30935E-07	
5-FU 0.1µM	4.75665E-05	4.33412E-05		5-FU 0.1µM	3.51921E-08	-3.57306E-08		5-FU 0.1µM	8.30539E-08	-9.63827E-08	

**b**

#1	Papp values [cm/s]			#2	Papp values [cm/s]			#3	Papp values [cm/s]		
Compounds	FITC 150 kDa	TRITC 4.4 kDa		Compounds	FITC 150 kDa	TRITC 4.4 kDa		Compounds	FITC 150 kDa	TRITC 4.4 kDa	
Alo 200µM	5.33144E-08	-4.98163E-08		Alo 200µM	1.35192E-07	1.33886E-07		Alo 200µM	-2.82054E-08	5.49692E-08	
Alo 100 µM	-6.94692E-08	-8.71208E-08		Alo 100 µM	1.28844E-07	1.28746E-07		Alo 100 µM	1.40487E-07	1.77902E-07	
Alo 30µM	-1.63152E-08	-7.14519E-08		Alo 30µM	1.3457E-07	9.03581E-08		Alo 30µM	4.80727E-08	5.34712E-08	
Alo 10µM	-2.92143E-09	-2.08918E-07		Alo 10µM	2.57269E-07	1.38994E-07		Alo 10µM	4.10303E-08	4.74303E-08	
Alo 3µM	-7.45069E-08	-1.45705E-07		Alo 3µM	1.45057E-07	1.00895E-07		Alo 3µM	9.0844E-08	3.66174E-08	
Alo 1µM	-1.36801E-09	-1.61613E-07		Alo 1µM	2.30886E-07	1.51313E-07		Alo 1µM	1.00312E-07	4.55846E-09	
Alo 0.3µM	7.4796E-08	1.05412E-08		Alo 0.3µM	4.22486E-07	2.02333E-07		Alo 0.3µM	1.56137E-07	4.96318E-10	
Alo 0.1µM	-2.56553E-07	-3.65648E-07		Alo 0.1µM	7.16611E-08	-6.2975E-08		Alo 0.1µM	1.55891E-07	2.06769E-08	

**c**

#1	Papp values [cm/s]			#2	Papp values [cm/s]			#3	Papp values [cm/s]		
Compounds	FITC 150 kDa	TRITC 4.4 kDa		Compounds	FITC 150 kDa	TRITC 4.4 kDa		Compounds	FITC 150 kDa	TRITC 4.4 kDa	
Diclo 300µM	7.79286E-08	1.41612E-07		Diclo 300µM	3.7318E-08	7.76478E-08		Diclo 300µM	1.70517E-08	8.2464E-08	
Diclo 100 µM	4.86416E-08	9.11917E-08		Diclo 100 µM	5.63964E-08	5.30297E-08		Diclo 100 µM	6.02109E-08	1.46196E-07	
Diclo 30µM	4.32671E-08	4.1518E-08		Diclo 30µM	1.60569E-08	1.56566E-08		Diclo 30µM	9.7288E-08	1.83121E-07	
Diclo 10µM	7.67023E-07	5.23045E-07		Diclo 10µM	-4.22297E-09	-3.85774E-09		Diclo 10µM	2.03486E-07	4.05776E-07	
Diclo 3µM	1.62542E-08	-2.87153E-08		Diclo 3µM	2.52829E-08	7.29068E-09		Diclo 3µM	-5.03419E-09	-9.32705E-07	
Diclo 1µM	1.46918E-08	5.75659E-08		Diclo 1µM	1.8555E-08	-7.30263E-07		Diclo 1µM	-1.63855E-08	-1.59794E-08	
Diclo 0.3µM	-5.41973E-08	-6.2279E-08		Diclo 0.3µM	-2.91788E-08	-6.4076E-07		Diclo 0.3µM	-3.54264E-08	-4.92228E-07	

Table 104: Papp values of the BI assay after treatment with Flavo (a), Gef (b) and Terf (c) in the Caco-2 OoC model.

**a**

#1	Papp values [cm/s]			#2	Papp values [cm/s]			#3	Papp values [cm/s]		
Compounds	FITC 150 kDa	TRITC 4.4 kDa		Compounds	FITC 150 kDa	TRITC 4.4 kDa		Compounds	FITC 150 kDa	TRITC 4.4 kDa	
Flavo 300µM	1.04265E-05	7.92253E-06		Flavo 300µM	2.25089E-06	2.90884E-06		Flavo 300µM	1.21761E-06	1.64852E-06	
Flavo 100 µM	4.0441E-08	1.34235E-07		Flavo 100 µM	2.71665E-07	3.45059E-07		Flavo 100 µM	2.77063E-08	6.5752E-08	
Flavo 30µM	3.69528E-08	2.46443E-07		Flavo 30µM	1.14676E-07	6.97868E-08		Flavo 30µM	4.59537E-08	6.18007E-08	
Flavo 10µM	3.69528E-08	1.03677E-07		Flavo 10µM	-8.46796E-09	3.12068E-09		Flavo 10µM	6.77255E-08	5.18297E-08	
Flavo 3µM	4.76374E-09	4.37275E-08		Flavo 3µM	-8.43841E-08	-3.26438E-08		Flavo 3µM	4.43917E-08	-2.25522E-08	
Flavo 1µM	-1.69789E-08	-4.94235E-08		Flavo 1µM	-4.29847E-07	-3.42394E-07		Flavo 1µM	-2.45582E-07	-6.73149E-07	
Flavo 0.3µM	2.21159E-08	1.9394E-07		Flavo 0.3µM	-2.31981E-07	-2.52133E-07		Flavo 0.3µM	-9.69017E-08	-1.58498E-07	
Flavo 0.1µM	3.02919E-07	5.97995E-07		Flavo 0.1µM	2.78667E-08	-6.53268E-07		Flavo 0.1µM	-4.98993E-07	-4.57555E-07	

**b**

#1	Papp values [cm/s]			#2	Papp values [cm/s]			#3	Papp values [cm/s]		
Compounds	FITC 150 kDa	TRITC 4.4 kDa		Compounds	FITC 150 kDa	TRITC 4.4 kDa		Compounds	FITC 150 kDa	TRITC 4.4 kDa	
Gef 300µM	3.54229E-07	9.20947E-07		Gef 300µM	2.24795E-06	1.20778E-06		Gef 300µM	4.16113E-07	3.6507E-07	
Gef 100 µM	-1.34091E-09	5.00173E-08		Gef 100 µM	3.90022E-06	2.15308E-06		Gef 100 µM	3.48394E-08	8.77603E-08	
Gef 30µM	7.10303E-08	1.10622E-07		Gef 30µM	2.42824E-07	2.53717E-07		Gef 30µM	6.06408E-06	3.21949E-06	
Gef 10µM	-1.45668E-08	-1.2914E-07		Gef 10µM	1.49619E-05	1.01551E-05		Gef 10µM	3.25822E-06	2.19366E-06	
Gef 3µM	-2.0632E-08	-4.60549E-08		Gef 3µM	1.02257E-05	7.49975E-06		Gef 3µM	2.22041E-07	2.18714E-07	
Gef 1µM	1.9213E-08	4.03938E-08		Gef 1µM	4.82059E-06	2.82689E-06		Gef 1µM	3.45308E-06	2.2469E-06	
Gef 0.3µM	1.85832E-08	2.94113E-08		Gef 0.3µM	4.26826E-07	3.31096E-07		Gef 0.3µM	1.50937E-07	1.57641E-07	
Gef 0.1µM	2.19289E-08	3.58042E-09		Gef 0.1µM	1.70481E-07	1.51821E-07		Gef 0.1µM	6.68971E-06	4.23046E-06	

**c**

#1	Papp values [cm/s]			#2	Papp values [cm/s]			#3	Papp values [cm/s]		
Compounds	FITC 150 kDa	TRITC 4.4 kDa		Compounds	FITC 150 kDa	TRITC 4.4 kDa		Compounds	FITC 150 kDa	TRITC 4.4 kDa	
Terf 300µM	1.65188E-05	1.10063E-05		Terf 300µM	1.81792E-05	1.15447E-05		Terf 300µM	1.42964E-05	1.08835E-05	
Terf 100 µM	1.63889E-05	1.20562E-05		Terf 100 µM	1.51258E-05	1.11116E-05		Terf 100 µM	1.2445E-05	1.03217E-05	
Terf 30µM	2.14297E-05	1.35648E-05		Terf 30µM	1.16208E-05	1.03034E-05		Terf 30µM	1.54622E-05	1.22013E-05	
Terf 10µM	2.88592E-06	1.86886E-06		Terf 10µM	6.4734E-08	-1.47936E-08		Terf 10µM	-1.0349E-09	-4.03367E-08	
Terf 3µM	6.73203E-06	4.22198E-06		Terf 3µM	3.36367E-08	2.29809E-08		Terf 3µM	-1.93452E-08	-1.55303E-07	
Terf 1µM	1.2364E-06	9.51376E-07		Terf 1µM	1.47869E-06	7.26396E-07		Terf 1µM	1.37625E-08	-8.54479E-08	
Terf 0.3µM	6.96504E-07	8.33075E-07		Terf 0.3µM	8.9009E-10	-2.26478E-08		Terf 0.3µM	2.7491E-08	-5.67749E-09	
Terf 0.1µM	8.84029E-08	-1.65655E-08		Terf 0.1µM	7.33017E-06	4.18137E-06		Terf 0.1µM	1.62371E-08	-1.55775E-08	



Table 105: Papp values of the BI assay after treatment with Lop in the Caco-2 OoC model.

#1	Papp values [cm/s]			#2	Papp values [cm/s]			#3	Papp values [cm/s]		
	Compounds	FITC 150 kDa	TRITC 4.4 kDa		Compounds	FITC 150 kDa	TRITC 4.4 kDa		Compounds	FITC 150 kDa	TRITC 4.4 kDa
Lop 300 μM	1.31594E-05	1.33106E-05		Lop 300 μM	1.28949E-05	1.11363E-05		Lop 300 μM	9.33536E-06	1.11131E-05	
Lop 100 μM	2.65991E-05	2.04444E-05		Lop 100 μM	2.45923E-05	1.65349E-05		Lop 100 μM	2.28804E-05	1.59536E-05	
Lop 30 μM	1.79558E-07	1.44521E-07		Lop 30 μM	1.28475E-07	1.32003E-07		Lop 30 μM	2.77185E-08	4.2831E-08	
Lop 10 μM	9.68889E-08	9.65985E-08		Lop 10 μM	1.14453E-07	1.78421E-07		Lop 10 μM	3.95572E-07	7.23525E-07	
Lop 3 μM	3.34933E-07	4.3312E-07		Lop 3 μM	7.80195E-07	9.46026E-07		Lop 3 μM	1.52977E-08	1.35012E-08	
Lop 1 μM	2.24543E-07	1.00133E-07		Lop 1 μM	3.15452E-07	5.26611E-07		Lop 1 μM	3.4447E-07	3.4243E-07	
Lop 0.3 μM	-1.18716E-08	-9.32529E-08		Lop 0.3 μM	3.26756E-07	1.11363E-05		Lop 0.3 μM	7.99949E-08	8.43037E-08	
Lop 0.1 μM	1.8649E-07	2.73427E-07		Lop 0.1 μM	2.28945E-07	4.04806E-08		Lop 0.1 μM	-2.29485E-08	-3.94033E-08	

## Appendix 10: Protein expression levels from the three different cell culture models

Table 106: Protein expression levels of tight junction proteins

Protein	Description	Caco-2 2D 21d	Caco-2 2D 21d	Caco-2 2D 21d	Caco-2 2D 21d	Caco-2 2 OoC 4d	Caco-2 2 OoC 4d	Caco-2 2 OoC 4d	Caco-2 2 OoC 4d	Caco-2 2 OoC 4d	Caco-2 Transwell 21d	Caco-2 Transwell 21d	Organoid 3D 10d	Organoid 3D 10d
CLDN18	Claudin-18	59851.5	57357.9	61702.4	55382.2	42661.2	45412.2	51706.2	57957.8	59270.6	68091.5	62283.9	47497.8	
CLDN3	Claudin-3	5975.9	8042.0	NA	NA	7142.3	5379.0	NA	NA	NA	NA	NA	NA	NA
CLDN4	Claudin-4	136211.4	137724.2	128821.2	132429.5	128656.5	132099.6	123935.0	138472.1	127173.4	122847.9	145806.0	153723.7	
CLDN1	Claudin domain-containing protein 1	6664.5	8338.8	20604.1	21078.9	2770.3	2843.1	24278.3	32528.2	33512.8	20560.0	271895.3	256114.3	
OCLN	Occludin	3834.4	3341.8	NA	NA	3002.5	3513.9	NA	NA	NA	NA	NA	NA	NA
TJAP1	Tight junction-associated protein	40100.7	40280.1	30431.7	31390.3	36580.2	36114.2	22329.1	22034.3	25125.5	24024.5	NA	NA	NA
TJP1	Tight junction protein ZO-1	13135.4	11654.5	NA	NA	9052.5	8241.5	NA	NA	NA	NA	NA	NA	NA
TJP2	Tight junction protein ZO-2	80692.2	78927.1	65710.4	73284.2	95886.4	95251.4	97360.6	99936.9	59545.9	51268.1	47395.1	52873.9	
TJP3	Tight junction protein ZO-3	17831.6	19729.6	14900.3	16208.4	NA	NA	9652.5	7811.8	14237.9	14391.7	NA	NA	NA

Table 107: Protein expression levels of adherens junction proteins

Protein	Description	Caco-2 2D 21d	Caco-2 2D 21d	Caco-2 2D 21d	Caco-2 2D 21d	Caco-2 2 OoC 4d	Caco-2 OoC 4d	Caco-2 OoC 4d	Caco-2 OoC 4d	Caco-2 Transwell 21d	Caco-2 Transwell 21d	Organoid 3D 10d	Organoid 3D 10d
CDH1	Cadherin-1	NA	NA	67278	64047	NA	NA	81090	99637	64984	75381	NA	NA
CDH10	Cadherin-10	178125.2	182919.1	181126.7	163939.3	108153.8	107697.0	101746.2	95285.3	127715.2	124445.9	141812.6	130566.2
CDH16	Cadherin-16	129487.8	129554.8	122838.4	115483.4	72121.5	77658.6	76184.6	70041.6	91326.3	91033.0	109244.1	83350.3
CDH17	Cadherin-17	70051.9	82296.9	62641.8	70581.3	39538.5	32105.4	39896.4	34475.1	82111.7	64215.7	23243.0	25630.7
CDH2	Cadherin-2	340253.6	338348.2	302354.6	298087.1	386018.9	384838.6	358914.1	343096.4	291406.3	280543.9	343581.9	302717.1
CDH3	Cadherin-3	223760.1	365922.9	302321.2	318961.8	424191.2	331753.0	376793.0	473402.9	288339.5	364054.3	130638.4	147283.0
CDH5	Cadherin-5	81702.4	74728.7	66025.2	81478.6	61507.2	67039.8	52936.2	56770.1	63885.5	60992.9	42844.4	49492.8
CDHR3	Cadherin-related family member 3	50740.6	45533.2	NA	NA	99237.2	77665.2	NA	NA	NA	NA	NA	NA
CDHR5	Cadherin-related family member 5	756676.7	731147.3	737545.8	648343.6	1007911.7	999615.7	799309.7	836249.6	670711.7	696918.5	858359.2	826999.91
CTNNA1	Catenin alpha-1	95224.0	90894.2	95142.7	95086.3	92246.1	90970.0	71897.8	75475.9	79951.2	78806.3	64108.7	62015.4
CTNNA2	Catenin alpha-2	42187.8	39998.2	37414.8	31938.0	35155.3	37086.4	31038.0	29267.1	39361.3	40748.1	NA	NA
CTNNB1	Catenin beta-1	372278.2	328670.4	316317.7	333429.6	361851.5	351807.5	354572.5	322025.9	290149.1	278960.0	360220.5	350257.8
CTNNB1	Beta-catenin-like protein 1	255357.8	249293.9	274337.6	261343.8	191669.5	184888.6	172039.1	199164.6	251315.9	259714.1	175014.0	173876.5
CTNND1	Catenin delta-1	NA	NA	NA	NA	NA	NA	NA	NA	NA	NA	NA	NA
VCL	Vinculin	NA	NA	7075	8090.5	NA	NA	7421.6	7522.7	7036.9	6178.3	NA	NA
ACTN1	Alpha-actinin-1	5112.6	5387.3	5749.6	5741.9	9725.3	9529.6	5425.9	5387.3	4858.7	4979.3	NA	NA
ACTN2	Alpha-actinin-2	15131.8	14080.7	NA	NA	10123.2	13013.1	NA	NA	NA	NA	NA	NA
ACTN3	Alpha-actinin-3	71928.9	65350.6	49172.8	48902.9	44398.4	55112.5	47212.5	50606.6	77091.4	90305.1	33208.6	40434.2
ACTN4	Alpha-actinin-4	NA	NA	NA	NA	NA	NA	NA	NA	NA	NA	NA	NA



Table 108: Protein expression levels of phase I enzymes

Protein	Description	Caco-2 2D 21d	Caco-2 2D 21d	Caco-2 OoC 4d	Caco-2 OoC 4d	Caco-2 2D 21d	Caco-2 2D 21d	Caco-2 OoC 4d	Caco-2 OoC 4d	Caco-2 2D 21d	Caco-2 2D 21d	Caco-2 OoC 4d	Caco-2 OoC 4d	Caco-2 Transwell 21d	Caco-2 Transwell 21d	Organoid 3D 10d	Organoid 3D 10d
CYP11B2	Cytochrome P450 11B2	1130154	2520322.2	2490417.7	1584371.5	2077654.0	2095674.2	1699432.43	1567824.3	2079071.3	2666651.1	2133070.7	2054714.4				
CYP1A1	Cytochrome P450 1A1	8046.5	9525.1	10785.5	9363.4	1278.2	8419.4	11635.7266	10293.8	7933.9	8557.2	NA	NA				
CYP1B1	Cytochrome P450 1B1	48942.0	47085.1	63599.0	58970.6	46897.3	47553.5	54302.5969	48129.6	44296.2	40761.9	32313.8	13590.0				
CYP20A1	Cytochrome P450 20A1	440483.8	473383.3	487479.2	499534.3	409013.9	434505.6	411107.233	470227.1	527454.8	514102.8	760677.1	738616.4				
CYP24A1	125-dihydroxyvitamin D(3) 24-hydroxylase	50932.7	38188.6	49487.7	56008.1	31771.7	31634.4	38543.0601	35312.7	226001.2	191777.1	NA	NA				
CYP26A1	Cytochrome P450 26A1	5846.6	5648.8	NA	NA	NA	NA	NA	NA	NA	NA	NA	NA				
CYP27A1	Sterol 26-hydroxylase mitochondrial	NA	NA	10362.3	10056.7	5729.2	6473.2	7380.93336	5619.3	5826.5	5263.9	6351.8	2541.2				
CYP27B1	25-hydroxyvitamin D-1 alpha hydroxylase	NA	NA	2652.3	3058.8	NA	NA	NA	NA	NA	NA	NA	NA				
CYP2C18	Cytochrome P450 2C18	1126.1	782.6	NA	NA	NA	NA	NA	NA	NA	NA	NA	NA				
CYP2C8	Cytochrome P450 2C8			2539.7	2650.1	NA	NA	NA	NA	NA	NA	NA	NA				
CYP2J2	Cytochrome P450 2J2	1300392.8	1871379.7	612967.2	638023.9	1622519.1	1333918.1	748875.784	797809.5	1058429.1	933120.9	302796.7	63022.0				
CYP2R1	Vitamin D 25-hydroxylase	49567.9	55056.7	53337.9	52105.9	54282.8	66315.6	59168.4674	52820.9	54136.8	51588.5	63352.7	57173.5				
CYP2S1	Cytochrome P450 2S1	119738.7	110633.4	139467.5	144500.1	115572.6	105093.2	148199.456	148627.3	90993.8	89730.6	102483.6	71813.8				
CYP2W1	Cytochrome P450 2W1	96848.6	88964.4	87307.3	92311.0	94243.0	85738.6	88016.9983	92172.2	100207.4	88210.9	239621.9	247659.2				
CYP3A4	Cytochrome P450 3A4	304023.1	415607.2	556454.6	508458.5	436060.3	458284.9	478843.477	476324.9	428523.9	486982.3	492671.3	486407.7				
CYP4B1	Cytochrome P450 4B1	81407.6	81473.5	80489.3	77666.4	NA	NA	NA	NA	NA	NA	NA	NA				
CYP4F2;CYP4F3;CYP4F12	Phylloquinone omega-hydroxylase CYP4F2	NA	NA	NA	NA	68038.8	69940.9	70246.2298	71071.8	67698.9	61700.9	74817.5	81015.5				
CYP4F22	Cytochrome P450 4F22	249.8	155.4	NA	NA	NA	NA	NA	NA	NA	NA	NA	NA				
CYP4F3	Docosahexaenoic acid omega-hydroxylase	1319954.1	1393229.9	1499455.8	1509220.0	1424223.2	1388153.4	1407791.42	1584600.3	1334449.5	1383945.3	2876661.8	2958114				

Table 109: Protein expression levels of phase II enzymes

Protein	Description	Caco-2 2D 21d	Caco-2 2D 21d	Caco-2 2D 21d	Caco-2 2D 21d	Caco-2 OoC 4d	Caco-2 OoC 4d	Caco-2 OoC 4d	Caco-2 OoC 4d	Caco-2 OoC 4d	Caco-2 OoC 4d	Caco-2 OoC 4d	Caco-2 OoC 4d	Caco-2 Transwell 21d	Caco-2 Transwell 21d	Organoid 3D 10d	Organoid 3D 10d
SULT1A1	Sulfotransferase 1A1	3188.2	3524.8	3337.6	2984.4	5082.1	5304.1	5248.5	5663.7	3332.7	2272.4	NA	NA				
SULT1A3	Sulfotransferase 1A3	33575.5	28690.7	29632.5	28200.3	21976.2	22678.2	22755.9	21533.3	34234.4	31077.1	NA	NA				
SULT1B1	Sulfotransferase family cytosolic 1B	38538.7	42317.1	42503.5	54686.4	46222.8	43728.2	52900.6	49904.2	39229.3	38088.4	44876.1	26509.2				
SULT1C2	Sulfotransferase 1C2	221192.0	200400.2	222873.8	235195.9	422528.9	425903.1	430787.5	376076.6	226977.1	207987.0	313633.3	273534.2				
SULT2A1	Bile salt sulfotransferase	46209.3	51224.8	44107.2	41978.0			21076.9	16217.6	39012.9	35666.0						
GSTA2	Glutathione S-transferase A2	30259.4	27641.2	30126.4	30896.8	30160.6	28336.8	31599.0	29098.7	28162.1	26257.0	26058.8	31739.5				
GSTA4	Glutathione S-transferase A4	355983.7	408920.5	374825.1	374370.0	442212.5	413425.9	384837.4	397546.3	375052.7	413755.7	405760.3	413805.0				
GSTA5	Glutathione S-transferase A5	33191.2	31592.4	40151.2	37027.2	29912.8	30122.5	32855.1	31587.5	36428.3	34374.8	105438.3	117458.4				
GSTC1	Glutathione S-transferase	67891.4	62625.1	59697.8	58141.5	57707.8	50032.7	51337.3	60341.6	28217.3	26859.5	NA	NA				
GSTK1	Glutathione S-transferase kappa 1	3886.8	4231.7	NA	NA	NA	NA	NA	NA	NA	NA	NA	NA				
GSTM1	Glutathione S-transferase Mu 1	11646.5	11007.8	NA	NA	14545.1	14179.4	NA	NA	NA	NA	NA	NA				
GSTM2	Glutathione S-transferase Mu 2	101757.7	94356.1	97566.5	103009.5	123730.7	115529.9	125237.97	112455.7	89925.3	83997.7	130047.2	131399.5				
GSTM3	Glutathione S-transferase Mu 3	15633.1	15716.9	15430.4	18034.2	17103.1	17503.0	18916.5	15473.5	18490.7	17661.9	20893.2	13697.4				
GSTP1	Glutathione S-transferase P	175532.5	187275.2	202659.5	176891.1	222016.4	235509.7	198323.3	211862.5	245445.3	235176.7	384005.1	385940.9				
GSTT1	Glutathione S-transferase theta-1	463051.4	526981.4	538755.2	595701.1	407715.7	380636.5	554514.9	667000.4	542365.1	579099.7	539469.1	498152.8				
GSTT2B	Glutathione S-transferase theta-2B	131479.8	130055.9	128010.3	123806.5	127991.0	124629.9	133048.6	140345.7	120322.6	116838.6	135039.1	127605.6				
UGDH	UDP-glucose 6-dehydrogenase	1102.4	1420.9	NA	NA	1572.9	1656.8	NA	NA	NA	NA	NA	NA				
UGT1	UDP-glucose:glycoprotein glucosyltransferase	5155.9	4935.2	3484.1	4372.2	5670.2	4243.2	3526.7	3455.5	3702.5	3644.1	NA	NA				
UGP2	UTP-glucose-1-phosphate uridylyltransferase	23252.9	23979.9	21346.8	24174.7	26308.0	26986.7	30655.4	24206.7	24143.4	23013.2	NA	NA				
UGT1A3	UDP-glucuronosyltransferase 1-3	7395.0	14835.5	19420.6	17000.4	29197.8	17531.3	18389.2	22810.8	19083.2	23518.4	15661.6	16940.7				
UGT1A6	UDP-glucuronosyltransferase 1-6			2438.9	2593.5	3214.0	3101.9	2733.8	1701.4	2663.6	2124.8	NA	NA				
UGT2A3	UDP-glucuronosyltransferase 2A3	60271.7	59829.3	58039.9	48241.2	83819.8	87332.8	86037.7	87025.9	57158.9	52369.2	86455.8	87889.7				
UGT2B17	UDP-glucuronosyltransferase 2B17	4904.1	6212.0	7554.6	8389.5	8681.5	8618.3	10572.6	9088.3	9066.8	9260.9	NA	NA				
UGT2B7	UDP-glucuronosyltransferase 2B7	6103.0	7541.9	7557.9	7615.5	9282.3	9721.9	9695.4	9825.4	6581.3	6816.3	NA	NA				
UGT8	2-hydroxyacyl sphingosine 1-beta-galactosyltransferase	NA	NA	11445.4	11966.6	15140.4	14089.4	14215.7	11691.5	11272.8	11414.3	NA	NA				
SULT1A2	Sulfotransferase 1A2	1230	1344.8	NA	NA	NA	NA	NA	NA	NA	NA	NA	NA				
NAT10	RNA cytidine acetyltransferase	NA	NA	NA	NA	3930.7	3963.5	NA	NA	NA	NA	NA	NA				
NAT14	N-acetyltransferase 14	NA	NA	NA	NA	35304	38234	NA	NA	NA	NA	NA	NA				
NAT6	N-acetyltransferase 6	2175.1	2511.6	NA	NA	3670.1	2690.4	NA	NA	NA	NA	NA	NA				

Table 110: Protein expression levels of phase III enzymes (SLC transporter)

Protein	Description	Caco-2 2D 21d	Caco-2 2D 21d	Caco-2 2D 21d	Caco-2 2D 21d	Caco-2 Ooc 4d	Caco-2 Ooc 4d	Caco-2 Ooc 4d	Caco-2 Ooc 4d	Caco-2 Trans 21d	Caco-2 Trans 21d	Organoids 10d	Organoids 10d
SLC11A2	Natural resistance-associated macrophage protein 2	7383.55	6695.07	6263.57	5870.10	8093.49	7433.18	6489.56	7623.02	5581.93	5055.13	12176.66	10176.79
SLC12A1	Solute carrier family 12 member 1	NA	NA	NA	NA	NA	15128	NA	NA	NA	NA	NA	NA
SLC12A2	Solute carrier family 12 member 2	952.75	819.61	NA	NA	1093.04	1022.13	NA	NA	NA	NA	NA	NA
SLC12A4	Solute carrier family 12 member 4	265690.52	223812.08	202054.25	197496.45	117657.75	122582.55	122882.84	122986.54	182800.87	190326.49	202759.73	189169.92
SLC12A6	Solute carrier family 12 member 6	39265.36	40096.28	50091.83	47397.85	65052.69	61305.63	67849.62	68388.42	36902.57	36588.27	29454.94	36648.38
SLC12A7	Solute carrier family 12 member 7	32618.58	41964.77	41698.76	46412.47	54406.06	52173.22	43171.96	38953.12	41808.83	42047.46	49811.92	49073.35
SLC12A8	Solute carrier family 12 member 8	18398.67	18917.45	22027.83	25386.49	32768.59	31840.46	24564.11	25289.04	18378.80	20040.02	23382.03	26945.15
SLC12A9	Solute carrier family 12 member 9	NA	NA	NA	NA	32.16	3468.50	NA	NA	NA	NA	NA	NA
SLC15A1	Solute carrier family 15 member 1	NA	NA	3736	3703.3	NA	NA	4457.20	3702.60	3557.50	2981.70	NA	NA
SLC15A2	Solute carrier family 15 member 2	NA	NA	NA	NA	NA	NA	NA	NA	NA	NA	NA	NA
SLC16A1	Monocarboxylate transporter 1	3955.57	3864.85	12142.81	11625.14	32107.29	32800.24	17765.99	20189.04	12226.59	9489.27	NA	NA
SLC16A10	Monocarboxylate transporter 10	6370.24	6899.82	9479.52	9695.19	9913.17	9529.77	12319.21	14169.46	8148.90	8136.29	8325.84	10728.38
SLC16A3	Monocarboxylate transporter 4	64949.11	61178.45	66107.54	66513.36	62893.59	66361.01	67209.86	59767.77	52353.84	55785.02	52118.78	55350.57
SLC17A5	Slain OS=Homo sapiens	70810.65	70675.92	64021.59	63749.02	59942.32	61717.63	61929.99	71759.36	61751.99	63142.68	65542.58	77873.28
SLC18B1	MFS-type transporter	384138.89	340243.13	331719.23	380655.54	510511.93	528683.08	537751.74	515713.04	375563.43	399063.15	357442.07	334859.07
SLC19A1	Folate transporter 1	NA	NA	NA	NA	3596.10	5046.30	NA	NA	NA	NA	NA	NA
SLC19A2	Thiamine transporter 1	NA	NA	NA	NA	NA	NA	NA	NA	NA	NA	NA	NA
SLC19A3	Thiamine transporter 2	89986.81	98825.46	105910.14	110593.65	149448.77	143096.76	127267.87	123421.35	107554.41	106313.79	74361.22	69056.79
SLC1A2	Excitatory amino acid transporter 2	888.55	1003.80	NA	NA	NA	NA	NA	NA	NA	NA	NA	NA
SLC1A5	Neutral amino acid transporter B(0) Sodium-dependent phosphate transporter 1	30771.32	30783.32	28148.80	28199.03	32457.32	33003.85	33593.74	34213.11	28600.41	28307.55	24362.24	0
SLC20A1	Sodium-dependent phosphate transporter 2	40796.59	47771.07	33595.54	36742.28	NA	NA	41879.01	49203.82	47038.26	56582.88	NA	NA
SLC20A2	Sodium-dependent phosphate transporter	NA	NA	2610.59	1508.29	1757.27	2093.53	1151.29	1584.78	3263.23	3134.68	2707.86	0
SLC22A12	Solute carrier family 22 member 12	264889.326	281631.83	244581.36	219065.02	17897.17	18806.25	124194.39	114176.92	18854.13	194297.25	153591.48	147735.48
SLC22A18	Solute carrier family 22 member 18	175004.64	168791.93	191294.95	158257.03	128849.03	137572.51	117025.30	112561.03	154651.49	169019.50	143279.99	143405.48
SLC22A23	Solute carrier family 22 member 23	NA	NA	3318	2507.80	NA	NA	2634.60	1193.10	2943	2039.40	NA	NA
SLC22A5	Solute carrier family 22 member 5	3239.1	3764.90	NA	NA	NA	NA	NA	NA	NA	NA	NA	NA
SLC23A1	Solute carrier family 23 member 1	4175.09	3664.08	NA	NA	3037.35	3264.44	NA	NA	NA	NA	NA	NA
SLC23A10	Tricarboxylate transport protein	73059.85	70546.27	66013.29	72034.09	107889.35	107917.03	105966.46	102533.04	66686.12	63513.67	48220.84	0
SLC25A10	Mitochondrial dicarboxylate carrier	6659.87	5324.22	NA	NA	6070.40	6689.72	NA	NA	NA	NA	NA	NA
SLC25A11	Mitochondrial 2-oxoglutarate/malate carrier protein	NA	NA	14271	16133	NA	NA	19165	16180	18736	20958	NA	NA
SLC25A12	Calcium-binding mitochondrial carrier protein Aralar1	1479.77	1621.32	NA	NA	1694.25	2076.23	NA	NA	NA	NA	NA	NA
SLC25A13	Calcium-binding mitochondrial carrier protein Aralar2	NA	NA	NA	NA	5707.20	4845.30	NA	NA	NA	NA	NA	NA
SLC25A15	Mitochondrial ornithine transporter 1	26221.35	28768.09	31118.01	28440.93	43492.18	42369.39	46106.59	55484.97	29665.93	29997.06	27837.16	24805.61
SLC25A16	Graves disease carrier protein	60967.87	72257.14	65057.29	65937.96	61902.92	63426.33	56777.49	50023.93	116174.26	114863.91	79549.71	96628.90
SLC25A17	Peroxisomal thiamine protein	141568.06	132865.89	140452.10	158161.28	86943.89	93673.46	86295.65	81724.05	119890.38	121337.57	66274.74	63220.11
SLC25A18	Mitochondrial thiamine pyrophosphate carrier	NA	NA	NA	NA	NA	4191.10	NA	NA	NA	NA	NA	NA
SLC25A19	Mitochondrial carnitine/acylcarnitine carrier protein	NA	NA	9570.82	10801.96	10425.09	9473.57	7941.18	7469.95	9567.11	10298.82	21822.98	16802.65
SLC25A22	Mitochondrial glutamate carrier 1	NA	NA	10646	13322	NA	NA	10542	9483.60	13421	9874.20	NA	NA
SLC25A23	Calcium-binding mitochondrial carrier protein ScaMC-3	10428.15	10900.34	18931.52	18708.14	9546.32	8200.69	17713.39	11717.89	15202.98	12077.39	NA	NA
SLC25A24	Calcium-binding mitochondrial carrier protein ScaMC-1	7670.97	5939.58	6503.57	4053.05	NA	NA	2932.49	3714.18	5401.38	5941.42	NA	NA
SLC25A25	Calcium-binding mitochondrial carrier protein ScaMC-2	22608.49	23080.62	22052.32	25165.29	28833.59	27468.66	30587.13	30142.23	24360.53	21512.82	NA	NA
SLC25A3	Phosphate carrier protein	17803.24	15047.17	19509.72	17571.41	23283.52	27290.02	22053.02	22477.46	15439.87	15131.59	12556.80	8859.62
SLC25A33	Solute carrier family 25 member 33	21214.54	19387.19	16202.95	17636.39	16072.46	16457.88	14397.43	15246.41	20319.98	19418.91	16372.58	13879.02
SLC25A36	Solute carrier family 25 member 36	NA	NA	5497	5231	NA	NA	3441.60	5862.90	3783.90	4900.60	NA	NA
SLC25A4	ADP/ATP translocase 1	16755.79	15322.39	10435.76	10438.12	NA	NA	11344.01	17127.71	11974.07	10791.16	NA	NA
SLC25A40	Solute carrier family 25 member 40	5777.38	6793.56	4846.85	4331.59	4335.22	4380.86	3248.07	2871.49	5651.69	5161.83	NA	NA
SLC25A42	Mitochondrial coenzyme A transporter	113647.84	108450.09	111430.35	105553.29	81631.61	84920.41	63637.75	77290.10	118237.82	124474.89	54373.50	50
SLC25A44	Solute carrier family 25 member 44	193040.57	173271.59	193462.05	199027.88	318317.50	310216.26	332836.46	323702.41	194369.36	175468.42	235303.91	204814.63
SLC25A46	Solute carrier family 25 member 46	121359.13	127242.67	113058.15	110738.98	79541.17	79847.98	70222.38	66692.68	9529.52	94372.93	106851.92	95484.25
SLC25A5	ADP/ATP translocase 2	NA	NA	3484	2649.90	NA	NA	4565.30	4742.80	4510.60	4636.70	NA	NA
SLC25A6	ADP/ATP translocase 3	NA	NA	NA	NA	NA	NA	NA	NA	NA	NA	NA	NA
SLC26A2	Sulfate transporter	5324.75	5192.00	4937.61	3356.73	4001.47	3558.28	4459.05	4657.97	6176.20	4041.81	3265.98	4432.52
SLC26A3	Chloride anion exchanger	295143.02	321539.14	309488.89	336058.16	427817.88	368817.79	359436.66	353234.54	302333.92	298004.32	235462.31	230992.92
SLC26A5	Prestin OS=Homo sapiens	13628.02	11865.66	11304.48	10846.45	15131.03	14940.69	14833.31	15430.55	10608.02	10474.96	14931.71	19953.85
SLC26A6	Solute carrier family 26 member 6	NA	NA	NA	NA	3989.40	3843.10	NA	NA	NA	NA	NA	NA
SLC27A1	Long-chain fatty acid transporter protein	11591.51	11800.03	14247.60	13029.43	NA	NA	10577.01	10218.21	19440.54	20833.27	NA	NA
SLC27A2	Very long-chain acyl-CoA synthetase	180850.23	182981.44	201219.11	187266.39	170171.39	168146.74	184475.84	179212.97	164721.72	163871.09	170466.36	158854.85
SLC27A3	Long-chain fatty acid transporter protein	26516.37	25967.98	39909.71	39422.72	36834.05	39615.58	51277.01	65241.59	28667.59	26331.32	NA	NA
SLC27A4	Long-chain fatty acid transporter protein	31962.86	30428.40	40112.68	38654.76	20845.59	20701.21	29209.59	27074.22	54358.55	51586.82	32812.32	31126.56
SLC28A3	Solute carrier family 28 member 3	4682.10	4141.40	NA	NA	NA	NA	NA	NA	NA	NA	NA	NA
SLC29A1	Equilibrative nucleoside transporter 1	8291.02	5402.02	4958.39	4907.75	7388.62	6638.57	4621.84	3768.49	5612.12	4080.05	NA	NA
SLC29A2	Equilibrative nucleoside transporter 2	14827.37	15303.36	15911.49	14547.88	11782.25	12052.90	15389.18	12286.92	12776.18	11831.42	17537.37	21711.92
SLC29A3	Equilibrative nucleoside transporter 3	9138.05	9171.83	7576.71	8343.23	8528.64	9576.39	8710.12	9798.66	9844.75	9064.88	9583.81	10741.67
SLC2A1	Solute carrier family 2, facilitated glucose transporter member 1	92836.66	92594.99	104594.94	102153.13	104817.21	109402.13	96003.61	81840.09	107348.95	103758.05	108265.85	105823.02
SLC2A10	Solute carrier family 2, facilitated glucose transporter member 10	5761.54	5230.98	7039.73	4860.01	10345.89	8867.31	9547.29	7604.28	5473.46	5865.64	NA	NA
SLC2A3	Solute carrier family 2, facilitated glucose transporter member 3	3808.13	8471.38	11786.25	11634.54	11517.19	11783.32	9650.84	9543.50	13213.94	12990.54	NA	NA
SLC2A5	Solute carrier family 2, facilitated glucose transporter member 5	NA	NA	NA	NA	5523.80	4268.01	NA	NA	NA	NA	NA	NA
SLC2A8	Solute carrier family 2, facilitated glucose transporter member 8	NA	NA	NA	NA	7890.40	8099.30	NA	NA	NA	NA	NA	NA
SLC30A1	Zinc transporter 1	77243.23	70174.68	84329.37	85710.91	82567.62	83240.51	95536.91	84789.58	69757.84	71569.63	146205.61	148971.69
SLC30A5	Zinc transporter 5	75073.76											





## Appendix 11: Fold changes in gene expression for the evaluation of potential biomarkers in all three used cell culture models

Table 111: Results from three replicates of the gene expression of potential novel tested biomarkers (*LCN-2*, *FABP-1*, *GSTA1*, *MLCK*, *CRP*, *HDC*, *GAST*) of the Caco-2 2D model. Values are normalized to the gene expression of the housekeepers *PPIA*, *PIB*, *HPRT1* and *LDHA* and given as fold changes towards the vehicle control.

	LCN2			FABP1			GSTA1			MLCK			CRP			HDC			GAST		
	N=1	N=2	N=3	N=1	N=2	N=3	N=1	N=2	N=3	N=1	N=2	N=3	N=1	N=2	N=3	N=1	N=2	N=3	N=1	N=2	N=3
Gefitinib 1µM	0.95	-1.7	-7.42	1.31	1.03	NA	2.97	3.01	2.36	0.73	0.96	NA	0.71	8.43	0.32	0.37	3.61	0.67	0.87	0.28	0.71
Gefitinib 0.1µM	0.27	-0.83	1.59	1.02	1.05	NA	2.68	1.71	2.06	1.15	0.96	NA	0.6	6.11	1.19	0.43	2.23	1.11	0.75	0.27	1.29
Gefitinib 0.01µM	-0.2	0	-2.3	0.74	0.81	NA	1.57	0.84	1.4	1.06	1	NA	0.75	0.52	0.52	0.32	0.67	0.54	1.3	0.18	1.22
Irinotecan 50µM	1.6	-0.17	1.4	0.75	1.07	NA	0.68	0.45	0.89	1.22	0.53	NA	0.7	3.13	0.79	0.55	1.21	0.64	1.92	0.75	1.22
Irinotecan 5µM	0.45	-0.17	9.43	1.04	1.13	NA	1.41	0.72	0.85	0.89	1.05	NA	0.5	3.4	1.38	0.46	1.08	0.93	1.11	0.41	1.02
Irinotecan 0.5µM	0.18	-0.6	-3.82	1.18	1.13	NA	1.66	0.75	1.43	0.77	1.29	NA	0.41	4.8	0.57	0.3	1.37	0.9	1.08	0.3	1.17
Oxaliplatin 5µM	-0.24	-1.12	6.94	0.97	1.11	NA	1.43	0.87	1.55	1.16	0.83	NA	0.45	6.25	0.96	0.5	2.13	0.68	0.92	0.3	1.13
Oxaliplatin 0.5µM	0.85	-2.43	-4.76	1.23	1.04	NA	1.91	0.64	1.37	0.86	1.15	NA	0.85	12.26	2.03	0.33	3.45	0.86	1.2	0.32	1.37
Oxaliplatin 0.05µM	0.22	-0.54	5.57	1.03	0.85	NA	1.52	0.48	1.14	1.06	1.26	NA	0.5	3.69	0.98	0.36	1.46	0.63	1.18	0.43	1.26
5FU 50µM	-0.24	-0.47	9.74	1.09	1.02	NA	1.47	0.71	1.34	1.14	1.11	NA	0.71	2.5	1.9	0.33	0.89	1.58	1.04	0.49	1.59
5FU 5µM	-1	-0.39	19.37	1	0.95	NA	2.26	0.53	1.08	1.05	1.1	NA	0.38	4.3	2.7	0.17	1.06	1.56	1.5	0.35	1.23
5FU 0.5µM	-0.7	0.35	14.49	0.94	0.85	NA	2.01	0.41	0.92	1.33	1.26	NA	0.79	1.41	1.81	0.22	0.25	1.39	1.11	0.21	0.81
Terfenadine 1µM	-0.23	-0.82	5.69	0.85	1.12	NA	1.21	0.6	1.24	1.28	1.39	NA	0.34	4.66	1.34	0.48	2.16	0.82	1.69	0.46	0.96
Terfenadine 0.1µM	-1.19	-0.84	0.32	0.96	1.18	NA	1.79	0.52	1.12	1.13	1.28	NA	0.53	6.32	0.85	0.6	2.31	0.47	1	0.34	1.36
Terfenadine 0.01µM	0.4	-0.97	-4.49	0.92	1	NA	1.74	0.38	1.12	1.21	1.46	NA	0.52	5.9	1.3	0.5	2.27	0.85	1.06	0.2	1.72
Loperamide 1µM	1.03	-0.77	0.99	1.04	1.15	NA	1.91	0.57	1.14	1.04	1.22	NA	0.39	5.18	1.49	0.65	2.1	1.05	1.7	0.34	0.53
Loperamide 0.1µM	-0.16	-0.85	5.49	0.91	1.15	NA	1.68	0.68	1.18	1.05	1.31	NA	0.71	4.45	1.3	0.55	1.33	0.89	0.69	0.34	0.99
Loperamide 0.01µM	-1.47	-0.15	5	0.86	0.99	NA	1.45	0.41	0.96	1.33	1.22	NA	0.98	1.39	0.9	0.68	0.86	0.67	0.69	0.28	0.71
Flavopiridol 1µM	5.22	2.93	4.98	1.06	1.6	NA	1.06	0.33	1.03	1.28	0.62	NA	1.17	-4.8	2.67	1.2	0.34	1.81	0.75	0.45	0.7
Flavopiridol 0.1µM	2.66	1.4	-3.9	1.16	1.82	NA	2.41	1.57	1.33	1.21	1.44	NA	0.4	0	2.3	2.95	1.2	1.87	1.44	0.5	1.23
Flavopiridol 0.01µM	0.31	0.31	-0.55	1.06	1.53	NA	1.33	0.89	1.14	1.28	1.32	NA	1.18	-0.4	1.86	0.94	0.86	1.51	1.08	1.17	1.81
Metformin 750µM	1.47	1.49	6.44	1.09	0.89	NA	1.75	0.61	1.3	0.93	0.67	NA	0.44	-3.14	1.45	0.61	0.64	1.29	1.29	0.92	1.23
DMSO 0.5%	1	1	1	1	1	NA	1	1	1	1	1	NA	1	1	1	1	1	1	1	1	1

Table 112: Results from three replicates of the gene expression of potential novel tested biomarkers (*LCN-2*, *FABP-1*, *GSTA1*, *MLCK*, *CRP*, *HDC*, *GAST*) of the Caco-2 OoC model. Values are normalized to the gene expression of the housekeepers *PPIA*, *PIB*, *HPRT1* and *LDHA* and given as fold changes towards the vehicle control.

	LCN2			FABP1			GSTA1			MLCK			CRP			HDC			GAST		
	N=1	N=2	N=3	N=1	N=2	N=3	N=1	N=2	N=3	N=1	N=2	N=3	N=1	N=2	N=3	N=1	N=2	N=3	N=1	N=2	N=3
Gefitinib 1µM	6.88	-0.48	0.91	0.98	1.07	1.02	6.01	12.61	8.64	1.61	0.81	0.96	2.1	0.56	0.58	0.37	0.64	0.54	0.43	NA	0.42
Gefitinib 0.1µM	3.07	-0.36	1.12	0.97	1.08	1.19	2.98	9.39	7.19	1.23	0.74	1.01	1.26	0.16	0.81	0.42	0.96	0.53	0.31	NA	0.34
Gefitinib 0.01µM	2.21	1.35	0.61	1.16	1.06	1.17	1.36	3.12	7.53	1.34	0.9	0.97	0.84	0.51	0.74	0.29	0.78	0.78	0.44	NA	0.33
Irinotecan 50µM	3.77	0.79	0.77	0.66	0.88	1.21	0.73	1.01	1.92	0.39	0.33	0.75	0.96	0.87	0.93	0.44	1.59	0.7	3.95	NA	1.45
Irinotecan 5µM	1.06	3.59	0.71	1.11	1.03	1.18	1.1	1.58	1.95	0.92	1	0.74	0.16	0.69	0.78	0.3	1.13	0.51	0.88	NA	1.14
Irinotecan 0.5µM	3.15	2.79	1.17	1.3	0.92	1.18	0.76	1.29	1.66	1.37	0.99	0.84	0.8	0.92	0.53	0.37	1.69	0.75	0.55	NA	1.34
Oxaliplatin 5µM		2.31	1.27		1.16	1.49		2.43	2.65		0.58	0.94		0.94	0.63		1.43	0.83		NA	0.62
Oxaliplatin 0.5µM	1.85	1.08	0.97	1.61	1.2	1.66	2.15	3.19	2.44	1.23	0.92	0.94	0.94	0.25	0.9	0.3	0.86	0.78	0.77	NA	0.85
Oxaliplatin 0.05µM	3.1	1.73	1.32	1.42	0.95	1.68	1.33	1.3	2.23	1.18	1.04	1	0.87	0.56	1.22	0.44	1.53	0.69	0.59	NA	0.66
5FU 50µM	2.53	4	4.37	1.05	0.96	1.06	1.48	2.44	3.02	0.81	0.74	0.98	0.79	0.77	2.26	0.36	1.15	1.98	0.55	NA	0.64
5FU 5µM	5.31	3.38	4.64	1.24	1.11	1.46	1.95	3.26	2.29	1.09	0.91	1.2	2.07	0.66	2.65	0.97	1.7	1.85	0.59	NA	0.58
5FU 0.5µM	21.43	2.61	9.44	1.29	1.09	1.51	1.7	1.38	2.29	1.23	1.04	1.22	8.22	0.3	5.26	3.2	1.27	3.79	0.7	NA	0.7
Terfenadine 1µM	3.48	4.36	1.5	1.42	1.12	1.29	1.23	1.91	2.42	1.18	0.92	1.01	1.38	0.67	0.69	0.7	1.43	0.91	0.7	NA	0.75
Terfenadine 0.1µM	1.74	1.12	0.82	1.55	1.12	1.5	1.55	2.26	2.26	1.21	1.07	1.16	1.14	0.69	0.49	0.52	1.49	0.57	0.94	NA	0.53
Terfenadine 0.01µM	2.71	0.23	0.95	1.23	1.02	1.48	1.71	1.41	1.59	1.14	1.03	1.25	1.91	0.44	0.89	0.47	1.35	0.8	0.71	NA	0.55
Loperamide 1µM	2.19	2.19	1.03	1.5	1.03	1.55	1.62	1.7	2.46	1.34	0.88	1.26	1.15	0.61	1.1	0.54	1.57	1.07	0.49	NA	0.54
Loperamide 0.1µM	2.32	-1.28	1.15	1.34	0.89	1.59	1.47	1.32	3.09	1.23	0.77	1.32	1.22	0.73	1.08	0.49	0.89	0.86	0.47	NA	0.57
Loperamide 0.01µM	2.06	1.99	2.11	1.33	0.92	1.65	1.18	1.33	2.46	1.3	0.89	1.33	0.84	0.21	1.22	0.48	0.96	1.1	0.53	NA	0.64
Flavopiridol 1µM	6.2	2.82	1.41	7.14	3.26	2.3	1.21	1	1.81	0.69	0.57	1.06	1.26	0.45	0.59	0.46	0.75	1.15	0.56	NA	1
Flavopiridol 0.1µM	37.77	2.61	0.93	2.22	0.98	2.2	1.36	1.19	1.76	0.43	0.49	1.05	14.07	0.96	1.16	7.25	3.73	1.83	3.65	NA	1.28
Flavopiridol 0.01µM	2.89	5.59	10.52	1.73	1.31	2.12	1.22	1.26	2.38	1.41	1.07	1.12	1.57	0.74	5.37	0.77	0.68	4.84	0.63	NA	1.33
Metformin 750µM	2.09	-0.76	1.58	1.13	1.02	1.2	1.28	1.57	1.67	1.02	0.99	1.26	1.24	0.65	1.68	0.34	1.41	1.04	0.66	NA	0.39
DMSO 0.5%	1	1	1	1	1	1	1	1	1	1	1	1	1	1	1	1	1	1	1	1	1

Table 113: Results from three replicates of the gene expression of potential novel tested biomarkers (*LCN-2*, *FABP-1*, *GSTA1*, *MLCK*, *CRP*, *HDC*, *GAST*) of the organoid 3D model. Values are normalized to the gene expression of the housekeepers *PPIA*, *PIB*, *HPRT1* and *LDHA* and given as fold changes towards the vehicle control.

	LCN2			FABP1			GSTA1			MLCK			CRP			HDC			GAST		
	N=1	N=2	N=3	N=1	N=2	N=3	N=1	N=2	N=3	N=1	N=2	N=3	N=1	N=2	N=3	N=1	N=2	N=3	N=1	N=2	N=3
Gefitinib 1µM	4.85	78.02	2.38	0.61	0.65	0.72	5.02	75	12.82	2.15	9.57	0.23	NA	62.5	2.04	NA	93.75	2.04	NA	NA	2.96
Gefitinib 0.1µM	2.21	4.06	1.18	0.89	1.04	1.01	0.66	1.06	1.96	2.44	1.09	0.9	NA	1.18	0.82	NA	1.77	1.36	NA	NA	0.83
Gefitinib 0.01µM	1.82	1.59	0.89	0.83	0.96	1.01	0.69	2.46	1.55	1.95	0.77	1.11	NA	9.28	0.48	NA	7.44	0.72	NA	NA	0.98
Irinotecan 50µM	1.77	1.16	1.02	0.56	0.35	0.53	0.6	5.89	0.95	0.68	-0.4	0.07	NA	6.54	2.86	NA	0	3.81	NA	NA	5.19
Irinotecan 5µM	2.39	33.08	2.52	0.57	0.14	0.82	0.62	7.5	1.28	0.74	-1.84	0.47	NA	0	0.7	NA	0	0.34	NA	NA	4.33
Irinotecan 0.5µM	1.35	5.82	1.74	0.6	0.61	0.89	0.75	1.14	2.3	0.92	0.08	0.71	NA	1.27	0	NA	0	1.97	NA	NA	2.4
Oxaliplatin 5µM	1.87	16.34	1.07	0.42	0.11	0.66	1.22	10.71	1.1	0.83	0	0.29	NA	64.25	0.91	NA	21.42	1.29	NA	NA	3.14
Oxaliplatin 0.5µM	1.57	4.49	0.66	0.79	0.81	0.93	1.63	1.28	2	1.72	0.61	0.83	NA	2.14	0.95	NA	2.14	0.47	NA	NA	2.22
Oxaliplatin 0.05µM	1.45	0.99	0.64	0.85	1.23	0.93	0.73	0.84	1.49	1.72	1	1.03	NA	0.31	0.5	NA	0.94	0.75	NA	NA	1.27
5FU 50µM	2.06	15.68	2.06	0.88	0.44	0.98	2.44	2.47	4	3.3	0.63	1.45	NA	0	2.93	NA	0	2.2	NA	NA	2.02
5FU 5µM	1.6	3.3	1.14	0.99	0.74	1	2.7	1.32	3.53	2.11	0.63	1.48	NA	0.73	1.34	NA	0.73	1.15	NA	NA	1.6
5FU 0.5µM	1.3	1.09	1.14	0.82	1.2	0.77	1.22	0.88	1.53	1.47	0.76	1.08	NA	0.49	0.4	NA	0.73	0.4	NA	NA	1.5
Terfenadine 1µM	1.55	1.08	0.9	0.83	1.16	1.06	0.75	1.16	1.49	1.76	0.95	1.24	NA	1.55	0.6	NA	1.39	0.89	NA	NA	1.43
Terfenadine 0.1µM	1.19	1.38	0.91	0.84	1.25	0.97	0.76	1.28	1.26	0.89	0.58	0.99	NA	2.44	0.53	NA	1.37	0.53	NA	NA	1.17
Terfenadine 0.01µM	1.21	1.27	0.84	0.76	1.05	0.9	0.77	1.01	1.84	1.08	0.89	1.14	NA	1.69	0.66	NA	1.63	0.66	NA	NA	1.37
Loperamide 1µM	2.28	1.26	0.21	0.78	1.28	1.07	0.97	1.68	1.29	1.45	1.2	0.78	NA	3.41	1.36	NA	3.91	0.34	NA	NA	0.81
Loperamide 0.1µM	2.01	1.42	0.68	0.89	1.11	1.03	0.78	1.16	1.63	1.22	0.62	0.79	NA	0.39	0.7	NA	0	1.05	NA	NA	0.88
Loperamide 0.01µM	1.91	1.45	0.71	0.76	1.1	0.97	1.68	1.2	2.73	1.86	0.69	0.82	NA	0.4	4.21	NA	0.6	1.93	NA	NA	1.61
Flavopiridol 1µM	3.32	NA	0.42	0.13	NA	0.12	-0.26	NA	4.74	1.13	NA	0.57	NA	NA	8.48	NA	NA	17.21	NA	NA	1.06
Flavopiridol 0.1µM	2.51	NA	0.39	0.07	NA	0.05	-0.23	NA	-0.89	0.63	NA	0.17	NA	NA	15.75	NA	NA	0	NA	NA	27.41
Flavopiridol 0.01µM	0.74	NA	0.39	0.77	NA	1.01	3.11	NA	1.69	1.84	NA	0.92	NA	NA	0.5	NA	NA	0.62	NA	NA	0.72
Metformin 750µM	1.26	1.73	1.89	1.2	1.02	0.94	1.71	0.87	1.54	1.16	1.19	0.57	NA	0	0.49	NA	0.65	1.49	NA	NA	0.9
DMSO 0.5%	1	1	1	1	1	1	1	1	1	1	1	1	NA	1	1	NA	1	1	NA	NA	1

Table 114: Statistically significant differences in gene expression between the DMSO control and treated samples. Caco-2 cells and colon organoids were treated for 48h in the advanced cell culture systems with GI toxic compounds and DMSO as control. After 48h potential genetic biomarkers were analyzed. Table showed calculated p-values. Statistical analysis was performed by Julian Kreis using one-sided-Wilcoxon test. p < 0.05 (red). N=3.

low dose	Gene	2D	OoC	3D
	CRP	0.565	0.533	0.953
	FABP2	0.65700	NA	NA
	HDC	0.799	0.629	0.714
	LCN2	0.101	0.041	0.349
	MLCK	0.075	0.033	0.395
low dose	Gene	2D	OoC	3D
	CRP	0.199	0.310	0.915
	FABP2	0.593	NA	NA
	HDC	0.396	0.669	0.812
	LCN2	0.022	0.006	0.060
	MLCK	0.049	0.049	0.684
low dose	Gene	2D	OoC	3D
	CRP	0.281	0.155	0.415
	FABP2	0.247	NA	NA
	HDC	0.597	0.618	0.147
	LCN2	0.101	0.002	0.057
	MLCK	0.208	0.238	0.592

## Appendix 12: Fold changes and statistical differences of mir194 expression

Table 115: Fold changes in mir194 expression after 7 days treatment in Caco-2 2D (a), caco-2 OoC (b) and organoid 3D (c).

	2D				OoC				3D		
	N=1	N=2	N=3		N=1	N=2	N=3		N=1	N=2	N=3
DMSO 0.5%	1	1	1	DMSO 0.5%	1	1	1	DMSO 0.5%	1	1	1
untreated	0.92	0.84	0.62	untreated	1.49	1.07	0.93	untreated	0.57	0.62	0.92
Gef 1µM	1.16	0.89	1.31	Gef 1µM	1.56	1.19	0.81	Gef 1µM	0.22	0.82	1.33
Oxali 5µM	1.22	0.91	1.47	Oxali 5µM	0.79	1.15	1.64	Oxali 5µM	0.14	0.6	0.91
Flavo 1µM	1.17	0.79	1.13	Flavo 1µM	1.02	0.79	0.6	Flavo 1µM	0.09	0.79	0.83
5FU 50µM	1.23	0.81	1.34	5FU 50µM	1.9	1.28	0.73	5FU 50µM	0.93	0.9	0.59
Diclo 300µM	0.98	1.03	1.27	Diclo 300µM	0.94	0.84	0.88	Met 750µM	0.41	0.73	NA
Diclo 30µM	1.15	1.18	1.31	Diclo 30µM	1.11	1.11	1.05				
Met 750µM	1.23	1.09	1.96	Met 750µM	2.07	1	0				

Table 116: Statistically significant differences in mir194 expression between treated and non-treated samples. Normal distribution was pretested with a Shapiro-Wilk test

		2D						OoC			
		Mean difference	95% Confidence Interval	p-value	Significance			Mean difference	95% Confidence Interval	p-value	Significance
DMSO 0.5%	untreated	0.2067	-0.3691 to 0.7825	0.8502	ns	DMSO 0.5%	untreated	-0.1633	-1.256 to 0.9291	0.9976	ns
	Met 750µM	-0.4267	-1.002 to 0.1491	0.2071	ns		Met 750µM	-0.02333	-1.116 to 1.069	>0.9999	ns
	Gef 1µM	-0.1200	-0.6958 to 0.4558	0.9905	ns		Gef 1µM	-0.1867	-1.279 to 0.9058	0.9969	ns
	Oxali 5µM	-0.2000	-0.7758 to 0.3758	0.8682	ns		Oxali 5µM	-0.1933	-1.286 to 0.8991	0.9950	ns
	Flavo 1µM	-0.03000	-0.6058 to 0.5458	0.9998	ns		Flavo 1µM	0.1967	-0.8958 to 1.289	0.9947	ns
	5-FU 50µM	-0.1267	-0.7025 to 0.4491	0.9866	ns		5-FU 50µM	-0.3033	-1.396 to 0.7891	0.9515	ns
	Diclo 30µM	-0.09333	-0.6691 to 0.4825	0.9972	ns		Diclo 30µM	0.1133	-0.9791 to 1.206	0.9996	ns
	Diclo 300µM	-0.2133	-0.7891 to 0.3625	0.8311	ns		Diclo 300µM	-0.09000	-1.182 to 1.002	0.9997	ns

ANOVA with Dunnett's multiple comparison P=0.05

ANOVA with Dunnett's multiple comparison P=0.05

		3D			
		Mean difference	95% Confidence Interval	p-value	Significance
DMSO 0.5%	untreated	0.2967	-0.5098 to 1.103	0.7719	ns
	Met 750µM	0.4300	-0.4717 to 1.332	0.5635	ns
	Gef 1µM	0.2100	-0.5965 to 1.016	0.9314	ns
	Oxali 5µM	0.4500	-0.3565 to 1.256	0.4187	ns
	Flavo 1µM	0.4300	-0.3765 to 1.236	0.4607	ns
	5-FU 50µM	0.1933	-0.6132 to 0.9998	0.9512	ns

ANOVA with Dunnett's multiple comparison P=0.05

## Appendix 13: Levels of secreted L-citrulline and statistical differences between the cell culture models

Table 117: Statistically significant differences in citrulline concentrations between the used cell culture models. Normal distribution was pretested with a Shapiro-Wilk test.

Dunn's multiple comparisons test	Mean rank difference	Summary	Adjusted P Value	Significance
2D vs. OoC	-15.77	*	0.0193	Yes
2D vs. 3D	19.73	**	0.0020	Yes
OoC vs. 3D	35.50	****	<0.0001	Yes

Table 118: Measured absorbance and interpolated concentrations of L-citrulline in the used cell culture models after 7days treatment with GI toxic and non-toxic compounds.

	Caco-2 2D						Caco-2 OoC					
	Absorbance (540nm)	Concentration (µM)	Absorbance (540nm)	Concentration (µM)	Absorbance (540nm)	Concentration (µM)	Absorbance (540nm)	Concentration (µM)	Absorbance (540nm)	Concentration (µM)	Absorbance (540nm)	Concentration (µM)
Gef 10µM	0.2695	138.38	0.2585	129.11	0.257	127.89	0.261	165.39	0.302	208.66	0.3285	241.04
5FU 10µM	0.2685	137.52	0.2515	123.48	0.266	135.38	0.3075	215.06	0.296	201.85	0.284	188.74
Lop 10µM	0.2775	145.45	0.2695	138.38	0.2695	138.38	0.3055	212.72	0.2935	199.06	0.3055	212.72
Flav 10µM	0.271	139.68	0.24	114.62	0.254	125.47	0.2495	154.52	0.249	154.06	0.247	152.22
Irino 10µM	0.238	113.13	0.2555	126.68	0.2625	132.43	0.2565	161.08	0.2565	161.08	0.247	152.22
Oxali 10µM	0.345	219.30	0.322	190.85	0.334	205.19	0.257	161.56	0.26	164.43	0.228	135.46
Terf 10µM	0.2645	134.10	0.263	132.84	0.277	144.99	0.2565	161.08	0.249	154.06	0.264	168.32
Diclo 300µM	0.34	212.77	0.3055	172.69	0.2995	166.50	0.635	NA	0.1925	107.16	0.1565	81.89
DMSO 0.5%	0.279	146.81	0.2815	149.09	0.279	146.81	0.2825	187.15	0.2395	145.45	0.22	128.75
Met 750µM	0.344	217.98	0.8885	NA	0.328	197.89	0.2455	150.85	0.2475	152.6	0.2325	139.32
untreated	0.339	211.49	0.3175	185.72	0.33	200.29	0.2655	169.79	0.285	189.81	0.29	195.21

	Organoid 3D					
	Absorbance (540nm)	Concentration (µM)	Absorbance (540nm)	Concentration (µM)	Absorbance (540nm)	Concentration (µM)
Gef 10µM	0.1465	115.69	0.1425	111.99	0.129	99.74
5FU 10µM	0.164	132.35	0.1685	136.76	0.1695	137.74
Lop 10µM	0.163	131.38	0.172	140.21	0.1675	135.77
Flav 10µM	0.1605	128.96	0.1575	126.08	0.156	124.65
Irino 10µM	0.1435	112.91	0.173	141.21	0.1125	85.29
Oxali 10µM	0.121	92.67	0.1285	99.29	0.1375	107.40
Terf 10µM	0.142	111.53	0.1465	115.69	0.1355	105.59
Diclo 300µM	0.1845	152.82	0.1765	144.70	0.18	148.23
DMSO 0.5%	0.0905	66.89	0.0905	66.89	0.092	68.11
Met 750µM	0.1125	85.29	0.11	83.16	0.107	80.60
untreated	0.118	90.05	0.123	94.42	0.13	100.63

Table 119: Statistically significant differences in L-citrulline concentrations between treated and non-treated samples. Normal distribution was pretested with a Shapiro-Wilk test.

		2D					OoC			
		Mean rank difference	p-value	Significance			Mean difference	95% Confidence Interval	p-value	Significance
DMSO 0.5%	untreated	-6.667	>0.9999	ns	DMSO 0.5%	untreated	-3.147	-46.24 to 39.95	0.9997	ns
	Met 750µM	-8.500	>0.9999	ns		Met 750µM	-6.281	-49.37 to 36.81	0.9994	ns
	Gef 10µM	11.00	>0.9999	ns		Gef 10µM	48.29	5.193 to 91.38	0.0232	*
	5-FU 10µM	11.33	>0.9999	ns		5-FU 10µM	43.76	0.6650 to 86.85	0.0454	*
	Lop 10µM	4.667	>0.9999	ns		Lop 10µM	48.07	4.978 to 91.16	0.0240	*
	Flavo 10µM	12.67	0.9803	ns		Flavo 10µM	40.73	-2.360 to 83.83	0.0700	ns
	Irino 10µM	15.33	0.4520	ns		Irino 10µM	107.4	59.18 to 155.5	<0.0001	****
	Oxali 10µM	-8.333	>0.9999	ns		Oxali 10µM	48.10	5.007 to 91.19	0.0238	*
	Terf 10µM	8.000	>0.9999	ns		Terf 10µM	54.27	11.18 to 97.36	0.0092	**
	Diclo 300µM	-5.000	>0.9999	ns		Diclo 300µM	16.95	-26.14 to 60.04	0.8354	ns

Kruskal-Wallis-Test with Dunn's multiple comparison. P=0.05

ANOVA with Dunnett's multiple comparison P=0.05

		3D			
		Mean difference	95% Confidence Interval	p-value	Significance
DMSO 0.5%	untreated	-27.74	-50.93 to -4.546	0.0140	*
	Met 750µM	-15.72	-38.92 to 7.470	0.3028	ns
	Gef 10µM	-41.85	-65.04 to -18.65	0.0002	***
	5-FU 10µM	-68.32	-91.51 to -45.13	<0.0001	****
	Lop 10µM	-68.49	-91.69 to -45.30	<0.0001	****
	Flavo 10µM	-59.27	-82.46 to -36.08	<0.0001	****
	Irino 10µM	-45.84	-69.04 to -22.65	<0.0001	****
	Oxali 10µM	-32.49	-55.69 to -9.300	0.0034	**
	Terf 10µM	-43.64	-66.84 to -20.45	0.0001	***
	Diclo 300µM	-81.29	-104.5 to -58.10	<0.0001	****

ANOVA with Dunnett's multiple comparison P=0.05

## Appendix 14: Levels of secreted calprotectin and statistical differences between the cell culture models

Table 120: Statistically significant differences in calprotectin concentrations between the used cell culture models. Normal distribution was pretested with a Shapiro-Wilk test.

Dunn's multiple comparisons test	Mean rank difference	Summary	Adjusted P Value	Significance
2D vs. OoC	-33.73	****	<0.0001	Yes
2D vs. 3D	-32.27	****	<0.0001	Yes
OoC vs. 3D	1.455	ns	>0.9999	no

Table 121: Measured absorbance and interpolated concentrations of calprotectin in the used cell culture models after 7days treatment with GI toxic and non-toxic compounds.

	2D						OoC					
	Absorbance (540nm)	Calprotectin conc. (pg/ml)	Absorbance (540nm)	Calprotectin conc. (pg/ml)	Absorbance (540nm)	Calprotectin conc. (pg/ml)	Absorbance (540nm)	Calprotectin conc. (pg/ml)	Absorbance (540nm)	Calprotectin conc. (pg/ml)	Absorbance (540nm)	Calprotectin conc. (pg/ml)
Flav 10µM	0.22	76.72	0.30	106.88	0.19	65.73	0.23	204.15	0.36	322.68	0.32	289.38
Oxali 10µM	0.27	95.42	0.35	126.40	0.15	51.35	0.21	187.36	0.28	249.49	0.36	326.92
Gef 10µM	0.32	114.62	0.34	122.45	0.19	65.73	0.25	218.28	0.36	322.68	0.47	432.35
5FU 10µM	0.38	138.37	0.29	103.04	0.15	51.35	0.26	230.18	0.30	269.37	0.23	206.42
Terf 10µM	0.2	69.37	0.45	167.09	0.20	69.37	0.28	247.18	0.34	302.94	0.32	283.32
Irino 10µM	0.19	65.73	0.32	114.62	0.27	95.42	0.26	228.34	0.36	327.39	0.30	267.52
Lop 10µM	0.23	80.42	0.16	54.92	0.20	69.37	0.21	181.03	0.36	325.98	0.36	321.26
Diclo 300µM	0.21	73.04	0.24	84.14	0.43	158.78	0.22	194.61	0.45	407.13	0.21	185.09
Met day 7	0.18	62.11	0.20	69.37	0.20	69.37	0.29	254.10	0.42	381.15	0.33	296.39
untreated	0.26	91.64	0.21	73.04	0.40	146.47	0.22	190.07	0.39	354.88	0.35	312.79
DMSO 0.5%	0.17	58.51	0.29	103.04	0.19	65.73	0.20	176.51	0.22	191.89	0.33	301.54

	3D					
	Absorbance (540nm)	Calprotectin conc. (pg/ml)	Absorbance (540nm)	Calprotectin conc. (pg/ml)	Absorbance (540nm)	Calprotectin conc. (pg/ml)
Flav 10µM	0.285	253.18	0.2795	248.10	0.1835	160.76
Oxali 10µM	0.76	722.49	0.318	283.79	0.1625	141.96
Gef 10µM	0.328	293.12	0.2025	177.87	0.1895	166.15
5FU 10µM	0.3355	300.13	0.9795	962.35	0.168	146.87
Terf 10µM	0.409	369.66	0.2205	194.15	0.1565	136.80
Irino 10µM	0.318	283.79	0.8445	812.97	0.2395	211.43
Lop 10µM	0.448	407.13	0.19	166.60	0.1415	123.26
Diclo 300µM	0.3635	326.45	0.9975	982.73	0.154	134.38
Met day 7	0.3475	311.38	0.8175	783.81	0.1575	137.49
untreated	0.424	384.02	0.486	444.05	0.1955	171.55
DMSO 0.5%	0.339	303.41	0.361	324.09	0.2035	178.77



Table 122: Statistically significant differences in calprotectin concentrations between treated and non-treated samples. Normal distribution was pretested with a Shapiro-Wilk test.

		2D			
		Mean rank difference	95% Confidence Interval	p-value	Significance
Medium	DMSO 0.5%	27.95	-54.76 to 110.7	0.9170	ns
	Met 750µM	36.76	-45.96 to 119.5	0.7402	ns
	Gef 10µM	2.776	-79.94 to 85.50	0.9999	ns
	5-FU 10µM	6.125	-76.59 to 88.84	0.9997	ns
	Lop 10µM	35.48	-47.24 to 118.2	0.7705	ns
	Flavo 10µM	20.60	-62.12 to 103.3	0.9864	ns
	Irino 10µM	11.79	-70.93 to 94.51	0.9994	ns
	Oxali 10µM	12.66	-70.06 to 95.37	0.9993	ns
	Terf 10µM	1.763	-80.96 to 84.48	>0.9999	ns
	Diclo 300µM	-1.603	-84.32 to 81.12	>0.9999	ns

ANOVA with Dunnett's multiple comparison P=0.05

		OoC			
		Mean rank difference	p-value	Significance	
Medium	DMSO 0.5%	10.00	>0.9999	ns	
	Met 750µM	-2.667	>0.9999	ns	
	Gef 10µM	-3.500	>0.9999	ns	
	5-FU 10µM	6.667	>0.9999	ns	
	Lop 10µM	1.667	>0.9999	ns	
	Flavo 10µM	1.833	>0.9999	ns	
	Irino 10µM	0.6667	>0.9999	ns	
	Oxali 10µM	4.000	>0.9999	ns	
	Terf 10µM	1.667	>0.9999	ns	
	Diclo 300µM	5.333	>0.9999	ns	

Kruskal-Wallis-Test with Dunn's multiple comparison. P=0.05

		3D		
		Mean rank difference	p-value	Significance
Medium	DMSO 0.5%	2.667	>0.9999	ns
	Met 750µM	2.667	>0.9999	ns
	Gef 10µM	8.667	>0.9999	ns
	5-FU 10µM	2.000	>0.9999	ns
	Lop 10µM	9.000	>0.9999	ns
	Flavo 10µM	8.667	>0.9999	ns
	Irino 10µM	0.5000	>0.9999	ns
	Oxali 10µM	4.167	>0.9999	ns
	Terf 10µM	7.667	>0.9999	ns
	Diclo 300µM	1.667	>0.9999	ns

Kruskal-Wallis-Test with Dunn's multiple comparison. P=0.05

## Appendix 15: Pictures of the long-term cultivation of iPSC derived colon organoids in the 3lane OrganoPlate®

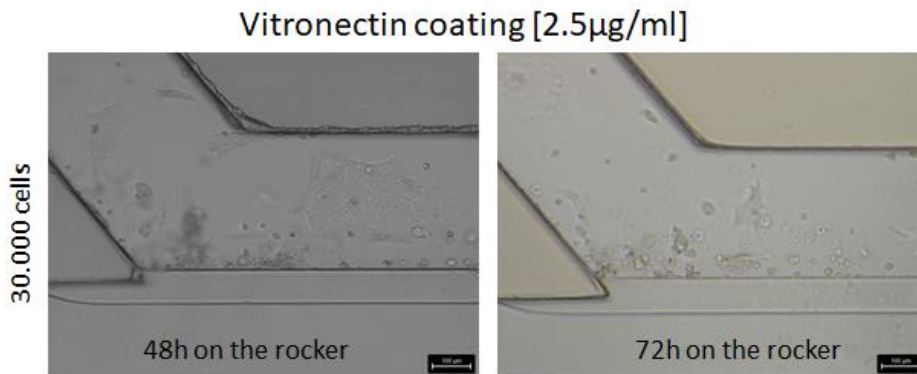


Figure 115: Pictures of the long-term cultivation of iPSC derived colon organoids. Organoids were dissociated to single cells and seeded into the top channel of a 3lane OrganoPlate®, which was coated with 2.5µg/ml vitronectin. Cultivation was performed for 48h and 72h on the rocker.

## Appendix 16: Hippo pathway

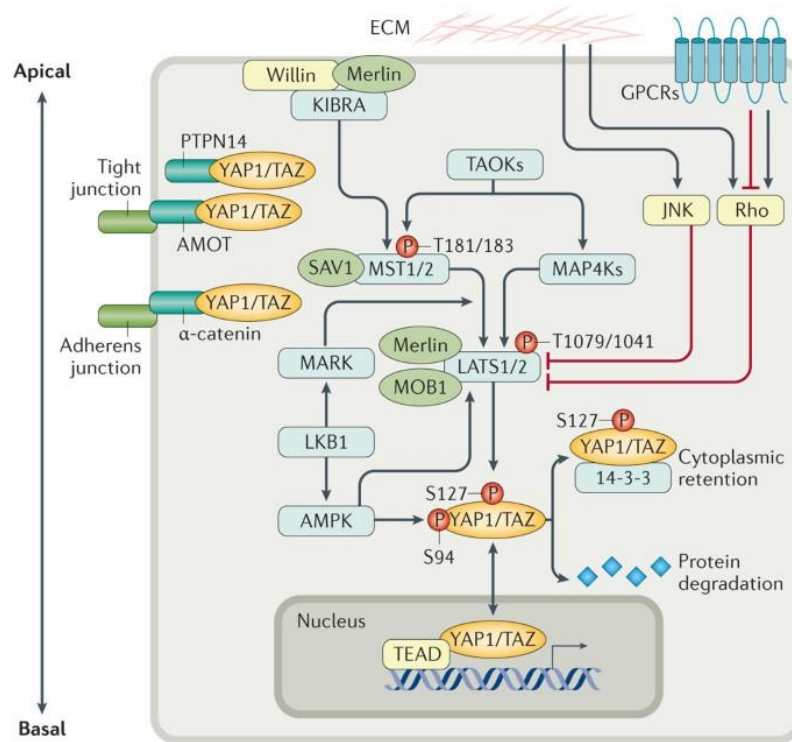


Figure 116: Schematic overview of the hippo pathway in intestinal

## Berufserfahrung

- 03/2023 - heute **Laborleiter „Advanced cell culture“**
- 10/2017 - 03/2020 **In vitro Toxikologie consultant**
- Zellkultur
  - Zyto-, Mitochondrien und Neurotoxikologische Assays
  - Erstellen von ROPs

## Ausbildung

---

- 03/2022 - 02/2023 **Post-Doc / Senior Scientist (Toxikologie)**
- Merck Healthcare KGaA, Darmstadt
- Etablierung von neuen in vitro Assays
  - Zellkultur (permanenten und primäre Zellen sowie iPSC)
  - Betreuung von Studenten
- 10/2018 - 02/2022 **Doktorarbeit (Toxikologie)**
- Merck Healthcare KGaA, Darmstadt
- 04/2014 - 09/2017 **Masterstudium (Technische Biologie)**
- Technische Universität, 64289 Darmstadt
- 10/2009 - 11/2013 **Bachelorstudium (Biologie)**
- Technische Universität, 64289 Darmstadt
- 08/2006 - 06/2009 **Abitur**
- Goethe Gymnasium, 64625 Bensheim

## Kenntnisse

---

- EDV-Kenntnisse
- Microsoft Office 365 (fortgeschritten)
  - Image J (gut)
  - GraphPad Prism (gut)
  - R (Statistik) (Grundkenntnisse)

---

Sprachkenntnisse Englisch (fließend)  
Französisch (Grundkenntnisse)  
Führerschein Klasse B & BE

## Interessen

---

Engagement Ehrenamtliches Retten von Lebensmitteln für Bedürftige  
Verein Share & Save  
Hobbys Mountainbiken  
Yoga  
Reisen

Lautertal, 06.04.2023

*Stefanie Hoffmann*

---

## Publications, posters, and awards

---

### Publications / Abstracts

Kevin Su, [Stefanie Hoffmann](#), Philip Hewitt and Vi Chu (2019): “Efficient differentiation of human pluripotent stem cells to colonic organoids and their applications in toxicology screens”

Kevin Su, [Stefanie Hoffmann](#), Philip Hewitt and Vi Chu (2019): „3dGRO™ human iPSC derived colon organoids” Data Sheet,  
(<https://www.merckmillipore.com/DE/de/search/human+iPSC+derived+colon+organoids?SearchTerm=human+iPSC+derived+colon+organoids&SelectedSearchResult=SFDocumentSearch&SearchContextPageletUUID=&SearchWithinResults=&SearchTermHistory=> )

### Posters

Kevin Su, [Stefanie Hoffmann](#), Philip Hewitt and Vi Chu (2019): “Enhancing well-to-well reproducibility of colon organoids for screening applications”

### Presentations

Stefanie Hoffmann (2022): “That Gut feeling - Comparison of advanced intestinal cell models for early safety assessment”. ICT 2022, The XVI<sup>th</sup> international congress of toxicology, Maastricht.

### Awards

Merck 3D animal welfare award 2019